

Physical and Optical Characterization of Anodized Aluminum-Tantalum Thin Films for use in

Thin Film Diagnostics

by

Matthew R Nickel

A thesis submitted in partial fulfillment of the requirements for the degree of

Doctor of Philosophy

in

Materials Engineering

Departments of Chemical and Materials Engineering and Biomedical Engineering

University of Alberta

© Matthew R Nickel, 2018

## **Abstract**

Thin film diagnostics have been proposed as a solution to the growing need for point-of-care diagnostic tests. Diagnostics based on anodized aluminum-tantalum thin films use interference colours to detect the adsorption of protein layers on a surface. The purpose of this work was to develop a stronger understanding of thin film diagnostics based on anodized aluminum-tantalum thin films with respect to: 1) deposition parameters of the metallic films and their effect on the optical properties, microstructure and sensitivity when developed for an immunoassay, 2) anodization parameters and their effect on the optical properties, microstructure and sensitivity when developed for an immunoassay, 3) effect of antigen size and surface density on the thin film interference colours, and 4) demonstration of a new binding technology to aluminum oxides to expand the use of these films for detecting other antigen-antibody pairs. Deposition of the tantalum and aluminum films is done using magnetron sputtering techniques. Adjusting the microstructure of the deposited tantalum films by changing the sputtering gas pressure had an effect on the optical reflectance, however no effects were found on the sensitivity of detecting adsorbed protein layers. The microstructure of the deposited aluminum films had minimal effect on the optical properties (refractive index and extinction coefficient) of the oxidized films after anodization. Sputtering parameters that achieved smoother, homogeneous films after anodization tended to show higher sensitivity to detecting adsorbed proteins. The electrolyte and voltage during anodization had significant effects on the optical properties, microstructure and sensitivity. Oxalic acid additive to a phosphoric acid bath was found to significantly improve film homogeneity and reduce surface roughness and pore size of the anodic alumina layer. This, in turn, was found to improve the sensitivity for detecting adsorbed protein and improve the tunability of the optical properties over films anodized strictly in phosphoric acid. Methods were also discovered, using sulphuric acid or

a voltage-step procedure, to tailor the pore size at the surface while simultaneously adjusting the optical properties of the anodic film. Antigen surface density was also found to have an effect on sensitivity for antibody assays. Spacing of an antigen on the film surface showed improved detection of a polyclonal antibody at lower concentrations. Finally, a new binding technology for proteins to aluminum oxides was applied to these diagnostics to expand the application for detecting secondary antibodies or antibodies for the Zika viral protein, non-structural protein 1 (NS1). Overall, these films showed significant tunability and high sensitivity, making them very useful for a variety of medical or research applications.

## **Preface**

The following articles were published or submitted for publication as a result from this thesis:

Nickel M., Melligan G., McMullen T. and Burrell R. (2018). The Effect of Chemical Additives in Phosphoric Acid Anodization of Aluminum-Tantalum Thin Films. *Thin Solid Films*, submitted July 2018. (Chapter 4.1).

Nickel M., Sweet H. and Burrell R. (2017). Anodizing Aluminum for Precision Medicine: The Future of Healthcare. *The Proceedings of the 2017 Aluminum Anodizing & Extrusion Summit*. 13-23. (Chapter 1).

The following articles were published during this PhD program, but are not a part of this thesis:

Nickel M., Rideout W., Shah N., Reintjes F., Chen J.Z., Burrell R., Pauly R. P. (2017). Estimating patient-borne water and electricity costs in home hemodialysis: a simulation. *CMAJ Open*. 5 (1), E61-E65.

## **Dedication**

This work is dedicated to the man who ignited the fire; thanks Ed, rest in peace.

## **Acknowledgments**

I would like to thank my supervisors Dr. Robert Burrell and Dr. Todd McMullen, as well as the other members on my committee: Dr. Anthony Young and Dr. Hasan Uludag, for all their help and advice. I would also like to express my thanks to my supervisory candidacy (Dr. Raimar Löbenberg and Dr. Jie Chen) and my defense committee (Dr. Ken Cadien and Dr. Benjamin Hatton).

I would also like to acknowledge the numerous students who worked with me in many of these studies and withstood my constant barrage of questioning: Gavin Melligan (Chapters 2, 3, and 4), Nicolas Linden (Chapter 4), Devon Stone (Chapters 4 and 5), and Kyle Moxham (Chapters 5 and 6). Also, many thanks to Ciaran Terry of Prominent Medical Inc. for working and collaborating on many of the studies. This work was funded by the Natural Sciences and Engineering Research Council (NSERC CGS-M) as well as the Jim Sorenson Chair in Biomedical Engineering.

I would also like to express my thanks to Hillary Sweet. Over the last few years we have had many fascinating discussions about science, technology, and life in general. This work is, in a large part, completed because of your inspiration.

Last, I would like to thank my parents, Marlis and Richard, and my wife, Kelsey, who helped me get to where I am today. I wouldn't be where I am if it wasn't for their unwavering support and belief in me.

# Table of Contents

Chapter 1 Introduction .....	1
1.0 Background .....	1
1.1 Point of Care Diagnostics – A Brief Review of the Literature .....	1
1.2 Thin Film Diagnostics .....	5
1.3 Optics .....	13
1.4 Atomic Sputter Deposition .....	17
1.5 Anodization of Aluminum .....	20
1.6 Immobilization of Proteins on Aluminum and Aluminum Oxides .....	25
2.0 Overview of Research Objectives .....	28
References .....	32
Chapter 2 Tantalum .....	42
The Effect of Tantalum Microstructure on Interference Colouring of Anodized Aluminum-Tantalum Thin Films .....	42
Introduction .....	42
Materials and Methods .....	43
Results .....	47
Discussion .....	61
Conclusion .....	65
References .....	66
Chapter 3 Aluminum .....	68
The Effect of Aluminum Sputtering Parameters on the Structural and Optical Properties of Anodized Aluminum-Tantalum Thin Films .....	68
Introduction .....	68
Materials and Methods .....	70
Results .....	76
Discussion .....	104
Conclusion .....	115
References .....	116
Chapter 4 Anodization of Aluminum-Tantalum Thin Films .....	119

4.1 The Effect of Chemical Additives in Phosphoric Acid Anodization of Aluminum-Tantalum Thin Films.....	119
Introduction.....	119
Materials and Methods.....	120
Results.....	125
Discussion.....	146
Conclusion .....	149
References.....	150
4.2 The Effects of Voltage on the Structure and Optical Properties of Anodized Aluminum-Tantalum Thin Films.....	153
Introduction.....	153
Materials and Methods.....	154
Results.....	158
Discussion.....	175
Conclusion .....	179
References.....	180
4.3 The Effects of Sequential Anodization with Sulphuric Acid and Phosphoric-Oxalic Acid on the Microstructure and Optical Properties of Aluminum-Tantalum Thin Films .....	182
Introduction.....	182
Materials and Methods.....	183
Results.....	187
Discussion.....	200
Conclusion .....	203
References.....	204
Chapter 5 Optical Sensitivity: Effects of Thin Film Microstructure and Antigen Surface Density on Visual Detection of IgG.....	207
5.1 The Effect of Thin Film Microstructure on a Visual Immunoassay for Anti-prothrombin IgG Based on Anodized Aluminum-Tantalum Thin Films .....	207
Introduction.....	207
Materials and Methods.....	209
Results.....	216
Discussion.....	239

Conclusion .....	249
References .....	250
5.2 The Effect of Antigen Size and Surface Density on a Visual Immunoassay Based on Anodized Aluminum-Tantalum Thin Films .....	252
Introduction.....	252
Materials and Methods.....	255
Results.....	260
Discussion.....	267
Conclusion .....	272
References.....	273
Chapter 6 Visual Immunoassay for Anti-Zika NS1 IgG and Goat Anti-Rabbit IgG on Anodized Aluminum-Tantalum Thin Films.....	275
Introduction.....	275
Materials and Methods.....	277
Results.....	285
Discussion.....	292
Conclusion .....	295
References.....	296
Chapter 7 Conclusion.....	300
Conclusions.....	300
Future Direction .....	302
References.....	305
References.....	307
Appendix 1 – Supplementary Data .....	331

## List of Tables

Table 2-1. Statistical results of one-way ANOVA and Tukey-Kramer post hoc tests for the change in reflectance measured at 555nm with the change in working Ar gas pressure during sputtering. If post hoc results were insignificant ( $p > 0.05$ ) then they were not listed. ....	49
Table 2-2. XRD peak analysis for tantalum films sputtered at 10, 15, 20, 25, and 30 mTorr. The phases and planes were identified using the work by Read and Hensler [3]. When possible overlapping of peaks was present, a best guess for the second peak was given. ....	57
Table 3-1. Experimental design matrix for sputtering aluminum at different powers and working gas pressures. T-S stands for target to substrate distance. ....	71
Table 3-2. The measured deposition rate and temperature range for each power/pressure parameter tested. ....	76
Table 3-3. EDX compositional data acquired from films sputtered at 9 W/cm <sup>2</sup> and either 1 or 10 mTorr working gas pressure (n=3). ....	82
Table 3-4. Measured aluminum thickness from SEM cross-sections of films sputtered at various parameters. Standard deviations represented by $\pm$ symbol (n=2). ....	83
Table 3-5. Ellipsometry of anodized aluminum-tantalum thin films, with aluminum sputtered under various powers and pressures. Sample size denoted by 'n'. ....	98
Table 3-6. Mean change in thickness of the aluminum films sputtered at various parameters after anodization at 4V in 0.4M phosphoric-0.1M oxalic acid. Sample number denoted by 'n'. ....	99
Table 3-7. Statistical results of the refractive index ( $\lambda=555\text{nm}$ , x-y plane) for aluminum films sputtered under various conditions and anodized at 4V in a 0.4M phosphoric and 0.1M oxalic acid mixture. Standard error is represented in brackets. ....	100
Table 3-8. Interference colours from anodized aluminum-tantalum films; aluminum films sputtered under different parameters and anodized in 0.4M phosphoric-0.1M oxalic acid at 4V. Films observed at approximately 75° from normal with a polarizing lens (s-polarized); n=2 for all data sets. ....	102
Table 3-9. Statistical results for RGB colour coordinate analysis for anodized aluminum-tantalum thin films, with aluminum sputtered at various powers and pressures and anodized in 0.4M phosphoric-0.1M oxalic acid at 4V (n=2 for all data sets). ....	103
Table 4-1. Concentrations and additives added to the 0.4M phosphoric acid anodization bath.	121

Table 4-2. Statistical results of current density during pore formation of each additive vs. the 0.4M phosphoric acid anodized control. n=3 for all data points. ....	128
Table 4-3. Statistical results for aluminum oxide RMS surface roughness as measured by SEM side-profile analysis for anodization with each additive vs. the 0.4M phosphoric acid control. ....	138
Table 4-4. Ellipsometry results for the porous aluminum oxide layer of aluminum-tantalum thin films anodized in various electrolytes. Standard deviations shown with $\pm$ symbol, n=3 for all data sets.....	143
Table 4-5. Observed interference colours and the recorded RGB coordinates from images taken at approximately 75° from normal with a polarizing lens (s-polarized light). ....	145
Table 4-6. Experimental design matrix for voltage-step anodization.....	156
Table 4-7. Ellipsometry results for anodized aluminum-tantalum thin films, with aluminum sputtered at various thicknesses and anodized under various voltages. Sample size n=3 for all data sets.....	160
Table 4-8. Statistical results from an analysis of refractive index for anodized aluminum-tantalum thin films, with aluminum sputtered at various thicknesses and then anodized at various voltages. Sample size n=3 for all data sets.....	161
Table 4-9. Statistical results for comparison of measured pore diameters between different anodizing conditions. Standard error represented by $\pm$ symbol.....	170
Table 4-10. Ellipsometry results for aluminum-tantalum films anodized in 0.4M phosphoric-0.1M oxalic acid at various voltage conditions. n=3 for all data sets. ....	172
Table 4-11. Statistical results for the aluminum oxide refractive index, as measured by ellipsometry, for the various anodizing conditions. For all data sets n=3. ....	173
Table 4-12. Interference colours and RGB coordinates measured from images of films anodized under various conditions. Sample size of n=3 for all data sets. ....	174
Table 4-13. Matrix of designed experiments for acid bath and voltage change. ....	184
Table 4-14. Statistical results for comparison of measured pore size between different anodizing conditions. Standard error represented by $\pm$ symbol. ....	196
Table 4-15. Ellipsometry results for the porous aluminum oxide layer anodized under various conditions. The first number indicates the time anodizing in 0.4M sulphuric acid at 4V, while the second number indicates the voltage anodizing in 0.4M phosphoric-0.1M oxalic acid mix.	

Standard deviations shown with  $\pm$  symbol, n=3 for all data sets. EMA=effective medium approximation; MSE=mean square error..... 198

Table 4-16. Statistical results for the aluminum oxide refractive index, as measured by ellipsometry, for the various anodizing conditions. For all data sets n=3. .... 199

Table 4-17. Interference colours and RGB coordinates measured from images of aluminum-tantalum films anodized under various conditions. Sample size n=3 for all data sets..... 200

Table 5-1. Experimental design matrix for sputtering aluminum at different power and working gas pressure. T-S stands for target to substrate distance..... 211

Table 5-2. Matrix of experiments for Part C – Effect of Electrolyte Mix and Aluminum Thickness on Optical Sensitivity..... 213

Table 5-3. Images and RGB coordinate analysis for protein adsorption studies on anodized aluminum-tantalum films with tantalum sputtered at various gas pressures. Sample size of n=3 for all data sets. Images taken at  $75^\circ$  from normal with a polarizing lens (s-polarized). .... 218

Table 5-4. Images and RGB coordinate analysis for protein adsorption studies on anodized aluminum-tantalum films with tantalum sputtered at various gas pressures. Sample size of n=3 for all data sets. Images taken at  $75^\circ$  from normal with a polarizing lens (s-polarized). .... 219

Table 5-5. Statistical results from ANOVA or Welch T-tests on colour differences ( $\Delta C$ ) with the application of prothrombin and anti-prothrombin on anodized aluminum-tantalum films with tantalum sputtered under various pressures. .... 220

*Table 5-6. Images and RGB coordinate analysis from sensitivity tests of anti-prothrombin on prothrombin for anodized aluminum-tantalum thin films. Aluminum was sputtered under various conditions. Sample size of n=2 for all data sets. Images taken at  $75^\circ$  from normal with a polarizing lens (s-polarized). .... 221*

*Table 5-7. Statistical results of a series of T-tests conducted on colour differences recorded from RGB coordinate analysis of protein adsorption studies on anodized aluminum-tantalum thin films with aluminum deposited at various power densities and gas pressures. Insignificant results ( $p>0.10$ ) not shown. The number indicates the concentration of antibody exposed to the surface in  $\mu\text{g/mL}$ , i.e. 200 vs. 50 is  $\Delta C(200\mu\text{g/mL})$  vs.  $\Delta C(50\mu\text{g/mL})$ . .... 223*

Table 5-8. Images and RGB coordinate analysis for protein adsorption studies on anodized aluminum-tantalum thin films with aluminum sputtered at various thicknesses and anodized in 0.4M phosphoric acid at 4V. Sample size of n=3 for all data sets..... 225

Table 5-9. Images and RGB coordinate analysis for protein adsorption studies on anodized aluminum-tantalum thin films with aluminum sputtered at various thicknesses and anodized in 0.4M phosphoric – 0.1M oxalic acid at 4V. Sample size of n=3 for all data sets. ....	227
Table 5-10. Images and RGB coordinate analysis for protein adsorption studies on anodized aluminum-tantalum thin films with aluminum sputtered at various thicknesses and anodized in 0.4M phosphoric – 0.4M oxalic acid at 4V. Sample size of n=3 for all data sets. ....	229
<i>Table 5-11. Statistical results for a one-way ANOVA performed on colour differences from various concentrations of antibody exposed to anodized aluminum-tantalum thin films with various aluminum thicknesses and anodized under various electrolytes at 4V. The number indicates the concentration of antibody exposed to the surface in <math>\mu\text{g/mL}</math>, i.e. 200 vs. 50 is <math>\Delta C(200\mu\text{g/mL})</math> vs. <math>\Delta C(50\mu\text{g/mL})</math>.</i> .....	230
Table 5-12. Images and RGB coordinate analysis for protein adsorption studies on anodized aluminum-tantalum thin films with aluminum sputtered at various thicknesses and anodized in 0.4M phosphoric – 0.1M oxalic acid at various voltages. Sample size of n=3 for all data sets.	234
Table 5-13. Statistical results for a one-way ANOVA performed on colour differences from various concentrations of antibody exposed to anodized aluminum-tantalum thin films with various aluminum thicknesses and anodized under voltages in 0.4M phosphoric – 0.1M oxalic acid. The number indicates the concentration of antibody exposed to the surface in $\mu\text{g/mL}$ , i.e. 100 vs. 50 is $\Delta C(100\mu\text{g/mL})$ vs. $\Delta C(50\mu\text{g/mL})$ . ....	236
Table 5-14. The molecular weight and dimensions of human prothrombin, fragment 1 and IgG antibodies. ....	253
Table 5-15. Cartoon drawings of the experimental design and the various proteins exposed to the anodized aluminum-tantalum surface. ....	257
Table 5-16. Application conditions for each protein solution in Part A. ....	258
Table 5-17. Results of Part A with various immobilized protein complexes on an anodized aluminum-tantalum thin film surface. Sample size of n=3 for all data sets. ....	261
Table 5-18. Results of Part B with various ratios of prothrombin and fragment 1 adsorbed to the anodized aluminum-tantalum thin film surface followed by treatment with anti-thrombin IgG (0.2 mg/mL) for 30 minutes. Sample size of n=3. ....	263

Table 5-19. Results of Part C: Anti-thrombin dilution series on anodized aluminum-tantalum thin films previously coated with 1.36 $\mu\text{M}$ prothrombin for 15 minutes. Sample size $n=3$ for all data sets.....	265
Table 5-20. Results of Part C: Anti-thrombin dilution series on anodized aluminum-tantalum thin films previously coated with a mixture of 25:75 (0.34 $\mu\text{M}$ : 1.02 $\mu\text{M}$ ) prothrombin to fragment 1 for 15 minutes. Sample size $n=3$ for all data sets. ....	266
Table 6-1. Experimental design for Part A: Immunoglobulin G and the expected result of protein binding on the surface. ....	279
Table 6-2. Experimental design for Part B: Zika NS1 and the expected result of protein binding on the surface. ....	281
Table 6-3. Results of Part A: Immunoglobulin G immobilization and detection with secondary antibody. Look to Table 6-1 for a detailed understanding of the treatment symbols. Sample size of $n=3$ for all experiments. ....	287
Table 6-4. Results of Part B: Zika NS1 immobilization and detection with specific monoclonal and polyclonal antibody solutions followed by secondary antibodies. Look to Table 6-2 for a detailed understanding of the treatment labels. Sample size of $n=3$ for all experiments. ....	289

## List of Figures

Figure 1-1. Design of a lateral flow assay such as those used in at-home pregnancy tests [5]. .....	3
Figure 1-2. Left: Interference colours resulting from gasoline on a wet tarmac [121]. Right: A schematic of light during thin film interference [122]. .....	5
Figure 1-3. continued. ....	7
Figure 1-4. Schematic of how mismatching refractive indices between the protein and surface oxide can produce a third reflection, which acts as noise in a thin film diagnostic system. ....	10
Figure 1-5. Scanning electron micrograph of nanostructured thin film device. ....	11
Figure 1-6. Schematic of how the light interacts with the device to generate an interference colour. As the thickness of the film increases, due to an adsorbed protein layer, there is an increase in the optical path length and therefore a change in the interference colour generated. ....	12
Figure 1-7. A: Order of interference colours generated with increasing thin film thickness from left to right [53]. B: CIE 1931 colour space chromaticity diagram (left) [54]; chromaticity coordinates for the interference colours produced from a dielectric layer ( $n=1.5$ ) over a substrate ( $n=2.25$ ). Each spot is an increase in the dielectric layer thickness with increments of 2nm from 0 to 600nm [27]. ....	15
Figure 1-8. Structure zone diagram for metal films deposited using magnetron sputtering. T is substrate temperature and $T_m$ is the melting point of the coating material [61]. ....	19
Figure 1-9. The nanostructure that develops during porous anodization of aluminum [74]. ....	21
Figure 1-10. The difference in current density ( $j$ ) graphs with time ( $t$ ) when potentiostatically anodizing to form either a barrier oxide or porous oxide [71]. ....	22
Figure 1-11. A schematic diagram of the 3-dimensional structure of prothrombin and its likely binding orientation on an aluminum oxide surface (modified from [115]; molecular dimensions from [116]). ....	27
Figure 2-1. Measured optical reflectance ( $\lambda=555\text{nm}$ ) of sputtered tantalum with increasing working gas pressure. Standard deviations are shown as error bars (10mTorr, $n=3$ ; 15 to 30 mTorr $n=6$ ). ....	48
Figure 2-2. Reflectivity vs. wavelength plot for tantalum films sputtered at 10, 15, 20, 25 and 30 mTorr through the visible light spectrum (400nm to 700nm). ....	49
Figure 2-3 continued. ....	50

Figure 2-4. Atomic (at.) % oxygen for tantalum films sputtered at various working gas pressures and then exposed to atmosphere. Sample size of n=3 for all data sets. ....	53
Figure 2-5 continued. ....	54
Figure 2-6. Current density-time plot during anodization of aluminum-tantalum thin films in 0.4M phosphoric acid-0.1M oxalic acid under potentiostatic conditions (4V). ....	58
Figure 2-7. Time to complete anodization (i.e. tantalum oxide barrier layer formation) for aluminum-tantalum thin films with tantalum sputtered at a working gas pressure of either 10, 15, 20, 25, or 30 mTorr (mT). Anodization was conducted under potentiostatic conditions (4V) in 0.4M phosphoric-0.1M oxalic acid mixture. ....	59
Figure 2-8. Current density during pore formation for aluminum-tantalum films with tantalum sputtered at a working gas pressure of either 10, 15, 20, 25, or 30 mTorr (mT). Anodization was conducted under potentiostatic conditions (4V) in 0.4M phosphoric-0.1M oxalic acid mixture. ....	59
Figure 2-9. Anodized aluminum-tantalum thin films, viewed at approximately 75° from normal through a polarizing lens (S-polarized light). From left-to-right tantalum sputtered at 10 mTorr, 15 mTorr, 20 mTorr, 25 mTorr and 30 mTorr. ....	60
Figure 2-10. Plot of reflectivity vs. wavelength for anodized aluminum-tantalum films with tantalum sputtered at 10 through 30 mTorr. ....	61
Figure 2-11. Cartoon depiction of an anodized aluminum-tantalum thin film device with an adsorbed layer of protein. The arrows show how a highly reflective metal could overwhelm any light coming off the protein/air interface. ....	65
Figure 3-1. Structure zone diagram for films deposited by magnetron sputtering. T is substrate temperature and $T_m$ is the melting temperature of the deposited species [6]. ....	69
Figure 3-2, continued. ....	77
Figure 3-3. FESEM of aluminum films sputtered at 9 W/cm <sup>2</sup> and 1 mTorr. Images are taken at 5,000X and 100,000X (inset). ....	82
Figure 3-4. FESEM of aluminum film surface sputtered at a constant current of 0.8A and an argon gas pressure of 2.5 mTorr (30 sccm). ....	84
Figure 3-5, continued. ....	85
Figure 3-6. XRD patterns of sputter deposited aluminum-tantalum thin films, with aluminum sputtered at 0.8A and 2.5 mTorr. ....	87
Figure 3-7, continued. ....	88

Figure 3-8, continued.....	92
Figure 3-9, continued.....	94
Figure 3-10, continued.....	95
Figure 3-11. XRD pattern from anodized aluminum-tantalum film with aluminum sputtered at 0.8A and 2.5 mTorr.....	97
Figure 3-12. Anodized aluminum-tantalum thin films, with aluminum sputtered under various conditions, viewed at appx. 75° from normal through a polarizing lens (s-polarized). Top: 0.9 W/cm <sup>2</sup> , left to right: 1 mTorr, 5 mTorr, and 10 mTorr. Middle: 5 W/cm <sup>2</sup> , left to right: 1 mTorr, 5 mTorr, and 10 mTorr. Bottom: 9 W/cm <sup>2</sup> , left to right: 1 mTorr and 10 mTorr.....	101
Figure 3-13. Anodized aluminum-tantalum thin film, with aluminum sputtered at 0.8A and 2.5 mTorr, viewed at appx. 75° from normal through a polarizing lens (s-polarized). .....	104
Figure 3-14. FESEM image of aluminum film sputtered to the conditions described in Chapter 4.1, with a base pressure of 1.0 x 10 <sup>-7</sup> Torr.....	107
Figure 3-15. Aluminum target 99.995% Al (Kurt J. Lesker Company, Jefferson Hills, PA) used in the magnetron sputtering machine at NAIT nanoFacility (photo courtesy of Ciaran Terry). Note the white oxide that has developed at the target center and edges after the target was exposed to atmosphere. ....	109
Figure 3-16. FESEM micrograph of anodized aluminum-tantalum thin film, with aluminum sputtered at 0.9 W/cm <sup>2</sup> and 10 mTorr. The circle outlines an aluminum oxide particle that was not porous anodized all the way through and was likely fully oxidized soon after pore formation initiated. ....	110
Figure 4-1. Current density-time plot during anodization of aluminum-tantalum thin films in 0.4M phosphoric acid under potentiostatic conditions (4V). ....	126
Figure 4-2. Time to complete anodization in each electrolyte mixture. From left to right: 0.4M phosphoric acid, 0.4M phosphoric and 0.1M citric acid, 0.4M phosphoric and 0.4M citric acid, 0.4M phosphoric acid and 3% (v/v) Norsol Anoad® , 0.4M phosphoric acid and 10% (v/v) Norsol Anoad® , 0.4M phosphoric and 0.1M oxalic acid, 0.4M phosphoric and 0.4M oxalic acid. Sample size of n=3 for all cases.....	127
Figure 4-3. Current density during pore formation in each electrolyte mixture. From left to right: 0.4M phosphoric acid, 0.4M phosphoric and 0.1M citric acid, 0.4M phosphoric and 0.4M citric acid, 0.4M phosphoric acid and 3% (v/v) Norsol Anoad® , 0.4M phosphoric acid and 10% (v/v)	

Norsol Anoadd <sup>®</sup> , 0.4M phosphoric and 0.1M oxalic acid, 0.4M phosphoric and 0.4M oxalic acid. Sample size of n=3 for all cases.....	127
Figure 4-4 continued. ....	129
Figure 4-5 continued. ....	134
Figure 4-6. Surface pore size measured from FESEM images for aluminum-tantalum thin films anodized in 0.4M phosphoric acid at 4V with various additives. Asterisk (*) indicates significant difference ( $p<0.05$ ) when compared to no additive using independent sample t-test. Sample size for each: None (n=157), 0.1M Oxalic (n=222), 0.4M Oxalic (n=242), 3% (v/v) Norsol (n=184), 10% (v/v) Norsol (n=168), 0.1M Citric (n=182), 0.4M Citric (n=152). ....	137
Figure 4-7. RMS surface roughness values as measured by SEM side-profile analysis of aluminum-tantalum films anodized in 0.4M phosphoric acid at 4V with various additives. ....	138
Figure 4-8 continued. ....	139
Figure 4-9. Refractive index values of the porous aluminum oxide layer determined by ellipsometry for aluminum-tantalum thin films anodized in 0.4M phosphoric acid at 4V with various additives. Asterisk (*) indicates significant difference ( $p<0.01$ ) when compared to no additive using; sample size of 3 for each case. ....	143
Figure 4-10. Aluminum oxide thicknesses determined by ellipsometry for aluminum-tantalum thin films anodized in 0.4M phosphoric acid at 4V with various additives. Asterisk (*) indicates significant difference ( $p<0.01$ ) when compared to no additive using; sample size of 3 for each case. .....	144
Figure 4-11. Anodized aluminum-tantalum thin films viewed at appx. 75° from normal through a polarizing lens (s-polarized). From left to right: 0.4M phosphoric acid, 0.4M phosphoric and 0.1M citric acid, 0.4M phosphoric and 0.4M citric acid, 0.4M phosphoric acid and 3% (v/v) Norsol Anoadd <sup>®</sup> , 0.4M phosphoric acid and 10% (v/v) Norsol Anoadd <sup>®</sup> , 0.4M phosphoric and 0.1M oxalic acid, 0.4M phosphoric and 0.4M oxalic acid. ....	145
Figure 4-12. Molecular structure and dimensions of (A) Citric acid, (B) Oxalic acid, and (C) Glycolic Acid. Carbon is yellow, oxygen is red, and hydrogen is white. Modelled using Molsoft MolBrowser Version 3.8-5 for Windows (Molsoft LLC, ©2017). Molecular structures and measurements from reference [18]. ....	149
Figure 4-13. Refractive indices of anodized aluminum-tantalum thin films, with various sputtered aluminum thicknesses and anodized under various voltages. Sample size n=3 for all data sets.	159

Figure 4-14. Aluminum-tantalum thin films anodized in 0.4M phosphoric-0.1M oxalic acid. Aluminum was deposited to thicknesses of either (A) 110nm, (B) 120nm, or (C) 130nm and then anodized at either 2, 4, 6, or 8V (shown from left to right in each image). Pictures were taken at approximately 75° from normal through a polarizing lens (s-polarized). ..... 162

Figure 4-15. Current density-time plot during anodization of aluminum-tantalum thin films in 0.4M phosphoric acid-0.1M oxalic acid with a voltage-step process (4V for 400s followed by 0.5V increase for 5s until 8V was reached). ..... 163

Figure 4-16. Current density-time plot during anodization of aluminum-tantalum thin films in 0.4M phosphoric acid-0.1M oxalic acid with a voltage-step process (4V for 400s followed by 0.5V increase for 5s until 8V was reached). Zoomed in time axis from 390 – 450s to show voltage step effect on current density..... 164

Figure 4-17 continued. .... 165

Figure 4-18. Measured pore diameter from FESEM surface images for the different anodizing conditions: from left to right, 1) 4V for 100s, stepped to 8V (n=357), 2) 4V for 100s, stepped to 10V (n=310), 3) 4V for 400s, stepped to 8V (n=370), 4) 4V for 400s, stepped to 10V (n=351), 5) 4V for 1000s, stepped to 8V (n=316), and 6) 4V for 1000s, stepped to 10V (n=353). ..... 169

Figure 4-19. XRD patterns from anodized aluminum-tantalum films in 0.4M phosphoric-0.1M oxalic acid: A) 4V for 100s, stepped to 8V; B) 4V for 1000s, stepped to 8V; C) 4V for 100s, stepped to 10V; D) 4V for 1000s, stepped to 10V..... 171

Figure 4-20. Anodized aluminum-tantalum thin films viewed at appx. 75° from normal through a polarizing lens (s-polarized). From left to right: A) 4V for 100s and then stepped to 8V; B) 4V for 400s, stepped to 8V; C) 4V for 1000s, stepped to 8V; D) 4V for 100s, stepped to 10V; E) 4V for 400s, stepped to 10V; F) 4V for 1000s, stepped to 10V..... 174

Figure 4-21. Typical current density vs. time graph for samples anodized for 200 sec in 0.4M sulphuric acid at 4V, followed by anodizing in 0.4M phosphoric-0.1M oxalic acid at 4V until completion..... 187

Figure 4-22. Typical current density vs. time graph for samples anodized for 200 sec in 0.4M sulphuric acid at 4V, followed by anodizing in 0.4M phosphoric-0.1M oxalic acid at 10V until completion..... 188

Figure 4-23, continued. .... 189

Figure 4-24, continued. .... 193

Figure 4-25. Measured pore size from FESEM surface images for the different anodizing conditions: from left to right, 1) anodized for 200s at 4V in 0.4M sulphuric acid (SA) followed by 4V in 0.4M phosphoric-0.1M oxalic acid mix (PO), n=311, 2) anodized for 200s at 4V in SA followed by 10V in PO, n=412, 3) anodized for 400s at 4V in SA followed by 4V in PO, n=492, 4) anodized for 400s at 4V in SA followed by 10V in PO, n=484. .... 196

Figure 4-26. XRD patterns of anodized aluminum-tantalum thin films in the various conditions: A) 200s and 4V in 0.4M sulphuric acid (SA) followed by 4V in 0.4M phosphoric-0.1M oxalic acid (PO), B) 400s and 4V in 0.4M SA followed by 4V in 0.4M-0.1M PO, C) 200s and 4V in 0.4M SA followed by 10V in 0.4M-0.1M PO, D) 400s and 4V in 0.4M SA followed by 10V in 0.4M-0.1M PO. .... 197

Figure 4-27. Interference colours produced when anodizing under the various conditions, from left to right: 1) 200s and 4V in 0.4M sulphuric acid (SA) followed by 4V in 0.4M phosphoric-0.1M oxalic acid (PO), B) 400s and 4V in 0.4M SA followed by 4V in 0.4M-0.1M PO, C) 200s and 4V in 0.4M SA followed by 10V in 0.4M-0.1M PO, D) 400s and 4V in 0.4M SA followed by 10V in 0.4M-0.1M PO. Pictures taken using a polarizer to visualize s-polarized light. .... 200

Figure 5-1. Recorded colour differences from RGB coordinate analysis for protein adsorption studies on anodized aluminum-tantalum thin films with aluminum sputtered under various power densities and gas pressures. Sample size of n=3 for all data sets. .... 222

*Figure 5-2. Recorded colour differences from RGB coordinate analysis for protein adsorption studies on anodized aluminum-tantalum thin films with various sputtered aluminum thicknesses and anodized in 0.4M phosphoric acid at 4V. Sample size of n=3 for all data sets. .... 226*

*Figure 5-3. Recorded colour differences from RGB coordinate analysis for protein adsorption studies on anodized aluminum-tantalum thin films with various sputtered aluminum thicknesses and anodized in 0.4M phosphoric – 0.1M oxalic acid at 4V. Sample size of n=3 for all data sets. .... 228*

*Figure 5-4. Recorded colour differences from RGB coordinate analysis for protein adsorption studies on anodized aluminum-tantalum thin films with various sputtered aluminum thicknesses and anodized in 0.4M phosphoric – 0.4M oxalic acid at 4V. Sample size of n=3 for all data sets. .... 230*

Figure 5-5. 1931 CIE colour diagram with selected films showing the average colour shift with increasing antibody concentration: 90nm Al, 0.4M phosphoric acid (■); 120nm, 0.4M phosphoric (x); 120nm, 0.4M phosphoric-0.1M oxalic (▲); 120nm, 0.4M phosphoric-0.4M oxalic (●)... 232

Figure 5-6. Colour differences recorded from RGB analysis of protein adsorption studies on anodized aluminum-tantalum thin films with aluminum sputtered at various thicknesses and anodized under various voltages in 0.4M phosphoric – 0.1M oxalic acid. Sample size of n=3 for all data sets..... 235

Figure 5-7. 1931 CIE colour diagram of average colour shift from films with prothrombin and either 100, 50, 20 or 0 µg/mL of anti-prothrombin antibody. With films of 120nm aluminum, and anodized at 2V (●); 4V (▲), 6V (X), 8V (■). OPL stands for optical path length. .... 237

Figure 5-8. 1931 CIE colour diagram of average colour shift from films with prothrombin and either 100, 50, 20, or 0 µg/mL of anti-prothrombin antibody. With films anodized at 4V in 0.4M phosphoric acid 0.1M oxalic acid and initial aluminum thickness of 110nm (●), 120nm (▲) and 130nm (X). OPL stands for optical path length..... 238

Figure 5-9. Cartoon depiction of light reflections with high and low protein surface density. The intensity of the light reflected off the protein layer reduces as less protein is adsorbed, and leads to a mismatch in reflections between the light off the tantalum metal and the protein. It was hypothesized that reducing tantalum metal reflectivity may help with detecting lower protein concentrations, however this study showed that lower tantalum metal reflectivity did not improve sensitivity and therefore this hypothesis is not true. .... 240

Figure 5-10. Cartoon depiction of how light interacts with protein adsorbed to the surface at high and low surface densities. The low surface density has a reduced refractive index because the composite refractive index consists of more air. The mismatch in refractive indices between the alumina and protein layer causes another reflection at the protein/alumina interface, which can act as noise in the system. The refractive indices were calculated using Equation (5.2) and either 50 or 24% of a monolayer of protein. .... 242

Figure 5-11. Cartoon depiction of how light may interact with a sparsely, prothrombin coated surface of alumina. The majority of light reflects off the aluminum oxide surface and interferes with light off the tantalum metal to produce orange, while a relatively small portion of light reflects off the adsorbed prothrombin to produce purple. Note the light reflecting off the tantalum metal is not shown in this diagram for simplicity. .... 243

*Figure 5-12. Left: CIE 1931 colour space chromaticity diagram [16]; Right: Chromaticity coordinates for the interference colours produced from a dielectric layer ( $\eta=1.5$ ) over a substrate ( $\eta=2.25$ ). Each spot is an increase in the dielectric layer thickness with increments of 2nm from 0 to 600nm [15].* ..... 245

Figure 5-13. A schematic diagram of the 3-dimensional structure of prothrombin and its binding orientation on an aluminum oxide surface (modified from [9]; molecular dimensions from [6]). ..... 254

Figure 5-14. Colour coordinate results of Part A, converted to Yxy coordinates and plotted on a 1931 CIE colour diagram. Base: aluminum oxide, II: prothrombin, F1: fragment 1, AII: anti-prothrombin antibody, AT: anti-thrombin antibody. .... 268

Figure 5-15. Cartoon depiction of A: theoretical thickness changes with the binding of anti-prothrombin to prothrombin (left) or fragment 1 (right) on a surface; B: Left – thickness change if antibody binds to the side or edge or fragment 1, Right – low affinity of anti-prothrombin to fragment 1 minimizes antibody binding, which results in less of an optical path length change. .... 270

Figure 5-16. Cartoon depiction of adsorbed prothrombin and fragment 1 on an aluminum oxide surface. Green areas show epitopes open and available for antibody binding. .... 271

Figure 6-1. Cartoon depiction of immobilization procedure and the reaction of the antigen with its antibody. Prothrombin is initially immobilized through the GLA domain to the alumina surface. This is then treated with glutaraldehyde, a homo-bifunctional crosslinker, followed by the antigen to attach the antigen to the surface without exposing it to the alumina surface. The surface is then coated in a capping agent, a small molecule that will react with the remaining glutaraldehyde. Finally, the surface is exposed to a solution containing the antibody, which will recognize epitopes on the antigen and bind. .... 277

Figure 6-2. Colour coordinate results of Part B, converted to Yxy coordinates and plotted on a 1931 CIE colour diagram. II: prothrombin, G: glutaraldehyde treatment, Cap: TBS treatment, NS1: Zika non-structural protein 1, Mab: monoclonal anti-NS1 antibody, Pab: polyclonal anti-NS1 antibody, Nab: polyclonal nonspecific antibody. .... 291

Figure 6-3. Glutaraldehyde reaction with amino groups via (1) Schiff base or (2) Michael-type addition reactions. Figure adapted from [26]. .... 293

## List of Symbols and Abbreviations

Abbreviation	Definition
AII	anti-prothrombin
ANOVA	analysis of variance
AT	anti-thrombin
at.%	atomic percent
$B_s$	blue coordinate, signal
$B_b$	blue coordinate, background
CIE	International Commission on Illumination or Commission Internationale de l'Éclairage
d	physical path length of light
Da	dalton
DHL	divergence high limiting
EDS	energy dispersive spectroscopy
EDX	energy dispersive X-ray spectroscopy
ELISA	enzyme linked immunosorbent assay
EMA	effective medium approximation
F1	human fragment 1
FESEM	field emission electron microscope
$G_s$	green coordinate, signal
$G_b$	green coordinate, background
ICDD	International Centre for Diffraction Data
IgG	immunoglobulin G
II	human prothrombin
k	extinction coefficient
k	Boltzmann's constant

LFA	lateral flow assay
M	molar, moles per liter
<i>m</i>	mass
MSE	mean square error
MW	molecular weight
NAIT	Northern Alberta Institute of Technology
nanoFAB	nano fabrication and characterization facility
NS1	non-structural protein 1
OPL	optical path length
P	pressure
<i>p</i>	partial pressure
PBS	phosphate buffered saline
PCR	polymerase chain reaction
pKa	acid dissociation constant
POCT	point-of-care testing
$R_s$	red coordinate, signal
$R_b$	red coordinate, background
SATW	super atmospheric thin window
SDD	silicon drift detector
SEM	scanning electron microscopy
SPR	surface plasmon resonance
T	temperature
$T_s$	substrate temperature
$T_m$	melting temperature of sputter deposited material
TBS	tris buffered saline
TTL	through-the-lens
U	anodization potential

v/v	volume by volume
wt. %	weight percent
XRD	X-ray diffraction
ZIKV	Zika virus
$\Delta C$	colour difference
$\mu$ PAD	micro paper-based analytical devices
$\varphi$	gas impingement rate
$\eta$	refractive index
$\lambda$	wavelength
$\lambda$	mean free path
$\omega$	glancing angle

# Chapter 1 Introduction

## 1.0 Background

### **1.1 Point of Care Diagnostics – A Brief Review of the Literature**

Almost all testing of patient samples, be it blood, urine, or tissue, is conducted in large central laboratories with highly trained staff and large sophisticated equipment. However, in the last few years there has been a huge movement towards point-of-care testing (POCT). There have been over 6,500 papers published just within the last 10 years on point-of-care diagnostics (Web of Science, July 10, 2017). The idea behind POCT has mainly been to miniaturize the big, bulky equipment of central laboratories down to the size of a phone or desktop computer and automate it. This is seen with emerging products such as the GeneXpert or i-STAT, where the current standard diagnostic technologies, PCR (polymerase chain reaction) for DNA-based sensors and ELISA (enzyme linked immunosorbent assay) for antibody-based sensors, are made to function in a portable benchtop or handheld device [1, 2]. Enzyme-linked immunosorbent assay (ELISA) has been the standard technique used in antibody-based sensors for the last 40 years [3]. It consists of covalently attaching an enzyme to an antibody which then reacts with a substrate, such as a dye to cause a colour change, and amplifies the protein signal. This signal can then be read visually or by a detector and compared to a standard curve to get a quantitative result. Other forms of this assay include radioimmunoassay (RIA), where a radiolabel marker is attached to the antibody, or fluorescence immunoassay, where the antibody is labeled with a molecule which fluoresces at a specific wavelength, for example a lanthanide chelate [4].

Point of care diagnostics can be broken up into two main categories: photometric and electrical-based systems. Photometric systems are usually based on some form of ELISA. Most photometric based systems involve some sort of signal amplification including fluorescence,

chemiluminescence, colloidal gold-conjugated antibodies, or an enzymatic substrate that produces a visible signal. The electrical systems can be potentiometric, impedimetric, or amperometric. Electrical systems will read changes in current or potential based on redox reactions occurring in the sample or by interaction of the analyte with an electrode surface. A short review of the most prominent technologies will be given here:

### *1.1.1 Lateral Flow Assays*

The most commonly known on-site diagnostic is the lateral flow assay (LFA). This is the technology of the at-home pregnancy test and has been commercially available to the public for the last 30 years [3]. LFA's work through capillary action of a fluid through test zones on polymeric strips. The fluid containing the analyte will flow through an area on the strip that contains antibodies conjugated to colored or fluorescent particles (e.g. colloidal gold, latex microspheres) [5]. If the analyte is present, visible or fluorescent lines will appear in the detection zone where an additional set of antibodies are immobilized to attach to any analyte passing through the zone, Figure 1-1. Detection is made by eye or a separate detection device.

LFA's are inexpensive, simple to use, and have a long shelf life. However, they currently suffer from poor sensitivity (mM to  $\mu$ M), requiring significant amplification for low concentration tests [1]. Another drawback is that they are difficult to develop as multiplex devices. An important aspect of future diagnostics is the ability to detect multiple analytes. For example, the identification of 8-30 microbe strains would allow for diagnosis of 80-90% of serious infections [6]. LFA's also require extensive sample preparation for testing of whole blood, with the reproducible filtration of solids, such as blood cells, from serum. This has been a large challenge of adapting lateral flow assays for whole blood samples in the past and a current area of research [7]. These drawbacks have led to research into other types of devices, such as microfluidics.

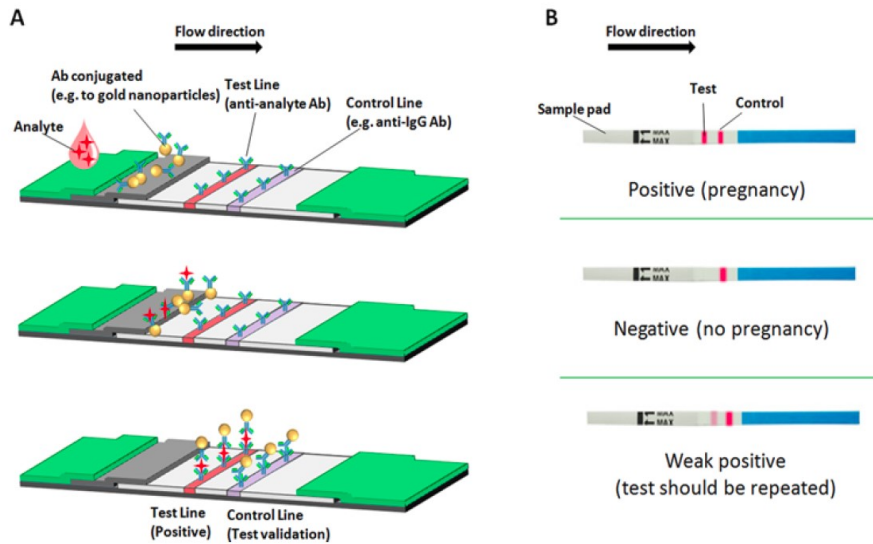


Figure 1-1. Design of a lateral flow assay such as those used in at-home pregnancy tests [5].

### 1.1.2 Emerging Microfluidic-based Technologies

Microfluidics involves the manipulation of fluids in micrometer-sized channels. Many diagnostic technologies have been developed within the last few years that utilize microfluidics. Micro paper-based analytical devices ( $\mu$ PADs) are an emerging technology where 3D patterned channels are made with hydrophobic and hydrophilic areas to guide fluid movement in three dimensions. The 3D system allows detection of multiple analytes. Diagnostics for All has developed a  $\mu$ PAD system for use in developing countries [8, 9]. These types of devices are inexpensive and easy to use, yet they experience challenges in mass production due to difficulties in reproducible manufacturing processes [2].

Other microfluidic-based technologies include: flow cytometry devices which measure fluorescent molecules in an ELISA-type assay, such as the xMAP by Luminex [10], or amplified ELISA tests such as the mChip diagnostic, which uses cassettes with all reagents self-contained in the cassette and is read by a handheld analyzer for quantitative results [11]. These systems are capable of high throughput and performance but they often require bulky, expensive instrumentation or have high

complexity to their manufacturing process making mass production difficult. Much of the recent Lab-on-a-Chip technology is based on microfluidics and has yet to see commercialization. New manufacturing methods are needed as current methods involve micromachining and lithography, which can be expensive processes for mass production [12].

### *1.1.3 Other Point-of-Care Technologies*

The other most common type of POC devices are electrochemical sensors. The glucose assays developed for diabetes patients involve the detection of redox reactions mediated by the enzymatic oxidation of glucose [6]. Recent advances in real-time polymerase chain reaction (PCR) have led to its use in diagnostics. PCR is extremely sensitive since both target and signal amplification are used, however the equipment required is complex, with the need for thermal cycling and fluorescent labelling of products to assess multiple analytes [6]. There are a few label-free methods such as surface plasmon resonance (SPR) and mechanical transduction techniques using piezoelectric materials such as nanocantilevers or acoustic wave devices. These systems tend to require highly complex and expensive instrumentation and are not simple to use.

New technologies, such as the mChip and xMAP, are improvements over the current standards for point-of-care testing, however they are not nearly as affordable as lateral flow assays and glucose sensors, with test strips/chips costing \$30-50 USD each and the handheld or benchtop readers being anywhere from \$1,000-\$15,000 USD [11, 13]. The World Health Organization lists a series of criteria, known as ASSURED, for an ideal point-of-care test [14]:

Affordable by those at risk of infection

Sensitive (few false-negatives)

Specific (few false-positives)

User-friendly (simple to perform and requiring minimal training)

**Rapid** (to enable treatment at first visit) and **Robust** (no refrigerated storage)

**Equipment-free**

**Delivered to those who need it**

Whereas the new microfluidic technologies achieve sensitive and specific output, they are not affordable, user-friendly, or equipment-free. On the other hand, lateral flow assays and electrochemical sensors are affordable and user-friendly but suffer from a lack of sensitive and specific output. The solution to this is in a fundamentally new approach to diagnostics.

## 1.2 Thin Film Diagnostics

If you have ever seen gasoline on a wet tarmac and noticed the rainbow of colours, you have experienced thin film interference. The colours are a result of the difference in optical properties between the water and the gasoline. Light is reflected off the interface between the gas and air and the interface between the gas and water. These two reflections will recombine and interfere with one another to create a colour, Figure 1-2. This colour is dependent on the thickness of the gas layer and thus the rainbow of colours you see are a result of the different thicknesses of gasoline on water.

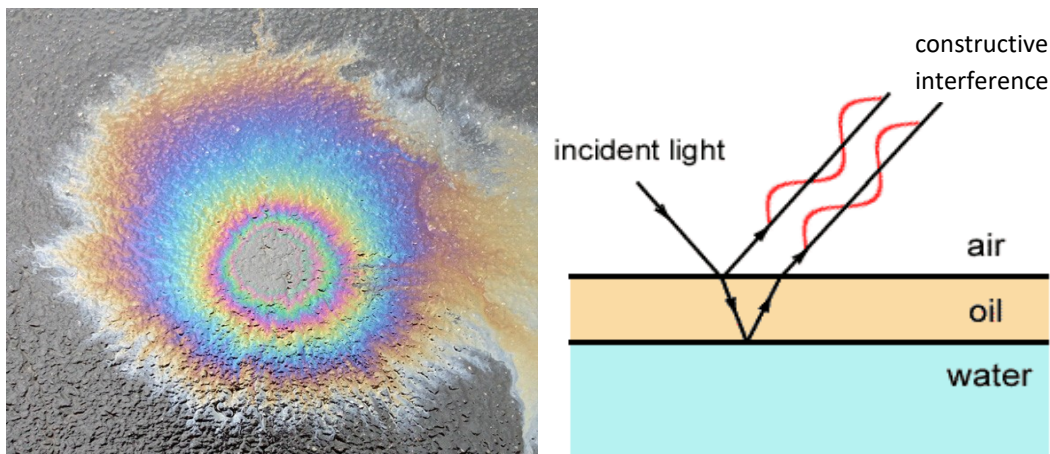


Figure 1-2. Left: Interference colours resulting from gasoline on a wet tarmac [121]. Right: A schematic of light during thin film interference [122].

In the same manner, interference colours are generated when certain types of metals (e.g. tantalum) are anodized at high voltages [15]. These colours are generated due to an oxide film on the surface of the metal. Whenever there is a change in the refractive index of the medium through which the light travels, there is a reflection. The film is thin enough to cause light reflected from the surface of the oxide and light reflected from the oxide-metal interface to interfere and generate different colours.

The colours observed in thin film interference depend on the optical path length (OPL), which is the product of the length of the film through which the light travels and the refractive index of the medium. In a medium of constant refractive index, the optical path length can be described as:

$$OPL = \eta d \quad (1.1)$$

where OPL is the optical path length,  $\eta$  is refractive index of the medium, and  $d$  is the physical length through which the light travels [16]. Thus, if there is a small change in the thickness of the film a change in color can be seen due to the change in the optical path length.

In the field of thin film diagnostics, this colour generating principle can be used to detect small molecules or proteins. The basis of this type of diagnostic device is to immobilize an antibody (or antigen) on a thin film surface to generate a colour. If a patient's fluid sample is placed on the surface of the device and contains the antigen (or antibody) associated with the immobilized antibody (or antigen), then an immune complex will form and create a visible colour change due to the increase in optical path length, Figure 1-3.

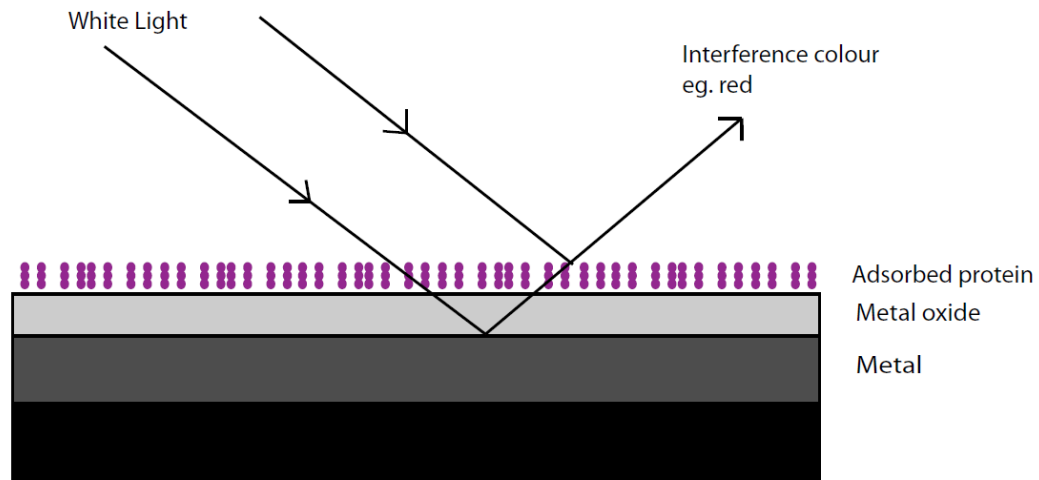


Figure 1-3. continued.

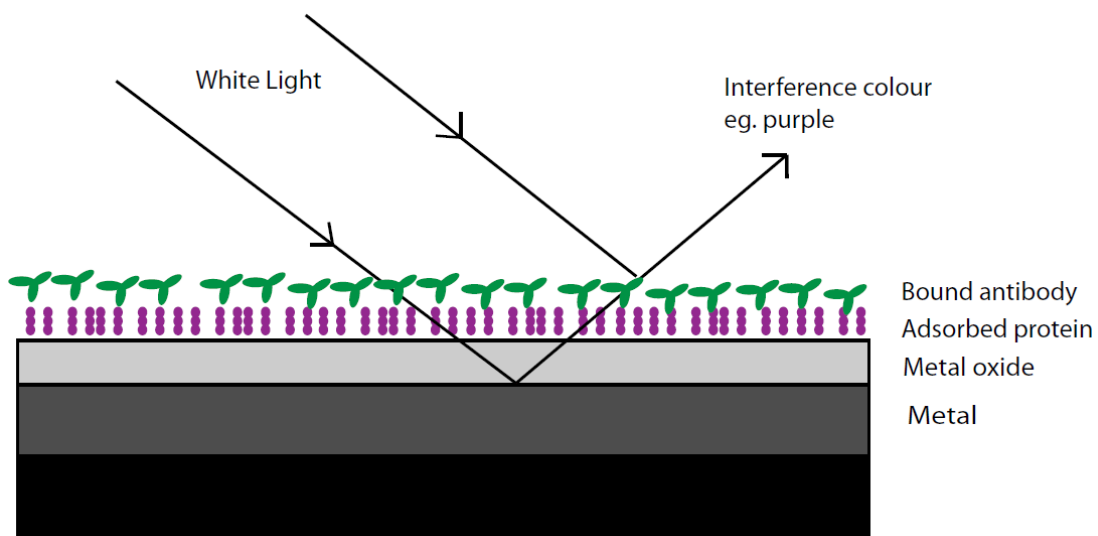


Figure 1-3, continued. A schematic of how light interacts with a thin film diagnostic device to produce interference colours from immunocomplexes forming on the surface.

### 1.2.1 History of Thin Film Diagnostics

Langmuir and Schaefer [17] were the first to study interference colours generated by thin organic films on a surface. They could approximate the thickness of an adsorbed molecule on water by comparing the colour with those generated by consecutive layers of barium stearate films on water. Shaffer and Dingle [18], as well as Porter and Pappenheimer [19] extended these studies to the

observance of antigen-antibody reactions. Many years later, Giaever developed a thin-film technology where antigen-antibody reactions could be observed on indium coated glass slides [20]. Adams et al. [21] conducted similar antigen-antibody studies on anodized tantalum coated glass slides.

Giaever made a significant amount of progress developing thin film diagnostics, filing three patents in '73 [22], '74 [23] and '75 [24]. The first patent was highly complex and involved the coating of the antigen-antibody complex with metal particles, followed by etching to create voids where biological particles were previously attached. The voids could be observed by a change in light transmission through the films. The following patent in '74, used a gold-indium alloy thin film, which was oxidized to generate an interference colour. Mono and bimolecular layers could be observed on the surface by changes in the interference colour, however contrast was low due to a mismatch in the refractive indices between protein and the oxidized substrate. This led to the patent in '75, which was composed of deposited metal globules on top of a dielectric layer. The metal globules were meant to scatter the light and increase the interference signal from the immobilized biological layers. An immunoassay for the detection of Hepatitis B antigen was eventually developed with a limit of detection of 22 ng/mL [25]. However, Giaever noted that the assay was limited by the time it takes for antibodies to diffuse to the surface, with higher sensitivity tests taking 16 hours to conduct. To improve sensitivity, a device was made to increase the contact time of solution to the surface by a wedge-shaped reservoir [24, 26].

A few years later, Nygren et al. [27, 28] developed a thin film device based on silicon dioxide films. Oxidation of silicon produced a thin silicon dioxide layer which generated an interference colour. The colour could be tuned by changing the time of oxidation and therefore changing the thickness of the oxide layer. Proteins and antibodies were then immobilized to the surface via

silanes. Direct visualization of protein layers was possible down to monomolecular films of 0.7nm thickness and as little as 100 ng of protein/cm<sup>2</sup> [29]. This technology was patented in 1997 [30] and commercialized by Biostar Inc. Tests were developed for group A and B streptococcus [31, 32], the influenza A and B viruses [33], chlamydia [34], rhinovirus [35], and an assay for the detection of snake venom [36]. However, many of the reports found that the optical immunoassay was not sensitive enough for clinical use [32, 33, 34].

The main drawback of this technology was that the refractive index of the thin silicon dioxide layer was fixed ( $n = 1.46\sim 1.47$ ,  $\lambda = 380\sim 700$  nm [37]) and could not be changed. This limited the sensitivity of the device as interference colours are most sensitive when the protein or molecular layers added are of a similar refractive index to their substrate. The refractive index of protein has been found to be nearly constant when measured in solution,  $n = 1.6$  [38]. However, an adsorbed protein layer on a surface will vary in refractive index due to density, protein-surface interactions, and composition. These variables contribute to an effective refractive index of the protein layer that has been found to vary from  $n = 1.36\text{-}1.55$  [39, 40, 41], when measured with ellipsometry. Every place where there is a change in refractive index, light experiences a reflection. If the substrate and protein layer are of different refractive indices, then a reflection will occur at the interface between these two layers and acts as noise in the system, Figure 1-4. To compensate for this, the test was developed with an ELISA format, where the thickness of the protein layer is increased by an enzyme-substrate reaction on the surface, amplifying the signal but also increasing the time and complexity of the test [42]. To perform this test without amplification and still retain strong colour shifts, a material is required where the refractive index can be tuned to match the substance you want to detect.

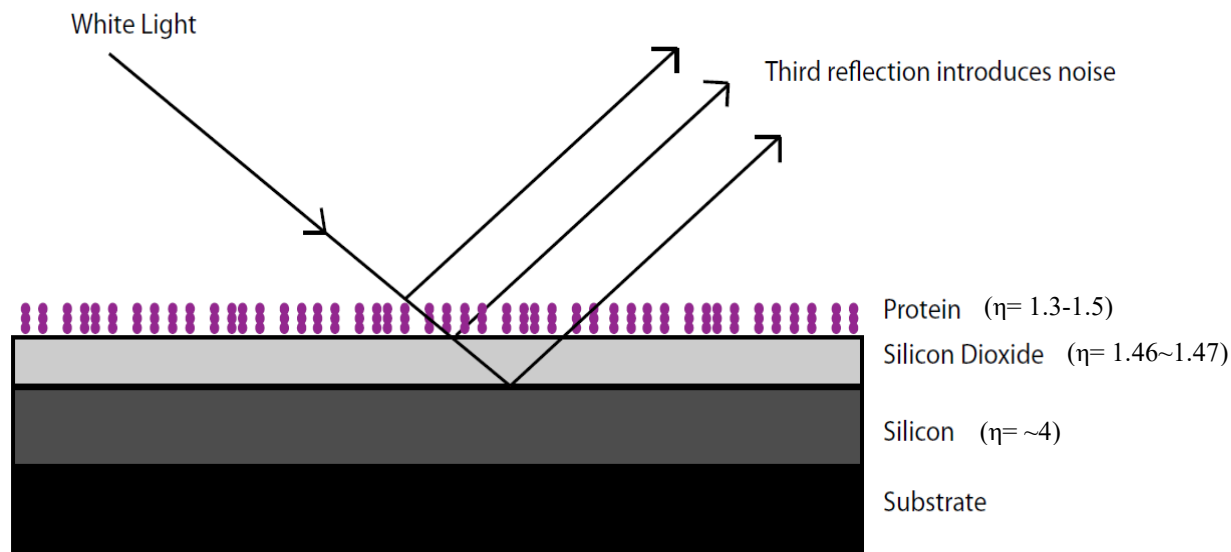


Figure 1-4. Schematic of how mismatching refractive indices between the protein and surface oxide can produce a third reflection, which acts as noise in a thin film diagnostic system.

### 1.2.2 Thin Film Diagnostic Based on Anodized Aluminum

Recently there has been an increase of interesting and new applications for anodized aluminum. The ability to create a regular hexagonal array of pores with diameters tailored in the nanometers has led to various research in nanostructured materials and the use of porous anodic alumina in the field of medicine for biosensors [43, 44], molecular and ion separation [45], drug delivery devices [46], and biocompatible implants for improved tissue integration [47]. With over 3000 papers published on porous aluminum oxide in the last 10 years, there appears to be no end to the applications of this material (Web of Science, July 2017).

As stated before, the problem with previous thin film diagnostics was the lack of a material with a tunable refractive index. To fix this problem, Burrell et al. patented a device to produce thin film interference colours based on anodized aluminum thin films [48, 49]. This device uses a thin, deposited layer of Ta (2000 Å) underneath a thin layer of Al (600-2400 Å). When the multi-layered material is electrochemically oxidized in an appropriate electrolyte, a layer of porous  $\text{Al}_2\text{O}_3$  is

formed, as well as a thin layer of  $Ta_2O_5$ , Figure 1-5. The  $Ta_2O_5$  forms an electrical barrier by limiting current flow proportional to the thickness of the oxide and thus acts as an internal process control [50]. At each point where there is a change in the refractive index, light is reflected. Reflected light exits the film and interferes constructively or destructively to generate a colour, as described earlier. When a very thin layer is added onto the  $Al_2O_3$ , such as a protein adsorbed onto the surface, there is a change in the optical path length and thus a different color is generated, Figure 1-6.

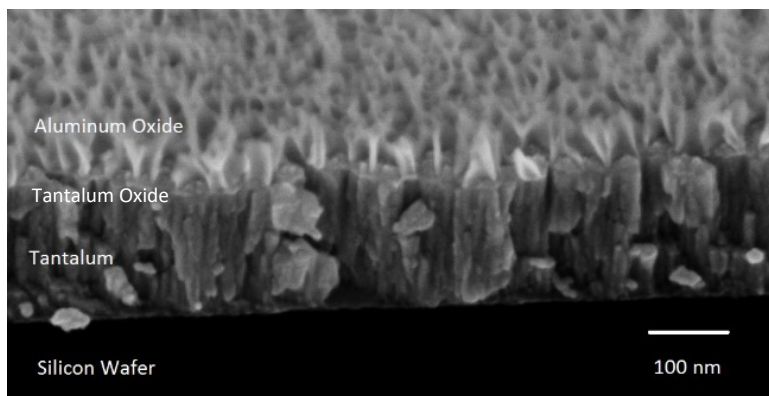


*Figure 1-5. Scanning electron micrograph of nanostructured thin film device.*

Over the visible spectrum, air has a refractive index of 1, alumina has a refractive index of about 1.7 [51], and adsorbed protein has a refractive index that varies between 1.36 and 1.55 [40, 39]. By tailoring the pore size and density in a porous aluminum oxide, the percentage of air in the film can be adjusted to tune the refractive index to match protein (explained in further detail in Section 1.3). The increased sensitivity brought about by tuning the refractive index allows for the most sensitive colour shifts and even picomolar ( $10^{-12}$ ) surface concentrations can be observed very clearly [48].

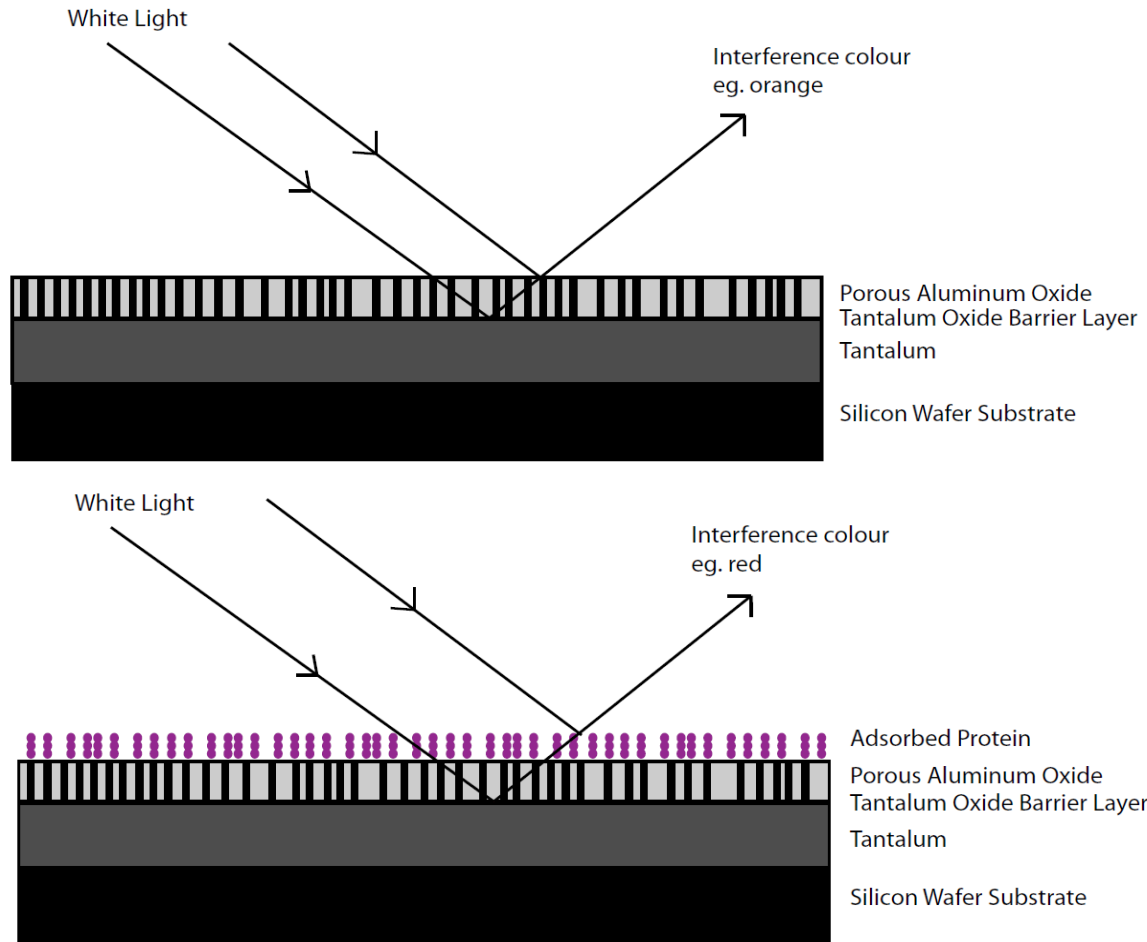


*Figure 1-6. Schematic of how the light interacts with the device to generate an interference colour. As the thickness of the film increases, due to an adsorbed protein layer, there is an increase in the optical path length and therefore a change in the interference colour generated.*

The benefits of this type of technology over other point-of-care tests are numerous. Thin film diagnostics based on anodized aluminum would be less expensive to produce and simpler to use than microfluidics, as the production methods (physical vapour deposition and anodization) are easily capable of mass manufacture. It would be easy to multiplex such a technology by immobilizing different antigens and antibodies to the surface. For example, a bar code of different colours could be made depending on the antigen or antibody being detected. No extra equipment would be necessary to read the test, as a simple colour change read by eye is all that is needed. If quantitative results were required, an imaging device could be used with some additional software

to determine protein concentration by the degree of colour change. Higher sensitivity can be achieved with a thin film assay than with a lateral flow assay since the detection method directly views a monolayer of analyte. A lateral flow assay requires amplification of the signal, typically with latex microsphere or gold-conjugated antibodies. Finally, no sample preparation is required, as in lateral flow assays, since no polymer matrix is needed for fluid transfer and sample solutions can be exposed directly to the surface. Such technology is capable of transforming the medical diagnostic industry and enabling precision medicine through point-of-care testing, however a more thorough understanding of the material and optical properties of these films is required before the commercialization of such a product can occur.

## **1.3 Optics**

### *1.3.1 Thin Film Interference of Oxidized Metal Films*

Thin film interference occurs due to differences in the optical properties of a thin film on top of a substrate. Some of the light is reflected off the film's surface, while some is refracted and travels through the film [16]. Due to the increased refractive index of the film compared to air, the light is retarded, reflects off the following substrate surface, and emits out of the film. These two light waves recombine and can interfere either constructively or destructively. Destructive interference occurs when light emerging from the film is shifted an integral number of half wavelengths. On the other hand, constructive interference occurs when the emerging light is an integral number of full wavelengths. Therefore, when the film thickness is one quarter of a wavelength, destructive interference occurs, with constructive interference occurring when a film thickness of half a wavelength is reached.

Figure 1-7A shows the progression of colours for thin film interference. The range of interference colours will start at black, work towards grays followed by gold, yellow, red and finally into second

order purples and blues. This occurs because, initially, a cancellation of all colours occurs leaving black. As the film gets thicker, intensity of all colours increases, producing greys and whites. This is followed by destructive interference of blue (smallest wavelengths) leaving yellow and then red [52]. As the film thickness increases, the colours progress into the second order colours, where a mix of destructive and constructive interference occurs. At larger thicknesses, multiple wavelengths can constructively and destructively interfere since both types of interference occur at integral numbers of either full or half wavelengths. The higher order colours eventually only switch between pinks and greens due to the mixing of destructive and constructive interference. Interference colours can be plotted on a CIE Standard Observer colour diagram, as shown in Figure 1-7B. CIE charts are used to quantitatively map all colours perceptible to a human. Interference colours follow a specific, circular path on these diagrams. Sandström et al. [27] showed how the most sensitive colour shifts to changes in thickness are in the first-order colours.

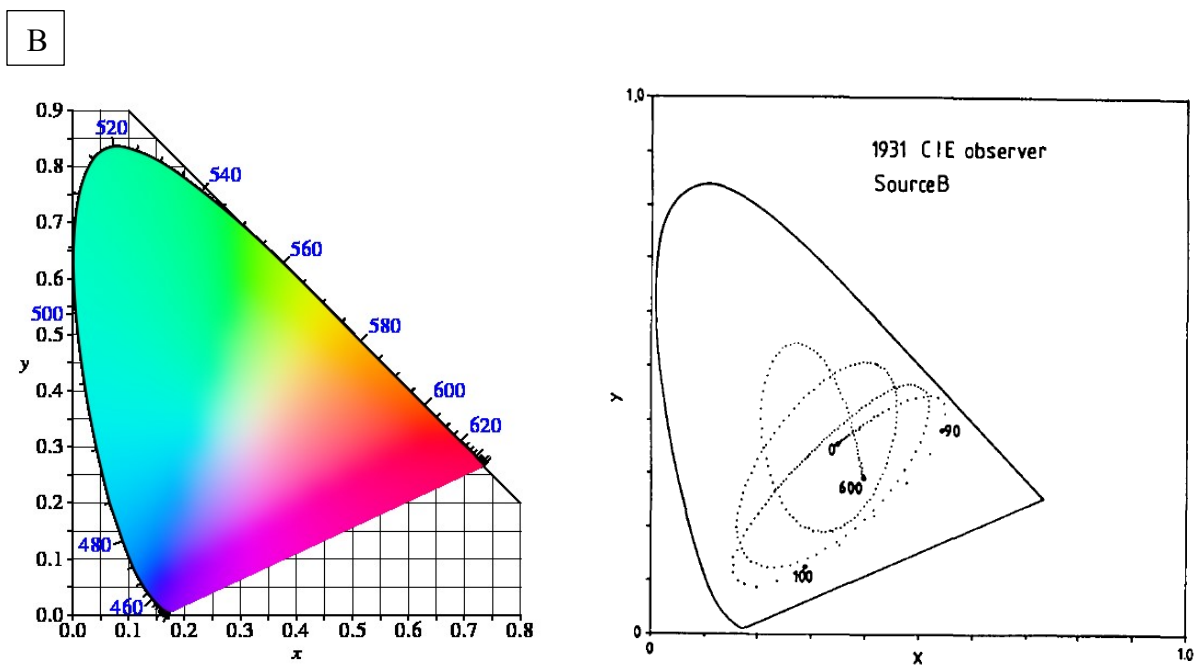
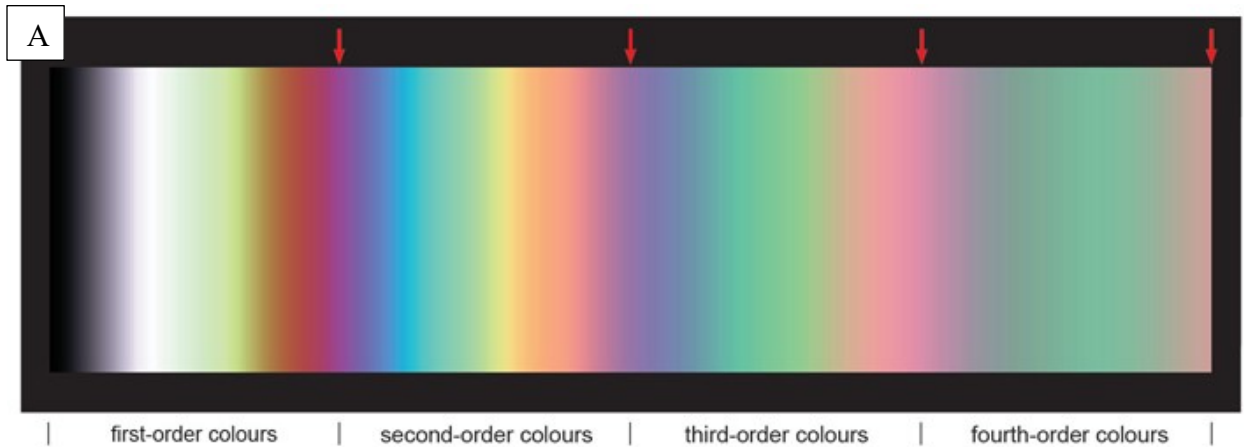


Figure 1-7. A: Order of interference colours generated with increasing thin film thickness from left to right [53]. B: CIE 1931 colour space chromaticity diagram (left) [54]; chromaticity coordinates for the interference colours produced from a dielectric layer ( $\eta=1.5$ ) over a substrate ( $\eta=2.25$ ). Each spot is an increase in the dielectric layer thickness with increments of 2nm from 0 to 600nm [27].

The production of interference colours from thin oxide films on tantalum has been well studied by Charlesby and Polling [15]. Two important points come to mind when considering their work and its relation to thin film diagnostics based on anodized aluminum:

(1) Production of an interference colour from an oxide film depends mostly on the reflectivity of the air/oxide interface. To create a saturated colour, the reflected light from the air/oxide interface and the light from the oxide/metal interface must each be 50% of the outgoing light. Thus, equal portions of light are interfering and producing the most saturated of interference colours. Tantalum is a very good material to use in this application since its reflectivity in the visible spectrum (390-700 nm) is on the order of 40-60 % [15]. The protein/alumina layer is fairly transparent, therefore a metal that absorbs a significant amount of light (such as Ta) needs to be used so that the light reflected off of the protein/air interface is not swamped by the light coming from the oxide/metal interface.

(2) The thickness of the oxide film determines the colour produced due to the increase in optical path length (as discussed in section 1.2). The protein layer by itself is not optically thick enough to create strong interference colours. Proteins are only a few nanometers in size, yet the wavelength of visible light varies from 390-700 nm's, with destructive interference occurring at a minimum of one quarter of a wavelength (min. ~100nm). Therefore, a layer of aluminum oxide is created on the surface with a refractive index near that of adsorbed protein (1.36~1.55 [39, 40, 55]) such that the effective optical thickness of the protein layer can be increased to achieve strong interference colours.

It is known that aluminum produces a porous alumina layer when anodized in certain electrolytes. The pore size of this material can be controlled on the scale of nanometers by changing the electrolyte or strength of the electric field during anodization [56]. Alumina has a refractive index in the visible range that is higher than that of protein, 1.7 vs. 1.36-1.55 respectively [51] [39]. By changing the pore size, the refractive index can be tuned to be the same as the protein layer added on the surface, as shown in Equation (1.2):

$$\eta = (1 - x)\eta_{film} + x\eta_{air} \quad (1.2)$$

Where  $x$  is the porosity of the film,  $\eta$  is the composite refractive index of the porous dielectric film,  $\eta_{film}$  is the refractive index of the dielectric (eg. alumina), and  $\eta_{air}$  is the refractive index of air (ie.  $\sim 1$ ) [57]. When the alumina layer and the protein layer have matching refractive indices, they act as one layer with response to light.

#### **1.4 Atomic Sputter Deposition**

The thin metallic films for this device are created with DC-magnetron sputter deposition, a form of physical vapor deposition. Sputter deposition involves bombardment of a target surface with energetic ions, which results in the ejection of atoms, ions, or clusters of the target material from the surface. These atoms land on a substrate surface opposite the target where a film starts to grow. The film will grow differently depending on the thermodynamic parameters of the deposit, the material properties of the substrate and target, as well as the processing parameters during sputtering (i.e. sputtering atmosphere, cathode and substrate geometry) [58, 59, 60, 61, 62, 63].

Magnetron sputtering uses a magnetic field to entrap electrons into a loop above the cathode surface. The trapping loop allows for more collisions between the electrons and the inert gas, typically Ar, thus producing more ions that will collide with the target surface and confine the produced plasma. Due to the confinement of the plasma, lower working gas pressures can be used in the chamber, allowing for higher deposition rates on the substrate [59]. DC magnetron sputtering is useful for producing highly pure thin films in a relatively short amount of time.

##### *1.4.1 Microstructural Zone Diagrams*

An extensive study of the microstructure of sputtered films has been conducted over the last 40 to 50 years. Movchan and Demchishin [59] were the first to develop structural zone diagrams, that

were a visual and qualitative way to describe the microstructure that develops from evaporation deposited films. They described a 3-zone model where the structure changed depending on the normalized temperature,  $T_s/T_m$ , where  $T_s$  is the substrate temperature and  $T_m$  is the melting temperature of the deposited material. Thornton [61] further developed this model for sputtering of thin films, considering the working gas pressure in the sputter chamber and expanding the model to include a transition zone between Zone 1 and 2 known as Zone T, Figure 1-8. Other models developed by Messier accounted for structure change with thickness as the film grew [64] and developed the diagram to encompass 5 zones.

Sputter-deposited film growth can be divided into three main steps: (1) Transport of the target species to the substrate, (2) adsorption of this species on the surface, and (3) diffusion of the atoms on the surface through processes such as bulk diffusion. Control of these three steps can lead to a variety of microstructures as described by Thornton [60]:

**Zone 1:** columnar, tapered crystals separated by open, voided boundaries.

**Zone T:** a transition region with a dense, fibrous structure and low surface roughness.

**Zone 2:** columnar grains separated by distinct boundaries.

**Zone 3:** structures are equiaxed, formed by recrystallization and grain growth.

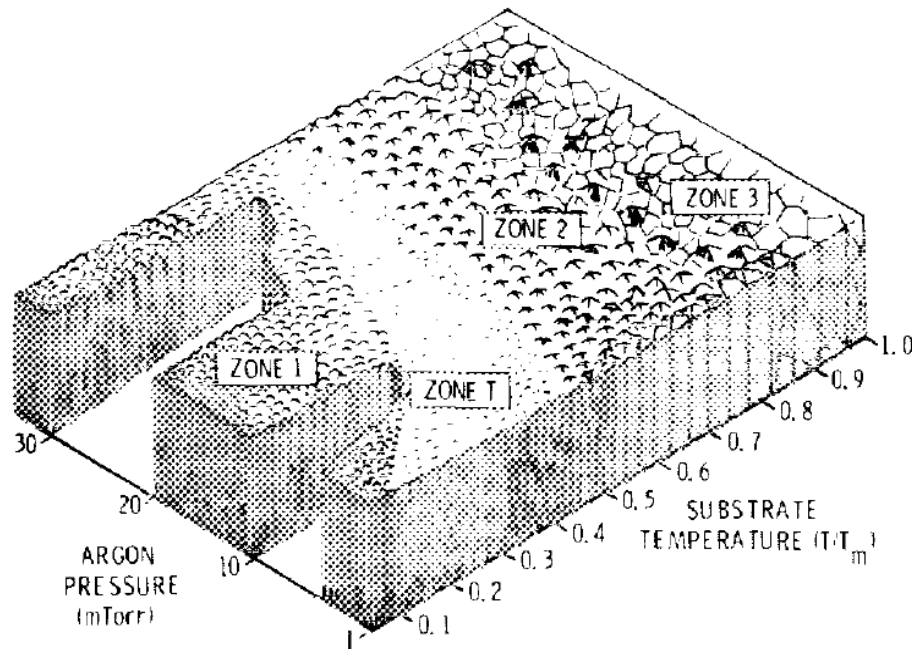


Figure 1-8. Structure zone diagram for metal films deposited using magnetron sputtering.  $T$  is substrate temperature and  $T_m$  is the melting point of the coating material [61].

The microstructure developed depends strongly on the energy by which the coating atoms are deposited. Increasing the energy of these atoms will transition a film from Zone 1, where low adatom mobility leads to a highly-voided structure, to Zone 3, where the high energy allows increased adatom mobility leading to grain growth and production of an equiaxed crystal structure. The energy of the deposited atoms can be controlled in various ways, including gas pressure, power density, substrate and target temperature, substrate bias voltage, and substrate-to-target distance [59]. The microstructure has a significant effect on the material properties of the sputtered film, including electrical properties [65, 66], film stress [62], and optical properties [67, 66].

## 1.5 Anodization of Aluminum

Aluminum metal always has a native oxide film about 2-3nm thick when under atmospheric conditions [68]. This oxide is stoichiometrically 1.5x the size of the metal and therefore is under a compressive stress when grown [56]. The compressive stress helps to achieve complete coverage of the aluminum metal by the oxide even when under deformation. In 1857, Buff found that aluminum could be electrochemically oxidized to increase the thickness of the oxide layer [68]. By the 1920's the process was being used in the manufacturing of seaplanes to increase their corrosion resistance [69].

Anodization involves setting up an electrolytic cell, where a metal to be oxidized is anodically polarized in an electrolyte [56]. There are two main types of oxides that can be grown electrolytically on aluminum: (i) barrier films, where a uniformly thick oxide layer grows on the aluminum surface and (ii) porous films, where oxide growth occurs such that a regular array of pores develops. The type of oxide grown is determined by the nature of the electrolyte, where neutral electrolytes, with a pH range of 5-7, grow barrier films and electrolytes in which aluminum oxide is sparingly soluble (phosphoric, sulphuric, oxalic, and chromic acids) will grow porous films [68, 70].

### *1.5.1 Growth, Structure, and Morphology of Anodic Porous Aluminum Oxide*

A significant amount of research has been done on the porous-type films, as the pore diameters can be manipulated on the scale of nanometers and very regular porous arrays can be grown. A brief discussion will be given here on the current understanding of how pore growth occurs during electrolytic oxidation; there are many detailed reviews on the subject [71, 72, 73, 70].

Electrolytic oxidation of aluminum in certain electrolytes can lead to a regular array of nanopores, with each pore contained within a hexagonal cell as shown in Figure 1-9. The pore structure and growth can be explained by the current-time (potentiostatic) or voltage-time (galvanostatic) graphs. Figure 1-10 shows the current-time graph for the potentiostatic anodization of aluminum to form either a barrier film or porous film. As the oxide coating thickens, the current must decrease as resistance increases. In porous films, as the current decreases it reaches a limiting value at which the current focuses on local imperfections in the oxide. The localized current initiates pore formation, leading to an increase in the current until steady-state pore growth results in a constant current.

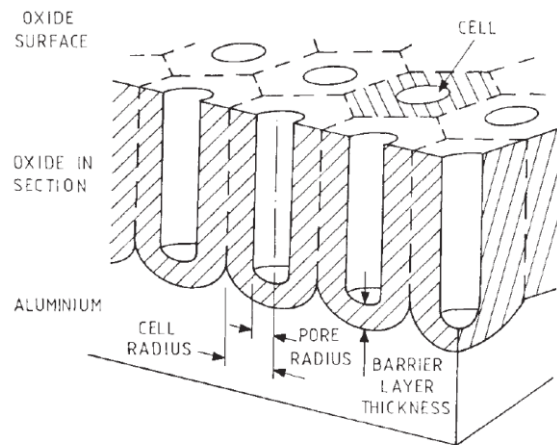


*Figure 1-9. The nanostructure that develops during porous anodization of aluminum [74].*

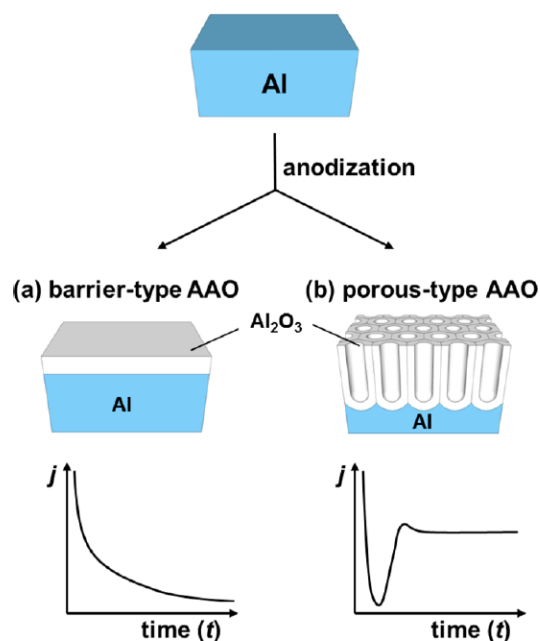


Figure 1-10. The difference in current density ( $j$ ) graphs with time ( $t$ ) when potentiostatically anodizing to form either a barrier oxide or porous oxide [71].

Radioactive tracer studies have shown that growth occurs at both the film/electrolyte and film/metal surfaces [75]. This occurs due to  $Al^{3+}$  egress and  $O^{2-}/OH^-$  ingress under the high electric field. Barrier films are formed at high current efficiencies. At high current efficiencies, all the  $Al^{3+}$  ions form material at the oxide/electrolyte interface. In contrast, at low efficiencies the outwardly migrating  $Al^{3+}$  ions are ejected directly into solution. This direct ejection results in higher dissolution rates of the oxide than would otherwise occur if no electric field were present. As the current efficiency decreases, a transition occurs where porous oxide formation starts to occur. The field also increases the polarization of the Al-O bond which makes attack of the molecule easier by the electrolyte acid [75]. The higher dissolution rate is very important; if the egressing aluminum ions formed an oxide at the surface, then no porous formation could result because the oxide film would “self-heal” preventing any cracks to form [75]. Since there is no aluminum oxide

growth at the oxide/electrolyte surface, the film is dissolved at preferential sites, such as grain boundaries, and the development of penetration paths occurs.

Finite-element method models have shown that below each penetration path, the potential is increased, resulting in an increase of the local electric field. An increased field leads to increased local dissolution and scalloped regions of the metal-film interface [76]. These scallops eventually merge until steady-state pore formation develops. This merging causes a cell morphology where the pore density at the surface of the oxide is much higher than further below. A steady-state formation develops because of an equilibrium between film growth and field assisted dissolution.

The above described theory of pore formation is called the field assisted dissolution model. There are other competing models for how the porous oxide forms, however the process discussed above is the most widely accepted. A recent study by Herbert et al. [77] provided a quantitative understanding of the relationship between the conditions of pore initiation and the dissolution chemistry, and provided further evidence for the field assisted dissolution model. Their model showed the dependence of pore formation on the current efficiency.

The pore size and density depend on several factors including electrolyte, pH, anodizing potential, time of anodization, and temperature. Pore diameter tends to increase with an increase in electrolyte concentration, decrease in pH, increase in potential or increase in anodization time. The barrier layer thickness is linearly dependent on the anodizing voltage. Pore density has been shown to be proportional to  $1/U^2$ , where U is the anodization potential. All these factors lead to a very tailorable nanostructured material, which can have strong effects on the optical properties of the anodic film. Wang, J., et al. [78] and Wang, Y., et al. [79] determined the optical constants of anodic oxide films formed in oxalic acid at various voltages and found that refractive index

increases with forming voltage. Hierro-Rodriguez et al. [80] and Rahman et al. [81] both measured the effect of post-anodization chemical treatments for pore widening on the optical properties of porous anodic alumina. As pore size increased with chemical etching, the refractive index decreased due to increased % air in the film. The ability to tune the refractive index of these films is what makes them so attractive for thin film diagnostic applications.

### *Importance of Anodization Parameters to Thin Film Diagnostics*

In this work, the Al/Ta thin films on silicon wafers will be anodized to produce  $\text{Al}_2\text{O}_3$  on  $\text{Ta}_2\text{O}_5$  on Ta. The main factors that need to be considered are: (1) electrolyte, (2) temperature, and (3) anodizing potential. Some important notes to consider are:

- (1) Pore size needs to be small enough such that protein is not entering the pores and changing the refractive index of the alumina layer. The addition of protein will increase the composite refractive index of the film.
- (2) Pore size and density need to be created such that the resulting refractive index of the alumina layer matches that of the protein layer. The refractive index can be adjusted by changing the voltage or electrolyte to adjust pore size and density.

Phosphoric acid electrolyte will be used due to its ability to produce alumina films that are highly porous, resistant to hydration and relatively inert in aqueous environments [74] [82]. Higher porosities allow for lower refractive indices, as more air is incorporated in the alumina-air layer. The oxide produced is inert in aqueous environments due to the resulting phosphate incorporated into the film from the electrolyte (typically 7.5 wt.%) [74] [82]. Davis et al. [83] showed that the surface consists of a monolayer of  $\text{AlPO}_4$  on top of an  $\text{Al}_2\text{O}_3$  substrate. The stability of the films in aqueous environments can be increased by incorporating more phosphate ions in the alumina

layer [84]. The stability of these films is an important factor in the shelf-life, since hydration of the film will lead to changes in the refractive index.

## **1.6 Immobilization of Proteins on Aluminum and Aluminum Oxides**

### *1.6.1 Protein and Ion Interactions with Aluminum Oxide Surfaces*

The most important sites for ion adsorption on metal oxides and hydroxides are the  $M\cdot OH$  and  $M\cdot OH_2$  sites on the surface, which become charged with  $H^+$  and  $OH^-$  ions [85]. These become Lewis acid/base sites which can partake in ligand exchange. In aluminum oxides and hydroxides,  $Al^{3+}$  ions exposed on crystal edges or defect sites become spots for  $H_2O$  and  $OH$  adsorption [86, 85]. These can then partake in ligand exchange reactions with anionic groups and can result in strong chemisorption to the surface [85, 87].

A review of amino acid and peptide adsorption to metals and oxides was discussed by Costa et al. [88]. The most common forms of bonding found were either ligand exchange with a hydroxyl on the surface or electrostatic binding, such as hydrogen bonds. Glycine was found to adsorb to boehmite ( $\gamma\text{-AlO}(\text{OH})$ ) via hydrogen bonding ( $NH_2\text{-HO}$ ). Alanine adsorbed to  $\alpha\text{-}$  and  $\gamma\text{-}$   $Al_2O_3$  via electrostatic binding. Greiner et al. [89] found that glutamic and aspartic acid adsorbed on  $\gamma\text{-}$   $Al_2O_3$  through either a bidentate or tetradentate conformation with 2 or 4 Al surface atoms via H-bonds or covalent bonding. Trujillo et al. [90] showed certain amino acids such as aspartate and glutamate can, when presented on the outside surface of a protein, enhance adsorption to aluminum hydroxides. Sepelyak et al. [91] showed that specific adsorption of pepsin occurs on aluminum hydroxides via anionic exchange of exposed carboxylate groups on the protein surface. Adsorption to aluminum hydroxides is mainly electrostatic based and dependent on the charge sign and magnitude of the material and protein surfaces. This needs to be taken into consideration when immobilizing protein to aluminum oxide surfaces.

### *1.6.2 Techniques for the Immobilization of Proteins to Aluminum Oxide Surfaces*

A large difficulty of using aluminum or aluminum oxides as a substrate for diagnostics in the past has been with problems in trying to functionalize the surface for protein binding. Aluminum and aluminum oxides have been shown to be catalytic to the degradation of biological materials such as viruses [92, 93, 94]. Other studies in enzymatic immobilization [95, 96] or pharmaceutical vaccine adjuvants [97, 98] have shown aluminum oxides and hydroxides capable of denaturing protein, reducing their functionality once adsorbed.

Previous techniques for functionalizing aluminum and aluminum oxide surfaces fall into 4 main categories: (1) silanization, (2) organophosphates or phosphonates, (3) coating of the alumina surface to provide a substitute material for protein attachment, and most recently (4) selectively bound peptides which can act as anchors to the surface. The most common method used in the past for protein immobilization to alumina has been silanization [99, 100, 101, 102, 103]. The surface is coated by silanes with functional groups which are then activated using various binding chemistries including carbodiimides or glutaraldehyde, and followed by protein immobilization. Some problems with silanization include low activation surface density and developing reproducible surfaces [104].

Hyndman et al. [105] [106] used organophosphate groups to functionalize the alumina surface for enzyme immobilization. Lu et al. [107] used organophosphonates to activate a nanoporous alumina surface for immobilization and detection of human odorant binding proteins. Another method for protein immobilization to aluminum oxide involves coating of the surface to provide a functional layer for protein immobilization. Dai et al. [108] used layer by layer deposition of polyelectrolyte multilayers. Oliveira et al. [109] deposited a polymer support for enzyme immobilization. Alvarez et al. [110] initially adsorbed protein A on alumina to bind IgG to the surface. More recently the

selective binding of peptides to aluminum by phage display has developed peptides that strongly adhere to aluminum [111, 112]. These have been used to immobilize antifreeze proteins to aluminum [113].

Another method of binding proteins to the surface was proposed by Burrell [114] and involves proteins or peptides with domains containing many anionic sites, such as vitamin-K dependent plasma proteins. These proteins are immobilized on the aluminum or aluminum oxide surface and then activated using typical homo- or heterobifunctional linkers.

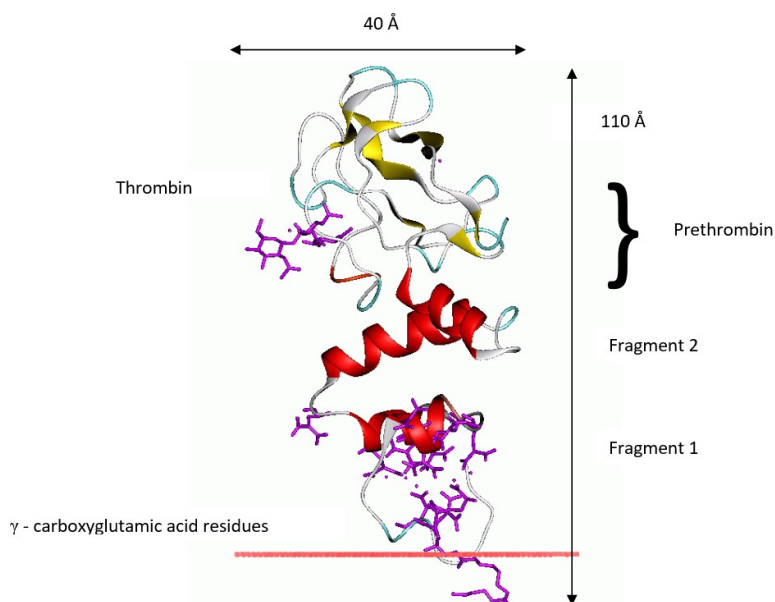


*Figure 1-11. A schematic diagram of the 3-dimensional structure of prothrombin and its likely binding orientation on an aluminum oxide surface (modified from [115]; molecular dimensions from [116]).*

Prothrombin is a vitamin K-dependent plasma protein that plays an important role in the coagulation cascade [115, 117]. It is a three-domain protein made up of fragment 1, fragment 2, and thrombin. Fragment 1 contains 10  $\gamma$ -carboxyglutamic acid residues in the first 40 amino acids, which help it bind to tissue lipid bilayers [118]. These anionic groups bind to the  $\text{Al}_2\text{O}_3$  surface almost irreversibly and keep the protein in the same orientation wherever it binds, as shown in

Figure 1-11. By having a large plurality of these anionic groups concentrated into a relatively small area, the binding strength is improved. Carboxyl groups are known to bind to aluminum oxides but can be pushed off the surface by larger anionic groups such as phosphates [119]. However, it has been shown that an increased number of carboxyl groups being able to bind to the surface from the same molecule improves the binding strength, as all bound groups must be removed simultaneously [120]. Each prothrombin molecule therefore has 20 anionic groups (2 carboxyl groups per  $\gamma$  - carboxyglutamic acid residue) within the first 40 amino acids, which are all attracted to the oxide surface. This allows for consistent antigen binding, minimal denaturation of the target protein, and a constant change in the optical path length, thus giving the best sensitivity for thin film diagnostic devices.

## 2.0 Overview of Research Objectives

The overarching goal of this work was to increase the understanding of a thin film diagnostic based on anodized aluminum-tantalum thin films. Following is a list of research objectives and hypotheses with a flow chart outlining the completed research below:

2.1.1 Establish how the sputtered tantalum microstructure affects the optical properties of the anodized aluminum-tantalum thin film.

*Hypothesis:* Increasing the working gas pressure while sputtering will decrease the reflectivity of tantalum due to a change in microstructural properties and result in stronger interference colours with protein adsorption. See Chapters 2 and 5.1.

2.1.2 Establish how the sputtered aluminum microstructure affects the optical properties of the anodized aluminum-tantalum thin films.

*Hypothesis:* Changing the working gas pressure and power density during sputtering of aluminum will change the microstructural properties of the thin film resulting in a change

in the final microstructure after anodization. Microstructural differences will change the optical properties of the thin film device, with denser, flatter films resulting in better sensitivity for detecting adsorbed protein layers. See Chapters 3 and 5.1.

- 2.1.3 Understand how the addition of chemical additives to phosphoric acid anodization bath affects microstructure and optical properties of anodized films.

*Hypothesis:* Chemical additives, or inhibitors, can be introduced into the anodization bath to improve uniformity and optical properties of anodized films. This will translate into better sensitivity for detecting adsorbed protein layers. See Chapters 4.1 and 5.1.

- 2.1.4 Engineer anodic alumina films that have both a reduced surface pore size and tunable refractive index.

*Hypothesis:* The porous anodic alumina can be developed such that a small surface pore size is developed, while simultaneously adjusting the porosity below the surface to tune the refractive index of the entire film. This can be done by either changing the voltage or electrolyte during the anodization process. See Chapters 4.2 and 4.3.

- 2.1.5 Understand how spatial distribution of prothrombin affects the sensitivity of the device.

*Hypothesis:* Spatial distribution of prothrombin (i.e. density on the surface) will affect the exposure of antigenic binding sites for a polyclonal anti-thrombin antibody to bind, and thus affect the sensitivity of detection. See Chapter 5.2.

- 2.1.6 Demonstrate a new technique developed by Burrell [108] that immobilizes an antigen to an alumina surface through prothrombin.

*Hypothesis:* An immunoassay can be developed for detecting IgG by immobilizing an antigen to the anodic alumina surface through prothrombin and detecting the bound antibody by changes of the interference colours produced. See Chapter 6.

Microstructural Investigation of Thin Film Diagnostic

What structure is ideal for thin film diagnostic?

2.1.1 How does tantalum microstructure affect interference colours?

See Ch. 2. Increased sputtering pressure reduces reflectivity off tantalum and causes a phase shift to occur. Small changes in interference colours occur due to both the phase shift and reduced reflectivity of the tantalum layer

2.1.2 How does aluminum sputtering parameters (pressure and power) affect surface microstructure and optical properties?

See Ch. 3. Increased pressure and decreased power both lead to inhomogeneous anodized films. Increased power leads to difficulty in controlling interference colours due to high deposition rate. Changes in the refractive index are minimal for anodization of these films in 0.4M phosphoric-0.1M oxalic acid mix, regardless of aluminum sputtered microstructure.

2.1.3 How does aluminum oxide microstructure and optical properties change with addition of inhibitors to the phosphoric acid anodization bath?

See Ch. 4.1. Inhibitors (oxalic acid, Norsol Anoad, citric acid) decrease surface roughness, increase refractive index and oxide thickness due to less etching during anodization. Strongest to weakest inhibitor: oxalic acid, Norsol Anoad, citric acid.

2.1.4 Can films be made with variable pore size to adjust refractive index without changing surface pore size?

Yes, see Ch. 4.2 and 4.3. Pore size can be manipulated by either changing the voltage during anodization or changing the electrolyte mid-anodization.

## Protein Immobilization on Thin Film Diagnostic

2.1.1/2.1.2/2.1.3 How does microstructure influence the sensitivity of an immunoassay based on anodized aluminum-tantalum thin films? Microstructure changes influenced by tantalum and aluminum deposition parameters, and anodization parameters of electrolyte and voltage.

See Ch. 5.1. Model system of prothrombin/anti-prothrombin used. Tantalum and aluminum deposition parameters have minimal effect on sensitivity of detecting adsorbed protein layers. Electrolyte and voltage have significant effects and can be adjusted to optimize interference colouring.

2.1.5 Can the sensitivity be increased by spacing out the antigen to open more available epitopes?

See Ch. 5.2. Slight improvement in detection limit for anti-thrombin polyclonal IgG when prothrombin is spaced out on the surface with fragment 1.

2.1.5 Demonstration of a new type of binding technology to aluminum oxides.

See Ch. 6. Immobilization of rabbit IgG and Zika NS1 was achieved by cross-linking to surface-immobilized prothrombin with glutaraldehyde. Detection of these antigens with their associated antibodies was visualized by a simple colour change after the antibody bound to the surface-immobilized antigen.

## References

- [1] C. D. Chin, V. Linder and S. K. Sia, "Commercialization of microfluidic point-of-care diagnostic devices," *Lab Chip*, vol. 12, pp. 2118-2134, 2012.
- [2] C. Dincer, R. Bruch, A. Kling, P. S. Dittrich and G. A. Urban, "Multiplexed Point-of-Care Testing - xPOCT," *Trends in Biotechnology*, pp. 1-15, 2017.
- [3] T. R. Holford, F. Davis and S. P. Higson, "Recent trends in antibody based sensors," *Biosensors and Bioelectronics*, vol. 34, pp. 12-24, 2012.
- [4] R. Burns, "Immunochemical techniques," in *Principles and Techniques of Biochemistry and Molecular Biology*, New York, NY, University Cambridge Press, 2010, pp. 263-299.
- [5] K. M. Koczula and A. Gallotta, "Lateral flow assays," *Essays in Biochemistry*, vol. 60, pp. 111-120, 2016.
- [6] V. Gubala, L. F. Harris, A. J. Ricco, M. X. Tan and D. E. Williams, "Point of Care Diagnostics: Status and Future," *Analytical Chemistry*, vol. 84, pp. 487-515, 2012.
- [7] EMD Millipore Corporation, "Rapid Lateral Flow Test Strips: Considerations for Product Development," EMD Millipore Corporation, Billerica, MA, 2013.
- [8] C. P. Chan, W. C. Mak, K. Y. Cheung, K. K. Sin, C. M. Yu, T. H. Rainer and R. Renneberg, "Evidence-Based Point-of-Care Diagnostics: Current Status and Emerging Technologies," *Annual Reviews of Analytical Chemistry*, vol. 6, pp. 191-211, 2013.
- [9] G. M. Whitesides, S. T. Phillips, A. W. Martinez, M. J. Butte, A. Wong, S. W. Thomas, H. Sindi, S. J. Vella, E. Carrilho, K. A. Mirica and Y. Liu, "Lateral flow and flow-through bioassay devices based on patterned porous media, methods of making same, and methods of using same". USA Patent 8,377,710 B2, 19 February 2013.
- [10] S. A. Dunbar, "Applications of Luminex® xMAP™ technology for rapid, high-throughput multiplexed nucleic acid detection," *Clinica Chimica Acta*, vol. 363, pp. 71-82, 2006.
- [11] C. D. Chin, Y. K. Cheung, T. Laksanasopin, M. M. Modena, S. Y. Chin, A. A. Sridhara, D. Steinmiller, V. Linder, J. Mushingantahe, G. Umvilighozo, E. Karita, L. Mwambarangwe, S. L. Braunstein, J. van de Wijgert, R. Sahabo, J. E. Justman, W. El-Sadr and S. K. Sia, "Mobile Device for Disease Diagnosis and Data Tracking in Resource-Limited Settings," *Clinical Chemistry*, vol. 59, no. 4, pp. 1-12, 2013.
- [12] H. Becker and L. E. Locascia, "Polymer microfluidic devices," *Talanta*, vol. 56, pp. 267-287, 2002.

- [13] J. Hu, X. Cui, Y. Gong, X. Xu, B. Gao, T. Wen, T. Lu and F. Xu, "Portable microfluidic and smartphone-based devices for monitoring of cardiovascular diseases at the point of care," *Biotechnology Advances*, vol. 34, pp. 305-320, 2016.
- [14] C. S. Kosack, A. Page and P. R. Klatser, "A guide to aid the selection of diagnostic tests," *Bullitin of the World Health Organization*, vol. 95, pp. 639-645, 2016.
- [15] A. Charlesby and J. J. Polling, "The Optical Properties of Thin Oxide Films on Tantalum," *Proceedings of the Royal Society of London. Series A, Mathematical and Physical Sciences*, vol. 227, pp. 434-447, 1955.
- [16] E. Hecht, *Optics*, Addison-Wesley Publishing Company, Inc., 1979.
- [17] I. Langmuir and V. J. Schaefer, "Optical measurement of the thickness of a film adsorbed from a solution," *Journal of the American Chemistry Society*, vol. 59, p. 1406, 1937.
- [18] M. F. Shaffer and I. H. Dingle, "A Study of Antigens and Antibodies by the Monolayer Film Technique of Langmuir," *Proceedings of the Society of Experimental Biology & Medicine*, vol. 38, p. 528, 1938.
- [19] E. F. Porter and A. M. Pappenheimer, "Antigen-antibody reactions between layers adsorbed on built up stearate films," *Journal of Experimental Medicine*, vol. 69, pp. 755-765, 1939.
- [20] I. Giaever, "The antigen-antibody reaction: a visual observation," *Journal of Immunology*, vol. 110, pp. 1424-1426, 1973.
- [21] A. L. Adams, M. Kling, G. C. Fischer and L. Vroman, "Three simple ways to detect antibody-antigen complex on flat surfaces," *Journal of Immunological Methods*, vol. 3, pp. 227-232, 1973.
- [22] I. Giaever, "Method and apparatus for immunological detection of biological particles". United States of America Patent 3,853,467, 10 December 1974.
- [23] I. Giaever, "Substrate for immunological tests and method of fabrication thereof". United States of America Patent 3,926,564, 16 December 1975.
- [24] I. Giaever, "Diagnostic device for visually detecting presence of biological particles". United States of America Patent 3,979,184, 7 September 1976.
- [25] I. Giaever and R. J. Laffin, "Visual detection of hepatitis B antigen," *Proceedings of the National Academy of Science USA*, vol. 71, pp. 4533-4535, 1974.
- [26] C. R. Keese and I. Giaever, "Measurement of antigen concentrations with a one-step inhibition assay," *Journal of Immunological Methods*, vol. 43, pp. 313-317, 1981.

- [27] B. H. Nygren, T. Sandstrom, J. E. Stenberg and L. B. Stilbert, "Method and member for detecting and/or measuring the concentration of a chemical substance". United States of America Patent 4,558,012, 10 December 1985.
- [28] H. Nygren, T. Sandström and M. Stenberg, "Direct Visual Detection of Protein Antigen: Importance of Surface Concentration," *Journal of Immunological Methods*, vol. 59, pp. 145-149, 1983.
- [29] T. Sandstrom, M. Stenberg and H. Nygren, "Visual detection of organic monomolecular films by interference colors," *Applied Optics*, vol. 24, no. 4, pp. 472-479, 1985.
- [30] T. Sandstrom, L. Stiblert and D. M. Maul, "Devices and methods for detection of an analyte based upon light interference". USA Patent 5,494,829, 27 February 1996.
- [31] J. M. Smith, M. C. Bauman and P. C. Fuchs, "An Optical Immunoassay for the Direct Detection of Group A Strep Antigen," *Laboratory Medicine*, vol. 26, no. 6, pp. 408-410, 1995.
- [32] T. M. Nguyen, D. W. Gauthier, T. D. Myles, B. S. Nuwayhid, M. A. Viana and P. C. Schreckenberger, "Detection of group B streptococcus: Comparison of an optical immunoassay with direct plating and broth-enhanced cultrue methods," *Journal of Maternal-Fetal Medicine*, vol. 7, pp. 172-176, 1998.
- [33] D. Schultze, Y. Thomas and W. Wunderli, "Evaluation of an Optical Immunoassay for the Rapid Detection of Influenza A and B Viral Antigens," *European Journal of Clinical Microbiology and Infectious Disease*, vol. 20, pp. 280-283, 2001.
- [34] C. I. Banda, E. H. Koumans, M. K. Sawyer, J. Dover, A. O'Connor, J. R. Papp, E. R. Unger, J. Braxton and C. M. Black, "Evaluation of the rapid BioStar optical immunoassay for detection of *Chlamydia trachomatis* in adolescent women," *Journal of Clinical Microbiology*, vol. 47, no. 1, pp. 215-216, 2009.
- [35] R. Ostroff, A. Ettinger, H. La, M. Rihanek, L. Zalman, J. Meador, A. K. Patick, S. Worland and B. Polisky, "Rapid multiserotype detection of human rhinoviruses on optically coated silicon surfaces," *Journal of Clinical Virology*, vol. 21, no. 2, pp. 105-117, 2001.
- [36] L. V. Dong, K. H. Eng, L. K. Quyen and P. Gopalakrishnakone, "Optical immunoassay for snake venom detection," *Biosensors and Bioelectronics*, vol. 19, pp. 1285-1294, 2004.
- [37] I. H. Malitson, "Interspecimen Comparison of the Refractive Index of Fused Silica," *Journal of the Optical Society of America*, vol. 55, no. 10, pp. 1205-1209, 1965.
- [38] T. L. McMeekin, M. L. Groves and N. J. Hipp, "Refractive Indices of Amino Acids, Proteins, and Related Substances," in *Amino Acids and Serum Proteins*, Philadelphia, American Chemical Society, 1964, pp. 54-66.

- [39] J. Vörös, "The Density and Refractive Index of Adsorbing Protein Layers," *Biophysics Journal*, vol. 87, no. 1, pp. 553-561, 2004.
- [40] J. Benesch, A. Askendal and P. Tengvall, "The determination of thickness and surface mass density of mesothick immunoprecipitate layers by null ellipsometry and protein 125iodine labeling," *Journal of Colloid and Interface Science*, vol. 249, no. 1, pp. 84-90, 2002.
- [41] R. G. C. Oudshoorn, R. P. H. Kooyman and J. Greve, "Refractive index and layer thickness of an adsorbing protein as reporters of monolayer formation," *Thin Solid Films*, Vols. 284-285, pp. 836-840, 1996.
- [42] T. Sandstrom, L. Stibler and D. M. Maul, "Method and instrument for detection of change of thickness or refractive index for a thin film substrate". USA Patent 5,613,171, 20 May 1997.
- [43] S. D. Alvarez, C. Li, C. E. Chiang, I. K. Schuller and M. J. Sailor, "A Label-Free Porous Alumina Interferometric Immunosensor," *ACS Nano*, vol. 3, no. 10, pp. 3301-3307, 2009.
- [44] S. Pan and L. J. Rothberg, "Interferometric Sensing of Biomolecular Binding Using Nanoporous Aluminum Oxide Templates," *Nano Letters*, vol. 3, no. 6, pp. 811-814, 2003.
- [45] H. U. Osmanbeyoglu, T. B. Hur and H. K. Kim, "Thin alumina nanoporous membranes for similar size biomolecule separation," *Journal of Membrane Science*, vol. 343, no. 1-2, pp. 1-6, 2009.
- [46] S. Simovic, D. Losic and K. Vasilev, "Controlled drug release from porous materials by plasma polymer deposition," *Chemical Communications*, vol. 46, no. 8, pp. 1317-1319, 2010.
- [47] K. C. Popat, E. E. Swan, V. Mukhatyar, K. Chatvanichkul, G. K. Mor, C. A. Grimes and T. A. Desai, "Influence of nanoporous alumina membranes on long-term osteoblast response," *Biomaterials*, vol. 26, no. 22, pp. 4516-4522, 2005.
- [48] R. E. Burrell, A. G. Naylor and A. M. Rosenfeld. US Patent 5,124,172, 1992.
- [49] S. S. Djokić and R. E. Burrell, "Visual detection of protein adsorption onto electrochemically oxidized aluminum surfaces," *Biosensors & Bioelectronics*, vol. 13, pp. 271-278, 1998.
- [50] D. A. Vermilyea, "The Kinetics of Formation and Structure of Anodic Oxide Films on Tantalum," *Acta Metallurgica*, vol. 1, pp. 283-294, 1953.
- [51] G. Wypych, *Handbook of Fillers 3rd Edition*, ChemTec Publishing, 2010.
- [52] K. Nassau, *The Physics and Chemistry of Color: The Fifteen Causes of Color*, NY: John Wiley & Sons, Inc., 1983.

- [53] "Interference colours," OpenLearn, [Online]. Available: <http://www.open.edu/openlearn/science-maths-technology/science/introduction-minerals-and-rocks-under-the-microscope/content-section-2.2.5>. [Accessed 05 05 2018].
- [54] R. G. Ben, "1931 Colour Space," Wikipedia, [Online]. Available: <https://commons.wikimedia.org/w/index.php?curid=7889658>. [Accessed 18 June 2018].
- [55] L. S. Jung, C. T. Campbell, T. M. Chinowsky, M. N. Mar and S. S. Yee, "Quantitative Interpretation of the Response of Surface Plasmon Resonance Sensors to Adsorbed Films," *Langmuir*, vol. 14, no. 19, pp. 5636-5648, 1998.
- [56] P. G. Sheasby and R. Pinner, *The Surface Treatment and Finishing of Aluminum and its Alloys - 6th Edition*, Finishing Publications Ltd., 2001.
- [57] A. G. Naylor, Interviewee, [Interview]. May 2016.
- [58] J. L. Vossen and W. Kern, *Thin Film Processes*, New York: Academic Press, Inc., 1978.
- [59] R. F. Bunshah, *Handbook of Deposition Technologies for Films and Coatings: Science, Technology and Applications Second Edition*, Park Ridge: Noyes Publications, 1994.
- [60] J. A. Thornton, "The microstructure of sputter-deposited coatings," *Journal of Vacuum Science and Technology*, vol. 4, no. 6, pp. 3059-3065, 1986.
- [61] J. A. Thornton, "Influence of apparatus geometry and deposition conditions on the structure and topography of thick sputtered coatings," *Journal of Vacuum Science & Technology*, vol. 11, pp. 666-670, 1974.
- [62] J. A. Thornton and D. W. Hoffman, "Stress-related Effects in Thin Films," *Thin Solid Films*, vol. 171, pp. 5-31, 1989.
- [63] J. G. Han, "Recent progress in thin film processing by magnetron sputtering with plasma diagnostics," *Journal of Physics D: Applied Physics*, vol. 42, p. 043001, 2009.
- [64] R. Messier, A. P. Giri and R. A. Roy, "Revised structure zone model for thin film physical structure," *Journal of Vacuum Science and Technology A*, vol. 2, pp. 500-503, 1984.
- [65] K. Chan and B. Teo, "Sputtering power and deposition pressure effects on the electrical and structural properties of copper thin films," *Journal of Materials Science*, vol. 40, pp. 5971-5981, 2005.
- [66] D. W. Hoffman and J. A. Thornton, "The compressive stress transition in Al, V, Zr, Nb and W metal films sputtered at low working pressures," *Thin Solid Films*, vol. 45, pp. 387-396, 1977.

- [67] S. Van Gils, T. Dimogerontakis, G. Buytaert, E. Stijns, P. Skeldon, G. E. Thompson and M. R. Alexander, "Optical properties of magnetron-sputtered and rolled aluminum," *Journal of Applied Physics*, vol. 98, 2005.
- [68] W. Lee and S. Park, "Porous Anodic Aluminum Oxide: Anodization and Templated Synthesis of Functional Nanostructures," *Chemical Reviews*, vol. 114, pp. 7487-7556, 2014.
- [69] G. D. Bengough and J. M. Stuart, "Improved process of protecting surfaces of aluminium or aluminium alloys". UK Patent 223,994, 2 August 1923.
- [70] G. D. Sulka, "Highly Ordered Anodic Porous Alumina Formation by Self-Organization Anodizing," in *Nanostructured Materials in Electrochemistry*, Weinheim, Wiley-VCH, 2008, pp. 1-97.
- [71] W. Lee and S. Park, "Porous Anodic Aluminum Oxide: Anodization and Templated Synthesis of Functional Nanostructures," *Chemical Reviews*, vol. 114, pp. 7487-7556, 2014.
- [72] G. E. Thompson, "Porous anodic alumina: fabrication, characterization and applications," *Thin Solid Films*, vol. 297, pp. 192-201, 1997.
- [73] A. Mutalib Md Jani, D. Losic and N. H. Voelcker, "Nanoporous anodic aluminium oxide: Advances in surface engineering and emerging applications," *Progress in Materials Science*, vol. 58, pp. 636-704, 2013.
- [74] R. C. Furneaux, W. R. Rigby and A. P. Davidson, "The formation of controlled-porosity membranes from anodically oxidized aluminum," *Nature*, vol. 337, no. 12, pp. 147-149, 1989.
- [75] G. E. Thompson, "Porous anodic alumina: fabrication, characterization and applications," *Thin Solid Films*, vol. 297, pp. 192-201, 1997.
- [76] G. E. Thompson, R. C. Furneaux, G. C. Wood, J. A. Richardson and J. S. Goode, "Nucleation and growth of porous anodic films on aluminum," *Nature*, vol. 272, pp. 433-435, 1978.
- [77] K. R. Herbert, S. P. Albu, I. Paramasivam and P. Schmuki, "Morphological instability leading to formation of porous anodic oxide films," *Nature Materials*, vol. 11, pp. 162-166, 2012.
- [78] J. Wang, C. Wang, Y. Li and W. Liu, "Optical constants of anodic aluminum oxide films formed in oxalic acid solution," *Thin Solid Films*, vol. 516, pp. 7689-7694, 2008.
- [79] Y. Wang, L. Chen, Z. Wu, S. Xu, H. Cui and W. Xu, "Subtle vertical structures of porous anodic alumina films for use as waveguides," *Nanotechnology*, vol. 28, no. 18, 2017.

- [80] A. Hierro-Rodriguez, P. Rocha-Rodrigues, F. Valdes-Bango, J. M. Alameda, P. A. Jorge, J. L. Santos, J. P. Araujo and J. M. Teixeira, "On the anodic aluminium oxide refractive index of nanoporous templates," *Journal of Physics D: Applied Physics*, vol. 48, no. 45, p. 455105, 2015.
- [81] M. M. Rahman, E. Garcia-Caurel, A. Santos, L. F. Marsal, J. Pallares and J. Ferrer-Borrull, "Effect of the anodization voltage on the pore-widening rate of nanoporous anodic alumina," *Nanoscale Research Letters*, vol. 7, no. 474, 2012.
- [82] G. E. Thompson, R. C. Furneaux and G. C. Wood, "The Morphology of Sealed Anodic Films Formed on Aluminium in Phosphoric Acid," *Transactions of the Institute of Metal Finishing*, vol. 53, pp. 97-102, 1975.
- [83] G. D. Davis, T. S. Sun, J. S. Ahearn and J. D. Venables, "Application of surface behaviour diagrams to the study of hydration of phosphoric acid-anodized aluminum," *Journal of Materials Science*, vol. 17, pp. 1807-1818, 1982.
- [84] J. D. Venables, M. E. Tadros and B. M. Ditchek. US Patent 4,308,079, 1981.
- [85] R. L. Parfitt, "Anion Adsorption by Soils and Soil Materials," in *Advances in Agronomy*, Academic Press Inc, 1978, pp. 1-50.
- [86] D. Muljadi, A. M. Posner and J. P. Quirk, "The Mechanism of Phosphate Adsorption by Kaolinite, Gibbsite, and Pseudoboehmite. Part 2. The Location of the Adsorption Sites," *Journal of Soil Science*, vol. 17, no. 2, pp. 230-237, 1966.
- [87] R. D. Ramsier, P. N. Henriksen and A. N. Gent, "Adsorption of Phosphorous Acids on Alumina," *Surface Science*, vol. 203, pp. 72-88, 1988.
- [88] D. Costa, L. Savio and C.-M. Pradier, "Adsorption of Amino Acids and Peptides on Metal and Oxide Surfaces in Water Environment: A Synthetic and Prospective Review," *The Journal of Physical Chemistry B*, vol. 120, pp. 7039-7052, 2016.
- [89] E. Greiner, K. Kumar, M. Sumit, A. Giuffre, W. Zhao, J. Pedersen and N. Sahai, "Adsorption of L-glutamic acid and L-aspartic acid to  $\gamma$ -Al<sub>2</sub>O<sub>3</sub>," *Geochimica et Cosmochimica Acta*, vol. 133, pp. 142-155, 2014.
- [90] M. Trujillo, J. Valencia and J. C. Calvo, "Peptide solubility, structure and charge position effect on adsorption by aluminium hydroxide," *Revista Colombiana de Química*, vol. 35, no. 2, pp. 135-146, 2006.
- [91] R. J. Sepelyak, J. R. Feldkamp, T. E. Moody, J. L. White and S. L. Hem, "Adsorption of Pepsin by Aluminum Hydroxide I: Adsorption Mechanism," *American Pharmaceutical Association*, vol. 73, no. 11, p. 1514, 1984.

- [92] J. P. Murray and S. J. Laband, "Degradation of Poliovirus by Adsorption on Inorganic Surfaces," *Applied and Environmental Microbiology*, vol. 37, no. 3, pp. 480-486, 1979.
- [93] J. P. Murray, *Physical Chemistry of Virus Adsorption and Degradation on Inorganic Surfaces: Its relation to wastewater treatment*, Cincinnati, OH: United States Environmental Protection Agency, 1980.
- [94] R. B. Thurman and C. P. Gerba, "Characterization of the effect of aluminum metal on poliovirus," *Journal of Industrial Microbiology*, vol. 3, pp. 33-38, 1988.
- [95] W. R. Bowen and Q. Gan, "Properties of Microfiltration Membranes: The Effects of Adsorption and Shear on the Recovery of an Enzyme," *Biotechnology and Bioengineering*, vol. 40, pp. 491-497, 1992.
- [96] D. C. Kim, A. Jang and D. J. Kang, "Biological functionality of active enzyme structures immobilized on various solid surfaces," *Current Applied Physics*, vol. 9, p. 1454, 2009.
- [97] A. Wittayanukulluk, D. Jiang, F. E. Regnier and S. L. Hem, "Effect of microenvironment pH of aluminum hydroxide adjuvant on the chemical stability of adsorbed antigen," *Vaccine*, vol. 22, p. 1172, 2004.
- [98] T. Clapp, P. Siebert, D. Chen and L. J. Braun, "Vaccines with Aluminum-Containing Adjuvants: Optimizing Vaccine Efficacy and Thermal Stability," *Journal of Pharmaceutical Science*, vol. 100, no. 2, p. 388, 2011.
- [99] P. Takmakov, I. Vlassiuk and S. Smirnov, "Application of anodized aluminum in fluorescence detection of biological species," *Analytical and Bioanalytical Chemistry*, vol. 385, no. 5, pp. 954-958, 2006.
- [100] S. Tanvir, J. Pantigny, P. Boulnois and S. Pulvin, "Covalent immobilization of recombinant human cytochrome CYP2E1 and glucose-6-phosphate dehydrogenase in alumina membrane for drug screening applications," *Journal of Membrane Science*, vol. 329, pp. 85-90, 2009.
- [101] G. Gonzalez, G. Priano, M. Gunther and F. Battaglini, "Mass transport effect of mesoscopic domains in the amperometric response of an electroactive species: Modeling for its applications in biomolecule detection," *Sensors and Actuators B: Chemical*, vol. 144, no. 2, pp. 349-353, 2008.
- [102] P. Milka, I. Krest and M. Keusgen, "Immobilization of alliinase on porous aluminum oxide," *Biotechnology and Bioengineering*, vol. 69, no. 3, pp. 344-348, 2000.
- [103] H. P. Jennissen, "Immobilizing mediator molecules via anchor molecules on metallic implant materials containing oxide layer". USA Patent 6,635,269 B1, 21 Oct 2003.

- [104] P. Rezvanian, M. Arroyo-Hernandez, M. Ramos, R. Daza, M. Elices, G. V. Guinea and J. Pérez-Rigueira, "Development of a versatile procedure for the biofunctionalization of Ti-6Al-4V implants," *Applied Surface Science*, vol. 387, pp. 656-660, 2016.
- [105] D. Hyndman, G. Lever, R. Burrell and T. G. Flynn, "Protein Immobilization to Alumina Supports: I. Characterization of Alumina-Organophosphate Ligand Interactions and Use in the Attachment of Papain," *Biotechnology and Bioengineering*, vol. 40, pp. 1319-1327, 1992.
- [106] D. Hyndman, R. Burrell, G. Lever and T. G. Flynn, "Protein Immobilization to Alumina Supports: II. Papain Immobilization to Alumina via Organophosphate Linkers," *Biotechnology and Bioengineering*, vol. 40, pp. 1328-1336, 1992.
- [107] Y. Lu, D. Zhang, Q. Zhang, Y. Huang, S. Luo, Y. Yao, S. Li and Q. Liu, "Impedance spectroscopy analysis of human odorant binding proteins immobilized on nanopore arrays for biochemical detection," *Biosensors and Bioelectronics*, vol. 79, p. 251, 2016.
- [108] J. Dai, G. L. Baker and M. L. Bruening, "Use of porous membranes modified with polyelectrolyte multilayers as substrates for protein arrays with low nonspecific adsorption," *Analytical Chemistry*, vol. 78, no. 1, pp. 135-140, 2005.
- [109] G. B. Oliveira, J. L. Filho, M. E. Chaves, W. M. Azevedo and L. B. Carvalho, "Enzyme immobilization on anodic aluminum oxide/polyethyleneimine or polyaniline composites," *Reactive and Functional Polymers*, vol. 68, no. 1, pp. 27-32, 2008.
- [110] S. D. Alvarez, C. Li, C. E. Chiang, I. K. Schuller and M. J. Sailor, "A label-free porous alumina interferometric immunosensor," *ACS Nano*, vol. 3, no. 10, pp. 3301-3307, 2009.
- [111] B. L. Adams, A. S. Finch, M. M. Hurley, D. A. Sarkes and D. N. Stratis-Cullum, "Genetically Engineered Peptides for Inorganics: Study of an Unconstrained Bacterial Display Technology and Bulk Aluminum Alloy," *Materials Views*, vol. 25, pp. 4585-4591, 2013.
- [112] R. Zuo, D. Ornek and T. K. Wood, "Aluminum- and mild steel-binding peptides from phage display," *Applied Genetics and Molecular Biotechnology*, vol. 68, pp. 505-509, 2005.
- [113] Y. Gwak, J. Park, M. Kim, H. S. Kim, M. J. Kwon, S. J. Oh, Y. Kim and E. Jin, "Creating Anti-icing Surfaces via the Direct Immobilization of Antifreeze Proteins on Aluminum," *Scientific Reports*, vol. 5, no. 12019, pp. 1-9, 2015.
- [114] R. E. Burrell, "Aluminum Oxide Surfaces and Interface Molecules". Provisional Patent. Filed Feb. 20, 2018.
- [115] M. Huang, A. C. Rigby, X. Morelli, M. A. Grant, G. Huang, B. Furie, B. Seaton and B. C. Furie, "Structural basis of membrane binding by Gla domains of vitamin K-dependent proteins," *Nature Structural Biology*, vol. 10, no. 9, pp. 751-756, 2003.

- [116] T. K. Lim, V. A. Bloomfield and G. L. Nelsestuen, "Structure of the Prothrombin- and Blood Clotting Factor X-Membrane Complexes," *Biochemistry*, vol. 16, no. 19, pp. 4177-4181, 1977.
- [117] K. G. Mann, M. E. Nesheim, W. R. Church, P. Haley and S. Krishnaswamy, "Surface-Dependent Reactions of the Vitamin K-Dependent Enzyme Complexes," *Blood*, vol. 76, no. 1, pp. 1-16, 1990.
- [118] D. A. Walz, D. Hewett-Emmett and W. H. Seegers, "Amino acid sequence of human prothrombin fragments 1 and 2," *Proceedings of the Natural Academy of Sciences USA*, vol. 74, no. 5, pp. 1969-1972, 1977.
- [119] A. Violante, C. Colombo and A. Buondonno, "Competitive Adsorption of Phosphate and Oxalate by Aluminum Oxides," *Soil Science Society of America Journal*, vol. 55, pp. 65-70, 1991.
- [120] J. van den Brand, O. Blajiev, P. C. Beentjes, H. Terryn and J. H. de Wit, "Interaction of Anhydride and Carboxylic Acid Compounds with Aluminum Oxide Surfaces Studied Using Infrared Reflection Absorption Spectroscopy," *American Chemical Society*, pp. 6308-6317, 2004.
- [121] R. Nave, "Oil Film Interference," *Hyperphysics*, [Online]. Available: <http://hyperphysics.phy-astr.gsu.edu/hbase/phyopt/oilfilm.html>. [Accessed 19 December 2016].
- [122] "Interference by Thin Film," *askIITians.com*, [Online]. Available: <https://www.askiitians.com/iit-jee-wave-optics/interference-by-thin-film/>. [Accessed 05 05 2018].

## Chapter 2 Tantalum

### The Effect of Tantalum Microstructure on Interference Colouring of Anodized

#### Aluminum-Tantalum Thin Films

##### **Introduction**

In a thin film diagnostic device, the tantalum metal layer is a crucial part of the colour generation. Tantalum, along with the other valve metals i.e. niobium, titanium, etc., can generate interference colours when oxidized, based on the oxide thickness. Microstructure has a strong effect on the optical properties of tantalum. Under equilibrium conditions bulk tantalum has a body-centered cubic crystal structure ( $\alpha$ -Ta) [1]. Since the 1960s, tantalum has been known to have a metastable tetragonal crystal structure ( $\beta$ -Ta) when sputter deposited under certain conditions [2, 3].  $\beta$ -Ta is known to have a higher electrical resistivity (170-210  $\mu\Omega$  cm) than  $\alpha$ -Ta (13-20  $\mu\Omega$  cm) and is a harder and more brittle material [1]. A study by Muth [4], showed significant differences in the optical properties between  $\alpha$  and  $\beta$  tantalum ( $\beta$ -Ta:  $\eta = 3.43-3.66i$ ,  $\alpha$ -Ta:  $\eta = 2.90-2.41i$ ;  $\lambda = 5461\text{\AA}$ ). Previous studies have shown that working gas pressure during sputter coating has a significant effect on the phase of tantalum deposited, with  $\alpha$ -Ta being deposited within certain pressure ranges and mixtures of  $\alpha$  and  $\beta$  forming at higher pressures [5, 6]. Thornton and Hoffman [7] showed how the optical reflectance of sputtered tantalum films decreased with increased sputter gas pressure. This decrease in reflectance was attributed to a shift of the microstructure from a smooth, dense film to a rough, open film, therefore leading to an increase in the amount of scattered light.

Interference colours from thin oxide films on tantalum were studied extensively by Charlesby and Polling [8] and Young [9]. A more recent study by Cui-Cui et al. [10] shows the range of the colors

produced from anodic tantalum oxide films. Production of an interference colour from an oxide film depends mostly on the reflectivity of the air/oxide interface. To create a saturated (or strong) interference colour, the reflected light from the air/oxide interface and the light from the oxide/metal interface must each be 50% of the outgoing light. Thus, equal portions of light are interfering and producing the most saturated of interference colours. For example, it is difficult to produce interference colours on pure aluminum because its reflectivity is on the order of 90% in the visible spectrum (390-700nm) [11]. Therefore, the light reflected off the metal surface overwhelms any light reflected off the surface oxide, diminishing the ability to see an interference colour. Tantalum is a good material to use in this application because its reflectivity in the visual spectrum is on the order of 40-60%, and therefore better balances the light off the oxide and metal surface [8].

The purpose of this study was to understand if tantalum microstructure has an effect on the interference colours produced by anodized aluminum-tantalum thin films. Silicon wafers were coated in a thin layer of tantalum (~230nm) at various gas pressures and then subsequently coated in a layer of aluminum (~120nm). These films were then anodized to produce a porous aluminum oxide over a tantalum oxide barrier layer over tantalum metal. The microstructure and optical properties were studied using scanning electron microscopy (SEM), X-ray diffraction (XRD), energy dispersive X-ray spectroscopy (EDX) and reflectance spectroscopy, and the resulting interference colours observed for differences.

## **Materials and Methods**

### *Deposition of tantalum thin films*

Tantalum thin films were deposited onto unprocessed <100> silicon wafers, 100mm in diameter (University Wafers, South Boston, MA), at the NAIT Nanotechnology Centre for Applied

Research using a Materials Research Corporation DC-magnetron planar sputtering machine to a thickness of  $226.5 \pm 3.8$  nm (wafer to wafer variation). A constant power density of  $1.54$  W/cm<sup>2</sup> and target-to-substrate distance of 70 mm was used. Sputtering was conducted at working Ar gas pressures of 10, 15, 20, 25, and 30 mTorr (135 sccm) with a tantalum target 20.3 cm in diameter and of 99.95% purity (Kurt J. Lesker Company, Jefferson Hills, PA). This gas pressure range was chosen from Thornton and Hoffman's work [12], as 10 mTorr was found to be the transition point from Zone T to Zone 1 for their work. The tantalum target was soldered to a water-cooled backing plate using indium. The base pressure of the system was  $1.8 \times 10^{-6}$  Torr. Sputtering was conducted with a static substrate, with flux normal to the surface. Thickness measurements were conducted by profilometry. A glass microscope slide was covered with a small square mask during deposition. The mask was removed post deposition and then step profiles were made using a KLA-Tencor Alpha Step 300 profilometer (KLA-Tencor Corporation, Milpitas, CA). An average thickness was taken from 3 to 5 measurements for each spot. A scan rate of 0.05 mm/sec was used over 0.5 mm and a stylus force of 2 mg.

### *Reflectance Spectroscopy*

The tantalum coated wafers were measured for optical reflectance to understand the change in reflectivity with deposited microstructure. A U-3900H Spectrophotometer (Hitachi Ltd., Tokyo, JP) was used to conduct scans with a wavelength range from 350 to 750 nm at 120 nm/min and at 5° from normal. An aluminum mirror was used as a base reference for reflectance. After coating with aluminum and anodizing, the films were measured for optical reflectance under the same conditions to understand both the surface colour generated and the reflectivity of each microstructure after anodization.

### *Scanning electron microscopy (SEM)*

SEM was used to observe microstructural and topographical changes with changes in sputtering gas pressure. Wafers of deposited tantalum thin films were fractured, and a small sample mounted onto aluminum stubs (Ted Pella Inc., Redding, CA) by carbon tape (PELCO Tabs™, Ted Pella Inc., Redding, CA), and visualized under a Zeiss Sigma Field Emission Scanning Electron Microscope (FESEM) at the nanoFAB – Fabrication and Characterization Center at the University of Alberta. Specimens were viewed at 5.00 keV, an aperture size of 30 µm, and a working distance of about 5 mm.

### *Energy dispersive X-ray spectroscopy (EDX)*

EDX was conducted on each tantalum thin film to measure oxygen content of films sputtered under various gas pressures. An Oxford X-Max detector (Oxford Instruments, Abingdon, UK) with a super atmospheric thin window (SATW) was used. The SEM settings during sample analysis were 5 keV, a working distance of 8.5mm, which was optimized for the EDX detector, and an aperture of 30 µm. All EDX profiles were analyzed using AZtecEnergy EDS analysis software, Version 3.1 (Oxford Instruments, Abingdon, UK).

### *X-Ray Diffraction (XRD)*

XRD was carried out to characterize microstructural differences in the sputtered tantalum films. A Rigaku Ultima IV (Cu-source) diffraction system was used with the thin film substrate holder attachment. Diffraction data was collected between 10 and 90° 2θ at 5.000°/min, using an incident divergence high limiting (DHL) slit of 10.00 mm and glancing angle  $\omega = 0.5^\circ$ . JADE 9™ software, Version 9.3 (Materials Data Inc., Livermore, CA) was used to analyze the XRD patterns along with the International Centre for Diffraction Data (ICDD) database to match peaks.

### *Deposition of aluminum thin films*

The tantalum coated wafers were cleaved into slides about 6.3 cm by 1.3 cm and then coated with aluminum. Aluminum was sputtered to a thickness of  $128.2 \pm 5.7$  nm (11 min at  $11.65 \pm 0.52$  nm/min as measured by SEM side profile analysis post-deposition, wafer to wafer variation) at the nanoFAB – Fabrication and Characterization Centre at the University of Alberta. A constant power density of  $6.6$  W/cm<sup>2</sup>, target-to-substrate distance of 125 mm and working Ar gas pressure of 7 mTorr (51 sccm) was used with a base pressure of  $1 \times 10^{-7}$  Torr. The aluminum target was 7.62 cm in diameter, 99.9995% pure (Kurt J. Lesker Company, Jefferson Hills, PA) and clamped to a water-cooled backing plate. The substrate was held at an angle of  $15^\circ$  with respect to the target and rotated at 20 RPM during deposition.

### *Anodization*

The aluminum-tantalum coated slides were anodized in a 0.4M phosphoric acid – 0.1M oxalic acid mix under potentiostatic conditions at 4V until the current decayed to  $<0.03$  mA/cm<sup>2</sup> using a PAR Model 273a potentiostat/galvanostat (AMETEK Inc., Oakridge, TN). Slides were rinsed before and after with MilliQ deionized water. A magnetic stir plate was used to agitate the solution and the electrolyte temperature was held constant at  $19 \pm 1^\circ\text{C}$ . An aluminum foil (Thermo Fisher Scientific, Waltham, MA) cathode was used with approximately 1:1 surface area ratio with the anode, and was held parallel and 40 mm from the anode. A saturated calomel electrode was used as a reference electrode (Thermo Fisher Scientific, Waltham, MA). Triplicates were performed to measure reproducibility. All anodized films were then viewed at approximately  $75^\circ$  from normal using a polarizing lens to view s-polarized light.

### *Statistics*

Standard deviations are represented by error bars on plots. Numerical results used a one-way ANOVA with a Tukey Multiple Comparisons post hoc test using IBM SPSS Statistics for Windows, Version 24.0 (IBM Corp., Released 2016, Armonk, NY). A Levene's test was used to check for similar sample variance between populations.

## **Results**

### *Reflectance Spectroscopy*

To understand the effects of deposited microstructure on the tantalum metal reflectivity, spectroscopy was used to record reflectance over the visible wavelengths of 350 to 750 nm. The changes in optical reflectance with working gas pressures have been recorded in Figure 2-1. There was a decrease in reflectance ( $\lambda=555\text{nm}$ ) with increased pressure from  $50.8 \pm 1.3\%$  at 10 mTorr to  $38.7 \pm 2.6\%$  at 30 mTorr. A typical plot of reflectance as a function of wavelength is shown in Figure 2-2 for each pressure. All reflectance plots can be found in Appendix 1. The results of the statistical analysis are shown in Table 2-1. The optical reflectance recorded after coating the tantalum with aluminum and anodizing is discussed in the Interference Colour section below.

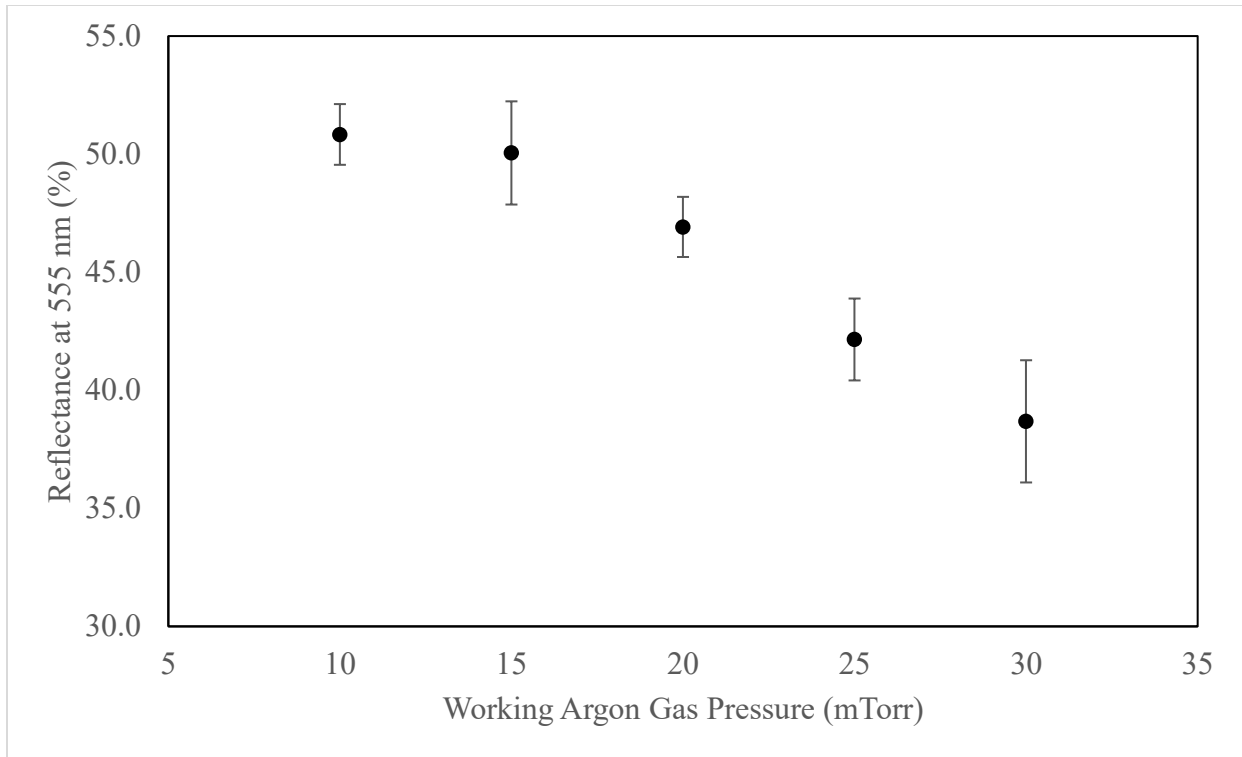


*Figure 2-1. Measured optical reflectance ( $\lambda=555\text{nm}$ ) of sputtered tantalum with increasing working gas pressure. Standard deviations are shown as error bars (10mTorr,  $n=3$ ; 15 to 30 mTorr  $n=6$ ).*

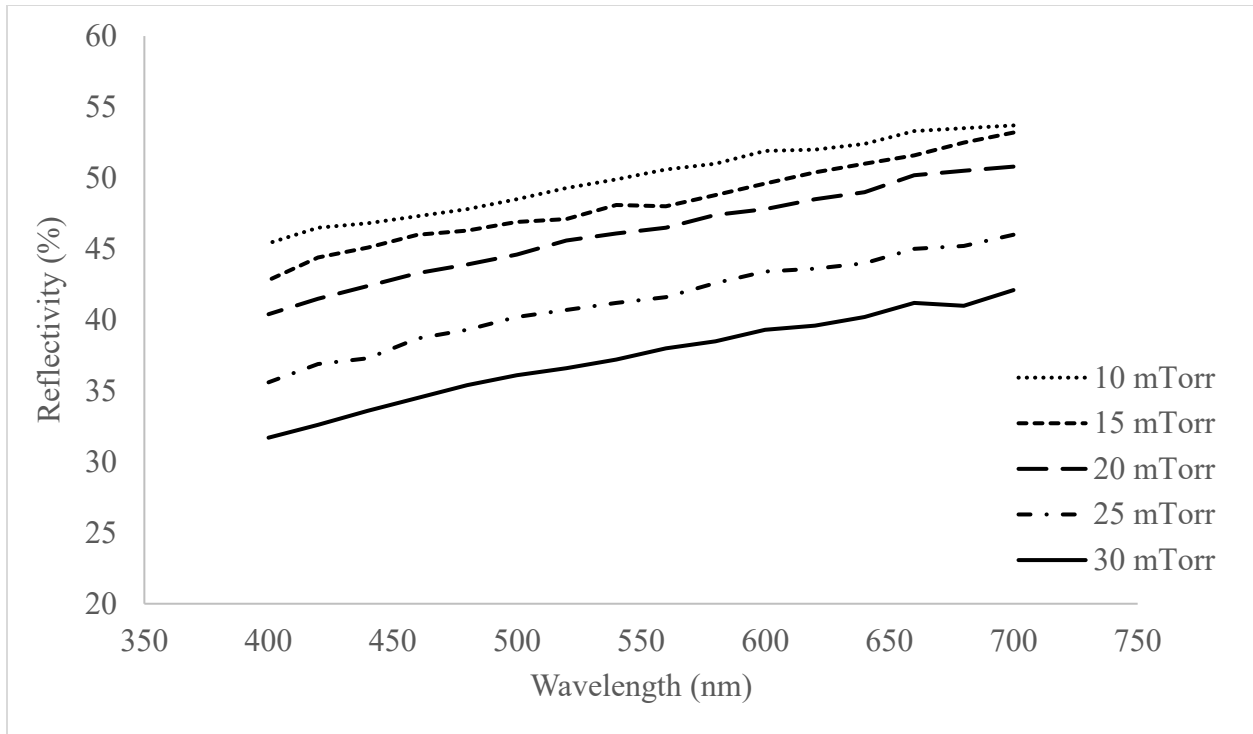


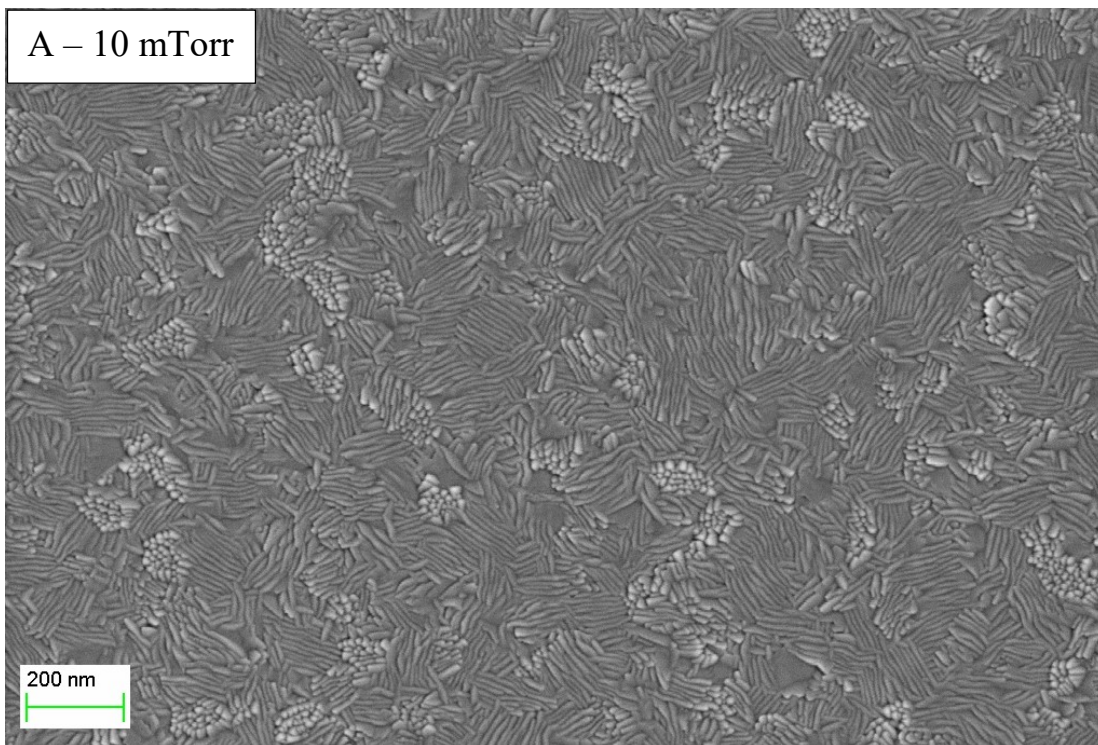
Figure 2-2. Reflectivity vs. wavelength plot for tantalum films sputtered at 10, 15, 20, 25 and 30 mTorr through the visible light spectrum (400nm to 700nm).

Table 2-1. Statistical results of one-way ANOVA and Tukey-Kramer post hoc tests for the change in reflectance measured at 555nm with the change in working Ar gas pressure during sputtering. If post hoc results were insignificant ( $p > 0.05$ ) then they were not listed.

Working Gas Pressure (mTorr)	ANOVA	Post Test Results
10	$p < 0.001$	$p < 0.05$ : 25mTorr ( $\uparrow$ ) $p < 0.001$ : 30mTorr ( $\uparrow$ )
15		$p < 0.05$ : 30mTorr ( $\uparrow$ )
20		$p < 0.05$ : 30mTorr ( $\uparrow$ )
25		$p < 0.05$ : 10mTorr ( $\downarrow$ )
30		$p < 0.05$ : 15mTorr ( $\downarrow$ ), 20mTorr ( $\downarrow$ ) $p < 0.001$ : 10mTorr ( $\downarrow$ )

### *SEM and EDX*

Figure 2-3 shows the change in tantalum microstructure as the working gas pressure was increased from 10 to 30 mTorr. A large change in the microstructure occurred between 15 and 20 mTorr, Figure 2-3B and 2-3C. Films sputtered at 10 and 15 mTorr show acicular particles on the surface. As the pressure is increased to 20 mTorr, the structure changes to round or spherical particles. As the working gas pressure is increased further, the structure becomes rougher and triangular particles start to grow amongst the spherical particles. EDX was used to analyze the change in oxygen content, Figure 2-4. An increase in oxygen was observed with increased pressure during deposition from  $8.2 \pm 3.0$  at.% at 10 mTorr to  $20.5 \pm 5.5$  at.% at 30 mTorr.



*Figure 2-3 continued.*

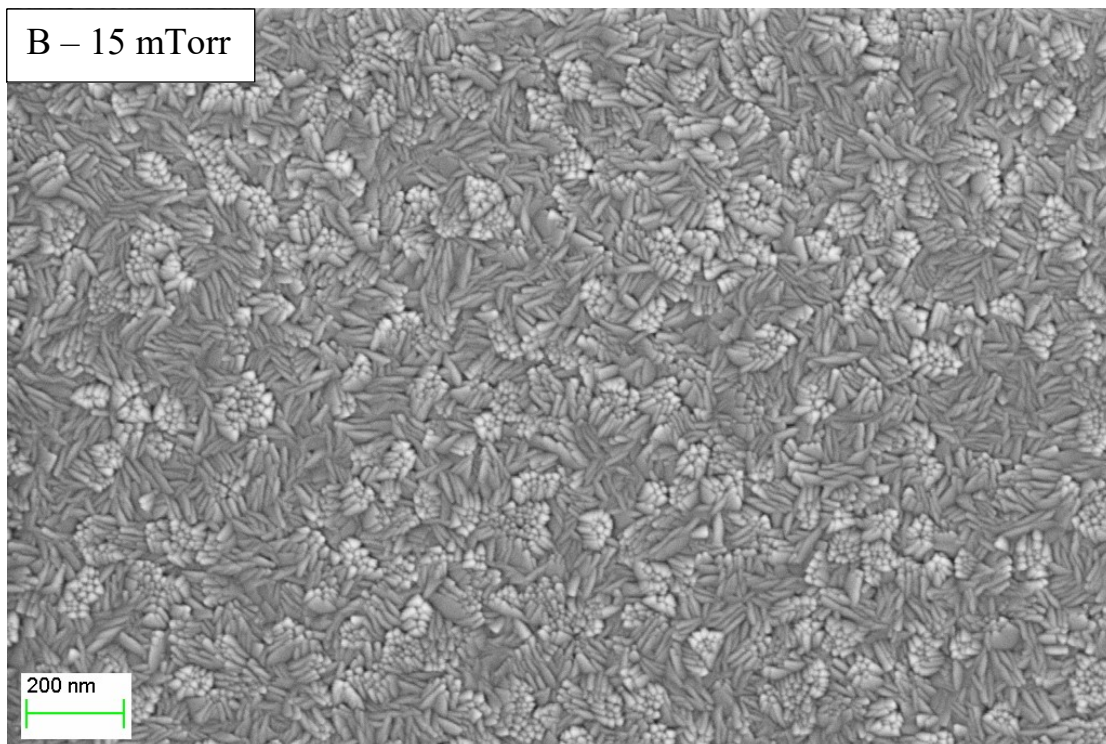


*Figure 2-3 continued.*

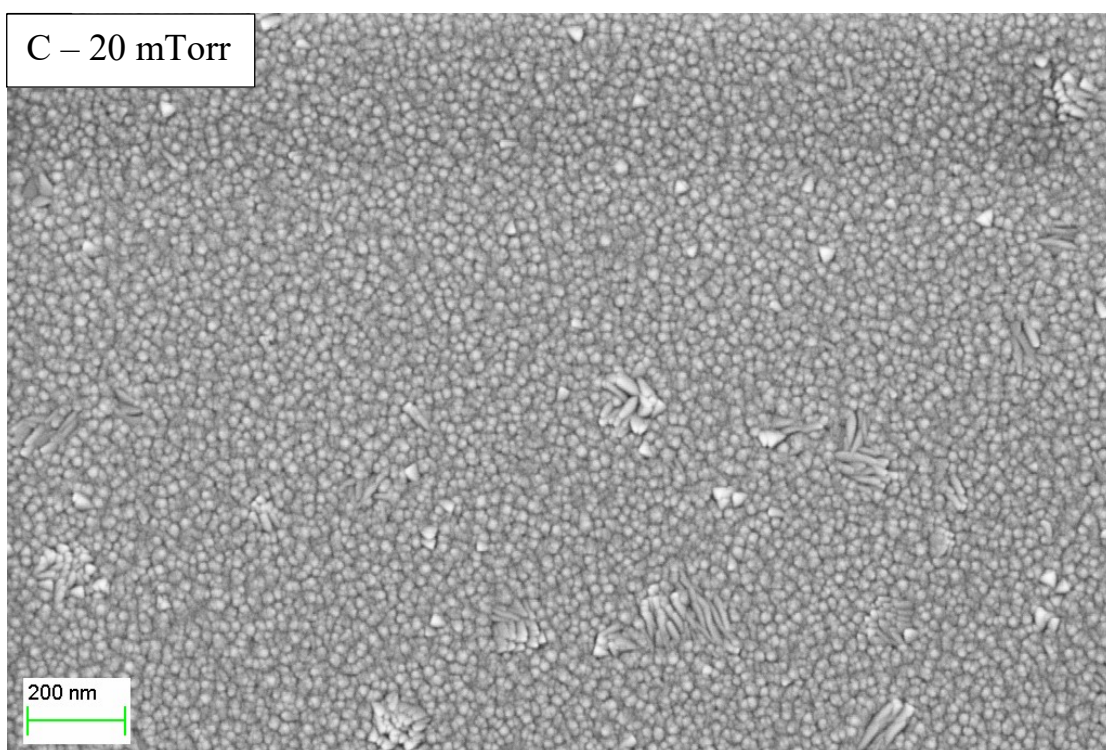


*Figure 2-3 continued.*

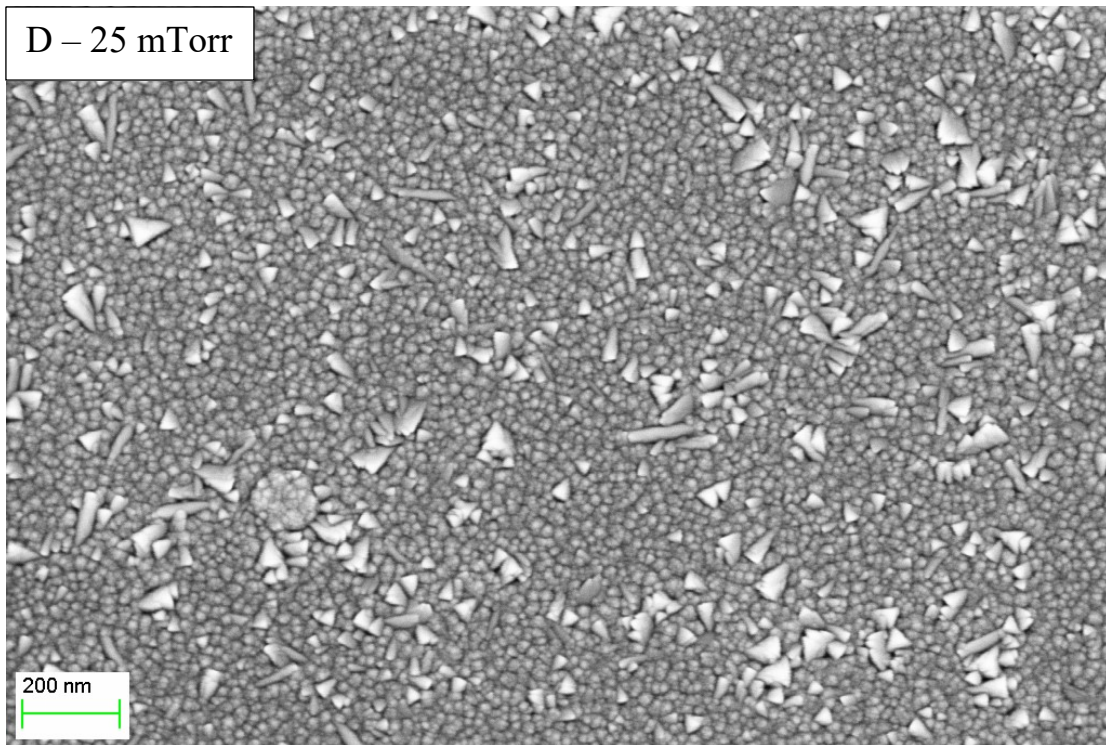


*Figure 2-3 continued.*

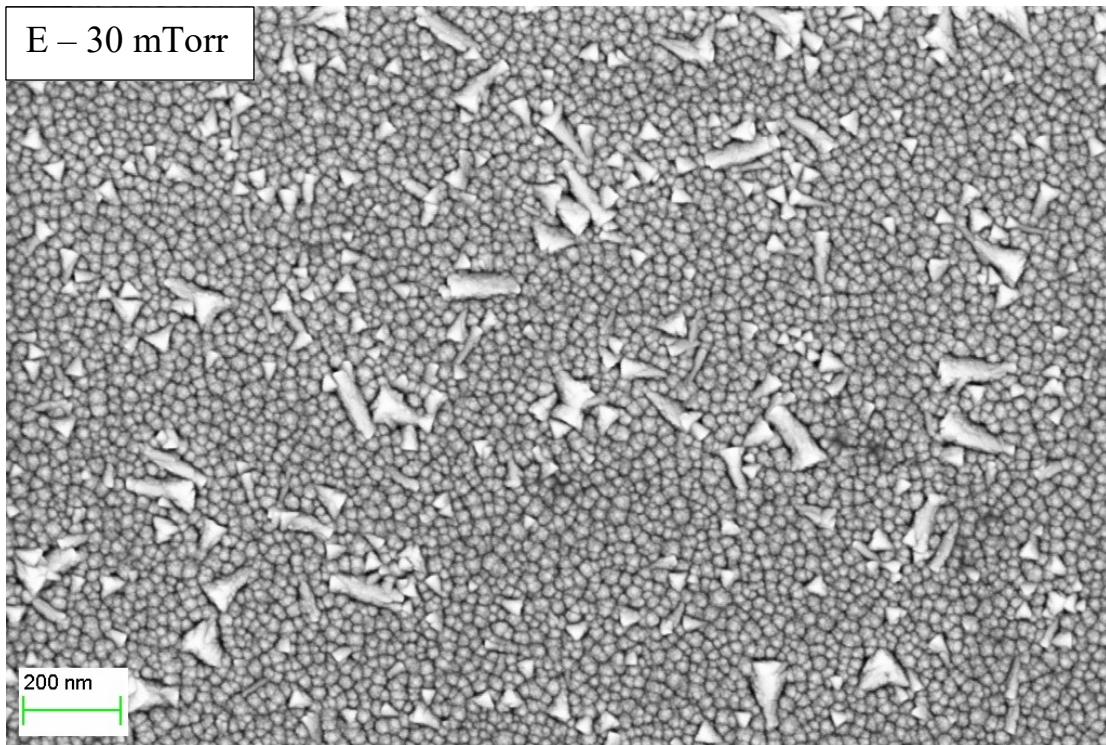


Figure 2-3 continued. FESEM surface images of tantalum films sputtered at different working gas pressures.

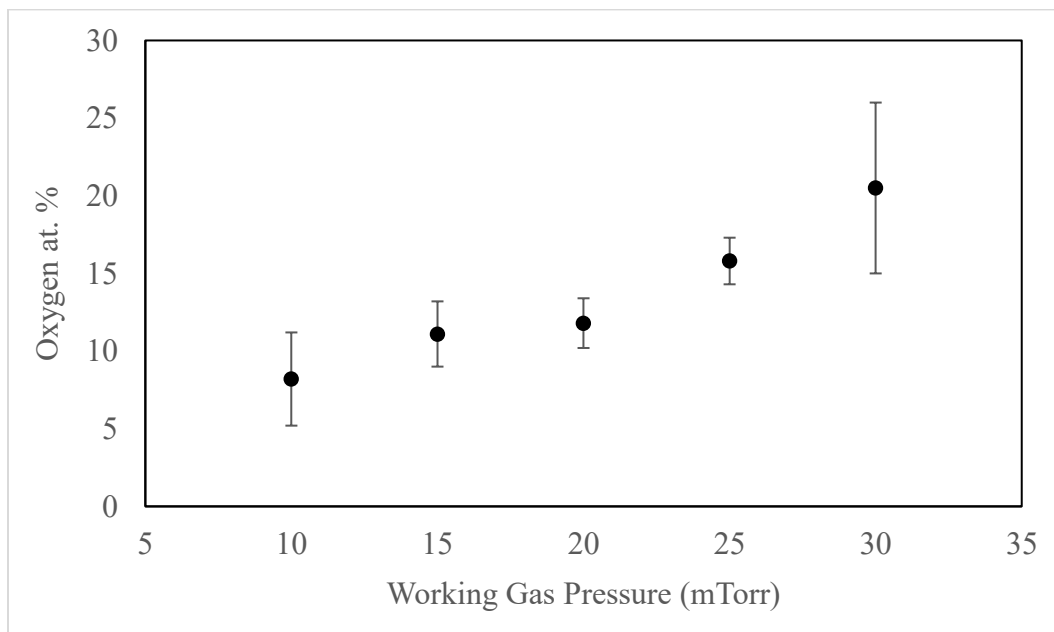


Figure 2-4. Atomic (at.) % oxygen for tantalum films sputtered at various working gas pressures and then exposed to atmosphere. Sample size of  $n=3$  for all data sets.

## XRD

The deposited films were analyzed for crystal structure changes using X-ray diffraction. The XRD patterns for each tantalum film can be seen in Figure 2-5. A summary of the peak analysis for films sputtered from 10 through 30 mTorr is shown in Table 2-2. At 10 mTorr, only peaks corresponding to  $\alpha$ -Ta were found. As the pressure increased, a mixture of peaks was found, corresponding to both  $\alpha$  and  $\beta$ -Ta.

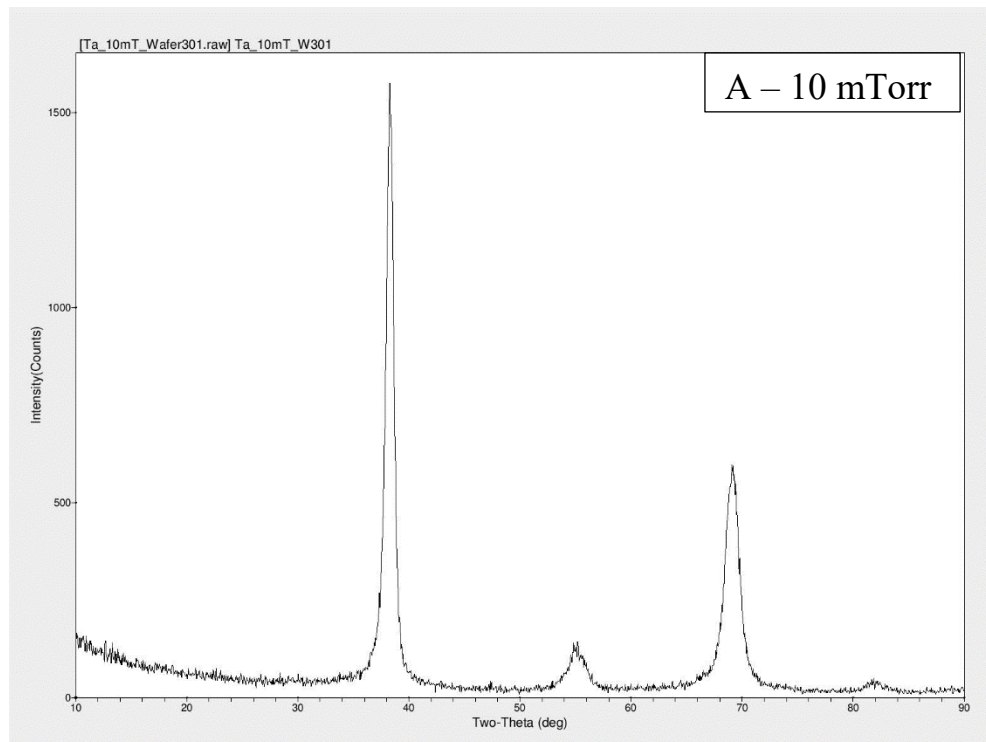


Figure 2-5 continued.

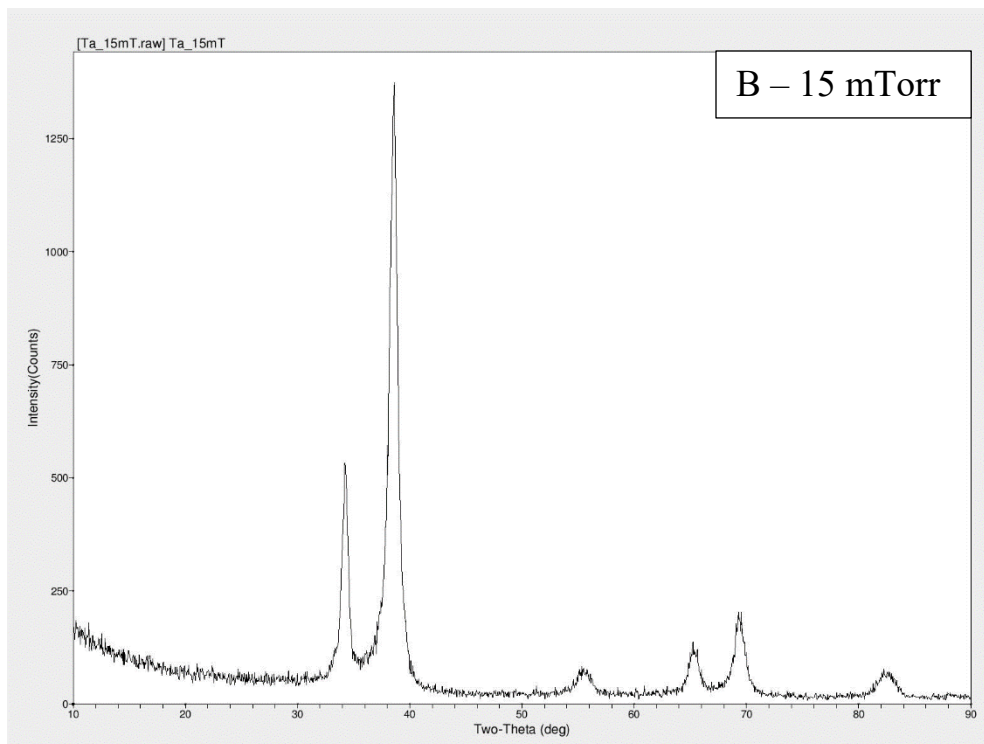


Figure 2-5 continued.

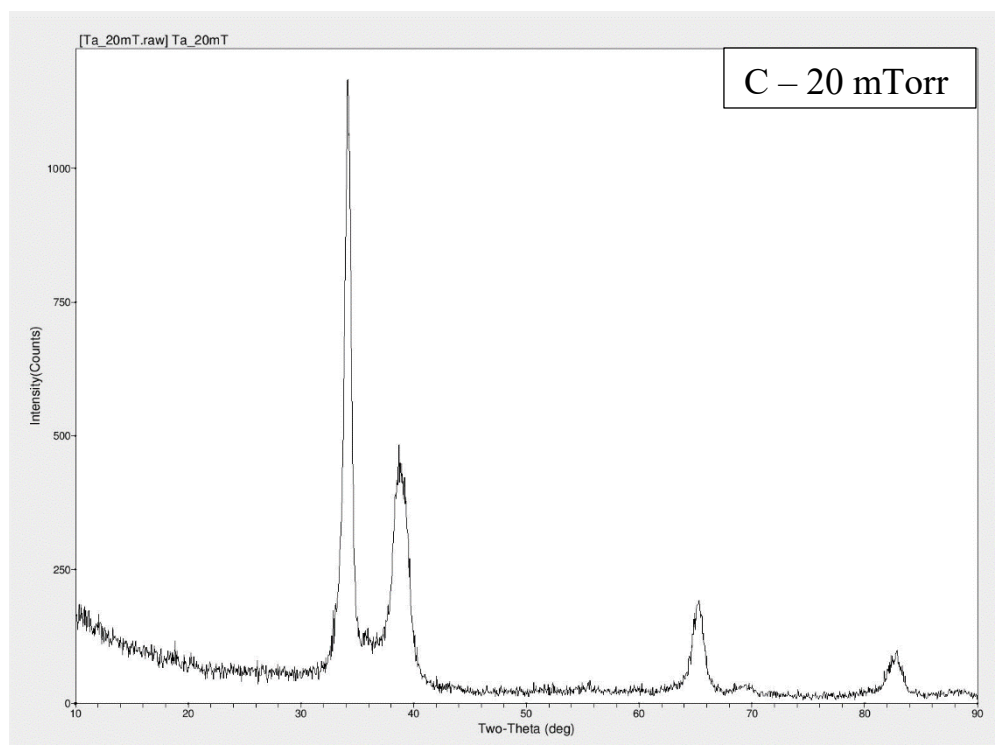


Figure 2-5 continued.

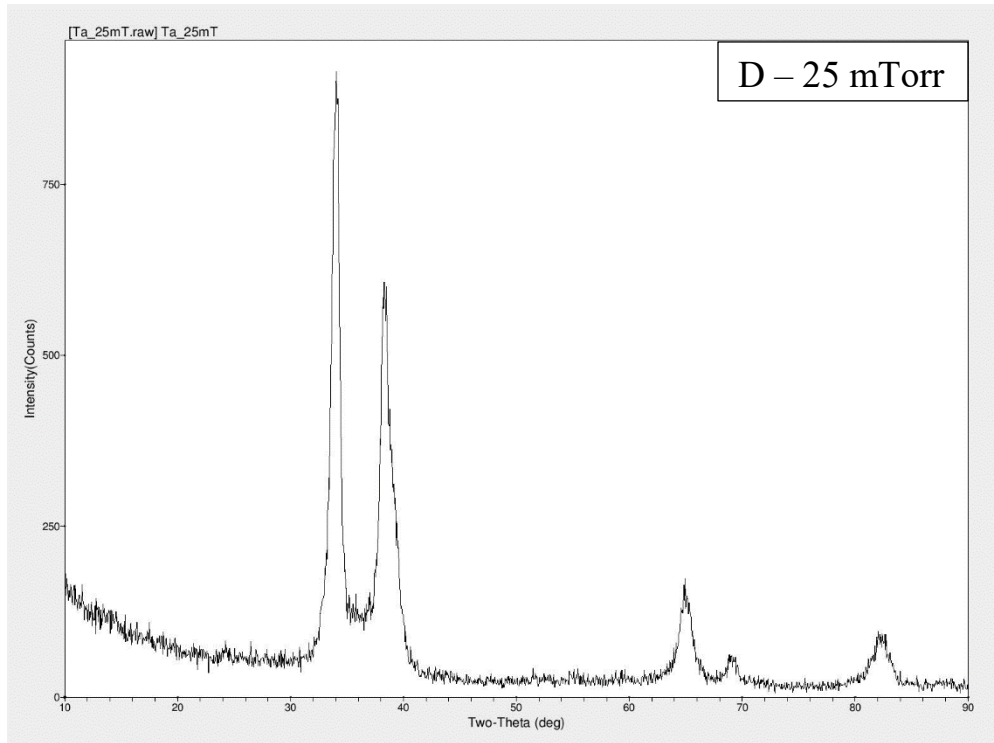


Figure 2-5 continued.

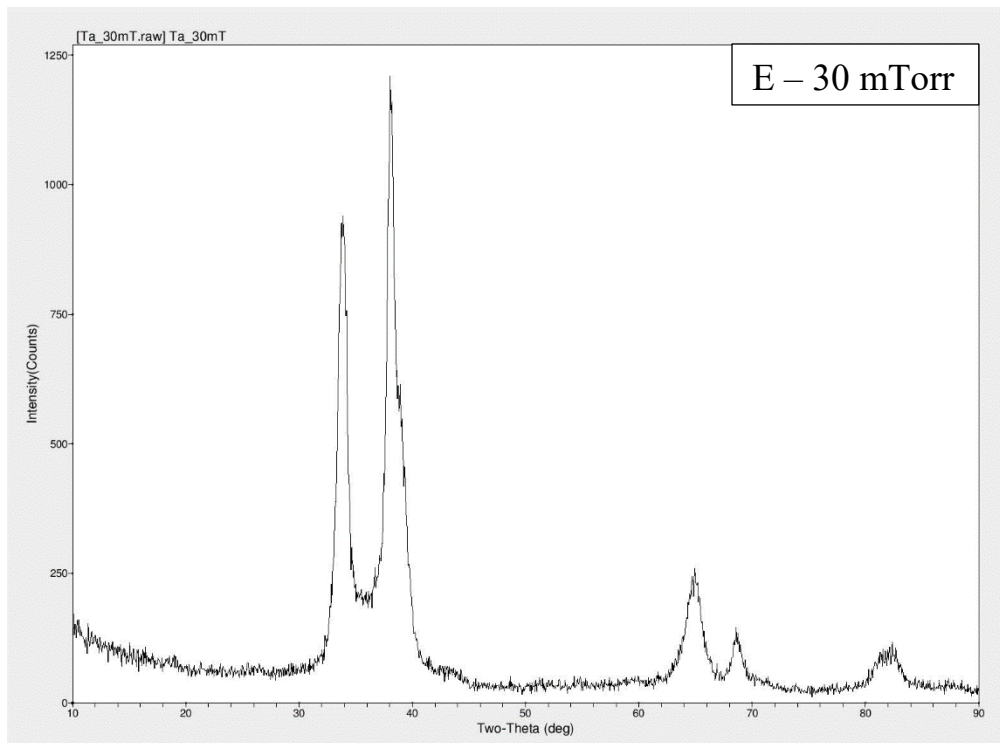


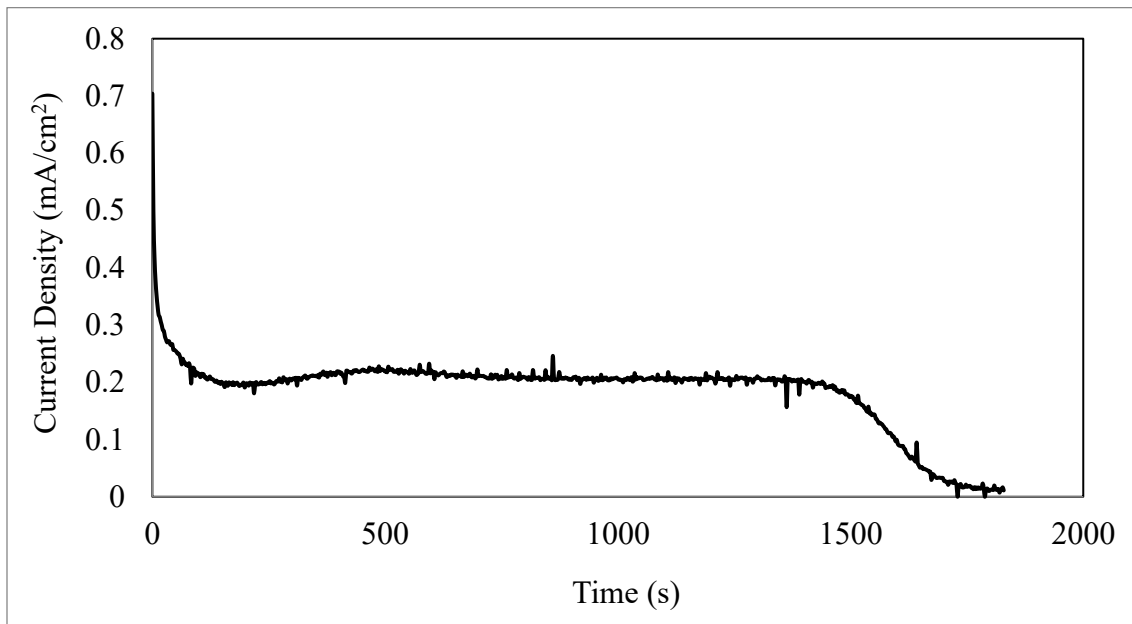
Figure 2-5 continued. XRD patterns of sputtered tantalum films at different working gas pressures.

Table 2-2. XRD peak analysis for tantalum films sputtered at 10, 15, 20, 25, and 30 mTorr. The phases and planes were identified using the work by Read and Hensler [3]. When possible overlapping of peaks was present, a best guess for the second peak was given.

Sputtering Pressure (mTorr)	2 $\Theta$ (°)	Lattice Parameter (Å)	Phase and Planes (hkl)
10	38.5	2.34	$\alpha$ -Ta (110)
	55.2	1.66	$\alpha$ -Ta (200)
	69	1.36	$\alpha$ -Ta (211)
	81.8	1.18	$\alpha$ -Ta (220)
15	34.2	2.62	$\beta$ -Ta (200)
	38.9	2.31	$\alpha$ -Ta (110) and/or $\beta$ -Ta (202)
	55.5	1.65	$\alpha$ -Ta (200)
	65.3	1.43	$\beta$ -Ta (304)
	69.4	1.35	$\alpha$ -Ta (211) and/or $\beta$ -Ta (400)
	82.4	1.17	$\alpha$ -Ta (220) and/or $\beta$ -Ta (404)
20	34.2	2.62	$\beta$ -Ta (200)
	38.8	2.32	$\alpha$ -Ta (110) and/or $\beta$ -Ta (202)
	65.3	1.43	$\beta$ -Ta (304)
	69.4	1.35	$\alpha$ -Ta (211) and/or $\beta$ -Ta (400)
	82.7	1.17	$\alpha$ -Ta (220) and/or $\beta$ -Ta (404)
25	34.2	2.62	$\beta$ -Ta (200)
	38.3	2.35	$\alpha$ -Ta (110) and/or $\beta$ -Ta (202)
	39.1	2.30	$\beta$ (211) - overlapping peak with 38.3°
	64.9	1.44	$\beta$ -Ta (304)
	68.9	1.36	$\alpha$ -Ta (211) and/or $\beta$ -Ta (400)
	82.2	1.17	$\alpha$ -Ta (220) and/or $\beta$ -Ta (404)
30	34.2	2.62	$\beta$ -Ta (200)
	38.2	2.35	$\alpha$ -Ta (110) and/or $\beta$ -Ta (202)
	38.9	2.31	$\beta$ (211) - overlapping peak with 38.2°
	65	1.43	$\beta$ -Ta (304)
	68.7	1.37	$\alpha$ -Ta (211) and/or $\beta$ -Ta (400)
	82	1.17	$\alpha$ -Ta (220) and/or $\beta$ -Ta (404)

### *Current Density Plots*

Current density was recorded to help understand if the tantalum microstructure influenced the anodization of the aluminum-tantalum films. An example of the current density recorded during anodization is shown in Figure 2-6. Each graph showed an initial drop in current due to an aluminum oxide barrier layer forming, followed by a steady-state current during pore formation of the aluminum oxide, and finally a drop in current density during tantalum oxide barrier layer formation. No difference in current density was found during porous aluminum oxide formation ( $p=0.93$ ), regardless of the initial tantalum microstructure. Time to complete anodization (current density  $<0.03 \text{ mA/cm}^2$ ) also showed no difference ( $p=0.54$ ). Plots of current density and completion time are shown in Figures 2-7 and 2-8.



*Figure 2-6. Current density-time plot during anodization of aluminum-tantalum thin films in 0.4M phosphoric acid-0.1M oxalic acid under potentiostatic conditions (4V).*

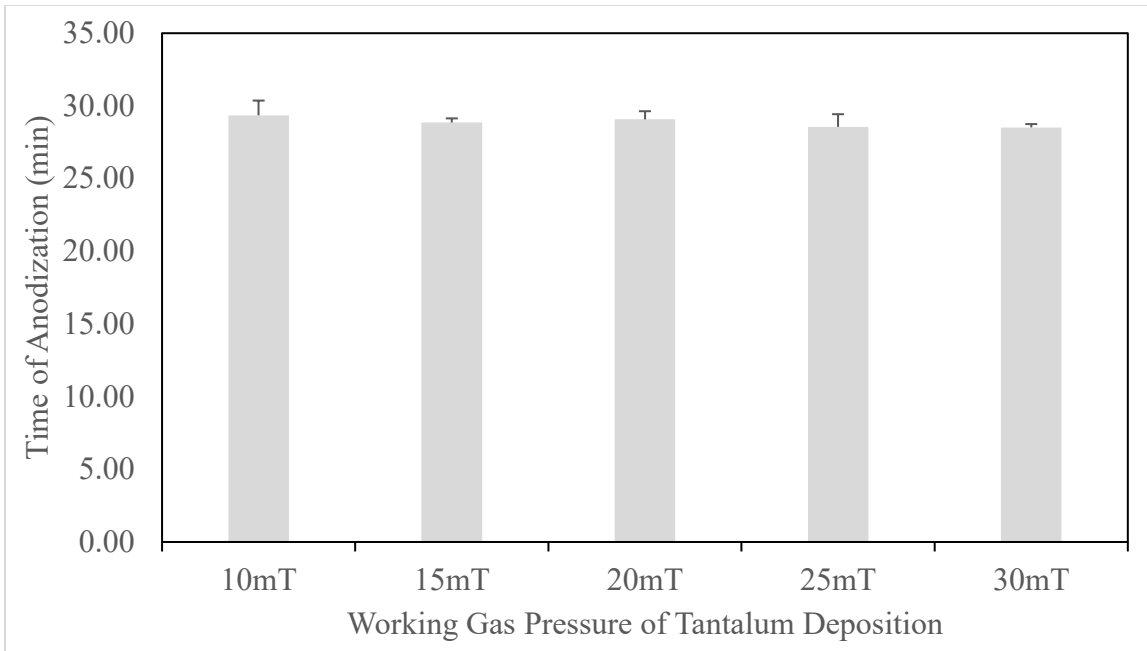


Figure 2-7. Time to complete anodization (i.e. tantalum oxide barrier layer formation) for aluminum-tantalum thin films with tantalum sputtered at a working gas pressure of either 10, 15, 20, 25, or 30 mTorr (mT). Anodization was conducted under potentiostatic conditions (4V) in 0.4M phosphoric-0.1M oxalic acid mixture.

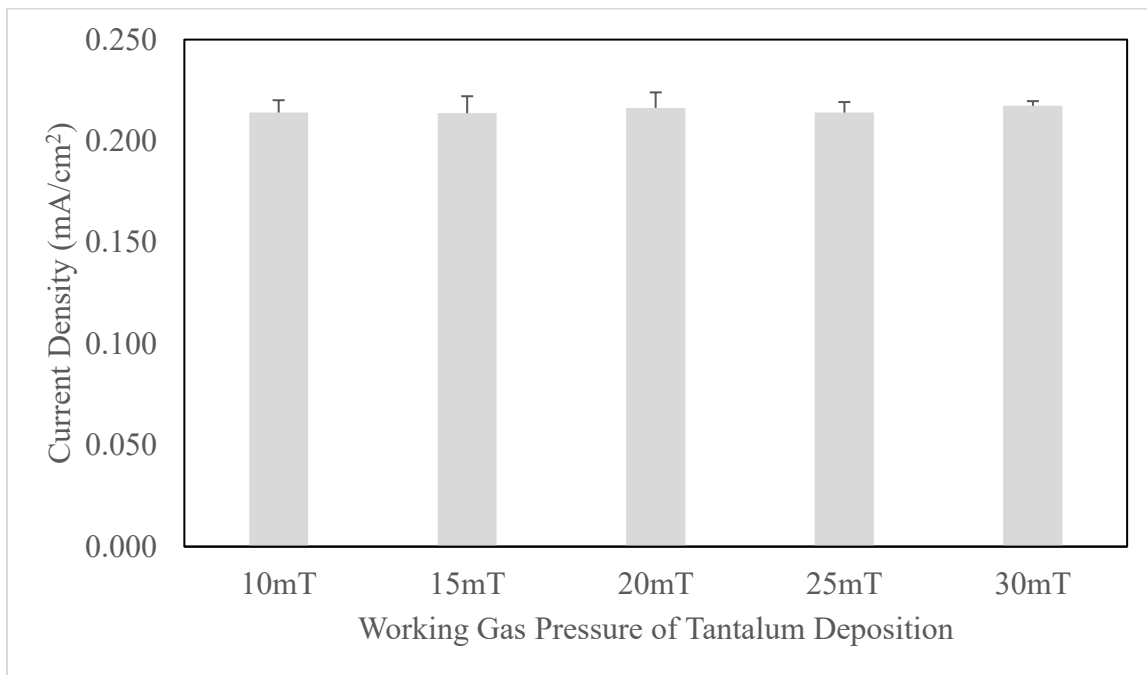


Figure 2-8. Current density during pore formation for aluminum-tantalum films with tantalum sputtered at a working gas pressure of either 10, 15, 20, 25, or 30 mTorr (mT). Anodization was conducted under potentiostatic conditions (4V) in 0.4M phosphoric-0.1M oxalic acid mixture.

### *Interference Colours*

The anodized slides were observed at approximately  $75^\circ$  from normal through a polarizing lens (S-polarized light) to increase interference colour contrast. Figure 2-9 shows the slides post-anodization, with tantalum sputtered at different pressures. Slides with tantalum sputtered at 15 through 30 mTorr appeared tan at  $75^\circ$ , while those sputtered at 10 mTorr were slightly more gold in colour. There was also a slight decrease in colour brightness observed from 10 to 30 mTorr. Reflectance spectrophotometry was used to better understand the differences in colour between the slides. Figure 2-10 is a sample graph of reflectivity vs. wavelength for the various tantalum microstructures after coating with aluminum and anodizing. Triplicates showed similar results and graphs of all reflectance curves can be found in Appendix 1. Samples sputtered at 10 mTorr showed a different reflectance curve from samples sputtered at 15 through 30 mTorr. The 15 through 30 mTorr samples showed a similar reflectance curve, however reflectivity decreased with increasing pressure.



*Figure 2-9. Anodized aluminum-tantalum thin films, viewed at approximately  $75^\circ$  from normal through a polarizing lens (S-polarized light). From left-to-right tantalum sputtered at 10 mTorr, 15 mTorr, 20 mTorr, 25 mTorr and 30 mTorr.*

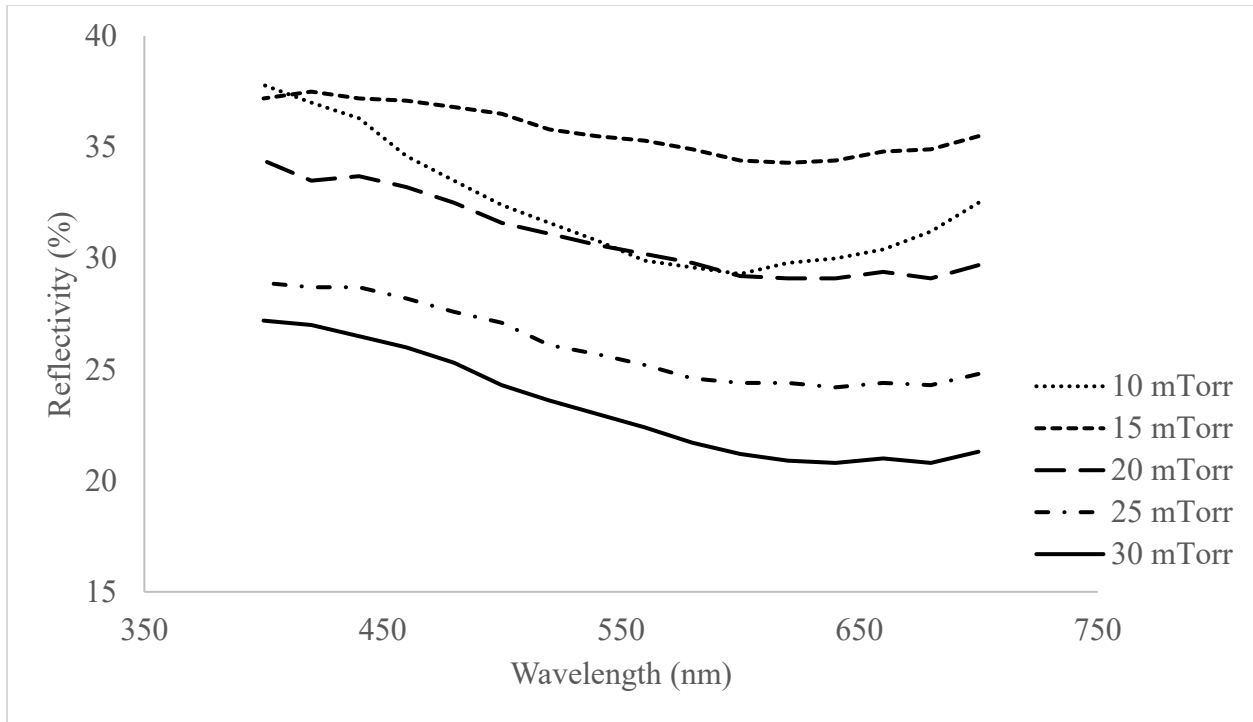


Figure 2-10. Plot of reflectivity vs. wavelength for anodized aluminum-tantalum films with tantalum sputtered at 10 through 30 mTorr.

## Discussion

Overall, various changes were found with the final interference colours due to changes in the tantalum microstructure, including changes in colour and reflectance. A decrease in reflectance was found due to a change in microstructure, as was also noted by Thornton and Hoffman [7]. As the working gas pressure increases, the mean free path of any sputtered atom will decrease. A decrease in the mean free path means that there will be more collisions between sputtered atoms and the gas and a more scattered or multi-directional flux will result. Eventually the flux will become thermalized (lacking kinetic energy) and film deposition is due to diffusion in the sputter chamber. A thermalized flux results in a rougher, less dense structure which scatters more light or traps it by internal reflections, leading to a decrease in reflectance [13, 7]. Thornton and Hoffman [12] found that in cylindrical post magnetron deposition, tantalum reflectivity at 555 nm decreased from about 50% at 10 mTorr to approximately 22% at 30 mTorr, an almost 20% larger drop than

seen here,  $50.8 \pm 1.3\%$  and  $38.7 \pm 2.6\%$  for 10 and 30 mTorr respectively, see Figure 2-1 and Figure 2-2. In this study, planar magnetron sputtering was used, whereas Thornton and Hoffman used cylindrical post magnetron sputtering. The geometry of cylindrical magnetron sputtering allows for a more oblique flux and thus causes a shift from a smooth to rough microstructure sooner than in planar sputtering [7].

The rougher topography with increased working gas pressure was confirmed using SEM and EDX analysis. The micrographs from SEM analysis show rougher surfaces as the argon pressure is increased from 10 to 30 mTorr, Figure 2-3A through 2-3E. The EDX data also points towards higher surface area developing. The increase in oxygen content of the sputtered tantalum film occurs due to an increase of exposed tantalum surface area, Figure 2-4. When the tantalum films are removed from the sputtering chamber, they are exposed to atmosphere where a native tantalum oxide film immediately starts to develop. The higher surface area of the films leads to a higher amount of oxide formed. The increased surface area could result from either increased surface roughness or from increased porosity and voided grain boundaries. As the pressure is increased from 20 to 30 mTorr, a noticeable increase in voided grain boundaries occurs and therefore the oxide is likely throughout the thickness of the film and not just on the surface. This porosity would result in both scattering and trapping of light within the film through internal reflections and is the reason why the reflectance drops significantly at 25 and 30 mTorr, see Figure 2-1 and Table 2-1.

The tantalum crystal structure was also found to shift with gas pressure. At 10 mTorr, a pure  $\alpha$ -phase tantalum (bcc) formed, Figure 2-5A. As the pressure increased, the  $\beta$ -phase tantalum starts to form, with random texturing of the surface, Figures 2-5B through 2-5E. Between 15 and 30 mTorr a mix of both  $\alpha$  and  $\beta$  tantalum was observed. It is important to note that the ratio of  $\beta$ -Ta to  $\alpha$ -Ta cannot be determined using a simple diffractometer trace, due to overlapping peaks

between the two phases, found at around  $38.4^\circ$ ,  $70^\circ$ , and  $82.3^\circ$ , see Table 2-2. Read and Hensler [3] discuss in detail why a diffraction photograph using the Debye-Scherrer technique must be used to distinguish mixtures of the two phases. The phase change that occurs between 10 and 15 mTorr is noticeable as a structural change on the micrographs by 20 mTorr. This work agrees with previous studies that have shown a metastable  $\beta$ -phase forms when sputtering tantalum under certain conditions [2, 3, 6, 1].

After coating with aluminum and anodizing, the interference colours were found to be gold to tan in colour. The 10 mTorr samples were gold, while the 15 to 30 mTorr samples were tan, Figure 2-9. One reason for this difference is likely the crystal structure of the underlying tantalum. As discussed in the introduction, the refractive index and extinction coefficient for  $\beta$  tantalum is higher than  $\alpha$  ( $\beta$ -Ta:  $\eta = 3.43-3.66i$ ,  $\alpha$ -Ta:  $\eta = 2.90-2.41i$ ;  $\lambda = 5461\text{\AA}$ ) [4]. The different optical properties would result in a different reflection off the tantalum metal surface over the visible spectrum, thereby changing the colour. This was supported by the reflectance spectroscopy data, Figure 2-10, which showed a very different reflectance curve over the visible spectrum for 10 mTorr samples compared to 15 through 30 mTorr. It was also found that the interference colours had a decrease in brightness as the pressure was increased from 15 to 30 mTorr. This decrease in brightness is due to the change in reflectance and topography of the tantalum sputtered films. Reducing the reflected light off the tantalum metal decreased the amount of light coming back to the eye (or camera), thereby creating a duller surface. It is interesting to note that the anodization process was not affected by the tantalum microstructure. Figure 2-6 shows the current density vs. time plot during anodization. The plot depicts a typical current graph for potentiostatic anodization, with (1) an initial decrease in current during barrier oxide formation, followed by (2) steady-state pore formation and (3) a final drop in current as a tantalum barrier oxide is formed, see Chapter 1

Section 1.5 for more details. The anodization time and current density during pore formation did not change regardless of the tantalum microstructure, Figures 2-7 and 2-8.

As was discussed in the introduction to this chapter, to create a saturated (or strong) interference colour, the reflected light from the air/oxide interface and the light from the oxide/metal interface must each be 50% of the outgoing light. Thus, equal portions of light are interfering and producing the most saturated of interference colours. In the case of this device, reducing the reflectance of the underlying metal may hinder the colour generation and reduce brightness, as we found here. However, there is the opportunity to tailor the tantalum for other coatings. Materials other than aluminum oxide may be coated on the tantalum surface. If these materials have a very low reflectivity, it is possible to tune the reflectance of the underlying tantalum metal such that 50% of the outgoing light is contributed from the material/metal interface and 50% is contributed from the air/material interface, and thus produce strong interference colours.

Another application of this tunable, nanostructured surface could be for increased sensitivity in thin film diagnostics. It is hypothesized that balancing the reflectance off the air/protein interface and the oxide/metal interface will result in a stronger interference colour due to a reduction of background noise. Figure 2-11 depicts how an overwhelming reflection off the metal surface can mask any signal coming off the air/protein interface. By lowering the reflectivity off the metal surface, the reflectance from the two surfaces can be brought into balance and thereby increase the sensitivity of the diagnostic device by reducing background noise. In Chapter 5, this work is continued to see if the different tantalum microstructures influence the sensitivity of observing adsorbed protein layers on these anodized aluminum-tantalum thin films.

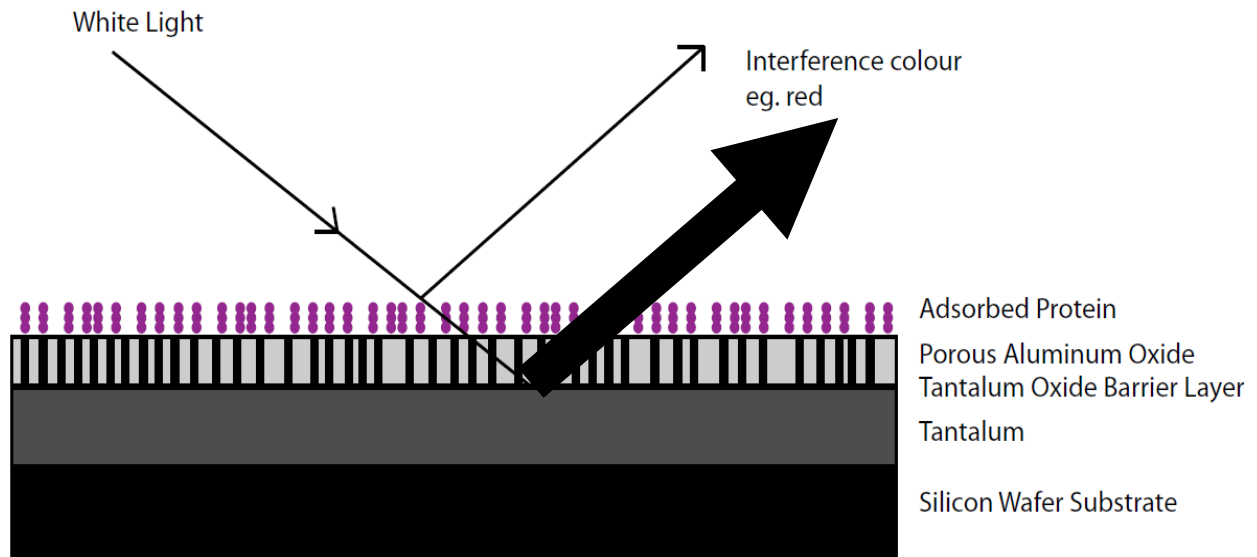


*Figure 2-11. Cartoon depiction of an anodized aluminum-tantalum thin film device with an adsorbed layer of protein. The arrows show how a highly reflective metal could overwhelm any light coming off the protein/air interface.*

## **Conclusion**

This work helped understand the optical and microstructural changes that occur with an increase in gas pressure during tantalum thin film sputtering and the effect that these changes had on interference colours produced by anodized aluminum-tantalum thin films. The following conclusions were found:

- 1) Increasing working argon gas pressure in the sputtering of tantalum films decreased the optical reflectance by creating rougher surfaces with voided grain boundaries, which scattered or trapped the light by internal reflections. The decreased reflectance reduced the interference colour brightness of the anodized aluminum-tantalum films.
- 2) Increasing the gas pressure during sputtering of tantalum produces a phase change from  $\alpha$ -Ta to  $\beta$ -Ta, which starts to occur between 10 and 15 mTorr (under the sputtering conditions used). After the tantalum is coated with aluminum and anodized, the phase

change contributes to a small colour shift from gold to tan, likely due to differences in the optical properties of the  $\alpha$  and  $\beta$  tantalum.

## References

- [1] J. J. Colin, G. Abadias, A. Michel and C. Jaouen, "On the origin of the metastable  $\beta$ -Ta phase stabilization in tantalum sputtered thin films," *Acta Materialia*, vol. 126, p. 481, 2017.
- [2] M. H. Read and C. Altman, "A New Structure in Tantalum Thin Films," *Applied Physics Letters*, vol. 7, p. 51, 1965.
- [3] M. H. Read and D. H. Hensler, "X-ray Analysis of Sputtered Films of Beta-Tantalum and Body-Centered Cubic Tantalum," *Thin Solid Films*, vol. 10, p. 123, 1972.
- [4] D. G. Muth, "Ellipsometer Study of Anodic Oxides Formed on Sputtered Tantalum and Tantalum-Aluminum Alloy Films," *Journal of Vacuum Science and Technology*, vol. 6, p. 749, 1969.
- [5] S. L. Lee, M. Doxbeck, J. Mueller, M. Cipollo and P. Cote, "Texture, structure and phase transformation in sputter beta tantalum coating," *Surface & Coatings Technology*, vol. 177, p. 44, 2004.
- [6] A. A. Navid and A. M. Hodge, "Nanostructured alpha and beta tantalum formation - Relationship between plasma parameters and microstructure," *Materials Science and Engineering A*, vol. 536, p. 49, 2012.
- [7] J. A. Thornton and D. W. Hoffman, "Stress-related Effects in Thin Films," *Thin Solid Films*, vol. 171, pp. 5-31, 1989.
- [8] A. Charlesby and J. J. Polling, "The Optical Properties of Thin Oxide Films on Tantalum," *Proceedings of the Royal Society of London. Series A, Mathematical and Physical Sciences*, vol. 227, pp. 434-447, 1955.
- [9] L. Young, "The determination of the thickness, dielectric constant, and other properties of anodic oxide films on tantalum from the interference colours," *Proceedings of the Royal Society A: Mathematical, Physical, and Engineering Sciences*, vol. 244, p. 41, 1958.
- [10] S. Cui-Cui, C. Yun-Yu, D. En-Mei and L. Chang-Hao, "Tunable structural color of anodic tantalum oxide films," *Chinese Physics B*, vol. 21, p. 088101, 2012.
- [11] D. Y. Smith, "The Optical Properties of Metallic Aluminum," in *Handbook of Optical Constants of Solids*, San Diego, Academic Press Inc., 1985, pp. 369-406.
- [12] J. A. Thornton and D. W. Hoffman, "Internal stresses in titanium, nickel, molybdenum, and tantalum films deposited by cylindrical magnetron sputtering," *Journal of Vacuum Science and Technology*, vol. 14, pp. 164-168, 1977.

[13] J. A. Thornton, "The microstructure of sputter-deposited coatings," *Journal of Vacuum Science and Technology*, vol. 4, no. 6, pp. 3059-3065, 1986.

## Chapter 3 Aluminum

### The Effect of Aluminum Sputtering Parameters on the Structural and Optical Properties of Anodized Aluminum-Tantalum Thin Films

#### Introduction

In the making of thin film diagnostics based on anodized aluminum-tantalum thin films, the microstructure, uniformity, and thickness of the deposited aluminum film are all important considerations that depend on the deposition process. The aluminum film is an important part of the system as the ability to visualize the binding of proteins to the thin film surface depends on the optical properties of the anodic oxide. The coating of materials with thin aluminum films has found a wide variety of applications, including integrated circuits [1], coatings for mirrors [2], conducting lines in liquid crystal display (LCD) panels [3], and the coating of polymer food packages for improved sealability and barrier properties [4], to mention just a few. Magnetron sputtering has become one of the main techniques to coat surfaces in these films due to its ability to precisely control the microstructure and properties of the deposited film.

The microstructure of sputtered films is dependent on the thermodynamic parameters of the deposit, the substrate and target materials, as well as the plasma and processing parameters during deposition [5, 6, 7, 8, 9, 10]. Structure - zone models have been used to understand how the deposition parameters can affect the microstructure of the resulting species. Thornton [6] described a structure - zone model for magnetron sputtered films which consisted of 4 zones dependent on the working argon pressure and the ratio of the substrate temperature ( $T$ ) to the melting temperature ( $T_m$ ) of the deposited species, Figure 3-1. Zone 1 is a columnar structure consisting of voided grain boundaries. Zone T is a smooth, dense structure since the higher substrate temperature increases diffusion processes to fill in inter-grain voids. Zone 2 consists of larger columnar grains with

metallurgical grain boundaries as opposed to voided grain boundaries. Finally, Zone 3 has such a high substrate temperature the grain structure becomes equiaxed due to bulk diffusion. Since the 1970s, many researchers have expanded on these zone diagrams accounting for film thickness [11] or ion impingement on the deposited surface due to a biased substrate [12].

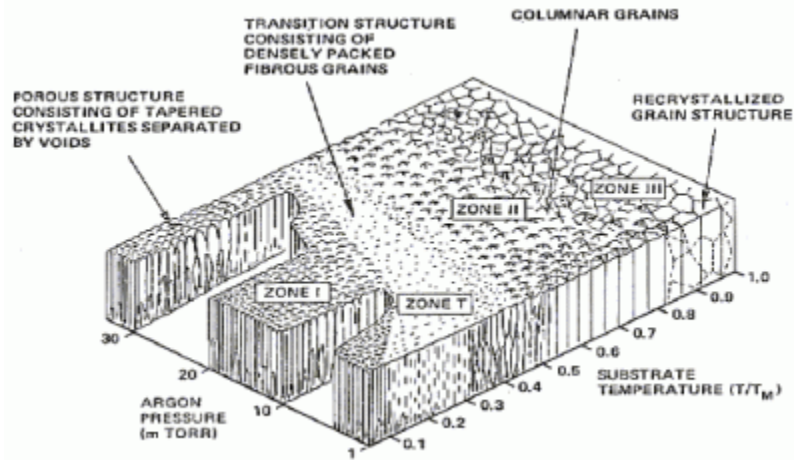


Figure 3-1. Structure zone diagram for films deposited by magnetron sputtering.  $T$  is substrate temperature and  $T_m$  is the melting temperature of the deposited species [6].

Previous studies have shown some of the effects that deposited microstructure has on anodized aluminum. Chin et al. [13] and Upreti et al. [14] showed the differences in topography and pore formation during anodization between sputtered and evaporated aluminum films. However, a fixed set of parameters was used in each study and they did not elaborate on the ability to tailor a deposited microstructure with each type of equipment. For example, Choudhury and Raghavan [15] discuss the connection between Thornton's structure zone diagram and the microstructures that result from porous anodization. They found that a Zone T or Zone 2 microstructure is ideal for homogenous anodization of Zr, Ti, and Al films, while the Zone 1 microstructure tends to yield a 'sponge-like' morphology. Adjusting the parameters of sputtering or evaporation can lead to different zone structures, as discussed above, and thereby change the anodized microstructure.

Other studies have shown the effects of grain size [16], surface topography [17, 18, 19], and defects [20] on the nanoporous structure.

What is currently not understood is the effect that deposition parameters have on the optical properties of anodic alumina films, specifically the complex refractive index. A key aspect in thin film diagnostics is the mismatch between the refractive index of the surface oxide and the adsorbed protein, as discussed in Chapter 1 Section 1.2. Porous anodization of aluminum allows for a tunable refractive index by adjustment of the voltage and electrolyte. It is unclear how the sputtered microstructure is involved in the final optical properties of the anodic film.

The purpose of this work was to (a) understand how the working gas pressure and power density in planar magnetron sputtering would affect the microstructure of aluminum thin coatings (~120 nm) sputtered onto tantalum films (~230 nm), and (b) to understand how these sputtering parameters affect the microstructure and optical properties of the nanostructured oxide after anodization of the films at 4V in a mixed 0.4M phosphoric-0.1M oxalic acid. Materials characterization was carried out using SEM, EDX, and XRD to understand changes in film topography, microstructure, and composition when sputtering under the various conditions and then anodizing. Ellipsometry was used after anodization to record the optical constants and final thickness of the anodic aluminum oxide.

## **Materials and Methods**

### *Magnetron Sputter Deposition - Tantalum*

Tantalum thin films were created by planar magnetron sputter deposition onto unprocessed <100> silicon wafers, 100 mm in diameter (University Wafers, South Boston, MA), at the Nanotechnology Centre for Applied Research at Northern Alberta Institute of Technology (NAIT).

Tantalum films were sputtered to a thickness of  $226.5 \pm 3.8$  nm using a 20.3 cm diameter tantalum target, 99.95% purity (Kurt J. Lesker Company, Jefferson Hills, PA). A constant power density of  $1.5 \text{ W/cm}^2$  and a target-to-substrate distance of 70 mm was used. A working Ar (99.9995%) gas pressure of 10 mTorr (132 sccm flow) was set with a base pressure of  $1.8 \times 10^{-6}$  Torr. The substrate was deposited statically with flux normal to the surface.

*Magnetron Sputter Deposition - Aluminum*

A. Power and Pressure Tests - Tantalum coated wafers were deposited with aluminum under various parameters. The matrix of experiments can be seen in Table 3-1. A timer was set on the power source to help with the deposition time consistency.

*Table 3-1. Experimental design matrix for sputtering aluminum at different powers and working gas pressures. T-S stands for target to substrate distance.*

	<b>Power Density</b>		
<b>Working Gas Pressure (Flow rate) [Argon]</b>	0.9 W/cm <sup>2</sup>	5 W/cm <sup>2</sup>	9 W/cm <sup>2</sup>
1 mTorr (9 sccm)	T-S distance: 70mm	T-S distance: 70mm	T-S distance: 70mm
5 mTorr (55 sccm)	T-S distance: 70mm	T-S distance: 70mm	N/A*
10 mTorr (135 sccm)	T-S distance: 70mm	T-S distance: 70mm	T-S distance: 70mm

\*Not tested due to high deposition rate at  $9\text{W/cm}^2$ ; too difficult to control thickness.

B. Constant Current Tests - After analysis of part A, an additional set of tantalum coated wafers were then deposited with aluminum under a constant current of 0.8A, and a working gas pressure of 2.5 mTorr (30 sccm).

A Materials Research Corporation DC-magnetron sputtering machine was used (New York, NY). The working gas in all experiments was argon (99.9995%). The aluminum target was 20.3 cm in

diameter and 99.995% purity (Kurt J. Lesker Company, Jefferson Hills, PA). Note that all cathodes were attached to the copper, water-cooled backing plate with the use of an indium solder to increase conductive heat transfer. A base pressure of  $1.8 \times 10^{-6}$  Torr was used. Sputtering was conducted with a target-to-substrate distance of 70 mm, where the substrate was held static with flux normal to the surface.

### *Temperature Sensors*

Temperature sensors were used to understand the change in substrate temperature with power and pressure. Vacuum Chamber Temp-Plates (Palmer Wahl Instrumentation Group, Asheville, NC) with a range from 48 - 260°C were used to record the temperature at the substrate. The irreversible temperature labels were attached to a piece of aluminum foil which was taped with Kapton tape to the substrate holder. Aluminum foil was used due to its high thermal conductivity. The temperature sensors showed a temperature range; if the box turned black then it signaled that the temperature went over the labelled temperature. Duplicate depositions were conducted at each parameter for a time required to deposit approximately 120 nm of Al.

### *Anodization*

The sputtered wafers were then cleaved into smaller sections of about 6.3 cm x 1.3 cm or 6.3 cm x 2.6 cm. These sections were electrolytically oxidized (anodized) in a 0.4M phosphoric acid and 0.1M oxalic acid mix at a constant voltage of 4V until the current decayed to  $<0.02 \text{ mA/cm}^2$  using a Princeton Applied Research Model 273a potentiostat/galvanostat (AMEKTEK Inc., Oak Ridge, TN). Aluminum foil (Thermo Fisher Scientific, Waltham, MA) was wrapped around a glass microscope slide and used as the cathode, where the cathode to anode area ratio was 1:1, with a cathode to anode distance of 40 mm. A saturated calomel electrode was used as a reference electrode (Thermo Fisher Scientific, Waltham, MA). A magnetic stir plate was used to agitate the

solution, and the temperature of the electrolyte was  $19 \pm 1^\circ\text{C}$ . All samples were rinsed before and after anodization with MilliQ deionized water. All anodized films were then viewed at approximately  $75^\circ$  from normal using a polarizing lens to view s-polarized light.

### *Scanning Electron Microscopy (SEM)*

SEM was conducted on the aluminum-tantalum films before and after anodization to understand changes in microstructure and topography. Samples of both pre- and post-anodized aluminum-tantalum thin films were fractured, mounted onto aluminum stubs (Ted Pella Inc., Redding, CA) using conductive carbon tape (PELCO Tabs<sup>TM</sup>, Ted Pella Inc., Redding, CA) and visualized under a Zeiss Sigma Field Emission Scanning Electron Microscope (FESEM) at the nanoFAB – Fabrication and Characterization Center at the University of Alberta. Unanodized specimens (sputtered aluminum-tantalum films) were viewed at 4.00 or 5.00 keV and an aperture size of 15  $\mu\text{m}$ . Anodized specimens were viewed at 3.00 or 4.00 keV and an aperture size of 15  $\mu\text{m}$ , at both  $0^\circ$  and  $45^\circ$  to acquire top and side profiles. The working distance was approximately 3 to 5 mm in both cases. A ‘through-the-lens’ (TTL) detector was used to decrease noise from SE3 electrons produced by the microscope chamber wall [21].

Side profiles were taken to measure the thickness of deposited aluminum films. Specimens were fractured and viewed at  $90^\circ$  with 4.00 keV, an aperture size of 15  $\mu\text{m}$ , 50,000 times magnification and a working distance of approximately 3 mm. Images were analyzed using ImageJ software (Rasband, WS, ImageJ, US National Institutes of Health, Bethesda, MD, <https://imagej.nih.gov/ij/>, 1997-2016). Each specimen had 2 cross-sectional images taken from randomly chosen areas. The thickness of the aluminum film was measured at 10 points across each image.

### *Energy-dispersive X-ray Spectroscopy (EDX)*

EDX was conducted on samples to analyze oxygen and nitrogen levels in the films. EDX was also performed on samples sputtered at  $9 \text{ W/cm}^2$  to analyze the elemental composition of the large particles ( $0.5\text{-}1 \text{ }\mu\text{m}$ ) found on the surface during SEM. EDX was conducted using an Oxford Instruments X-Max silicon drift detector (SDD) (Oxford Instruments, Abingdon, UK) with a super-atmospheric thin window (SATW). The SEM was set to 5 keV and a working distance of 8.5mm (optimized for the EDX detector). A deadtime of  $\sim 20\%$  was maintained and the scans were set to finish at 100,000 counts. AZtecEnergy EDS analysis software Version 3.1 (Oxford Instruments, Abingdon, UK) was used to determine film composition from the EDX spectrum.

### *X-Ray Diffraction (XRD)*

XRD was carried out to check for microstructural differences and confirm the consumption anodization of the aluminum films. A Rigaku Ultima IV (Cu-source) diffraction system with a thin film, substrate holder attachment was used. Diffraction data was collected between  $10$  and  $90^\circ 2\theta$  at  $5.000^\circ/\text{min}$ , using an incident divergence high limiting (DHL) slit of 10.00 mm and glancing angle  $\omega = 0.5^\circ$ . JADE 9<sup>TM</sup> software (Materials Data Inc., Livermore, CA) was used to analyze the XRD patterns along with the International Centre for Diffraction Data (ICDD) database to match peaks.

### *Ellipsometry*

Ellipsometry was used to understand changes in the optical constants of the aluminum oxide layer post-anodization. Final aluminum oxide thickness and the optical constants (refractive index,  $n$ , and extinction coefficient,  $k$ ) were determined using a J.A. Woollam M-2000V spectroscopic ellipsometer (J.A. Woollam Co., Lincoln, NE). A model was built, using CompleteEASE®

software (J.A. Woollam Co., Lincoln, NE), to represent each layer of the final anodized films, as described elsewhere (Chapter 4.1). For all layers,  $\Psi$  and  $\Delta$  values were recorded for wavelengths 370 nm to 1000 nm at angles of 55°, 65°, and 75° from normal. The CompleteEASE® software was then used to record the refractive index, extinction coefficient, aluminum oxide film thickness, and the porosity (%void). For additional details, see Chapter 4.1.

### *Colour Coordinates*

Photos of the interference colours were taken at approximately 75° from normal using a phone camera and a polarizing lens (s-polarized). Slides were placed on white cardboard paper with a matte, white background. The images were then analyzed for RGB coordinates using ImageJ software (Rasband, WS, ImageJ, US National Institutes of Health, Bethesda, MD, <https://imagej.nih.gov/ij/>, 1997-2016). A rectangular area of each slide was selected in the photo, encompassing between 32,000 and 46,000 pixels. The mean and standard deviation were recorded for the RGB coordinates of each area.

### *Statistics*

The standard deviations are shown on all plots and graphs using error bars. Numerical results used a one-way ANOVA with a Tukey Multiple Comparison post hoc test using IBM SPSS Statistics for Windows, Version 24.0 (IBM Corp., Released 2016, Armonk, NY). A Levene's test was used to check for similar sample variance between populations. An independent samples t-test was conducted on the EDX data to compare oxygen content between the sputtered film and the large particles found on films sputtered at 9 W/cm<sup>2</sup> (equal variances not assumed due to failed Levene's test).

## Results

### *Sputtering Temperature & Deposition Rate*

The sputtering parameters strongly affect the deposition rate and uniformity of a sputtered film, therefore an analysis of the deposition rates and the substrate temperature under each set of parameters was conducted. The deposition rates for each set of sputtering parameters are shown in Table 3-2. A 10x increase in power led to an approximately 8-9x increase in deposition rate and about an 8-15x increase in variability. The recorded temperature also increased with power density. At 0.9 W/cm<sup>2</sup> the temperature never reached above 48°C and was therefore outside the temperature gauge range. As the power was increased to 9 W/cm<sup>2</sup> the temperature reached a maximum of between 82°C and 93°C.

The pressure was also found to influence the temperature and deposition rate. Increasing pressure reduced the deposition rate at all power densities. At 5 W/cm<sup>2</sup>, the temperature was also found to decrease as the pressure increased.

*Table 3-2. The measured deposition rate and temperature range for each power/pressure parameter tested.*

Power (W/cm <sup>2</sup> )	Pressure (mTorr)	Deposition Rate (Å/s), (n=2)	Temperature Range (°C) (n=2)
0.9	1	11.0 ± 0.5	T < 48
	5	8.1 ± 0.8	T < 48
	10	7.7 ± 0.6	T < 48
5	1	52.5 ± 5.5	71 < T < 93
	5	46.4 ± 2.4	71 < T < 82
	10	40.9 ± 1.4	60 < T < 82
9	1	87.8 ± 4.4	82 < T < 93
	N/A		
	10	69.4 ± 8.9	82 < T < 93

### *SEM and EDX of Sputtered Aluminum Films*

Surface images of the aluminum sputtered films are shown in Figure 3-2. A simple visual inspection of the SEM images shows an increase in roughness and voided grain boundaries as the power is decreased, or the pressure increased. In particular, films sputtered at  $0.9 \text{ W/cm}^2$  and 10 mTorr showed large voids, Figure 3-2C. Films sputtered at 5 and  $9 \text{ W/cm}^2$  and 1 mTorr were very dense with a noticeably smaller grain size. Films sputtered at either 5 or 10 mTorr had bright, 50-100 nm, particles on the surface.

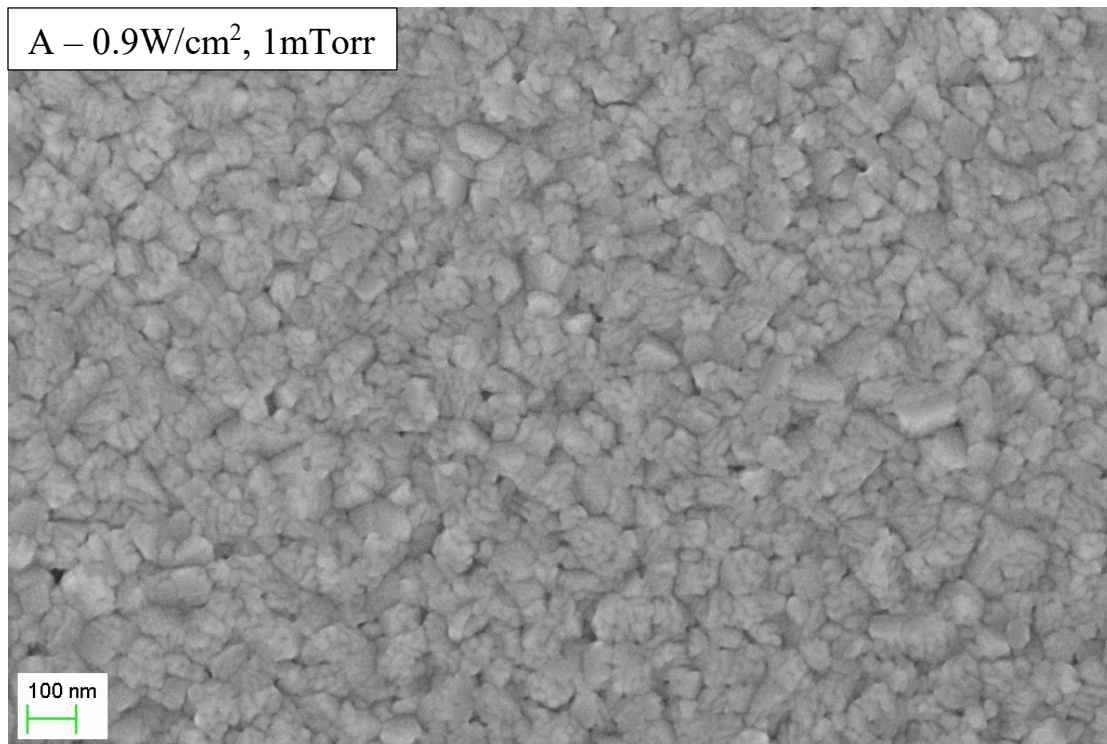


*Figure 3-2, continued.*

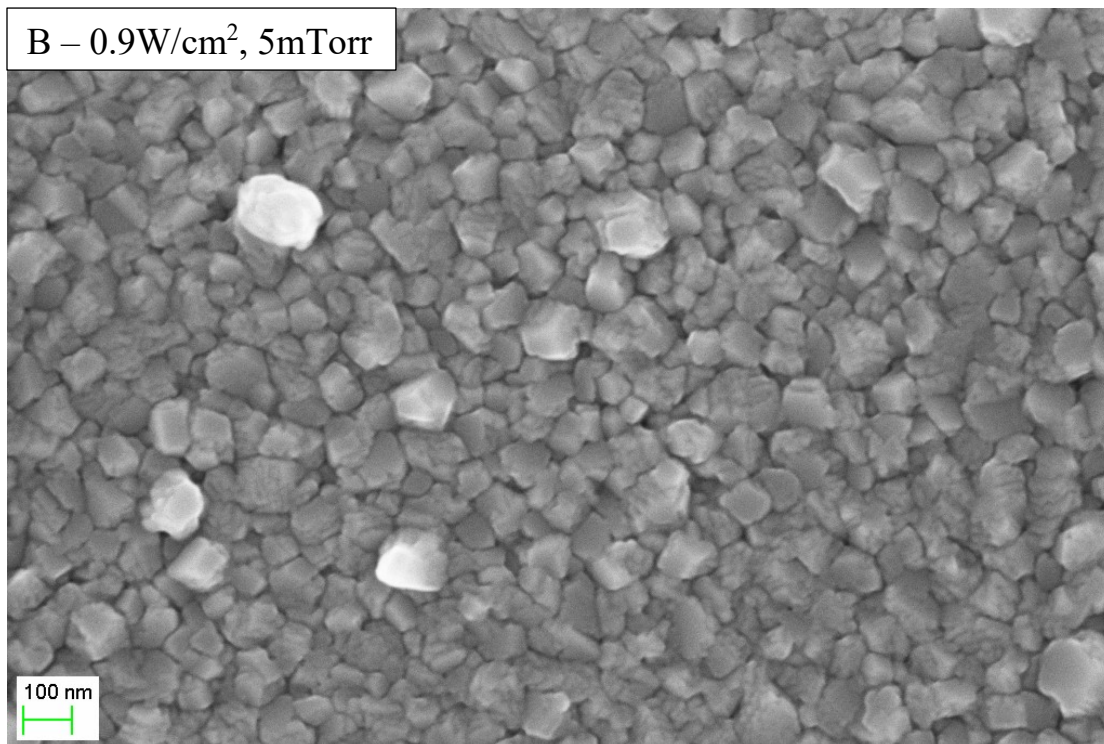


*Figure 3-2, continued.*

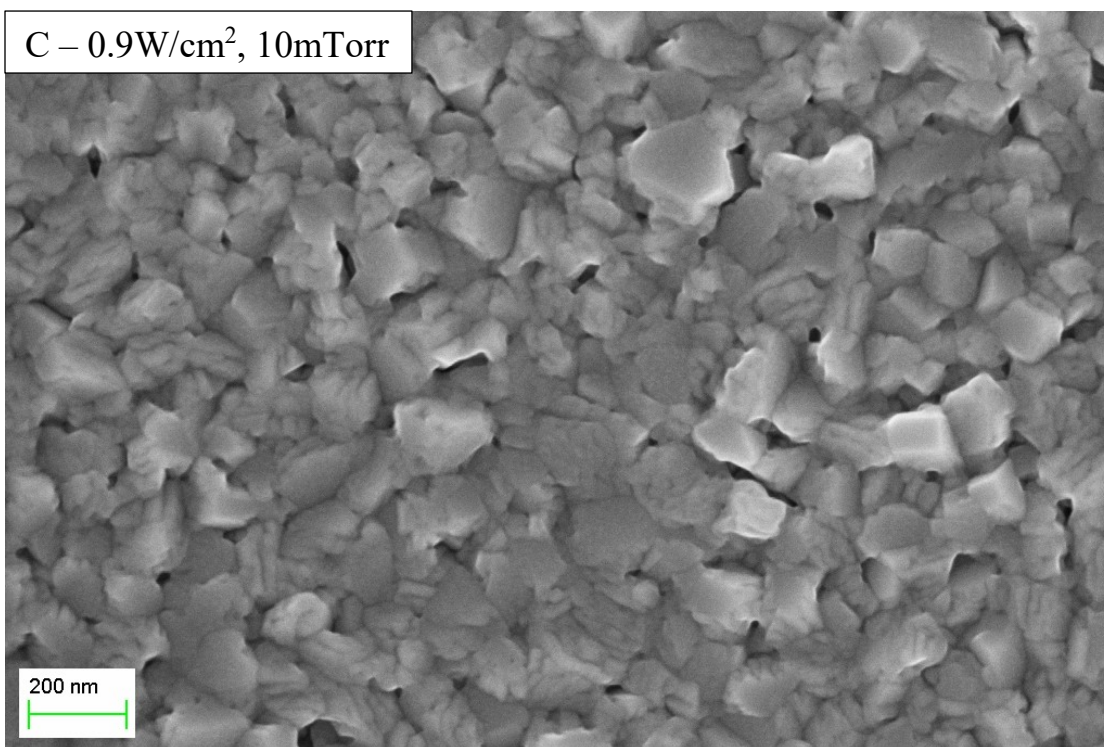


*Figure 3-2, continued.*

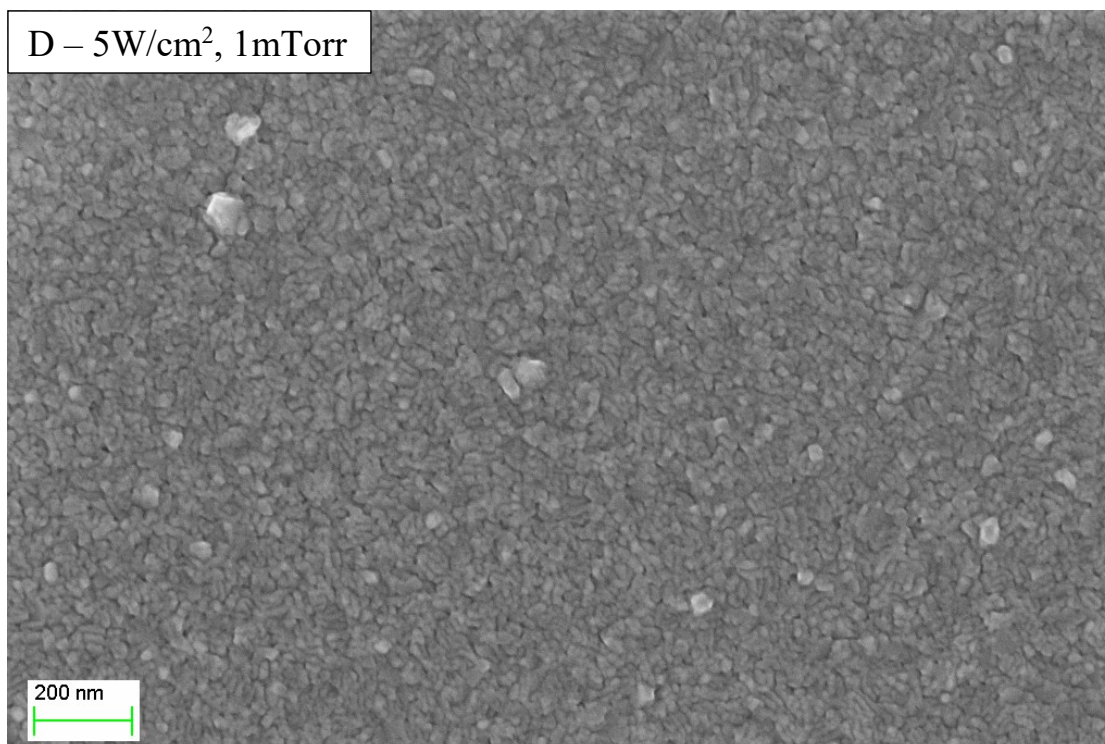


*Figure 3-2, continued.*

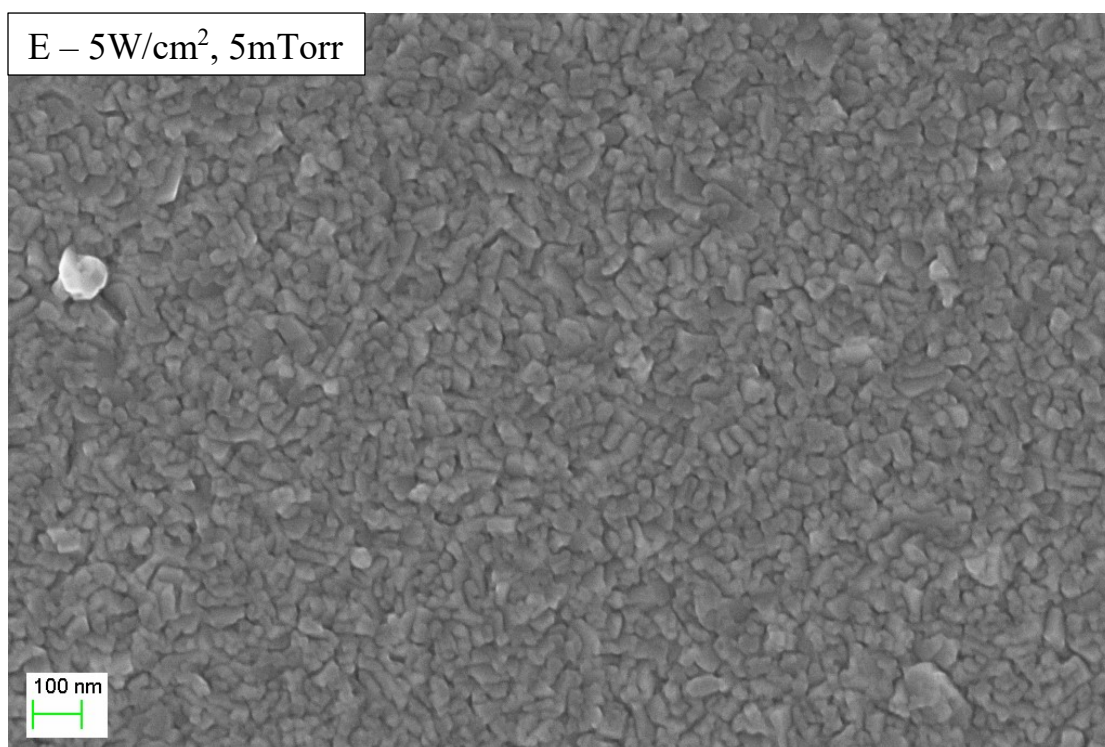


*Figure 3-2, continued.*

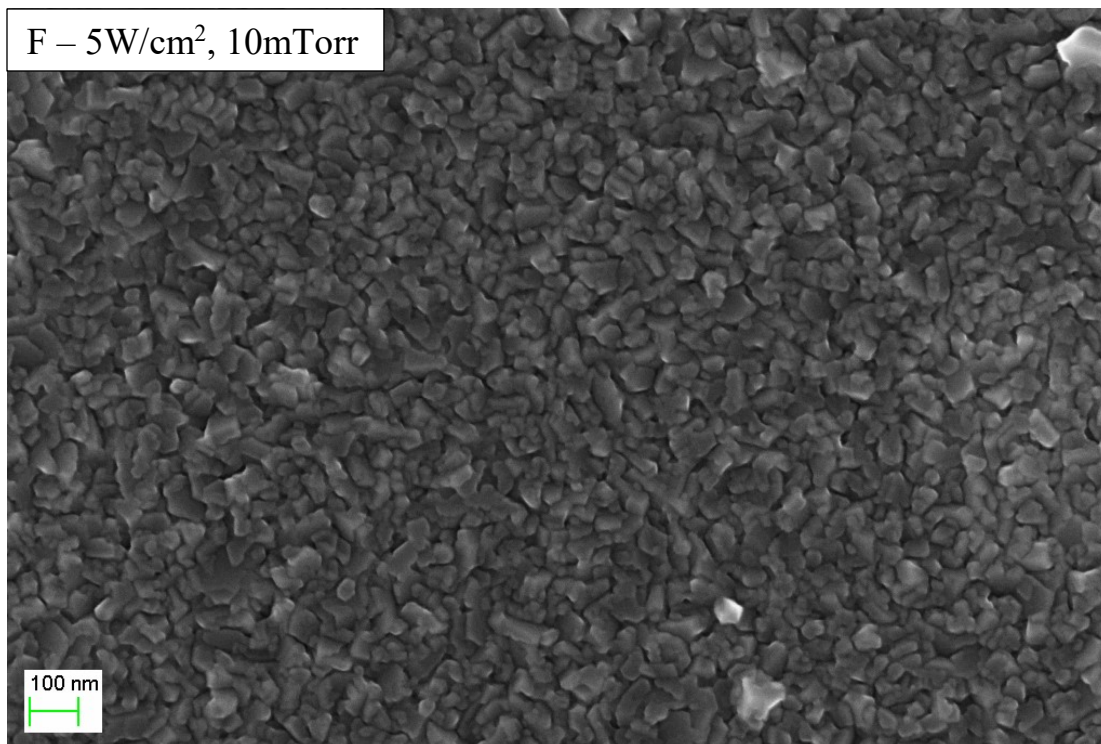


*Figure 3-2, continued.*

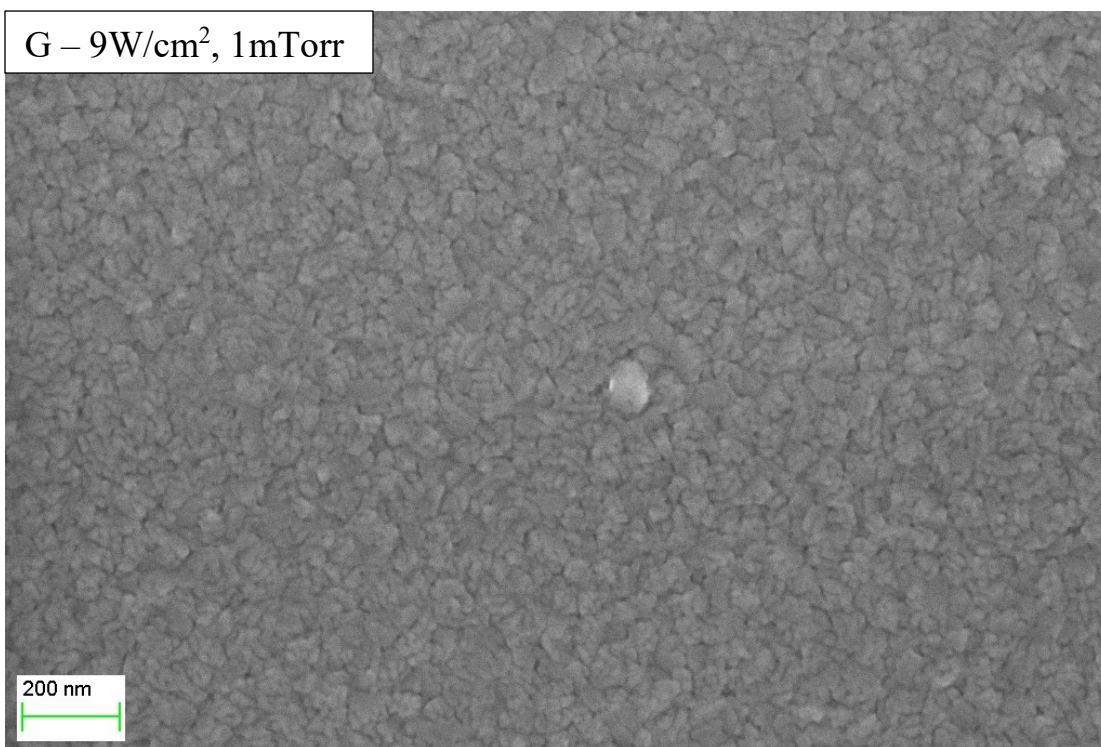


*Figure 3-2, continued.*

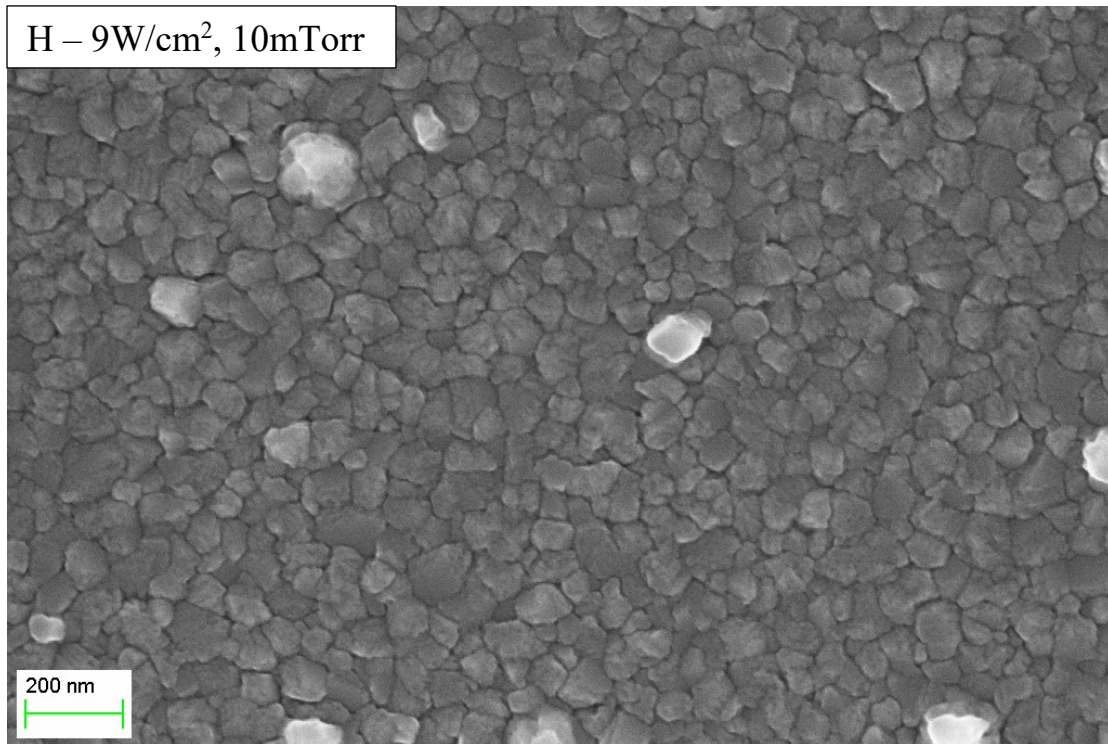


*Figure 3-2 continued. FESEM of sputtered aluminum films deposited at different power densities and working Ar gas pressures.*

Additionally, at the high-power densities ( $9 \text{ W/cm}^2$ ) the sputtered surface was covered with large, bright particles, about 0.5 to 1 microns across, Figure 3-3. An EDX point scan was performed on these particles to determine their elemental makeup. Table 3-3 shows the difference in composition between the aluminum surface and bright particles as measured by EDX. No significant difference was found in the oxygen content between the particles or the sputtered surface ( $9 \text{ W/cm}^2$  and 10 mTorr:  $p=0.231$ ;  $9 \text{ W/cm}^2$  and 1 mTorr:  $p=0.225$ ).

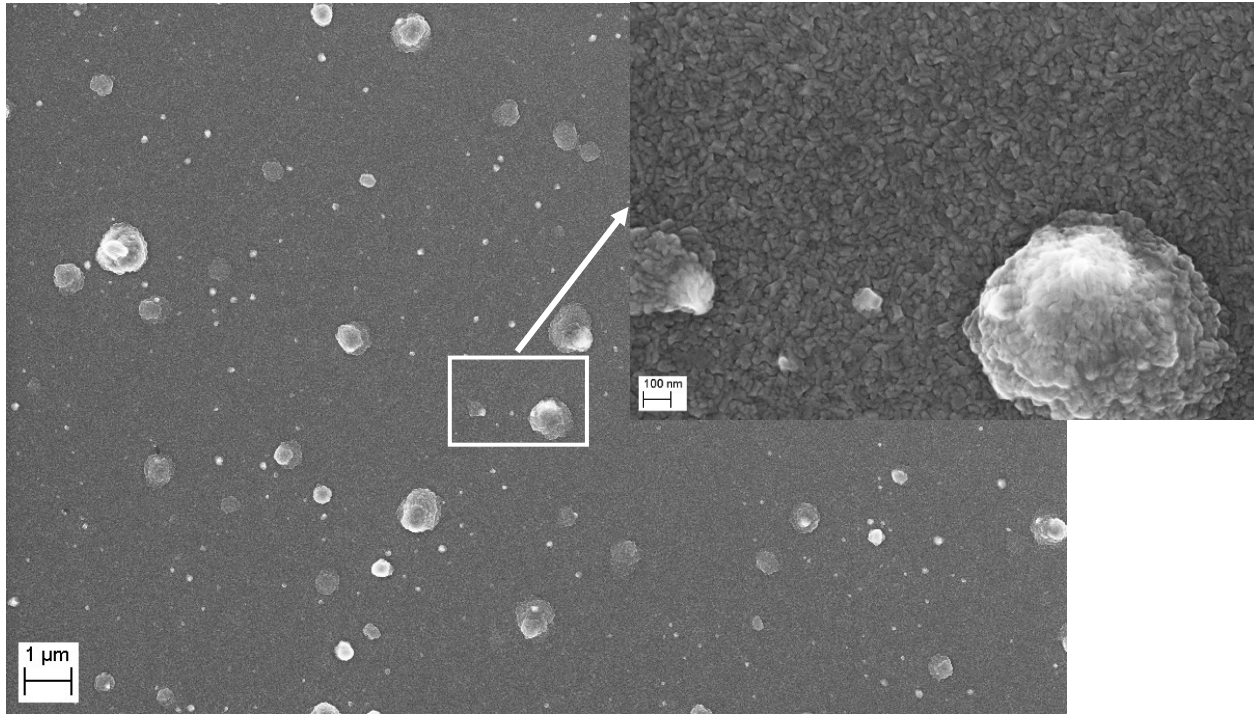


Figure 3-3. FESEM of aluminum films sputtered at  $9 \text{ W/cm}^2$  and  $1 \text{ mTorr}$ . Images are taken at  $5,000X$  and  $100,000X$  (inset).

Table 3-3. EDX compositional data acquired from films sputtered at  $9 \text{ W/cm}^2$  and either  $1$  or  $10 \text{ mTorr}$  working gas pressure ( $n=3$ ).

<b><math>9 \text{ W/cm}^2</math> and <math>10 \text{ mTorr}</math></b>		
<b>Element</b>	<b>Atomic % in Surface</b>	<b>Atomic % in Particle</b>
Aluminum	$81.27 \pm 0.52$	$80.38 \pm 3.75$
Tantalum	$11.93 \pm 0.63$	$11.09 \pm 1.62$
Nitrogen	$2.43 \pm 0.29$	$1.89 \pm 0.75$
Oxygen	$4.36 \pm 0.20$	$6.65 \pm 2.34$

<b><math>9 \text{ W/cm}^2</math> and <math>1 \text{ mTorr}</math></b>		
<b>Element</b>	<b>Atomic % in Surface</b>	<b>Atomic % in Particle</b>
Aluminum	$80.82 \pm 0.46$	$84.36 \pm 6.75$
Tantalum	$11.41 \pm 0.27$	$7.11 \pm 3.82$
Nitrogen	$3.47 \pm 0.23$	$2.18 \pm 0.93$
Oxygen	$4.31 \pm 0.18$	$6.35 \pm 2.04$

The measured thickness of the SEM cross-sections can be found in Table 3-4. Films sputtered at 0.9 W/cm<sup>2</sup> were ~10-30nm thicker than those sputtered at 5 or 9 W/cm<sup>2</sup>. Initially, a profilometer was used to measure step height of the sputtered aluminum films on a glass slide. This method was checked by the SEM cross-sections and found to be inaccurate. All analysis for this chapter was therefore done using the SEM cross-sections.

*Table 3-4. Measured aluminum thickness from SEM cross-sections of films sputtered at various parameters. Standard deviations represented by ± symbol (n=2).*

<b>Sputtering Parameters</b>	<b>Measured Al Thickness (nm)</b>
0.9 W/cm <sup>2</sup> , 1 mTorr	141.9 ± 6.0
0.9 W/cm <sup>2</sup> , 5 mTorr	129.3 ± 12.4
0.9 W/cm <sup>2</sup> , 10 mTorr	147.3 ± 11.0
5 W/cm <sup>2</sup> , 1 mTorr	125.9 ± 13.2
5 W/cm <sup>2</sup> , 5 mTorr	125.4 ± 6.4
5 W/cm <sup>2</sup> , 10 mTorr	122.8 ± 4.2
9 W/cm <sup>2</sup> , 1 mTorr	122.9 ± 6.1
9 W/cm <sup>2</sup> , 10 mTorr	117.9 ± 15.2

The SEM micrograph for aluminum films sputtered at constant current (0.8A) and 2.5 mTorr is shown in Figure 3-4. These surfaces looked very similar to those sputtered at 0.9 W/cm<sup>2</sup> and either 1 or 5 mTorr, Figures 3-2A or 3-2B.

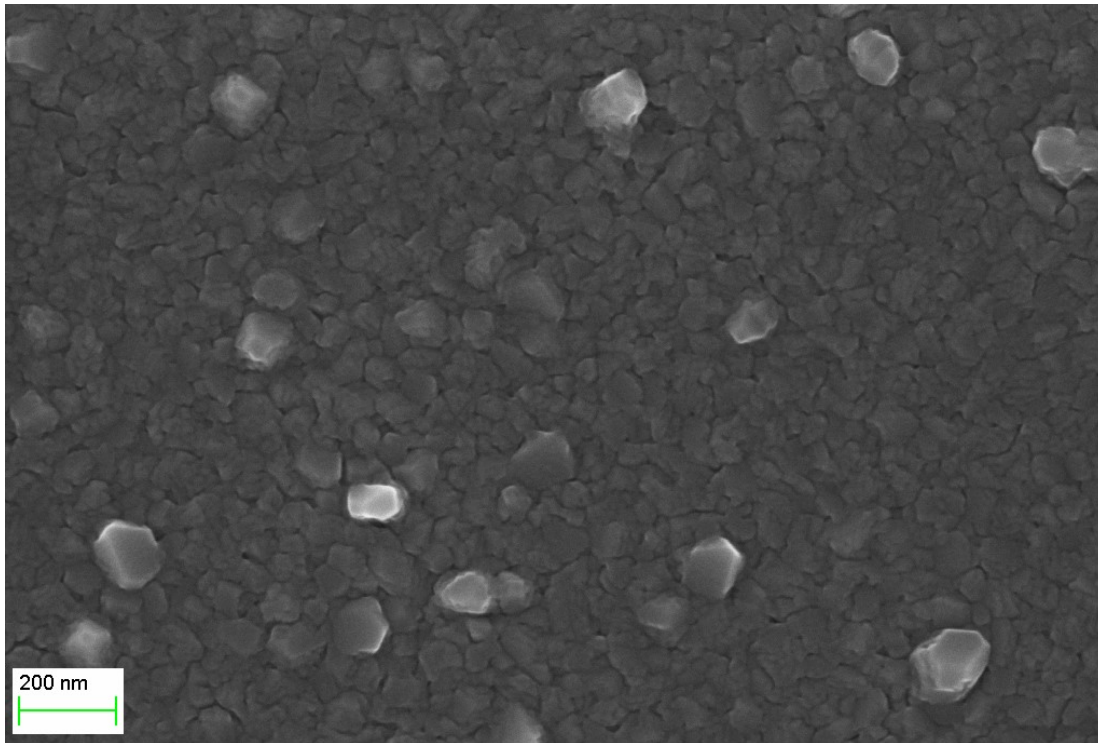


*Figure 3-4. FESEM of aluminum film surface sputtered at a constant current of 0.8A and an argon gas pressure of 2.5 mTorr (30 sccm).*

#### *XRD of Sputtered Aluminum-Tantalum Films*

The XRD patterns for films sputtered at the various parameters are shown in Figure 3-5. Aluminum (fcc) peaks  $44.7^\circ$   $2\theta$  (200),  $65.1^\circ$   $2\theta$  (220) and  $78.2^\circ$   $2\theta$  (311) were found at all sputtering parameters. The aluminum  $38.5^\circ$   $2\theta$  (111) and  $82.4^\circ$  (222) peaks overlap with tantalum peaks  $38.4^\circ$  (110) and  $82.3^\circ$  (220). Tantalum ( $\alpha$ -Ta) peaks  $55.5^\circ$  (200) and  $69.6^\circ$  (211) are also apparent in all XRD patterns. An additional set of peaks was found in all films, except those sputtered at  $9 \text{ W/cm}^2$  and 10 mTorr, at  $39.5^\circ$   $2\theta$ ,  $45.5^\circ$ ,  $66.2^\circ$ , and  $79.2^\circ$ . JADE 9<sup>TM</sup> software identified these peaks as possibly gamma aluminum oxide ( $\text{Al}_{2.144}\text{O}_{3.2}$ ),  $39.4^\circ$   $2\theta$  (222),  $45.8^\circ$  (400),  $66.9^\circ$  (440), and  $79.4^\circ$  (533). Films sputtered at a constant current of 0.8A and 2.5 mTorr showed similar results, Figure 3-6, with peaks present for aluminum (fcc), gamma aluminum oxide ( $\text{Al}_{2.144}\text{O}_{3.2}$ ), and tantalum ( $\alpha$ -Ta). Note that a significant broadening was found at the overlapping aluminum

(111) and tantalum (110) peaks, for films sputtered at  $9 \text{ W/cm}^2$  and 10 mTorr. This broadening was also found in the anodized film XRD patterns and is due to the underlying tantalum, Figure 3-10C.

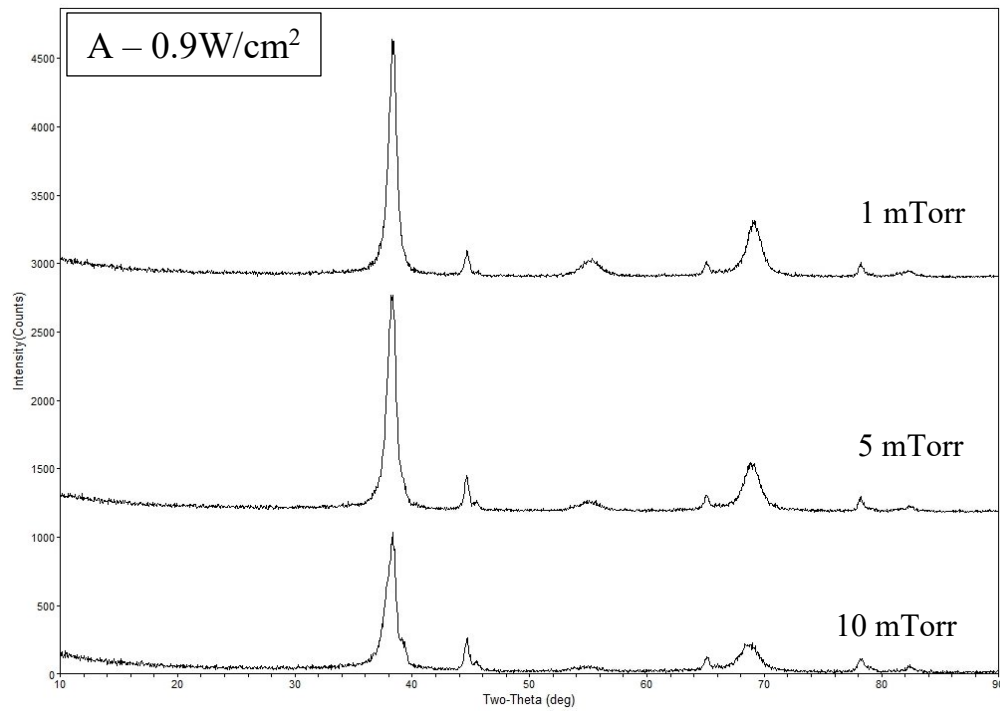


*Figure 3-5, continued.*

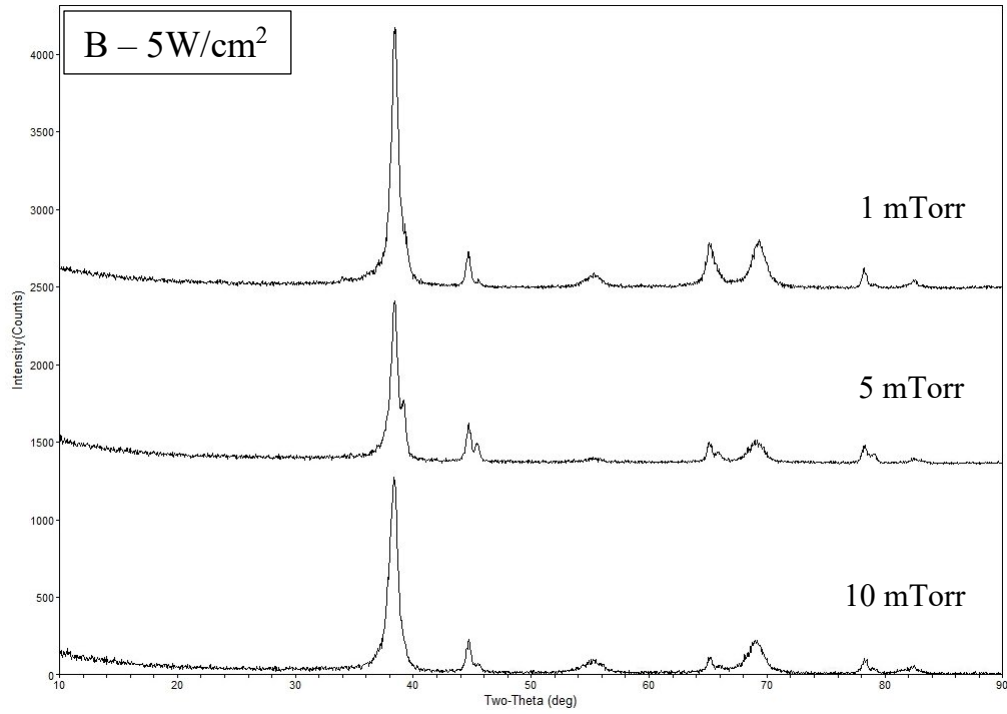


Figure 3-5, continued.

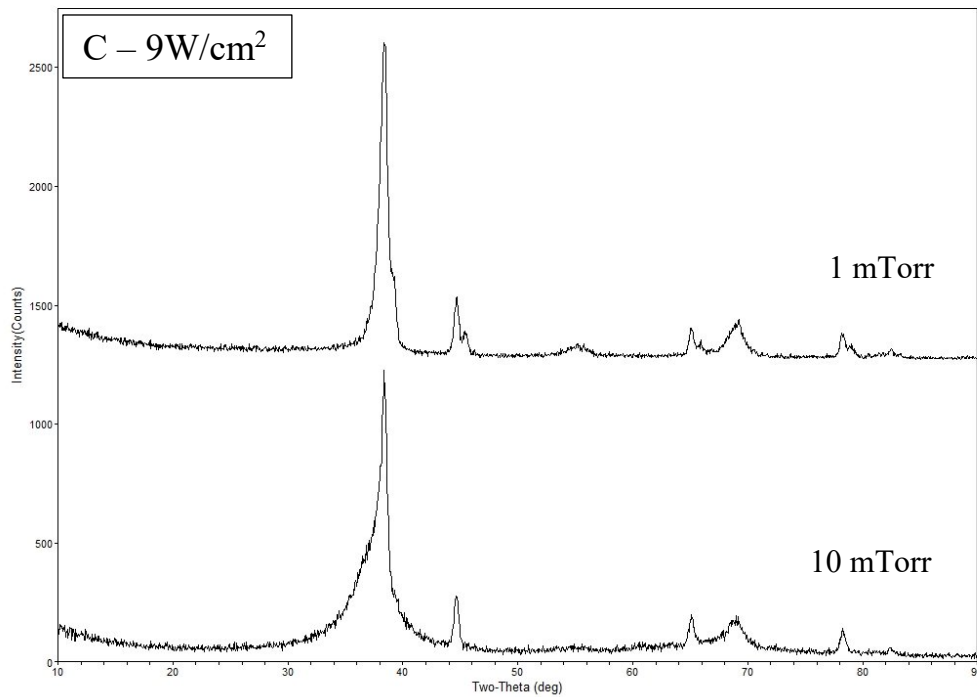
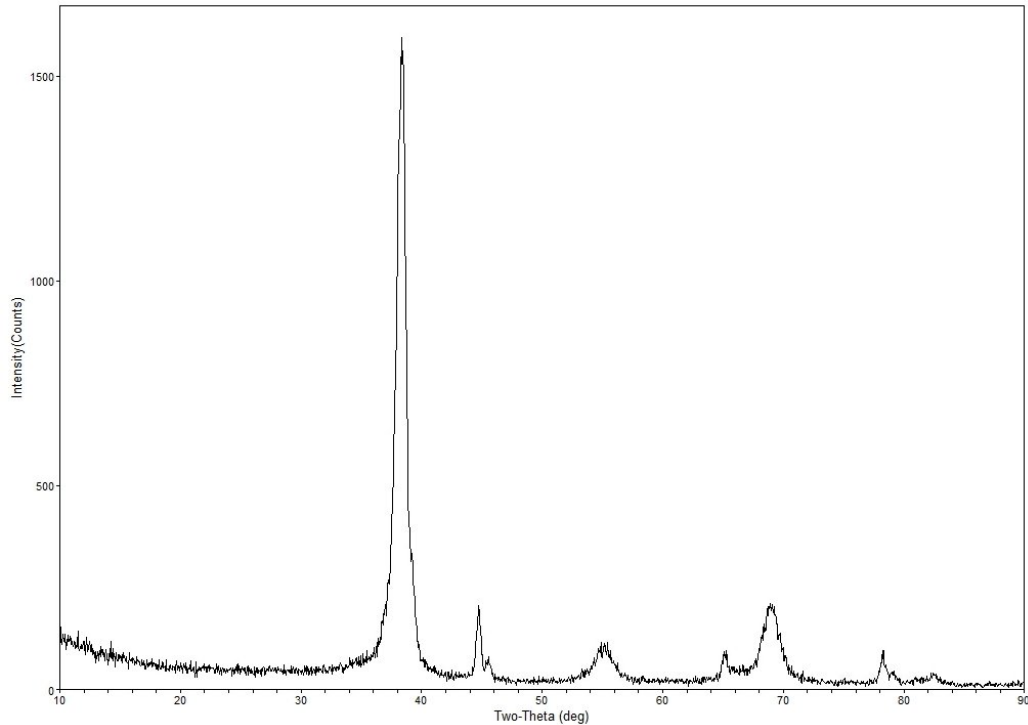


Figure 3-5, continued. XRD patterns of sputter deposited aluminum-tantalum thin films, with aluminum sputtered at various power densities and gas pressures.



*Figure 3-6. XRD patterns of sputter deposited aluminum-tantalum thin films, with aluminum sputtered at 0.8A and 2.5 mTorr.*

#### *SEM of Anodized Aluminum-Tantalum Films*

The surface SEM images of each anodized aluminum-tantalum film are shown in Figure 3-7. There is a change in anodized microstructure as the gas pressure is increased, resulting in an inhomogeneous surface with interspersed particles (50~100nm). This was noticed most significantly at 0.9 W/cm<sup>2</sup> and 10 mTorr, Figure 3-7C, and was reduced as the power was increased, or pressure decreased. Significant pitting of the surface was also apparent at 0.9 W/cm<sup>2</sup> and 10 mTorr, which was also reduced by either increased power, or decreased pressure. Films sputtered at 1 mTorr were the most homogeneous, regardless of power.

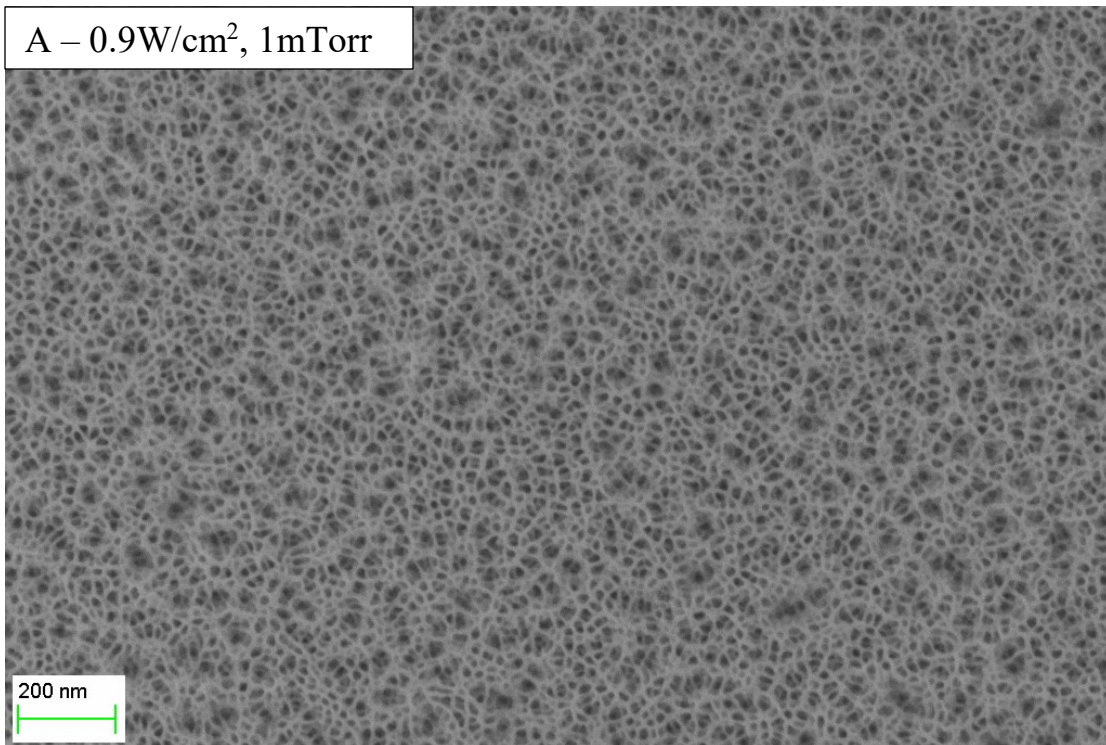


*Figure 3-7, continued.*

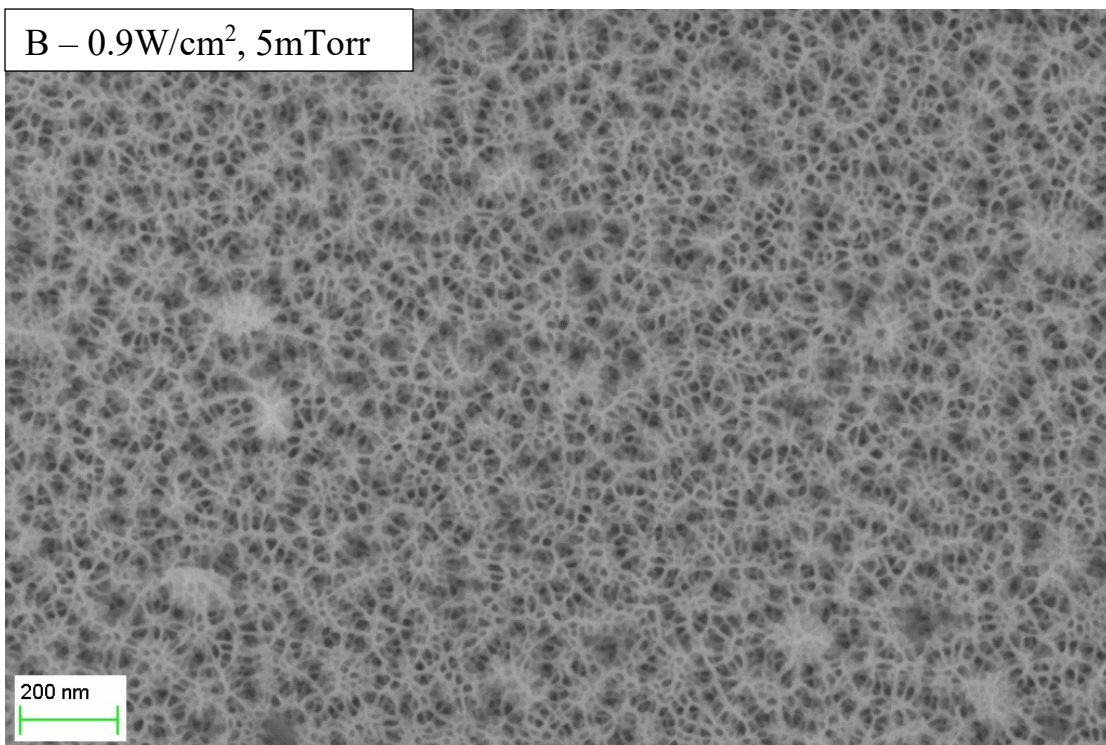


*Figure 3-7, continued.*

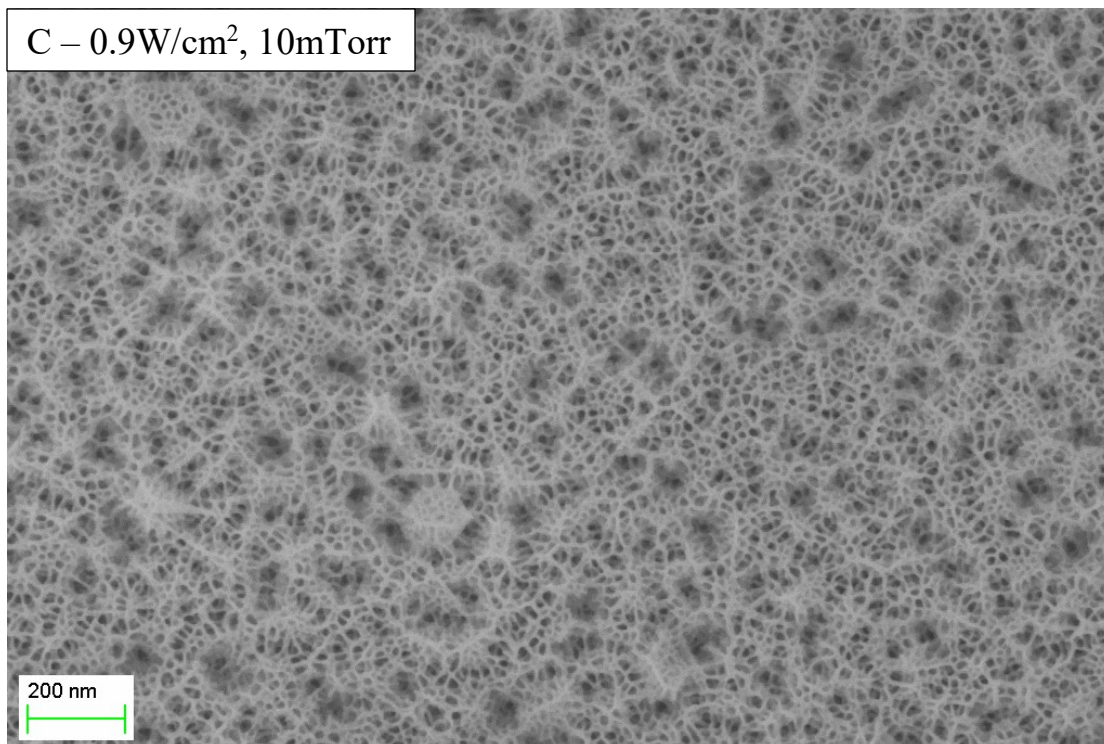


*Figure 3-7, continued.*

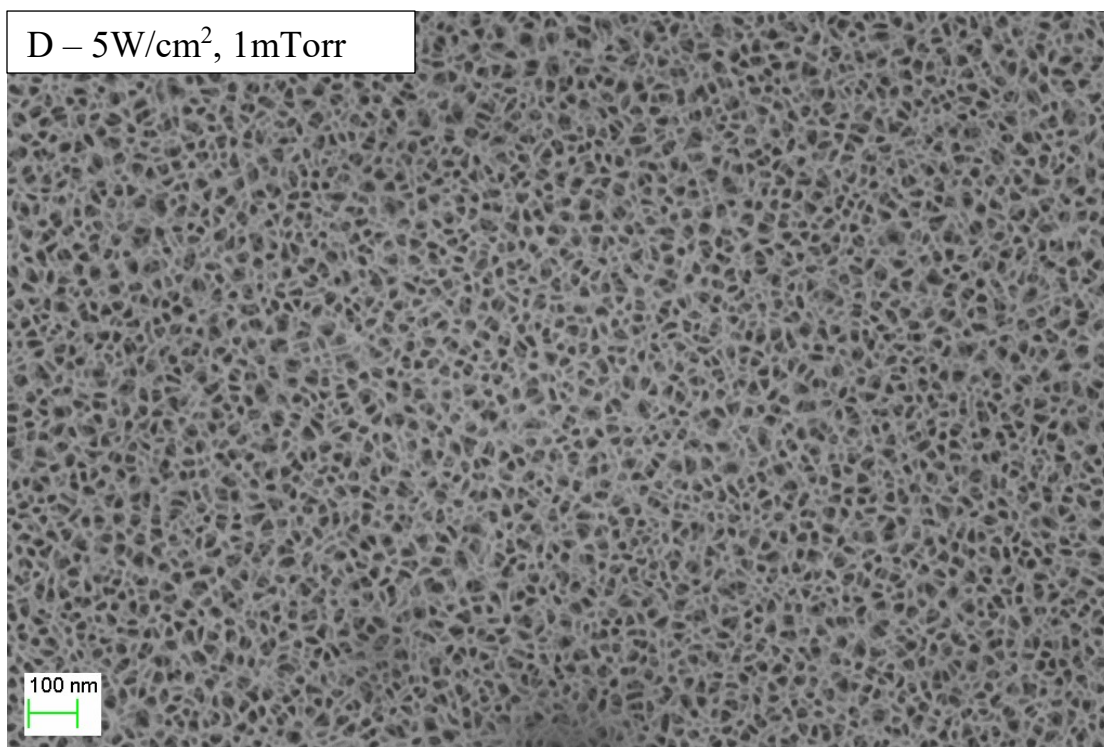


*Figure 3-7, continued.*

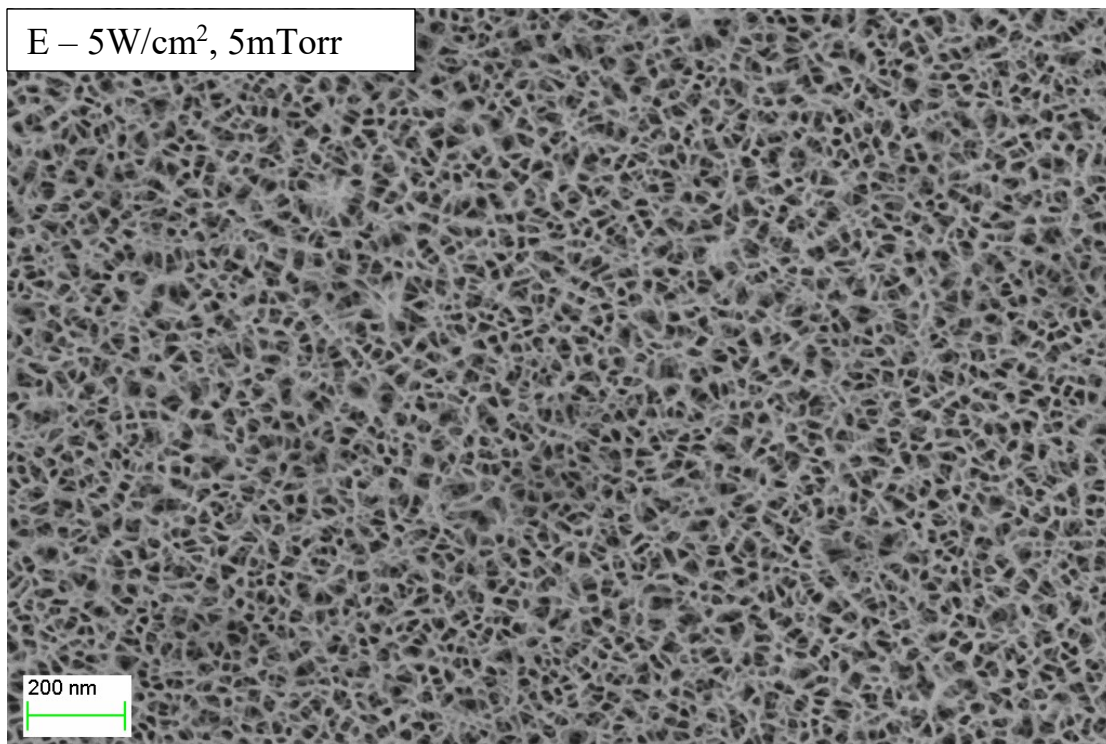


*Figure 3-7, continued.*

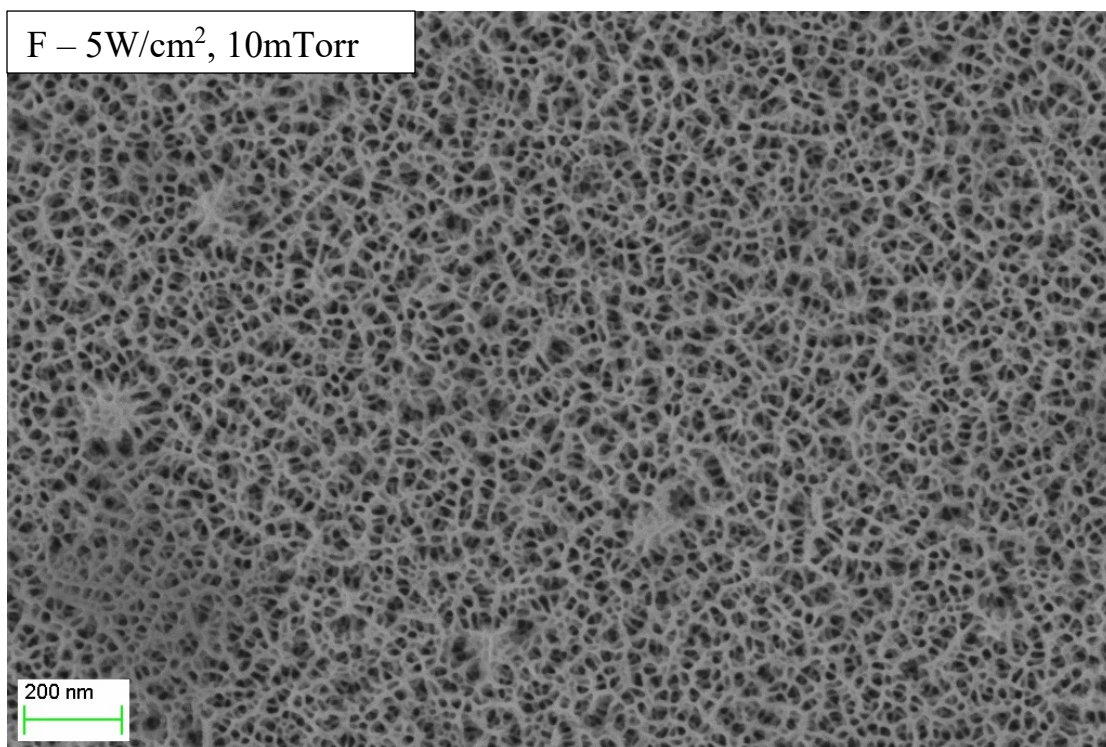


*Figure 3-7, continued.*

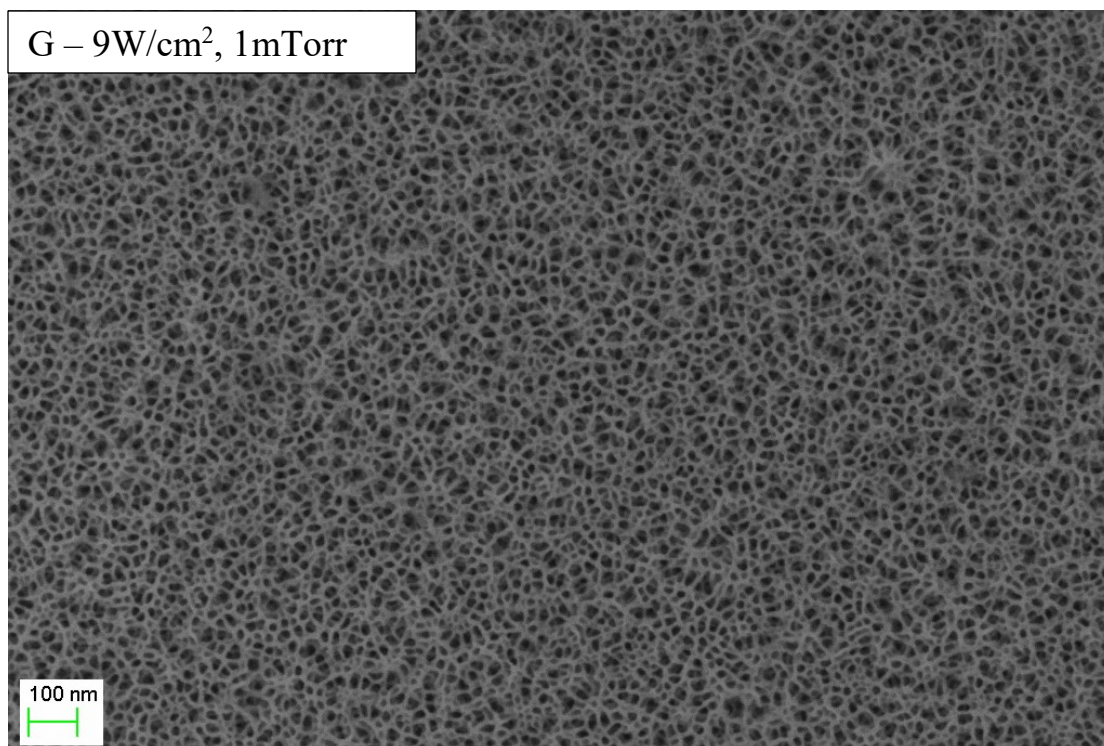


*Figure 3-7, continued.*

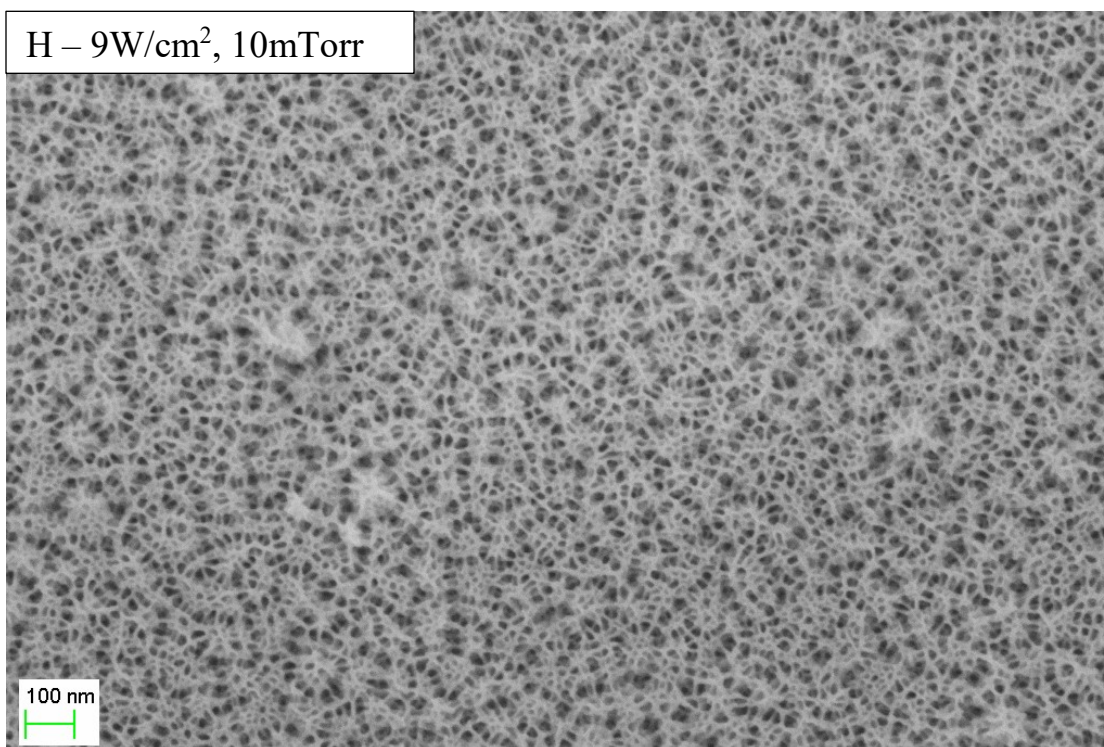


*Figure 3-7, continued. FESEM surface images of aluminum-tantalum thin films anodized at 4V in 0.4M phosphoric acid – 0.1M oxalic acid mix, with aluminum films deposited at different power densities and working Ar gas pressures.*

The TTL detector gives a unique look at the surface since it can look down through the pores. It was found that many surface pores would separate or converge, developing new pores below the surface. Edge profiles of anodized specimens are shown in Figure 3-8, for films sputtered at 0.9 W/cm<sup>2</sup>, and give a much better understanding of what is happening below the surface. The pore tortuosity increases noticeably with increased pressure from 1 to 10 mTorr. Figure 3-9 shows the surface and edge of a film sputtered at constant current (0.8A) and 2.5 mTorr. These films look very similar to those sputtered at 0.9 W/cm<sup>2</sup> and 1 or 5 mTorr.

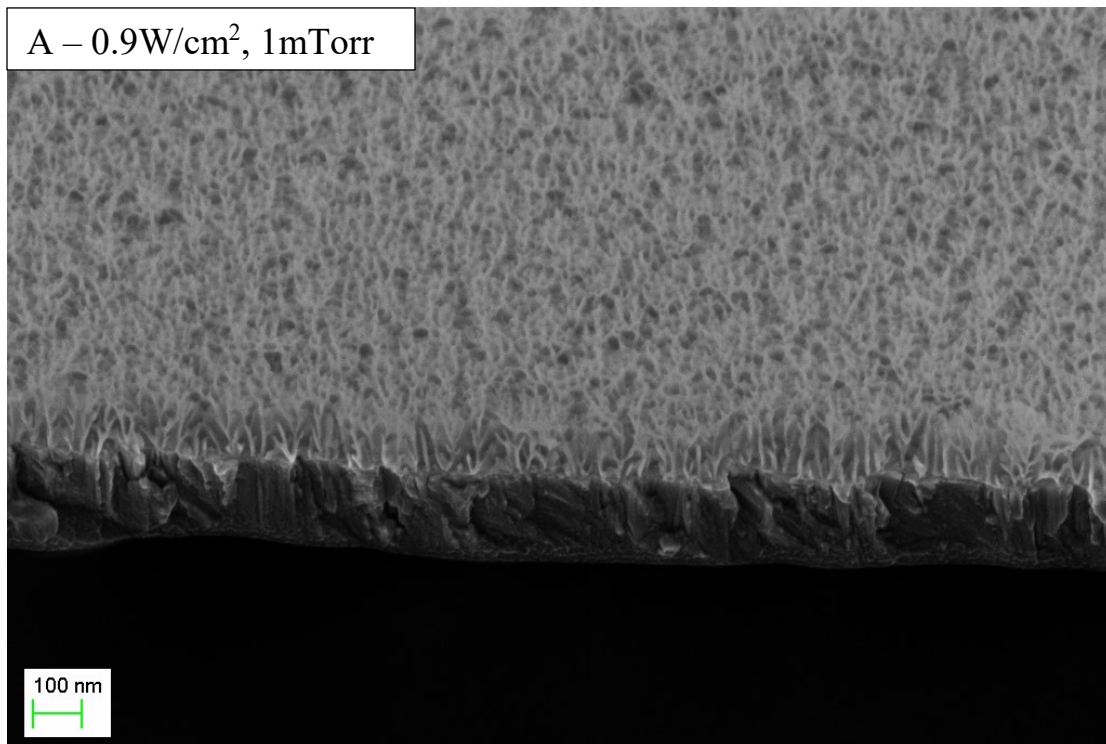


*Figure 3-8, continued.*

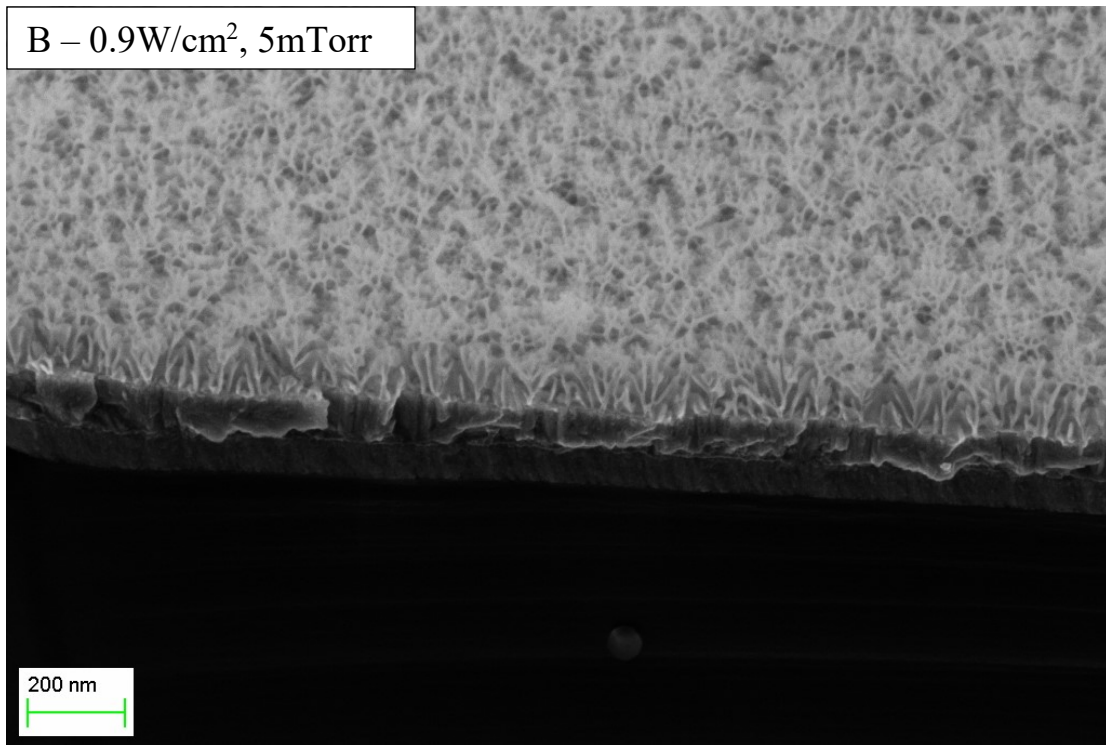


Figure 3-8, continued.

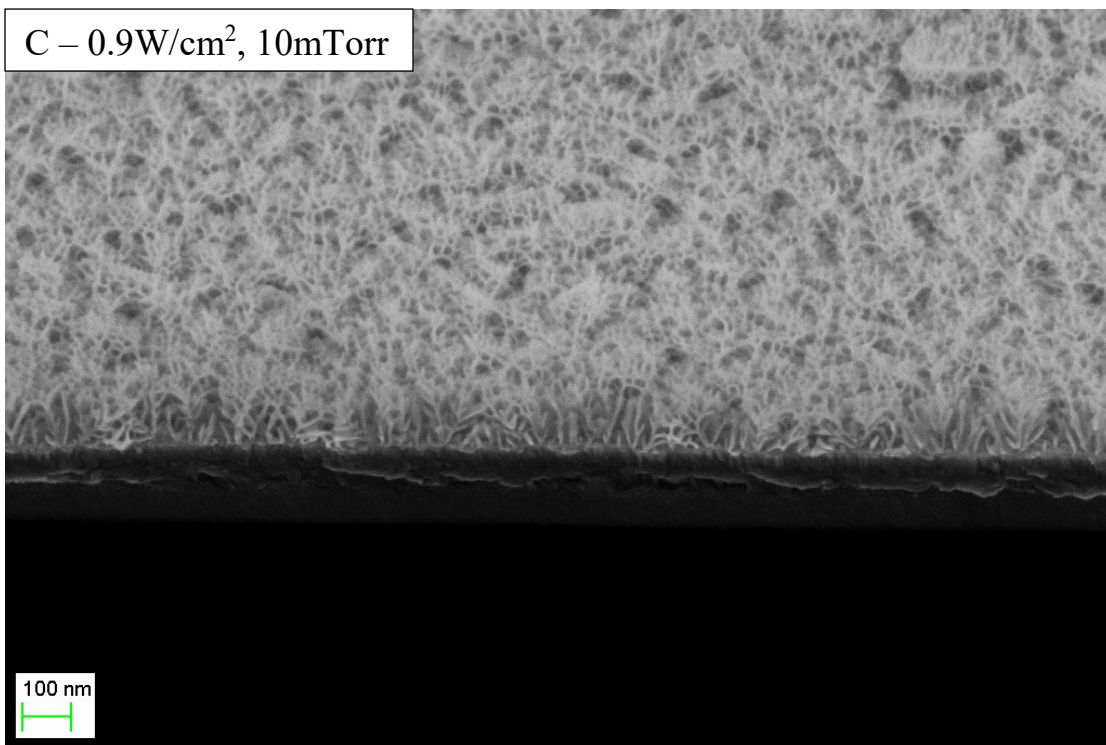
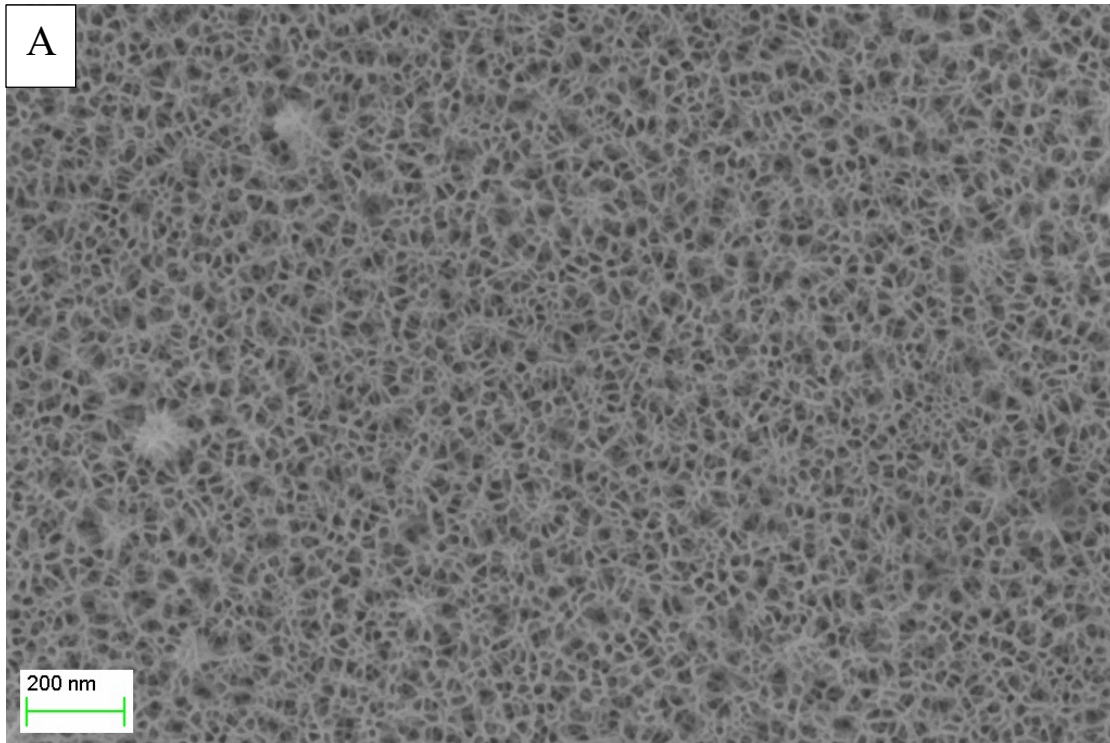
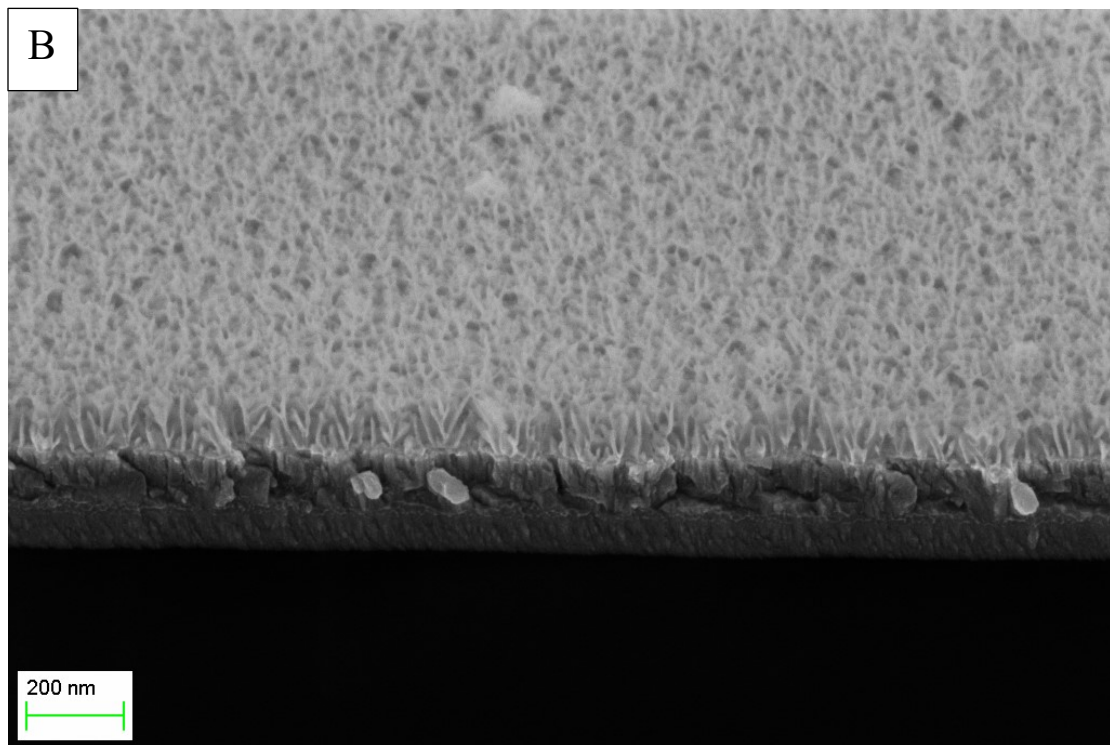


Figure 3-8, continued. FESEM fractured edge images of aluminum-tantalum sputtered thin films anodized in a 0.4M phosphoric – 0.1M oxalic acid mix at 4V, with aluminum sputtered at 0.9 W/cm<sup>2</sup> and at a gas pressure of either A) 1 mTorr, B) 5 mTorr, or C) 10 mTorr.



*Figure 3-9, continued.*



*Figure 3-9, continued. FESEM images of surface and fractured edge of an aluminum-tantalum thin film anodized in 0.4M phosphoric – 0.1M oxalic acid mix and at 4V, with aluminum sputtered at a constant current of 0.8A and argon gas pressure of 2.5 mTorr (30 sccm).*

### *XRD of Anodized Aluminum-Tantalum Films*

The XRD patterns for all anodized aluminum-tantalum films are shown in Figure 3-10. The aluminum peaks are no longer present, with only peaks corresponding to  $\alpha$  - tantalum remaining;  $2\theta$  values =  $38.4^\circ$  ( $\alpha$ -Ta 110),  $55.5^\circ$  ( $\alpha$ -Ta 200),  $69.6^\circ$  ( $\alpha$ -Ta 211), and  $82.3^\circ$  ( $\alpha$ -Ta 220). The films sputtered at  $9 \text{ W/cm}^2$  and 10 mTorr showed very broad tantalum peaks. The XRD pattern for a film sputtered at 0.8A and 2.5 mTorr is shown in Figure 3-11. Again, only peaks corresponding to  $\alpha$  - tantalum remained after anodization.

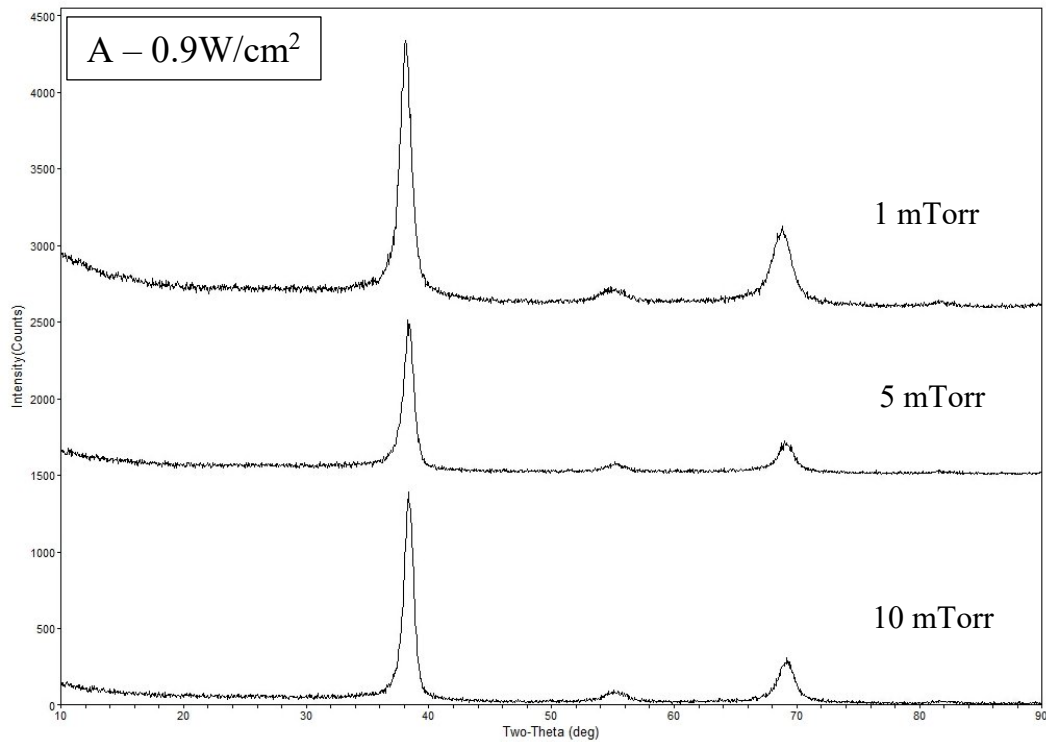


*Figure 3-10, continued.*

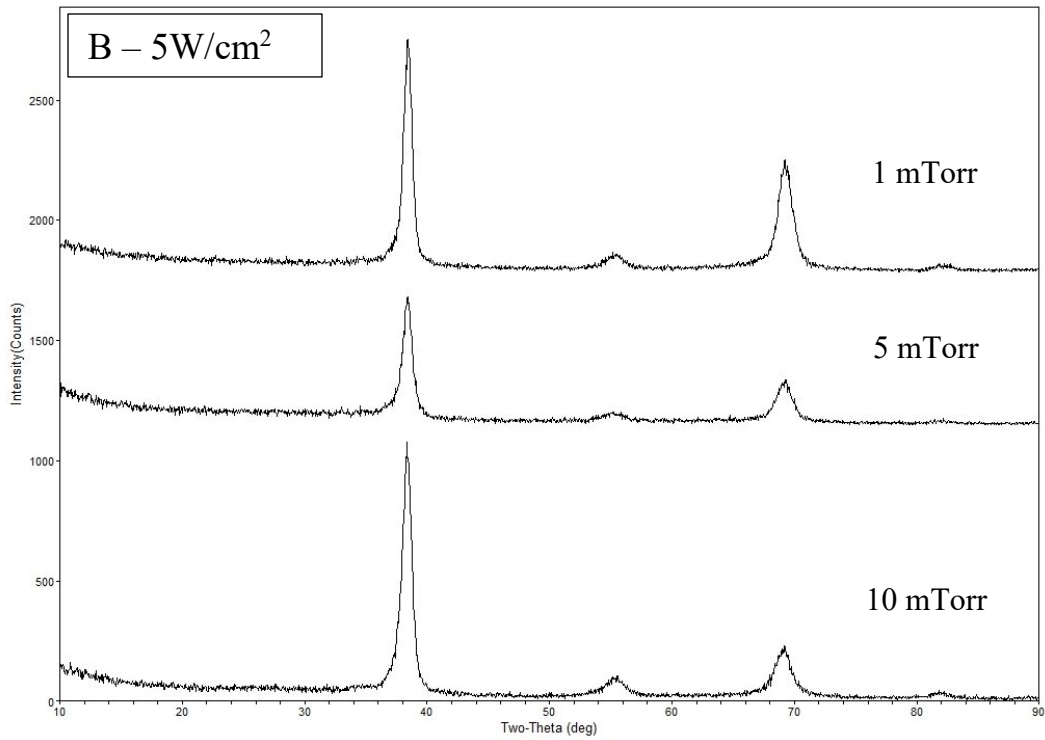


Figure 3-10, continued.

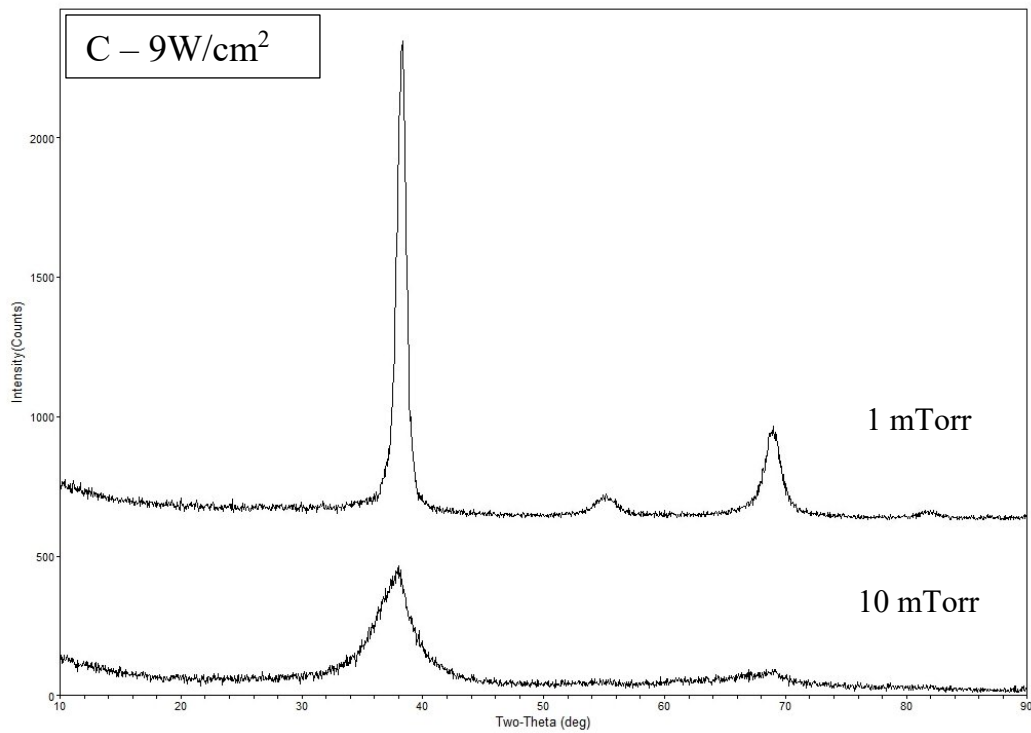
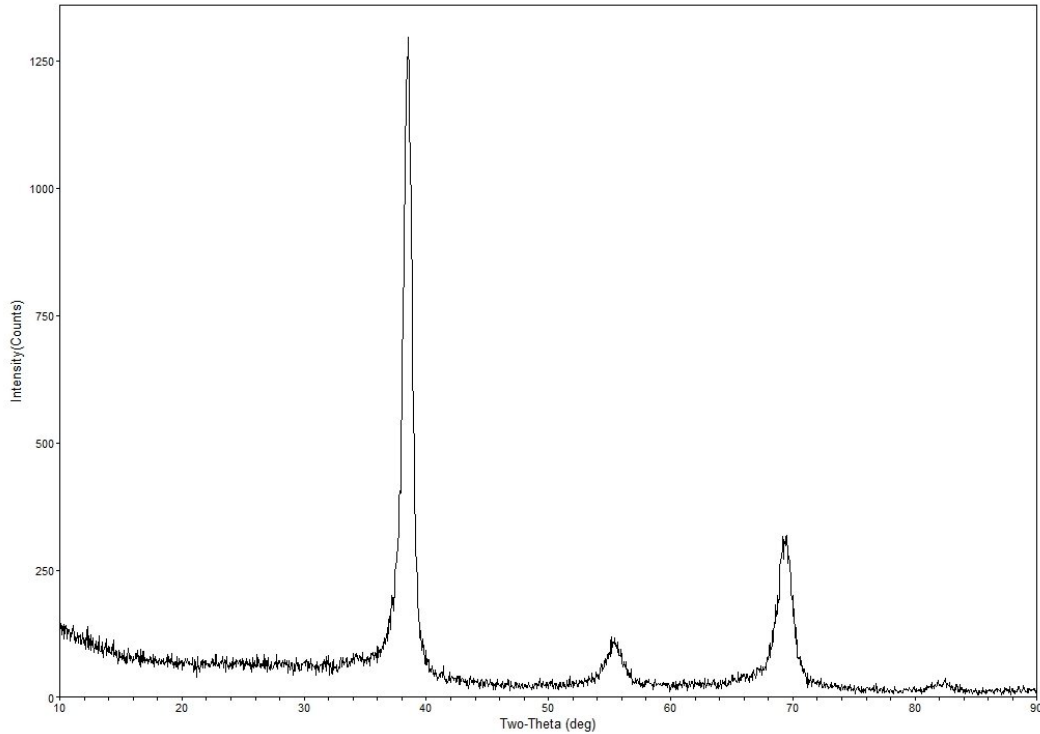


Figure 3-10, continued. XRD patterns of anodized aluminum-tantalum thin films with aluminum sputtered under various power densities and pressures.



*Figure 3-11. XRD pattern from anodized aluminum-tantalum film with aluminum sputtered at 0.8A and 2.5 mTorr.*

### *Ellipsometry*

The optical constants (refractive index,  $n$ , and extinction coefficient,  $k$ ) as well as the porous aluminum oxide thicknesses were determined using ellipsometry. Table 3-5 shows the recorded ellipsometry values for aluminum oxide thickness, refractive index ( $\lambda=555\text{nm}$ , x-y plane parallel to surface), the percent air (% void) in the effective medium approximation (EMA) model, and the mean square error (MSE).

The change in thickness for the aluminum sputtered films after anodization was recorded from the ellipsometry anodic oxide data and the SEM cross-sections taken before anodization, Table 3-6. Films sputtered at  $0.9\text{ W/cm}^2$  and 10 mTorr showed the largest change in thickness, with a  $29 \pm 12.6\text{ nm}$  reduction in thickness from anodization.

Table 3-5. Ellipsometry of anodized aluminum-tantalum thin films, with aluminum sputtered under various powers and pressures. Sample size denoted by 'n'.

Parameters	0.9 W/cm <sup>2</sup> (n=4)		
	1 mTorr	5 mTorr	10 mTorr
Thickness (nm)	136.5 ± 1.8	130.0 ± 2.0	118.0 ± 6.1
Refractive Index (λ=555nm, x-y plane)	1.308 ± 0.003	1.301 ± 0.005	1.301 ± 0.004
EMA (% void)	53.0 ± 0.4	53.8 ± 0.7	53.7 ± 0.5
MSE	12.9 ± 2.8	17.1 ± 4.0	22.9 ± 7.6
	5 W/cm <sup>2</sup> (n=2)		
	1 mTorr	5 mTorr	10 mTorr
Thickness (nm)	120.8 ± 1.1	116.9 ± 1.0	119.3 ± 4.5
Refractive Index (λ=555nm, x-y plane)	1.324 ± 0.001	1.325 ± 0.001	1.327 ± 0.001
EMA (% void)	50.9 ± 0.1	50.8 ± 0.2	50.6 ± 0.1
MSE	13.1 ± 0.5	12.7 ± 0.4	16.8 ± 3.7
	9 W/cm <sup>2</sup> (n=2)		
	1 mTorr	5 mTorr	10 mTorr
Thickness (nm)	121.6 ± 0.7	-	122.4 ± 3.1
Refractive Index (λ=555nm, x-y plane)	1.324 ± 0.005	-	1.323 ± 0.006
EMA (% void)	50.9 ± 0.6	-	51.0 ± 0.8
MSE	14.3 ± 2.0	-	39.6 ± 3.1

Films sputtered at 0.9 W/cm<sup>2</sup> had lower refractive indices (p<0.01) than those sputtered at either 5 or 9 W/cm<sup>2</sup>. No differences were found in the refractive index between those sputtered at 5 or 9 W/cm<sup>2</sup> (p>0.90). Pressure also made no significant difference (p>0.25) to the refractive index at any set power. See Table 3-7 for all statistical results on the refractive indices. The maximum difference in refractive index was found between films sputtered at 0.9 W/cm<sup>2</sup>, 10 mTorr, and 5 W/cm<sup>2</sup>, 10 mTorr, which resulted in a mean difference of 0.025 or a 1.9% change. The largest standard deviation was found for films sputtered at 9 W/cm<sup>2</sup> and 10 mTorr, which was ± 0.006 or ± 0.5%. MSE values were generally found to increase with pressure. Note that the extinction coefficient, k, in all films was found to be 0. The refractive index of films sputtered under constant

current conditions was  $1.317 \pm 0.003$  ( $\lambda=555\text{nm}$ , x-y plane), with an extinction coefficient of 0 (see Chapter 4.2 for more details on constant current sputtered films).

*Table 3-6. Mean change in thickness of the aluminum films sputtered at various parameters after anodization at 4V in 0.4M phosphoric-0.1M oxalic acid. Sample number denoted by 'n'.*

Parameters	Change in Thickness (nm)	T-test result
0.9 W/cm <sup>2</sup> , 1 mTorr (n=4)	-5.4 ± 6.3	p<0.05: 0.9W/cm <sup>2</sup> , 10 mTorr*
0.9 W/cm <sup>2</sup> , 5 mTorr (n=4)	0.7 ± 12.6	p<0.05: 0.9W/cm <sup>2</sup> , 10 mTorr
0.9 W/cm <sup>2</sup> , 10 mTorr (n=4)	-29.3 ± 12.6	p<0.10: 5W/cm <sup>2</sup> , 1mTorr; 5W/cm <sup>2</sup> , 5mTorr* p<0.05: 5W/cm <sup>2</sup> , 10mTorr*; 9W/cm <sup>2</sup> , 1mTorr*; 9W/cm <sup>2</sup> , 10mTorr
5 W/cm <sup>2</sup> , 1 mTorr (n=2)	-5.1 ± 13.2	-
5 W/cm <sup>2</sup> , 5 mTorr (n=2)	-8.5 ± 6.5	-
5 W/cm <sup>2</sup> , 10 mTorr (n=2)	-3.5 ± 6.2	-
9 W/cm <sup>2</sup> , 1 mTorr (n=2)	-1.3 ± 6.1	-
9 W/cm <sup>2</sup> , 10 mTorr (n=2)	4.5 ± 15.5	-

\*Equal variances not assumed.

Table 3-7. Statistical results of the refractive index ( $\lambda=555\text{nm}$ ,  $x\text{-}y$  plane) for aluminum films sputtered under various conditions and anodized at 4V in a 0.4M phosphoric and 0.1M oxalic acid mixture. Standard error is represented in brackets.

Parameters	ANOVA Test Result	test vs.	Post Hoc Test Results	Mean Difference
0.9 W/cm <sup>2</sup> , 1 mTorr	p<0.001	0.9 W/cm <sup>2</sup> , 5 mTorr	p>0.10	No difference
		0.9 W/cm <sup>2</sup> , 10 mTorr	p>0.10	No difference
		5 W/cm <sup>2</sup> , 1 mTorr	p<0.01, decrease	-0.016 (0.003)
		5 W/cm <sup>2</sup> , 5 mTorr	p<0.01, decrease	-0.018 (0.003)
		5 W/cm <sup>2</sup> , 10 mTorr	p<0.01, decrease	-0.019 (0.003)
		9 W/cm <sup>2</sup> , 1 mTorr	p<0.01, decrease	-0.016 (0.003)
		9 W/cm <sup>2</sup> , 10 mTorr	p<0.01, decrease	-0.016 (0.003)
0.9 W/cm <sup>2</sup> , 5 mTorr		0.9 W/cm <sup>2</sup> , 10 mTorr	p>0.10	No difference
		5 W/cm <sup>2</sup> , 1 mTorr	p<0.001, decrease	-0.023 (0.003)
		5 W/cm <sup>2</sup> , 5 mTorr	p<0.001, decrease	-0.024 (0.003)
		5 W/cm <sup>2</sup> , 10 mTorr	p<0.001, decrease	-0.026 (0.003)
		9 W/cm <sup>2</sup> , 1 mTorr	p<0.001, decrease	-0.023 (0.003)
		9 W/cm <sup>2</sup> , 10 mTorr	p<0.001, decrease	-0.022 (0.003)
0.9 W/cm <sup>2</sup> , 10 mTorr		5 W/cm <sup>2</sup> , 1 mTorr	p<0.001, decrease	-0.022 (0.003)
		5 W/cm <sup>2</sup> , 5 mTorr	p<0.001, decrease	-0.024 (0.003)
		5 W/cm <sup>2</sup> , 10 mTorr	p<0.001, decrease	-0.025 (0.003)
		9 W/cm <sup>2</sup> , 1 mTorr	p<0.001, decrease	-0.022 (0.003)
		9 W/cm <sup>2</sup> , 10 mTorr	p<0.001, decrease	-0.022 (0.003)
5 W/cm <sup>2</sup> , 1 mTorr		5 W/cm <sup>2</sup> , 5 mTorr	p>0.10	No difference
		5 W/cm <sup>2</sup> , 10 mTorr	p>0.10	No difference
		9 W/cm <sup>2</sup> , 1 mTorr	p>0.10	No difference
		9 W/cm <sup>2</sup> , 10 mTorr	p>0.10	No difference
5 W/cm <sup>2</sup> , 5 mTorr		5 W/cm <sup>2</sup> , 10 mTorr	p>0.10	No difference
		9 W/cm <sup>2</sup> , 1 mTorr	p>0.10	No difference
		9 W/cm <sup>2</sup> , 10 mTorr	p>0.10	No difference
5 W/cm <sup>2</sup> , 10 mTorr		9 W/cm <sup>2</sup> , 1 mTorr	p>0.10	No difference
		9 W/cm <sup>2</sup> , 10 mTorr	p>0.10	No difference
9 W/cm <sup>2</sup> , 1 mTorr		9 W/cm <sup>2</sup> , 10 mTorr	p>0.10	No difference

### Interference Colours

The anodized slides, visualized under s-polarized light at approximately  $75^\circ$  from normal, can be found in Figure 3-12, while Table 3-8 lists the observed colours and their RGB coordinates. The statistical results for comparison between RGB values is shown in Table 3-9. Finally, films sputtered at 0.8A and 2.5 mTorr are shown in Figure 3-13; these films were tan (R:  $106.15 \pm 11.61$ , G:  $51.01 \pm 9.99$ , B:  $22.97 \pm 2.81$ ) in colour.

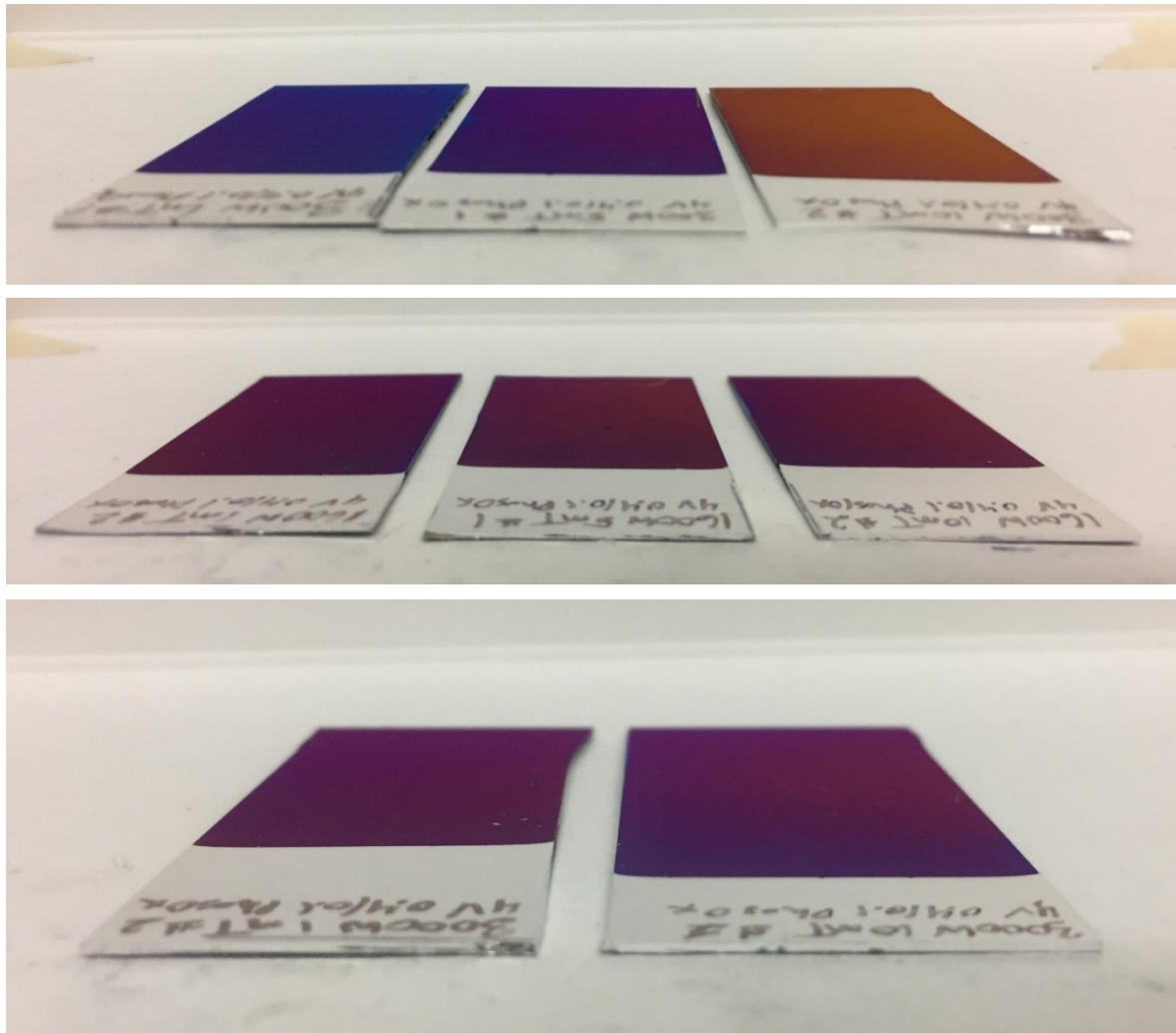


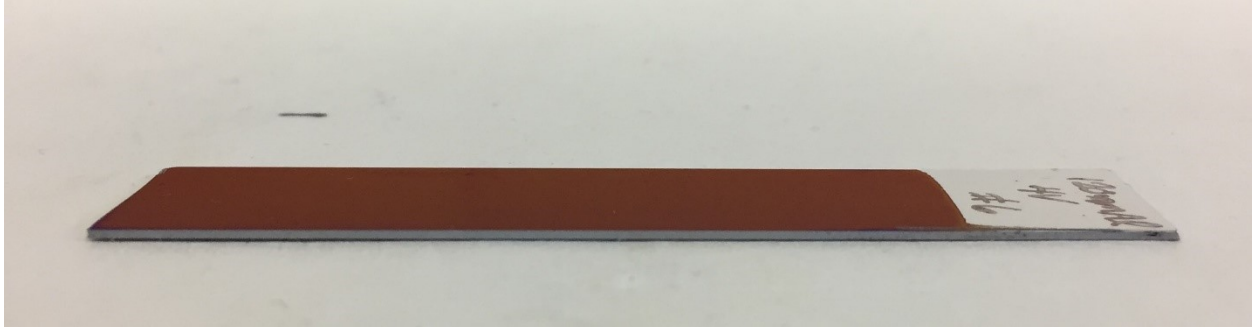
Figure 3-12. Anodized aluminum-tantalum thin films, with aluminum sputtered under various conditions, viewed at appx.  $75^\circ$  from normal through a polarizing lens (s-polarized). Top:  $0.9 \text{ W/cm}^2$ , left to right: 1 mTorr, 5 mTorr, and 10 mTorr. Middle:  $5 \text{ W/cm}^2$ , left to right: 1 mTorr, 5 mTorr, and 10 mTorr. Bottom:  $9 \text{ W/cm}^2$ , left to right: 1 mTorr and 10 mTorr.

Table 3-8. Interference colours from anodized aluminum-tantalum films; aluminum films sputtered under different parameters and anodized in 0.4M phosphoric-0.1M oxalic acid at 4V. Films observed at approximately 75° from normal with a polarizing lens (s-polarized); n=2 for all data sets.

Working Gas Pressure	Power Density		
	0.9 W/cm <sup>2</sup>	5 W/cm <sup>2</sup>	9 W/cm <sup>2</sup>
1 mTorr	Dark blue R: 35.48 ± 3.16 G: 25.07 ± 2.94 B: 90.71 ± 4.38	Plum R: 77.84 ± 6.64 G: 16.73 ± 2.43 B: 61.10 ± 6.81	Purple R: 75.61 ± 5.12 G: 18.20 ± 3.27 B: 63.25 ± 4.53
5 mTorr	Dark purple R: 60.56 ± 7.19 G: 20.84 ± 2.81 B: 84.49 ± 4.96	Plum R: 84.41 ± 6.99 G: 24.10 ± 2.62 B: 47.90 ± 4.13	N/A
10 mTorr	Tan R: 110.05 ± 7.14 G: 53.58 ± 4.94 B: 28.23 ± 3.52	Plum R: 80.79 ± 7.76 G: 23.09 ± 3.27 B: 57.06 ± 8.77	Purple R: 79.20 ± 9.20 G: 21.29 ± 2.38 B: 70.22 ± 6.50

Table 3-9. Statistical results for RGB colour coordinate analysis for anodized aluminum-tantalum thin films, with aluminum sputtered at various powers and pressures and anodized in 0.4M phosphoric-0.1M oxalic acid at 4V (n=2 for all data sets).

Parameters	ANOVA Test Result	test vs.	Post Hoc Test Results
0.9 W/cm <sup>2</sup> , 1 mTorr	p<0.001 for Red, Green, and Blue comparisons	0.9 W/cm <sup>2</sup> , 5 mTorr	p<0.10, R
		0.9 W/cm <sup>2</sup> , 10 mTorr	p<0.001, RGB
		5 W/cm <sup>2</sup> , 1 mTorr	p<0.01, RB
		5 W/cm <sup>2</sup> , 5 mTorr	p<0.01, RB
		5 W/cm <sup>2</sup> , 10 mTorr	p<0.01, RB
		9 W/cm <sup>2</sup> , 1 mTorr	p<0.05, RB
		9 W/cm <sup>2</sup> , 10 mTorr	p<0.10, RB
0.9 W/cm <sup>2</sup> , 5 mTorr		0.9 W/cm <sup>2</sup> , 10 mTorr	p<0.01, RGB
		5 W/cm <sup>2</sup> , 1 mTorr	p<0.05, B
		5 W/cm <sup>2</sup> , 5 mTorr	p<0.10, RB
		5 W/cm <sup>2</sup> , 10 mTorr	p<0.05, B
		9 W/cm <sup>2</sup> , 1 mTorr	p<0.10, B
0.9 W/cm <sup>2</sup> , 10 mTorr		9 W/cm <sup>2</sup> , 10 mTorr	No difference
		5 W/cm <sup>2</sup> , 1 mTorr	p<0.05, RGB
		5 W/cm <sup>2</sup> , 5 mTorr	p<0.10, RGB
		5 W/cm <sup>2</sup> , 10 mTorr	p<0.05, RGB
		9 W/cm <sup>2</sup> , 1 mTorr	p<0.05, RGB
5 W/cm <sup>2</sup> , 1 mTorr		9 W/cm <sup>2</sup> , 10 mTorr	p<0.05, RGB
		5 W/cm <sup>2</sup> , 5 mTorr	No difference
		5 W/cm <sup>2</sup> , 10 mTorr	No difference
		9 W/cm <sup>2</sup> , 1 mTorr	No difference
5 W/cm <sup>2</sup> , 5 mTorr		9 W/cm <sup>2</sup> , 10 mTorr	No difference
		5 W/cm <sup>2</sup> , 10 mTorr	No difference
		9 W/cm <sup>2</sup> , 1 mTorr	No difference
5 W/cm <sup>2</sup> , 10 mTorr		9 W/cm <sup>2</sup> , 10 mTorr	No difference
		9 W/cm <sup>2</sup> , 1 mTorr	No difference
9 W/cm <sup>2</sup> , 1 mTorr		9 W/cm <sup>2</sup> , 10 mTorr	No difference
		9 W/cm <sup>2</sup> , 10 mTorr	No difference



*Figure 3-13. Anodized aluminum-tantalum thin film, with aluminum sputtered at 0.8A and 2.5 mTorr, viewed at appx. 75° from normal through a polarizing lens (s-polarized).*

### **Discussion**

The results of this study show that the sputtering parameters (gas pressure and power) influence both the sputtered aluminum and the porous aluminum oxide that results after potentiostatic anodization. Power and pressure both had an effect on the morphology of the sputtered films mainly due to the amount of energy of the deposited atoms. The increase in temperature found during deposition occurs due to increased energy of the aluminum atom flux. As the power was increased at the target, there was an increase of both the voltage and current. The current density is related to the number of ions impacting the target, while the voltage is related to the ion energy [8]. As the voltage is increased, the potential difference across the cathode dark space increases and the plasma ions approach the target with greater energy, resulting in an increase in sputter yield and energy transferred to the sputtered ions [9]. This increased energy is taken with the sputtered atoms to the substrate, thereby increasing the deposition temperature. As the current is increased, the number of ions impacting the target per unit time increases, which leads to higher sputter rates. A 10x increase in power led to an ~8-9x increase in the deposition rate, see Table 3-2, and an ~8-15x increase in variability of the deposition rate. As discussed in Chapter 1 Section 1.2, the colour generated from thin film interference is extremely sensitive to changes in thickness

with previous works showing thickness changes as small as 0.7nm [22] to 2.7nm [23] generating colour shifts. Therefore, a strong control on deposition rate, with as little variance as possible, is required to create consistent film colour.

As the working gas pressure increases in the chamber, the mean free path ( $\lambda$ ) of sputtered atoms is decreased ( $\lambda \propto P^{-1}$ , where P is the total pressure in the gas chamber [24]). A smaller mean free path means that more collisions occur between the sputtered atoms and gas atoms in the chamber. These collisions reduce the kinetic energy of the sputtered atoms and therefore the atoms land with less energy on the substrate. The energy loss eventually leads to thermalization of the flux, where the sputtered atoms have transitioned from a ballistic to diffusion regime [10]. This energy loss is noticed at 5 W/cm<sup>2</sup>, where the recorded temperature decreases when the pressure is increased, from 71°C < T < 93°C to 60°C < T < 82°C for 1 to 10 mTorr, respectively. The increase in pressure also reduces the deposition rate due to both thermalization of the flux, causing slower movement of sputtered atoms through the chamber, and backscattering of sputtered atoms.

The amount of kinetic or thermal energy an atom has when it reaches the substrate surface is very important for adatom (adsorbed atom) surface diffusion. At low powers and high pressures, there is limited adatom surface mobility and therefore atoms cannot diffuse to high energy crystal edge sites after they condense on the substrate surface. Instead, the deposited nuclei will grow in the direction of the sputtered flux [9]. The adatom diffusion is responsible for the difference between Thornton's zone 1 and zone T [6]. As the energy of the adsorbed atom is increased, diffusion increases on the surface and the voids between growing nuclei are filled in, developing smoother, denser films. This can be seen when observing the differences between films sputtered at low and high power, e.g. Figures 3-2A and 3-2G, or low and high pressure, e.g. Figures 3-2A and 3-2C. All micrographs showed an increase in voided grain boundaries or surface roughness when the

power was decreased, or the gas pressure increased. In other words, the lower the energy of the flux, the more voided and rougher the deposited film.

The study by Choudhury and Raghavan [15] found that large changes to the energy of a sputtered aluminum flux did not significantly affect the anodized microstructure. Their sputtering was conducted at very high pressures (40 mTorr) and a substrate to target separation of 75 mm. The low melting point of aluminum (933K) was used to explain the lack of microstructural change, as even at room temperature  $T/T_m$  is 0.32, where  $T$  is the substrate temperature and  $T_m$  is the melting point of aluminum. According to Thornton's structure zone diagram [6], this temperature ratio is already in the dense transition zone (Zone T) and therefore significant adatom surface mobility exists, making it difficult to generate the voided Zone 1 structures. However, our study more resembled the works of Chung et al. [18] and Liao et al. [17]. Choudhury and Raghavan used a much lower base pressure ( $10^{-7}$  Torr) than Chung or Liao (both at  $2.7 \times 10^{-4}$  Torr) or our study ( $1.8 \times 10^{-6}$  Torr). Previous works have shown the effects that residual gases and the base pressure have on sputtered aluminum films [25, 26]. Higher concentrations of oxygen can lead to the formation of oxide particles and microcrystalline aluminum, with oxide particles pinning the grain boundaries [25]. Therefore, the residual oxygen and nitrogen in the chamber contribute significantly to the sputtered microstructure and explains why some studies show more effects than others from the sputtering parameters.

The incorporation of oxygen into the film is dependent on both the gas impingement rate,  $\phi$ , and the aluminum deposition rate, as follows:

$$\phi_{O_2} = (2\pi m_{O_2} kT)^{-0.5} p_{O_2} \quad (3.1)$$

$$\% \text{ Oxygen in Film} = \frac{\phi_{O_2}}{\text{Al flux} + \phi_{O_2}} \times 100 \quad (3.2)$$

Where  $\varphi_{O_2}$  is the oxygen gas impingement rate (atoms/cm<sup>2</sup>·s),  $m_{O_2}$  is the mass of oxygen (g),  $k$  is Boltzmann's constant,  $T$  is the temperature (K),  $p_{O_2}$  is the partial pressure of oxygen (Pa), and  $Al\ flux$  is the aluminum deposition rate (atoms/cm<sup>2</sup>·s), [27]. Therefore, from Equation (3.2), higher deposition rates lead to lower oxygen contamination when sputtering. The base pressure is another contributor to the oxygen and nitrogen content in the films. All films were sputtered with a base pressure of  $1.8 \times 10^{-6}$  Torr. Figure 3-14 shows a surface SEM image of an aluminum film sputtered under the conditions listed in Chapter 4.1 (base pressure of  $1.0 \times 10^{-7}$  Torr). Observing Equation (3.1) above, higher O<sub>2</sub> partial pressures lead to a higher O<sub>2</sub> impingement rate ( $\varphi$ ) and thus higher levels of oxygen contamination.

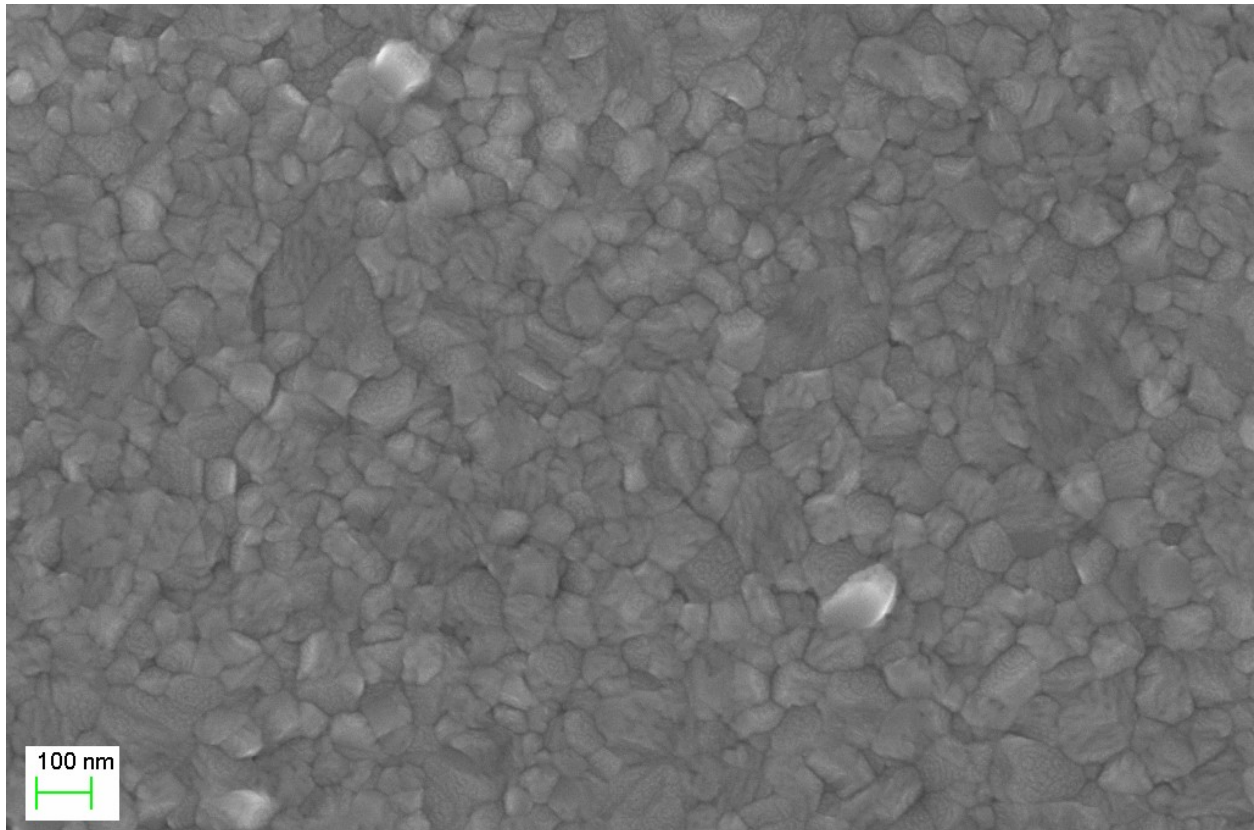


*Figure 3-14. FESEM image of aluminum film sputtered to the conditions described in Chapter 4.1, with a base pressure of  $1.0 \times 10^{-7}$  Torr.*

The EDX and XRD data confirm the presence of oxide impurities. From EDX, the sputtered film had up to  $4.36 \pm 0.20$  at.% oxygen, and the XRD patterns showed a series of peaks corresponding to gamma aluminum oxide ( $Al_{2.144}O_{3.2}$ ). The only film that did not contain aluminum oxide peaks was that sputtered at  $9W/cm^2$  and 10 mTorr. The higher power results in a larger aluminum deposition rate (*Al flux*) and therefore a lower % oxygen in the film, Equation (3.2). Also, a higher pressure was accompanied by a larger working gas flow rate, 135 sccm (10 mTorr) vs. 9 sccm (1 mTorr). The higher pressure and flow rate would reduce both the partial pressure of oxygen in the chamber and help mask any residual gases coming back into the chamber from leaks in the system. It was hypothesized that defects in the film, such as voids or oxide particles, would cause differences during the anodization process; the results of anodization are discussed later.

Figure 3-3 shows the SEM images of large particles that were deposited on the substrate surface at  $9 W/cm^2$ . EDX demonstrated that these particles were comprised primarily of aluminum with some oxygen and nitrogen, Table 3-3, at levels not significantly varying from the remainder of the film ( $p>0.2$ ). The system is a sputter-down configuration; therefore, it is likely that these are particles of aluminum that were redeposited on the target surface and fell onto the substrate when the power was significantly increased ( $9 W/cm^2$  or 3 kW vs. historical operation of the machine at  $1.54 W/cm^2$  or 500W). The high temperature and increased size of the plasma could cause these aluminum particles to break off from the target and fall onto the substrate surface. Strain likely builds up to cause these particles to break off, with the strain caused by the mismatch in thermal expansion coefficients between aluminum metal ( $21-24 \times 10^{-6}/^{\circ}C$ ) and aluminum oxide ( $7-10.9 \times 10^{-6}/^{\circ}C$ ) [28]. A picture of the target is shown in Figure 3-15. Note the white oxide build up on everywhere but the sputter tracks. The re-deposition of aluminum that occurs on this part of the target produces a rough surface that, when exposed to atmosphere, develops a thick oxide layer

which can be seen as white. The deposition of large aluminum particles is not favorable from an optics perspective. Not only would this create a non-uniform film thickness and thus generate a mixture of interference colours, however it is also likely that these particles increase the scattering of light and introduce noise into the thin film system. In Chapter 5 the effects of this microstructure on the sensitivity of detecting adsorbed proteins is further studied.

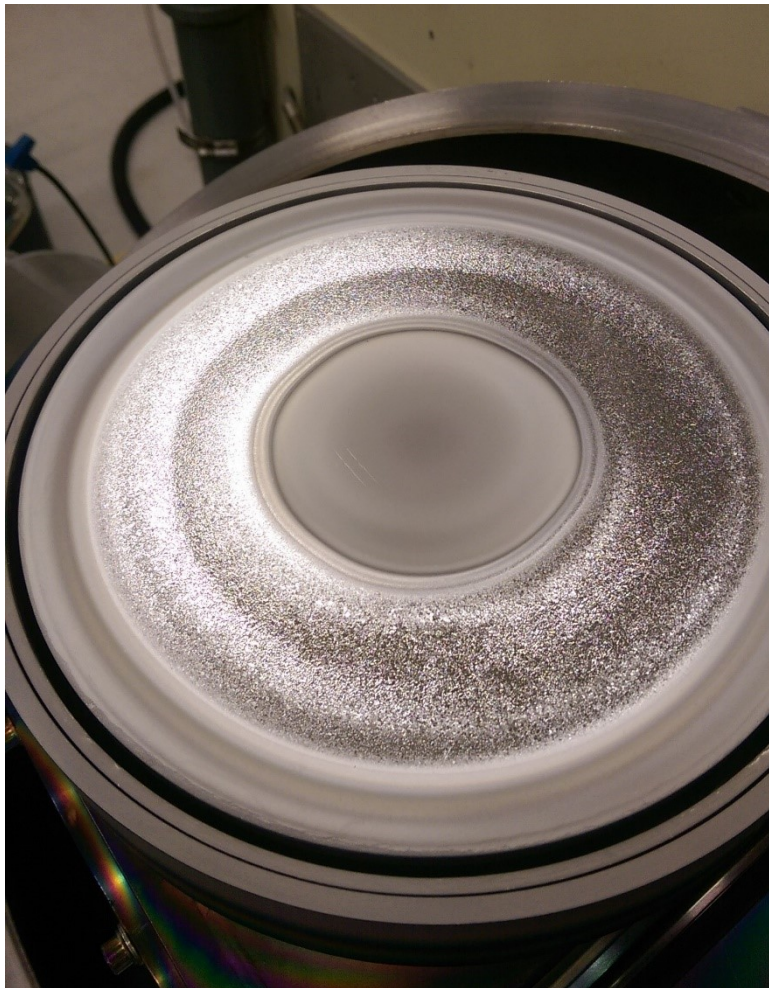


*Figure 3-15. Aluminum target 99.995% Al (Kurt J. Lesker Company, Jefferson Hills, PA) used in the magnetron sputtering machine at NAIT nanoFacility (photo courtesy of Ciaran Terry). Note the white oxide that has developed at the target center and edges after the target was exposed to atmosphere.*

Films sputtered at either 5 or 10 mTorr formed small oxide particles (50 – 100nm) during anodization, e.g. Figures 6B and 6C. These small, anodized particles may occur due to topography. The open, voided structure of the films formed at higher pressures allows for more oxidation when exposed to atmosphere. These particles may then completely oxidize during the barrier oxide formation phase or soon after pore formation initiates; look to Chapter 1 Section 1.5 for an understanding of the phases of porous anodization of aluminum. Figure 3-16 shows how pore formation appeared to start but was not completed in one of these particles. A study by Lebyedeva et al. [19] showed a similar result, where non-through pores formed on protruding grains.

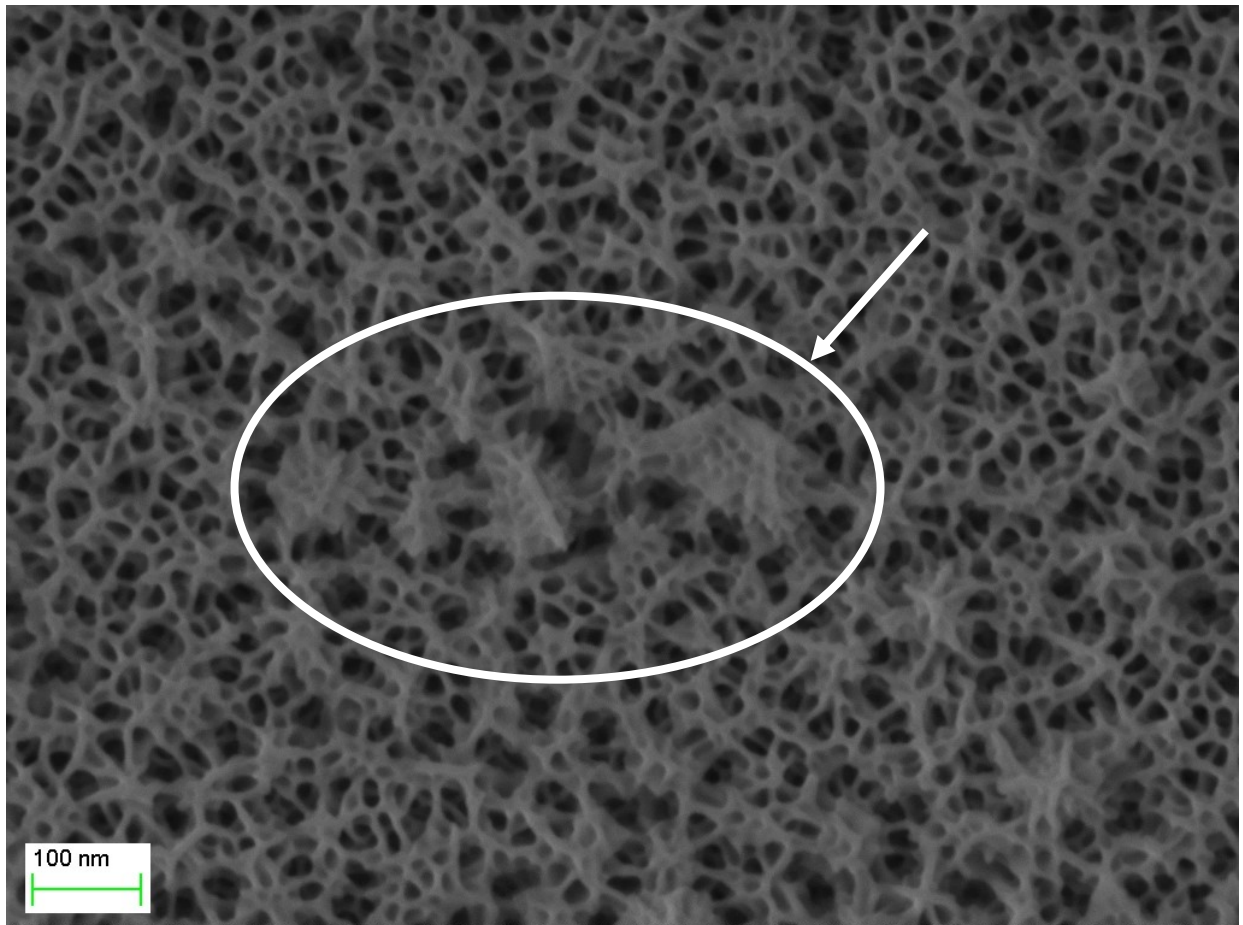


*Figure 3-16. FESEM micrograph of anodized aluminum-tantalum thin film, with aluminum sputtered at  $0.9 \text{ W/cm}^2$  and 10 mTorr. The circle outlines an aluminum oxide particle that was not porous anodized all the way through and was likely fully oxidized soon after pore formation initiated.*

Another feature of films sputtered at 5 and 10 mTorr appears to be large pitting of the surface, similar to that found when anodizing in pure phosphoric acid as opposed to a phosphoric-oxalic mix (see Chapter 4.1). This pitting is due to the aggressiveness of the electrolyte attacking active sites on the aluminum surface, such as defects and grain boundaries. As discussed earlier, films sputtered at higher pressures were found to have rougher surfaces and voided boundaries. XRD also showed gamma aluminum oxide which is contributing to the pinning of grain boundaries. The electrolyte is therefore able to more aggressively attack surfaces sputtered at higher pressures, leaving the pitted surfaces found. On the other hand, films sputtered at 1 mTorr were more uniform and showed little to no pitting. The edge profiles in Figure 3-7 clearly show the change in the porous nanostructure as the pressure is increased. Films sputtered at 10 mTorr, Figure 3-7C, show irregular pore growth (highly tortuous) and rougher surfaces than those sputtered at 1 mTorr, Figure 3-7A. As the pores grow down into the aluminum film, they would deviate based on encountered defects, such as oxide impurities or voids. Kim and Lee [29] showed how impurities in an aluminum film act as defects, changing the pore formation during anodization by inducing imbalances in the electric field.

It is interesting to note that the XRD patterns obtained after anodization all showed strictly  $\alpha$ -Ta peaks. Even though almost every sputtered microstructure contained gamma aluminum oxide to begin with, the anodization process appeared to consume this crystalline oxide and produce only an amorphous oxide. It is also interesting to note that consumption anodization of aluminum occurred regardless of the initial microstructure, also evident by a lack of peaks other than tantalum. One unusual observation found was the broad tantalum peaks for the films sputtered at  $9\text{W}/\text{cm}^2$  and 10 mTorr. Peak broadening occurs due to a smaller crystallite size and more

amorphous structure. Therefore, there was inconsistencies in the tantalum deposition which contributed to the broad peaks in these samples.

Theoretically, an ideal film for use in thin film diagnostics would be optically smooth and homogenous. Surface roughness, pore tortuosity, and non-through anodized oxide particles would all lead to an increase in the amount of scattered light and noise in the system. In Chapter 5, the effect of these microstructures on the visible sensitivity of adsorbed protein layers is studied. Ultimately, it is very interesting to note that sputtering parameters had a less significant effect on the optical properties of the anodized aluminum. For example, the ellipsometry results show that the refractive index is relatively robust to changes in sputtered aluminum microstructure with a maximum change of no larger than  $1.9 \pm 0.2\%$  between all sputtered and anodized films, Table 3-7. The only changes found were between  $0.9 \text{ W/cm}^2$  and the higher power densities used (5 and  $9 \text{ W/cm}^2$ ). In other words, the ellipsometry results under the current model show that pressure has no significant effect on the refractive index in the x-y plane (plane parallel with the surface). However, notice the increased mean square error found with increased pressure, Table 3-5. The current model uses a depolarization factor of 0 in the z plane and 0.5 in the x-y plane, which simulates a structure of perfectly straight pores consisting of air with the remainder being aluminum oxide. Films sputtered at 10 mTorr show very irregular pore growth and little to no straight pore formation. This tortuous pore growth is likely the reason why error increased with pressure.

The change in refractive index between films sputtered at  $0.9 \text{ W/cm}^2$  or 5 and  $9 \text{ W/cm}^2$  is attributed to film and defect density. The low power films contain more defects and voids, and are therefore attacked more aggressively by the electrolyte. This would lead to higher dissolution rates, more air in the anodized film, and lower refractive indices. However, the change in refractive index is

minimal, with only a maximum mean difference of 0.026 or 1.9% occurring between 0.9 W/cm<sup>2</sup>, 5 mTorr and 5 W/cm<sup>2</sup>, 10 mTorr (see Table 3-7). This relatively small difference shows the robustness of the anodic film porosity to changes in aluminum microstructure.

As discussed in Chapter 1 Section 1.3.1, interference colours follow a specific order based on the constructive and destructive interference of smallest to largest wavelengths. The interference colours observed appear to follow the first order interference regime of yellow to red and eventually progress into second order purples and blues. Colour differences were found to occur with both changes in thickness and refractive index, as would be expected. Films sputtered at 0.9 W/cm<sup>2</sup> showed no significant differences in refractive index with change in pressure, however they did show differences in colour, Table 3-9, which is due to the difference in oxide thickness, Table 3-5. On the other hand, films sputtered at 0.9 W/cm<sup>2</sup> and 10 mTorr showed a significant difference ( $p < 0.05$ ) in colour compared to 5 and 9 W/cm<sup>2</sup> despite a similar thickness; therefore, the colour difference here is probably from the difference in refractive index as well as the large particles found on the surface.

SEM cross-sections were taken of the sputtered aluminum films to confirm whether they all had the same starting thickness, Table 3-4. It was found that the starting thicknesses were not the same and the change in thickness after anodization was also different, depending on the sputtering conditions. Almost all films showed a reduction in thickness after anodizing, with the largest change occurring with aluminum sputtered at 0.9 W/cm<sup>2</sup> and 10 mTorr, Table 3-6. These films showed the largest voids, Figure 3-2C, and the most uneven anodization, Figure 3-6C. The large voids and high density of defects in these films likely allows for higher dissolution rates in the acid electrolyte, as discussed earlier. It is important to reduce the amount of dissolution occurring during anodization for two reasons: (1) more dissolution leads to larger pore size, which can then

allow the infiltration of protein into the pore. If protein infiltrates the pores, there is a change in the anodic film refractive index and a lower sensitivity of the device due to mismatch between the protein and porous alumina refractive indices. (2) Reducing the dissolution rate helps to keep a consistent film thickness and allows for stronger quality control during manufacturing.

In Chapter 4.1, it was found that anodizing in phosphoric acid versus a phosphoric-oxalic mix led to higher surface roughness and thinner anodic films after anodization. The oxalic acid acts as an inhibitor to the alumina dissolution and allows for smoother, thicker film growth. Sweet [31] found that higher voltages lead to higher dissolution rates for phosphoric acid anodization of aluminum-tantalum thin films in the range of 3-10V, however in Chapter 4.2 of this work the voltage range of 2-8V found minimal change in thickness when using a phosphoric-oxalic acid mix. Therefore, when this study states that the refractive index change is robust to microstructure, that is considering that an inhibited electrolyte is being used. It is likely that using a film with a large number of defects, such as those made at  $0.9 \text{ W/cm}^2$  and 10 mTorr, as well as an aggressive electrolyte, such as pure phosphoric acid, would lead to much larger variability of film thickness, refractive index, and interference colours.

In part B of this study, films were sputtered under constant current conditions to improve thickness tolerance. Current is the most significant parameter to control the deposition rate, since the number of particles colliding with the cathode target is proportional to the current [30]. The microstructure of these films, before and after anodization, is similar to those sputtered at  $0.9 \text{ W/cm}^2$  and either 1 or 5 mTorr. Future work in this thesis (see Chapters 4.2, 5 and 6) used this microstructure as it allowed for a consistent deposited thickness over the lifetime of the aluminum target.

## Conclusion

Overall, this work has contributed to the understanding of how sputtering parameters affect the anodization of sputtered aluminum-tantalum films, as well as the structural and optical properties of the anodic oxide. Based on the results of this study, the following conclusions have been made for films anodized at 4V in 0.4M phosphoric-0.1M oxalic acid:

1. The structure and topography of anodized aluminum is highly dependent on the sputtered microstructure. Sputtering parameters that lead to voided grain boundaries and more defects cause increased pore tortuosity, inhomogeneity of the porous anodized surface, pitting, and higher dissolution rates.
2. Regardless of the sputtered aluminum microstructure, consumption anodization of the aluminum occurs, producing amorphous aluminum and tantalum oxides.
3. The optical properties of the porous anodic alumina, specifically the refractive index in the x-y plane, are robust to changes in the sputtered aluminum microstructure. However, this cannot be extrapolated to anodization in other electrolytes or voltages.

With respect to the manufacturing of thin films diagnostics, based on anodized aluminum-tantalum thin films, a few recommendations follow. Sputtering parameters should be under tight quality control with careful attention to: (a) maintain a low base pressure,  $10^{-6}$  Torr or preferably  $10^{-7}$  Torr, as oxygen and nitrogen can affect the anodized structure and introduce impurities and defects; (b) aluminum deposition parameters should be carefully chosen to produce dense films (Zone T or Zone 2) at low deposition rates, which helps to control the final oxide (and thus interference colour generated) by producing optically flat, uniform films, with consistent thicknesses.

## References

- [1] C. R. Fuller and P. B. Ghate, "Magnetron-sputtered aluminum films for integrated circuit interconnections," *Thin Solid Films*, vol. 64, pp. 25-37, 1979.
- [2] L. D. Hartsough and P. S. McLeod, "High-rate sputtering of enhanced aluminum mirrors," *Journal of Vacuum Science and Technology*, vol. 14, no. 1, p. 123, 1977.
- [3] I. Hong, C. Chiu, H. Huang and R. Hsieh, "A Study of the Microstructure, Texture and Sputtering Properties of 5N High-purity Aluminum Target," *China Steel Technical Report*, vol. 24, p. 56, 2011.
- [4] L. Piergiovanni and S. Limbo, "Metal Packaging Materials," in *Food Packaging Materials*, NY, Springer, Cham, 2016, pp. 13-21.
- [5] J. A. Thornton, "The microstructure of sputter-deposited coatings," *Journal of Vacuum Science and Technology*, vol. 4, no. 6, pp. 3059-3065, 1986.
- [6] J. A. Thornton, "Influence of apparatus geometry and deposition conditions on the structure and topography of thick sputtered coatings," *Journal of Vacuum Science & Technology*, vol. 11, pp. 666-670, 1974.
- [7] J. A. Thornton and D. W. Hoffman, "Stress-related Effects in Thin Films," *Thin Solid Films*, vol. 171, pp. 5-31, 1989.
- [8] R. K. Waits, "Planar Magnetron Sputtering," in *Thin Film Processes*, New York, Academic Press, Inc., 1978, pp. 131-170.
- [9] R. F. Bunshah, *Handbook of Deposition Technologies for Films and Coatings*, Science, Technology and Applications, Second Edition, New Jersey: Noyes Publications, 1994, pp. 29-.
- [10] J. G. Han, "Recent progress in thin film processing by magnetron sputtering with plasma diagnostics," *Journal of Physics D: Applied Physics*, vol. 42, p. 043001, 2009.
- [11] R. Knepper and R. Messier, "Thin Film Morphology at Low Adatom Mobility," *Proceedings of SPIE*, vol. 4467, p. 87, 2001.
- [12] K. H. Guenther, "Revisiting structure zone models for thin film growth," *SPIE*, vol. 1324, p. 2, 1990.
- [13] I. K. Chin, F. K. Yam, Y. Chai and Z. Hassan, "Comparative study of porous anodic alumina: effects of aluminium deposition methods," *Materials Science and Technology*, vol. 31, no. 6, p. 709, 2015.

- [14] S. Upreti, K. Mukherjee, M. Palit, A. Bag, S. Mallik, S. Chattopadhyay and C. K. Maiti, "Porous Anodic Alumina Template Formation: Deposition Technique Dependence," in *Physics of Semiconductor Devices, Environmental Science and Engineering*, Cham, Springer, 2014, pp. 725-728.
- [15] T. H. Choudhury and S. Raghavan, "Anodization of sputtered metallic films: The microstructural connection," *Scripta Materialia*, vol. 105, pp. 18-21, 2015.
- [16] A. F. Feil, M. V. da Costa, L. Amaral, S. R. Teixeira, P. Migowski, J. Dupont, G. Machado and S. B. Peripolli, "The influence of aluminum grain size on alumina nanoporous structure," *Journal of Applied Physics*, vol. 107, p. 026103, 2010.
- [17] M. W. Liao and C. K. Chung, "Growth of porous anodized alumina on the sputtered aluminum films with 2D-3D morphology for high specific surface area," *Applied Surface Science*, vol. 309, pp. 290-294, 2014.
- [18] C. K. Chung, M. W. Liao, O. K. Khor and H. C. Chang, "Enhancement of pore size distribution in one-step hybrid pulse anodization of aluminum thin films sputtered on Si substrates," *Thin Solid Films*, vol. 544, pp. 374-379, 2013.
- [19] T. Lebyedyeva, S. Kryvyi, P. Lytvyn, M. Skoryk and P. Shpylovyi, "Formation of Nanoporous Anodic Alumina by Anodization of Aluminum Films on Glass Substrates," *Nanoscale Research Letters*, vol. 11, no. 203, 2016.
- [20] W. H. Yu, G. T. Fei, X. M. Chen, F. H. Xue and X. J. Xu, "Influence of defects on the ordering degree of nanopores made from anodic aluminum oxide," *Physics Letters A*, vol. 350, pp. 392-395, 2006.
- [21] J. Goldstein, D. Newbury, D. Joy, C. Lyman, P. Echlin, E. Lifshin, L. Sawyer and J. Michael, *Scanning Electron Microscopy and X-Ray Microanalysis*, 3rd Ed., New York: Springer Science + Business Media LLC, 2003.
- [22] T. Sandström, M. Stenberg and H. Nygren, "Visual detection of organic monomolecular films by interference colors," *Applied Optics*, vol. 24, no. 4, pp. 472-479, 1985.
- [23] R. E. Burrell, A. G. Naylor and A. M. Rosenfeld, "Thin Film Diagnostic". US Patent 5,124,172, 23 June 1992.
- [24] P. Chiggiato, "Vacuum Technology for Ion Sources," in *CAS CERN Accelerator School: Ion Sources*, Senec, Slovakia, CERN, 2013, pp. 463-502.
- [25] S. Van Gils, T. Dimogerontakis, G. Buytaert, E. Stijns, P. Skeldon, G. E. Thompson and M. R. Alexander, "Optical properties of magnetron-sputtered and rolled aluminum," *Journal of Applied Physics*, vol. 98, 2005.

- [26] R. S. Nowicki, "Influence of residual gases on the properties of dc magnetron-sputtered aluminum-silicon," *Journal of Vacuum Science and Technology* , vol. 17, no. 1, p. 384, 1980.
- [27] H. H. Gatzert, V. Saile and J. Leuthold, "Vacuum Technology," in *Micro and Nano Fabrication: Tools and Processes*, Berlin, Springer-Verlag, 2015, pp. 7-63.
- [28] M. F. Ashby, *Materials Selection in Mechanical Design*, Fourth Edition, Burlington, MA: Elsevier Ltd., 2011.
- [29] B. Kim and J. S. Lee, "Formation of Anodic Aluminum Oxide with Branched or Meshed Pores," *Journal of Nanoscience and Nanotechnology*, vol. 16, no. 6, p. 6575, 2016.
- [30] L. Maissel and R. Glang, *Handbook of Thin Film Technology*, NY: McGraw-Hill, 1970.
- [31] H. Sweet, *Development of a Thin Film Device and Optics System for Protein Detection*, Edmonton, AB: University of Alberta, 2018.

## Chapter 4 Anodization of Aluminum-Tantalum Thin Films

### 4.1 The Effect of Chemical Additives in Phosphoric Acid Anodization of Aluminum-Tantalum Thin Films

#### **Introduction**

Anodization is a very important process in the creation of interference colours with aluminum-tantalum thin films. Under ambient conditions aluminum is covered by an oxide or hydroxide film. This native oxide film is generally 3-10 nm thick [1]. The film can be grown when aluminum is electrolytically oxidized (anodized) in certain electrolytes. Of particular interest is the growth of porous anodic alumina when aluminum is electrolytically oxidized in acids such as sulphuric, oxalic, or phosphoric acid. In such cases, a regular array of cells forms with each containing a cylindrical pore [2]. The diameter of these pores can be controlled in the range of 10-400 nm by anodizing in potentiostatic conditions and varying the voltage, where the pore diameter appears to increase linearly with anodizing voltage [3]. Previous works have used this voltage-pore diameter relationship to create interference colours resulting from changes in the optical path length (material refractive index and film thickness) of the light travelling through the thin oxide films, as described in Chapter 1 [4, 5, 6, 7]. However, there has been little published work on the creation of these interference colours when anodizing under various electrolytes or mixtures thereof.

The rate of dissolution of alumina in an electrolyte is dependent on the nature of the anionic groups in solution [8]. Phosphoric acid has a very high dissolving power for anodic alumina surfaces. Chemical additives, such as oxalic or citric acid, are commonly used in anodization baths to reduce the chemical dissolution of aluminum oxide [1, 9, 10, 11]. These additives help to increase the life-

time of the chemical bath since less aluminum is being dissolved into the electrolyte, as well as contribute to thicker grown oxide films [1].

The purpose of this study was to see the effects on microstructure and the optical properties of anodized aluminum-tantalum thin films when a chemical inhibitor has been added to a phosphoric acid anodization bath. Three inhibitors were used at various concentrations: oxalic acid, citric acid, and an industrially produced inhibitor Norsol Anoad®<sup>®</sup>, which is composed of glycolic acid and glycerol. Material characterization was carried out using SEM, XRD, and ellipsometry to understand the changes in topography, microstructure, and optical properties with each electrolyte mix.

## **Materials and Methods**

### *Magnetron Sputter Deposition*

Aluminum-tantalum thin films were created by planar magnetron sputter deposition onto unprocessed <100> silicon wafers 100 mm in diameter (University Wafers, South Boston, MA). Tantalum films were sputtered at the NAIT Nanotechnology Centre for Applied Research to a thickness of  $226.5 \pm 3.8$  nm using an 20.3 cm diameter tantalum target 99.95% purity (Kurt J. Lesker Company, Jefferson Hills, PA). A constant power density of  $1.5 \text{ W/cm}^2$ , target-to-substrate distance of 70 mm was used and a working Ar (99.9995%) gas pressure of 10 mTorr (132 sccm) with a base pressure of  $1.8 \times 10^{-6}$  Torr. Tantalum was sputtered with a static substrate, flux normal to the surface. Tantalum thickness measurements were determined using profilometry as described in Chapter 2.

Aluminum films were then sputtered onto the tantalum thin film to a thickness of  $139.8 \pm 6.3$  nm (12 min at  $11.65 \pm 0.52$  nm/min as measured by SEM side profile post-deposition), using a 7.6 cm

diameter aluminum target 99.9995% purity (Kurt J. Lesker Company, Jefferson Hills, PA) at the nanoFAB - Fabrication and Characterization Centre at the University of Alberta. For the aluminum, a constant power density of 6.6 W/cm<sup>2</sup>, target-to-substrate distance of 125 mm and working Ar gas pressure of 7 mTorr (55 sccm) was used with a base pressure of 1 x 10<sup>-7</sup> Torr. The substrate was at an angle of 15° with respect to the target and rotated at 20 RPM during the deposition.

### *Anodization*

Aluminum-tantalum coated wafers were then cleaved into pieces approximately 6.3 cm x 1.3 cm. These were then anodized in various electrolyte mixtures under potentiostatic conditions at 4V until the current decayed to <0.02 mA/cm<sup>2</sup> using a Princeton Applied Research Model 273a potentiostat/galvanostat (AMETEK Inc., Oakridge, TN). A 0.4M phosphoric acid electrolyte was used with the addition of oxalic acid, citric acid, or Norsol Anoadd<sup>®</sup>, Table 4-1 (phosphoric acid, oxalic acid dihydrate, and citric acid anhydrous: Thermo Fisher Scientific, Waltham, MA; Norsol Anoadd<sup>®</sup>: Northern Technical Solutions, Guelph, ON).

*Table 4-1. Concentrations and additives added to the 0.4M phosphoric acid anodization bath.*

<b>Additive</b>	<b>Concentrations</b>
Oxalic Acid	0.1M 0.4M
Citric Acid	0.1M 0.4M
Norsol Anoadd <sup>®</sup>	3% (v/v) 10% (v/v)

Slides were rinsed before and after with MilliQ deionized water. A magnetic stir plate was used to agitate the solution, and the temperature of the electrolyte was 19 ± 1°C. Aluminum foil (Thermo Fisher Scientific, Waltham, MA) was wrapped around a glass microscope slide and used as a

cathode. The separation distance between the cathode and anode was 40 mm. A saturated calomel electrode was used as a reference electrode (Thermo Fisher Scientific, Waltham, MA). Triplicates were performed to measure reproducibility. All anodized films were then viewed at approximately 75° from normal using a polarizing lens to view s-polarized light.

### *Scanning Electron Microscopy (SEM)*

SEM analysis was conducted to visualize microstructural and topographical changes of the samples anodized in different electrolytes. The anodized aluminum-tantalum thin films were fractured and mounted onto aluminum stubs (Ted Pella Inc., Redding, CA) using conductive carbon tape (PELCO Tabs™, Ted Pella Inc., Redding, CA). A Zeiss Sigma Field Emission Scanning Electron Microscope (FESEM) at the nanoFAB - Fabrication and Characterization Center at the University of Alberta was used to examine each sample. Specimens were viewed at 3.00 keV and an aperture size of 15 µm to reduce charging effects from the electron beam, and at both 0° and 45° from vertical. Images were taken at 50,000 and 100,000 times, with a working distance of approximately 3 mm. SEM surface micrographs taken at 100,000 times magnification were analyzed using ImageJ software (Rasband, W.S., ImageJ, U.S. National Institutes of Health, Bethesda, Maryland, USA, <https://imagej.nih.gov/ij/>, 1997-2016) for pore diameter measurements. Three evenly spaced lines were drawn horizontally and another three vertically across the micrograph. The pores along these lines were measured for diameter.

Side profiles were taken to acquire RMS measurements for surface roughness. Specimens were viewed at 90° with either 3.00 or 4.00 keV, an aperture size of either 15 or 20 µm, 100,000 times magnification and working distance of approximately 3 mm. Images were then analyzed using ImageJ software (Rasband, W.S., ImageJ, U. S. National Institutes of Health, Bethesda, Maryland, USA, <https://imagej.nih.gov/ij/>, 1997-2016). Each specimen had 2 or 3 cross-sectional images

taken from randomly chosen areas. The thickness of the porous aluminum oxide was measured at 20 points across each cross-section.

### *X-Ray Diffraction (XRD)*

XRD was carried out to check for microstructural differences and confirm the consumption anodization of the aluminum film. A Rigaku Ultima IV (Cu-source) diffraction system with a thin film, substrate holder attachment was used. Diffraction data was collected between 10 and 90° 2 $\theta$  at 5.000°/min, using a DHL slit of 10.00 mm and glancing angle  $\omega = 0.5^\circ$ . A sputtered aluminum-tantalum wafer was analyzed as a control for initial phases present. Anodized slides from all acid mixtures were then analyzed under the same conditions. Note that an initial scan was collected at 2.000°/min to see whether the higher resolution scan would show peaks that the faster scan would not. There was no observed difference between the fast and slow scans, therefore the remaining scans were done at 5.000°/min. JADE 9<sup>TM</sup> software (Materials Data Inc., Livermore, CA) was used to analyze the XRD patterns along with the International Centre for Diffraction Data (ICDD) database to match peaks.

### *Ellipsometry*

The samples that showed the largest interference colour and microstructural differences were analyzed using ellipsometry. The optical constants (refractive index,  $n$ , and extinction coefficient,  $k$ ) as well as the final oxide thicknesses were determined using a J.A. Woollam M-2000V spectroscopic ellipsometer (J.A. Woolam Co., Lincoln, NE). A model was built to represent each layer of the final anodized films: tantalum substrate, tantalum oxide film, and aluminum oxide porous film.

Optical constants were measured for each layer, tabulated, and used in the subsequent model. A B-Spline was used to model the tantalum metal. A series of tantalum slides were anodized under the same conditions as described previously to generate a tantalum oxide layer and a Cauchy model was used to represent this tantalum oxide film. Duplicates were performed of the tantalum and tantalum oxide layers to measure reproducibility of the optical constants. Variance was found to be minimal and had little effect on the final model. The tantalum and tantalum oxide layers that showed the lowest mean square error (MSE) values were used as the models for the final anodized films. Finally, the aluminum-tantalum slides were analyzed post anodization and an Effective Medium Approximation (EMA) model was used to represent the porous alumina layer with the use of two mediums, aluminum oxide and void (i.e. air). Specifically, the Bruggeman Anisotropic model was used, with depolarization constants of  $z=0$  and  $x-y=0.5$  to represent a material composed of parallel cylinders [12]. Only the refractive index in the x-y plane was recorded as this is the most important parameter for interference colour generation. The tabulated tantalum and tantalum oxide optical constants were used to represent the underlying layers.

For all layers,  $\Psi$  and  $\Delta$  values were recorded for wavelengths 370 nm to 1000 nm at angles of  $55^\circ$ ,  $65^\circ$ , and  $75^\circ$  from normal. CompleteEASE<sup>®</sup> software for Windows (J.A. Woolam Co., Lincoln, NE) was used to develop the ellipsometry model and tabulate refractive index and oxide thickness values. Note that a Cauchy model was initially used to represent the aluminum oxide, however the model produced non-physical results (increasing refractive index with wavelength) and was thus abandoned in favor of EMA.

### *Colour Coordinates*

Photos of the interference colours were taken at approximately  $75^\circ$  from normal using a phone camera and a polarizing lens (s-polarized). The images were then analyzed for RGB coordinates

using ImageJ software (Rasband, WS, ImageJ, US National Institutes of Health, Bethesda, MD, <https://imagej.nih.gov/ij/>, 1997-2016). A rectangular area of each slide was selected in the photo, encompassing between 11,000 and 41,000 pixels. The mean and standard deviation were recorded for the RGB coordinates of each area.

### *Statistics*

Standard deviations are shown on all plots using error bars. Numerical results used a one-way ANOVA with a Tukey Multiple Comparisons post hoc test using IBM SPSS Statistics for Windows, Version 24.0 (IBM Corp., Released 2016, Armonk, NY). A Levene's test was used to check for similar sample variance between populations. The numerical results for pore size were analyzed using an independent t-test, taking into account unequal sample size and variance.

## **Results**

### *Current Density Plots*

The current density over time was recorded for anodization in each electrolyte mixture to better understand how the electrolyte effects pore formation and the state of the electrolytic cell. A typical plot of current density with time is shown in Figure 4-1. The plot shows the regular stages of pore growth during anodization, as discussed in Chapter 1 – Section 1.5. Once the aluminum is consumed and porous oxide formation complete, a tantalum oxide barrier layer starts to form which results in a drop in the current as the oxide thickens. The time to complete anodization in each electrolyte mixture (i.e. current density reaches  $<0.02 \text{ mA/cm}^2$  after tantalum oxide barrier formation) is shown below in Figure 4-2, as well as the current density during pore formation, Figure 4-3. The comparison for current density during pore formation was chosen at 50% completion, i.e. If 700 seconds was time of completion, then 350 seconds was the time chosen. This was chosen as the current density remained relatively constant during pore formation, giving

a steady-state value. Statistical results for the change in current density during pore formation are shown in Table 4-2; each mixture is compared with the 0.4M phosphoric acid anodized control. Citric acid only appeared to have an influence at 0.4M with a decrease of the current density to  $0.553\pm 0.006$  mA/cm<sup>2</sup> and increase in time to  $12.8\pm 0.2$  min. Norsol Anoad® was found to have the next strongest change; current density was decreased to  $0.409\pm 0.005$  mA/cm<sup>2</sup> for 3% (v/v) additive and  $0.416\pm 0.020$  mA/cm<sup>2</sup> for 10% (v/v), and time was increased to  $18.1\pm 0.6$  min and  $15.8\pm 0.6$  min respectively. Oxalic acid appears to have the strongest effect on the current density and time. A decrease in the current density was observed from  $0.677\pm 0.021$  mA/cm<sup>2</sup> in straight 0.4M phosphoric acid to  $0.212\pm 0.005$  or  $0.218\pm 0.018$  mA/cm<sup>2</sup> for 0.1M and 0.4M oxalic acid additive respectively. A corresponding increase in time for complete anodization was also observed from  $10.8\pm 0.1$  min to  $32.2\pm 0.7$  or  $31.5\pm 1.4$  min for 0.1M and 0.4M oxalic acid. These both correspond to an approximately 60-70% change in current density and time.

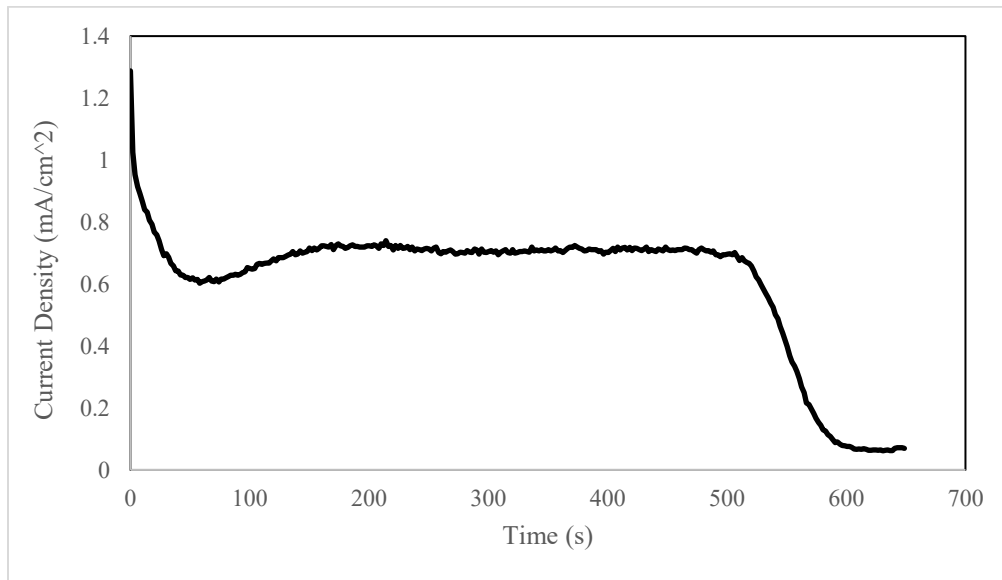


Figure 4-1. Current density-time plot during anodization of aluminum-tantalum thin films in 0.4M phosphoric acid under potentiostatic conditions (4V).

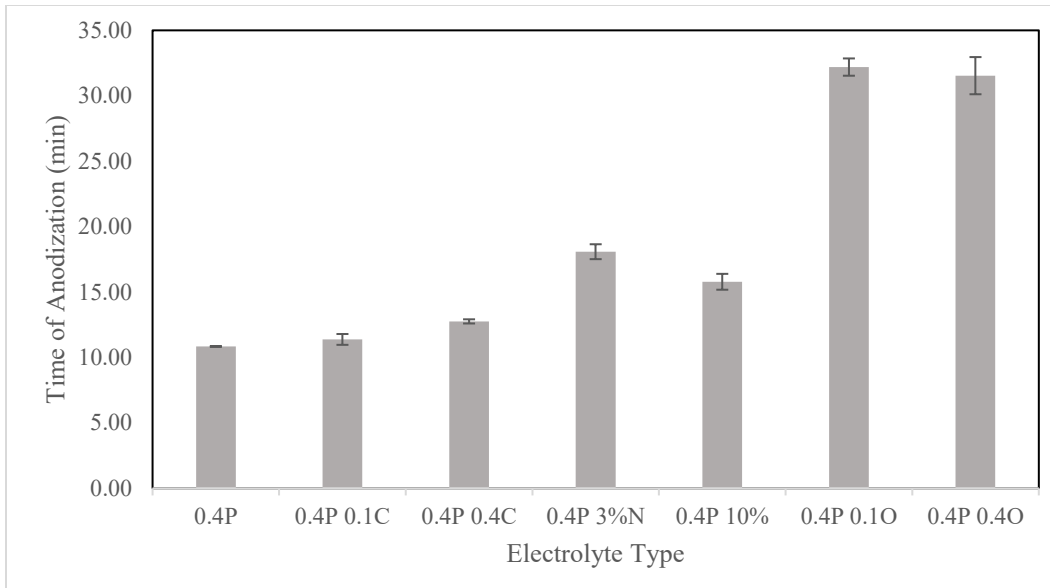


Figure 4-2. Time to complete anodization in each electrolyte mixture. From left to right: 0.4M phosphoric acid, 0.4M phosphoric and 0.1M citric acid, 0.4M phosphoric and 0.4M citric acid, 0.4M phosphoric acid and 3% (v/v) Norsol Anoadd<sup>®</sup>, 0.4M phosphoric acid and 10% (v/v) Norsol Anoadd<sup>®</sup>, 0.4M phosphoric and 0.1M oxalic acid, 0.4M phosphoric and 0.4M oxalic acid. Sample size of  $n=3$  for all cases.

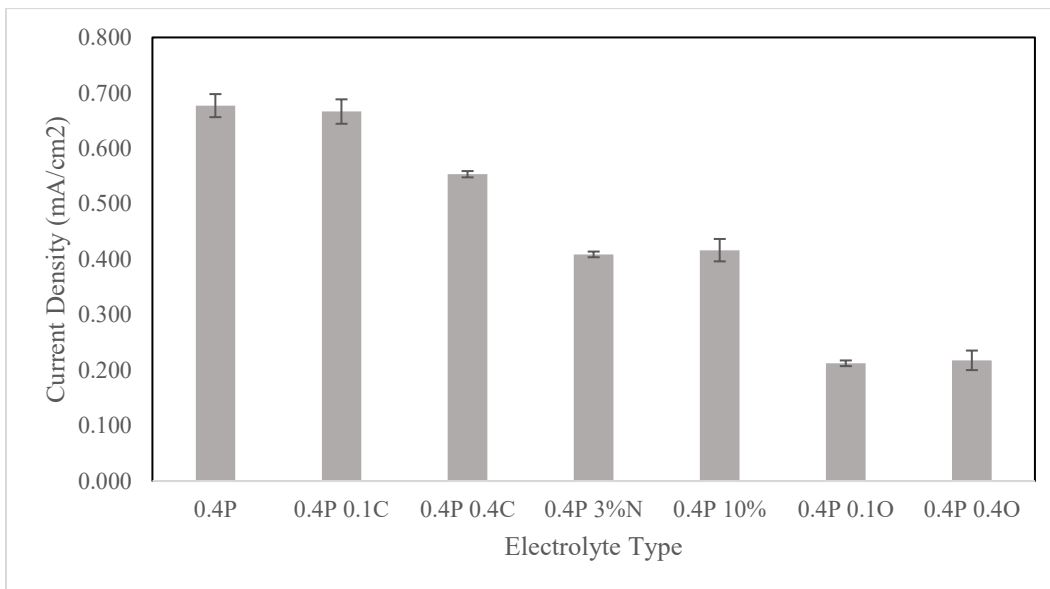


Figure 4-3. Current density during pore formation in each electrolyte mixture. From left to right: 0.4M phosphoric acid, 0.4M phosphoric and 0.1M citric acid, 0.4M phosphoric and 0.4M citric acid, 0.4M phosphoric acid and 3% (v/v) Norsol Anoadd<sup>®</sup>, 0.4M phosphoric acid and 10% (v/v) Norsol Anoadd<sup>®</sup>, 0.4M phosphoric and 0.1M oxalic acid, 0.4M phosphoric and 0.4M oxalic acid. Sample size of  $n=3$  for all cases.

Table 4-2. Statistical results of current density during pore formation of each additive vs. the 0.4M phosphoric acid anodized control. n=3 for all data points.

Additive	ANOVA p-value	Post Hoc Test Results
0.1M Citric	p<0.001	p=0.977, not significant
0.4M Citric		p<0.001, decrease
3% (v/v) Norsol		p<0.001, decrease
10% (v/v) Norsol		p<0.001, decrease
0.1M Oxalic		p<0.001, decrease
0.4M Oxalic		p<0.001, decrease

### SEM Microstructural Images and RMS

SEM images were taken of the aluminum-tantalum films anodized in each electrolyte mixture to check for microstructural differences. Figure 4-4 shows the surface images of each anodized film. Images were taken at 45° for films anodized in 0.4M phosphoric acid, 0.4M phosphoric and 0.1M citric, 0.4M phosphoric and 3% (v/v) Norsol Anoad®<sup>®</sup>, and 0.4M phosphoric and 0.1M oxalic mixtures to get a better understanding of the surface topography differences, Figure 4-5.

The 0.4M phosphoric acid film appeared to have a very rough surface with highly tortuous pores and pits anywhere from 50 to 100nm across. Citric acid, when added at 0.1M, showed a small difference in microstructure with an apparent reduction in the size and number of pits, however this change was not noticed at 0.4M. The Norsol Anoad®<sup>®</sup> also appeared to have an affect at 3% (v/v), which resulted in a flatter surface, and less tortuous pore growth. However, when the strength was increased to 10% (v/v) the effects disappeared and the microstructure again looked similar to 0.4M phosphoric acid. The oxalic acid had the greatest effect on microstructure. Both the 0.1M and the 0.4M showed much flatter surfaces and straighter, more uniform pores. It was also more apparent in oxalic mixtures that anodization starts to occur at grain boundaries, as the pores tend to be larger there, creating a unique topographical feature that outlines each grain. Figure 4-6

shows the measured pore diameter for films anodized in each electrolyte. Phosphoric acid anodized films had a mean pore diameter of  $18.6 \pm 8.1$  nm. A significant decrease in pore size was found for films anodized in all mixes except those with 10% (v/v) Norsol. However, the difference was largest with 0.1M and 0.4M oxalic acid, reducing the pore size to  $10.7 \pm 4.5$  nm and  $9.5 \pm 4.1$  nm, respectively.

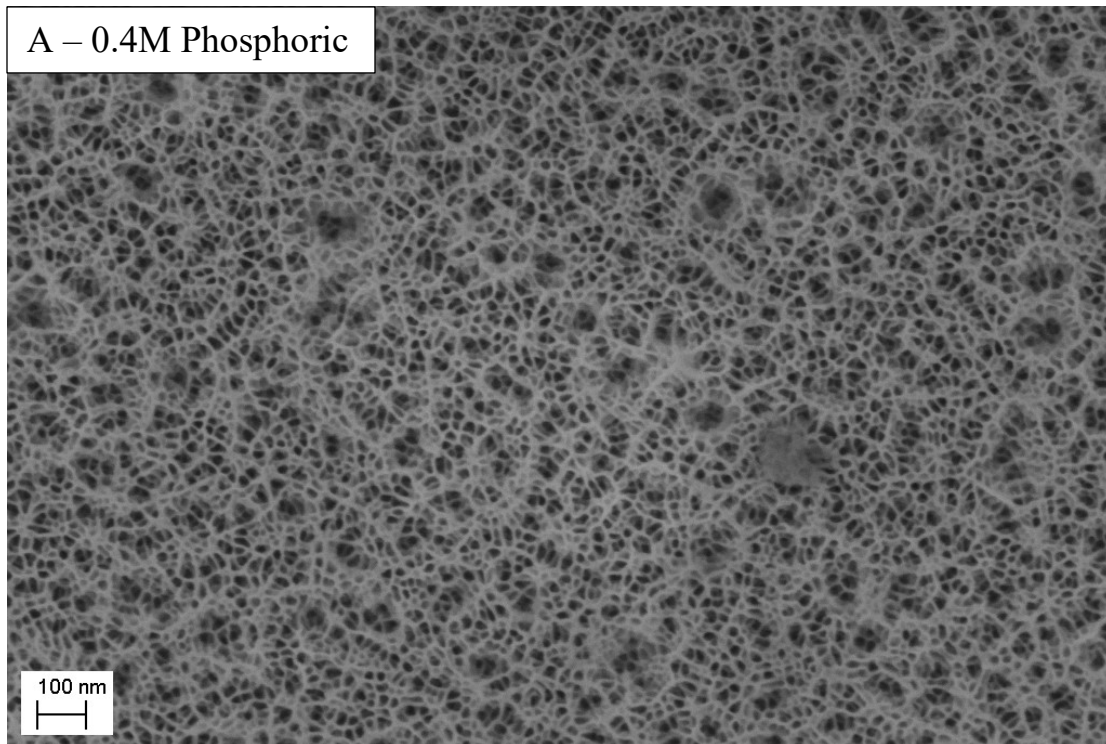


*Figure 4-4 continued.*

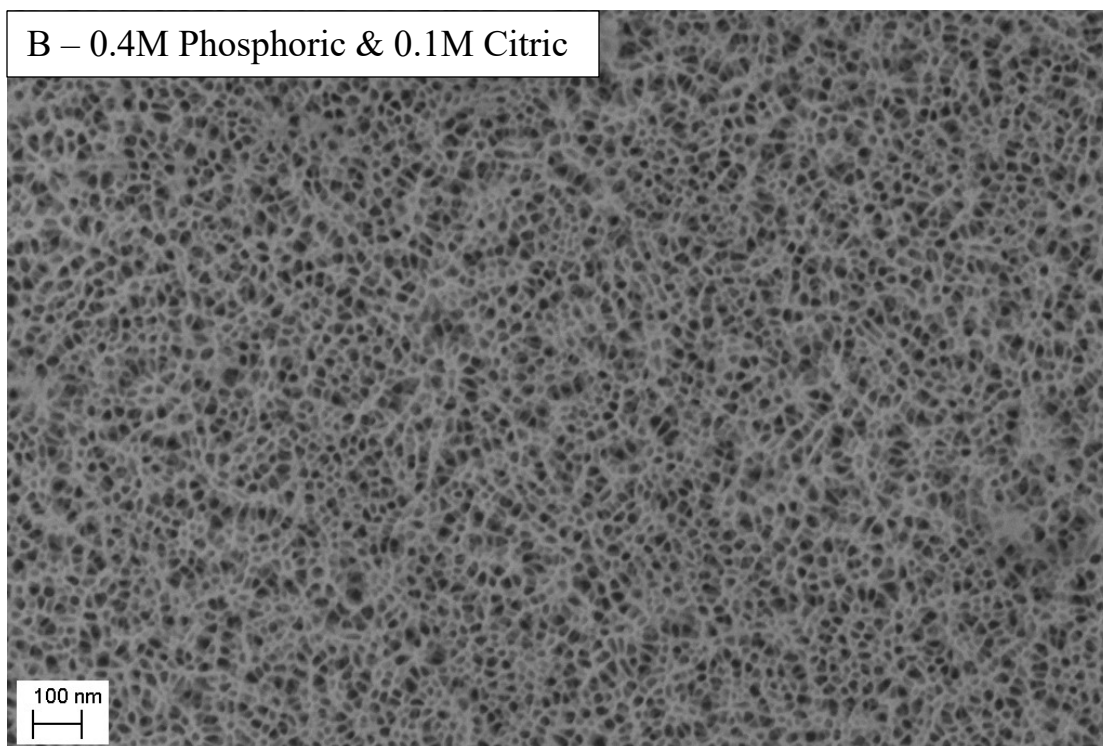


*Figure 4-4, continued.*

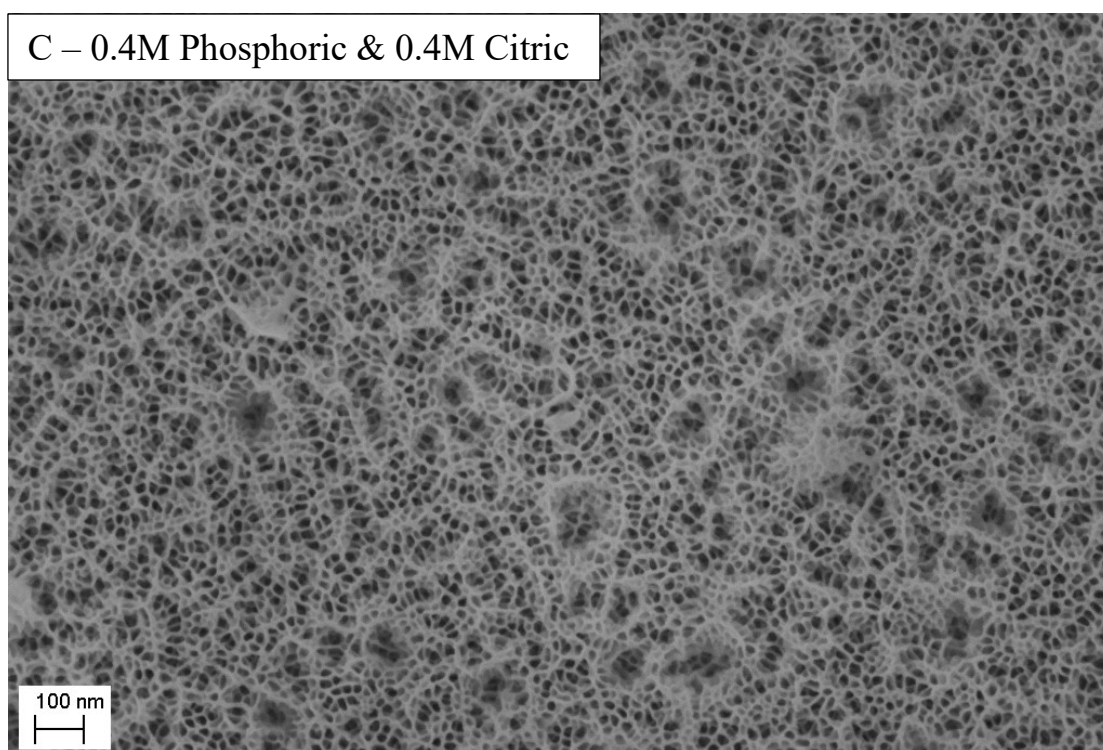


*Figure 4-4, continued.*

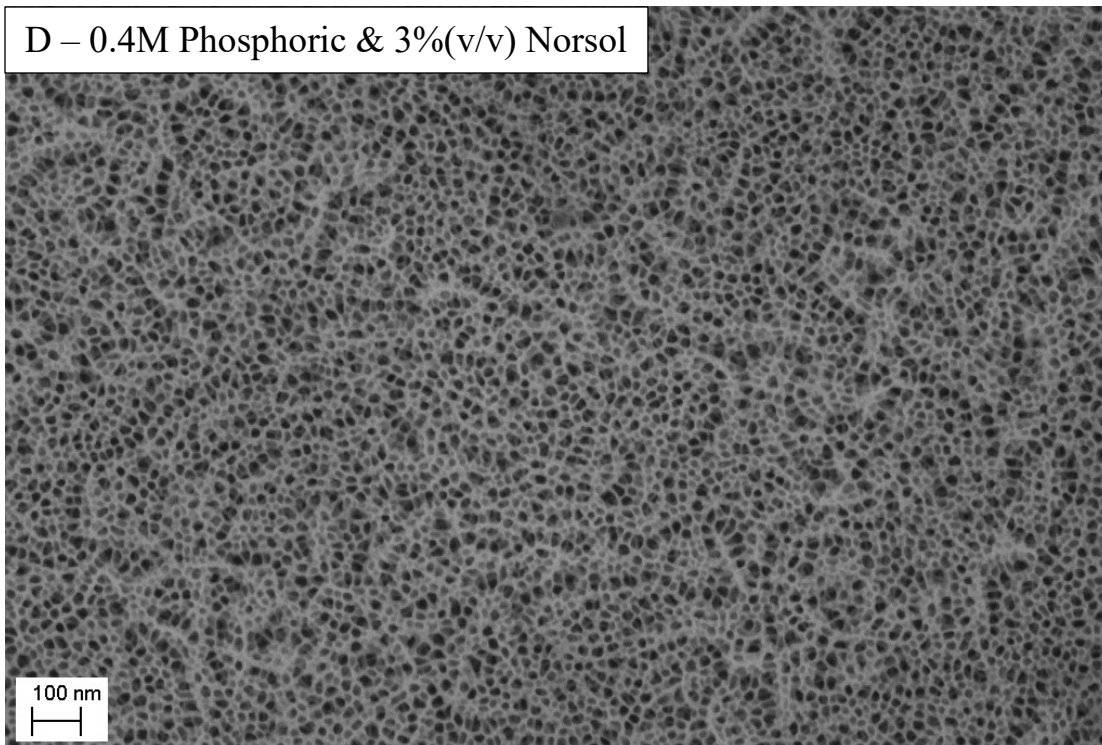


*Figure 4-4, continued.*

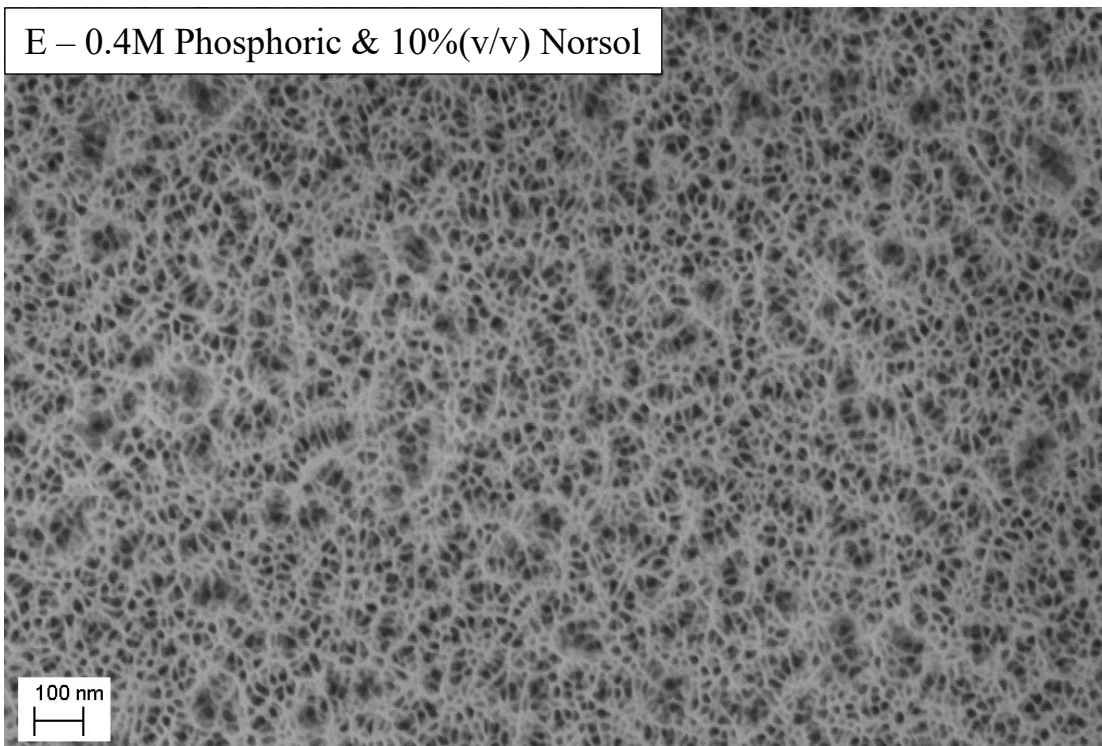


*Figure 4-4, continued.*

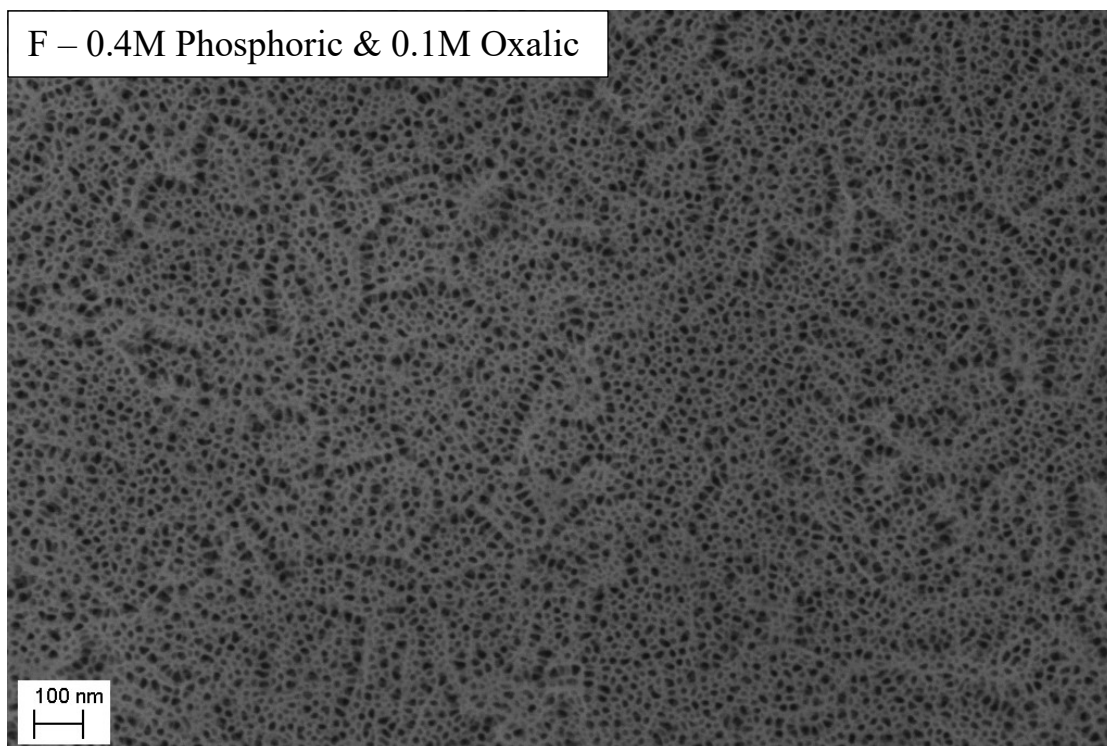


*Figure 4-4, continued.*

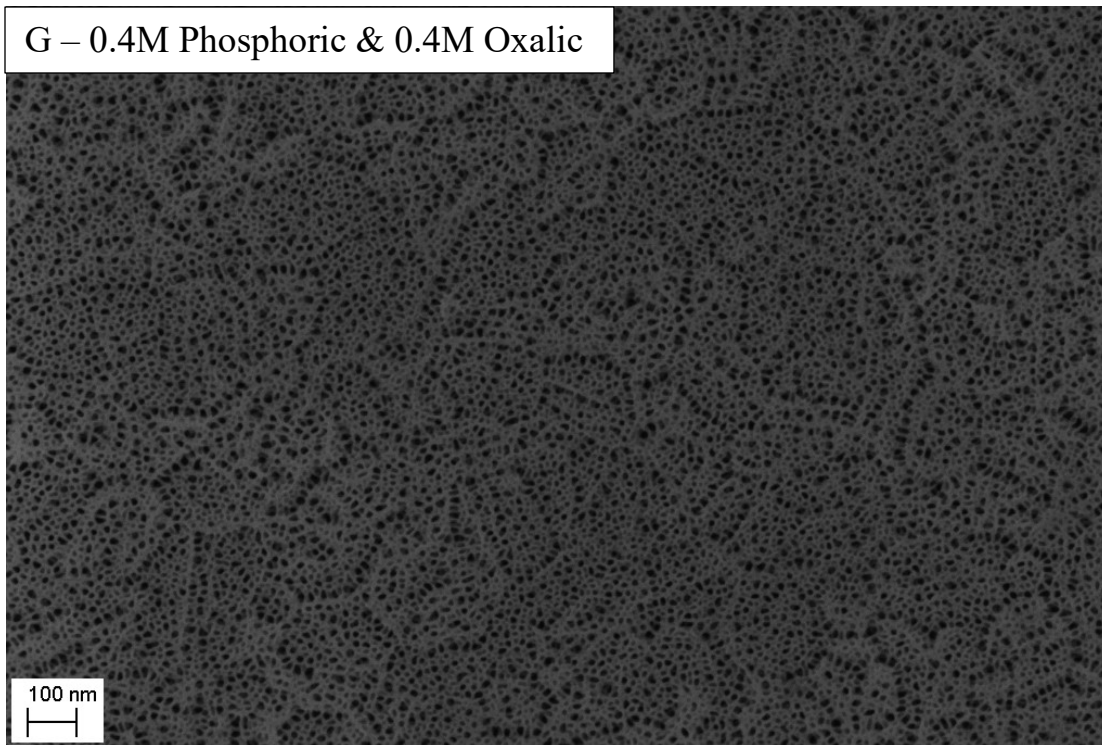


*Figure 4-4, continued. Surface FESEM images of aluminum-tantalum sputtered thin films anodized in various electrolytes.*

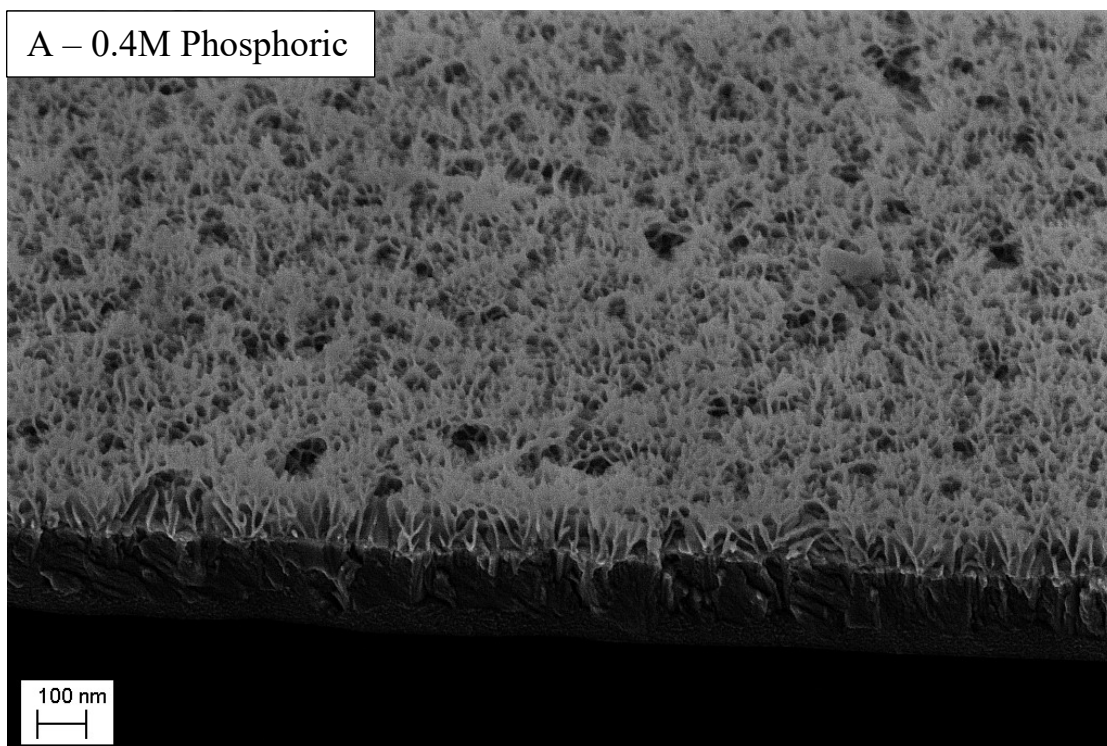


*Figure 4-5 continued.*

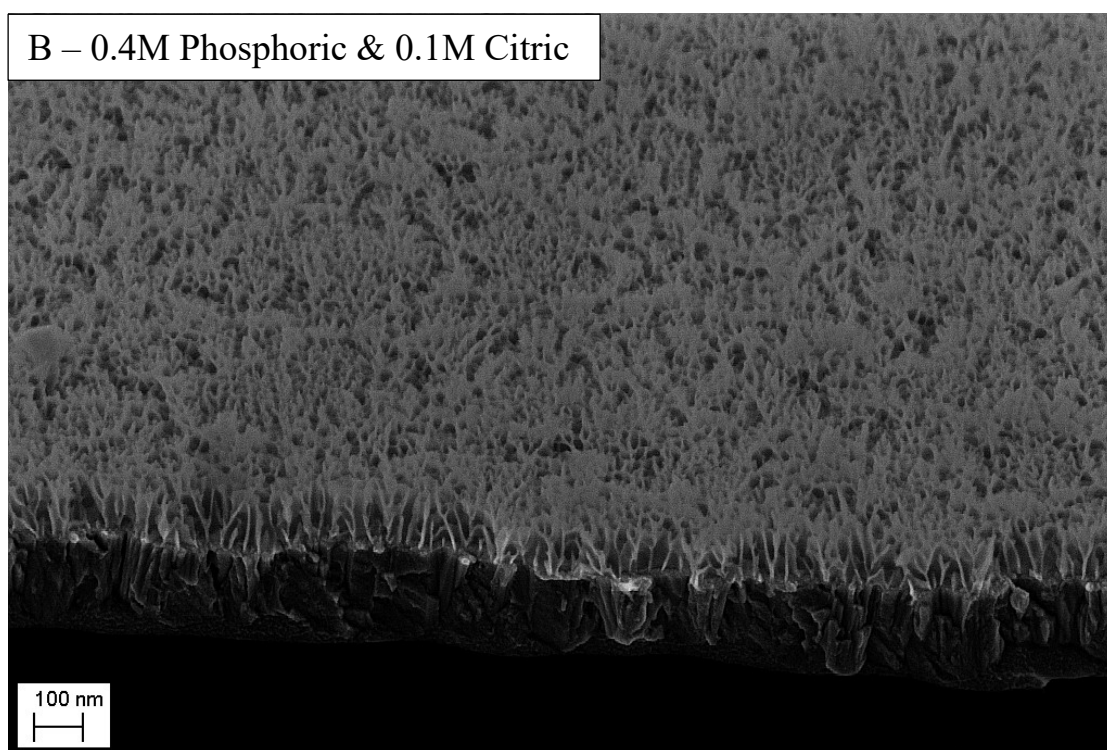


*Figure 4-5, continued.*

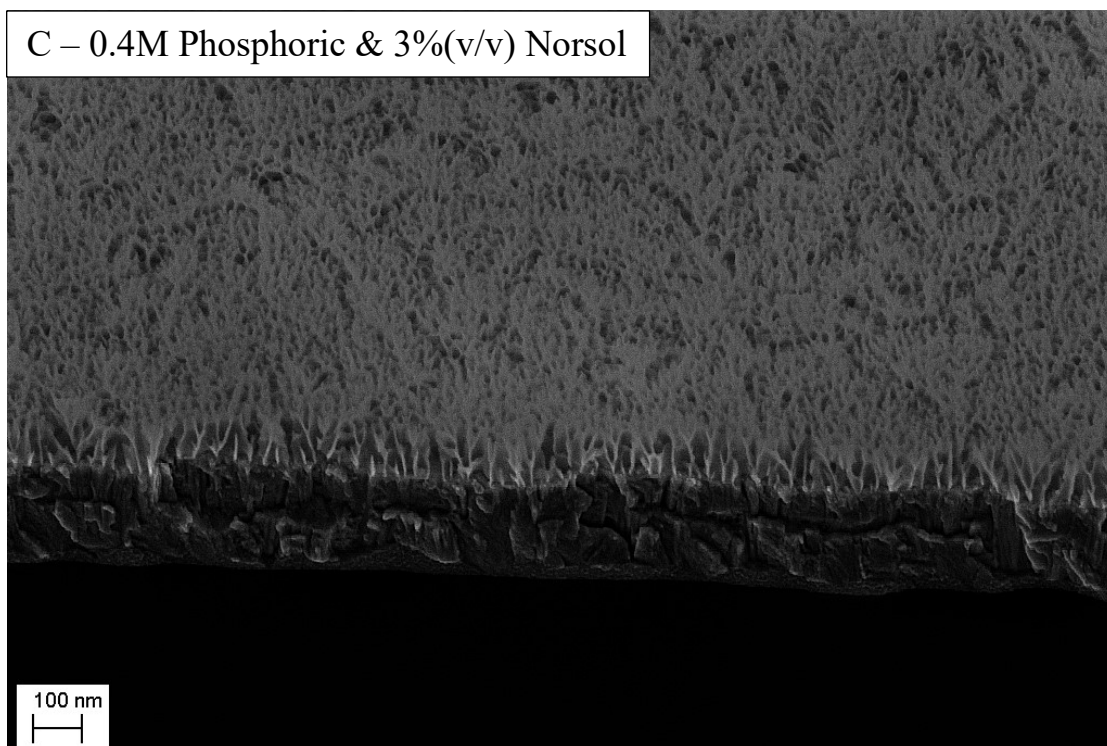


*Figure 4-5, continued.*

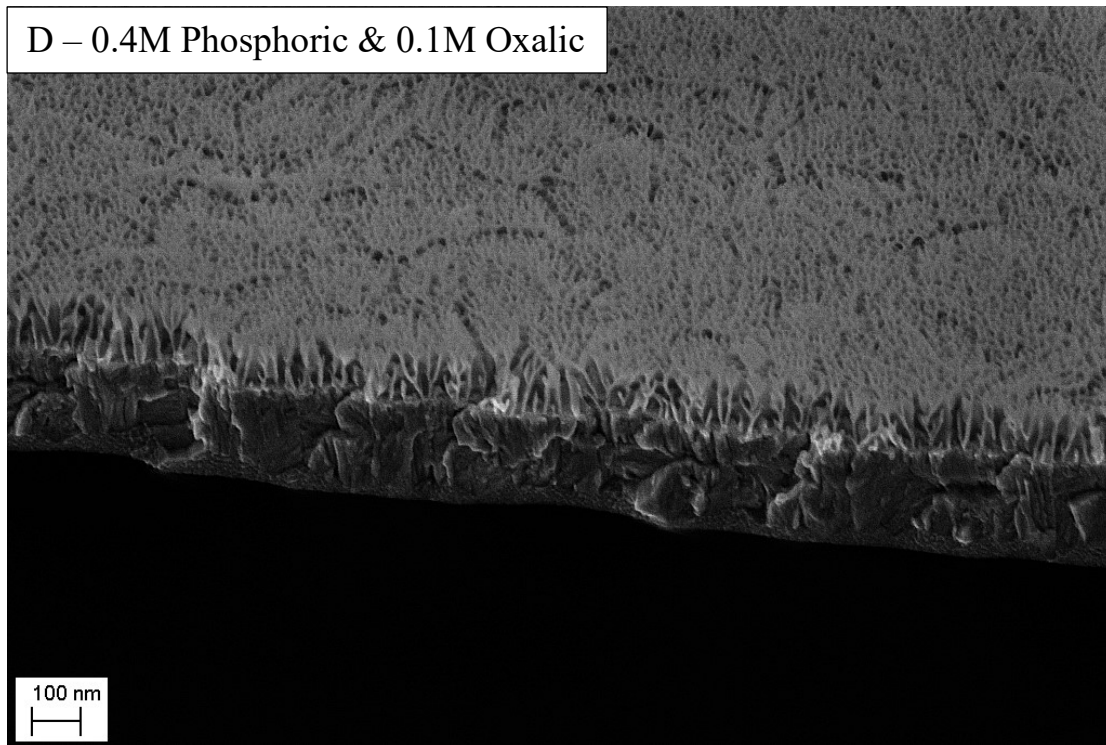


*Figure 4-5, continued. FESEM fractured edge images of aluminum-tantalum sputtered thin films anodized in various electrolytes.*

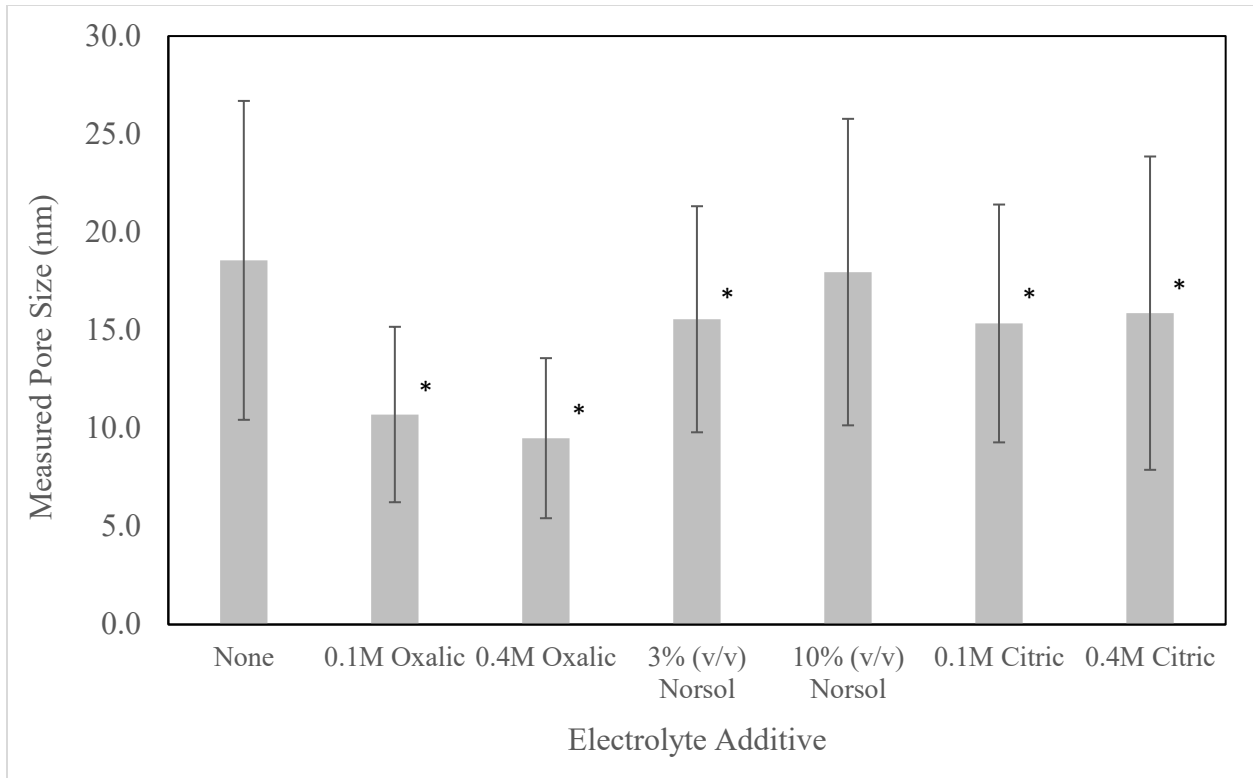


Figure 4-6. Surface pore size measured from FESEM images for aluminum-tantalum thin films anodized in 0.4M phosphoric acid at 4V with various additives. Asterisk (\*) indicates significant difference ( $p < 0.05$ ) when compared to no additive using independent sample t-test. Sample size for each: None ( $n=157$ ), 0.1M Oxalic ( $n=222$ ), 0.4M Oxalic ( $n=242$ ), 3% (v/v) Norsol ( $n=184$ ), 10% (v/v) Norsol ( $n=168$ ), 0.1M Citric ( $n=182$ ), 0.4M Citric ( $n=152$ ).

SEM side-profiles were analyzed to acquire root mean square (RMS) values for the aluminum oxide surface, Figure 4-7. The results of a one-way ANOVA, followed by a Tukey-Kramer multiple comparisons test are shown in Table 4-3. RMS measurements confirm the qualitative analysis from the SEM micrographs, showing a decrease in surface roughness for all additives except 10% (v/v) Norsol and 0.4M citric acid when compared to straight phosphoric acid.

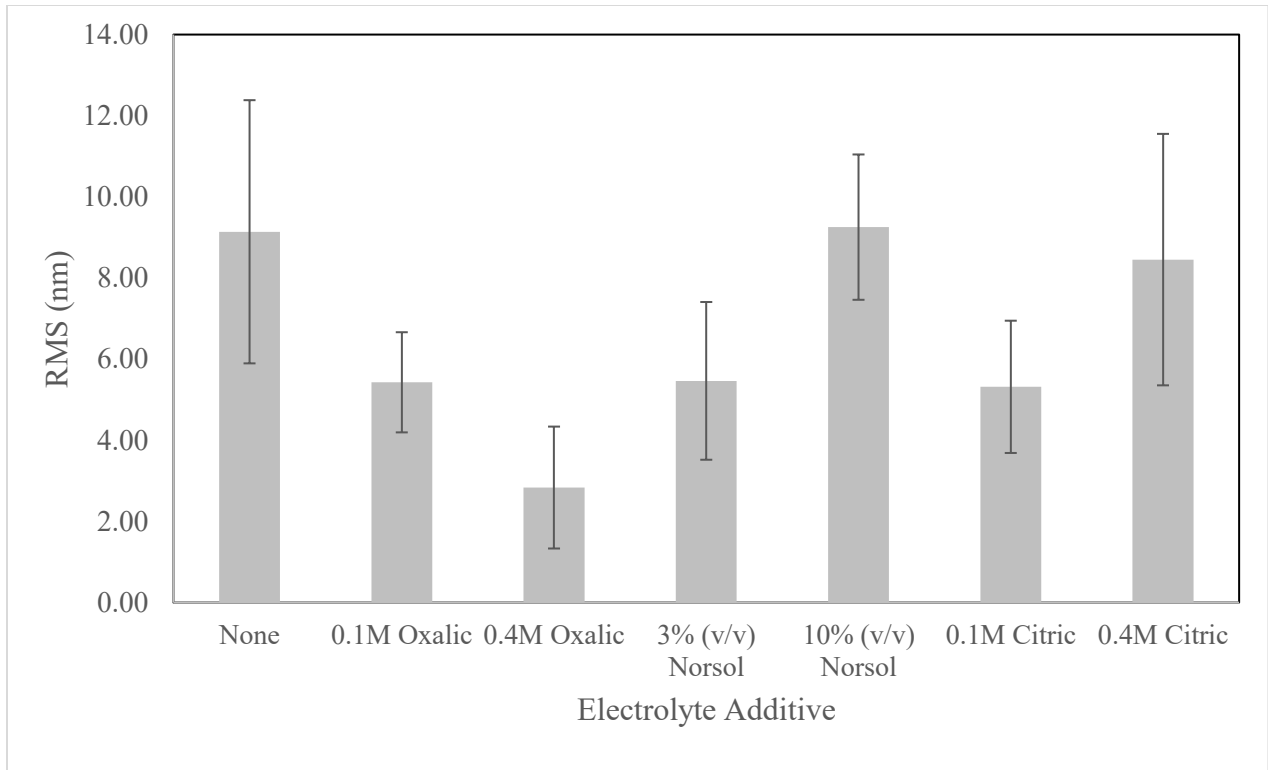


Figure 4-7. RMS surface roughness values as measured by SEM side-profile analysis of aluminum-tantalum films anodized in 0.4M phosphoric acid at 4V with various additives.

Table 4-3. Statistical results for aluminum oxide RMS surface roughness as measured by SEM side-profile analysis for anodization with each additive vs. the 0.4M phosphoric acid control.

Additive	ANOVA	Post Test Results
0.4M Phosphoric, no additive (n=6)	p < 0.0001	N/A
0.1M Oxalic (n=8)		p<0.05, decrease
0.4M Oxalic (n=5)		p<0.05, decrease
3% (v/v) Norsol (n=9)		p<0.05, decrease
10% (v/v) Norsol (n=6)		p=1.000, no change
0.1M Citric (n=7)		p<0.05, decrease
0.4M Citric (n=9)		p=0.997, no change

## XRD

The XRD patterns obtained after anodization in each electrolyte, along with the initial aluminum-tantalum sputtered film are shown in Figure 4-8. From these patterns, two things can be observed: the disappearance of the aluminum peaks and the absence of any peaks other than  $\alpha$  phase tantalum after anodization.

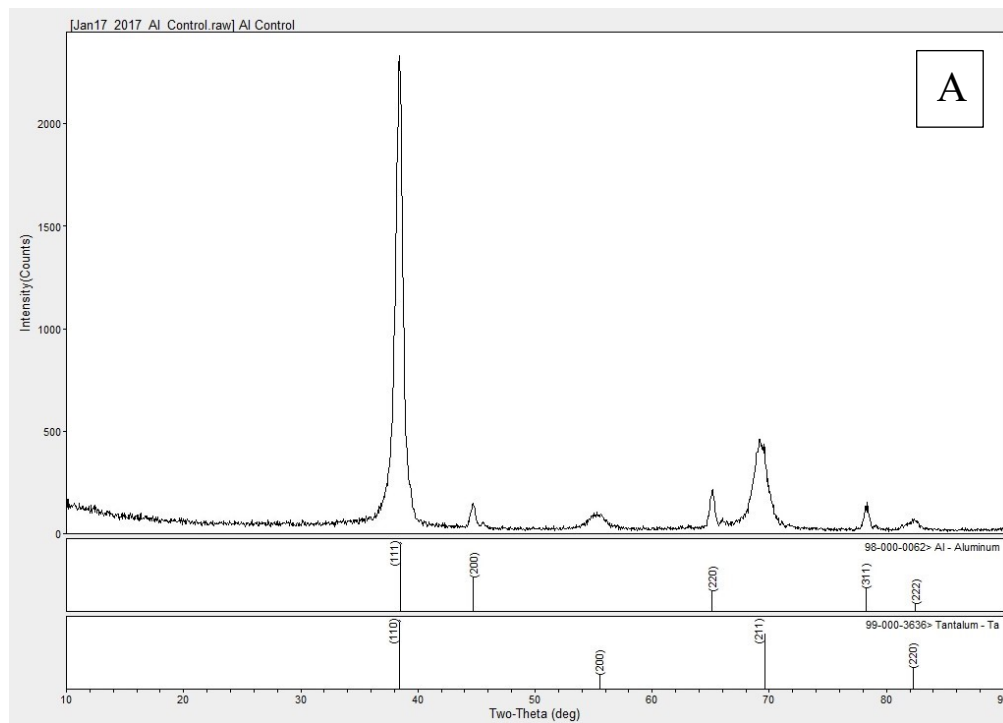


Figure 4-8 continued.

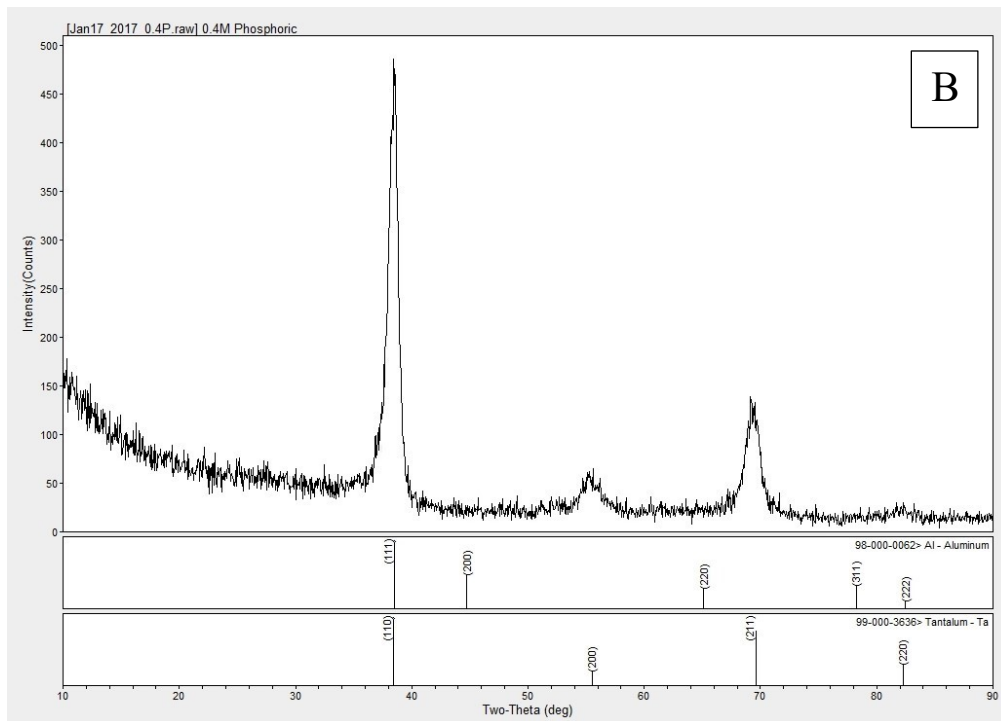


Figure 4-8, continued.

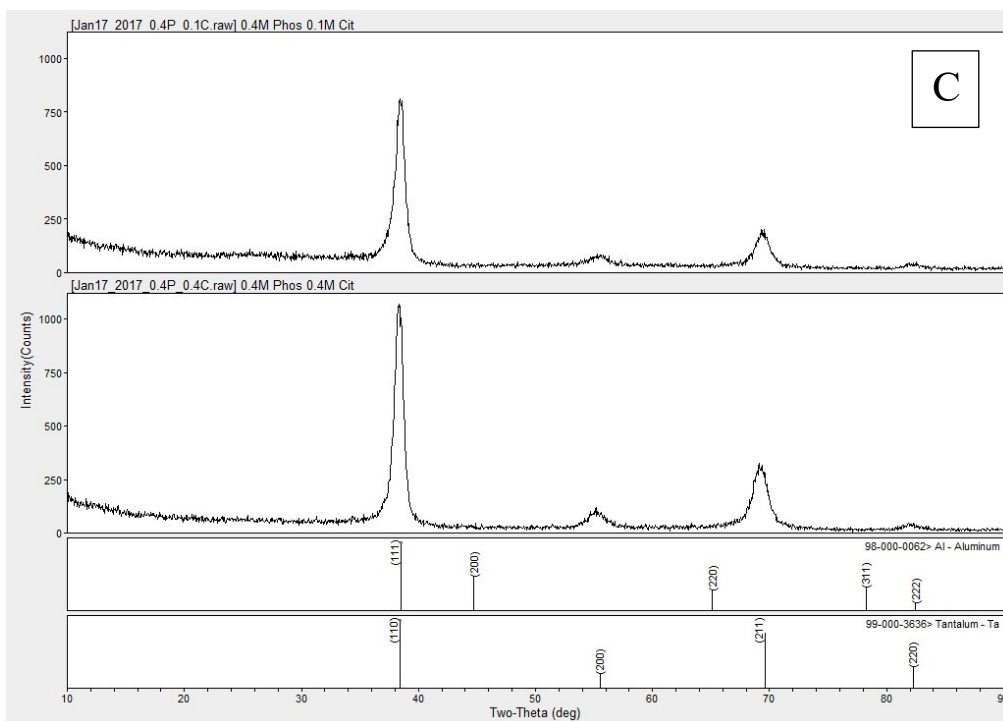


Figure 4-8, continued.

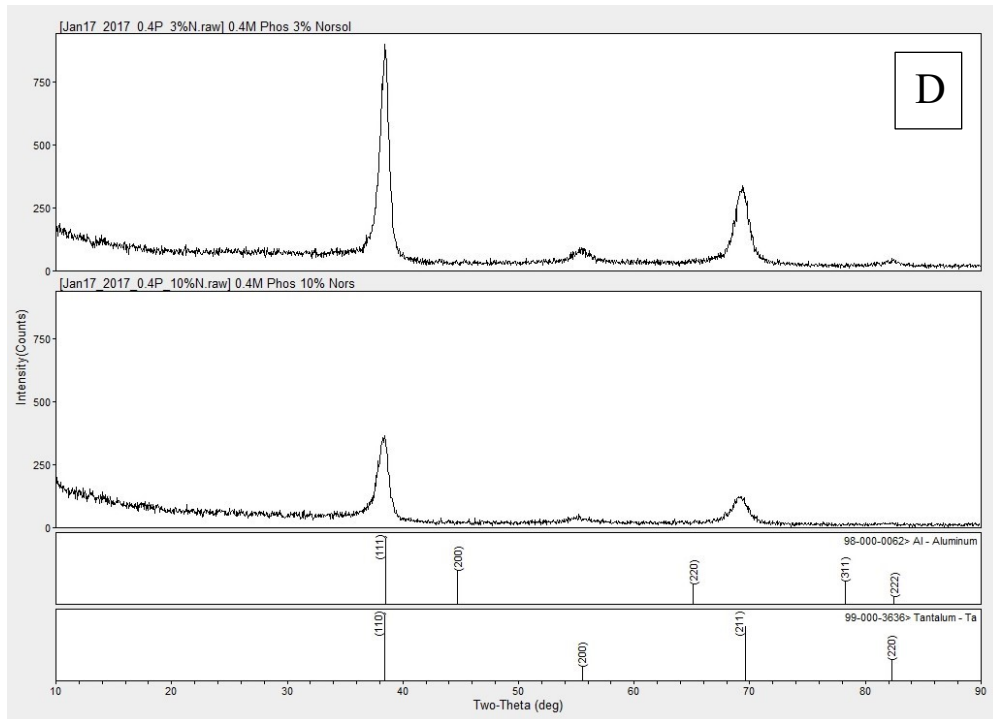


Figure 4-8, continued.

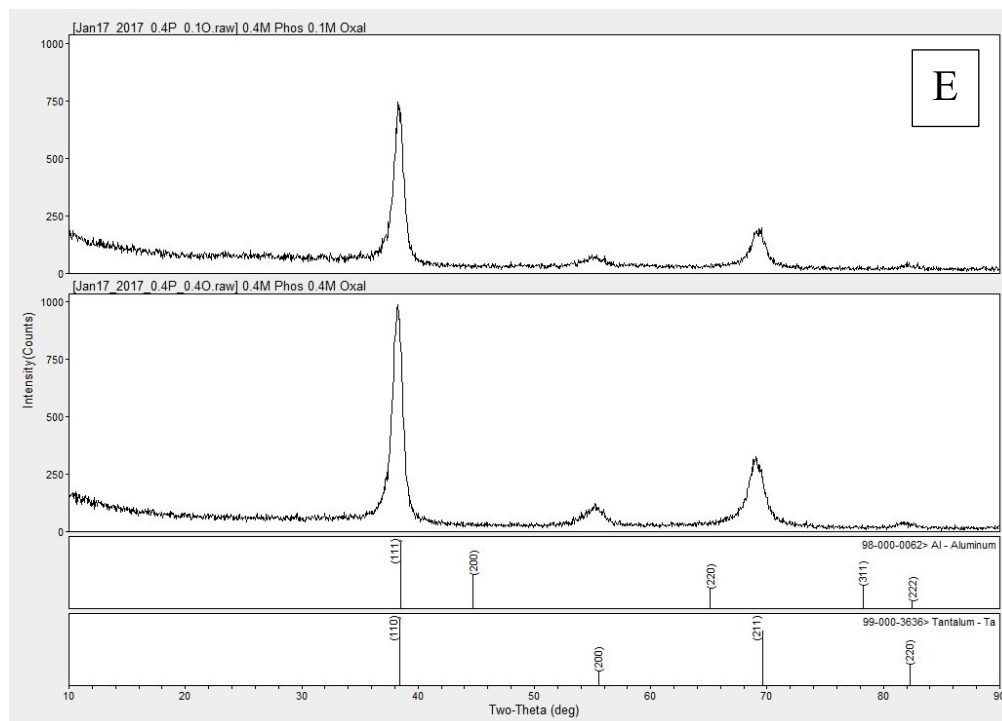


Figure 4-8, continued. XRD patterns with the aluminum and tantalum ICDD peaks labelled: A) aluminum-tantalum films pre-anodization; B) 0.4M phosphoric acid; C) 0.4M phosphoric acid with 0.1M (top) and 0.4M (bottom) citric acid; D) 0.4M phosphoric acid with 3% (v/v) (top) and 10% (v/v) (bottom) Norsol Anoadd; E) 0.4M phosphoric acid with 0.1M (top) and 0.4M (bottom) oxalic acid.

### Ellipsometry

Ellipsometry was conducted on phosphoric acid anodized films and inhibited films that showed the strongest change in microstructure: 3% (v/v) Norsol Anoadd<sup>®</sup>, 0.1M oxalic, and 0.4M oxalic acid. Figures 4-9 and 4-10 show the measured refractive indices ( $\lambda=555\text{nm}$ ) and anodic film thickness, respectively. The thickness, refractive index, measured % void, and mean square error (MSE) for each model are shown Table 4-4. The extinction coefficient,  $k$ , was found to be 0 for all anodic oxide films.

No change was found for the refractive index ( $\lambda=555\text{nm}$ ) or the final aluminum oxide thickness with the addition of Norsol Anoadd<sup>®</sup> at 3% (v/v) ( $p=0.822$ ). Oxalic acid mixtures showed increases in refractive index and thickness at both 0.1M ( $p<0.005$ ) and 0.4M ( $p<0.001$ )

concentrations. Increasing the concentration of oxalic acid from 0.1M to 0.4M led to a larger increase in anodic oxide thickness and refractive index.

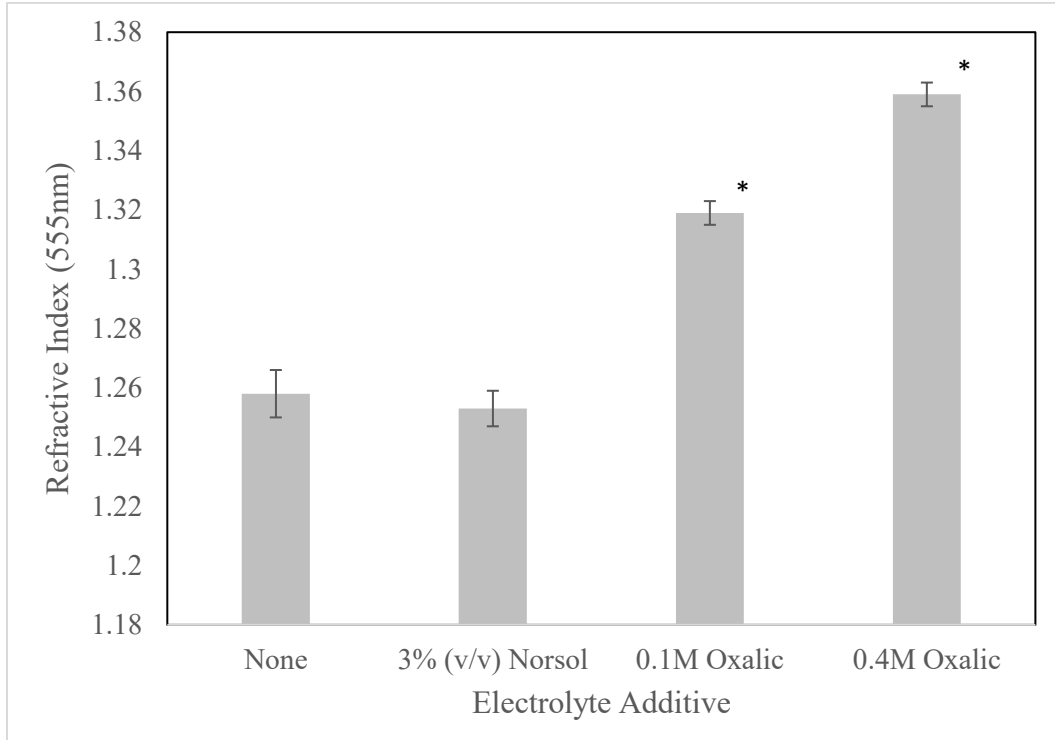


Figure 4-9. Refractive index values of the porous aluminum oxide layer determined by ellipsometry for aluminum-tantalum thin films anodized in 0.4M phosphoric acid at 4V with various additives. Asterisk (\*) indicates significant difference ( $p < 0.01$ ) when compared to no additive using; sample size of 3 for each case.

Table 4-4. Ellipsometry results for the porous aluminum oxide layer of aluminum-tantalum thin films anodized in various electrolytes. Standard deviations shown with  $\pm$  symbol,  $n=3$  for all data sets.

	0.4M Phosphoric	0.4M Phosphoric, 3% (v/v) Norsol	0.4M Phosphoric, 0.1M Oxalic	0.4M Phosphoric, 0.4M Oxalic
<b>Thickness (nm)</b>	119.7 ± 1.2	121.3 ± 0.3	123.2 ± 0.5	129.4 ± 3.2
<b>Refractive Index (<math>\lambda=555\text{nm}</math>)</b>	1.258 ± 0.008	1.253 ± 0.006	1.319 ± 0.004	1.359 ± 0.004
<b>EMA (% void)</b>	59.3 ± 1.0	60.0 ± 0.9	51.4 ± 0.5	46.4 ± 0.5
<b>MSE</b>	17.3 ± 0.5	20.8 ± 2.4	11.8 ± 0.6	21.9 ± 2.0

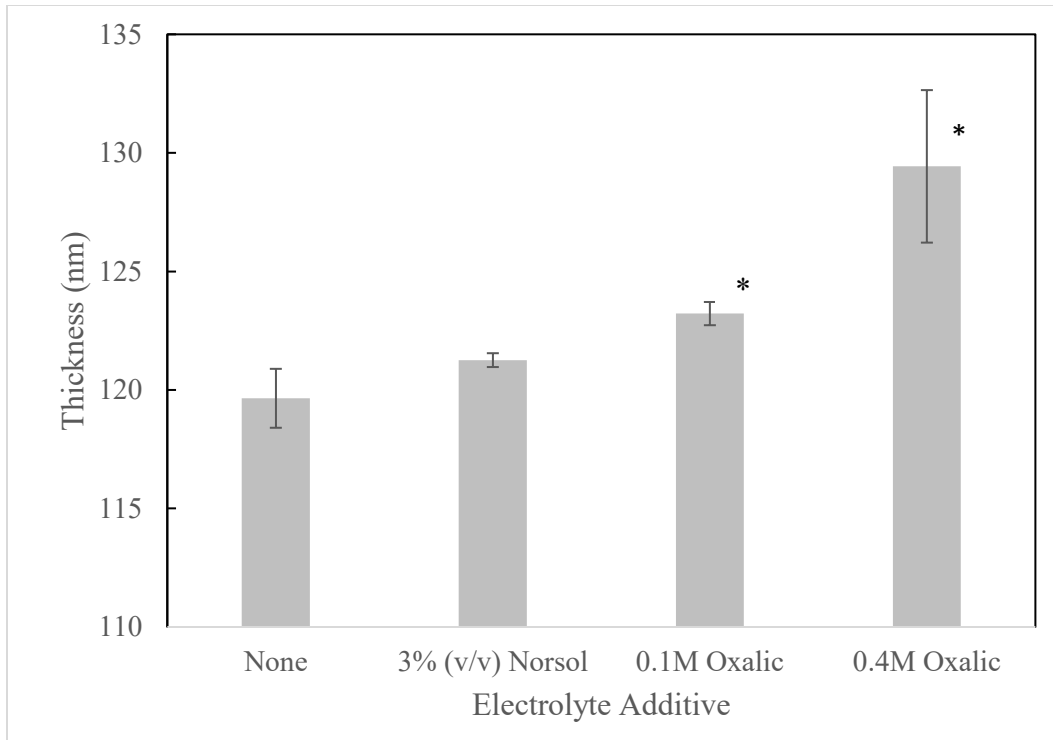


Figure 4-10. Aluminum oxide thicknesses determined by ellipsometry for aluminum-tantalum thin films anodized in 0.4M phosphoric acid at 4V with various additives. Asterisk (\*) indicates significant difference ( $p < 0.01$ ) when compared to no additive using; sample size of 3 for each case.

#### Interference Colours

The interference colours generated after anodization in each electrolyte are shown in Figure 4-11. The observed colours and their colour coordinates are in Table 4-5. The films anodized in straight phosphoric acid, or in phosphoric acid with citric acid or Norsol Anoad® additives all showed a similar tan to yellow colour. The films anodized in phosphoric/oxalic acid showed purple and dark blue for 0.1M and 0.4M oxalic acid respectively. Significant differences were found for all RGB coordinates for films anodized with 0.1M ( $p < 0.01$ ) and 0.4M ( $p < 0.05$ ) oxalic acid. Films with 3% (v/v) Norsol Anoad® or 0.1M citric acid only showed a significant difference in the blue coordinate ( $p < 0.05$  for both). The 10% (v/v) Norsol Anoad® and 0.4M citric acid films showed no difference in any colour coordinate.

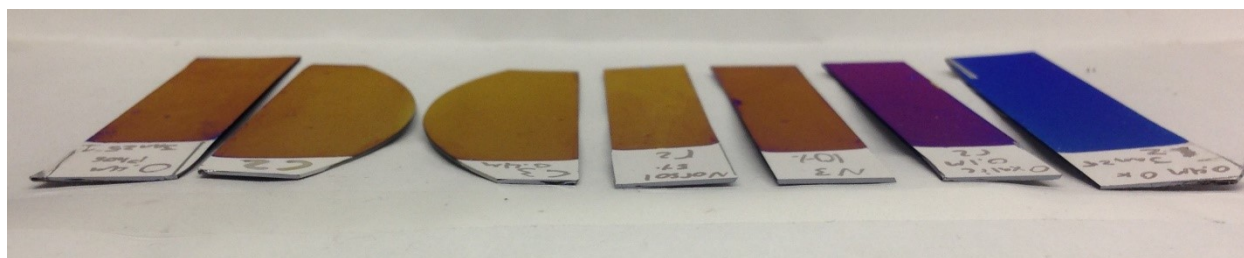


Figure 4-11. Anodized aluminum-tantalum thin films viewed at appx. 75° from normal through a polarizing lens (s-polarized). From left to right: 0.4M phosphoric acid, 0.4M phosphoric and 0.1M citric acid, 0.4M phosphoric and 0.4M citric acid, 0.4M phosphoric acid and 3% (v/v) Norsol Anoad® , 0.4M phosphoric acid and 10% (v/v) Norsol Anoad®, 0.4M phosphoric and 0.1M oxalic acid, 0.4M phosphoric and 0.4M oxalic acid.

Table 4-5. Observed interference colours and the recorded RGB coordinates from images taken at approximately 75° from normal with a polarizing lens (s-polarized light).

Electrolyte	Interference Colour
0.4M Phosphoric	Tan R: 159.8 ± 3.3 G: 106.7 ± 3.5 B: 43.3 ± 2.1
0.4M Phosphoric & 0.1M Citric	Yellow-tan R: 144.0 ± 8.6 G: 105.8 ± 6.3 B: 61.9 ± 2.7
0.4M Phosphoric & 0.4M Citric	Yellow-tan or Tan R: 146.7 ± 6.8 G: 102.6 ± 7.0 B: 44.5 ± 5.0
0.4M Phosphoric & 3% (v/v) Norsol	Yellow-tan R: 152.1 ± 4.6 G: 117.5 ± 4.4 B: 66.0 ± 3.9
0.4M Phosphoric & 10% (v/v) Norsol	Tan R: 150.1 ± 7.7 G: 103.3 ± 8.0 B: 47.7 ± 3.1
0.4M Phosphoric & 0.1M Oxalic	Purple R: 108.1 ± 7.9 G: 49.0 ± 3.8 B: 101.4 ± 5.3
0.4M Phosphoric & 0.4M Oxalic	Blue R: 23.9 ± 3.7 G: 53.6 ± 3.2 B: 123.5 ± 5.7

## Discussion

The ability to manipulate interference colour can be achieved by tailoring the anodization electrolyte, as it was found that the addition of chemical inhibitors had a range of effects on the anodization, microstructure and the optical properties of the anodic oxide.

It was concluded that oxalic acid acts as the strongest inhibitor of the additives chosen, followed by the Norsol Anoad® and then citric acid. The rate of anodization was slowed up to 60-70% depending on the inhibitor used by dropping the pore formation current density. Since all slides were sputtered to the same initial aluminum thickness, the amount of charge passed during oxidation should be the same. By reducing the current density, the amount of charge passing per unit time is reduced, thereby increasing the required time for complete anodization. The current density is associated with the movement of ions through the oxide when under a high electric field [3, 13]. By decreasing the current density, the rate of  $O^{2-}/OH^-$  ingress to the oxide/metal interface and  $Al^{3+}$  egress to the oxide/electrolyte interface is reduced, thereby slowing the rate of oxidation. It is interesting to note that the Norsol product at 3% (v/v) had a microstructural effect, and yet did not significantly affect the final thickness or refractive index. The glycolic acid/glycerol mixture appears to improve how evenly the aluminum film anodizes without changing the air to alumina ratio in the film, Table 4-4. Oxalic acid, on the other hand, promotes even anodization as well as strongly reduced dissolution, evident by the smoother surfaces, smaller standard deviation of pore size and visible grain boundaries. Pore formation occurs initially at sites of high energy such as crystal defects and grain boundaries [13]. Therefore, these initial pores along the grain boundary were exposed to the acid for a longer period causing an increased pore size relative to the center of crystal grains due to etching. Although this form of dissolution likely occurs in all mixes, the topography is more apparent in the phosphoric/oxalic mixes because the surface is still intact and

has not been as strongly degraded from chemical etching by the electrolyte. Regardless of the electrolyte used, the XRD patterns showed complete anodization of the aluminum film and the generation of amorphous oxides, as is evident by the lack of any peaks in the patterns other than  $\alpha$  phase tantalum. The colour difference is a result of the higher refractive indices and oxide thicknesses, thereby increasing the optical path length of these films relative to the straight phosphoric acid films. Larger optical path lengths produce higher order colours as discussed in Chapter 1 Section 1.3.1. The increase in refractive index of the phosphoric-oxalic acid films is a result of the reduced chemical etching which leads to smaller pores and lower void fraction in the thin film, Figure 4-6 and Table 4-4. As discussed in Chapter 1 - Section 1.2.2, the lower air content in the film will increase the refractive index and thus lead to an increase in the optical path length (OPL). It is this increased OPL that results in a change in the interference colour. Both citric acid and Norsol Anoadd<sup>®</sup> do not lead to changes in refractive index or thickness and therefore the colour remains the same.

Previous studies have stated that the inhibition process is a result of the mixing of a strong acid with a weak acid, thereby weakening the acidity of the electrolyte and promoting oxide growth over dissolution [10]. This study more strongly supports Mardilovich et al. [8], where there appears to be no correlation between the dissolving power of the acid and its basicity or dissociation constant. Oxalic acid is a diprotic acid, dissociation constants of  $k_{a1}=5.6 \times 10^{-2}$  and  $k_{a2}=5.42 \times 10^{-5}$  [14]. Phosphoric acid, on the other hand, is a weaker triprotic acid,  $k_{a1}=7.11 \times 10^{-3}$ ,  $k_{a2}=6.32 \times 10^{-8}$ , and  $k_{a3}=4.5 \times 10^{-13}$  [14]. Despite being a weaker acid, phosphoric acid has a higher dissolving ability for anodic alumina. It has been postulated that the ability of the acidic anion to form complexes with  $Al^{3+}$  determines the solubility rate [8]. Phosphate and oxalate anions have been shown to compete for surface binding sites on aluminum oxides [15]. The competition between

these two anions is what likely decreases the dissolution rate in the phosphoric/oxalic acid mixtures as oxalate anions, with a weaker dissolving ability for alumina, will compete against phosphate ions to interact with the surface.

Figure 4-12 shows the 3D structure of glycolic (monocarboxylic), oxalic (dicarboxylic) and citric (tricarboxylic) acid. This work found that oxalic acid acted as the strongest inhibitor in phosphoric acid solutions, followed by the glycolic acid/glycerol mixture, and then the citric acid. The strength of these inhibitors is likely due to their ability to interact with the oxide surface. It is well known that dicarboxylic acids bind more strongly to aluminum oxides than monocarboxylic, likely due to the increased energy required to simultaneously remove two chemisorbed carboxylates as opposed to one [16, 17]. The increased bond strength probably allows oxalic acid to compete more effectively with phosphoric acid and thus acts as a stronger inhibitor to dissolution. Citric acid is a tricarboxylic acid; however, its carboxyl groups are spread further apart. The stereochemistry will either prevent two carboxyl groups from the formation of a bidentate bond or reduce the number of molecules that can associate with the surface due to its size (i.e. steric hindrance). Therefore, citric acid is the weakest of the three inhibitors chosen.

With respect to thin film diagnostics, this study provides an understanding of how the electrolyte strongly affects both the microstructure and optical properties of the anodic alumina film. Using a strong inhibitor in a phosphoric acid electrolyte, such as oxalic acid, can help achieve a number of important goals including, the high porosity needed for low refractive index films, a small pore size required to keep protein from adsorbing inside the pores and thus changing the refractive index, as well as an optically smooth surface to provide a uniform light reflecting substrate for the adsorption of protein.

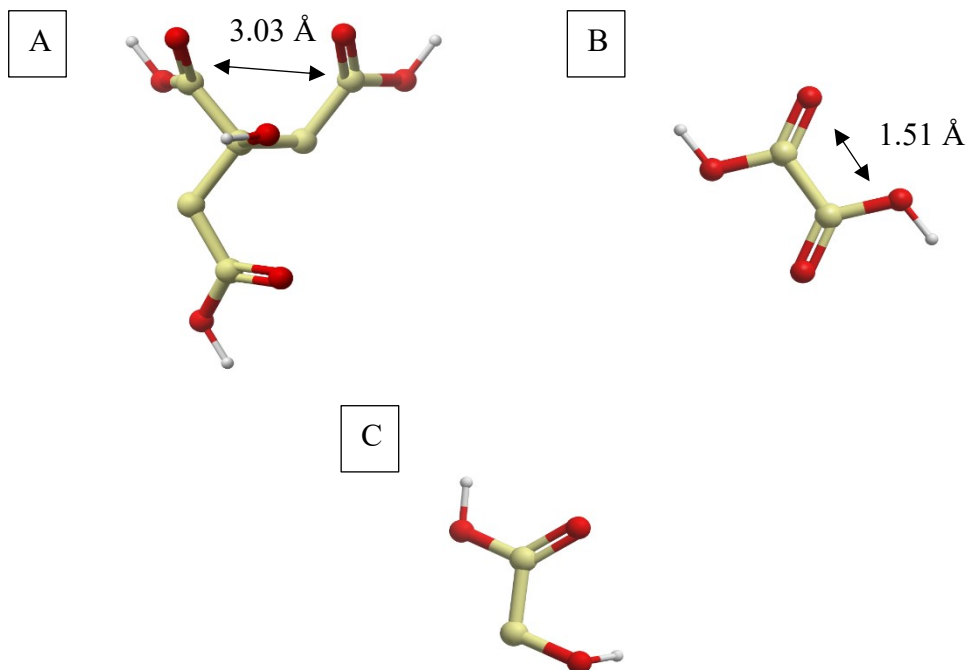


Figure 4-12. Molecular structure and dimensions of (A) Citric acid, (B) Oxalic acid, and (C) Glycolic Acid. Carbon is yellow, oxygen is red, and hydrogen is white. Modelled using Molsoft MolBrowser Version 3.8-5 for Windows (Molsoft LLC, ©2017). Molecular structures and measurements from reference [18].

## Conclusion

These results helped to improve the understanding of how adding chemical additives to the anodization bath affect the microstructural and optical properties of the anodized aluminum-tantalum thin films. A list of important conclusions follows:

1. 0.4M Phosphoric acid anodized aluminum-tantalum films are highly rough and appear to have high pore tortuosity when anodized at 4V.
2. The addition of 0.1M citric acid had an effect on the microstructure, reducing the surface roughness, pore size and the number of pits in the porous anodic layer. However, the change was

relatively minor. 0.4M citric acid reduced the current density during anodization, however there was no change in microstructure or the interference colours generated compared to phosphoric acid films.

3. Addition of 3% (v/v) Norsol Anoadd<sup>®</sup> reduced the apparent roughness of the surface and created more uniform pores, however there was no change found in the resulting porous aluminum oxide thickness or refractive index. In comparison, 10% (v/v) Norsol Anoadd<sup>®</sup> appeared to have no effect on microstructure or the resulting interference colour.

4. Addition of oxalic acid at 0.1M and 0.4M produced flatter, more uniform surfaces, reduced pore tortuosity and size, and was found to decrease the current density during pore formation which resulted in approximately tripling the time of anodization. Significant changes in the interference colours were found, which was caused by an increase in porous aluminum oxide thickness and refractive index.

5. All electrolyte mixtures consumption anodized the aluminum and produced amorphous aluminum oxide and tantalum oxide films.

## References

[1] P. G. Sheasby and R. Pinner, *The Surface Treatment and Finishing of Aluminum and its Alloys* - 6th Edition, Finishing Publications Ltd., 2001.

[2] R. C. Furneaux, W. R. Rigby and A. P. Davidson, "The formation of controlled-porosity membranes from anodically oxidized aluminum," *Nature*, vol. 337, no. 12, pp. 147-149, 1989.

[3] W. Lee and S. Park, "Porous Anodic Aluminum Oxide: Anodization and Templated Synthesis of Functional Nanostructures," *Chemical Reviews*, vol. 114, pp. 7487-7556, 2014.

[4] R. E. Burrell, A. G. Naylor and A. M. Rosenfeld. "Thin Film Diagnostic Device. " US Patent 5,124,172, 1992.

- [5] M. A. Jozefowicz and A. M. Rosenfeld, "Optical Interference Structures". US Patent 5,218,472, 8 June 1993.
- [6] A. M. Rosenfeld and P. Smits, "Colour Change Devices Incorporating Thin Anodic Films". US Patent 4,994,314, 19 February 1991.
- [7] P. Smits, A. M. Rosenfeld and H. F. DeFerrari, "Tamper-Evident Structures". US Patent 4,837,061, 6 June 1989.
- [8] P. P. Mardilovich, A. N. Govyadinov, N. I. Mazurenko and R. Paterson, "New and modified anodic alumina membranes Part II. Comparison of solubility of amorphous (normal) and polycrystalline anodic alumina membranes," *Journal of Membrane Science*, vol. 98, pp. 143-155, 1995.
- [9] V. Moutarlier, M. P. Gigandet, J. Pagetti and B. Normand, "Influence of oxalic acid addition to chromic acid on the anodising of Al 2024 alloy," *Surface Coatings and Technology*, vol. 182, pp. 117-123, 2004.
- [10] W. Bensalah, M. Feki, M. Wery and H. F. Ayed, "Chemical dissolution resistance of anodic oxide layers formed on aluminum," *Transactions of Nonferrous Metals Society of China*, vol. 21, pp. 1673-1679, 2011.
- [11] Y. Shang, L. Wang, D. Niu, Z. Liu, Y. Wang and C. Liu, "Effects of Additive for Anodizing Electrolyte on Anodic Film of High Silicon Aluminum Alloy," *International Journal of Electrochemical Science*, vol. 11, pp. 1549-1557, 2016.
- [12] K. Hinrichs and K. Eichhorn, "Ch. 7 Detection of Organic Attachment onto Highly Ordered Three-Dimensional Nanostructured Thin Films by Generalized Ellipsometry and Quartz Crystal Microbalance with Dissipation Techniques," in *Ellipsometry of Functional Organic Surfaces and Films*, Heidelberg: Springer, 2014, pp. 142-143.
- [13] G. E. Thompson, "Porous anodic alumina: fabrication, characterization and applications," *Thin Solid Films*, vol. 297, pp. 192-201, 1997.
- [14] D. A. Skoog, D. M. West and F. J. Holler, "Appendix 4 – Dissociation Constants for Acids," in *Fundamentals of Analytical Chemistry – 5<sup>th</sup> Edition*, New York, W. B. Saunders Company, 1988, p. 817.
- [15] A. Violante, C. Colombo and A. Buondonno, "Competitive Adsorption of Phosphate and Oxalate by Aluminum Oxides," *Soil Science Society of America Journal*, vol. 55, pp. 65-70, 1991.
- [16] J. van den Brand, O. Blajiev, P. C. Beentjes, H. Terryn and J. H. de Wit, "Interaction of Anhydride and Carboxylic Acid Compounds with Aluminum Oxide Surfaces Studied Using

Infrared Reflection Absorption Spectroscopy," American Chemical Society, pp. 6308-6317, 2004.

[17] P. Benoit, J. G. Hering and W. Stumm, "Comparative study of the adsorption of organic ligands on aluminum oxide by titration calorimetry," *Applied Geochemistry*, vol. 8, pp. 127-139, 1993.

[18] "National Center for Biotechnology Information," PubChem Compound Database, [Online]. Available: <https://pubchem.ncbi.nlm.nih.gov/>. [Accessed 13 September 2017].

## 4.2 The Effects of Voltage on the Structure and Optical Properties of Anodized Aluminum-Tantalum Thin Films

### **Introduction**

The nanostructure of anodic alumina is a critical component of diagnostics based on anodized aluminum-tantalum thin films, as it controls both the optical and chemical properties of the surface. The structure of anodic alumina can be controlled by many aspects of the anodization process, including electrolyte, temperature, current, voltage, and post-anodization processing [1, 2, 3, 4]. Of these various parameters, voltage is one of the most studied and is known to control the pore size in the range of 10's to 100's of nanometers [5]. Voltage also controls the thickness of the barrier layer and the pore population density [3, 4, 5]. Steady state pore growth is a dynamic equilibrium between anodic oxide growth and field-assisted dissolution. Increasing the voltage leads to an increase in the local field at the base of each pore, resulting in a thicker barrier layer and larger radius of curvature of the field distribution. The increased radius of curvature leads to field-assisted dissolution such that a larger pore base is established and the pore diameter increases [3, 4] (see Chapter 1 – Section 1.5 for more details). This knowledge has been applied in many areas, including molecular membranes of controlled pore size [6, 7], waveguides [8], and many other applications in the biomedical and electronics industries.

Some studies show the effect voltage has on the optical properties of anodized aluminum. Wang, J., et al. [9] and Wang, Y., et al. [8] determined the optical constants of anodic oxide films formed in oxalic acid at various voltages. Shih et al. [10] analyzed reflectance and refractive index values of anodic aluminum oxides on Al 1050 alloys. Hierro-Rodriguez et al. [11] and Rahman et al. [12] both measured the effect of post-anodization chemical treatments for pore widening on the optical properties of porous anodic alumina. Sweet [13] studied the effects of voltage on sputtered

aluminum-tantalum thin films anodized in phosphoric acid. The general consensus in the literature is that increasing voltage results in an increase of the refractive index. However, of these studies only Sweet showed the optical properties for films anodized at low voltages (less than 20V). No studies have shown the effects of low voltages (<20V) on the optical properties of aluminum films anodized in a phosphoric-oxalic acid mix, nor have there been any studies showing the ability to tailor both the topography of the nanostructured alumina and the optical properties by a voltage-step process, whereby the voltage is adjusted during anodization to change the structure of the oxide as the film grows.

The purpose of this work was to understand the effects voltage has on the structure and optical properties of aluminum-tantalum thin films anodized in a phosphoric-oxalic acid mix. Two sets of experiments were conducted: A) a series of films were sputtered with varied aluminum thicknesses (110-130 nm) and anodized at a series of voltages (2, 4, 6, 8 V), and B) a voltage-step process was used, initializing anodization at 4V and stepping up to either 8 or 10V after a pre-set time. The anodized films were studied using SEM, XRD, and ellipsometry to characterize topography, microstructure, and the optical properties of the anodic alumina films.

## **Materials and Methods**

### *Thin Film Deposition*

#### Study A: Voltage/thickness

Aluminum-tantalum thin films were synthesized as described in Chapter 4.1. Sputtering was conducted at the NAIT Nanotech Centre for Applied Research for both the tantalum and aluminum portion of these films. Slides were sputtered with  $226.5 \pm 3.8$  nm of tantalum, followed by either 110, 120 or 130 nm of aluminum. Glass slides were used as witness slides in the chamber with a

mask during deposition. After deposition, profilometry was used to measure the thicknesses, as described in Chapter 2. Variation was found to be within  $\pm 2$ nm.

#### Study B: Voltage step process

Thin aluminum-tantalum films were made as described previously, Chapter 4.1. Tantalum was sputtered to a thickness of  $226.5 \pm 3.8$  nm and aluminum to a thickness of  $128.2 \pm 5.7$  nm.

#### *Anodization*

Aluminum-tantalum coated wafers were then cleaved into pieces approximately 6.3 cm x 1.3 cm. These were anodized in a 0.4M phosphoric acid, 0.1M oxalic acid mixture (phosphoric acid and oxalic acid dehydrate, Thermo Fisher Scientific, Waltham, MA) using a PAR Model 273a potentiostat/galvanostat (AMETEK Inc., Oak Ridge, TN). Slides were rinsed before and after with MilliQ deionized water. A magnetic stir plate was used to agitate the solution and the temperature of the electrolyte was  $19 \pm 1^\circ\text{C}$ . Aluminum foil (Thermo Fisher Scientific, Waltham, MA) was wrapped around a glass microscope slide and used as a cathode. The separation distance between the cathode and anode was 40 mm. A saturated calomel electrode was used as a reference electrode (Thermo Fisher Scientific, Waltham, MA). Triplicates were performed to measure reproducibility. All anodized films were viewed at approximately  $75^\circ$  from normal using a polarizing lens to view s-polarized light.

#### Study A: Voltage/thickness

The PAR Model 273a was set in potentiostatic mode at either 2, 4, 6, or 8V and anodization carried out until the current decayed to  $<0.05$  mA/cm<sup>2</sup>. Each of the 4 voltages was carried out for aluminum films of 110, 120, and 130 nm thicknesses.

## Study B: Voltage-step Process

An automated program was made in Electrochemistry PowerSuite<sup>®</sup> (Princeton Applied Research, Oak Ridge, TN) which held the potential of the cell at 4V for a specified period and then increased the voltage by 0.5V, holding for 5 seconds and repeating until the final voltage was reached. The final voltage was then held until the current decayed to  $<0.05 \text{ mA/cm}^2$  as a result of the electrical properties of the tantalum oxide barrier layer. Table 4-6 lists the conditions tested.

*Table 4-6. Experimental design matrix for voltage-step anodization.*

<b>Time held at 4V</b>	<b>Final Voltage</b>
100 s (1.67 min)	8V or 10V
400 s (6.67 min)	8V or 10V
1000 s (16.67 min)	8V or 10V

## SEM

SEM analysis was conducted to examine microstructural changes of the samples. Samples were mounted as described previously, Chapter 4.1. A Zeiss Sigma Field Emission Scanning Electron Microscope (FESEM) at the nanoFAB - Fabrication and Characterization Center at the University of Alberta was used to view each sample. Specimens were examined at 3.00 keV and an aperture size of 15  $\mu\text{m}$  to reduce charging effects from the electron beam, and at both 0° and 45° from vertical. A magnification of 50,000 or 100,000 times was used with a working distance of approximately 3 mm. SEM surface micrographs taken at 100,000 times magnification were analyzed using ImageJ software (Rasband, W.S., ImageJ, U.S. National Institutes of Health, Bethesda, Maryland, USA, <https://imagej.nih.gov/ij/>, 1997-2016) for pore diameter measurements. Three evenly spaced lines were drawn horizontally and another three vertically

across the micrograph. The pores along these lines were measured for diameter. Two samples from each experiment were measured this way. Samples were very homogenous and therefore only a single micrograph was used from each.

### *XRD*

The specimens were analyzed post-anodization by XRD for both crystal structure changes and to check for any remaining aluminum metal in the films. A Rigaku Ultima IV (Cu-source) diffraction system with a thin-film substrate holder attachment was used. Data was collected between 10 and 90° 2 $\theta$  at 5.000°/min, using a glancing angle of  $\omega=0.5^\circ$  and a DHL slit of 10 mm. Peaks were analyzed using JADE 9™ software (Materials Data Inc., ©2014) and the International Centre for Diffraction Data (ICDD) database.

### *Ellipsometry*

The optical constants (refractive index,  $n$ , and extinction coefficient,  $k$ ) as well as the final oxide thicknesses were determined using a J.A. Woollam M-2000V spectroscopic ellipsometer. A model was built as described previously, Chapter 4.1. For all layers,  $\Psi$  and  $\Delta$  values were recorded for wavelengths 370 nm to 1000 nm at angles of 55°, 65°, and 75° from normal. CompleteEASE® software for Windows (J.A. Woolam Co., Lincoln, NE) was used to develop the ellipsometry model and tabulate refractive index and oxide thickness values. Note that an anisotropic model was used to describe the porous alumina layer.

### *Colour Coordinates*

Photos of the interference colours were taken at approximately 75° from normal using a phone camera and a polarizing lens (s-polarized). The images were then analyzed for RGB coordinates using ImageJ software (Rasband, WS, ImageJ, US National Institutes of Health, Bethesda, MD,

<https://imagej.nih.gov/ij/>, 1997-2016). A rectangular area of each slide was selected in the photo, encompassing between 32,000 and 46,000 pixels. The mean and standard deviation were recorded for the RGB coordinates of each area.

### *Statistics*

Standard deviations are shown on all plots using error bars. Numerical results used IBM SPSS Statistics for Windows, Version 24.0 (IBM Corp., Released 2016, Armonk, NY). A Levene's test was used to check for similar sample variance between populations. Pore size populations were analyzed using an independent t-test. ANOVA was unsuitable for this test due to unequal sample size and variance. The refractive index values were tested using a Welch T-test with a Games-Howell post test for unequal sample variance. Aluminum oxide thickness and the colour coordinate results were tested using a one-way ANOVA with Tukey multiple comparison post hoc tests.

## **Results**

### *Study A: Voltage-Thickness*

#### Ellipsometry

The final oxide thickness and optical properties were measured with ellipsometry. Significant changes to the refractive index were found with changes in voltage. The results of the ellipsometry analysis can be found in Table 4-7. Figure 4-13 shows the recorded refractive indices (in the x-y plane,  $\lambda=555\text{nm}$ ) and Table 4-8 summarizes the statistics. The refractive index remained constant for each voltage and showed no significant change with increased aluminum thickness. As voltage was increased from 2 to 8 V the refractive index increased, which was correlated with the decrease in percent air in the film. No significant change in thickness was found with a change in voltage (ANOVA p-values:  $p>0.30$  for 110nm,  $p>0.10$  for 120nm, and  $p>0.30$  for 130nm). The maximum standard deviation of the refractive index was found for 110 nm films sputtered at 2V, however

the deviation was minimal at  $\pm 0.011$  or  $\pm 0.9\%$ . The extinction coefficient,  $k$ , was found to be near 0 in all cases.

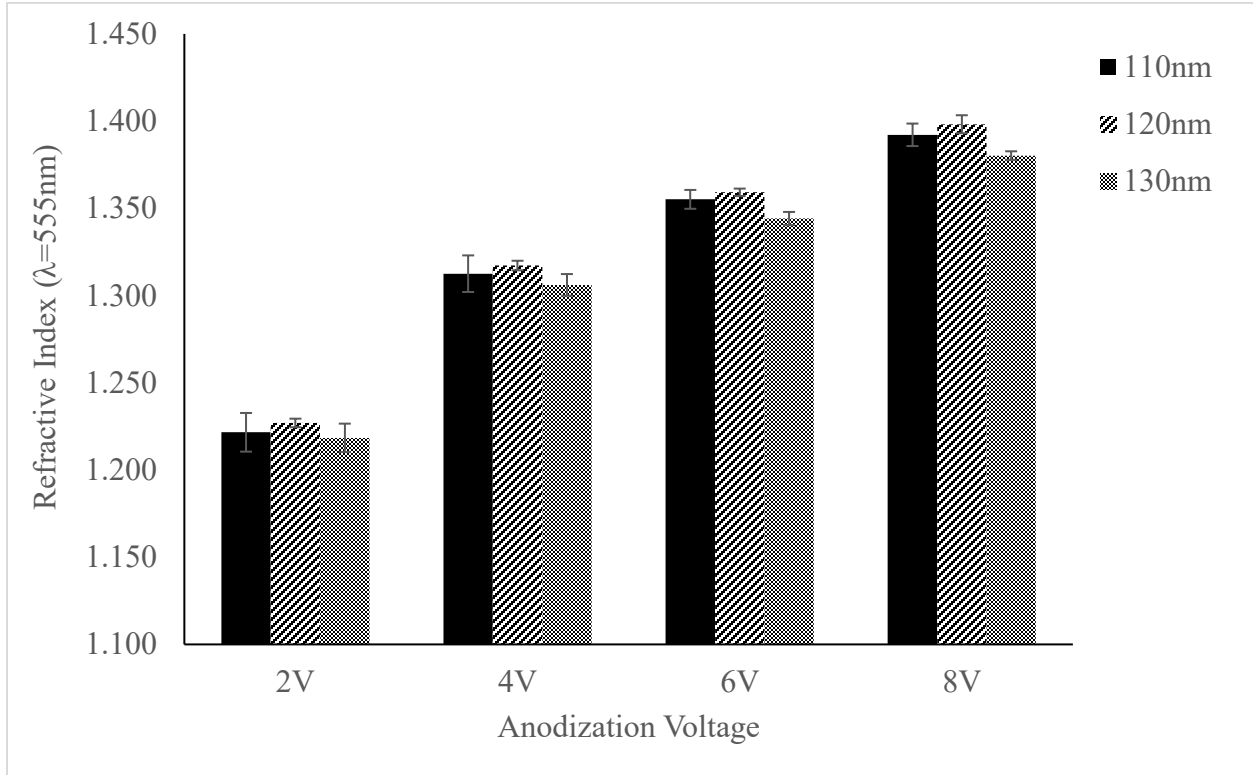


*Figure 4-13. Refractive indices of anodized aluminum-tantalum thin films, with various sputtered aluminum thicknesses and anodized under various voltages. Sample size  $n=3$  for all data sets.*

Table 4-7. Ellipsometry results for anodized aluminum-tantalum thin films, with aluminum sputtered at various thicknesses and anodized under various voltages. Sample size  $n=3$  for all data sets.

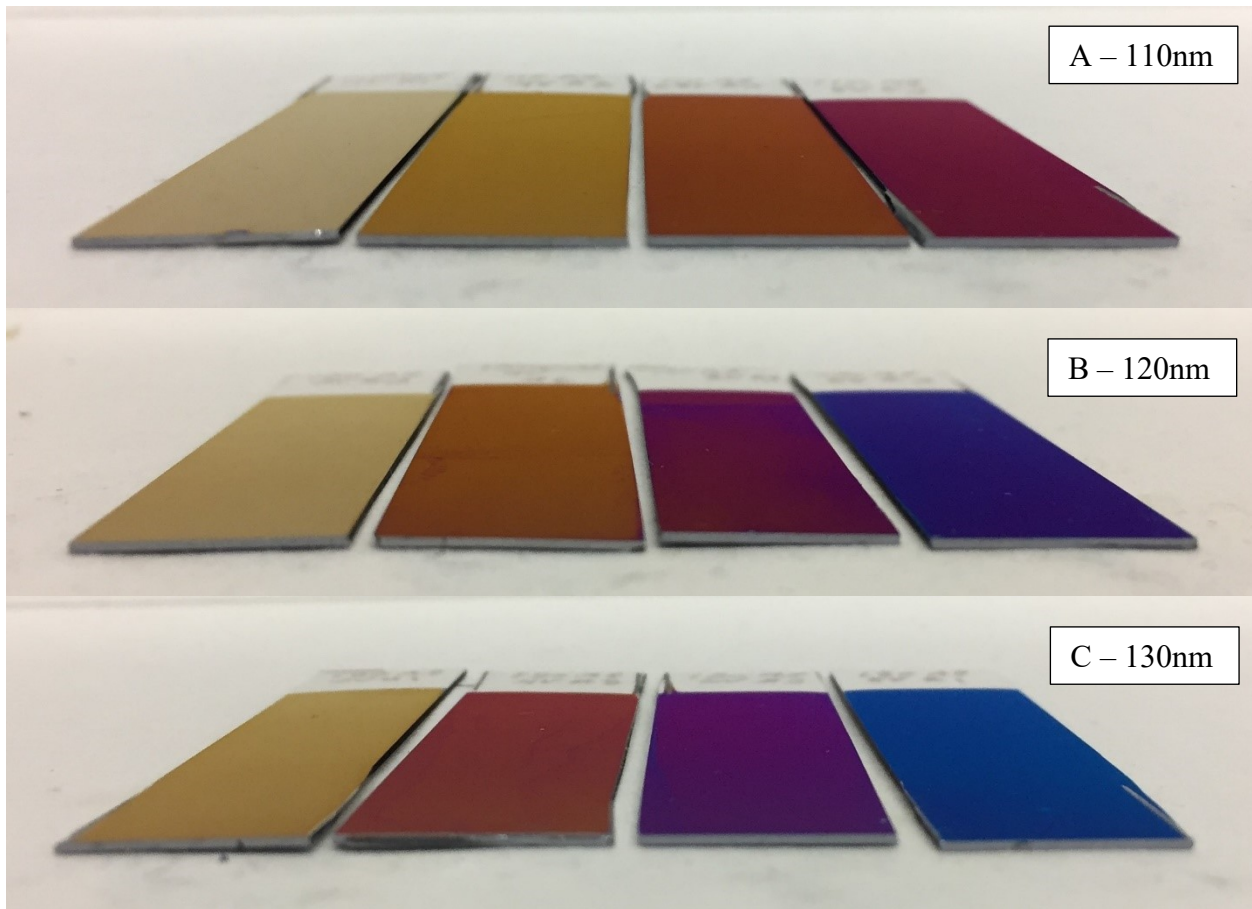
Parameters	Deposited Al Thickness 110 nm			
	2V	4V	6V	8V
Thickness (nm)	$101.4 \pm 0.8$	$100.9 \pm 1.4$	$99.5 \pm 0.8$	$98.2 \pm 1.5$
Refractive Index ( $\lambda=555\text{nm}$ , x-y plane)	$1.222 \pm 0.011$	$1.313 \pm 0.010$	$1.355 \pm 0.005$	$1.392 \pm 0.006$
EMA (% void)	$64.3 \pm 1.5$	$52.3 \pm 1.3$	$47.0 \pm 0.6$	$42.5 \pm 0.8$
MSE	$18.2 \pm 5.8$	$13.3 \pm 6.2$	$11.3 \pm 3.7$	$8.6 \pm 1.2$
Parameters	Deposited Al Thickness 120 nm			
	2V	4V	6V	8V
Thickness (nm)	$109.5 \pm 0.5$	$110.0 \pm 1.4$	$109.0 \pm 1.6$	$107.0 \pm 0.7$
Refractive Index ( $\lambda=555\text{nm}$ , x-y plane)	$1.227 \pm 0.002$	$1.317 \pm 0.003$	$1.359 \pm 0.002$	$1.398 \pm 0.005$
EMA (% void)	$63.5 \pm 0.3$	$51.7 \pm 0.3$	$46.5 \pm 0.3$	$41.8 \pm 0.6$
MSE	$19.4 \pm 4.1$	$12.1 \pm 3.2$	$9.4 \pm 1.9$	$6.9 \pm 1.2$
Parameters	Deposited Al Thickness 130 nm			
	2V	4V	6V	8V
Thickness (nm)	$118.2 \pm 0.6$	$119.9 \pm 1.1$	$118.0 \pm 0.4$	$117.0 \pm 1.2$
Refractive Index ( $\lambda=555\text{nm}$ , x-y plane)	$1.218 \pm 0.008$	$1.306 \pm 0.006$	$1.344 \pm 0.004$	$1.380 \pm 0.002$
EMA (% void)	$64.7 \pm 1.1$	$53.1 \pm 0.8$	$48.3 \pm 0.5$	$43.9 \pm 0.3$
MSE	$22.8 \pm 9.5$	$15.4 \pm 8.4$	$14.9 \pm 7.5$	$13.7 \pm 5.4$

Table 4-8. Statistical results from an analysis of refractive index for anodized aluminum-tantalum thin films, with aluminum sputtered at various thicknesses and then anodized at various voltages. Sample size  $n=3$  for all data sets.

Thickness (nm)	Voltage (V)	Welch test p-value	Games-Howell post test results
110	2	p<0.001	p<0.05: 4V 120nm (↓) p<0.01: 4V & 110, 130nm, 6V & 110, 120, 130 nm, 8V & 110, 120, 130nm (↓)
	4		p<0.10: 6V & 110, 120nm (↓) p<0.05: 2V 120nm (↑), 8V & 120, 130nm (↓) p<0.01: 2V & 110, 130nm (↑), 110nm 8V (↓)
	6		p<0.10: 4V 110nm (↑) p<0.05: 4V 120nm (↑), 8V 110nm (↓) p<0.01: 2V & 110, 120, 130nm, 4V 130nm (↑), 8V & 120, 130nm (↓)
	8		p<0.10: 6V 120nm (↑) p<0.05: 6V & 110, 130nm (↑) p<0.01: 2V & 110, 120, 130nm, 4V & 110, 120, 130nm (↑)
120	2		p<0.05: 4V 110nm (↓) p<0.01: 4V & 120, 130nm, 6V & 110, 120, 130nm, 8V & 110, 120, 130nm (↓)
	4		p<0.05: 2V 110nm (↑), 6V 110nm (↓) p<0.01: 2V & 120, 130nm (↑), 6V & 120, 130nm, 8V & 110, 120, 130nm (↓)
	6		p<0.10: 4V 110nm, 6V 130nm (↑), 8V 110nm (↓) p<0.05: 4V 130nm (↑), 8V 120nm (↓) p<0.01: 2V & 110, 120, 130nm, 4V 120nm (↑), 8V 130nm (↓)
	8		p<0.05: 4V 110nm, 6V 120nm (↑) p<0.01: 2V & 110, 120, 130nm, 4V & 120, 130nm, 6V & 110, 130nm (↑)
130	2		p<0.01: 4V & 110, 120, 130nm, 6V & 110, 120, 130nm, 8V & 110, 120, 130nm (↓)
	4		p<0.05: 6V & 120, 130nm (↓) p<0.01: 2V & 110, 120, 130nm (↑), 6V 110nm (↓), 8V & 110, 120, 130nm (↓)
	6		p<0.10: 6V 120nm (↓) p<0.05: 2V 120nm (↑), 4V 130nm (↑) p<0.01: 2V & 110, 120, 130nm (↑), 4V 120nm (↑), 8V & 120, 130nm (↓)
	8		p<0.05: 4V 110nm, 6V 110nm (↑) p<0.01: 2V & 110, 120, 4V & 120, 130nm, 6V & 120, 130nm (↑)

## Interference Colours

The interference colours produced at each voltage and thickness are shown in Figure 4-14. As voltage increases, the colours appear to span the first order interference colour regime (yellow to red) and then progress into the second order (purple and blue). Increasing the thickness of the initial aluminum also changes the colour observed. Replicates showed good reproducibility of colour.



*Figure 4-14. Aluminum-tantalum thin films anodized in 0.4M phosphoric-0.1M oxalic acid. Aluminum was deposited to thicknesses of either (A) 110nm, (B) 120nm, or (C) 130nm and then anodized at either 2, 4, 6, or 8V (shown from left to right in each image). Pictures were taken at approximately 75° from normal through a polarizing lens (s-polarized).*

## Study B: Voltage-Step Process

### Current Density Plots

A typical current density plot for the voltage-step process is shown in Figures 4-15 and 4-16, where Figure 4-16 is focused on the current density during the voltage step procedure. Every time the voltage was increased by 0.5V the current responded with a spike followed by immediate decay. After the stepping process was complete, a steady state current density, higher than the initial 4V, was reached. This steady current was followed by an eventual drop, where the process was stopped when the current density was  $<0.05\text{mA/cm}^2$ .

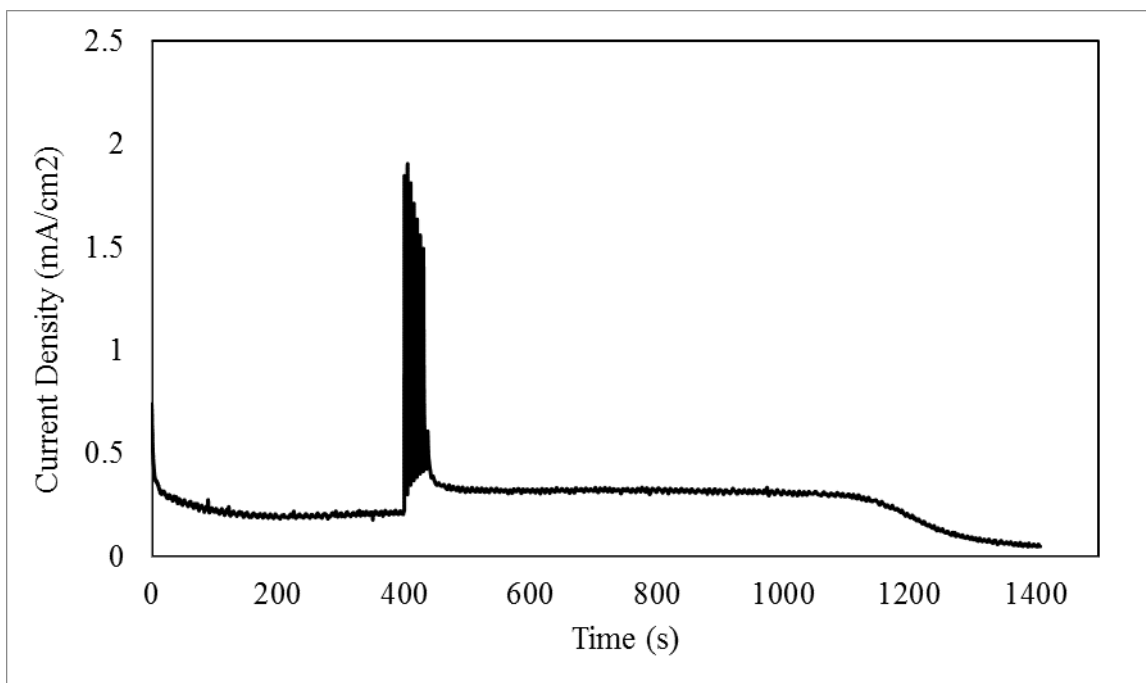
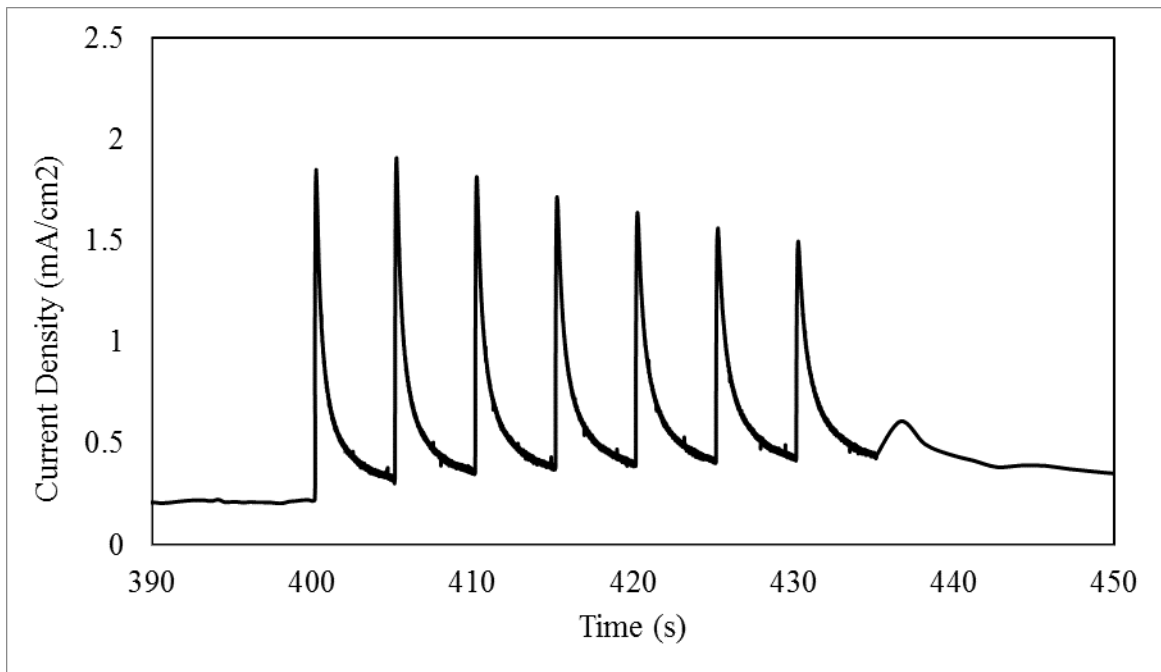


Figure 4-15. Current density-time plot during anodization of aluminum-tantalum thin films in 0.4M phosphoric acid-0.1M oxalic acid with a voltage-step process (4V for 400s followed by 0.5V increase for 5s until 8V was reached).



*Figure 4-16. Current density-time plot during anodization of aluminum-tantalum thin films in 0.4M phosphoric acid-0.1M oxalic acid with a voltage-step process (4V for 400s followed by 0.5V increase for 5s until 8V was reached). Zoomed in time axis from 390 – 450s to show voltage step effect on current density.*

## SEM

SEM images were taken of the cross-sections (at 45°) to examine the change in pore structure, Figure 4-17. The images show the development of bottle-shaped pores. This bottle neck structure was more noticeable when either (a) the voltage was stepped up earlier on in the process, or (b) when the final voltage was higher. At 100s, the structure changes about a third of the way down the pore, with some pores being cut off to make space for larger pore development. At 400s this change occurs at about halfway down the pore, and at 1000s the change is difficult to see.

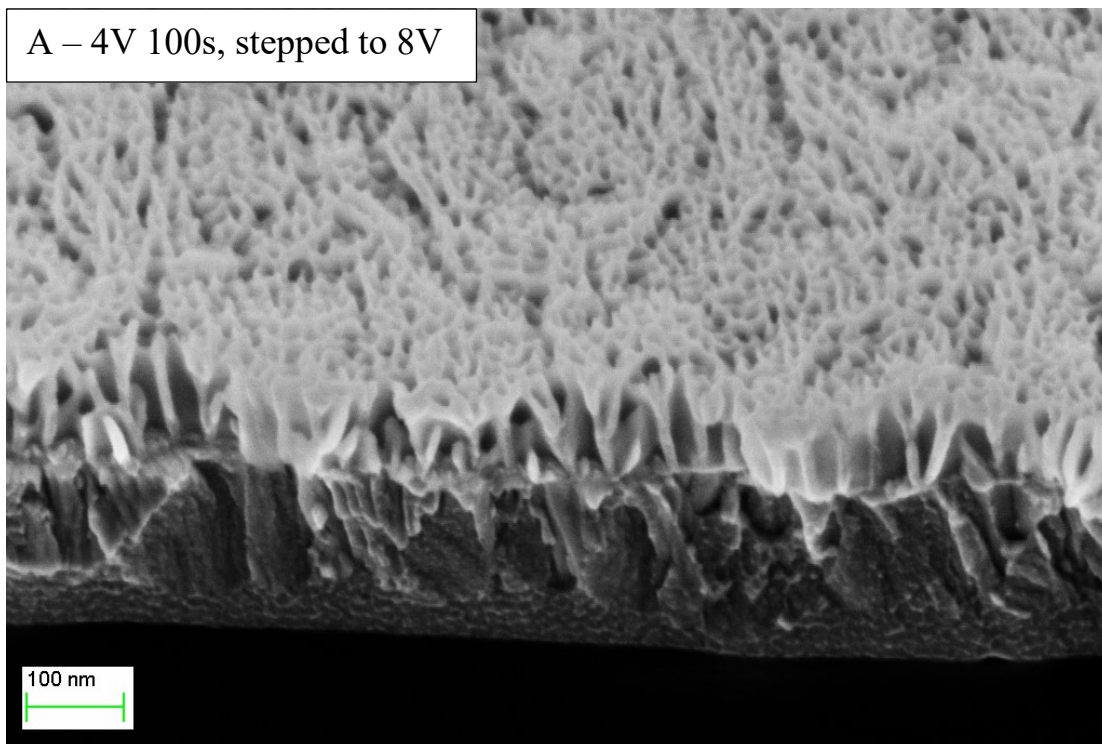


*Figure 4-17 continued.*

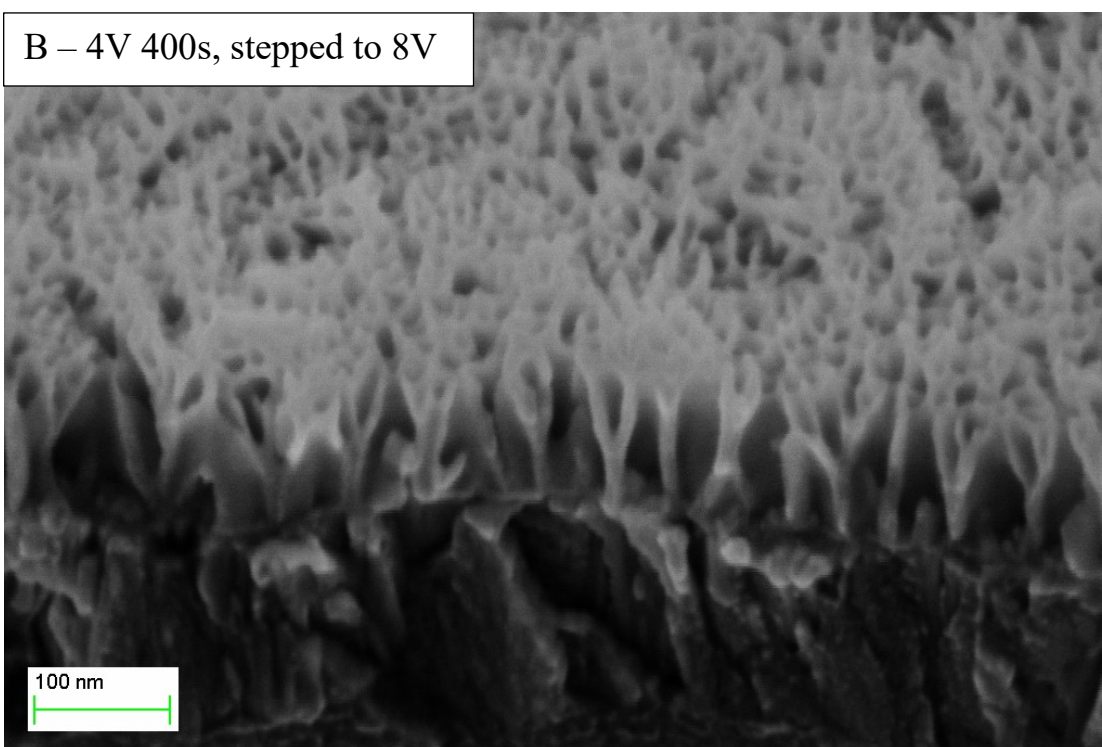


*Figure 4-17 continued.*

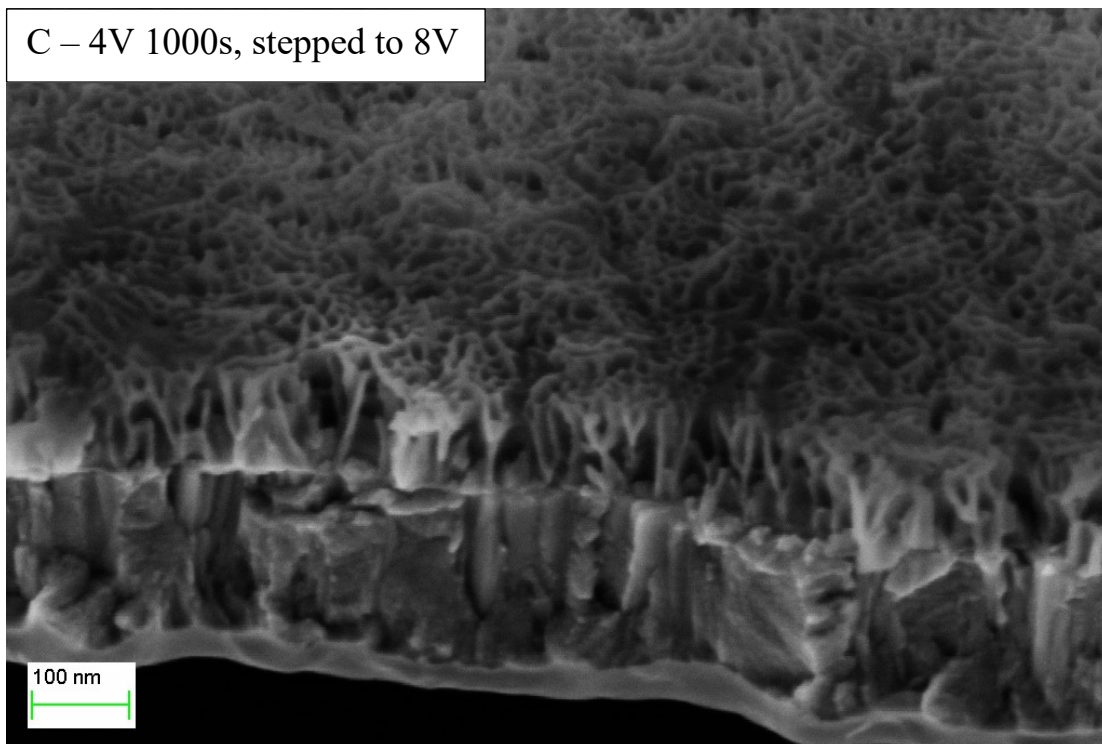


*Figure 4-17 continued.*

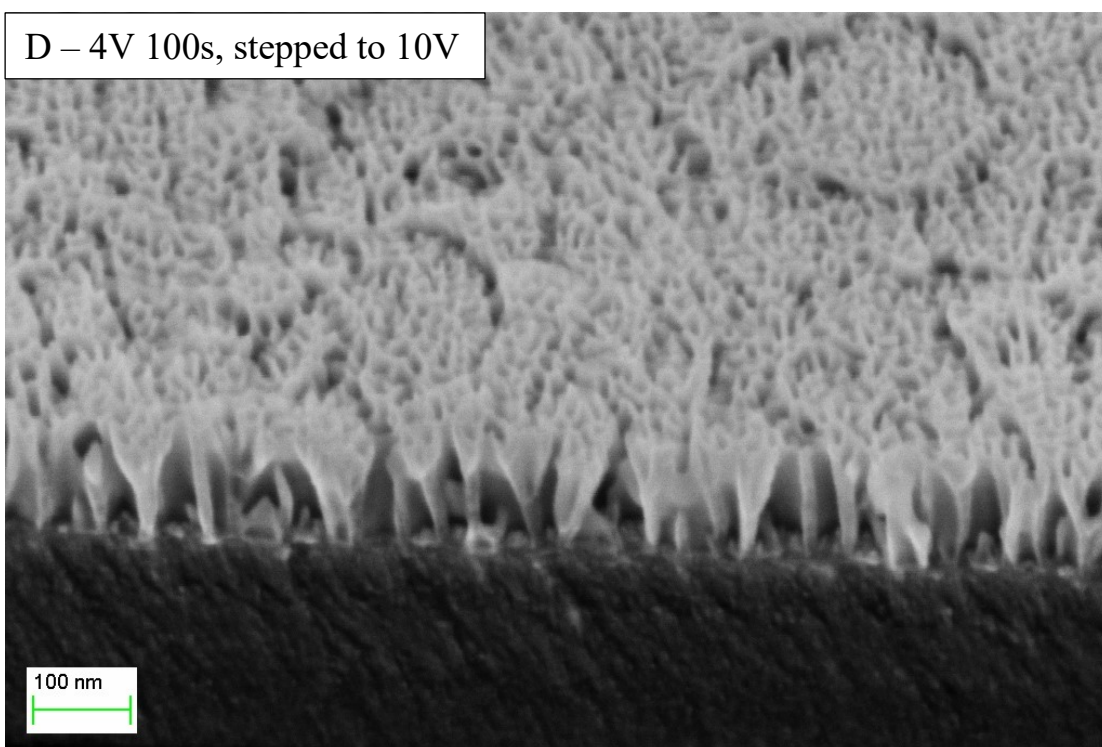


*Figure 4-17 continued.*

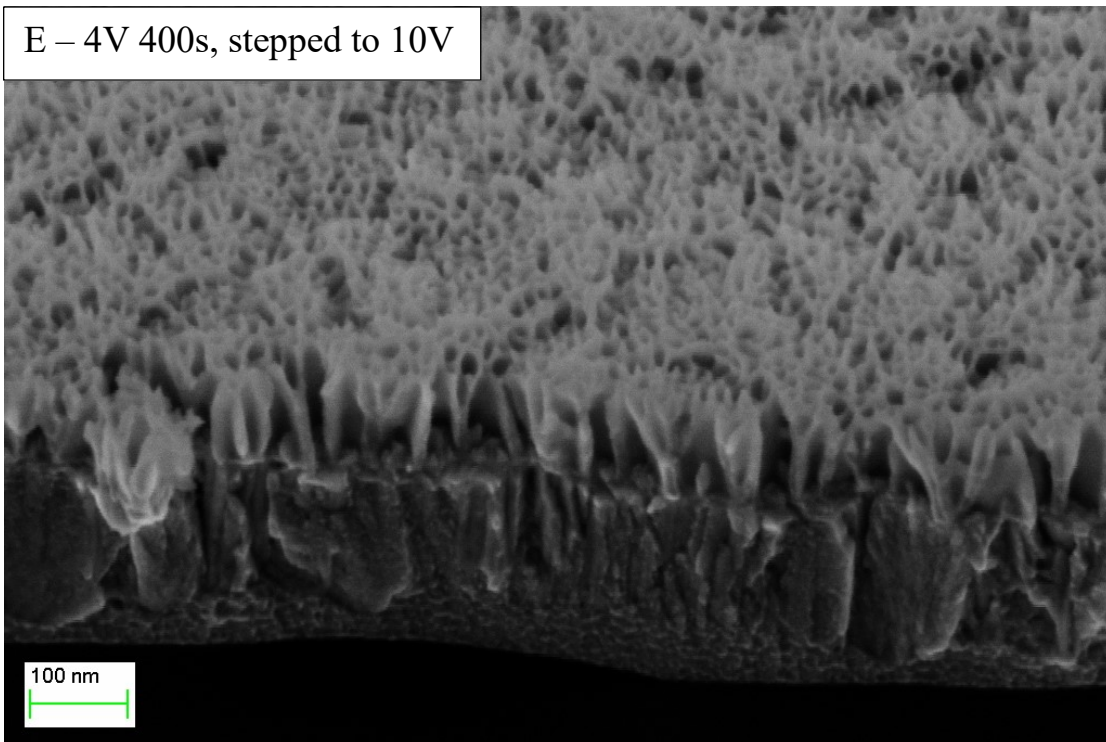


*Figure 4-17 continued.*

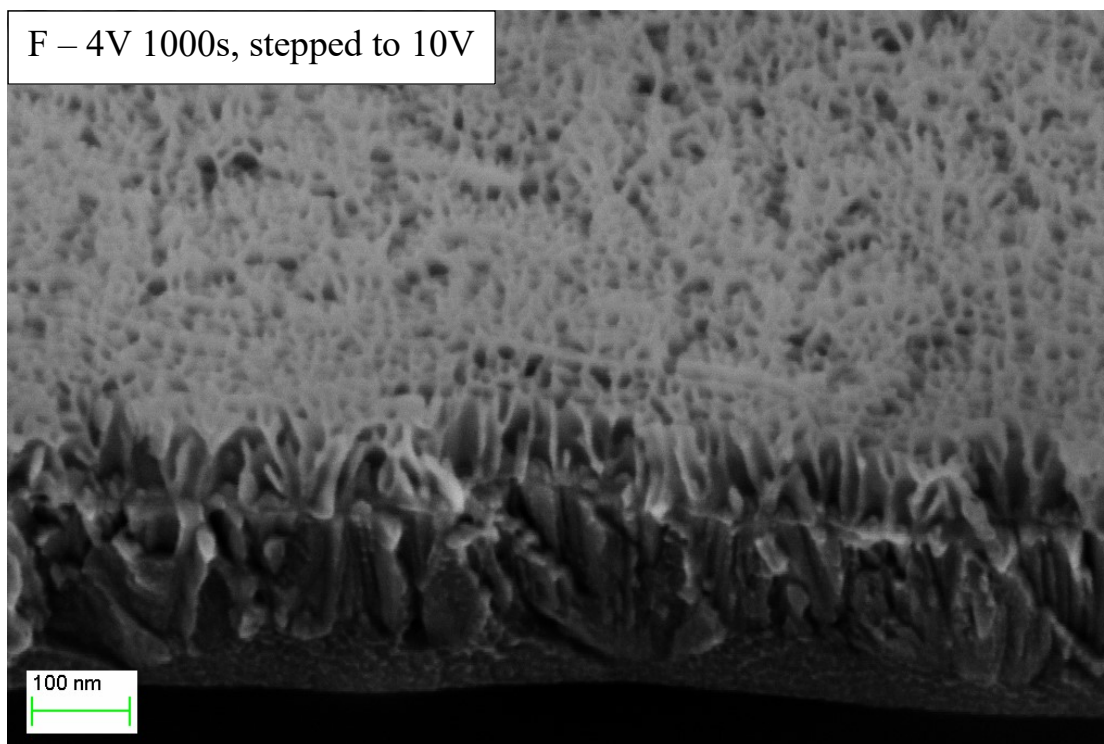


*Figure 4-17 continued. FESEM images of anodized aluminum-tantalum thin films, anodized in 0.4M phosphoric-0.1M oxalic acid under various voltage step parameters.*

The measured pore sizes showed variability depending on the final voltage and the time at which the voltage step process was initiated, Figure 4-18. Samples at 10V showed a consistent increase in the surface pore size compared to 8V, except for when the voltage was stepped up after 1000s, Table 4-9. Pore sizes ranged from  $10.7 \pm 2.6$  nm (4V for 1000s followed by 10V) to  $14.3 \pm 4.0$  nm (4V for 100s followed by 10V) and the variation in pore size appeared to be larger the sooner the secondary voltage was applied, Figure 4-18. Therefore, a longer time at the lower voltage (4V) reduces the effects of the secondary voltage (8 or 10V) on the surface pore size.

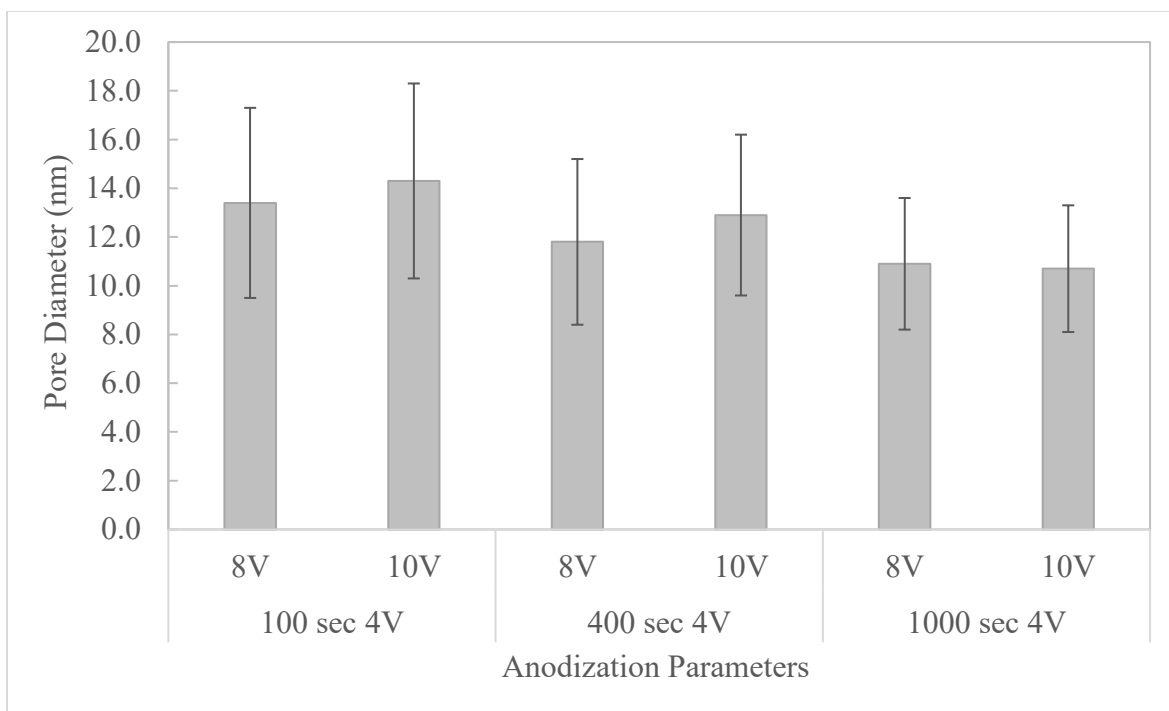


Figure 4-18. Measured pore diameter from FESEM surface images for the different anodizing conditions: from left to right, 1) 4V for 100s, stepped to 8V ( $n=357$ ), 2) 4V for 100s, stepped to 10V ( $n=310$ ), 3) 4V for 400s, stepped to 8V ( $n=370$ ), 4) 4V for 400s, stepped to 10V ( $n=351$ ), 5) 4V for 1000s, stepped to 8V ( $n=316$ ), and 6) 4V for 1000s, stepped to 10V ( $n=353$ ).

Table 4-9. Statistical results for comparison of measured pore diameters between different anodizing conditions. Standard error represented by  $\pm$  symbol.

Time at 4V (sec)	Voltage Step-up (V)	test vs.	t-test p Value	Mean Difference (nm)
100	8 (n=357)	100s/10V	<0.01	-0.9 $\pm$ 0.3
		400s/8V	<0.001*	1.6 $\pm$ 0.3
		400s/10V	<0.10*	0.5 $\pm$ 0.3
		1000s/8V	<0.001*	2.5 $\pm$ 0.2
		1000s/10V	<0.001*	2.7 $\pm$ 0.2
	10 (n=310)	100s/8V	<0.01	0.9 $\pm$ 0.3
		400s/8V	<0.001*	2.5 $\pm$ 0.3
		400s/10V	<0.001*	1.4 $\pm$ 0.3
		1000s/8V	<0.001*	3.5 $\pm$ 0.3
		1000s/10V	<0.001*	3.6 $\pm$ 0.3
400	8 (n=370)	100s/8V	<0.001*	-1.6 $\pm$ 0.3
		100s/10V	<0.001*	-2.5 $\pm$ 0.3
		400s/10V	<0.001	-1.1 $\pm$ 0.3
		1000s/8V	<0.001*	0.9 $\pm$ 0.2
		1000s/10V	<0.001*	1.1 $\pm$ 0.2
	10 (n=351)	100s/8V	<0.10*	-0.5 $\pm$ 0.3
		100s/10V	<0.001*	-1.4 $\pm$ 0.3
		400s/8V	<0.001	1.1 $\pm$ 0.3
		1000s/8V	<0.001*	2.0 $\pm$ 0.2
		1000s/10V	<0.001*	2.2 $\pm$ 0.2
1000	8 (n=316)	100s/8V	<0.001*	-2.5 $\pm$ 0.2
		100s/10V	<0.001*	-3.5 $\pm$ 0.3
		400s/8V	<0.001*	-0.9 $\pm$ 0.2
		400s/10V	<0.001*	-2.0 $\pm$ 0.2
		1000s/10V	No difference	-
	10 (n=353)	100s/8V	<0.001*	-2.7 $\pm$ 0.2
		100s/10V	<0.001*	-3.6 $\pm$ 0.3
		400s/8V	<0.001*	-1.1 $\pm$ 0.2
		400s/10V	<0.001*	-2.2 $\pm$ 0.2
		1000s/8V	No difference	-

\*Equal variances not assumed, failed Levene's test for equality of variance.

## XRD

Films were characterized using XRD to determine any changes in microstructure with the anodization parameters. Figure 4-19 shows XRD patterns for samples anodized at 4V for 100 and

1000s and then stepped up to 10V. When compared to XRD patterns before anodization, the peaks that overlap between tantalum and aluminum are significantly decreased and the remaining aluminum peaks are no longer present. The only remaining peaks were found to be  $\alpha$  – tantalum (peaks for crystal planes (110), (200), (211), and (220)), therefore the anodic aluminum and tantalum oxides must be amorphous, which is consistent with all other studies in this thesis. The tantalum shows some variability of its crystallinity, as can be seen in Figure 4-19C where the peaks are noticeably broader than the other samples.

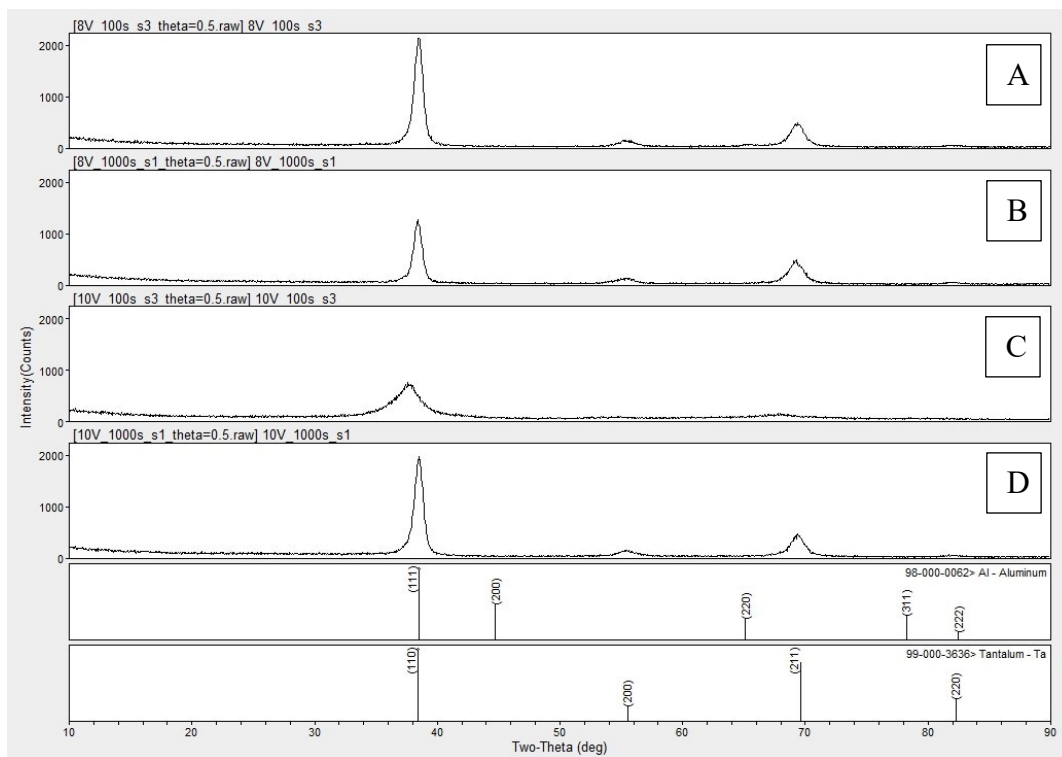


Figure 4-19. XRD patterns from anodized aluminum-tantalum films in 0.4M phosphoric-0.1M oxalic acid: A) 4V for 100s, stepped to 8V; B) 4V for 1000s, stepped to 8V; C) 4V for 100s, stepped to 10V; D) 4V for 1000s, stepped to 10V.

### Ellipsometry

Overall, both the time anodized at 4V and the strength of the final electric field (8 or 10V) had effects on the optical properties of the anodized films. The results of the ellipsometry study are

shown in Tables 4-10 and 4-11. As the anodization time at the lower voltage is increased, there is a decrease in the aluminum oxide thickness and the refractive index. Films anodized at 4V for 100 or 400s showed no significant differences in refractive index, however films anodized at 4V for 1000s were found to be have a significantly lower refractive index. No difference was found between samples anodized at 8 or 10V. The deviation of the refractive index remained relatively small, with a maximum standard deviation of  $\pm 0.018$  or  $\pm 1.3\%$  for samples anodized at 4V for 100s and then stepped up to 10V. Tantalum oxide thickness increased as the final voltage was increased. The extinction coefficient,  $k$ , was found to be 0 in all cases.

*Table 4-10. Ellipsometry results for aluminum-tantalum films anodized in 0.4M phosphoric-0.1M oxalic acid at various voltage conditions.  $n=3$  for all data sets.*

	100s/8V	400s/8V	1000s/8V	100s/10V	400s/10V	1000s/10V
Thickness Al <sub>2</sub> O <sub>3</sub>	110.5 $\pm$ 0.7	107.5 $\pm$ 0.2	105.4 $\pm$ 0.5	109.8 $\pm$ 1.5	106.8 $\pm$ 1.0	105.3 $\pm$ 0.8
Refractive Index ( $\lambda=555\text{nm}$ ), x-y plane	1.427 $\pm$ 0.005	1.409 $\pm$ 0.003	1.368 $\pm$ 0.015	1.418 $\pm$ 0.018	1.418 $\pm$ 0.008	1.361 $\pm$ 0.003
EMA (% void)	38.3 $\pm$ 0.6	40.5 $\pm$ 0.4	45.4 $\pm$ 1.8	39.5 $\pm$ 2.1	39.5 $\pm$ 1.0	46.2 $\pm$ 0.4
MSE	9.0 $\pm$ 0.1	10.7 $\pm$ 1.4	12.5 $\pm$ 2.9	23.3 $\pm$ 11.5	10.7 $\pm$ 2.0	11.7 $\pm$ 1.1
Thickness TaO	9.2 $\pm$ 0.2	11.0 $\pm$ 0.3	12.9 $\pm$ 0.9	12.1 $\pm$ 0.4	13.5 $\pm$ 0.6	14.1 $\pm$ 0.2

Table 4-11. Statistical results for the aluminum oxide refractive index, as measured by ellipsometry, for the various anodizing conditions. For all data sets  $n=3$ .

Time at 4V (sec)	Voltage Step Up (V)	test vs.	ANOVA p Value	Post Hoc Test Results
100	8	100s/10V	<0.001	No difference
		400s/8V		No difference
		400s/10V		No difference
		1000s/8V		$p < 0.001$ (↑)
		1000s/10V		$p < 0.001$ (↑)
	10	400s/8V		No difference
		400s/10V		No difference
		1000s/8V		$p < 0.001$ (↑)
		1000s/10V		$p < 0.001$ (↑)
		400		8
1000s/8V	$p < 0.01$ (↑)			
1000s/10V	$p < 0.001$ (↑)			
10	1000s/8V		$p < 0.001$ (↑)	
	1000s/10V		$p < 0.001$ (↑)	
1000	8	1000s/10V	No difference	

### Interference Colours

Visual inspection of the slides post-anodization showed a small range of interference colours was produced, in the blue and purple range, Figure 4-20. The RGB coordinates were recorded and can be found in Table 4-12. Films anodized at 4V for either 100s or 400s were blue and showed no significant differences in the RGB coordinates, regardless of the secondary voltage. Films anodized at 4V for 1000s were different shades of purple depending on whether the secondary voltage was 8 or 10V; the 8V films had a stronger red hue than the 10V films, confirmed by RGB coordinate analysis, indicating a shorter optical path length since red comes before purple in the colour progression, see Chapter 1 Section 1.3 for more details.

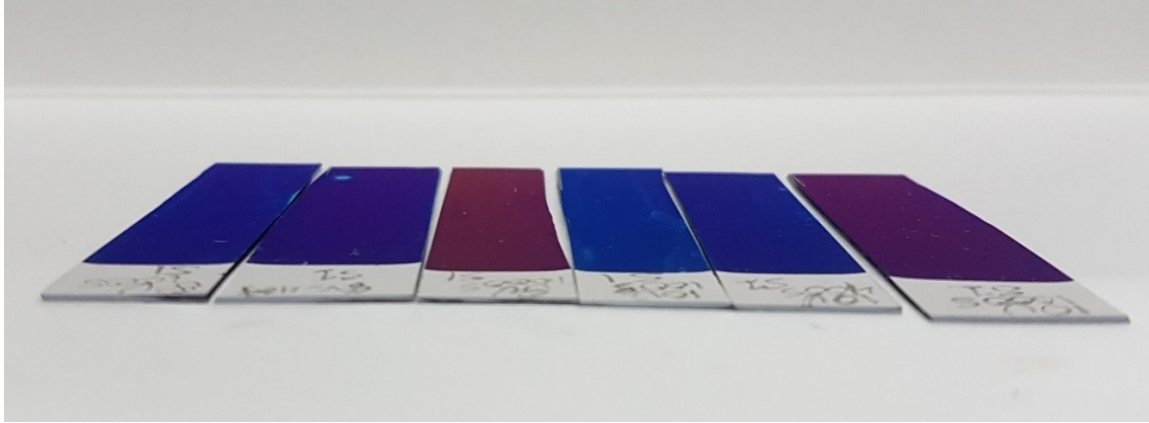


Figure 4-20. Anodized aluminum-tantalum thin films viewed at appx. 75° from normal through a polarizing lens (s-polarized). From left to right: A) 4V for 100s and then stepped to 8V; B) 4V for 400s, stepped to 8V; C) 4V for 1000s, stepped to 8V; D) 4V for 100s, stepped to 10V; E) 4V for 400s, stepped to 10V; F) 4V for 1000s, stepped to 10V.

Table 4-12. Interference colours and RGB coordinates measured from images of films anodized under various conditions. Sample size of  $n=3$  for all data sets.

Anodizing Conditions	Interference Colour and RGB Coordinates
4V 100s, stepped to 8V	Blue R: $36.0 \pm 6.1$ G: $27.8 \pm 3.8$ B: $118.6 \pm 5.8$
4V 400s, stepped to 8V	Blue R: $55.9 \pm 7.1$ G: $29.3 \pm 9.0$ B: $107.5 \pm 7.5$
4V 1000s, stepped to 8V	Plum R: $112.1 \pm 11.1$ G: $47.6 \pm 6.4$ B: $92.4 \pm 12.4$
4V for 100s, stepped to 10V	Blue R: $28.0 \pm 10.0$ G: $35.6 \pm 3.4$ B: $116.6 \pm 5.9$
4V for 400s, stepped to 10V	Blue R: $17.6 \pm 3.7$ G: $23.2 \pm 3.8$ B: $102.6 \pm 5.2$
4V for 1000s, stepped to 10V	Purple R: $81.7 \pm 5.6$ G: $30.5 \pm 3.8$ B: $86.5 \pm 3.6$

## Discussion

It is apparent from both the ellipsometry data and interference colours generated, that voltage has a strong effect on the complex refractive index of the porous aluminum oxide layer. Study A showed that as voltage was increased, the refractive index also increased, in accordance with previous studies [11, 12, 13]. This is counter intuitive as one would assume that a larger pore size would result in higher air content in the film, and thus a lower refractive index. Although pore size increases linearly with voltage, the pore spacing is inversely correlated to voltage ( $U$ ) by  $1/U^2$  [5]. Therefore, the volume of air in the anodic layer decreases with an increase in voltage.

Previous works by Sweet [13] used a 0.4M phosphoric acid electrolyte and found that at very low voltages, 2V, the dissolution from the electrolyte starts to significantly effect the final oxide thickness. This work used a 0.4M phosphoric-0.1M oxalic acid mix. As shown in Chapter 4.1, the oxalic acid acts as an inhibitor for the phosphoric acid electrolyte and reduces the amount of dissolution that occurs during anodization. Less dissolution reduces the amount of etching at the surface and leads to a maintained thickness all the way down to 2V, see Table 4-7. Starting at 2V and increasing to 8V, the interference colours progress along the first-order interference colour regime (white through red) and into second-order purples and blues (for more details on the interference colour orders see Chapter 1 Section 1.3). Increasing the thickness of the initial aluminum layer also results in an increase of the interference colour. This shows the ability to tailor the refractive index via the voltage and the order of interference via the sputtered aluminum film thickness. The refractive index and order of interference are both important aspects when it comes to thin film diagnostics. When adsorbing protein to the aluminum oxide surface, it is very important to tailor the refractive index of the alumina layer to match the refractive index of the protein. As discussed in Chapter 1, a mismatch between these two refractive indices can lead to an

extra reflection of light occurring between the protein and alumina layer, which acts as noise in the system and reduces the sensitivity to detect small molecules. The order of interference is also an important aspect of sensitivity. Higher order colours occur when more than one wavelength of light can constructively or destructively interfere at the same time. As a thin film gets thicker, the interference colours eventually stop progressing as a rainbow and only switch back and forth between pinks and greens. At this point, multiple wavelengths interfere and the combination of these results in a mixed colour of either pink or green, see Chapter 1 Figure 1-7. Therefore, the colours must be maintained in the first-order regime so that the smallest changes in the optical path length can be observed. For the conditions studied, the refractive index can be tailored between  $\sim 1.2$  and  $1.4$  by simply adjusting the voltage between  $2$  and  $8\text{V}$ . If a higher refractive index is required, and this refractive index increases the optical path length such that second-order colours are produced, then a thinner aluminum layer can be sputtered to push the colour back into the first-order regime. This is exemplified by the films anodized at  $6\text{V}$  and with either  $110$  or  $130\text{nm}$  of aluminum, Figure 4-14. Note how the  $130\text{nm}$  films are purple when anodized at  $6\text{V}$ , a second-order colour. However, when the aluminum thickness is reduced to  $110\text{nm}$ , the final interference colour is tan, a first-order colour. Examples of tailoring the surface for protein detection can be found in Chapters 5 and 6 of this work.

Study B demonstrated the ability to engineer both the structural and optical properties of anodized alumina films by tight controls on the voltage during anodization. The current density plots showed a spike in the current every time the voltage stepped up. These spikes and following decays correspond to growth of the barrier layer at the bottom of the pore [2]. Every  $0.5\text{V}$  step resulted in a slight increase in the barrier layer thickness and a widening of the pore bottom. These structural changes were observed in the SEM images and the production of the bottle-neck shaped pores.

The SEM results show the effects of anodization time at the initial voltage and the strength of the secondary voltage. Increasing the time at the initial voltage (4V) controlled how far down the film the pore size changed, as well as the surface pore diameter. The longer the time at 4V, the further down the film before the pores widened. At 1000s, the surface pore diameter did not change significantly between 8 and 10V, Table 4-9. However, at 100 and 400s, the mean pore diameter was larger for 10V than 8V. The lack of a change for the 1000s films occurs because anodization has progressed far enough down the film that the voltage is no longer having a significant effect on the dissolution rate at the surface. After anodizing for only 100 or 400s, the electric field still contributes significantly to field-assisted dissolution and the ejection of  $\text{Al}^{3+}$  into the electrolyte at the surface. Therefore, to reduce the effects of the final voltage on the pore size, anodization must be carried out for a longer period of time before ramping. The downside is that at 1000s the ~120nm films are already mostly anodized and the voltage increase will not significantly increase the refractive index of the film.

Another important microstructural parameter of the anodic film is the crystal structure and phases present. The XRD patterns showed complete anodization of aluminum, as no peaks other than  $\alpha$  – tantalum were present. Therefore, the voltage-step process left no pockets of unanodized aluminum in the film. This is important for thin film diagnostics, as unanodized aluminum particles could act as light scatter centers and introduce noise into the optical system.

Ellipsometry showed that the microstructural changes found in SEM contributed to a change in the optical parameters of the films. Increasing the anodization time at the initial voltage, resulted in lower refractive indices. As shown in Study A, increasing voltage leads to increased refractive index, therefore leaving the films at 4V for a longer period of time results in films with more air (higher % void) and lower refractive indices. The lack of any change in refractive index for films

anodized at 100 or 400s indicates that the extra 300s of anodizing at 4V was not enough to significantly change the optical properties. It is interesting to note that when the voltage ramp was initiated at 100s the pore diameter change was not found to occur in the SEM images until around a third of the way down the film, see Figures 4-17A and 4-17D. Future work should include a study of inducing the higher voltage at shorter times, perhaps within the first minute of anodization. This may help create the bottle-neck structure closer to the surface and allow for stronger shifts in the refractive index.

The change in refractive index correlated with the change in interference colouring. For example, the 100 and 400s films showed no significant difference in refractive index and no difference in colour, Tables 4-11 and 4-12. The interference colours differed only slightly, with a small range of purples and blues. One reason for this could be the small difference in the final voltage (either 8 or 10V) leading to small differences in pore size and density. However, the results from Study A showed that strong differences in colour and refractive index occur with only a 2V change, in the range of 2-8V. Therefore, it could also be an effect of increased variability. Future work should involve a larger range of voltages, perhaps increasing all the way to 50V. It would be expected that the interference colours would change significantly in this case, not only from the refractive index changes of the aluminum oxide, but also from the thickness of the underlying tantalum oxide. Many previous studies have shown the voltage-dependent thickness of anodic tantalum oxides [14, 15, 16]. Increasing the tantalum oxide thickness would also increase the optical path length and lead to interference colour shifts. The effects of this on a thin film diagnostic are uncertain. One can speculate that introducing a thick tantalum oxide layer may introduce another reflection from the change in refractive index between the porous aluminum oxide ( $n = 1.3-1.4$ ,  $\lambda = 55\text{nm}$ ) and the barrier tantalum oxide ( $n = \sim 2.1$ ,  $\lambda = 555\text{nm}$  [17]). This extra reflection may contribute to noise

in the system and lower the sensitivity of the device. A parallel study on the surface pore size would also be beneficial, since extending the surface pore diameter above 20 nm would be detrimental for use in thin film diagnostics. The pore size needs to remain small enough such that protein and other biomolecules are excluded from the pore and thus cannot change the complex refractive index of the alumina layer.

## **Conclusion**

Overall this study increased our understanding of the voltage effects on anodized aluminum-tantalum thin films in a phosphoric-oxalic acid mix. The following conclusions were made:

- 1) Increasing voltage during anodization results in an increase of the refractive index of the porous alumina layer in the range of 2 to 8V, in agreement with the literature for films anodized in other electrolytes.
- 2) Anodizing in a 0.4M phosphoric-0.1M oxalic acid mix reduces the dissolution that occurs when anodizing at lower voltages (2V) when compared to similar films anodized in only 0.4M phosphoric acid (comparison with work from Sweet [13]).
- 3) Increasing the thickness of the sputtered aluminum layer results in a larger optical path length, and a change in the interference colours generated.
- 4) Bottle-neck shaped pores can be produced by using a voltage step procedure, starting at a lower voltage (4V) and increasing after a set period of time to a higher voltage (8 or 10V).
- 5) The refractive index can be tailored by changing the time of anodization at the lower voltage or the strength of the final voltage. Increasing the time of anodization at the lower voltage decreases the refractive index, thereby shifting to smaller optical path length interference colours.

Increasing the final voltage causes an increase in the refractive index, and thus a shift to larger optical path length interference colours.

## References

- [1] G. E. Thompson and G. C. Wood, "Porous anodic film formation on aluminium," *Nature*, vol. 290, pp. 230-232, 1981.
- [2] P. G. Sheasby and R. Pinner, *The Surface Treatment and Finishing of Aluminum and its Alloys - 6th Edition*, Finishing Publications Ltd., 2001.
- [3] J. P. O'Sullivan and G. C. Wood, "The morphology and mechanism of formation of porous anodic films on aluminium," *Proceedings of the Royal Society of London A*, vol. 317, pp. 511-543, 1970.
- [4] W. Lee and S. Park, "Porous Anodic Aluminum Oxide: Anodization and Templated Synthesis of Functional Nanostructures," *Chemical Reviews*, vol. 114, pp. 7487-7556, 2014.
- [5] G. D. Sulka, "Highly Ordered Anodic Porous Alumina Formation by Self-Organization Anodizing," in *Nanostructured Materials in Electrochemistry*, Weinheim, Wiley-VCH, 2008, pp. 1-97.
- [6] H. U. Osmanbeyoglu, T. B. Hur and H. K. Kim, "Thin alumina nanoporous membranes for similar size biomolecule separation," *Journal of Membrane Science*, vol. 343, no. 1-2, pp. 1-6, 2009.
- [7] R. C. Furneaux, W. R. Rigby and A. P. Davidson, "The formation of controlled-porosity membranes from anodically oxidized aluminum," *Nature*, vol. 337, no. 12, pp. 147-149, 1989.
- [8] Y. Wang, L. Chen, Z. Wu, S. Xu, H. Cui and W. Xu, "Subtle vertical structures of porous anodic alumina films for use as waveguides," *Nanotechnology*, vol. 28, no. 18, 2017.
- [9] J. Wang, C. Wang, Y. Li and W. Liu, "Optical constants of anodic aluminum oxide films formed in oxalic acid solution," *Thin Solid Films*, vol. 516, pp. 7689-7694, 2008.
- [10] T. Shih, P. Wei and Y. Huang, "Optical properties of anodic aluminum oxide films on Al 1050 alloys," *Surface & Coatings Technology*, vol. 202, pp. 3298-3305, 2008.
- [11] A. Hierro-Rodriguez, P. Rocha-Rodrigues, F. Valdes-Bango, J. M. Alameda, P. A. Jorge, J. L. Santos, J. P. Araujo and J. M. Teixeira, "On the anodic aluminium oxide refractive index of nanoporous templates," *Journal of Physics D: Applied Physics*, vol. 48, no. 45, p. 455105, 2015.

- [12] M. M. Rahman, E. Garcia-Caurel, A. Santos, L. F. Marsal, J. Pallares and J. Ferrer-Borrull, "Effect of the anodization voltage on the pore-widening rate of nanoporous anodic alumina," *Nanoscale Research Letters*, vol. 7, no. 474, 2012.
- [13] H. Sweet, *Development of a Thin Film Device and Optics System for Protein Detection*, Edmonton, AB: University of Alberta, 2018.
- [14] A. Charlesby and J. J. Polling, "The Optical Properties of Thin Oxide Films on Tantalum," *Proceedings of the Royal Society of London. Series A, Mathematical and Physical Sciences*, vol. 227, pp. 434-447, 1955.
- [15] L. Young, *Anodic Oxide Films*, New York: Academic Press, 1961.
- [16] L. Young, "The determination of the thickness, dielectric constant, and other properties of anodic oxide films on tantalum from the interference colours," *Proceedings of the Royal Society A: Mathematical, Physical, and Engineering Sciences*, vol. 244, p. 41, 1958.
- [17] S. Cui-Cui, C. Yun-Yu, D. En-Mei and L. Chang-Hao, "Tunable structural color of anodic tantalum oxide films," *Chinese Physics B*, vol. 21, p. 088101, 2012.

### 4.3 The Effects of Sequential Anodization with Sulphuric Acid and Phosphoric-Oxalic Acid on the Microstructure and Optical Properties of Aluminum-Tantalum Thin Films

#### **Introduction**

As discussed in Chapter 1, the porosity, pore size, and surface chemistry are all important in thin film diagnostics. Being able to tune the refractive index of the porous, anodic aluminum oxide layer to match protein, as well as maintain an optically flat surface to reduce light scatter are both critical to achieving optimal sensitivity. It is also important to maintain a relatively small pore size with respect to protein. If protein can enter the pore, a change will occur in the composite refractive index of the alumina/air layer leading to variability in test results and noise in the system. The refractive index and pore size of nanoporous alumina can be tailored by adjusting the anodization process. Anodization of aluminum to create porous films can be carried out in many electrolytes, including sulphuric, oxalic, or phosphoric acid among others [1, 2]. The electrolyte has been found to affect many aspects of the resulting porous films including barrier layer thickness [3], pore wall structure and composition [4], crystal structure [5], porosity, pore size [6], hardness [7], and volume expansion of the oxide [2]. A good review of these effects is covered by Sulka [6], Lee and Park [2] and Sheasby and Pinner [1].

Few studies have looked at anodizing aluminum thin films in a sequential, multi-electrolyte process. Liu et al. [8] look at anodizing films under various electrolytes and voltages to change the pore size throughout the film. Sequential anodization in sulphuric, oxalic, malonic and tartaric acid was carried out to create a continuously larger pore size with each change in electrolyte. Zaraska et al. [9] conducted sequential anodization of aluminum starting with an oxalic acid and then following with phosphoric acid. A smaller diameter pore was developed with the oxalic acid and then larger diameters with the phosphoric acid.

The purpose of this study was to see if an aluminum-tantalum thin film could initially be anodized in sulphuric acid to produce smaller pores on the surface, and then sequentially anodized in a phosphoric-oxalic acid mixture to produce larger pores underneath. Manipulating the nanostructure in this way would demonstrate tunability of not only the optical properties of the film, but also the size and structure of the pores on the surface. Aluminum-tantalum films were anodized in sulphuric acid for various times and then switched to a mixed phosphoric-oxalic acid bath for the remainder of the anodization. The anodic films were analyzed using SEM, XRD, and ellipsometry to better understand the resulting microstructure, topography, and optical properties.

## **Materials and Methods**

### *Thin Film Deposition*

Thin films of aluminum and tantalum were sputtered onto unprocessed silicon wafers as described previously (Chapter 4.1). Tantalum metal was sputtered to a thickness of  $226.5 \pm 3.8$  nm and aluminum to a thickness of  $128.2 \pm 5.7$  nm.

### *Anodization*

All chemicals were acquired from Thermo Fisher Scientific, Waltham, MA. The aluminum-tantalum coated wafers were then cleaved into pieces about 6.3 cm x 1.3 cm. These were anodized using a PAR Model 273a potentiostat/galvanostat (AMETEK Inc., Oakridge, TN) under potentiostatic conditions. The cleaved wafer pieces were rinsed before and after with MilliQ deionized water. A magnetic stir plate was used to agitate the solution, and the temperature of the electrolyte was  $19 \pm 1^\circ\text{C}$ . Aluminum foil (Thermo Fisher Scientific, Waltham, MA) was wrapped around a glass microscope slide and used as a cathode with a separation distance of 40 mm between the cathode and anode. A saturated calomel electrode (Thermo Fisher Scientific, Waltham, MA) was used as a reference electrode for the cell.

The films were initially anodized at 4V in 0.4M sulphuric acid for either 200 or 400s. They were then rinsed thoroughly with deionized water and placed in a 0.4M phosphoric-0.1M oxalic acid mixture and anodized at either 4 or 10V until the current decayed to  $<0.02 \text{ mA/cm}^2$ . Table 4-13 shows the matrix of experiments conducted. A set of slides was initially anodized in sulphuric acid until completion (current decayed to  $<0.02 \text{ mA/cm}^2$ ). From the current vs. time plot, the times of 200s and 400s were decided on as times to switch the acid. These times were chosen because, (a) 200s was just after the start of the steady-state pore formation in sulphuric acid and therefore the surface porosity would have already been well established; (b) 400s was well into the pore formation phase of anodizing for sulphuric acid and most of the oxide film would have developed by this point. Triplicates were performed on all experiments to measure reproducibility. All anodized films were then viewed at approximately  $75^\circ$  from normal using a polarizing lens to view s-polarized light.

*Table 4-13. Matrix of designed experiments for acid bath and voltage change.*

<b>0.4M Sulfuric Acid Bath</b>		<b>0.4M Phosphoric/ 0.1M Oxalic Acid Bath</b>	
Voltage (V)	Time (s)	Voltage (V)	Time (s)
4	200	4	To completion
-	400	4	-
-	200	10	-
-	400	10	-

### *SEM*

SEM was used to analyze the microstructural and topographical changes of the anodized specimens. Specimens from all experiments described in Table 4-13 were analyzed, as well as a film anodized exclusively in 0.4M sulphuric acid at 4V. This sulphuric acid anodized film was used as a reference to understand how the films would anodize exclusively in sulphuric acid. The

anodized aluminum-tantalum thin films were fractured and mounted on stubs using conductive carbon tape. The Zeiss Sigma FESEM was set to 3.00 keV and a 15  $\mu\text{m}$  aperture to reduce surface charging effects. Images were taken at  $0^\circ$  and  $45^\circ$  from normal, at 50,000 or 100,000 times magnification and a working distance of approximately 3 mm. SEM surface micrographs were taken at 100,000 times magnification and analyzed using ImageJ software (Rasband, W.S., ImageJ, U. S. National Institutes of Health, Bethesda, Maryland, USA, <https://imagej.nih.gov/ij/>, 1997-2016) for pore size analysis. Three evenly spaced lines were drawn horizontally and another three vertically across the micrograph. Pores along these lines were measured for diameter. This was done for two samples from each experiment. The micrograph was taken randomly from the sample surface; the anodized surfaces were very homogenous and therefore only a single micrograph was used for each sample.

### *XRD*

XRD was used to analyze post-anodized specimens for microstructural differences and consumption anodization of the aluminum films. The Rigaku Ultima IV (Cu-source) diffraction system with a thin film, substrate holder attachment was used. Diffraction data was collected between  $10$  and  $90^\circ 2\theta$  at  $5.000^\circ/\text{min}$ , using a DHL slit of 10.00 mm and glancing angle  $\omega = 0.5^\circ$ . JADE 9<sup>TM</sup> software (Materials Data Inc., Livermore, CA) was used to analyze XRD patterns with the International Centre for Diffraction Data (ICDD) database to match peaks.

### *Ellipsometry*

Ellipsometry was used to measure the optical constants (refractive index and extinction coefficient) of post-anodized specimens. A J.A. Woollam M-2000V spectroscopic ellipsometer was used with a model for the thin film layers, as described in Chapter 4.1. The  $\Psi$  and  $\Delta$  values were recorded for wavelengths 370 nm to 1000 nm at angles of  $55^\circ$ ,  $65^\circ$ , and  $75^\circ$  from normal.

The aluminum oxide thickness and optical constants were derived from these values using an anisotropic, Bruggeman effective medium approximation model. CompleteEASE<sup>®</sup> software for Windows (J.A. Woolam Co., Lincoln, NE) was used to develop the ellipsometry model and tabulate refractive index and oxide thickness values. More detail of the model can be found in Chapter 4.1 – Materials and Methods.

### *Colour Coordinates*

A phone camera was used to take photos of the interference colours at approximately 75° from normal with a polarizing lens (s-polarized). The images were then analyzed for RGB coordinates using ImageJ software (Rasband, WS, ImageJ, US National Institutes of Health, Bethesda, MD, <https://imagej.nih.gov/ij/>, 1997-2016). A rectangular area of each slide was selected in the photo, encompassing between 15,000 and 21,000 pixels. The mean and standard deviation were recorded for the RGB coordinates of each area.

### *Statistics*

Numerical results were processed using IBM SPSS Statistics for Windows, Version 24.0 (IBM Corp., Released 2017, Armonk, NY). A Levene's test was used to check for similar sample variance between populations. The SEM analysis of pore size used an independent T-test to compare between populations, as ANOVA was unsuitable due to unequal sample size and variance. Refractive index and RGB colour coordinate values used a one-way ANOVA with Tukey multiple comparison post hoc tests. Standard deviations are shown by error bars in all graphs.

## Results

### *Current Density Plots*

The current density was recorded in each case for a better understanding of how the films anodize under each set of conditions. Two current density vs. time graphs are shown in Figures 4-21 and 4-22. When the secondary anodizing step was carried out at 4V there was an initial drop in the current density for the first couple seconds and then a slow increase to a steady state current density until finally the current dropped to near 0 mA, Figure 4-21. On the other hand, when the secondary anodizing step was carried out using 10V there was a drop from a much higher current density followed by a steady state current after a few minutes, Figure 4-22. This was consistent, whether the films were anodized initially for 200 sec or 400 sec in sulphuric acid.

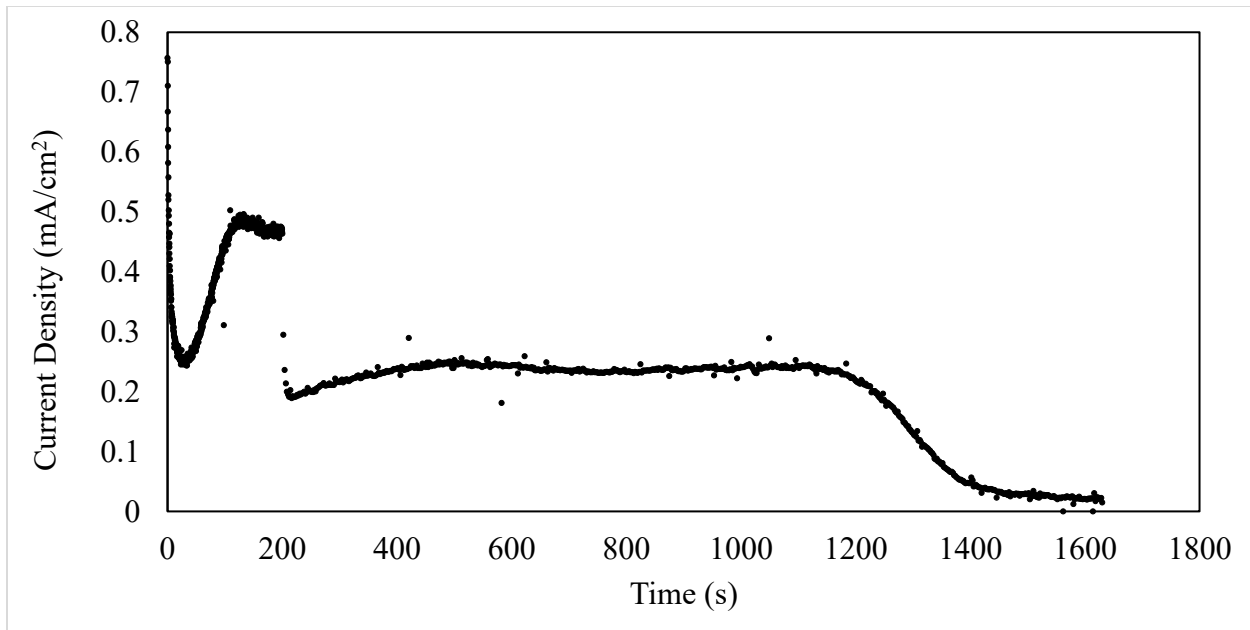


*Figure 4-21. Typical current density vs. time graph for samples anodized for 200 sec in 0.4M sulphuric acid at 4V, followed by anodizing in 0.4M phosphoric-0.1M oxalic acid at 4V until completion.*

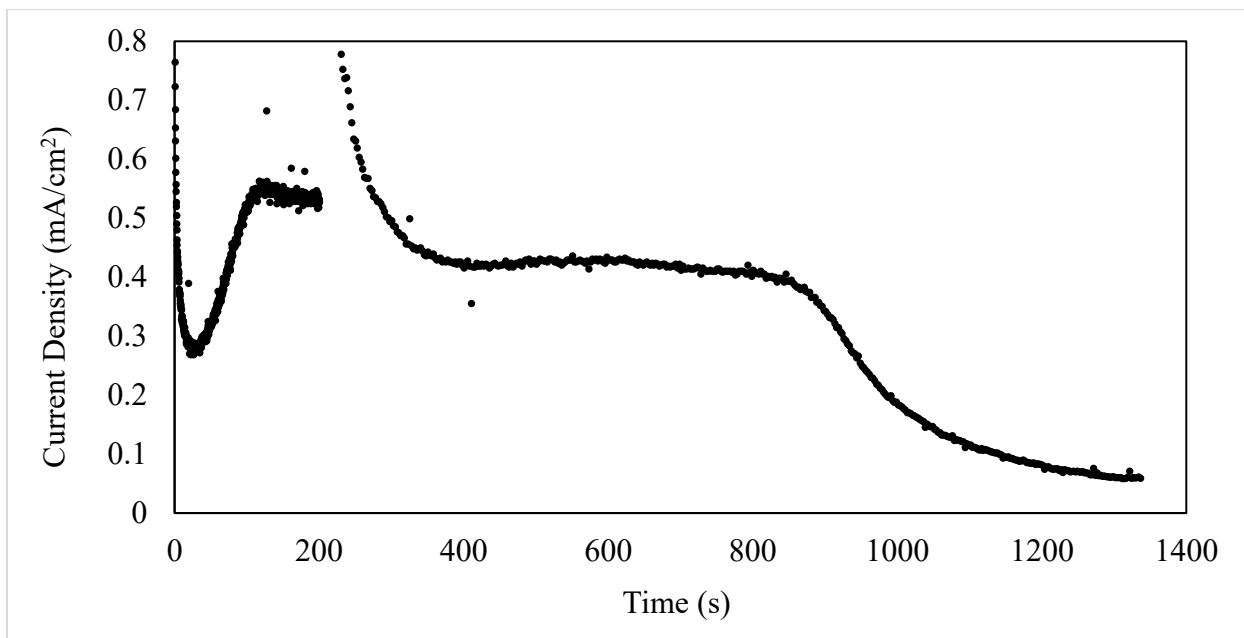
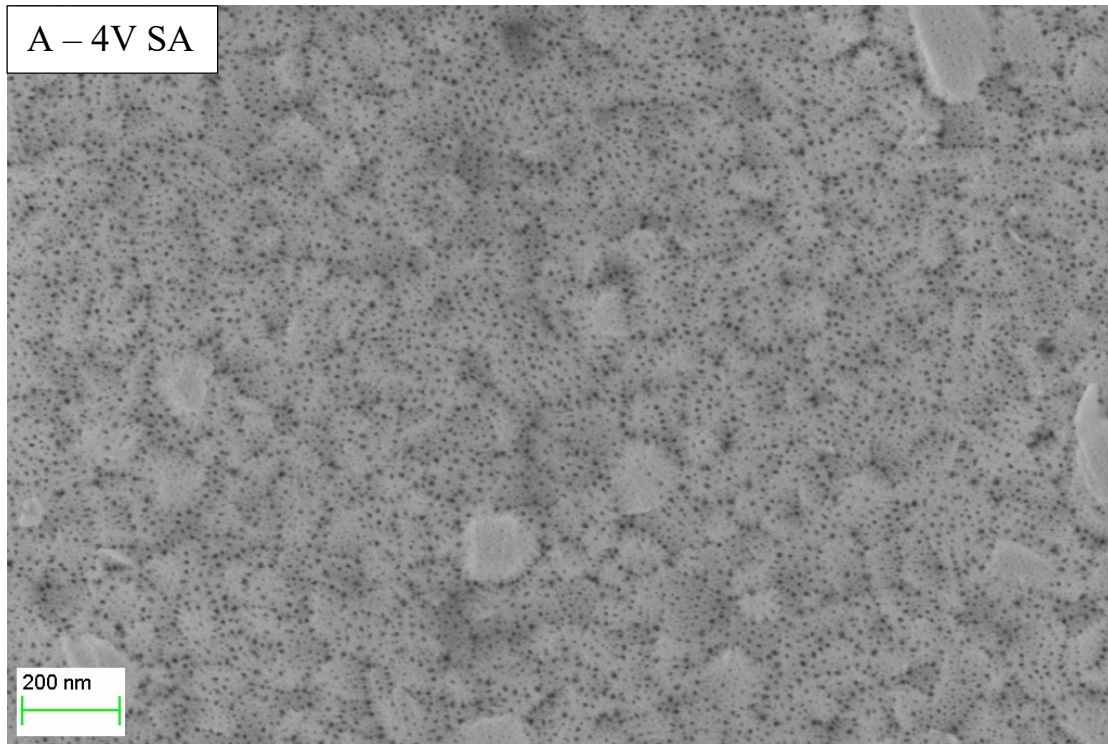


Figure 4-22. Typical current density vs. time graph for samples anodized for 200 sec in 0.4M sulphuric acid at 4V, followed by anodizing in 0.4M phosphoric-0.1M oxalic acid at 10V until completion.

### SEM

Overall, SEM showed strong differences in microstructure between the various anodizing conditions. Figure 4-23 shows the surfaces created when anodizing at the various parameters. The cross-sections taken at 45° are shown in Figure 4-24. Surfaces anodized only in 0.4M sulphuric acid had both a reduced pore density and pore size compared to surfaces anodized sequentially in 0.4M sulphuric acid and then in a 0.4M phosphoric-0.1M oxalic acid mix, see Figure 4-23A. The cross-section of these films, Figure 4-24A, shows that pore tortuosity is also much higher than those anodized in a phosphoric/oxalic mix. Anodizing in the phosphoric/oxalic mix after either 200 or 400 sec in sulphuric caused a noticeable increase in the pore size of the surface, Figure 4-23, and larger pores below, Figure 4-24, compared to films anodized completely in sulphuric acid. The longer the films were anodized in sulphuric acid, the higher the visible tortuosity of the porous structure below, compare Figure 4-24D and 4-24E. The transition from a sulphuric to

phosphoric/oxalic pore structure is apparent in the samples anodized in sulphuric acid for 200 sec, which gives the film a canopy-like structure with smaller pores on top, which expand to larger pores once the electrolyte and voltage is changed.



*Figure 4-23, continued.*

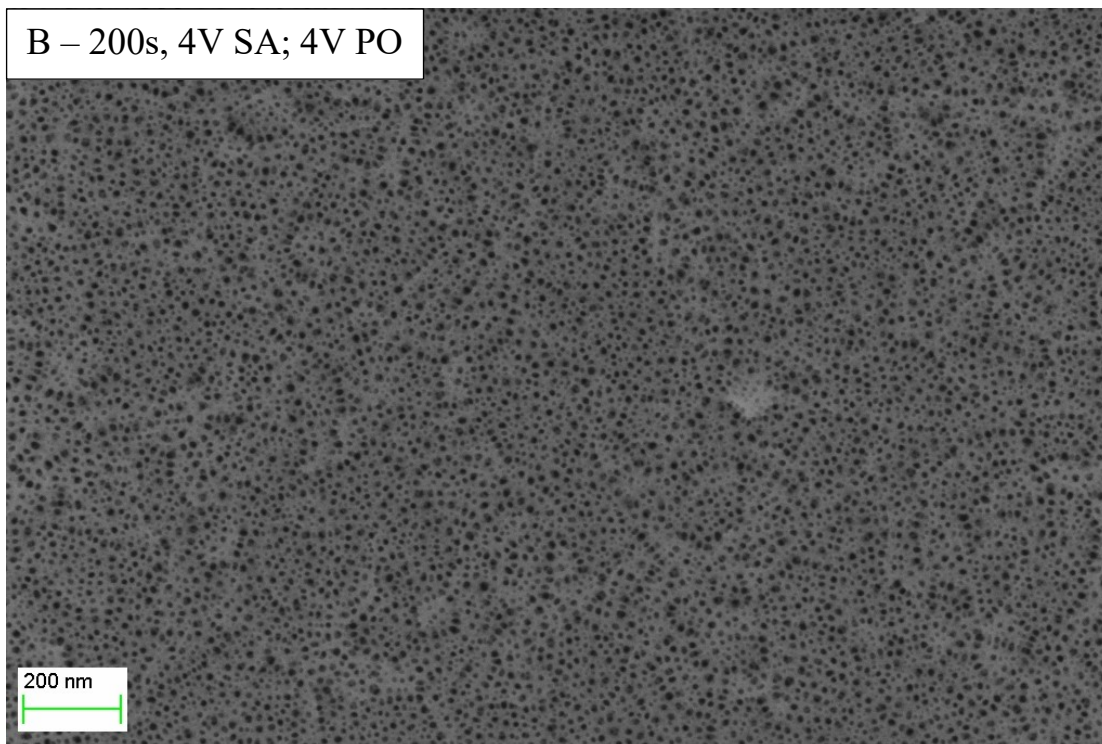


*Figure 4-23, continued.*

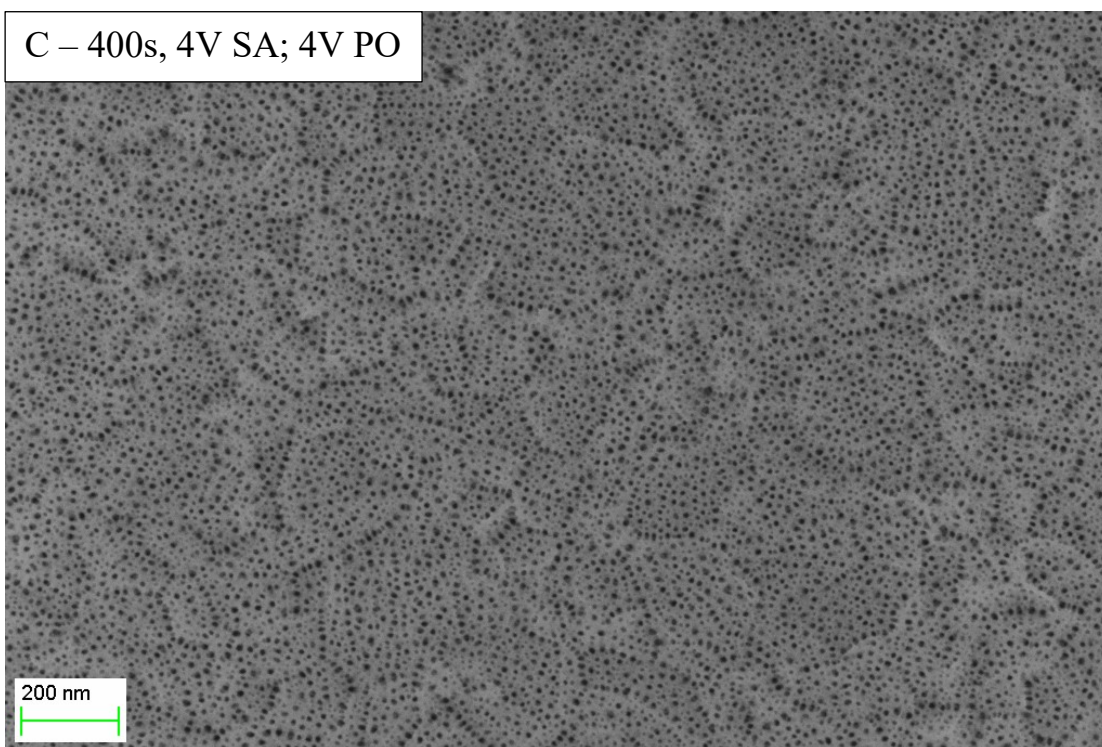


*Figure 4-23, continued.*

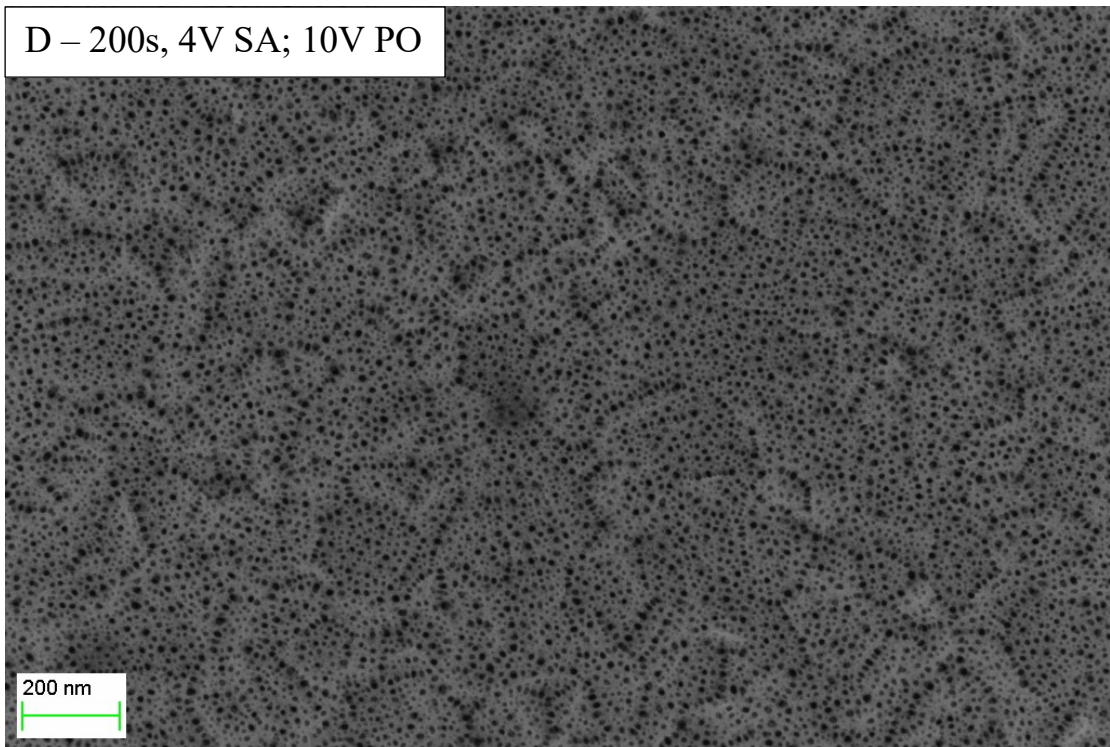


*Figure 4-23, continued.*

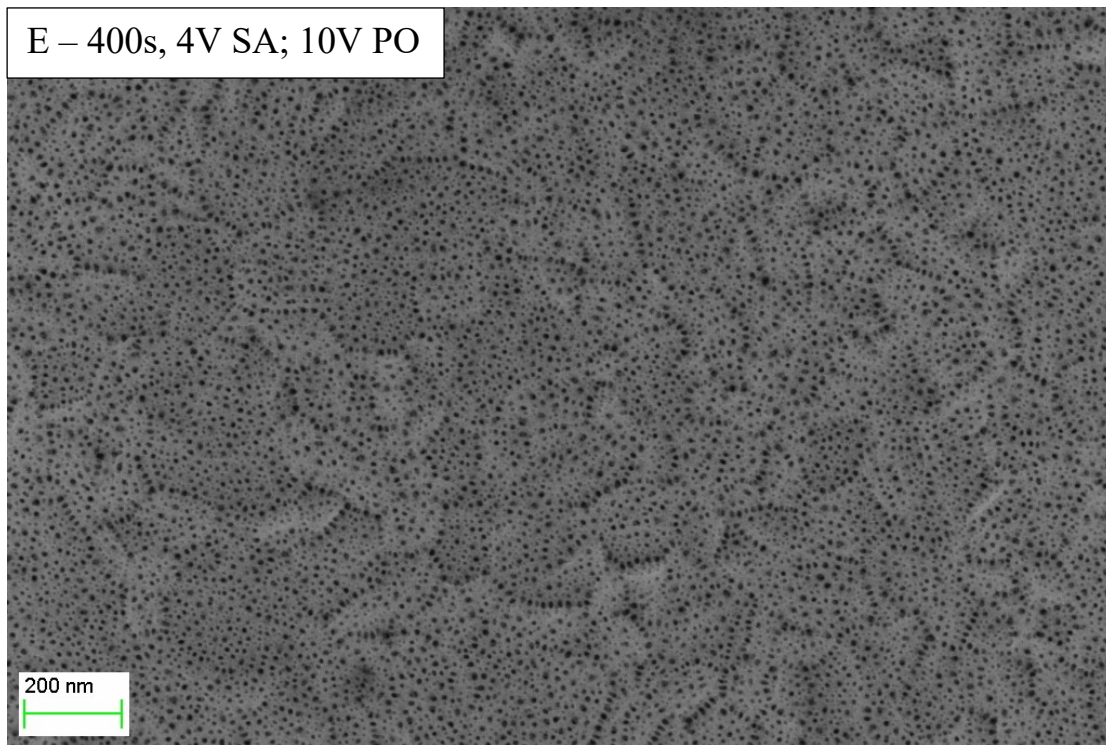


*Figure 4-23, continued. FESEM surface images of anodized aluminum-tantalum thin films, anodized under various parameters: A) 4V in 0.4M sulphuric acid, B) 200s and 4V in 0.4M sulphuric acid (SA) followed by 4V in 0.4M phosphoric-0.1M oxalic acid (PO), C) 400s and 4V in 0.4M SA followed by 4V in 0.4M-0.1M PO, D) 200s and 4V in 0.4M SA followed by 10V in 0.4M-0.1M PO, E) 400s and 4V in 0.4M SA followed by 10V in 0.4M-0.1M PO.*

The results of the pore size analysis are shown in Figure 4-25 with statistical results in Table 4-14.

The analysis showed that surface pore size ranged from 7.4 to 8.6 nm with standard deviations of no more than  $\pm 2.7$  nm. The longer the films were anodized in sulphuric acid, the smaller the pores at the surface. Increasing the voltage of the phosphoric/oxalic anodization step from 4 to 10 V increased surface pore size no more than  $0.5 \pm 0.2$  nm (sulphuric acid step 200s), and when the sulphuric anodization step was increased to 400s no significant difference was found. Most samples showed statistically significant differences in pore size, however the difference is relatively small (maximum  $1.2 \pm 0.2$ nm), Table 4-14.

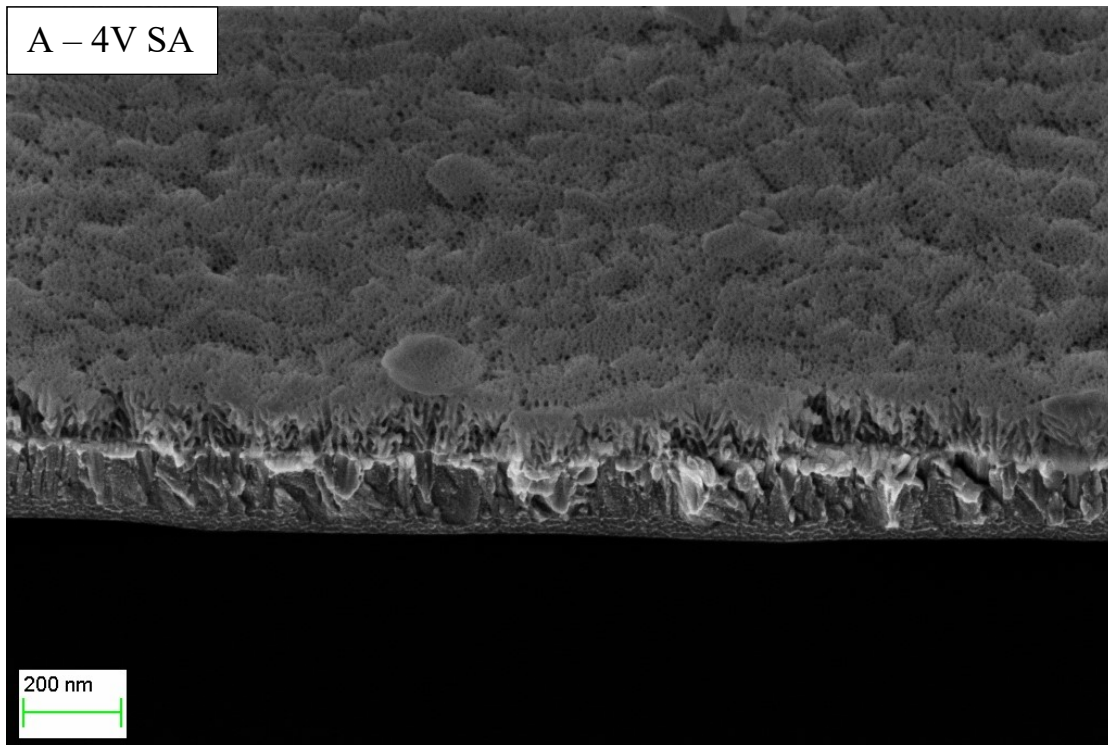


*Figure 4-24, continued.*

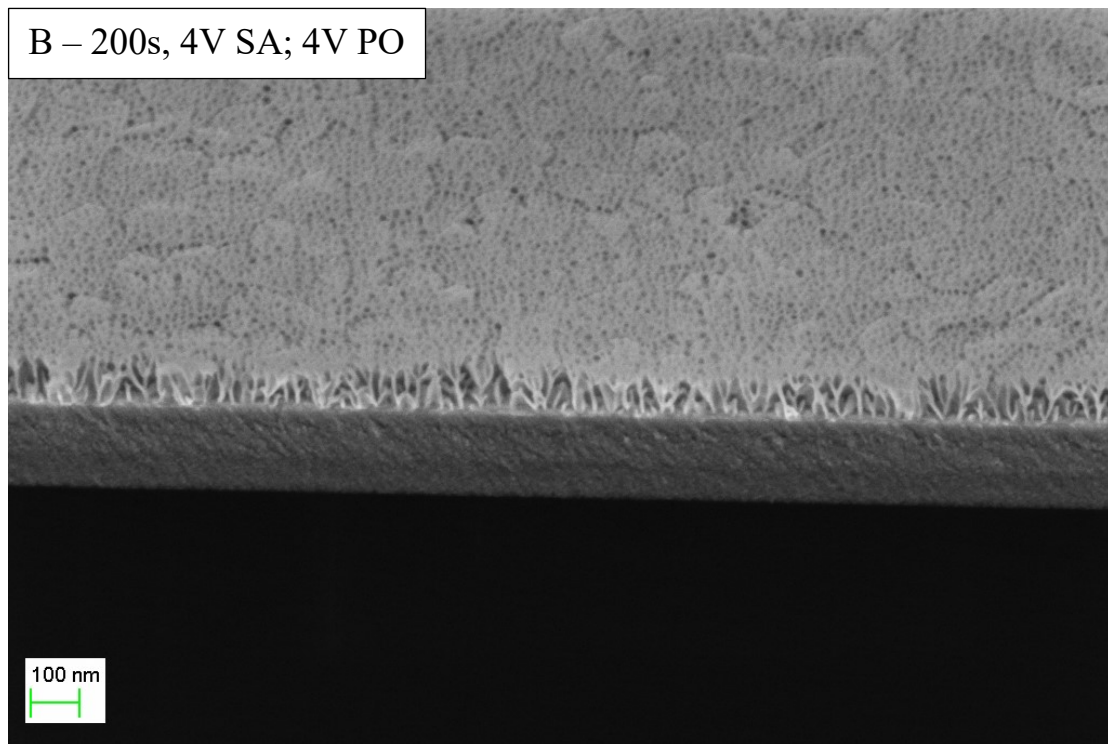


*Figure 4-24, continued.*

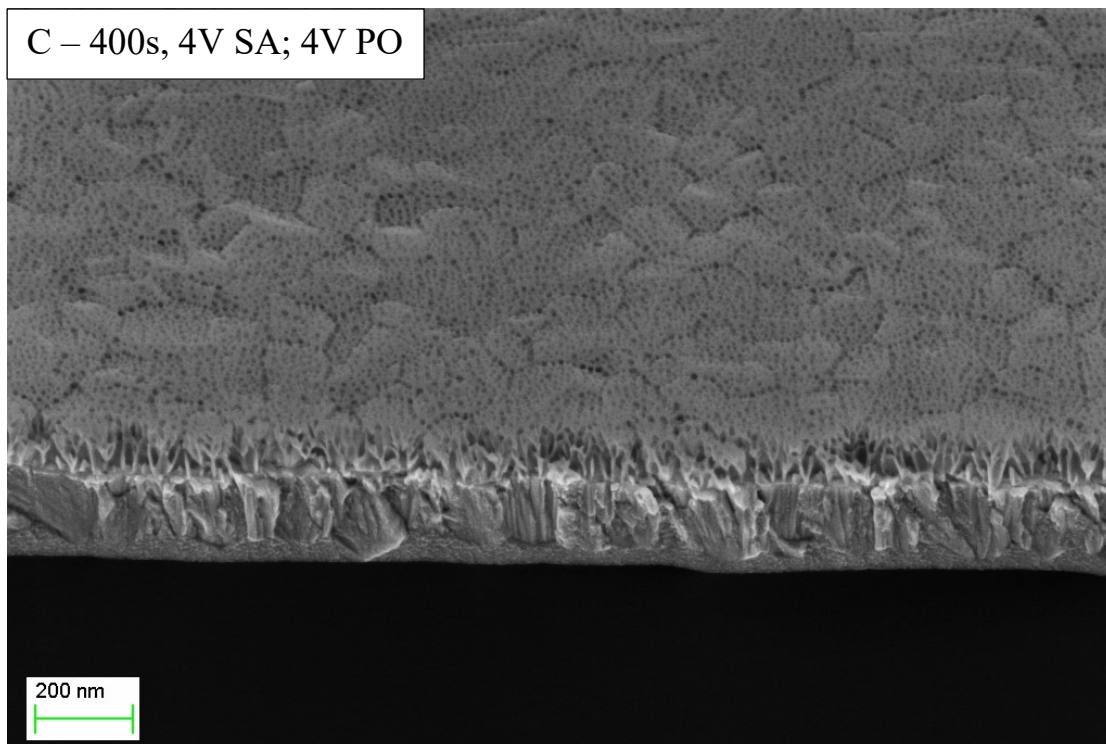


*Figure 4-24, continued.*

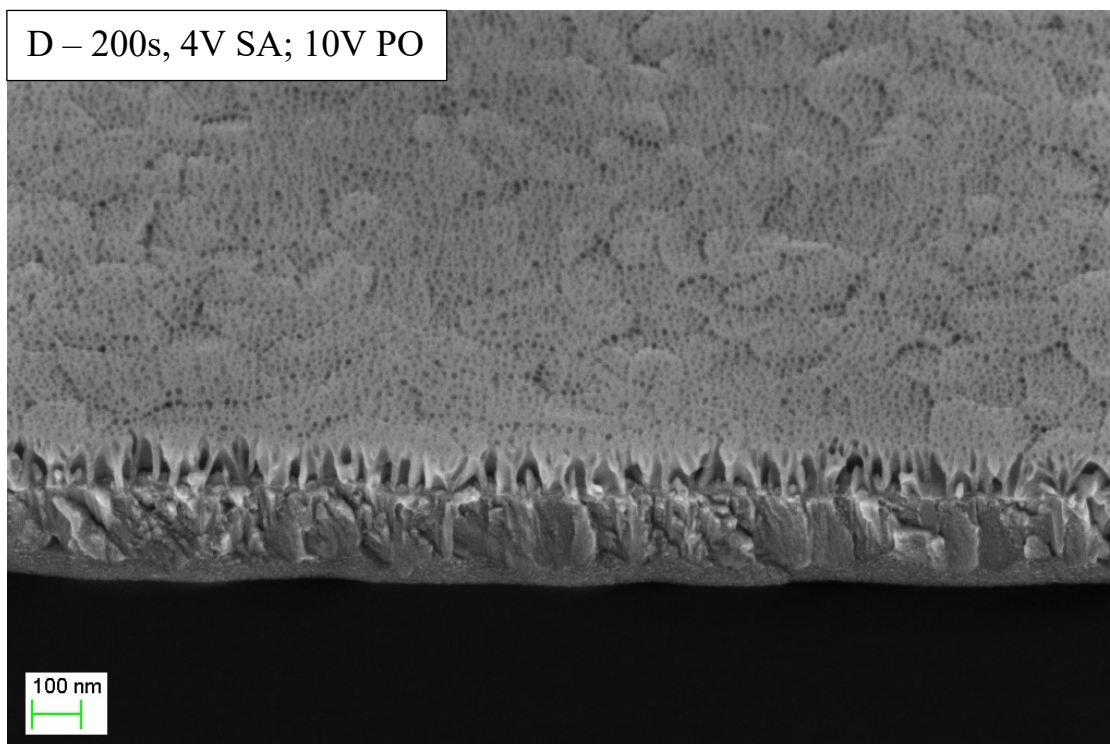


*Figure 4-24, continued.*

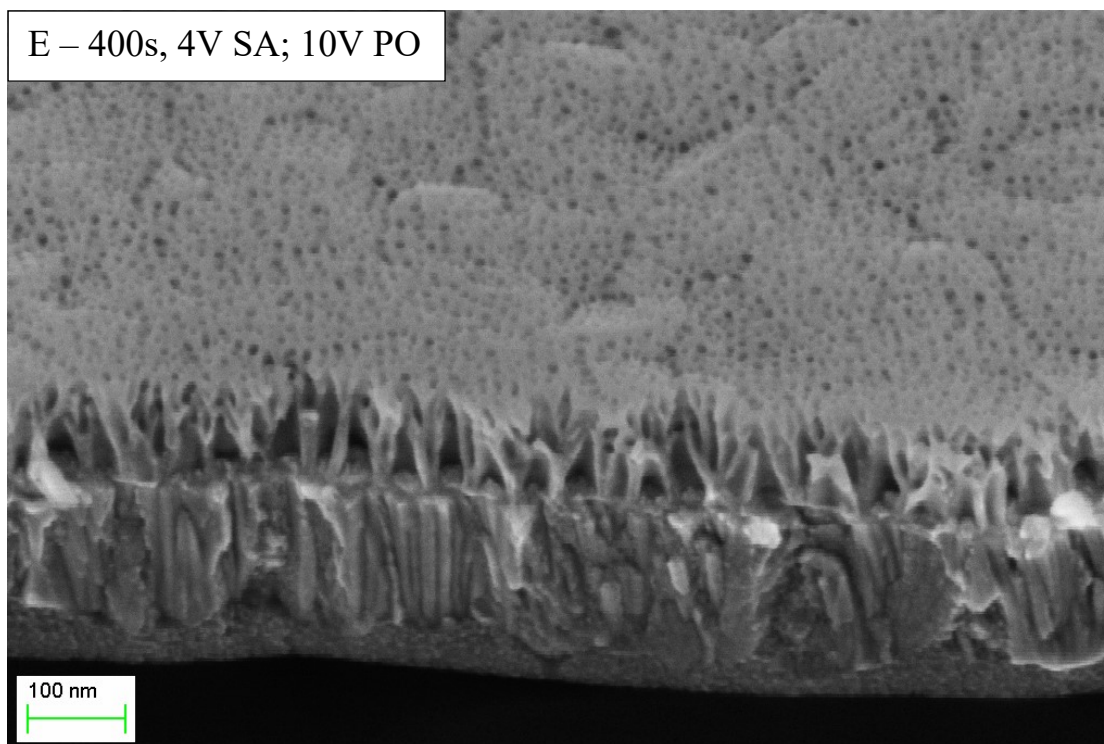


*Figure 4-24 continued. FESEM cross-sectional images of anodized aluminum-tantalum thin films, anodized under various parameters. Images A through D are at 50 kX magnification, while image E is at 100 kX. A) 4V in 0.4M sulphuric acid, B) 200s and 4V in 0.4M sulphuric acid (SA) followed by 4V in 0.4M phosphoric-0.1M oxalic acid (PO), C) 400s and 4V in 0.4M SA followed by 4V in 0.4M-0.1M PO, D) 200s and 4V in 0.4M SA followed by 10V in 0.4M-0.1M PO, E) 400s and 4V in 0.4M SA followed by 10V in 0.4M-0.1M PO.*

A similar pore analysis was conducted on samples anodized only in the 0.4M phosphoric-0.1M oxalic mix at 4V until completion in Chapter 4.1 of this work. The results showed a pore size of  $10.7 \pm 4.5\text{nm}$ ; therefore, a significant decrease in surface pore size results when the films are initially anodized in sulphuric acid for the first 200 or 400 seconds (t-test:  $p < 0.001$  for all 4 cases in this study compared to 0.4M phosphoric-0.1M oxalic mix). A Levene's test for equality of variances showed that when the samples were first anodized in sulphuric acid for 200 or 400s and then anodized in the phosphoric-oxalic mix, the variance also decreased significantly compared to those just anodized in the phosphoric-oxalic mix ( $p < 0.001$  for all cases).

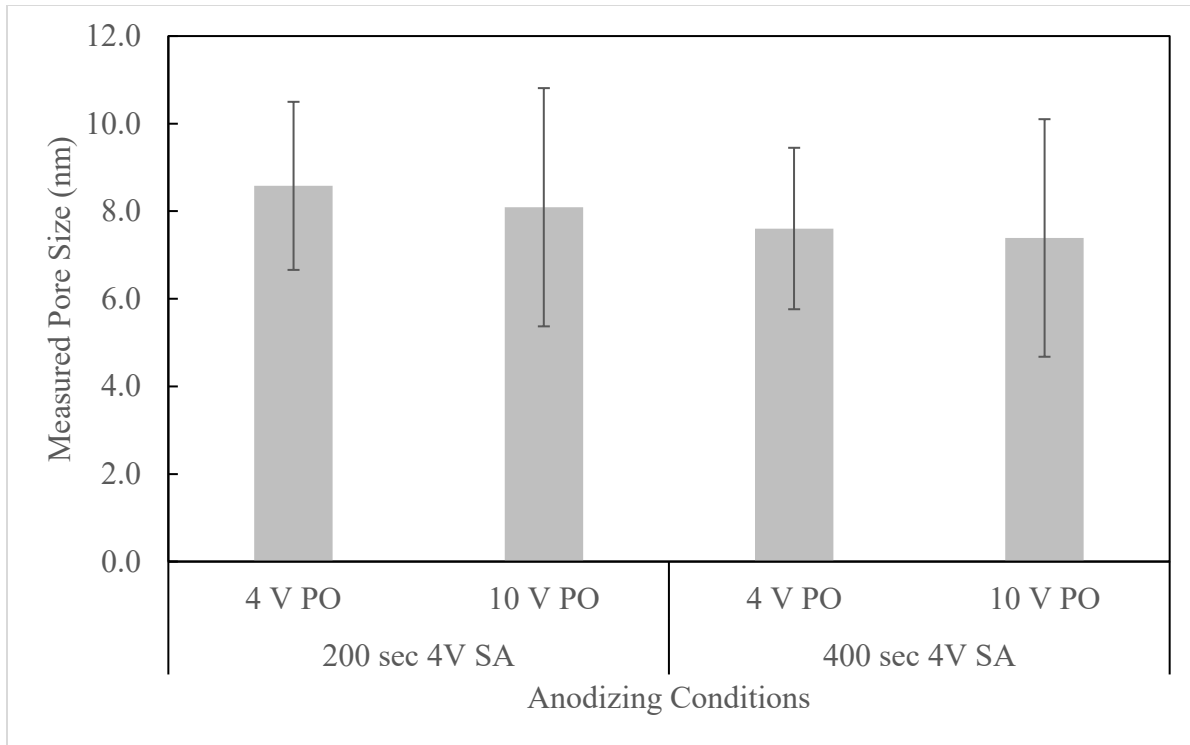


Figure 4-25. Measured pore size from FESEM surface images for the different anodizing conditions: from left to right, 1) anodized for 200s at 4V in 0.4M sulphuric acid (SA) followed by 4V in 0.4M phosphoric-0.1M oxalic acid mix (PO), n=311, 2) anodized for 200s at 4V in SA followed by 10V in PO, n=412, 3) anodized for 400s at 4V in SA followed by 4V in PO, n=492, 4) anodized for 400s at 4V in SA followed by 10V in PO, n=484.

Table 4-14. Statistical results for comparison of measured pore size between different anodizing conditions. Standard error represented by  $\pm$  symbol.

Time in 0.4M Sulphuric Bath at 4V (sec)	Voltage in 0.4M Phosphoric-0.1M Oxalic Bath (V)	test vs.	t-test p Value	Mean Difference (nm)
200	4 (n=311)	200s/10V	<0.01*	0.5 $\pm$ 0.2
		400s/4V	<0.001	1.0 $\pm$ 0.1
		400s/10V	<0.001*	1.2 $\pm$ 0.2
200	10 (n=412)	200s/4V	<0.01*	-0.5 $\pm$ 0.2
		400s/4V	<0.01*	0.5 $\pm$ 0.2
		400s/10V	<0.001	0.7 $\pm$ 0.2
400	4 (n=492)	200s/4V	<0.001	-1.0 $\pm$ 0.1
		200s/10V	<0.01*	-0.5 $\pm$ 0.2
		400s/10V	No difference	-
400	10 (n=484)	200s/4V	<0.001*	-1.2 $\pm$ 0.2
		200s/10V	<0.001	-0.7 $\pm$ 0.2
		400s/4V	No difference	-

\*Equal variances not assumed, failed Levene's test for equality of variance

## XRD

The X-ray diffraction patterns are shown in Figure 4-26. When compared to an aluminum-tantalum thin film control, aluminum peaks were not present post anodization for all conditions (look to Chapter 4.1 for the aluminum-tantalum control XRD pattern). The peaks present correspond to  $\alpha$ -Ta (bcc): (110), (200), (211), (220). Figure 4-26A showed much broader peaks than the others.

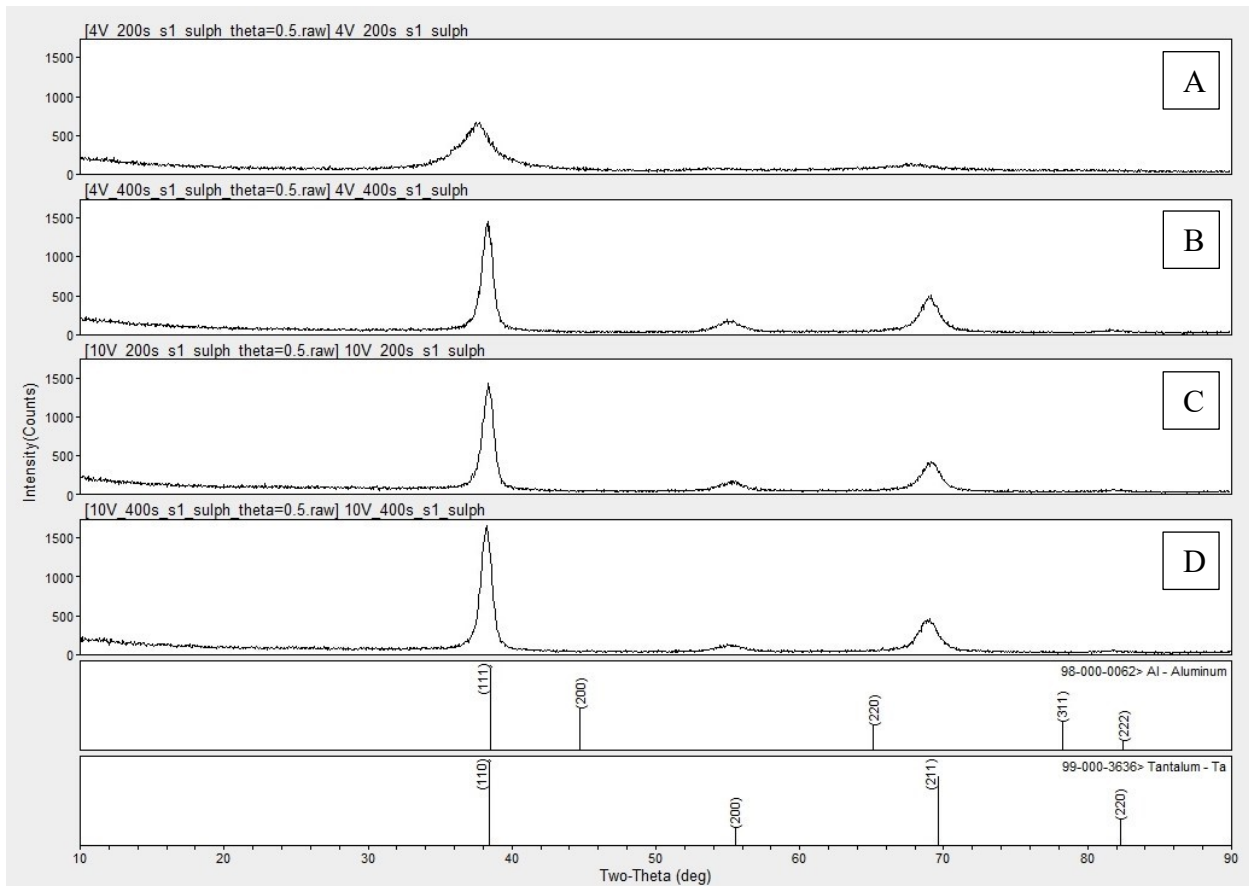


Figure 4-26. XRD patterns of anodized aluminum-tantalum thin films in the various conditions: A) 200s and 4V in 0.4M sulphuric acid (SA) followed by 4V in 0.4M phosphoric-0.1M oxalic acid (PO), B) 400s and 4V in 0.4M SA followed by 4V in 0.4M-0.1M PO, C) 200s and 4V in 0.4M SA followed by 10V in 0.4M-0.1M PO, D) 400s and 4V in 0.4M SA followed by 10V in 0.4M-0.1M PO.

### Ellipsometry

Ellipsometry measured both the optical constants (refractive index and extinction coefficient) and the thickness of the aluminum oxide film. The refractive index and thickness recorded for each of the different test parameters are shown in Table 4-15. Statistical results are shown in Table 4-16. Increasing the voltage of the phosphoric-oxalic step from 4 to 10V results in an increase of the refractive index value, and a decrease of the % void in the film. Increasing the time of anodization in sulphuric acid from 200 to 400s also resulted in higher refractive indices. It was also noticed that the error in the model (MSE values) decreased when higher voltages were used. The extinction coefficient (k) for all aluminum oxide films was found to be 0.

*Table 4-15. Ellipsometry results for the porous aluminum oxide layer anodized under various conditions. The first number indicates the time anodizing in 0.4M sulphuric acid at 4V, while the second number indicates the voltage anodizing in 0.4M phosphoric-0.1M oxalic acid mix. Standard deviations shown with  $\pm$  symbol,  $n=3$  for all data sets. EMA=effective medium approximation; MSE=mean square error.*

	200s/4V	200s/10V	400s/4V	400s/10V
Thickness (nm)	123.1 $\pm$ 0.1	124.0 $\pm$ 2.0	125.3 $\pm$ 0.9	120.4 $\pm$ 1.6
Refractive Index ( $\lambda=555\text{nm}$ ), x-y plane	1.343 $\pm$ 0.012	1.418 $\pm$ 0.011	1.444 $\pm$ 0.005	1.462 $\pm$ 0.008
EMA (% void)	48.4 $\pm$ 1.5	36.4 $\pm$ 0.6	39.5 $\pm$ 1.3	34.4 $\pm$ 0.9
MSE	32.2 $\pm$ 11.4	8.4 $\pm$ 1.4	40.9 $\pm$ 0.7	14.0 $\pm$ 8.9

Table 4-16. Statistical results for the aluminum oxide refractive index, as measured by ellipsometry, for the various anodizing conditions. For all data sets  $n=3$ .

Time in Sulphuric Bath (sec)	Voltage in Phosphoric-Oxalic Bath (V)	test vs.	ANOVA p Value	Post Hoc Test Results
200	4	200s/10V	<0.001	p=0.005, decrease
		400s/4V		p=0.004, decrease
		400s/10V		p=0.001, decrease
200	10	200s/4V		p=0.005, increase
		400s/4V		p=0.100, decrease
		400s/10V		p=0.022, decrease
400	4	200s/4V		p=0.004, increase
		200s/10V		p=0.100, increase
		400s/10V		p=0.108, decrease
400	10	200s/4V		p=0.001, increase
		200s/10V		p=0.022, increase
		400s/4V		p=0.108, increase

### Interference Colours

Figure 4-27 shows the resulting interference colours produced when observed with s-polarized light at approximately  $75^\circ$  from normal. Colours varied from dark blue (200 sec sulphuric acid (SA) and 4V phosphoric oxalic (PO)) to blue (200 sec SA and 10V PO; 400 sec SA and 4V PO) to light blue (400 sec SA, 10V PO). Table 4-17 shows the RGB colour coordinates measured from each image. Significant differences in colour coordinates were found for each set of anodizing conditions ( $p < 0.05$ ).

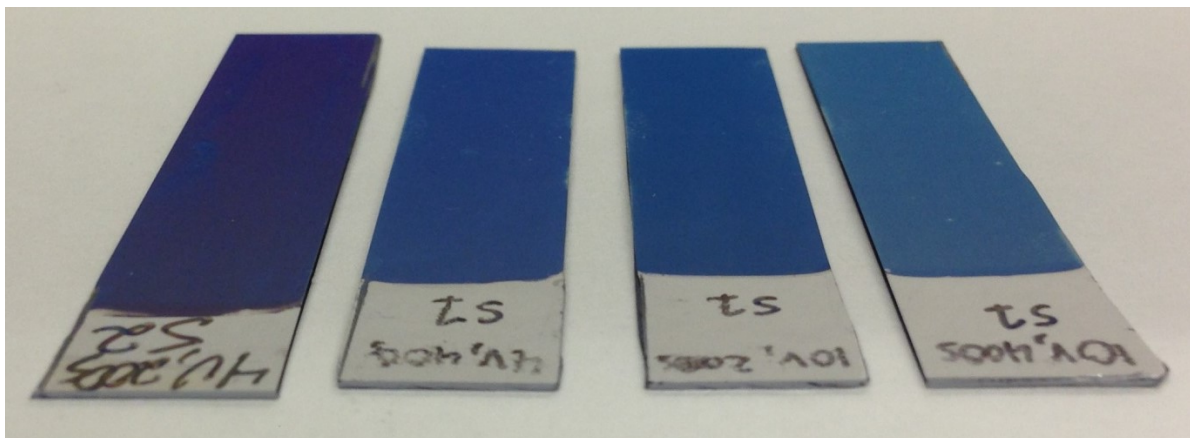


Figure 4-27. Interference colours produced when anodizing under the various conditions, from left to right: 1) 200s and 4V in 0.4M sulphuric acid (SA) followed by 4V in 0.4M phosphoric-0.1M oxalic acid (PO), B) 400s and 4V in 0.4M SA followed by 4V in 0.4M-0.1M PO, C) 200s and 4V in 0.4M SA followed by 10V in 0.4M-0.1M PO, D) 400s and 4V in 0.4M SA followed by 10V in 0.4M-0.1M PO. Pictures taken using a polarizer to visualize s-polarized light.

Table 4-17. Interference colours and RGB coordinates measured from images of aluminum-tantalum films anodized under various conditions. Sample size  $n=3$  for all data sets.

Anodizing Conditions	Interference Colours and RGB Coordinates
200s in Sulphuric bath, 4V in Phosphoric-Oxalic bath	Dark Blue R: $79.2 \pm 17.4$ G: $32.0 \pm 5.3$ B: $100.8 \pm 6.7$
200s in Sulphuric bath, 10V in Phosphoric-Oxalic bath	Blue R: $7.7 \pm 2.4$ G: $70.0 \pm 10.4$ B: $135.7 \pm 5.4$
400s in Sulphuric bath, 4V in Phosphoric-Oxalic bath	Blue R: $15.0 \pm 6.3$ G: $96.8 \pm 7.7$ B: $155.8 \pm 5.3$
400s in Sulphuric bath, 10V in Phosphoric-Oxalic bath	Light Blue R: $44.3 \pm 9.8$ G: $129.2 \pm 7.1$ B: $167.7 \pm 4.1$

## Discussion

The ability to engineer both the optical properties and structure of the porous aluminum oxide was achieved by a sequential, multi-electrolyte anodization process. Anodizing initially in sulphuric

acid led to smaller surface pore size and then following with phosphoric-oxalic acid produced highly porous films below the surface with a tailorable refractive index via the final voltage.

The current density acted as would be predicted. The initial decrease of the current is a result of barrier oxide growth and the thickness of the barrier oxide is proportional to the voltage [1, 2]. When the same voltage was used for both anodization steps, the oxide barrier layer does not thicken. Therefore, in a matter of seconds the current went to a steady state value where pore formation occurs. The electrolyte is known to affect the current density of pore formation due to differences in the composition of the aluminum oxide formed [10]. Figure 4-21 shows the lower current density that occurs when anodizing at the same voltage in phosphoric-oxalic acid as opposed to sulphuric. When 10V was used in the second step, the barrier oxide layer thickens before steady state pore formation begins. This growth shows up as a drop from a high current density down to a steady state value over the course of a few minutes, Figure 4-22. Finally, the current drops to near 0 as the tantalum oxide barrier layer is formed.

Initially anodizing in sulphuric acid leads to a decrease in the surface pore diameter compared to films fully anodized in a phosphoric/oxalic acid mix. As shown in the SEM images, this creates a canopy-like structure, or bottle-neck pores, Figure 4-24B through 4-24E. It is commonly known that porous alumina films formed in phosphoric acid produce a larger pore size and pore volume than those formed in sulphuric acid [11]. Increasing the voltage causes an increase in the pore size, decrease in pore density, and increase in refractive index. This corresponds well with other studies [12, 13, 14, 15, 16]. The pore volume increases significantly below 20V for any of the major electrolytes including sulphuric, phosphoric, oxalic, and chromic acids [11]. Increasing the pore volume leads to higher air content in the film and lower refractive indices as the forming voltage is dropped.

The aluminum oxide that develops appears to be amorphous. After anodization, only peaks corresponding to  $\alpha$ -tantalum were present in the XRD patterns. The patterns also showed no sign of aluminum, and therefore consumption anodization still occurs. Consumption anodization is critical when producing these films for thin film diagnostics. Unanodized aluminum particles in the film can act as scatter centers for light, introducing noise and decreasing the sensitivity of such devices to detecting small biological molecules on the surface. It is interesting to note that some variability was observed in the underlying tantalum metal. Figure 4-26A shows wider tantalum peaks corresponding to a more amorphous tantalum substrate. The same tantalum can be observed via SEM in Figure 4-24B. This problem likely occurs due to a lack of quality control during sputtering of tantalum. An intermittent leak in the sputtering chamber could cause the tantalum to be less pure and reduce crystallinity, with more oxygen and nitrogen being integrated into the film. As shown in Chapter 2 of this work, the tantalum microstructure has an effect on the resulting interference colour. An increased variability in the RGB coordinates was found for films sputtered and anodized on this tantalum, Table 4-17 (200s in sulphuric acid, 4V in phosphoric-oxalic mix). This increased variability is attributed to the varying tantalum microstructure of these films.

This study demonstrates the ability to tune the refractive index of the porous aluminum oxide, while maintaining a small (<10nm) pore diameter at the surface. To tune the refractive index, the porosity of the film must be adjusted using the voltage during anodization. However, increasing the voltage leads to a proportional increase in the pore diameter. In thin film diagnostics, the pore size must be kept smaller than the size of the molecule of interest, otherwise the biomolecule may be adsorbed in the pore and cause a change in the refractive index of the anodic oxide. As described in Chapter 1, the most sensitive of interference colour shifts occur when the refractive index of the oxide matches that of the adsorbed biological layer. In this work, the refractive index was changed

from  $1.343 \pm 0.012$  to  $1.418 \pm 0.011$  by simply changing the voltage of the phosphoric-oxalic anodization step from 4 to 10V, Table 4-15, (sulphuric acid anodization initially carried out for 200s at 4V). At the same time, the pore diameter at the surface was only changed by  $0.5 \pm 0.2\text{nm}$ . This is a significant result as it shows that it is possible to tailor the optical properties of the anodic film without significantly changing the structure of the top few nanometers of the surface.

Recommended future works for this project would be expansion of the voltages and times used to get a better understanding of the limits of tunability of the refractive index. It would also be important to study the protein binding characteristics and composition of these films, as the surface would be different from films only anodized in phosphoric/oxalic mixtures. These films likely have a high sulphate content at the surface as it is well known that the electrolyte anion is incorporated into the film [4, 17]. It is unknown how this affects the binding of proteins, especially vitamin K dependent proteins such as prothrombin, since these are used for surface functionalization of aluminum oxides [18]. Another important question is the change in shelf-life for the interference colours produced. Phosphoric acid anodization is commonly used to increase the hydration resistance of anodic alumina films [19]. Anodic films produced in sulphuric and oxalic acid tend to be less resistant to microstructural changes associated with hydration due to their lack of phosphate content [20]. Preventing hydration is key to maintain the interference colours, as microstructural changes will result in shifts of the complex refractive index.

## **Conclusion**

Overall, this study showed the capability of tailoring the optical properties of anodized aluminum-tantalum thin films, while at the same time controlling the nanostructure of the surface. This study presents the following conclusions:

- 1) Engineering the optical properties and structure of anodized aluminum films can be achieved using a sequential, multi-electrolyte anodization process, with a sulphuric acid bath followed by a phosphoric-oxalic mixed bath.
- 2) Anodizing initially in 0.4M sulphuric acid at 4V reduces the pore size when compared to films anodized only in 0.4M phosphoric-0.1M oxalic acid. This creates a canopy-like microstructure of the oxide where pores are smaller on the film surface and grow larger when the electrolyte is changed and voltage increased.
- 3) The refractive index of the alumina film can be tailored by varying the time in each electrolyte and the voltage. A small (<10nm) pore size on the surface can still be maintained while the refractive index is tailored, by adjusting the porosity of the film below the top few nanometers of the surface.
- 4) Consumption anodization of aluminum still occurs as shown by XRD. The oxide films developed are amorphous.

## References

- [1] P. G. Sheasby and R. Pinner, *The Surface Treatment and Finishing of Aluminum and its Alloys* - 6th Edition, Finishing Publications Ltd., 2001.
- [2] W. Lee and S. Park, "Porous Anodic Aluminum Oxide: Anodization and Templated Synthesis of Functional Nanostructures," *Chemical Reviews*, vol. 114, pp. 7487-7556, 2014.
- [3] S. Z. Chu, K. Wada, S. Inoue, M. Isogai, Y. Katsuta and A. Yasumori, "Large-Scale Fabrication of Ordered Nanoporous Alumina Films with Arbitrary Pore Intervals by Critical-Potential Anodization," *Journal of the Electrochemical Society*, vol. 153, no. 9, pp. B384-B391, 2006.
- [4] G. E. Thompson and G. C. Wood, "Porous anodic film formation on aluminium," *Nature*, vol. 290, pp. 230-232, 1981.

- [5] I. Farnan, R. Dupree, A. J. Forty, Y. S. Jeong, G. E. Thompson and G. C. Wood, "Structural information about amorphous anodic alumina from  $^{27}\text{Al}$  MAS NMR," *Philosophical Magazine Letters*, vol. 59, no. 4, pp. 189-195, 1989.
- [6] G. D. Sulka, "Highly Ordered Anodic Porous Alumina Formation by Self-Organization Anodizing," in *Nanostructured Materials in Electrochemistry*, Weinheim, Wiley-VCH, 2008, pp. 1-97.
- [7] A. W. Brace and P. G. Sheasby, *The Technology of Anodizing Aluminium*, Gloucestershire : Technicopy Ltd, 1968.
- [8] S. Liu, S. Tang, H. Zhou, C. Fu, Z. Huang, H. Liu and Y. Kuang, "Fabrication of AAO films with controllable nanopore size by changing electrolytes and electrolytic parameters," *Journal of Solid State Electrochemistry*, vol. 17, pp. 1931-1938, 2013.
- [9] L. Zaraska, M. Jaskula and G. D. Sulka, "Porous anodic alumina layers with modulated pore diameters formed by sequential anodizing in different electrolytes," *Materials Letters*, vol. 171, pp. 315-318, 2016.
- [10] G. E. Thompson and G. C. Wood, "Porous anodic film formation on aluminium," *Nature*, vol. 290, pp. 230-232, 1981.
- [11] F. Keller, M. S. Hunter and D. L. Robinson, "Structural features of oxide coatings on aluminum," *Journal of the Electrochemical Society*, vol. 100, no. 9, pp. 411-419, 1953.
- [12] Y. Xu, H. Liu, X. Li, W. Kang, B. Cheng and X. Li, "A novel method for fabricating self-ordered porous anodic alumina with wide interpore distance using phosphoric/oxalic acid mixed electrolyte," *Materials Letters*, vol. 151, pp. 79-81, 2015.
- [13] M. M. Rahman, E. Garcia-Cauarel, A. Santos, L. F. Marsal, J. Pallares and J. Ferrer-Borrull, "Effect of the anodization voltage on the pore-widening rate of nanoporous anodic alumina," *Nanoscale Research Letters*, vol. 7, no. 474, 2012.
- [14] T. Shih, P. Wei and Y. Huang, "Optical properties of anodic aluminum oxide films on Al 1050 alloys," *Surface & Coatings Technology*, vol. 202, pp. 3298-3305, 2008.
- [15] J. Wang, C. Wang, Y. Li and W. Liu, "Optical constants of anodic aluminum oxide films formed in oxalic acid solution," *Thin Solid Films*, vol. 516, pp. 7689-7694, 2008.
- [16] H. Sweet, *Development of a Thin Film Device and Optics System for Protein Detection*, Edmonton, AB: University of Alberta, 2018.
- [17] Y. Fukuda and T. Fukushima, "Behavior of Sulfate Ions during Formation of Anodic Oxide Film on Aluminium," *Bulletin of the Chemical Society of Japan*, vol. 53, no. 11, pp. 3125-3130, 1980.

[18] R. E. Burrell, "Aluminum Oxide Surfaces and Interface Molecules". Provisional Patent. Filed Feb. 20, 2018.

[19] R. C. Furneaux, W. R. Rigby and A. P. Davidson, "Porous Films and Method of Forming Them". US Patent 4,687,551, 18 August 1987.

[20] G. E. Thompson, R. C. Furneaux and G. C. Wood, "The Morphology of Sealed Anodic Films Formed on Aluminium in Phosphoric Acid," Transactions of the Institute of Metal Finishing, vol. 53, pp. 97-102, 1975.

## Chapter 5 Optical Sensitivity: Effects of Thin Film Microstructure and Antigen Surface Density on Visual Detection of IgG

### 5.1 The Effect of Thin Film Microstructure on a Visual Immunoassay for Anti-prothrombin IgG Based on Anodized Aluminum-Tantalum Thin Films

#### **Introduction**

Thin film diagnostics based on anodized aluminum have been proposed as a novel method for rapid, point-of-care detection of antigen-antibody complexes [1]. Enzyme-linked immunosorbent assay (ELISA) has been the gold standard in antibody-based testing for the last 40 years [2]. A typical ELISA test consists of covalently attaching an enzyme to an antibody designed to detect your analyte. This enzyme then reacts with a substrate, such as a dye to cause a colour change, and amplifies the protein signal [3]. There are many formats of this test, such as the radioimmunoassay (RIA) where the antibody is attached to a radioactive isotope, or fluorescence immunoassay, where a fluorescent molecule is attached to the antibody. In all cases, an antibody with some sort of amplification signal is required to read the test. ELISA assays have a number of steps including blocking, washing, incubation of the antibodies and substrates, which can take a number of hours to complete [4]. Thin film diagnostics, on the other hand, are capable of direct visualization of the antibody by a change in the interference colour in a matter of minutes. No need for sample preparation or waiting for incubation times of a substrate. However, more research needs to be conducted on the variables that affect the colour shifts and how these affect the sensitivity of an immunoassay based on thin film interference.

Prothrombin and its associated antibody, anti-prothrombin IgG, can be used as a model system for antigen-antibody reactions on an alumina surface. Prothrombin is a vitamin K dependent protein,

containing an anionic rich domain known as the GLA domain. This domain contains 10  $\gamma$ -carboxyglutamic acid residues which help prothrombin with membrane binding during the coagulation cascade [5, 6]. Such residues bind strongly with aluminum and aluminum oxides allowing for oriented and specific binding of prothrombin to an alumina surface [7, 8].

In this work, a variety of anodized aluminum-tantalum thin films were tested as outlined in previous chapters:

A) manipulation of the tantalum microstructure and optical properties by changing deposition parameters (Chapter 2),

B) manipulation of the aluminum microstructure and optical properties by changing deposition parameters (Chapter 3),

C) adjusting the aluminum oxide nanostructure and optical properties by addition of an inhibitor (oxalic acid) to the phosphoric acid bath during anodization (Chapter 4.1),

D) manipulation of the aluminum oxide nanostructure and optical properties by varying the thickness of the sputtered aluminum and the voltage during anodization (Chapter 4.2).

Prothrombin was adsorbed to the surface of these films and the colour shifts recorded. The prothrombin coated films were then exposed to anti-prothrombin IgG at various concentrations to test the performance characteristics of an immunoassay based on the interference colour shifts observed. The results of the various effects of microstructure on the interference colour shifts is then discussed.

## **Materials and Methods**

### *Materials*

All thin films were supplied by Prominent Medical Inc. (Edmonton, AB). Proteins and antibodies were acquired from Aniera Diagnostica, LLC (West Chester, OH), from the A-CoA division: Human prothrombin, purified protein (SKU #: PT-1099T); anti-human prothrombin, sheep, affinity purified IgG (SKU#: A5D-11164S). Unless otherwise specified, all proteins and antibodies were stored in 1 mL Eppendorf<sup>TM</sup> snap-cap microcentrifuge tubes (Thermo Fisher Scientific, Waltham, MA). Antibodies were dialyzed overnight at 4°C in phosphate buffered saline (PBS), pH 7.4, using an 8-10 kDa Micro Float-A-Lyzer<sup>®</sup> (Spectrum Laboratories Inc., Rancho Dominguez, CA). All other materials, unless specified, were acquired from Thermo Fisher Scientific (Waltham, MA).

### *Part A – Effect of Sputtered Tantalum Microstructure on Optical Sensitivity*

#### Thin Film Sample Preparation

Unprocessed <100> silicon wafers (University Wafers, South Boston, MA), 100 mm in diameter, were deposited with thin films of tantalum followed by aluminum using planar magnetron sputtering. Approximately 230 nm of tantalum was deposited at either 10, 15, 20, 25, or 30 mTorr argon gas pressure. These wafers were then coated with  $120 \pm 2$  nm of aluminum and potentiostatically anodized at 4V in 0.4M phosphoric acid-0.1M oxalic acid, as described in Chapter 2. These wafers were cleaved into slides approximately 6.3 cm x 1.3 cm for protein adsorption studies.

#### Protein Adsorption

To determine the detection limit of a protein directly adsorbed on the anodized slides, human prothrombin was adsorbed at 3 concentrations, covering 3 orders of magnitude. Human

prothrombin was diluted to 1 mg/mL (13.9  $\mu$ M), 100  $\mu$ g/mL (1.39  $\mu$ M), and 10  $\mu$ g/mL (139 nM) in tris buffered saline (TBS), pH 7.4. Four 1 cm diameter circles were drawn on the slide with a Sharpie® permanent marker (Sharpie, Oak Brook, IL) using a plastic template. The marker was used as a hydrophobic barrier to contain protein solutions within a constant surface area. A 20  $\mu$ L drop of each prothrombin concentration was placed on the surface within each circle using a micropipette. The drop spread to wet the entire area within the circle and was then pipetted up and down several times to mix the drop on the surface. The slides were then left for 30 minutes at  $20 \pm 2^\circ\text{C}$  on top of wet paper towel in a Petri dish to keep a high relative humidity and prevent the protein solution from drying on the surface. After 30 minutes, the drops were removed with a pipette and then the slides were rinsed thoroughly with deionized water and left to air dry. The slides were then viewed at approximately  $75^\circ$  from normal with a polarizing lens (s-polarized) and the colours recorded.

Anti-human prothrombin, sheep IgG, was diluted to a concentration of 200  $\mu$ g/mL (1.33  $\mu$ M) using PBS, pH 7.4. Using a micropipette, 20 $\mu$ L drops were placed on the prothrombin coated surface to wet the entire area within each circle. In a similar fashion, spots of anti-prothrombin were placed directly on the alumina surface for a negative control. The drops were then pipetted up and down several times to mix well on the surface and then left for 30 minutes with wet paper towel underneath in a closed Petri dish at  $20 \pm 2^\circ\text{C}$ . The antibody solutions were then removed with a pipette and the slides were rinsed thoroughly with deionized water and left to air dry. After drying, slides were observed at approximately  $75^\circ$  from normal with a polarizing lens (s-polarized) and colours recorded.

## Part B – Effect of Sputtered Aluminum Microstructure on Optical Sensitivity

### Thin Film Sample Preparation

Unprocessed <100> silicon wafers (University Wafers, South Boston, MA), 100 mm in diameter, were deposited with thin films of tantalum followed by aluminum using planar magnetron sputtering. Tantalum was sputtered to  $226.5 \pm 3.8$  nm and then subsequently coated with aluminum under various power and pressure parameters, see Table 5-1, as described in Chapter 3. After coating with aluminum, the films were potentiostatically anodized at 4V in 0.4M phosphoric acid-0.1M oxalic acid (details in Chapter 3). These wafers were cleaved into slides approximately 6.3 cm x 2.6 cm for protein adsorption studies.

Table 5-1. Experimental design matrix for sputtering aluminum at different power and working gas pressure. T-S stands for target to substrate distance.

Working Gas Pressure (Flow rate) [Argon]	Power Density		
	0.9 W/cm <sup>2</sup>	5 W/cm <sup>2</sup>	9 W/cm <sup>2</sup>
1 mTorr (9 sccm)	T-S distance: 70mm	T-S distance: 70mm	T-S distance: 70mm
5 mTorr (55 sccm)	T-S distance: 70mm	T-S distance: 70mm	N/A*
10 mTorr (135 sccm)	T-S distance: 70mm	T-S distance: 70mm	T-S distance: 70mm

\*Not tested due to high deposition rate at 9W/cm<sup>2</sup>; too difficult to control thickness

### Protein Adsorption

To determine the detection limit of each aluminum microstructure for an antibody-antigen complex, human prothrombin was adsorbed to the surface and an anti-human prothrombin IgG dilution series was carried out. Human prothrombin was diluted to 100 µg/mL (1.39 µM) with TBS, pH 7.4. Six 1 cm diameter circles were drawn on the slide with a Sharpie® permanent marker (Sharpie, Oak Brook, IL) using a plastic template. A 20 µL drop of prothrombin solution was

placed on the surface within each circle using a micropipette. The drop was spread to wet the entire area within the circle and was then pipetted up and down several times to mix the drop on the surface. The slides were then left for 30 minutes on top of wet paper towel in a Petri dish to maintain a high relative humidity and at  $20 \pm 2^\circ\text{C}$ . After 30 minutes, the drops were removed with a pipette and then the slides were rinsed thoroughly with deionized water and left to air dry. The slides were then observed at  $75^\circ$  from normal with a polarizing lens (s-polarized) and the colours recorded.

Anti-human prothrombin, sheep IgG, was diluted to the following concentrations using PBS, pH 7.4: 200  $\mu\text{g/mL}$  (1.33  $\mu\text{M}$ ), 100  $\mu\text{g/mL}$  (667 nM), 50  $\mu\text{g/mL}$  (333 nM), 20  $\mu\text{g/mL}$  (133 nM), and 10  $\mu\text{g/mL}$  (66.7 nM). A 20  $\mu\text{L}$  drop of each concentration was applied in the same manner as described above on an area previously coated with prothrombin. Additionally, a 20  $\mu\text{L}$  drop of PBS was placed on a prothrombin coated area to act as a negative control for the buffer solution. The antibody solutions were left on the films for 30 minutes at  $20 \pm 2^\circ\text{C}$  and then rinsed off thoroughly with deionized water. The slides were allowed to air dry and were then viewed at  $75^\circ$  from normal with a polarizing lens (s-polarized) and the colours recorded.

### *Part C – Effect of Electrolyte Mix and Aluminum Thickness on Optical Sensitivity*

#### Thin Film Sample Preparation

Unprocessed <100> silicon wafers (University Wafers, South Boston, MA), 100 mm in diameter, were deposited with  $226.5 \pm 3.8$  nm of tantalum followed by either 90, 100, 110, 120, 130, or 140 nm of aluminum. Sputtering conditions were the same as found in Chapter 4.2 Study A. Wafers were then anodized at 4V in either: 0.4M phosphoric acid, 0.4M phosphoric-0.1M oxalic acid mix, or 0.4M phosphoric-0.4M oxalic acid mix, as described in Chapter 4.1. Table 5-2 shows the matrix of experiments conducted.

*Table 5-2. Matrix of experiments for Part C – Effect of Electrolyte Mix and Aluminum Thickness on Optical Sensitivity.*

<b>Electrolyte</b>	<b>Sputtered Aluminum Thickness (nm)</b>
0.4M phosphoric acid	90, 100, 110, 120, 130, 140
0.4M phosphoric acid-0.1M oxalic acid mix	90, 100, 110, 120, 130
0.4M phosphoric acid-0.4M oxalic acid mix	90, 100, 110, 120, 130

### Protein Adsorption

To test the detection limit of an antibody for each anodized film, human prothrombin was adsorbed onto the surface and then a series of anti-human prothrombin IgG dilutions was applied. Eighteen 1 cm diameter circles were drawn on each wafer using a Sharpie® permanent marker (Sharpie, Oak Brook, IL) and a plastic template. Prothrombin was diluted to 100 µg/mL (1.39 µM) in TBS, pH 7.4, and then applied as described previously (Part B). Sweet [8] showed that a surface monolayer of prothrombin formed on alumina after 15 minutes when 100 µg/mL was used, therefore this work was carried out using 15 minutes as the time of prothrombin application. Anti-human prothrombin, sheep IgG, was diluted in PBS, pH 7.4, to the following concentrations: 500 µg/mL (3.33 µM), 200 µg/mL (1.33 µM), 50 µg/mL (333 nM), 20 µg/mL (133 nM). 20 µL drops of each concentration were placed on a prothrombin coated circle with a micropipette, as described previously (Part B). After 30 minutes, the drops were removed with a pipette and the wafer rinsed thoroughly with deionized water and left to air dry. Once dry, the wafers were observed at approximately 75° from normal through a polarizing lens (s-polarized) and colours recorded.

## *Part D – Effect of Anodization Voltage and Aluminum Thickness on Optical Sensitivity*

### Thin Film Sample Preparation

Unprocessed <100> silicon wafers (University Wafers, South Boston, MA), 100 mm in diameter, were deposited with  $226.5 \pm 3.8$  nm of tantalum followed by either 110, 120, or 130 nm of aluminum, under the conditions described in Chapter 4.2. The wafers were cleaved into sections about 6.3 cm x 1.3 cm and then anodized in 0.4M phosphoric – 0.1M oxalic acid at either 2, 4, 6, or 8V, using the conditions described in Chapter 4.2.

### Protein Adsorption

To test the colour shifts occurring from an antigen-antibody complex, human prothrombin was adsorbed onto the surface and then a series of anti-human prothrombin IgG dilutions were applied. Four 1 cm diameter circles were drawn on the slide with a Sharpie® permanent marker (Sharpie, Oak Brook, IL) using a plastic template. 20  $\mu$ L drops of prothrombin were applied at 100  $\mu$ g/mL (1.36  $\mu$ M) to each circle for 30 minutes, as described in Part B. These solutions were then rinsed off with deionized water and left to air dry. Anti-human prothrombin, sheep IgG, was then applied using the following concentrations in PBS, pH 7.4: 100  $\mu$ g/mL (667 nM), 50  $\mu$ g/mL (333 nM), 20  $\mu$ g/mL (133 nM). For this experiment, LoBind Eppendorf<sup>TM</sup> microcentrifuge tubes (Thermo Fisher Scientific, Waltham, MA) were used to reduce protein adsorption to the surface of the container. Application of the antibody solutions was the same as described in Part B. Additionally, a single spot of prothrombin on each slide was exposed to 20  $\mu$ L of PBS as a negative control. After 30 minutes, these solutions were rinsed off with deionized water and the slides were allowed to air dry. They were then observed at approximately 75° from normal with a polarizing lens (s-polarized) and the colours recorded.

### *Colour Coordinates*

Photos of the interference colours were taken at approximately 75° from normal using a phone camera and a polarizing lens (s-polarized). The slides were placed on a white cardboard sheet and imaged with a matte, white background under regular, white fluorescent ceiling lighting. The images were then analyzed for RGB coordinates using ImageJ software (Rasband, WS, ImageJ, US National Institutes of Health, Bethesda, MD, <https://imagej.nih.gov/ij/>, 1997-2016). A circular area of each slide was selected in the photo, encompassing between 5,000 and 30,000 pixels. The mean and standard deviation were recorded for the RGB coordinates of each area. Colour difference was calculated using the Euclidean distance between the R, G, and B coordinates, as shown in Equation (5.1):

$$\Delta C = \sqrt{(R_s - R_b)^2 + (G_s - G_b)^2 + (B_s - B_b)^2} \quad (5.1)$$

Where R, G and B are the RGB coordinates measured, s is the signal or the test spot exposed to both antigen (prothrombin) and antibody (anti-prothrombin IgG), b is the background or the spot only coated in antigen (prothrombin). Note that this method does not consider differences in colour due to human perception and only calculates the differences in the collected data.

The colour difference was measured for each antibody test spot compared to the background; these differences were then pooled and analyzed statistically. For Part B, the colour differences were analyzed using an independent samples T-test. A T-test was used as opposed to ANOVA due to a sample size of n=2 and unequal variance. For Parts A, C and D with a sample size of n=3, a one-way ANOVA was used with a Tukey post-hoc test to check for differences between populations. A Levene's test was initially used to check for equal sample variance. If the Levene's test failed, then a Welch T-test was carried out, which is more robust against inequality of means. All

statistical analysis was conducted using IBM SPSS Statistics for Windows, Version 24.0 (IBM Corp., Released 2016, Armonk, NY). All standard deviations are represented by error bars on plots or the '±' symbol in tables.

The colour differences were then used to analyze the performance characteristics of the immunoassay, including analytical range and limit of detection. Where the analytical range is the range of concentrations that have significant differences in colour, and limit of detection is the smallest concentration that showed a significant change in colour from the background [6].

## **Results**

### *Part A – Effect of Tantalum Microstructure on Optical Sensitivity*

Changes in the tantalum microstructure showed no differences to the sensitivity of the slides for detecting adsorbed protein layers. Table 5-3 and 5-4 show the results of the protein immobilization studies on anodized aluminum-tantalum thin films with change in deposited tantalum microstructure. When observed and analyzed by eye, no differences were found for the detection limit of protein on the surfaces (100 µg/mL), regardless of tantalum microstructure. The RGB coordinate analysis supported these observations, showing that the colour difference was not significantly different for any microstructure, see Table 5-5 for statistical results. Prothrombin adsorbed to the surface at 10 µg/mL showed no difference in colour from the bare surface. At 100 µg/mL the colour of the surface changed to reddish-purple and at 1 mg/mL the colour was dark purple. After exposing the surface to 200 µg/mL of anti-prothrombin IgG, the area previously exposed to 10 µg/mL of prothrombin changed from tan to red, the area exposed to 100 µg/mL changed from reddish-purple to dark purple and the area exposed to 1 mg/mL changed from dark purple to dark blue. Again, no significant differences were found for colour changes ( $\Delta C$ ) with the addition of anti-prothrombin regardless of microstructure, see Table 5-5. The negative control

spots, where anti-prothrombin was placed directly onto the alumina surface, showed no colour change. When the colour difference ( $\Delta C$ ) was measured from RGB coordinate data, each slide showed a small shift in colour for the negative control, see Table 5-4.

Table 5-3. Images and RGB coordinate analysis for protein adsorption studies on anodized aluminum-tantalum films with tantalum sputtered at various gas pressures. Sample size of n=3 for all data sets. Images taken at 75° from normal with a polarizing lens (s-polarized).

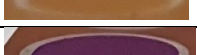
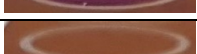
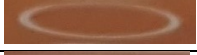
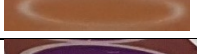
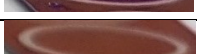
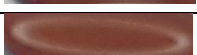
Tantalum Sputtering Pressure	Prothrombin		RGB Colour Difference ( $\Delta C$ ) Prothrombin vs. base slide
	Concentration	Image	
10 mTorr	1 mg/mL		88.2 ± 28.0
	0.1 mg/mL		66.1 ± 15.0
	0.01 mg/mL		14.9 ± 0.4
	Blank		-
15 mTorr	1 mg/mL		76.4 ± 10.2
	0.1 mg/mL		58.2 ± 5.9
	0.01 mg/mL		11.3 ± 3.4
	Blank		-
20 mTorr	1 mg/mL		85.2 ± 12.3
	0.1 mg/mL		67.8 ± 5.4
	0.01 mg/mL		14.3 ± 0.9
	Blank		-
25 mTorr	1 mg/mL		82.6 ± 10.3
	0.1 mg/mL		64.4 ± 4.9
	0.01 mg/mL		14.0 ± 1.9
	Blank		-
30 mTorr	1 mg/mL		75.8 ± 12.5
	0.1 mg/mL		57.3 ± 8.4
	0.01 mg/mL		11.7 ± 5.8
	Blank		-

Table 5-4. Images and RGB coordinate analysis for protein adsorption studies on anodized aluminum-tantalum films with tantalum sputtered at various gas pressures. Sample size of n=3 for all data sets. Images taken at 75° from normal with a polarizing lens (s-polarized).

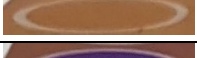
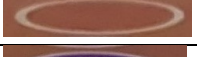
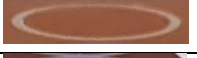
Tantalum Sputtering Pressure	Prothrombin [varied concentration] & Anti-prothrombin [0.2 mg/mL]		RGB Colour Difference ( $\Delta C$ ) Prothrombin + Anti-prothrombin vs. Prothrombin
	Prothrombin Concentration	Image	
10 mTorr	1 mg/mL		36.9 ± 3.95
	0.1 mg/mL		47.2 ± 15.5
	0.01 mg/mL		25.1 ± 11.0
	Blank		13.3 ± 9.9
15 mTorr	1 mg/mL		48.7 ± 13.1
	0.1 mg/mL		53.9 ± 13.6
	0.01 mg/mL		22.2 ± 1.2
	Blank		10.5 ± 0.1
20 mTorr	1 mg/mL		49.5 ± 14.8
	0.1 mg/mL		52.3 ± 13.7
	0.01 mg/mL		21.1 ± 2.8
	Blank		8.4 ± 2.3
25 mTorr	1 mg/mL		51.8 ± 13.7
	0.1 mg/mL		52.0 ± 10.5
	0.01 mg/mL		19.1 ± 2.6
	Blank		9.9 ± 3.8
30 mTorr	1 mg/mL		51.2 ± 24.9
	0.1 mg/mL		54.7 ± 24.0
	0.01 mg/mL		26.3 ± 10.8
	Blank		11.2 ± 2.4

Table 5-5. Statistical results from ANOVA or Welch T-tests on colour differences ( $\Delta C$ ) with the application of prothrombin and anti-prothrombin on anodized aluminum-tantalum films with tantalum sputtered under various pressures.

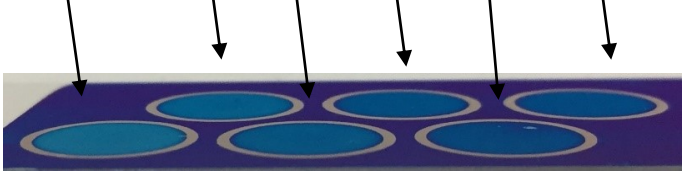
Prothrombin Concentration	Prothrombin ANOVA p-value	Prothrombin + Anti-prothrombin ANOVA p-value
1 mg/mL	p=0.817	p=0.868
0.1 mg/mL	p=0.426	p=0.989
0.01 mg/mL	p=0.546*	p=0.623*

\*Welch T-test used due to unequal sample variance

#### Part B – Effect of Aluminum Microstructure on Optical Sensitivity

Few differences were found for the sensitivity between various sputtered and anodized aluminum microstructures. The interference colours produced by prothrombin and anti-prothrombin are shown in Table 5-6. Colour differences for each antibody concentration are plotted in Figure 5-1 and the statistical results can be found in Table 5-7. When the films were observed and analyzed by eye, no difference in the sensitivity or limit of detection was found, with a limit of 50  $\mu\text{g/mL}$  of IgG. The RGB coordinate analysis of the images showed some differences between the various microstructures. The analytical range was greatest for films sputtered at 0.9  $\text{W/cm}^2$  & 5 mTorr, 5  $\text{W/cm}^2$  & 1 mTorr, and 9  $\text{W/cm}^2$  & 1 mTorr, i.e. more significant colour differences were found between each concentration of antibody on these films compared to the other films, see Table 5-7. The limit of detection was found to be 50  $\mu\text{g/mL}$  for films sputtered at 9  $\text{W/cm}^2$  and 1 or 10 mTorr, 0.9  $\text{W/cm}^2$  and 10 mTorr, and 5  $\text{W/cm}^2$  and 1 mTorr. When compared against one another, no aluminum microstructure showed a significantly larger colour difference ( $\Delta C$ ) than any other, at any antibody concentration ( $p > 0.10$  for all concentrations). Overall, there appeared to be very little difference between all aluminum microstructures and their ability to detect adsorbed protein layers.

Table 5-6. Images and RGB coordinate analysis from sensitivity tests of anti-prothrombin on prothrombin for anodized aluminum-tantalum thin films. Aluminum was sputtered under various conditions. Sample size of  $n=2$  for all data sets. Images taken at  $75^\circ$  from normal with a polarizing lens (*s*-polarized).

Aluminum Sputtering Parameters	Prothrombin [100 $\mu\text{g}/\text{mL}$ ] + Anti-prothrombin [varied concentration]						RGB Colour Difference ( $\Delta C$ ) Prothrombin + Anti-prothrombin vs. Prothrombin
	200 $\mu\text{g}/\text{mL}$	100 $\mu\text{g}/\text{mL}$	50 $\mu\text{g}/\text{mL}$	20 $\mu\text{g}/\text{mL}$	10 $\mu\text{g}/\text{mL}$	0 $\mu\text{g}/\text{mL}$	
0.9 W/cm <sup>2</sup> , 1 mTorr							200 $\mu\text{g}/\text{mL}$ : $34.81 \pm 0.10$ 100 $\mu\text{g}/\text{mL}$ : $17.95 \pm 5.40$ 50 $\mu\text{g}/\text{mL}$ : $9.51 \pm 2.77$ 20 $\mu\text{g}/\text{mL}$ : $3.49 \pm 1.59$ 10 $\mu\text{g}/\text{mL}$ : $8.80 \pm 2.96$
0.9 W/cm <sup>2</sup> , 5 mTorr							200 $\mu\text{g}/\text{mL}$ : $29.62 \pm 2.59$ 100 $\mu\text{g}/\text{mL}$ : $17.41 \pm 1.87$ 50 $\mu\text{g}/\text{mL}$ : $7.64 \pm 1.91$ 20 $\mu\text{g}/\text{mL}$ : $4.13 \pm 1.85$ 10 $\mu\text{g}/\text{mL}$ : $8.23 \pm 2.60$
0.9 W/cm <sup>2</sup> , 10 mTorr							200 $\mu\text{g}/\text{mL}$ : $42.73 \pm 8.64$ 100 $\mu\text{g}/\text{mL}$ : $29.38 \pm 6.59$ 50 $\mu\text{g}/\text{mL}$ : $12.04 \pm 0.96$ 20 $\mu\text{g}/\text{mL}$ : $7.23 \pm 0.78$ 10 $\mu\text{g}/\text{mL}$ : $6.08 \pm 0.39$
5 W/cm <sup>2</sup> , 1 mTorr							200 $\mu\text{g}/\text{mL}$ : $36.64 \pm 3.48$ 100 $\mu\text{g}/\text{mL}$ : $19.94 \pm 3.61$ 50 $\mu\text{g}/\text{mL}$ : $14.75 \pm 1.94$ 20 $\mu\text{g}/\text{mL}$ : $5.65 \pm 2.56$ 10 $\mu\text{g}/\text{mL}$ : $6.94 \pm 1.09$
5 W/cm <sup>2</sup> , 5 mTorr							200 $\mu\text{g}/\text{mL}$ : $51.12 \pm 16.56$ 100 $\mu\text{g}/\text{mL}$ : $31.56 \pm 14.81$ 50 $\mu\text{g}/\text{mL}$ : $15.22 \pm 8.80$ 20 $\mu\text{g}/\text{mL}$ : $6.48 \pm 6.52$ 10 $\mu\text{g}/\text{mL}$ : $4.91 \pm 1.83$
5 W/cm <sup>2</sup> , 10 mTorr							200 $\mu\text{g}/\text{mL}$ : $32.53 \pm 0.79$ 100 $\mu\text{g}/\text{mL}$ : $13.14 \pm 8.53$ 50 $\mu\text{g}/\text{mL}$ : $7.88 \pm 1.76$ 20 $\mu\text{g}/\text{mL}$ : $5.82 \pm 0.64$ 10 $\mu\text{g}/\text{mL}$ : $5.74 \pm 2.17$
9 W/cm <sup>2</sup> , 1 mTorr							200 $\mu\text{g}/\text{mL}$ : $37.04 \pm 1.95$ 100 $\mu\text{g}/\text{mL}$ : $22.86 \pm 3.54$ 50 $\mu\text{g}/\text{mL}$ : $12.86 \pm 1.37$ 20 $\mu\text{g}/\text{mL}$ : $7.43 \pm 3.26$ 10 $\mu\text{g}/\text{mL}$ : $4.45 \pm 2.19$

9 W/cm <sup>2</sup> , 10 mTorr		200 µg/mL: 39.69 ± 11.13 100 µg/mL: 24.25 ± 9.81 50 µg/mL: 13.45 ± 1.21 20 µg/mL: 8.43 ± 2.65 10 µg/mL: 7.10 ± 0.19
-----------------------------------	--	---

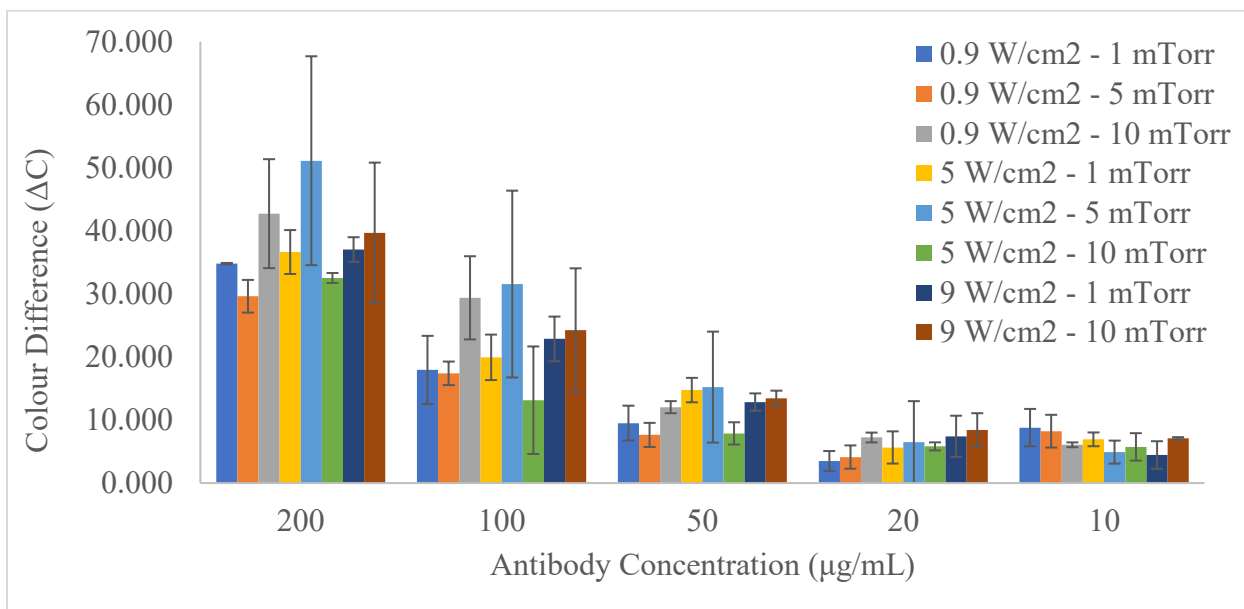


Figure 5-1. Recorded colour differences from RGB coordinate analysis for protein adsorption studies on anodized aluminum-tantalum thin films with aluminum sputtered under various power densities and gas pressures. Sample size of  $n=3$  for all data sets.

Table 5-7. Statistical results of a series of T-tests conducted on colour differences recorded from RGB coordinate analysis of protein adsorption studies on anodized aluminum-tantalum thin films with aluminum deposited at various power densities and gas pressures. Insignificant results ( $p > 0.10$ ) not shown. The number indicates the concentration of antibody exposed to the surface in  $\mu\text{g/mL}$ , i.e. 200 vs. 50 is  $\Delta C(200\mu\text{g/mL})$  vs.  $\Delta C(50\mu\text{g/mL})$ .

Aluminum Sputtering Parameters	T-test Results
0.9 W/cm <sup>2</sup> , 1 mTorr	200 vs. 50: $p < 0.05$ 200 vs. 20: $p < 0.05$ 200 vs. 10: $p < 0.10$
0.9 W/cm <sup>2</sup> , 5 mTorr	200 vs. 100: $p < 0.05$ 200 vs. 50: $p < 0.05$ 200 vs. 20: $p < 0.05$ 200 vs. 10: $p < 0.05$ 100 vs. 50: $p < 0.05$ 100 vs. 20: $p < 0.05$ 100 vs. 10: $p < 0.10$
0.9 W/cm <sup>2</sup> , 10 mTorr	50 vs. 20: $p < 0.05$ 50 vs. 10: $p < 0.05$
5 W/cm <sup>2</sup> , 1 mTorr	200 vs. 100: $p < 0.05$ 200 vs. 50: $p < 0.05$ 200 vs. 20: $p < 0.05$ 200 vs. 10: $p < 0.05$ 100 vs. 20: $p < 0.10$ 100 vs. 10: $p < 0.10$ 50 vs. 20: $p < 0.10$ 50 vs. 10: $p < 0.10$
5 W/cm <sup>2</sup> , 5 mTorr	No differences
5 W/cm <sup>2</sup> , 10 mTorr	200 vs. 50: $p < 0.05$ 200 vs. 20: $p < 0.01$ 200 vs. 10: $p < 0.05$
9 W/cm <sup>2</sup> , 1 mTorr	200 vs. 100: $p < 0.10$ 200 vs. 50: $p < 0.01$ 200 vs. 20: $p < 0.05$ 200 vs. 10: $p < 0.01$ 100 vs. 20: $p < 0.05$ 100 vs. 10: $p < 0.05$ 50 vs. 10: $p < 0.10$
9 W/cm <sup>2</sup> , 10 mTorr	50 vs. 10: $p < 0.10$

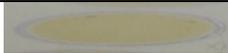
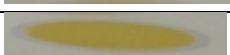
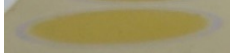
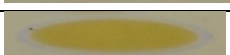
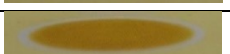
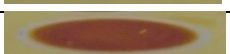
### *Part C – Effect of Electrolyte Mix and Aluminum Thickness on Optical Sensitivity*

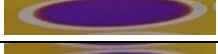
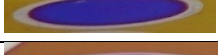
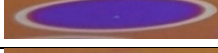
The effects of electrolyte and aluminum thickness on the interference colours produced by prothrombin and anti-prothrombin are shown in Tables 5-8 through 5-10. The colour differences are plotted in Figures 5-2 through 5-4 and statistical results can be found in Table 5-11. When the wafers were observed by eye, the strongest colour differences were found for films with 120 or 130 nm of aluminum, anodized in 0.4M phosphoric acid or the 0.4M phosphoric – 0.1M oxalic acid mix. The RGB coordinate analysis showed that the greatest colour differences, for each electrolyte, varied based upon the aluminum thickness. Films anodized in 0.4M phosphoric acid showed the largest differences for 120 through 140 nm. The 0.4M phosphoric – 0.1M oxalic acid films showed the greatest differences for 110 through 130 nm and the 0.4M phosphoric – 0.4M oxalic films showed the greatest differences for 100 through 120 nm. The detection limit for most films was found to be 50 µg/mL, however only the following films were found to have statistically significant differences between 50 and 20 µg/mL and therefore the best analytical sensitivity: 120 and 130 nm anodized in 0.4M phosphoric – 0.1M oxalic acid, and 120 nm anodized in 0.4M phosphoric – 0.4M oxalic acid.

The 120 through 140 nm films anodized in 0.4M phosphoric acid were found to have strong colour differences at 20 µg/mL, however the colour shift was found to move down the interference colour spectrum and not up, as in all other films. This was confirmed by converting to the Yxy coordinate system. The average RGB coordinates for a few of the tested films were converted to the Yxy colour coordinate system and plotted on a 1931 CIE colour diagram, Figure 5-5. Note that as optical path length increases, the interferences colours start near white in the center and then progress in a circle out to yellow and orange and then across to purple and blue. When looking at the colour shift for the 120nm films anodized in 0.4M phosphoric acid, the 20µg/mL treatment of

antibody showed a colour further back in the spectrum than prothrombin alone, indicating a reduction in the optical path length. This was different from the films anodized in the oxalic acid mixes, as they never showed a decreasing optical path length with antibody treatment. This discrepancy is discussed later.

*Table 5-8.* Images and RGB coordinate analysis for protein adsorption studies on anodized aluminum-tantalum thin films with aluminum sputtered at various thicknesses and anodized in 0.4M phosphoric acid at 4V. Sample size of n=3 for all data sets.

Aluminum Thickness	Prothrombin [100µg/mL] & Anti-prothrombin [varied concentration]		RGB Colour Difference (ΔC) Prothrombin + Anti-prothrombin vs. Prothrombin
	Antibody [µg/mL]	Image	
90 nm	0		-
	20		9.31 ± 2.73
	50		13.43 ± 3.90
	200		28.02 ± 2.71
	500		48.35 ± 1.54
100 nm	0		-
	20		5.66 ± 2.74
	50		7.25 ± 4.70
	200		41.35 ± 3.10
	500		52.59 ± 2.94
110 nm	0		-
	20		13.92 ± 3.82
	50		18.34 ± 5.41
	200		48.97 ± 4.99
	500		74.07 ± 4.79
120 nm	0		-
	20		17.19 ± 10.65
	50		21.92 ± 8.74
	200		92.18 ± 1.73

	500		$126.37 \pm 9.16$
130 nm	0		-
	20		$35.79 \pm 6.90$
	50		$32.60 \pm 7.77$
	200		$82.66 \pm 7.10$
	500		$115.60 \pm 2.77$
	140 nm	0	
20			$25.12 \pm 11.55$
50			$38.90 \pm 20.78$
200			$89.12 \pm 7.59$
500			$95.61 \pm 3.89$

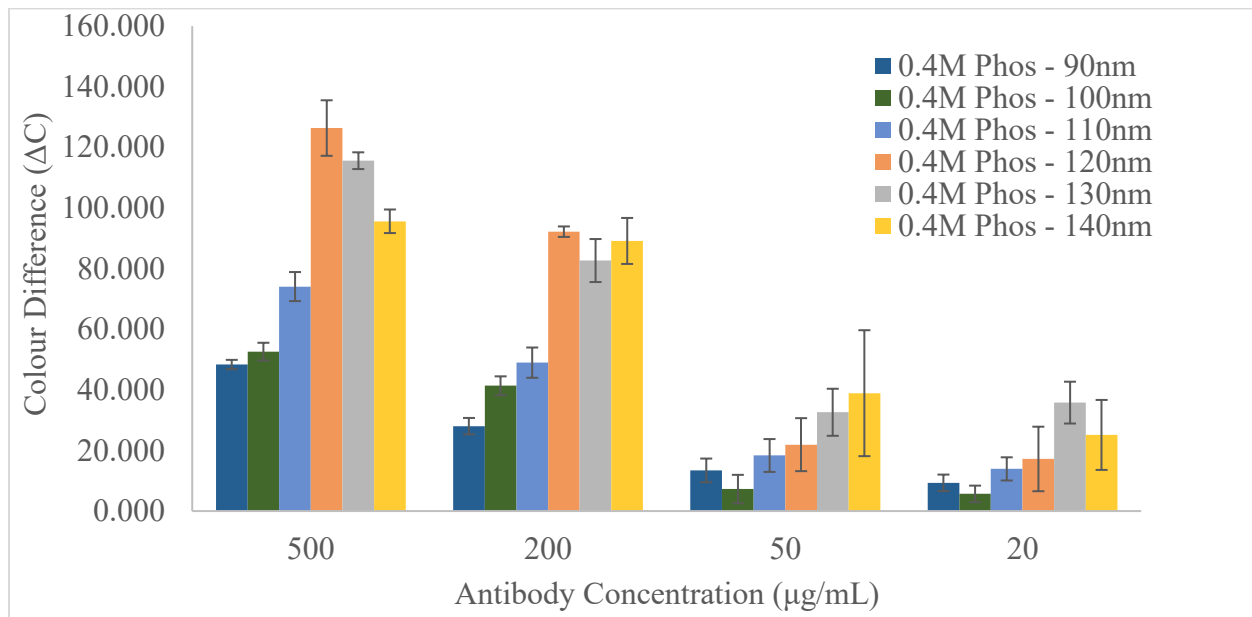
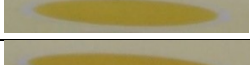
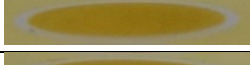
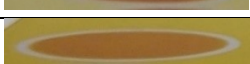
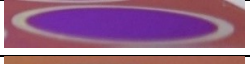
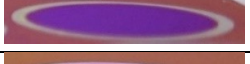
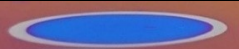


Figure 5-2. Recorded colour differences from RGB coordinate analysis for protein adsorption studies on anodized aluminum-tantalum thin films with various sputtered aluminum thicknesses and anodized in 0.4M phosphoric acid at 4V. Sample size of  $n=3$  for all data sets.

Table 5-9. Images and RGB coordinate analysis for protein adsorption studies on anodized aluminum-tantalum thin films with aluminum sputtered at various thicknesses and anodized in 0.4M phosphoric – 0.1M oxalic acid at 4V. Sample size of n=3 for all data sets.

Aluminum Thickness	Prothrombin [100µg/mL] & Anti-prothrombin [varied concentration]		Colour Difference (ΔC) Prothrombin + Anti-prothrombin vs. Prothrombin
	Antibody [µg/mL]	Image	
90 nm	0		-
	20		15.19 ± 6.57
	50		15.35 ± 4.17
	200		24.00 ± 5.22
	500		30.03 ± 5.22
100 nm	0		-
	20		15.32 ± 4.59
	50		13.34 ± 1.61
	200		22.69 ± 5.84
	500		33.24 ± 2.76
110 nm	0		-
	20		11.63 ± 2.93
	50		21.41 ± 5.62
	200		78.39 ± 5.68
	500		89.79 ± 3.03
120 nm	0		-
	20		8.86 ± 1.23
	50		35.17 ± 11.45
	200		79.87 ± 11.70
	500		104.38 ± 7.56
130 nm	0		-
	20		9.25 ± 0.62
	50		35.08 ± 12.43
	200		89.22 ± 7.80

	500		115.35 ± 1.19
--	-----	---	---------------

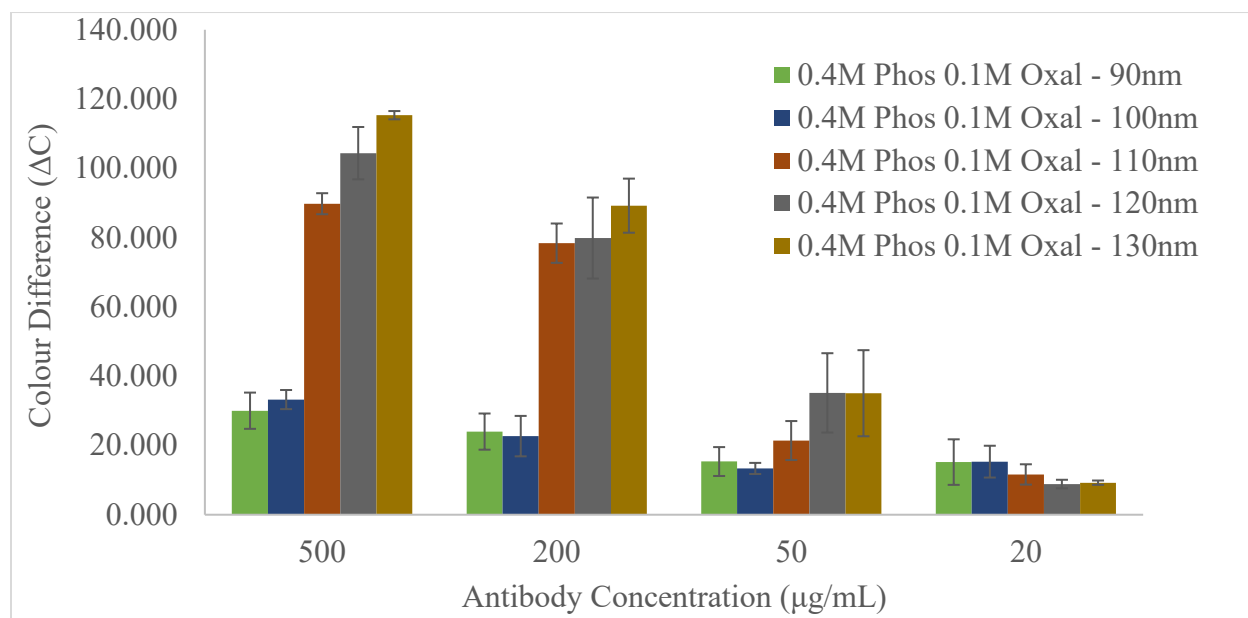
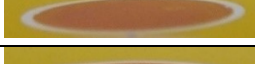
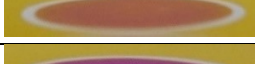
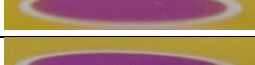
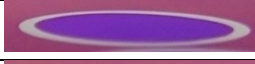
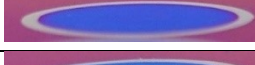
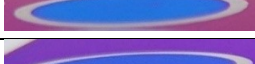
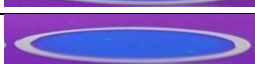


Figure 5-3. Recorded colour differences from RGB coordinate analysis for protein adsorption studies on anodized aluminum-tantalum thin films with various sputtered aluminum thicknesses and anodized in 0.4M phosphoric – 0.1M oxalic acid at 4V. Sample size of  $n=3$  for all data sets.

Table 5-10. Images and RGB coordinate analysis for protein adsorption studies on anodized aluminum-tantalum thin films with aluminum sputtered at various thicknesses and anodized in 0.4M phosphoric – 0.4M oxalic acid at 4V. Sample size of n=3 for all data sets.

Aluminum Thickness	Prothrombin [100µg/mL] & Anti-prothrombin [varied concentration]		RGB Colour Difference (ΔC) Prothrombin + Anti-prothrombin vs. Prothrombin
	Antibody [µg/mL]	Image	
90 nm	0		-
	20		2.91 ± 0.58
	50		5.81 ± 2.04
	200		28.53 ± 6.39
	500		46.61 ± 3.20
100 nm	0		-
	20		16.00 ± 5.16
	50		33.24 ± 11.72
	200		88.03 ± 11.44
	500		95.78 ± 5.61
110 nm	0		-
	20		13.23 ± 7.33
	50		22.56 ± 13.36
	200		77.47 ± 15.43
	500		98.07 ± 12.84
120 nm	0		-
	20		19.37 ± 3.26
	50		48.63 ± 18.75
	200		95.58 ± 14.53
	500		119.78 ± 6.15
130 nm	0		-
	20		22.76 ± 3.61
	50		14.73 ± 7.73
	200		61.62 ± 7.72

	500		66.54 ± 5.63
--	-----	---	--------------

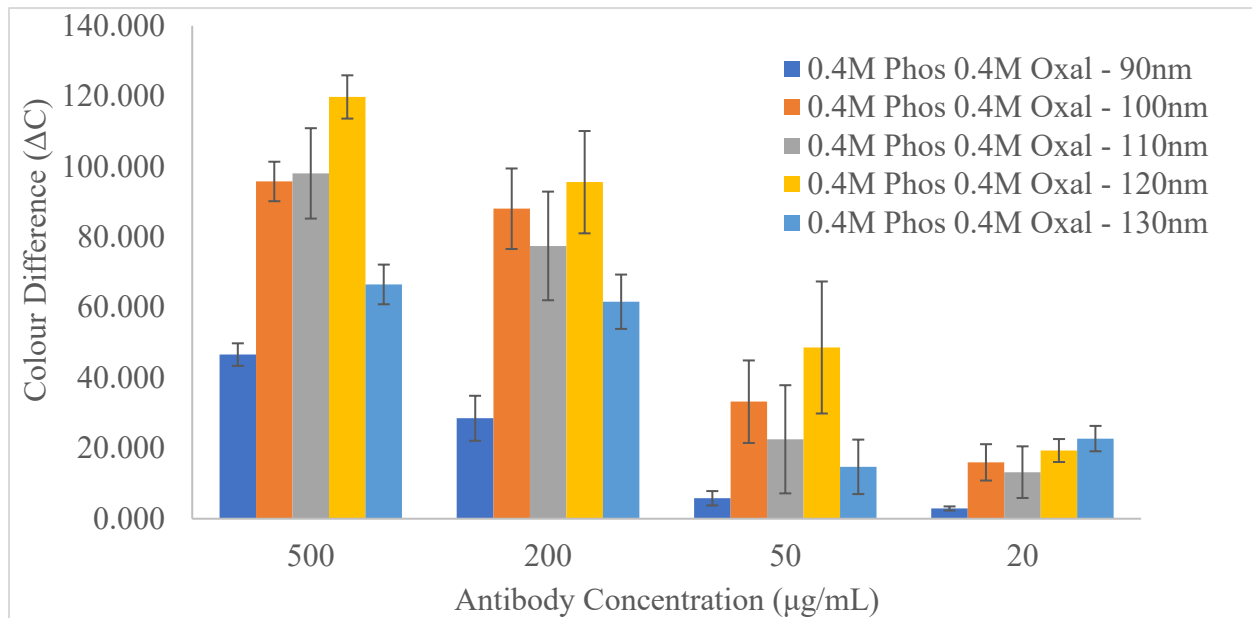


Figure 5-4. Recorded colour differences from RGB coordinate analysis for protein adsorption studies on anodized aluminum-tantalum thin films with various sputtered aluminum thicknesses and anodized in 0.4M phosphoric – 0.4M oxalic acid at 4V. Sample size of n=3 for all data sets.

Table 5-11. Statistical results for a one-way ANOVA performed on colour differences from various concentrations of antibody exposed to anodized aluminum-tantalum thin films with various aluminum thicknesses and anodized under various electrolytes at 4V. The number indicates the concentration of antibody exposed to the surface in  $\mu\text{g/mL}$ , i.e. 200 vs. 50 is  $\Delta C(200\mu\text{g/mL})$  vs.  $\Delta C(50\mu\text{g/mL})$ .

Electrolyte and Aluminum Thickness	ANOVA p-value	Post hoc Test Results
0.4M Phosphoric, 90 nm	P<0.001	500 vs. 200, 50, 20: p<0.001 200 vs. 50, 20: p<0.001
0.4M Phosphoric, 100 nm	P<0.001	500 vs. 200: p<0.05 500 vs. 50, 20: p<0.001 200 vs. 50, 20: p<0.001
0.4M Phosphoric, 110 nm	P<0.001	500 vs. 200, 50, 20: p<0.001 200 vs. 50, 20: p<0.001
0.4M Phosphoric, 120 nm	P<0.001	500 vs. 200: p<0.01 500 vs. 50, 20: p<0.001 200 vs. 50, 20: p<0.001
0.4M Phosphoric, 130 nm	P<0.001	500 vs. 200, 50, 20: p<0.001 200 vs. 50, 20: p<0.001

0.4M Phosphoric, 140 nm	P<0.001	500 vs. 50, 20: p<0.01 200 vs. 50, 20: p<0.01
0.4M Phosphoric – 0.1M Oxalic, 90 nm	P<0.05	500 vs. 50, 20: p<0.05
0.4M Phosphoric – 0.1M Oxalic, 100 nm	P<0.001	500 vs. 200: p<0.05 500 vs. 50, 20: p<0.01 200 vs. 50: p<0.10
0.4M Phosphoric – 0.1M Oxalic, 110 nm	P<0.001	500 vs. 200: p<0.10 500 vs. 50, 20: p<0.001 200 vs. 50, 20: p<0.001
0.4M Phosphoric – 0.1M Oxalic, 120 nm	P<0.001	500 vs. 200: p<0.05 500 vs. 50, 20: p<0.001 200 vs. 50: p<0.01 200 vs. 20: p<0.001 50 vs. 20: p<0.05
0.4M Phosphoric – 0.1M Oxalic, 130 nm	P<0.001	500 vs. 200: p<0.05 500 vs. 50, 20: p<0.001 200 vs. 50, 20: p<0.001 50 vs. 20: p<0.05
0.4M Phosphoric – 0.4M Oxalic, 90 nm	P<0.001	500 vs. 200: p<0.01 500 vs. 50, 20: p<0.001 200 vs. 50, 20: p<0.001
0.4M Phosphoric – 0.4M Oxalic, 100 nm	P<0.001	500 vs. 50, 20: p<0.001 200 vs. 50, 20: p<0.001
0.4M Phosphoric – 0.4M Oxalic, 110 nm	P<0.001	500 vs. 50, 20: p<0.001 200 vs. 50, 20: p<0.01
0.4M Phosphoric – 0.4M Oxalic, 120 nm	P<0.001	500 vs. 50, 20: p<0.001 200 vs. 50: p<0.01 200 vs. 20: p<0.001 50 vs. 20: p<0.10
0.4M Phosphoric – 0.4M Oxalic, 130 nm	P<0.001	500 vs. 50, 20: p<0.001 200 vs. 50, 20: p<0.001

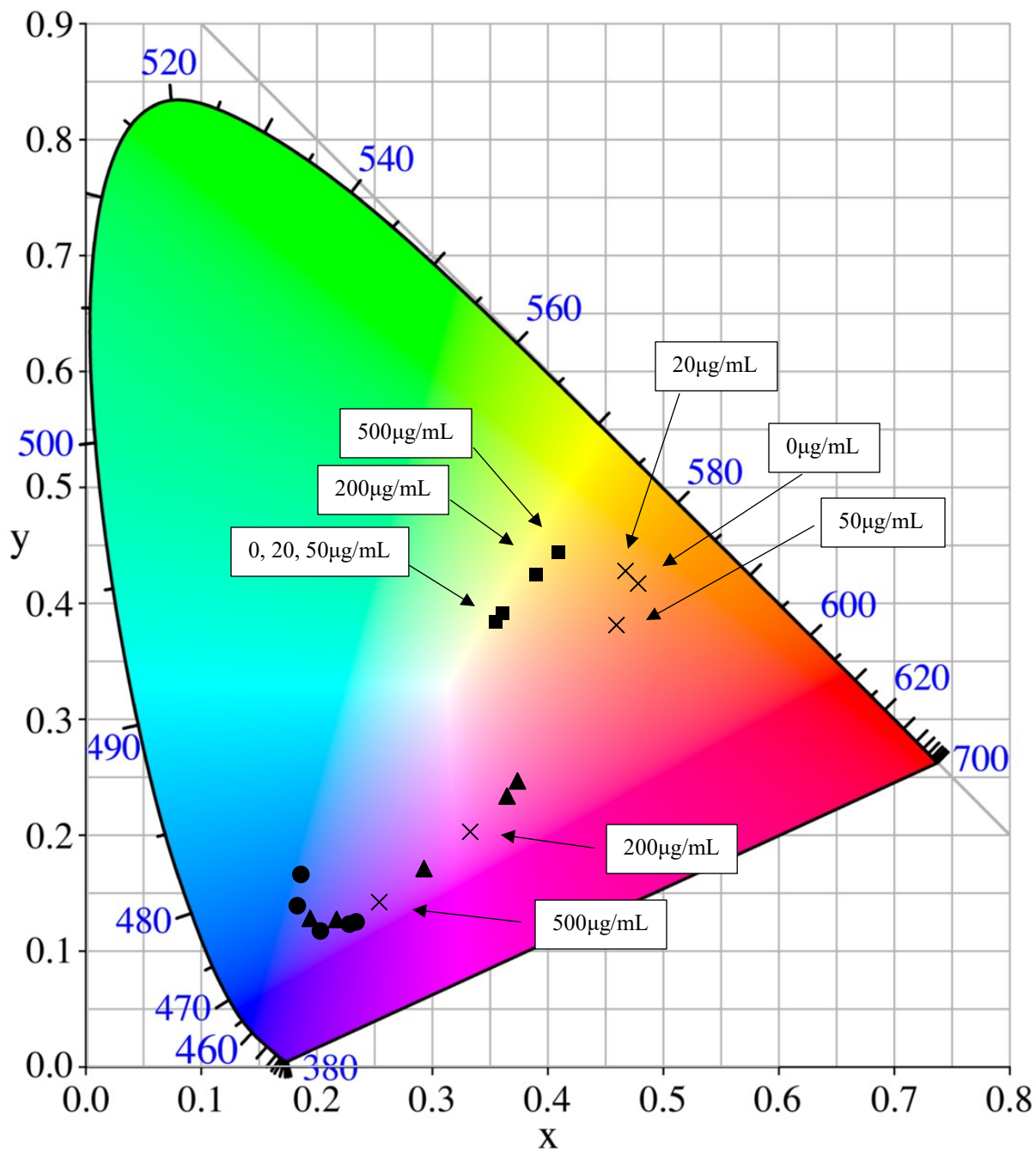


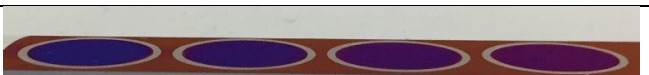
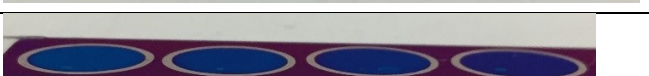
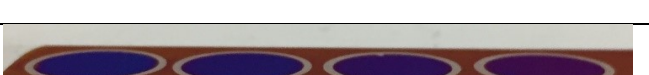
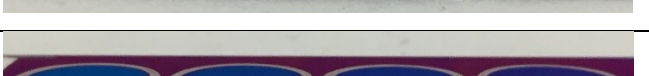
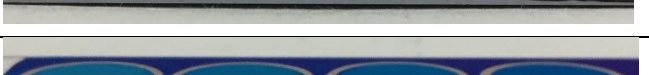
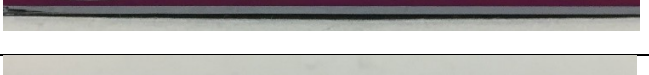
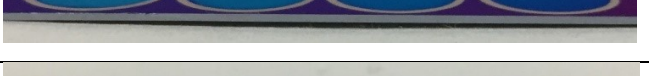
Figure 5-5. 1931 CIE colour diagram with selected films showing the average colour shift with increasing antibody concentration: 90nm Al, 0.4M phosphoric acid (■); 120nm, 0.4M phosphoric (x); 120nm, 0.4M phosphoric-0.1M oxalic (▲); 120nm, 0.4M phosphoric-0.4M oxalic (●).

#### *Part D – Effect of Anodization Voltage and Aluminum Thickness on Optical Sensitivity*

The results of Part C found that at 4V, 0.4M phosphoric – 0.1M oxalic showed the strongest results with respect to analytical sensitivity and detection limit for a prothrombin – anti-prothrombin immunoassay; therefore, a series of tests was carried out using this electrolyte and varying both the voltage during anodization and the starting aluminum thickness. The results of these tests can be found in Table 5-12, with RGB colour differences plotted in Figure 5-6. Statistical results of the colour differences can be found in Table 5-13. When observed and analyzed by eye, the films that started with either a yellow or tan colour tended to show the strongest differences with addition of prothrombin and anti-prothrombin antibody. Films that started out purple or blue in colour were more difficult to distinguish between the various antibody concentrations. The detection limit was found to be 20 µg/mL in all cases. RGB coordinate analysis confirmed that colour differences were higher for the 2 and 4V films (yellow and tan films). However, the following films showed the strongest significant differences between antibody concentrations: 110nm & 4V, 120nm & 4V, 130nm & 2V.

For ease of analysis, two CIE colour diagrams plotted the average RGB coordinates from the prothrombin – anti-prothrombin test spots. Figure 5-7 shows films with 120nm of aluminum, anodized at 2, 4, 6, and 8V, while Figure 5-8 shows films anodized at 4V with 110, 120, and 130nm of aluminum. As the antibody concentration was increased from 0 to 100µg/mL, the colour moved across the CIE chart in a circular pattern. In the same fashion, the colour changed as voltage or film thickness were increased. Only one series is labelled with the concentrations of antibody in each figure, however the pattern was similar for all samples.

Table 5-12. Images and RGB coordinate analysis for protein adsorption studies on anodized aluminum-tantalum thin films with aluminum sputtered at various thicknesses and anodized in 0.4M phosphoric – 0.1M oxalic acid at various voltages. Sample size of n=3 for all data sets.

Aluminum Thickness and Anodizing Voltage	Prothrombin (100 µg/mL) + Anti-prothrombin (varied concentration)				RGB Colour Difference (ΔC) Prothrombin + Anti-prothrombin vs. Prothrombin
	100 µg/mL	50 µg/mL	20 µg/mL	0 µg/mL	
110 nm, 2V					100 µg/mL: 46.95 ± 7.24 50 µg/mL: 38.28 ± 5.87 20 µg/mL: 22.42 ± 4.21
110 nm, 4V					100 µg/mL: 46.67 ± 2.84 50 µg/mL: 35.45 ± 2.99 20 µg/mL: 22.00 ± 4.24
110 nm, 6V					100 µg/mL: 42.70 ± 8.00 50 µg/mL: 33.85 ± 4.49 20 µg/mL: 17.97 ± 3.27
110 nm, 8V					100 µg/mL: 36.72 ± 6.10 50 µg/mL: 29.41 ± 2.86 20 µg/mL: 18.08 ± 1.66
120 nm, 2V					100 µg/mL: 53.68 ± 9.06 50 µg/mL: 45.79 ± 6.46 20 µg/mL: 28.79 ± 9.37
120 nm, 4V					100 µg/mL: 41.27 ± 3.18 50 µg/mL: 35.29 ± 2.74 20 µg/mL: 19.24 ± 2.13
120 nm, 6V					100 µg/mL: 40.57 ± 6.80 50 µg/mL: 33.51 ± 5.37 20 µg/mL: 21.02 ± 4.06
120 nm, 8V					100 µg/mL: 27.01 ± 3.88 50 µg/mL: 18.34 ± 3.26 20 µg/mL: 9.16 ± 2.30
130 nm, 2V					100 µg/mL: 48.04 ± 5.61 50 µg/mL: 37.89 ± 3.05 20 µg/mL: 20.41 ± 1.50
130 nm, 4V					100 µg/mL: 47.42 ± 7.13 50 µg/mL: 36.87 ± 7.20 20 µg/mL: 20.15 ± 4.81
130 nm, 6V					100 µg/mL: 32.54 ± 10.26 50 µg/mL: 23.03 ± 7.96 20 µg/mL: 13.35 ± 6.21
130 nm, 8V					100 µg/mL: 37.66 ± 11.67 50 µg/mL: 26.05 ± 9.25 20 µg/mL: 13.17 ± 9.55

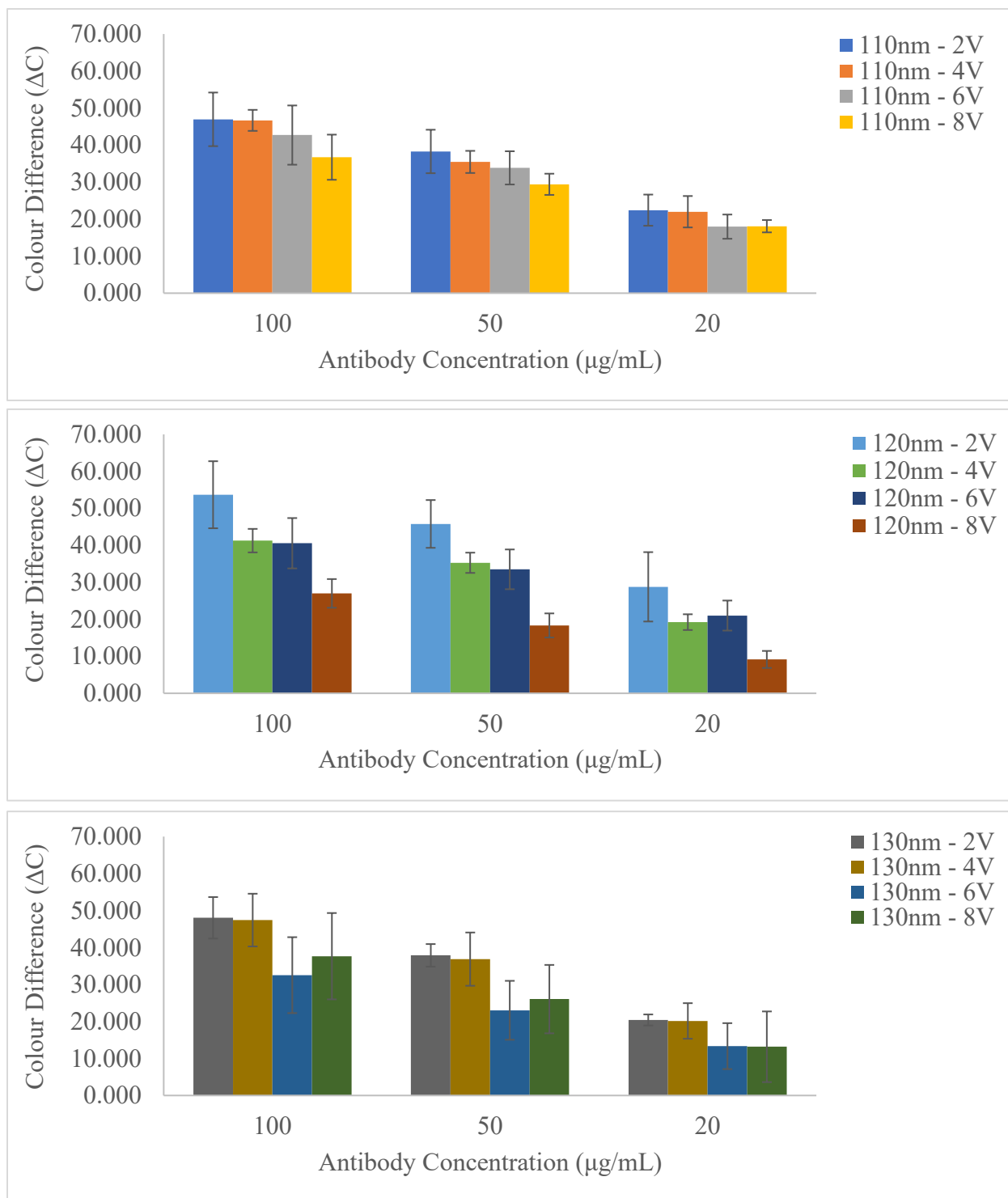


Figure 5-6. Colour differences recorded from RGB analysis of protein adsorption studies on anodized aluminum-tantalum thin films with aluminum sputtered at various thicknesses and anodized under various voltages in 0.4M phosphoric – 0.1M oxalic acid. Sample size of  $n=3$  for all data sets.

Table 5-13. Statistical results for a one-way ANOVA performed on colour differences from various concentrations of antibody exposed to anodized aluminum-tantalum thin films with various aluminum thicknesses and anodized under voltages in 0.4M phosphoric – 0.1M oxalic acid. The number indicates the concentration of antibody exposed to the surface in  $\mu\text{g/mL}$ , i.e. 100 vs. 50 is  $\Delta C(100\mu\text{g/mL})$  vs.  $\Delta C(50\mu\text{g/mL})$ .

<b>Aluminum Thickness and Anodizing Voltage</b>	<b>ANOVA p-value</b>	<b>Post hoc Test Results</b>
110 nm, 2V	P<0.01	100 vs. 20: p<0.01 50 vs. 20: p<0.05
110 nm, 4V	P<0.001	100 vs. 50: p<0.05 100 vs. 20: p<0.01 50 vs. 20: p<0.01
110 nm, 6V	P<0.01	100 vs. 20: p<0.01 50 vs. 20: p<0.05
110 nm, 8V	P<0.01	100 vs. 20: p<0.01 50 vs. 20: p<0.05
120 nm, 2V	P<0.05	100 vs. 20: p<0.05
120 nm, 4V	P<0.001	100 vs. 50: p<0.10 100 vs. 20: p<0.001 50 vs. 20: p<0.001
120 nm, 6V	P<0.05	100 vs. 20: p<0.05 50 vs. 20: p<0.10
120 nm, 8V	P<0.01	100 vs. 50: p<0.05 100 vs. 20: p<0.01 50 vs. 20: p<0.05
130 nm, 2V	P<0.001	100 vs. 50: p<0.05 100 vs. 20: p<0.001 50 vs. 20: p<0.01
130 nm, 4V	P<0.01	100 vs. 20: p<0.01 50 vs. 20: p<0.05
130 nm, 6V	P<0.10	100 vs. 20: p<0.10
130 nm, 8V	P<0.10	100 vs. 20: p<0.10

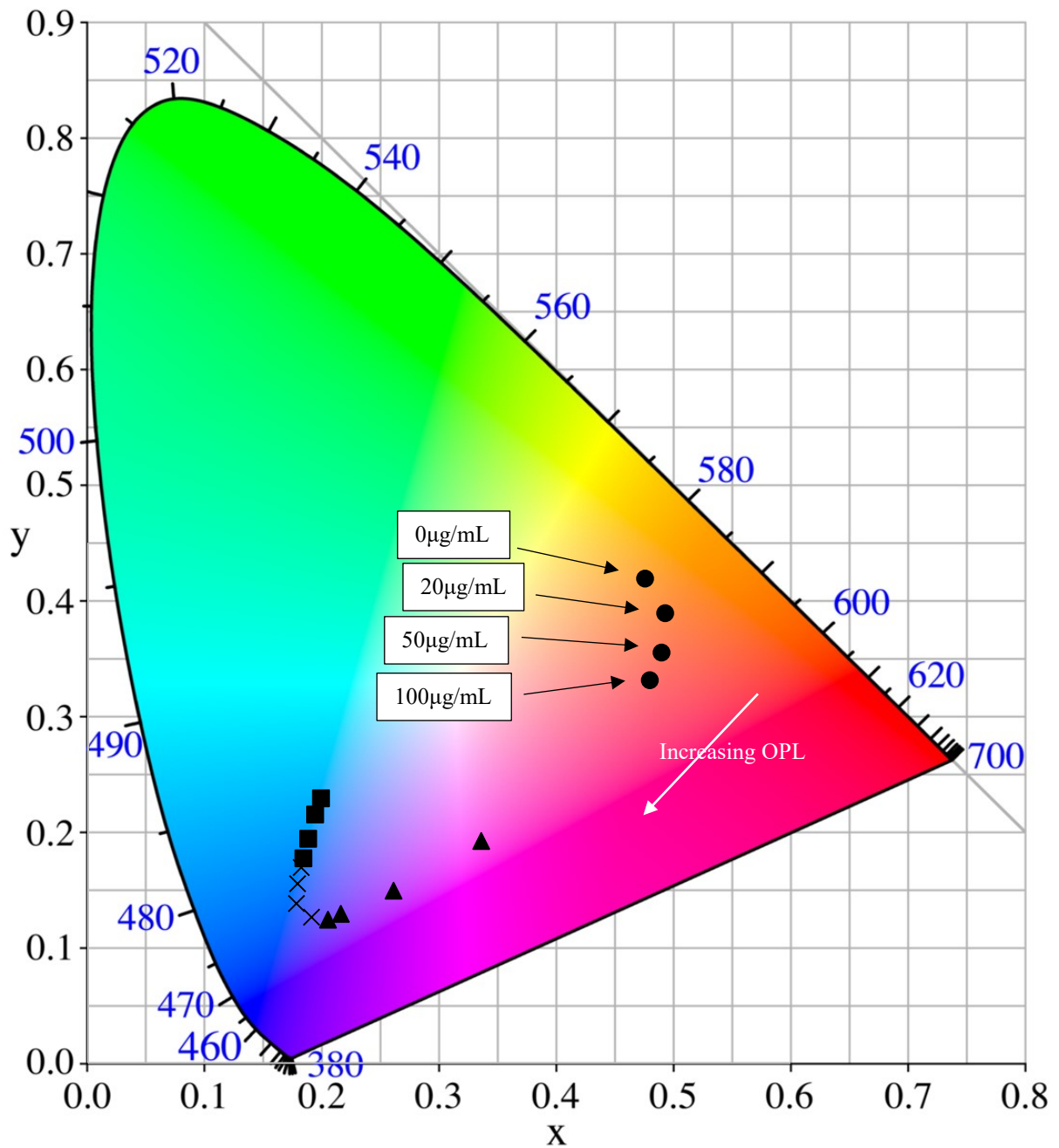


Figure 5-7. 1931 CIE colour diagram of average colour shift from films with prothrombin and either 100, 50, 20 or 0  $\mu\text{g}/\text{mL}$  of anti-prothrombin antibody. With films of 120nm aluminum, and anodized at 2V ( $\bullet$ ); 4V ( $\blacktriangle$ ), 6V (X), 8V ( $\blacksquare$ ). OPL stands for optical path length.

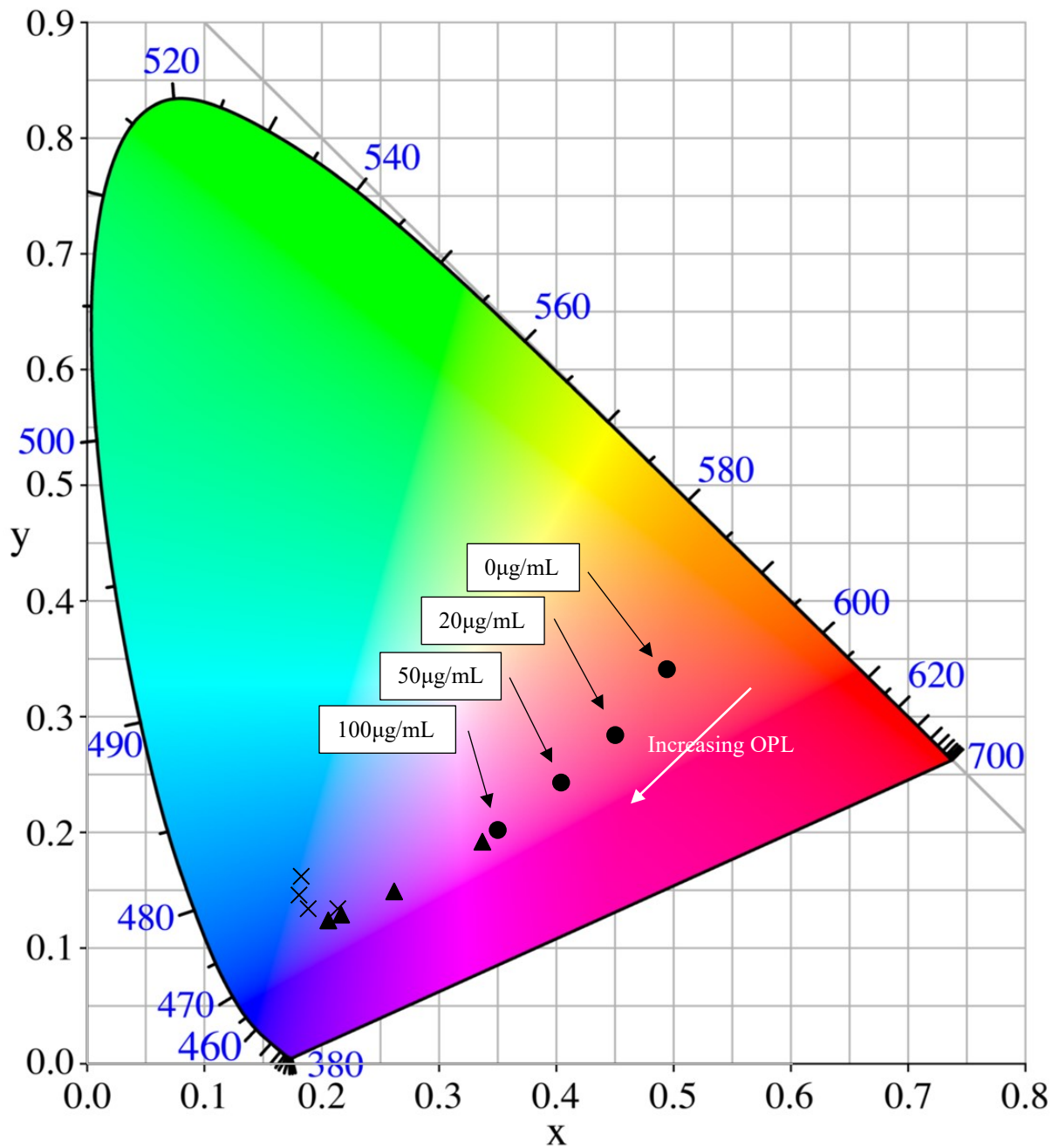


Figure 5-8. 1931 CIE colour diagram of average colour shift from films with prothrombin and either 100, 50, 20, or 0  $\mu\text{g}/\text{mL}$  of anti-prothrombin antibody. With films anodized at 4V in 0.4M phosphoric acid 0.1M oxalic acid and initial aluminum thickness of 110nm ( $\bullet$ ), 120nm ( $\blacktriangle$ ) and 130nm (X). OPL stands for optical path length.

## Discussion

Overall this study showed that, with the model prothrombin/anti-prothrombin system, certain aspects of the nanostructure of the anodized aluminum-tantalum thin films have a significant effect on the colours produced for an immunoassay. The deposited tantalum and aluminum microstructure showed little effect on the sensitivity of the immunoassay, however anodizing conditions and the thickness of the starting aluminum had significant effects.

Reducing tantalum reflectance by 10% through deposition parameters had no effect on the sensitivity of detecting protein on the thin film surface. Charlesby and Polling [10] discussed interference colours produced by thin oxide films in detail. The interference colour from an oxide film depends strongly on the reflectivity at the air/oxide interface. A saturated colour arises when the light reflected at the air/oxide interface matches the intensity of light reflected at the oxide/metal interface. As discussed in Chapter 1, tantalum produces strong interference colours because it has a relatively low reflectivity for light in the visible wavelengths, around 50% as shown in Chapter 2, which allows for a balance of intensities off the two interfaces. It was expected that by reducing the reflectivity of the tantalum via a microstructural shift, the interference colours produced by adsorbed protein would strengthen. As the amount of protein on the surface decreases, less light is reflected at the air/protein interface and thus the intensity of light reflected off the oxide/metal interface must be reduced to rebalance the light intensities, see Figure 5-9. However, there appears to be no effect on the colour difference from adsorbed protein as the tantalum reflectivity is reduced from 50 to 40% by increased sputtering pressures. The lack of any observable effect may be due to a minimal drop in reflectivity (only 10%), and therefore not enough to balance the intensities off the two surfaces. However, it is possible that the sensitivity limit for detecting low surface concentrations of protein does not come about because of

mismatched light intensities, but because of mismatched refractive indices between the sparse protein layer and the porous aluminum oxide.

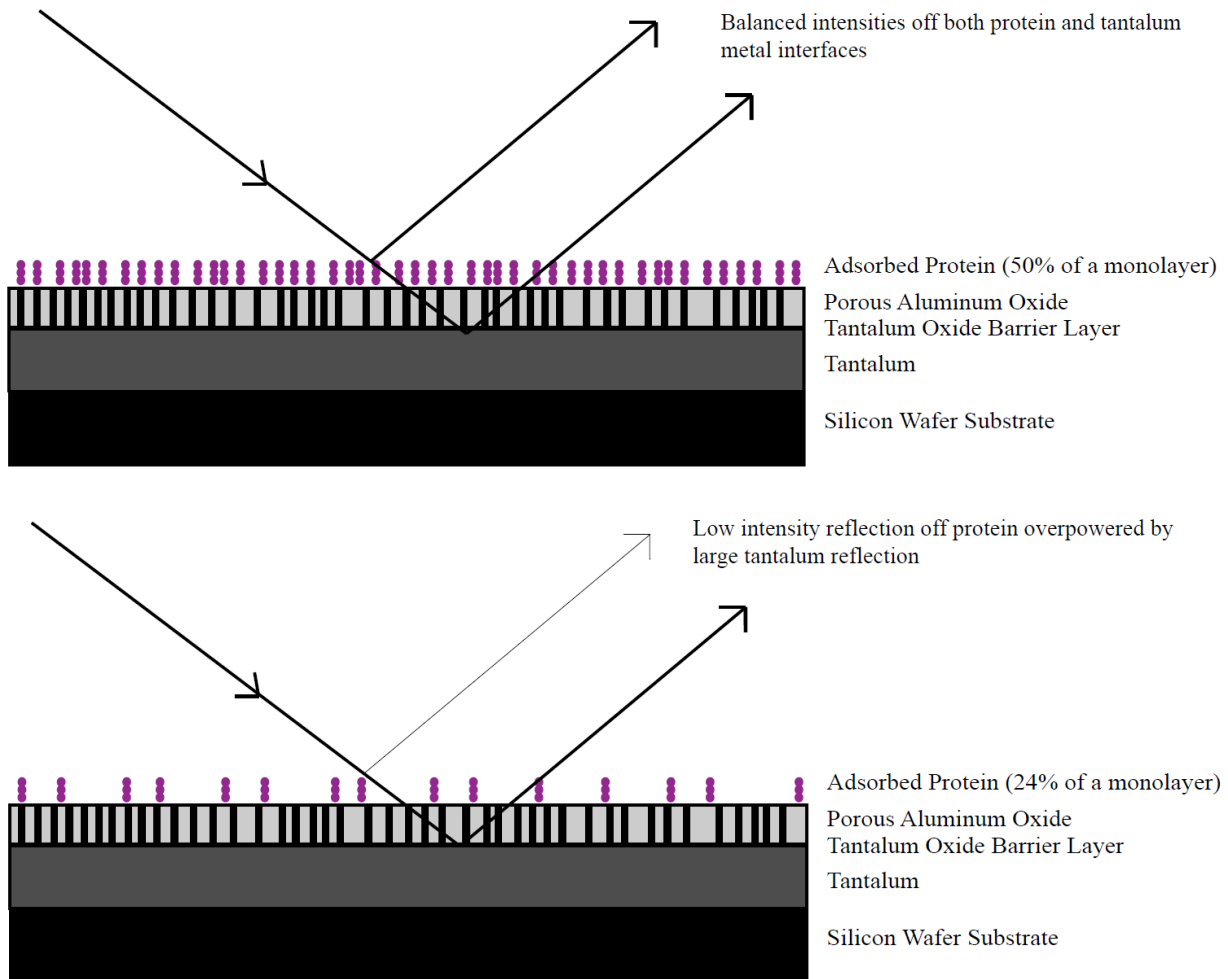


*Figure 5-9. Cartoon depiction of light reflections with high and low protein surface density. The intensity of the light reflected off the protein layer reduces as less protein is adsorbed, and leads to a mismatch in reflections between the light off the tantalum metal and the protein. It was hypothesized that reducing tantalum metal reflectivity may help with detecting lower protein concentrations, however this study showed that lower tantalum metal reflectivity did not improve sensitivity and therefore this hypothesis is not true.*

Previous works have shown that the refractive index of an adsorbed protein layer is dependent on the density of the adsorbed protein, which is determined by various factors such as protein size and composition, solvent, and material surface properties [11]. The lowest concentration of

prothrombin used in this study was 10  $\mu\text{g/mL}$ , which equates to 2.78 picomoles in a 20 $\mu\text{L}$  drop. If we assume prothrombin takes up an area of 4nm x 4nm on the surface (diameter of prothrombin [9]), we can estimate how many molecules would be required to create a monolayer for a 1cm diameter circle. Assuming 100% coverage and a perfectly flat surface this amounts to 8.15 picomoles, a high estimate considering the surface tends to be around 50% porous (look to Chapter 4 results). Sweet [8] found that 71% of prothrombin in a 20  $\mu\text{L}$  drop of 0.009 mg/mL adsorbs to an anodic alumina surface in 15 minutes. Therefore, if we assume 71% of the 2.78 picomoles adsorbs (1.97 picomoles) then we only have 48% coverage of the surface or 24% of a full monolayer of protein at the lowest prothrombin concentration. The refractive index of the protein layer will be a composite between air and protein. This composite refractive index may be calculated as shown in Equation (5.2):

$$\eta = (1 - x)\eta_{protein} + x\eta_{air} \quad (5.2)$$

Where  $x$  is the porosity of the protein layer,  $\eta$  is the composite refractive index of the protein/air layer,  $\eta_{protein}$  is the refractive index of the protein (typically  $\sim 1.6$  [12]), and  $\eta_{air}$  is the refractive index of air (ie.  $\sim 1$ ). Using this equation and a refractive index of 1.6 for prothrombin, the composite refractive index can be calculated for each protein layer. Figure 5-10 shows the theoretical surface density and refractive index for prothrombin adsorbed at high (i.e. 1mg/mL) and low (i.e. 0.01 mg/mL) surface densities. As the protein becomes sparser on the surface there is a mismatch introduced between the refractive index in the visible spectrum of the porous alumina layer ( $\eta = \sim 1.3$ ) and the protein layer ( $\eta = \sim 1.14$ , 24% of a monolayer of protein). This mismatch would introduce another reflection at the alumina/protein interface, which could now be acting as noise in the system and become the limiting factor for sensitivity. As shown in Parts C and D, the electrolyte and voltage can be used to tune the porous alumina refractive index to

optimize the colour shift. Theoretically, it may be possible to reduce the refractive index further by lowering the voltage during anodization such that lower protein concentrations can be detected on the surface.

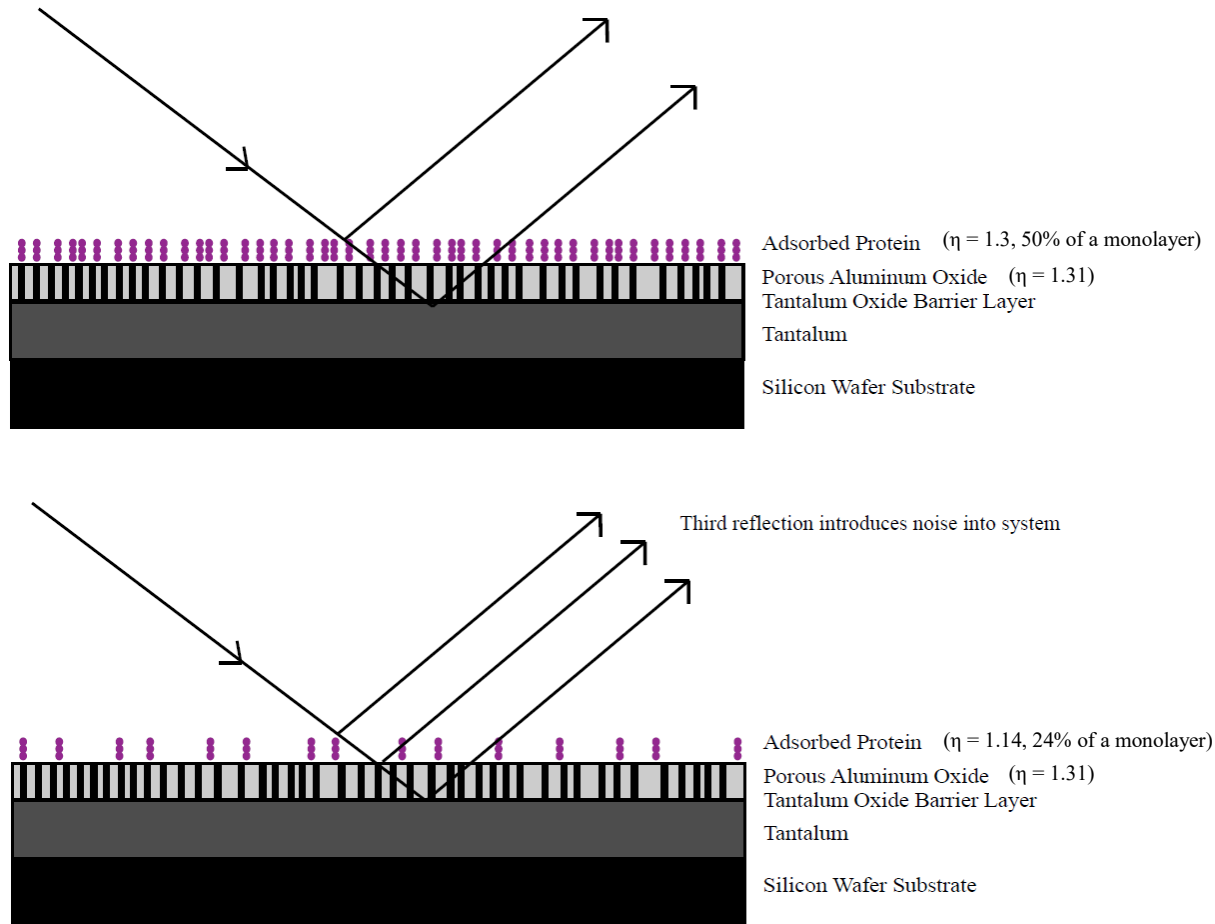
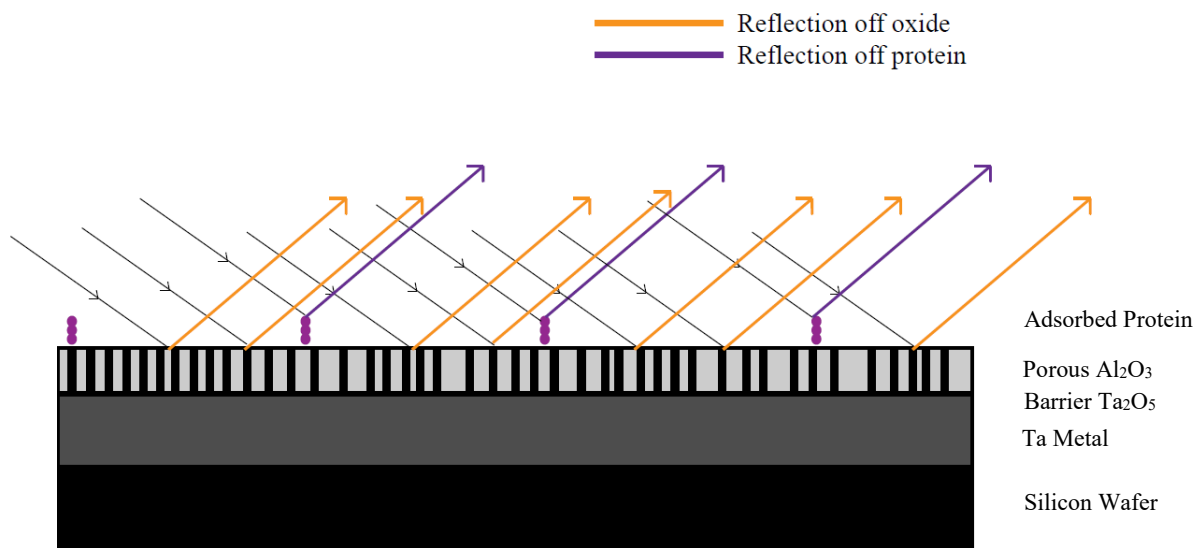


Figure 5-10. Cartoon depiction of how light interacts with protein adsorbed to the surface at high and low surface densities. The low surface density has a reduced refractive index because the composite refractive index consists of more air. The mismatch in refractive indices between the alumina and protein layer causes another reflection at the protein/alumina interface, which can act as noise in the system. The refractive indices were calculated using Equation (5.2) and either 50 or 24% of a monolayer of protein.

On the other hand, there may be a limit at which there is so little protein adsorbed to the surface that the light which interacts with it to produce an interference colour is simply overpowered by the light interacting with the alumina surface, see Figure 5-11. It is not understood at what point the protein layer stops behaving as a composite refractive index and only as individual proteins. It

may be possible to simulate all this by computer software. Recommended future work is to experiment with a multi-physics simulation software, such as COMSOL Multiphysics®, to gain a better understanding of the optics.



*Figure 5-11. Cartoon depiction of how light may interact with a sparsely, prothrombin coated surface of alumina. The majority of light reflects off the aluminum oxide surface and interferes with light off the tantalum metal to produce orange, while a relatively small portion of light reflects off the adsorbed prothrombin to produce purple. Note the light reflecting off the tantalum metal is not shown in this diagram for simplicity.*

An interesting discovery from this first set of experiments was that a protein (prothrombin) could be adsorbed to the surface in such low quantities that no colour shift is observed, and then the antibody could be exposed to the surface and bind to create a visible colour shift. As the density and height of the adsorbed protein layer increased from the binding antibody, there was a significant enough change in the optical path length that the adsorbed layer became visible, see Table 5-4. This knowledge could be useful in designing tests where a ‘just noticeable’ effect is required for positive results.

The aluminum microstructure had slightly more effect on the sensitivity of the assay compared to tantalum, however differences were still found to be minimal within the parameters tested. It appeared that lower pressures were generally better to observe differences in the amount of adsorbed antibody. This could be due to the microstructural differences found in Chapter 3. Films sputtered at lower pressures had less pitting and more uniform surfaces after anodization than those sputtered at higher pressures. The 5 and 9 W/cm<sup>2</sup> films at 1 mTorr were the densest structures and produced smooth surfaces post-anodization with little pitting. This could contribute to their ability to better distinguish between various concentrations of adsorbed antibody. For example, Nagata et al. [13] found that increasing the surface roughness of sputtered aluminum films from 5.5 to 10.5 nm reduced interference colour effects from a thin resist film on the sputtered aluminum. Therefore, when observing Thornton's diagram [14] (see Figure 1-8), the Zone T and 2 structures appear to be the best starting structure for homogenous anodization and thus improve the interference effects from adsorbed protein layers. However, overall the differences in strength of colour change were insignificant between each microstructure and this is probably due to the low variation in the optical properties. Chapter 3 of this work found that the refractive index varied by no more than 1.9% for each structure after anodization. Since matching of the protein and alumina film refractive indices is a key parameter for sensitivity, the low variation in refractive index explains why minimal change was found between protein detection on the various microstructures.

Another important parameter is the film thickness and starting optical path length. As discussed in Chapter 1, higher order interference colours are less sensitive to changes in film thickness. Interference colours follow a very specific order. Sandström et al. [15] plotted the order of interference colours on a 1931 CIE Standard Observer colour diagram, see Figure 5-12. The colours start in white and then progress in a circular pattern from yellow around to purple and blue,

and then back to yellow. Eventually, the colours start to flip back and forth through green and pink. The most sensitive colour shifts to changes in optical path length are found in the first order colour regime from yellow over to second order purple, see the dot spacing in Figure 5-12. The films sputtered at 0.9 W/cm<sup>2</sup> and 1 mTorr had the highest starting optical path length (OPL) due to their thickness post-anodization (OPL =  $\eta d$ ,  $\eta$  is refractive index and  $d$  is physical path length). Therefore, the reduced sensitivity from these films compared to the 5 and 9 W/cm<sup>2</sup> films could be due to the higher order interference colour.

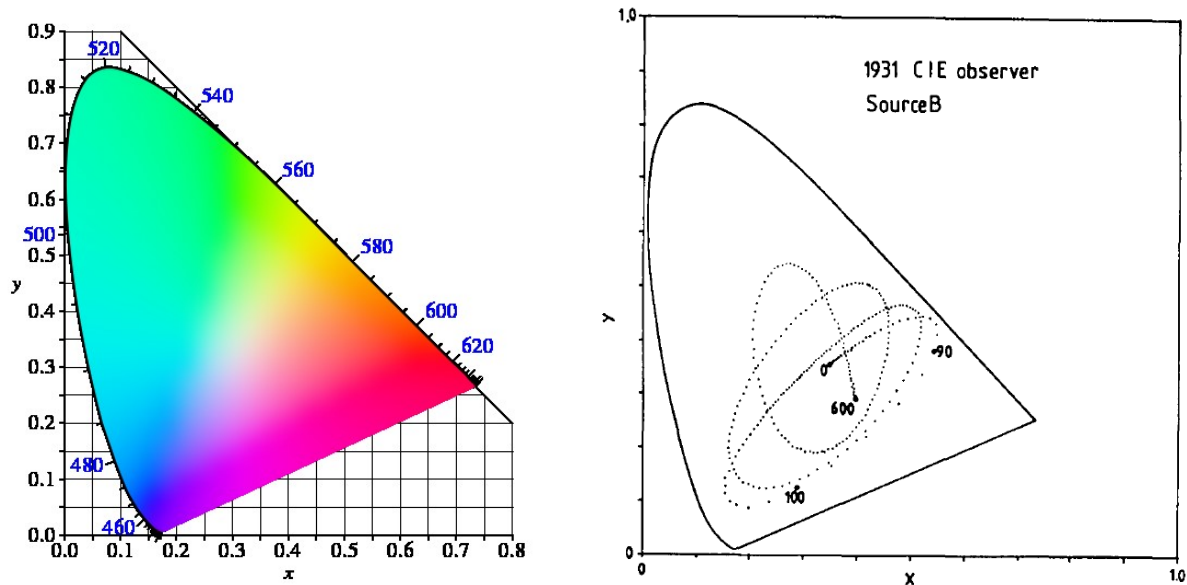


Figure 5-12. Left: CIE 1931 colour space chromaticity diagram [16]; Right: Chromaticity coordinates for the interference colours produced from a dielectric layer ( $\eta=1.5$ ) over a substrate ( $\eta=2.25$ ). Each spot is an increase in the dielectric layer thickness with increments of 2nm from 0 to 600nm [15].

From Part C, a few things can be understood about the sensitivity of these films to detecting adsorbed proteins and how the electrolyte can be tailored to improve sensitivity. Films that showed the greatest colour differences started out tan or yellow before protein was adsorbed. Once the second order interference colours were reached (purple and blue) the difference in colour was

found to be more difficult to discern. This is due to the reduced sensitivity with higher order colours, as discussed earlier. Once more wavelengths can interfere, constructively or destructively, due to a thicker film, the multiple interferences can act as noise in the system and reduce the sensitivity. The amount of oxalic acid added to the anodization bath effects the final microstructure and refractive index, as shown in Chapter 4.1. Increasing the amount of oxalic acid reduces the etching caused by phosphoric acid during anodization and leads to thicker, more homogeneous films with higher refractive indices and lower surface roughness. For example, films anodized in 0.4M phosphoric acid at 4V had refractive indices of  $1.258 \pm 0.008$ , however, with the addition of 0.1M or 0.4M oxalic acid, the refractive index increased to either  $1.319 \pm 0.004$  or  $1.359 \pm 0.004$  respectively. When using Equation (5.2) the refractive index of an adsorbed IgG layer can be calculated at approximately  $\eta=1.3$  (50% air, 50% protein with  $\eta_{\text{protein}}=1.6$ ). Therefore, the films anodized with 0.1M oxalic acid showed the strongest analytical sensitivity and lowest detection limits due to the best match of refractive index between the protein and alumina layers.

The 0.4M phosphoric acid films showed significant colour differences at  $20\mu\text{g/mL}$  for 120 and 130nm of Al, however the colour showed a reduced optical path length with respect to the spot with adsorbed prothrombin, see Figure 5-5. To test if this was related to colour variation across the wafer, the colour of the anodized aluminum-tantalum film was measured on each side of the wafer. The 120nm films anodized in 0.4M phosphoric acid had nearly double the colour differential across the wafer than 120nm films anodized in the 0.4M phosphoric – 0.1M oxalic acid mix when taken under similar lighting conditions,  $\Delta C = 17.24 \pm 1.02$  vs.  $\Delta C = 8.94 \pm 1.18$  respectively. The 0.4M phosphoric acid films showed significantly higher variability in colour across the wafer ( $p<0.001$ ), which accounts for the colour differences from the  $20\mu\text{g/mL}$  antibody spots. The experiment was conducted such that the prothrombin coated area was on the opposite

side of the wafer as the prothrombin – anti-prothrombin coated area; therefore, differences in the initial prothrombin colour are likely due to occur simply due to variation in colour of the wafer surface. As discussed above, the lack of an inhibitor, such as oxalic acid, in the electrolyte leads to a higher dissolution rate of alumina during anodization and less homogeneous surfaces. This variation would make quality control in mass manufacturing very difficult and is a strong reason to use the inhibited films over non-inhibited. Since the sensitivity, detection limit, and colour homogeneity were all greatest for 0.4M phosphoric – 0.1M oxalic acid anodized films, these were used for Part D.

Part D showed how these anodic thin films can be tuned to create optimal colour shifts for a certain antibody-antigen reaction. A base colour of yellow or tan, before protein adsorption, produced the most easily visible shifts. This result appears to align with the work of Sandström et al. [15] who found that thickness changes are most noticeable in the tan to purple region of first order interference colours when adsorbing organic films on silicon dioxide. Figures 5-7 and 5-8 show how increasing the thickness and voltage both increase the optical path length of the interference colours produced, progressing in a circular pattern in the CIE colour diagrams similar to that shown in Figure 5-12. The optical path length is a function of both physical film thickness and refractive index ( $OPL = \eta d$ , where  $\eta$  is refractive index and  $d$  is physical path length). As found in Chapter 4, increasing voltage raises the refractive index of the alumina film, thereby increasing the optical path length. Films that showed the strongest colour changes were anodized at either 2 or 4V. These films have refractive indices of  $\sim 1.22$  (2V) and  $\sim 1.31$  (4V), compared to the higher refractive indices found for 6 and 8V of  $\sim 1.35$  and  $\sim 1.39$  respectively. The lower refractive index better matches the optical properties of the protein layer, as a refractive index of  $\sim 1.3$  was found for a layer of 50% air and 50% protein using Equation (5.2).

Note how the detection limit was lower for Part D than Parts A through C, 20  $\mu\text{g}/\text{mL}$  vs. 50  $\mu\text{g}/\text{mL}$  respectively. The use of LoBind Eppendorf<sup>TM</sup> tubes for storing antibody solutions helped reduced adherence of IgG to the wall of the container, thereby increasing the amount available for binding to the thin film surface. These polypropylene tubes are commonly used in proteomic and genomic studies to reduce adsorption of the biological sample to the container surface.

It was also noted that for  $0.2 < x < 0.5$  in  $Y_{xy}$  colour coordinates, the largest differences in colour occurred with increased antibody concentration, see Figures 5-7 and 5-8. We can conclude that, for optimal sensitivity, future tests should all be designed considering two critical aspects: (1) the thickness must be deposited such that the immunoassay is run in the first order x-colour coordinate range of 0.2 to 0.5; (2) the refractive index of the porous alumina must be tailored, preferably by adjusting voltage or electrolyte, so that the alumina layer has identical optical properties as the protein layer.

Overall, sensitivity compared well with previous works and may have shown improvement over previous anodized aluminum-tantalum thin films. Sweet [8] showed how aluminum-tantalum films anodized in 0.4M phosphoric acid at 8V have a limit of 25  $\mu\text{g}/\text{mL}$  when tested under similar conditions as this study (20  $\mu\text{L}$  of anti-prothrombin on a 1cm diameter prothrombin coated, circular area). This work found 20  $\mu\text{g}/\text{mL}$  produced a strong colour shift and it is hypothesized that smaller concentrations would still produce a shift. Assuming a molecular weight of 150 kDa for IgG, this is a detection limit of 133nM, or more appropriately, 850  $\text{fmol}/\text{cm}^2$  (assuming perfectly flat surface, 1cm diameter circle, and all protein in 20  $\mu\text{L}$  solution binds to the surface). It is important to note that sensitivity limits of these films should not be determined as a weight per volume or molar basis, since it is surface saturation that is most important to establish a colour difference. For example, the surface could be exposed to a higher volume of solution at a lower concentration

and still produce a colour shift. In such cases, the limiting factor would be the antigen-antibody affinity and their association/dissociation constants.

Future work should expand on this study by exposing surfaces to larger volumes of solution at lower IgG concentrations. This work also does not show limits of specificity and the affinity of an antibody for an antigen. Many factors affect antigen-antibody affinities including, temperature, pH, ionic strength, the solvent medium, duration of incubation, antigen surface density and steric availability of epitopes [17, 18, 19, 20]. The aspect of antigen surface density is addressed in Chapter 5.2, however much more work needs to be done to better define antigen-antibody binding kinetics on an alumina surface.

## **Conclusion**

This work helped to understand the effects of microstructure on an immunoassay based on thin film interference of anodized aluminum-tantalum thin films. The following conclusions were found:

- 1) Reducing the tantalum reflectivity by adjusting the sputtered microstructure did not significantly improve the colour differences from adsorbed protein layers.
- 2) The sputtered microstructure of the aluminum film does not create significant differences in detection limits. However, it appears that sputtering at lower pressures to produce optically flat films post-anodization may help with analytical sensitivity and determining differences in surface protein concentrations.
- 3) The electrolyte controls surface microstructure and refractive index. The sensitivity for detecting adsorbed protein layers can be increased by changing the electrolyte, with 0.4M

phosphoric – 0.1M oxalic acid mixtures showing the best sensitivity over 0.4M phosphoric acid or a 0.4M phosphoric – 0.4M oxalic acid mix, when anodized at 4V.

4) Films anodized with an oxalic acid additive showed less variation of colour across a 10mm diameter wafer, which led to higher sensitivity and reproducibility of colour from adsorbed protein layers compared to those anodized without additive.

5) For best sensitivity, the thickness of the sputtered aluminum layer must be controlled to produce films which will move through first order interference colours when protein is adsorbed (approximately,  $0.2 < x < 0.5$  in Yxy colour coordinate system). This must be combined with matching the refractive index of the alumina layer with the protein layer, preferably through changes in voltage or electrolyte.

## References

[1] R. E. Burrell, A. G. Naylor and A. M. Rosenfeld, "Thin Film Diagnostic". US Patent 5,124,172, 23 June 1992.

[2] T. R. Holford, F. Davis and S. P. Higson, "Recent trends in antibody based sensors," *Biosensors and Bioelectronics*, vol. 34, pp. 12-24, 2012.

[3] R. Burns, "Immunochemical techniques," in *Principles and Techniques of Biochemistry and Molecular Biology*, New York, NY, University Cambridge Press, 2010, pp. 263-299.

[4] B. Bryne, E. Stack, N. Gilmartin and R. O'Kennedy, "Antibody-Based Sensors: Principles, Problems and Potential for Detection of Pathogens and Associated Toxins," *Sensors*, vol. 9, pp. 4407-4445, 2009.

[5] D. A. Walz, D. Hewett-Emmett and W. H. Seegers, "Amino acid sequence of human prothrombin fragments 1 and 2," *Proceedings of the Natural Academy of Sciences USA*, vol. 74, no. 5, pp. 1969-1972, 1977.

[6] M. Huang, A. C. Rigby, X. Morelli, M. A. Grant, G. Huang, B. Furie, B. Seaton and B. C. Furie, "Structural basis of membrane binding by Gla domains of vitamin K-dependent proteins," *Nature Structural Biology*, vol. 10, no. 9, pp. 751-756, 2003.

[7] R. E. Burrell, "Aluminum Oxide Surfaces and Interface Molecules". Provisional Patent. Filed Feb. 20, 2018.

- [8] H. Sweet, *Development of a Thin Film Device and Optics System for Protein Detection*, Edmonton, AB: University of Alberta, 2018.
- [9] K. Wilson, "Basic Principles," in *Principles and Techniques of Biochemistry and Molecular Biology*, Seventh Edition, New York, NY, Cambridge University Press, 2010, pp. 1-37.
- [10] A. Charlesby and J. J. Polling, "The Optical Properties of Thin Oxide Films on Tantalum," *Proceedings of the Royal Society of London. Series A, Mathematical and Physical Sciences*, vol. 227, pp. 434-447, 1955.
- [11] J. Vörös, "The Density and Refractive Index of Adsorbing Protein Layers," *Biophysical Journal*, vol. 87, pp. 553-561, 2004.
- [12] T. L. McMeekin, M. L. Groves and N. J. Hipp, "Refractive Indices of Amino Acids, Proteins, and Related Substances," in *Amino Acids and Serum Proteins*, Philadelphia, American Chemical Society, 1964, pp. 54-66.
- [13] H. Nagata, A. Yamaguchi and A. Kawai, "Characterization of Thin-Film Interference Effect due to Surface Roughness," *Japan Journal of Applied Physics*, vol. 34, pp. 3754-3758, 1995.
- [14] J. A. Thornton, "Influence of apparatus geometry and deposition conditions on the structure and topography of thick sputtered coatings," *Journal of Vacuum Science & Technology*, vol. 11, pp. 666-670, 1974.
- [15] T. Sandström, M. Stenberg and H. Nygren, "Visual detection of organic monomolecular films by interference colors," *Applied Optics*, vol. 24, no. 4, pp. 472-479, 1985.
- [16] R. G. Ben, "1931 Colour Space," Wikipedia, [Online]. Available: <https://commons.wikimedia.org/w/index.php?curid=7889658>. [Accessed 18 June 2018].
- [17] R. Reverberi and L. Reverberi, "Factors affecting the antigen-antibody reaction," *Blood Transfus*, vol. 5, pp. 227-240, 2007.
- [18] B. Demeule, S. J. Shire and J. Liu, "A therapeutic antibody and its antigen form different complexes in serum than in phosphate-buffered saline: A study by analytical ultracentrifugation," *Analytical Biochemistry*, vol. 388, pp. 279-287, 2009.
- [19] M. Hadzhieva, A. D. Pashov, S. Kaveri, S. Lacroix-Desmazes, H. Mouquet and J. D. Dimitrov, "Impact of Antigen Density on the Binding Mechanism of IgG Antibodies," *Scientific Reports*, vol. 7, p. 3767, 2017.
- [20] H. Nygren, M. Werthen and M. Stenberg, "Kinetics of antibody binding to solid-phase-immobilised antigen," *Journal of Immunological Methods*, vol. 101, pp. 63-71, 1987.

## 5.2 The Effect of Antigen Size and Surface Density on a Visual Immunoassay Based on Anodized Aluminum-Tantalum Thin Films

### **Introduction**

The specificity of antibody – antigen interactions are vital to the successful use of immunoassays, whether in solution or for thin film diagnostics. Antibodies are recognition molecules of the adaptive immune system designed to identify antigens and contain as few as 2 and as many as 10 identical antigen binding sites [1]. Immunoglobulin G (IgG) is a Y-shaped antibody that contains 2 antigen-binding sites on the Fab (fragment of antigen-binding) arms. The bottom fragment is known as the Fc arm (fragment crystallisable or fragment constant). IgG is commonly used in immunoassays for the detection of specific biological markers.

An important factor of immunoassays developed on solid-liquid interfaces, varying from assays in solution, is the antigen surface density and the steric interactions of antibodies and antigens at the solid surface. For example, Hadzhieva et al. [2] showed how antigen surface density has significant effects on the binding of low affinity antibodies compared to high affinity antibodies. They found that low affinity antibodies tend to have significantly lower dissociation constants at higher antigen surface densities, due to the binding of both antibody arms. An antibody only has a reach of around 150 Å between the two arms, and higher antigen spacing allows only one arm to bind. On the other hand, Nygren et al. [3] found that antibody binding to a surface is limited from steric interactions between bound antibodies. In their study, they found that the rate of binding antibodies to an immobilized antigen decreases suddenly around 1.5 pmol/cm<sup>2</sup> of bound antibody. This correlated with a distance between antibody molecules of 10 nm, about the molecular diameter of IgG. Therefore, further binding would be prevented by steric effects. Another issue that could limit antibody binding is too high of an antigen surface density. If antigens were packed very close

together, then only certain epitopes would be available to bind. Certain antibodies may have an increased capacity to bind due to spacing of the antigens, which opens more epitopes for recognition.

Nygren et al. [4] discussed the importance of antigen surface concentration on the detection limit for thin film diagnostics based on silicon dioxide films on silicon. Their hypothesis was that a certain level of bound antibody or antigen must exist before a colour change could be visualized. Sweet [5] confirmed this for protein immobilized on anodized aluminum-tantalum thin films. Using a radiolabel, it was found that approximately 34-38% surface area coverage was required to produce a visible colour shift for immobilized prothrombin.

This study used prothrombin as a model system for detecting antibody-antigen reactions at an anodized aluminum-tantalum thin film surface. Table 5-12 shows the molecular weight and dimensions of prothrombin, fragment 1 and IgG antibody. The size of these molecules will change the colour of a thin film diagnostic surface by differences in the optical path length, as discussed in detail in Chapter 1.

*Table 5-14. The molecular weight and dimensions of human prothrombin, fragment 1 and IgG antibodies.*

<b>Protein</b>	<b>Molecular Weight (kDa)</b>	<b>Dimensions (Å)</b>
Human Prothrombin (II)	72 [6]	110 x 38 x 38 [6]
Human Fragment 1 (F1)	23 [6]	15 x 30 x 35 [10]
Immunoglobulin G [anti-prothrombin (AII) or anti-thrombin (AT)]	150 [11]	142 x 85 x 38 [11]

The purpose of this work was to test the sensitivity of a binding antibody when the spacing of a surface-bound antigen is adjusted on an anodized aluminum-tantalum thin film. Prothrombin,

fragment 1 and anti-human thrombin IgG were used as a model system. Prothrombin was adsorbed to the surface in a mixture with fragment 1 at varying concentrations. Prothrombin is a 3-segment protein consisting of thrombin, fragment 2 and fragment 1, see Figure 5-9 [6, 7]. Fragment 1 is the first 156 residues of prothrombin and contains a GLA domain consisting of 10  $\gamma$ -carboxyglutamic acid residues which bind strongly to aluminum oxides and help with oriented binding on an alumina surface [8, 9]. Since both prothrombin and fragment 1 contain the GLA domain, both will bind strongly to alumina. The smaller fragment 1 can therefore act as a spacer between prothrombin molecules immobilized on the surface. The sensitivity of anti-human thrombin IgG was then tested by analyzing the associated colour changes of the thin film surface. Anti-thrombin antibody was used since it will not recognize sites on fragment 1 and will only recognize the top of prothrombin.

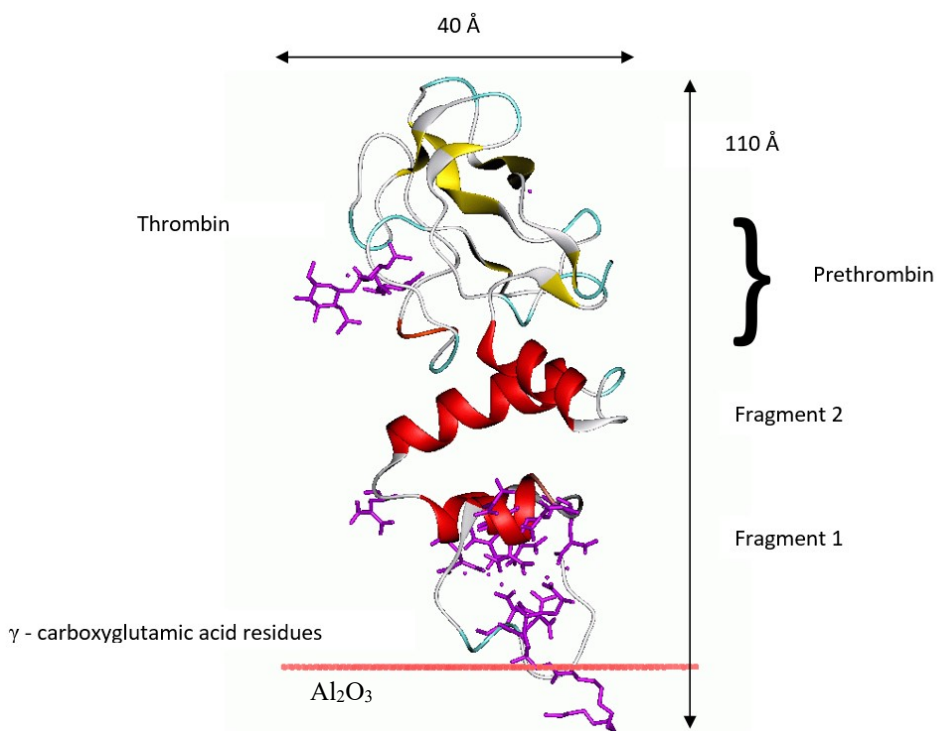


Figure 5-13. A schematic diagram of the 3-dimensional structure of prothrombin and its binding orientation on an aluminum oxide surface (modified from [9]; molecular dimensions from [6]).

## Materials and Methods

### *Materials*

All anodized aluminum-tantalum thin films were provided by Prominent Medical Inc. (Edmonton, AB). Tantalum thin films of  $226.5 \pm 3.8$  nm were sputtered onto unprocessed <100> silicon wafers (University Wafers, South Boston, MA) 100 mm in diameter. This was followed by an aluminum deposition of 120 nm where the thickness was within  $\pm 2$  nm. Deposition conditions were the same as those in Part A of Chapter 4.2. Wafers were anodized using a 0.4M phosphoric and 0.1M oxalic acid mixture at 4V, as described in Chapter 4.1.

All proteins and antibodies were acquired from Aniera Diagnostica, LLC (West Chester, OH), from the A-CoA division: Human prothrombin, purified protein (SKU #: PT-1099T), human fragment 1 (SKU #: PT1-1099T), anti-human prothrombin, sheep, affinity purified IgG (SKU #: PT-1030B), anti-human thrombin, sheep, affinity purified IgG (SKU #: THR-1030B). Prothrombin and fragment 1 were stored in tris buffered saline (TBS), pH 7.4, and the antibodies, anti-prothrombin and anti-thrombin, were stored in phosphate buffered saline (PBS), pH 7.4. Prothrombin and fragment 1 were not stored in PBS since phosphate adsorbs strongly to an alumina surface and can reduce the effectiveness of binding between these proteins and the surface. All antibodies were purchased in a 50% glycerol solution and were therefore dialyzed overnight in PBS, pH 7.4, using a Micro Float-A-Lyzer<sup>®</sup> (Spectrum Laboratories Inc., Rancho Dominguez, CA) before use. All experiments were conducted in triplicate to measure reproducibility.

### *Methods - Protein Adsorption*

#### Part A – Fragment 1, Prothrombin, Anti-prothrombin and Anti-thrombin

To understand the changes in interference colouring that occurs from molecules of different sizes, human prothrombin and fragment 1 were adsorbed to the thin film surface in equimolar quantities

and their colours recorded after washing and drying the slides. Afterwards, polyclonal anti-prothrombin and anti-thrombin IgGs were placed on the spots previously coated with prothrombin or fragment 1. The two antibodies were used to check the affinity of each antibody for each antigen, and act as a specificity test for the device to different antigens. Fragment 1 does not contain the thrombin domain and therefore it was hypothesized that the anti-thrombin would not show a colour change for spots coated with fragment 1, whereas anti-prothrombin would recognize epitopes in both antigens. The experimental design is shown in Table 5-15.

Circles of 1 cm diameter were then drawn on an anodized aluminum-tantalum coated wafer using a Sharpie® permanent marker (Sharpie, Oak Brook, IL). The marker was used as a hydrophobic barrier to contain the applied solutions within a constant surface area. 20 µL drops of protein were applied to the surface with a micropipette and spread to wet the entire surface area inside the drawn circle. The drops were left for a specified time in a Petri dish with wet paper towel underneath at  $20 \pm 2^\circ\text{C}$ . The humid environment was required to prevent the evaporation of the 20 µL drop off the surface. Afterwards, the solution was removed with the pipette and the wafer was rinsed thoroughly with deionized water. The application conditions are shown in Table 5-16. After rinsing, the wafers were left to air dry and were then observed at approximately  $75^\circ$  from normal using a polarizing lens (s-polarized).

Table 5-15. Cartoon drawings of the experimental design and the various proteins exposed to the anodized aluminum-tantalum surface.

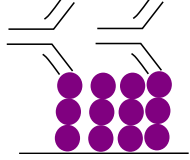
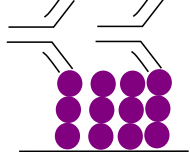
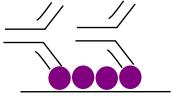
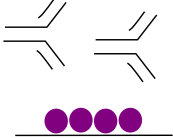
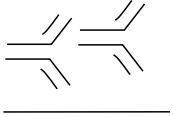
Treatment	Cartoon Depiction
None	
Prothrombin (II)	
Prothrombin (II) + Anti-prothrombin IgG (AII)	
Prothrombin (II) + Anti-thrombin IgG (AT)	
Fragment 1 (F1)	
Fragment 1 (F1) + Anti-prothrombin IgG (AII)	
Fragment 1 (F1) + Anti-thrombin IgG (AT)	
Anti-prothrombin (AII) or anti-thrombin IgG (AT)	

Table 5-16. Application conditions for each protein solution in Part A.

Treatment	Concentration	Application Time
Prothrombin	1.39 $\mu$ M (0.100 mg/mL)	15 minutes
Fragment 1	1.39 $\mu$ M (0.030 mg/mL)	15 minutes
Anti-prothrombin IgG	1.33 $\mu$ M (0.200 mg/mL)	30 minutes
Anti-thrombin IgG	1.33 $\mu$ M (0.200 mg/mL)	30 minutes

#### Part B – Prothrombin and Fragment 1 Mix

Prothrombin and fragment 1 were mixed to create solutions varying in the molar concentration of each molecule to see whether fragment 1 could be used as a spacer between prothrombin molecules, and whether this spacing could be observed by a colour difference of the surface. Mixtures of the following ratios were made in 1 mL Eppendorf<sup>TM</sup> snap-cap microcentrifuge tubes (Thermo Fisher Scientific, Waltham, MA): Prothrombin (II) : Fragment 1 (F1) – 100:0 (1.36  $\mu$ M : 0  $\mu$ M), 80:20 (1.09  $\mu$ M : 0.27  $\mu$ M), 60:40 (0.82  $\mu$ M : 0.54  $\mu$ M), 40:60 (0.54  $\mu$ M : 0.82  $\mu$ M), 20:80 (0.27  $\mu$ M : 1.09  $\mu$ M), 0:100 (0  $\mu$ M : 1.36  $\mu$ M). Sharpie permanent marker was then used to draw 1 cm diameter circles on an anodized aluminum-tantalum wafer and the mixed protein solutions were applied for 15 minutes, in the manner described in Part A. After washing and allowing the wafer to air dry, the spots were observed using a polarizing lens.

After the various prothrombin and fragment 1 mixtures were applied to the thin film surface, a solution containing anti-human thrombin, sheep, affinity purified IgG (200  $\mu$ g/mL, PBS, pH 7.4) was applied to each spot for 30 minutes, using the method described in Part A. The anti-thrombin antibody will only bind to the top domain of prothrombin (thrombin) and it was hypothesized that the various mixtures would show stronger or weaker colour shifts depending on the steric availability of the epitopes. After the 30 minute application time, the solution was removed with a pipette and the wafer thoroughly rinsed with deionized water. After air drying, the wafer was observed at approximately 75° using a polarizing lens.

### Part C – Dilution Series of Anti-thrombin

The final experiment was to test whether the detection limit for a polyclonal anti-thrombin antibody was increased by spacing out the prothrombin on the surface. Two mixtures of prothrombin and fragment 1 were adsorbed onto the surface and then followed with a series of dilutions of the anti-thrombin antibody. The first mixture consisted of only prothrombin, II:F1 = 100:0 (1.36  $\mu\text{M}$  : 0  $\mu\text{M}$ ), while the second was a 25:75 (0.34  $\mu\text{M}$  : 1.02  $\mu\text{M}$ ) mix of prothrombin and fragment 1. Part B of this study found that the largest colour difference from anti-thrombin IgG occurred when prothrombin was adsorbed to the surface alone. However, it was decided to still compare the detection limit of anti-thrombin IgG for a surface that had adsorbed both prothrombin as well as a mixture (25:75 of prothrombin to fragment 1).

A Sharpie permanent marker was used to draw 1 cm diameter circles on the wafer. The 100:0 prothrombin to fragment 1 ratio was applied to 21 circles and the 25:75 mixture was applied another 21 circles for 15 minutes in a humid environment, as described in Part A. After rinsing with deionized water and allowing to air dry, the anti-thrombin antibody was placed on each prothrombin and fragment 1 coated spot for 30 minutes. The following dilutions were used: 200  $\mu\text{g}/\text{mL}$  (1.33  $\mu\text{M}$ ), 100  $\mu\text{g}/\text{mL}$  (0.67  $\mu\text{M}$ ), 50  $\mu\text{g}/\text{mL}$  (0.33  $\mu\text{M}$ ), 20  $\mu\text{g}/\text{mL}$  (0.13  $\mu\text{M}$ ), 10  $\mu\text{g}/\text{mL}$  (0.07  $\mu\text{M}$ ), 0  $\mu\text{g}/\text{mL}$  (PBS solution). The antibody solutions were then removed with a pipette and the wafer was rinsed thoroughly with deionized water and allowed to air dry. The colours were then observed at about  $75^\circ$  from normal using a polarizing lens.

#### *Colour Coordinates*

Photos of the interference colours were taken at approximately  $75^\circ$  from normal using a phone camera and a polarizing lens (s-polarized). Slides were placed on white cardboard paper and images taken with a matte, white background. The images were then analyzed for RGB coordinates

using ImageJ software (Rasband, WS, ImageJ, US National Institutes of Health, Bethesda, MD, <https://imagej.nih.gov/ij/>, 1997-2016). A circular area of each slide was selected in the photo, encompassing between 5,000 and 30,000 pixels. The mean and standard deviation were recorded for the RGB coordinates of each area. Colour difference was calculated using the Euclidean distance between the R, G, and B coordinates:

$$\Delta C = \sqrt{(R_s - R_b)^2 + (G_s - G_b)^2 + (B_s - B_b)^2} \quad (5.1)$$

Where  $R$ ,  $G$  and  $B$  are the RGB coordinates measured,  $s$  is the signal or test spot exposed to both antigen and antibody,  $b$  is the background or the spot only coated in antigen.

For Part B, the colour differences were analyzed statistically using an independent samples Welch T-test, followed by a Games Howell post hoc test (assuming unequal variance, due to failed Levene's test of homogeneity). Part C numerical results were analyzed using a one-way ANOVA with Tukey post hoc testing (assuming equal variances, due to passing Levene's test of homogeneity). All statistical analysis was conducted using IBM SPSS Statistics for Windows, Version 24.0 (IBM Corp., Released 2016, Armonk, NY).

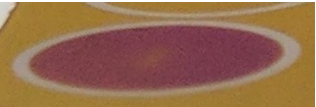
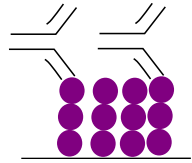
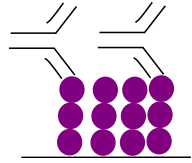
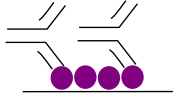
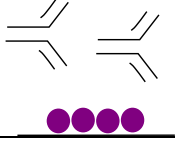
## Results

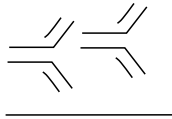
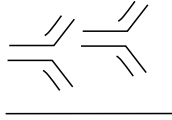
### *Part A – Fragment 1, Prothrombin, Anti-prothrombin and Anti-thrombin*

The results of Part A are shown in Table 5-17. The surface of the anodized aluminum-tantalum thin film is initially yellow. When individual drops of prothrombin and fragment 1 are placed on films in equimolar concentrations (1.36  $\mu\text{M}$ ) it was found that prothrombin produced a plum colour, while fragment 1 produced an orange. When a polyclonal anti-prothrombin antibody is added to both (1.33  $\mu\text{M}$ ), prothrombin goes from plum to dark blue, while fragment 1 goes from orange to dark pink. When anti-thrombin antibody is added to both (1.33  $\mu\text{M}$ ), prothrombin

changes to purple, while fragment 1 remains orange. As a negative control, the antibody solutions were placed directly on the thin film surface for 30 minutes. No colour change of the surface was observed.

*Table 5-17. Results of Part A with various immobilized protein complexes on an anodized aluminum-tantalum thin film surface. Sample size of n=3 for all data sets.*

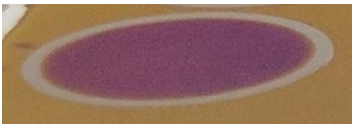
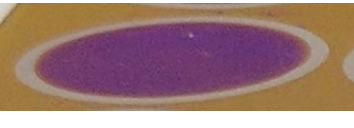
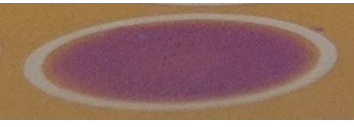
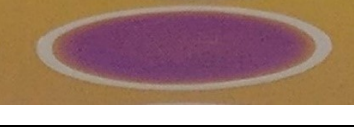
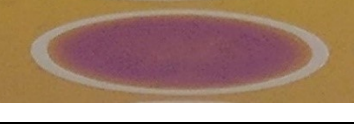
Treatment	Cartoon Depiction of Expected Result	Image with Polarizing Lens (75° from normal, s-polarized light)	Observed Colour & RGB Coordinates
None			Yellow R: 176.87 ± 4.21 G: 137.78 ± 4.28 B: 39.80 ± 4.49
II			Plum R: 136.51 ± 9.87 G: 68.52 ± 5.50 B: 77.74 ± 3.82
II & AII			Dark Blue R: 95.56 ± 8.99 G: 41.94 ± 3.21 B: 132.00 ± 7.78
II & AT			Purple R: 113.14 ± 17.10 G: 45.67 ± 3.09 B: 104.39 ± 3.08
F1			Orange R: 164.73 ± 5.99 G: 113.27 ± 6.21 B: 43.28 ± 4.82
F1 & AII			Dark Pink R: 152.69 ± 4.39 G: 85.86 ± 1.96 B: 70.37 ± 2.17
F1 & AT			Orange R: 162.07 ± 6.34 G: 110.94 ± 5.94 B: 45.33 ± 6.98

AII			Yellow R: 168.18 ± 7.95 G: 129.52 ± 10.04 B: 40.86 ± 7.45
AT			Yellow R: 171.63 ± 6.33 G: 133.39 ± 7.62 B: 39.80 ± 3.11

### *Part B – Fragment 1 and Prothrombin Mix*

The results of Part B are shown in Table 5-18. As the ratio of prothrombin to fragment 1 progressed from 100:0 to 0:100, the colour shifted from plum to orange. When anti-thrombin was applied (1.33  $\mu$ M), colour shifts were observed on all spots except those consisting of only fragment 1. The largest colour shift ( $\Delta C = 17.69 \pm 1.40$ ) was found for a ratio of 100:0 of prothrombin to fragment 1. For a ratio of 0:100 of prothrombin to fragment 1, a colour shift was not observed with treatment of antibody, however the phone camera showed a small colour difference after RGB coordinate analysis ( $\Delta C = 7.54 \pm 2.12$ ). A Welch t-test was conducted to compare colour differences for each ratio with anti-thrombin antibody. Significant differences were only found between the 100:0 and 0:100 ratios ( $p=0.02$ ). Overall, it was concluded that adsorbing prothrombin in mixture with fragment 1 did not appear to significantly improve the colour difference detected from 200  $\mu$ g/mL of anti-thrombin antibody.

Table 5-18. Results of Part B with various ratios of prothrombin and fragment 1 adsorbed to the anodized aluminum-tantalum thin film surface followed by treatment with anti-thrombin IgG (0.2 mg/mL) for 30 minutes. Sample size of n=3.

Treatment	Image with Polarizing Lens (75° from normal, s-polarized light)	Observed Colour & RGB Coordinates	Colour Difference and Observed Difference (Yes/No)
100 II : 0 F1		Plum R: 121.84 ± 5.23 G: 70.60 ± 4.55 B: 96.87 ± 4.56	17.69 ± 1.40 Yes
100 II : 0 F1 AT		Purple R: 113.01 ± 5.32 G: 57.36 ± 4.53 B: 113.93 ± 4.93	
80 II : 20 F1		Plum R: 122.11 ± 5.00 G: 72.55 ± 4.67 B: 96.52 ± 4.35	17.55 ± 10.50 Yes
80 II : 20 F1 AT		Purple R: 117.75 ± 6.81 G: 59.67 ± 4.11 B: 108.46 ± 4.53	
60 II : 40 F1		Light Plum R: 124.89 ± 4.13 G: 76.53 ± 3.92 B: 96.33 ± 3.70	13.82 ± 8.52 Yes
60 II : 40 F1 AT		Purple R: 124.92 ± 7.23 G: 65.93 ± 4.57 B: 99.73 ± 5.61	
40 II : 60 F1		Light Plum R: 138.31 ± 3.07 G: 90.25 ± 3.41 B: 89.71 ± 3.02	15.04 ± 8.26 Yes
40 II : 60 F1 AT		Light Purple R: 134.99 ± 5.74 G: 77.45 ± 3.90 B: 93.41 ± 4.56	
20 II : 80 F1		Orange R: 148.99 ± 2.75 G: 104.30 ± 2.94 B: 84.53 ± 2.87	14.01 ± 7.35 Yes
20 II : 80 F1 AT		Very Light Plum R: 147.77 ± 4.36 G: 93.45 ± 3.65	

		B: $86.35 \pm 4.63$	
0 II : 100 F1		Orange R: $156.36 \pm 2.94$ G: $112.02 \pm 3.00$ B: $83.63 \pm 2.95$	7.54 ± 2.12* No
0 II : 100 F1 AT		Orange R: $160.75 \pm 3.46$ G: $113.44 \pm 2.93$ B: $74.72 \pm 3.70$	

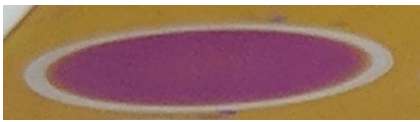
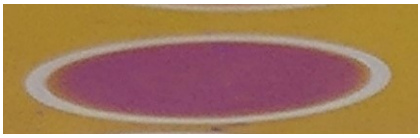
\*Significant difference in measured colour difference ( $p < 0.10$ ) when compared to 100:0 ratio of prothrombin to fragment 1 (equal variances not assumed).

#### *Part C – Dilution Series of Anti-thrombin*

The results of Part C can be found in Tables 5-19 and 5-20. When observed by eye, no difference in the detection limit for anti-thrombin antibody was found between the surfaces coated in prothrombin or the 25:75 prothrombin to fragment 1 mix; both showed no observable change for treatments lower than 50  $\mu\text{g}/\text{mL}$  anti-thrombin antibody. Immediately after the test, the slides were observed at  $75^\circ$  from normal with a polarizing lens. A change in colour could be seen between the spots treated with the PBS blank (0  $\mu\text{g}/\text{mL}$  anti-thrombin IgG) and with either 200, 100 or 50  $\mu\text{g}/\text{mL}$  of anti-thrombin antibody for both the 100:0 and 25:75 mix. However, in the images taken with the phone camera and then analyzed for RGB coordinates, the difference was only observed for the 200 and 100  $\mu\text{g}/\text{mL}$  treated areas.

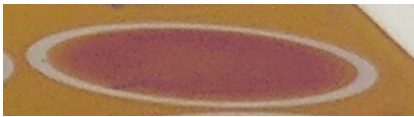
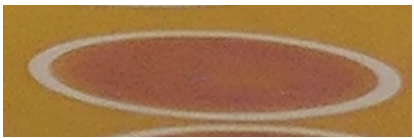
A difference in colour was also observed between areas that were treated with prothrombin, and those treated with the PBS solution for 30 minutes after prothrombin. This was also observed for the 25:75 prothrombin to fragment 1 mix. It appeared that the PBS solution reduced the amount of colour shift that initially occurred from prothrombin and fragment 1, see Table 5-19 and 5-20. For this reason, the colour difference between antibody treated areas was compared with the area treated with PBS solution, as opposed to the initial prothrombin/fragment 1 spot.

Table 5-19. Results of Part C: Anti-thrombin dilution series on anodized aluminum-tantalum thin films previously coated with 1.36  $\mu\text{M}$  prothrombin for 15 minutes. Sample size  $n=3$  for all data sets.

Treatment	Image with Polarizing Lens (75° from normal, s-polarized light)	Observed Colour & RGB Coordinates	Colour Difference and Observed Difference (Yes/No)
II		Plum R: $126.32 \pm 2.36$ G: $63.78 \pm 3.64$ B: $102.58 \pm 2.39$	$12.25 \pm 2.82$ Yes
II & PBS		Light Plum R: $133.34 \pm 4.50$ G: $69.36 \pm 2.00$ B: $108.25 \pm 5.84$	
			<b>Compared vs. PBS Treatment</b>
II & AT (0.07 $\mu\text{M}$ or 10 $\mu\text{g/mL}$ )		Light Plum R: $135.62 \pm 2.82$ G: $72.24 \pm 2.97$ B: $117.11 \pm 10.32$	$9.66 \pm 5.17$ No
II & AT (0.13 $\mu\text{M}$ or 20 $\mu\text{g/mL}$ )		Light Plum R: $137.24 \pm 2.34$ G: $72.98 \pm 2.07$ B: $119.85 \pm 11.08$	$12.86 \pm 5.84$ No
II & AT (0.33 $\mu\text{M}$ or 50 $\mu\text{g/mL}$ )		Light Plum R: $135.89 \pm 2.97$ G: $70.24 \pm 2.17$ B: $116.82 \pm 6.52$	$9.32 \pm 1.24$ Yes
II & AT (0.67 $\mu\text{M}$ or 100 $\mu\text{g/mL}$ )		Light Purple R: $124.33 \pm 2.33$ G: $59.81 \pm 3.52$ B: $117.16 \pm 1.74$	$16.16 \pm 6.29$ Yes
II & AT (1.33 $\mu\text{M}$ or 200 $\mu\text{g/mL}$ )		Purple R: $110.29 \pm 1.55$ G: $51.03 \pm 2.83$ B: $114.67 \pm 6.55$	$31.46 \pm 6.39^*$ Yes

\*Significant difference in measured colour difference ( $p < 0.10$ ) when compared to all other anti-thrombin (AT) treated ratios.

Table 5-20. Results of Part C: Anti-thrombin dilution series on anodized aluminum-tantalum thin films previously coated with a mixture of 25:75 (0.34  $\mu\text{M}$  : 1.02  $\mu\text{M}$ ) prothrombin to fragment 1 for 15 minutes. Sample size  $n=3$  for all data sets.

Treatment	Image with Polarizing Lens (75° from normal, s-polarized light)	Observed Colour & RGB Coordinates	Colour Difference and Observed Difference (Yes/No)
25 II : 75 F1		Light Red R: 140.97 $\pm$ 4.76 G: 77.63 $\pm$ 3.16 B: 80.71 $\pm$ 0.88	12.77 $\pm$ 3.92 Yes
25 II : 75 F1 & PBS		Orange R: 141.76 $\pm$ 7.47 G: 82.31 $\pm$ 6.02 B: 69.33 $\pm$ 2.55	
			<b>Compared vs. PBS Treatment</b>
25 II : 75 F1 & AT (0.07 $\mu\text{M}$ or 10 $\mu\text{g/mL}$ )		Orange R: 138.58 $\pm$ 9.82 G: 80.80 $\pm$ 8.43 B: 65.79 $\pm$ 4.43	5.90 $\pm$ 0.90 No
25 II : 75 F1 & AT (0.13 $\mu\text{M}$ or 20 $\mu\text{g/mL}$ )		Orange R: 134.83 $\pm$ 11.26 G: 78.34 $\pm$ 9.56 B: 64.97 $\pm$ 4.08	9.73 $\pm$ 3.67 No
25 II : 75 F1 & AT (0.33 $\mu\text{M}$ or 50 $\mu\text{g/mL}$ )		Orange R: 132.77 $\pm$ 11.78 G: 75.39 $\pm$ 9.00 B: 68.70 $\pm$ 3.05	11.39 $\pm$ 5.24 Yes
25 II : 75 F1 & AT (0.67 $\mu\text{M}$ or 100 $\mu\text{g/mL}$ )		Light Red R: 129.49 $\pm$ 9.77 G: 69.15 $\pm$ 5.66 B: 78.30 $\pm$ 0.39	20.32 $\pm$ 0.34* Yes
25 II : 75 F1 & AT (1.33 $\mu\text{M}$ or 200 $\mu\text{g/mL}$ )		Light Purple R: 125.62 $\pm$ 7.40 G: 64.96 $\pm$ 3.19 B: 86.41 $\pm$ 2.26	29.33 $\pm$ 4.58* Yes

\*Significant difference in measured colour difference ( $p<0.10$ ) when compared to all other anti-thrombin (AT) treated ratios.

Statistical analysis of the colour differences showed that the mixture may improve sensitivity. On prothrombin coated spots, a significant difference was found between areas treated with 200  $\mu\text{g}/\text{mL}$  of anti-thrombin and all other concentrations ( $p < 0.05$ ). No significant difference was found between areas treated from 0 to 100  $\mu\text{g}/\text{mL}$  of anti-thrombin ( $p > 0.30$ ). On the other hand, for the 25:75 mixture, significant differences were found for 200 and 100  $\mu\text{g}/\text{mL}$  of anti-thrombin compared to all other concentrations ( $p < 0.10$ : 200 vs. 100  $\mu\text{g}/\text{mL}$  and 100 vs. 50  $\mu\text{g}/\text{mL}$ ;  $p < 0.05$ : 200 vs. 50, 20, 10  $\mu\text{g}/\text{mL}$  and 100 vs. 50, 20, 10  $\mu\text{g}/\text{mL}$ ).

## **Discussion**

Overall, this study showed that thin film diagnostics based on anodized aluminum-tantalum thin films: (1) can distinguish between various antibodies and antigens via differences in colour, (2) separation of prothrombin on the surface can be achieved by adding fragment 1 which is observed as a difference in colour, and (3) separation of prothrombin (antigen) may increase the sensitivity of an immunoassay for anti-thrombin (antibody).

In part A of this study, strongly visible colour changes were observed between prothrombin and fragment 1. As discussed in Chapter 1 – Section 1.3.1, interference colours progress in a very specific order, from black to yellow to red, in first order colours, and then into purple and blue for the second order colours. A larger change in thickness of the thin film surface will result in a larger optical path length and progression up this spectrum of colours. The recorded average RGB coordinates were converted into the Yxy colour coordinate system and placed on a 1931 CIE colour diagram for ease of analysis, see Figure 5-14. This study successfully showed that a smaller protein (Fragment 1, MW = 23 kDa) will actually show a smaller shift up the spectrum than a larger protein (Prothrombin, MW = 72 kDa), yellow to orange for fragment 1 vs. yellow to plum for prothrombin. Fragment 1 corresponds to an approximately 4 nm increase in the surface

thickness when a monolayer adsorbs, as opposed to the 11 nm increase in thickness that occurs with prothrombin.

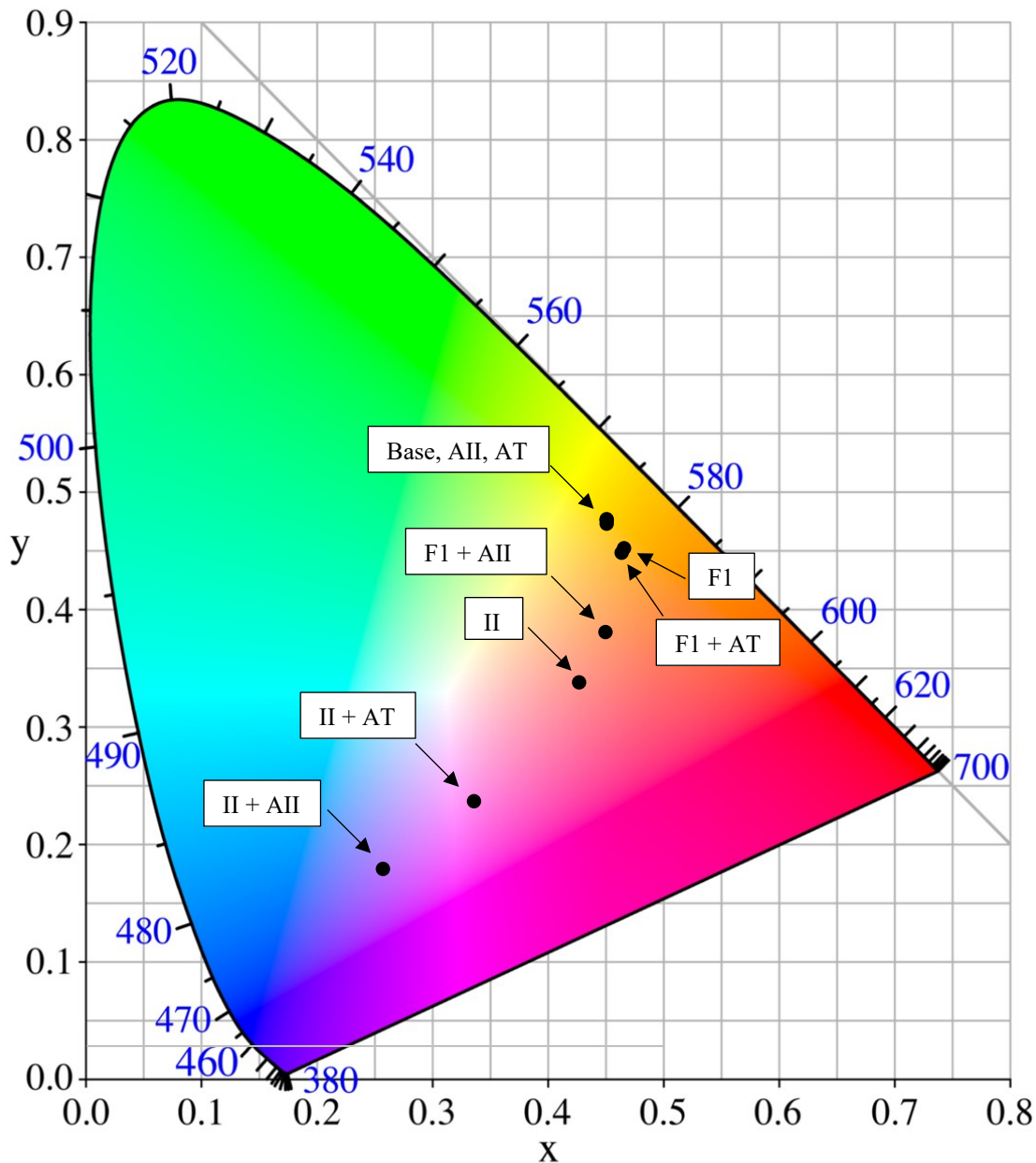


Figure 5-14. Colour coordinate results of Part A, converted to Yxy coordinates and plotted on a 1931 CIE colour diagram. Base: aluminum oxide, II: prothrombin, F1: fragment 1, AII: anti-prothrombin antibody, AT: anti-thrombin antibody.

Unlike other diagnostic platforms using enzymes or chromogens, these thin films can distinguish between molecular sizes on the order of a few nanometers. This colour differentiation with

thickness also carries forward with the antibodies. The polyclonal anti-prothrombin can bind to both fragment 1 and prothrombin, as it will recognize epitopes in both molecules, since fragment 1 is the first 156 amino acid residues of prothrombin [10]. Surfaces coated with both prothrombin and fragment 1 showed changes with the binding of anti-prothrombin, however the colour change was not identical, see Table 5-17 or Figure 5-14. Anti-prothrombin caused a shift to dark blue when placed on prothrombin, and a shift to dark pink when placed on fragment 1. Depending on the orientation of binding, the thickness change due to a bound IgG can be from 4.5 to 14.2 nm, or an average of 9.4 nm [11]. Figure 5-15A shows a cartoon depiction of these layers and the theoretical thickness changes. From the drawing we see that fragment 1 and anti-prothrombin should be thicker than prothrombin alone (16.4 nm vs. 11 nm), and therefore the resulting colour should be higher up the interference spectrum. However, prothrombin is more purple than fragment 1 and anti-prothrombin, making it higher on the inference spectrum and therefore a larger optical path shift. This occurs because either the anti-prothrombin molecule only recognizes epitopes on the edge of fragment 1 or because the affinity is lower for fragment 1 than prothrombin, resulting in less antibody binding, see Figure 5-15B. This could easily be tested by radiolabelling the antibody and comparing the difference in density between antibody bound to prothrombin and fragment 1.

Study A also demonstrated the specificity for an immunoassay based on thin film interference. The films coated with fragment 1 did not change colour with the treatment of anti-thrombin. However, films coated with prothrombin showed a change with anti-thrombin treatment. This is because prothrombin contains the thrombin molecule as one of its domains, see Figure 5-13. Therefore, the anti-thrombin could recognize prothrombin and bind, causing a shift in the optical path length and a colour change. However, note how anti-thrombin did not cause the same shift in colour as anti-

prothrombin. This is likely due to a lower affinity of anti-thrombin for prothrombin. When prothrombin is cleaved to release thrombin, a structural change occurs and the anti-thrombin antibody probably has a higher affinity for this cleaved structure [7]. No colour change was found for either IgG when they were placed on the surface alone. IgG has a low affinity for alumina and therefore non-specific binding is insignificant [12].

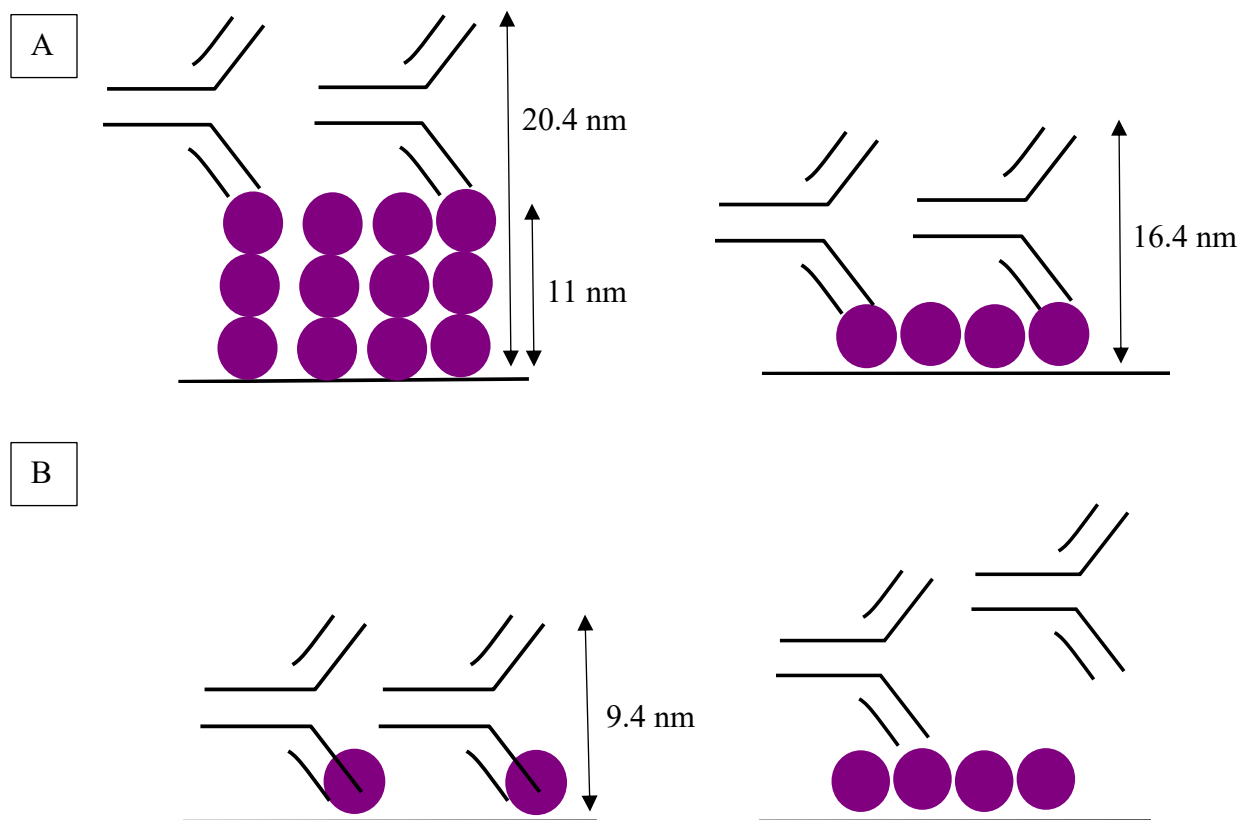


*Figure 5-15. Cartoon depiction of A: theoretical thickness changes with the binding of anti-prothrombin to prothrombin (left) or fragment 1 (right) on a surface; B: Left – thickness change if antibody binds to the side or edge of fragment 1, Right – low affinity of anti-prothrombin to fragment 1 minimizes antibody binding, which results in less of an optical path length change.*

Part B of this study demonstrated the ability to lower the prothrombin surface density with the addition of fragment 1. The progressive change in colour from plum to orange occurs due to less prothrombin adsorbing to the surface in exchange for fragment 1, see Table 5-18. The colour observed is dependent on a mixture of the various path length changes and therefore it slowly

transitions from plum to orange as the overall optical path length decreases. Initially it was hypothesized that spacing the prothrombin out on the surface would allow for a higher sensitivity to detecting anti-thrombin IgG. If each prothrombin molecule had more space between one another, then there would be more available epitopes for antibody binding, see Figure 5-16. However, the colour difference was found only to decrease as prothrombin surface density was decreased.

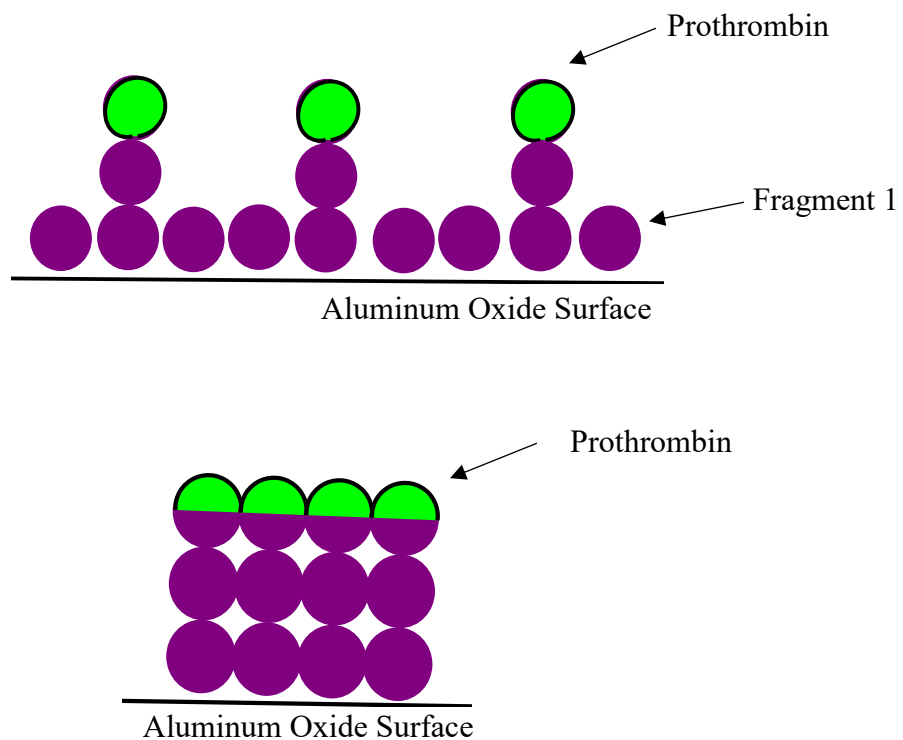


*Figure 5-16. Cartoon depiction of adsorbed prothrombin and fragment 1 on an aluminum oxide surface. Green areas show epitopes open and available for antibody binding.*

To confirm that the sensitivity for anti-thrombin IgG was not improved by lower prothrombin surface density, part C tested a dilution series of anti-thrombin against a 100% prothrombin coated surface and a surface treated with a 25:75 prothrombin to fragment 1 ratio. Displacement of prothrombin and fragment 1 appeared to occur with phosphate buffer. Films initially treated with

prothrombin or fragment 1 and then treated with phosphate buffered saline (PBS) showed a small shift in colour. Phosphate has a higher affinity to alumina than carboxyl groups and therefore it is likely that a small percentage of the prothrombin and fragment 1 are being removed by the buffer, thereby causing the small change in colour observed. This was found to be important when comparing the colour differences for Parts B and C. In Part B, no significant improvement in colour difference was found for the mixtures compared to pure prothrombin coated surfaces. However, Part C found statistically significant differences in colour at 200 and 100  $\mu\text{g}/\text{mL}$  for the 25:75 mixture, where the prothrombin coated surfaces were only significant for 200  $\mu\text{g}/\text{mL}$ . The reason this difference was not noticed in Part B is due to the baseline spot used for comparison. In Part B, the baseline spot was not treated with PBS and therefore, it is not a proper control and likely contributes to the difference in results between Parts B and C. The marginal improvement in analytical sensitivity of the mixture could be due to one of two things, either (a) the spacing of prothrombin allowed for more antibodies to bind and a larger colour shift, or (b) the spacing caused the initial colour to start off lower in the spectrum, making the test more sensitive. As discussed in Chapter 1, the first order interference colours are the most sensitive to changes in the optical path length and therefore the mixture coated surface would be more sensitive than the 100% prothrombin coated surface simply due to where it started in the interference spectrum. To confirm whether or not more antibodies are binding, future work should run the same set of tests with a radiolabelled antibody and determine the exact amount of antibody bound in each case.

## **Conclusion**

This work helped to understand the effects of antigen size and surface density on the colours produced by an immunoassay based on anodized aluminum-tantalum thin films. The following conclusions were made:

1. Molecular size can be visibly detected based on the thickness change from the adsorbed molecule
2. Spacing of prothrombin on the surface can be achieved by adding fragment 1 which is observed as a difference in colour of the surface
3. Spacing of prothrombin (antigen) may increase the sensitivity of an immunoassay for anti-thrombin IgG (antibody) by increasing the colour difference of the analyzed images at lower concentrations of antibody, however the improvement is small and the detection limit was not strongly reduced by spacing.

## References

- [1] K. D. Elgert, *Immunology: Understanding the Immune System*, Hoboken, NJ: John Wiley & Sons, Inc., 2009.
- [2] M. Hadzhieva, A. D. Pashov, S. Kaveri, S. Lacroix-Desmazes, H. Mouquet and J. D. Dimitrov, "Impact of Antigen Density on the Binding Mechanism of IgG Antibodies," *Scientific Reports*, vol. 7, p. 3767, 2017.
- [3] H. Nygren, M. Werthen and M. Stenberg, "Kinetics of antibody binding to solid-phase-immobilised antigen," *Journal of Immunological Methods*, vol. 101, pp. 63-71, 1987.
- [4] H. Nygren, T. Sandström and M. Stenberg, "Direct Visual Detection of Protein Antigen: Importance of Surface Concentration," *Journal of Immunological Methods*, vol. 59, pp. 145-149, 1983.
- [5] H. Sweet, *Development of a Thin Film Device and Optics System for Protein Detection*, Edmonton, AB: University of Alberta, 2018.
- [6] T. K. Lim, V. A. Bloomfield and G. L. Nelsestuen, "Structure of the Prothrombin- and Blood Clotting Factor X-Membrane Complexes," *Biochemistry*, vol. 16, no. 19, pp. 4177-4181, 1977.
- [7] S. Krishnaswamy, "The Transition of Prothrombin to Thrombin," *Journal of Thrombosis and Haemostasis*, vol. 11, pp. 265-276, 2013.

- [8] R. E. Burrell, "Aluminum Oxide Surfaces and Interface Molecules". Provision Patent. Filed Feb. 20, 2018.
- [9] M. Huang, A. C. Rigby, X. Morelli, M. A. Grant, G. Huang, B. Furie, B. Seaton and B. C. Furie, "Structural basis of membrane binding by Gla domains of vitamin K-dependent proteins," *Nature Structural Biology*, vol. 10, no. 9, pp. 751-756, 2003.
- [10] A. Tulinsky, C. H. Park and T. J. Rydel, "The Structure of Prothrombin Fragment 1 at 3.5 Å Resolution," *The Journal of Biological Chemistry*, vol. 260, no. 19, p. 10771, 1985.
- [11] V. R. Sarma, E. W. Silverton, D. R. Davies and W. D. Terry, "The Three-Dimensional Structure at 6 Å Resolution of a Human  $\gamma$ G1 Immunoglobulin Molecule," *The Journal of Biological Chemistry*, vol. 246, no. 11, p. 3753, 1971.
- [12] S. D. Alvarez, C. Li, C. E. Chiang, I. K. Schuller and M. J. Sailor, "A label-free porous alumina interferometric immunosensor," *ACS Nano*, vol. 3, no. 10, pp. 3301-3307, 2009.

## Chapter 6 Visual Immunoassay for Anti-Zika NS1 IgG and Goat Anti-Rabbit IgG on Anodized Aluminum-Tantalum Thin Films

### Introduction

Protein degradation and orientation have been fundamental challenges in functionalizing thin film aluminum oxide surfaces. As discussed in Chapter 1, Section 1.6.2, there are a few methods to immobilize proteins onto these surfaces including silanization [1, 2, 3, 4, 5], organophosphates and phosphonates [6, 7], substitute surface coatings [8, 9], and selectively bound peptides [10, 11, 12]. The protein of interest must be kept off the surface, as aluminum, as well as its oxides and hydroxides, have been shown to be catalytic to the degradation of biological materials [13, 14, 15], and are capable of denaturing the secondary and tertiary structures resulting in loss of biological activity of the protein [16, 17, 18, 19]. Burrell [20] proposed using proteins or peptides with domains containing many polyanionic sites, such as the vitamin K dependent proteins, to bridge molecules to an aluminum oxide surface. The binding strength of vitamin K dependent proteins, such as prothrombin, comes from a GLA domain containing 10  $\gamma$  - carboxyglutamic acid residues [21]. In prothrombin, the GLA domain is contained in the Fragment 1 section of the protein (see Chapter 1 Section 1.6.2 for more details). The relatively high density of anionic sites (di-carboxyl groups) allow for a multitude of binding sites to the alumina surface through association with surface protonated hydroxyl groups or uncoordinated aluminum atoms on crystal edge or defect sites [22, 23, 24]. Prothrombin can then be activated using a variety of binding chemistries such as carbodiimides or glutaraldehyde. Being 4 nm wide and 11 nm tall, prothrombin also acts as a spacer between the aluminum oxide surface and the protein of interest [25]. This keeps the immobilized protein away from the active surface, eliminating the potential for structural damage.

The purpose of this work was to demonstrate the use of prothrombin as a bridging molecule to the alumina surface for other proteins, followed by the detection of these immobilized proteins (antigens) with their associated antibodies. Glutaraldehyde is used as the cross-linking molecule between prothrombin and the antigen. Glutaraldehyde is a linear, 5-carbon dialdehyde that is soluble in all proportions of water, alcohol, and organic solvents [26]. It reacts very rapidly with amine groups around neutral pH and has been used as a fixative and protein immobilization agent for decades [27, 28]. Glutaraldehyde reacts well with the  $\epsilon$ -amino groups of lysine residues on proteins and thus it can be used to link proteins via these residues. Following treatment with glutaraldehyde a protein or surface can then be treated with a small, amine containing molecule, for example tris(hydroxymethyl)aminomethane buffered saline (TBS), to effectively cap any remaining glutaraldehyde and prevent reactions occurring when exposed to other protein containing solutions.

In this study, rabbit polyclonal IgG and Zika virus (ZIKV) non-structural protein 1 (NS1) were immobilized on the surface. These immobilized antigens were then detected using their associated antibodies. Figure 6-1 depicts the immobilization procedure and the resulting immunoassay developed. The rabbit IgG was used as a simple demonstration to visibly detect an antigen-antibody complex, whereas the Zika virus NS1 was used to demonstrate a current, real world application. The Zika virus is part of the Flaviviridae family of viruses and has caused concern lately due to its ability to cause microcephaly and neurological complications in unborn fetuses [29]. It is spread by the Aedes genus of mosquito as well as sexual contact. ZIKV non-structural protein 1 functions in many aspects of the virus's life cycle including viral replication, immune evasion, and pathogenesis [29, 30]. NS1 is a soluble complement fixing antigen and is therefore studied for its ability to evoke an immune response from the adaptive immune system. Detection

of antibodies against ZIKV NS1 in the blood would identify a previous exposure to ZIKV and be helpful in tracking the global spread of the disease. This work demonstrates proof of concept of this device for use as an immunoassay.

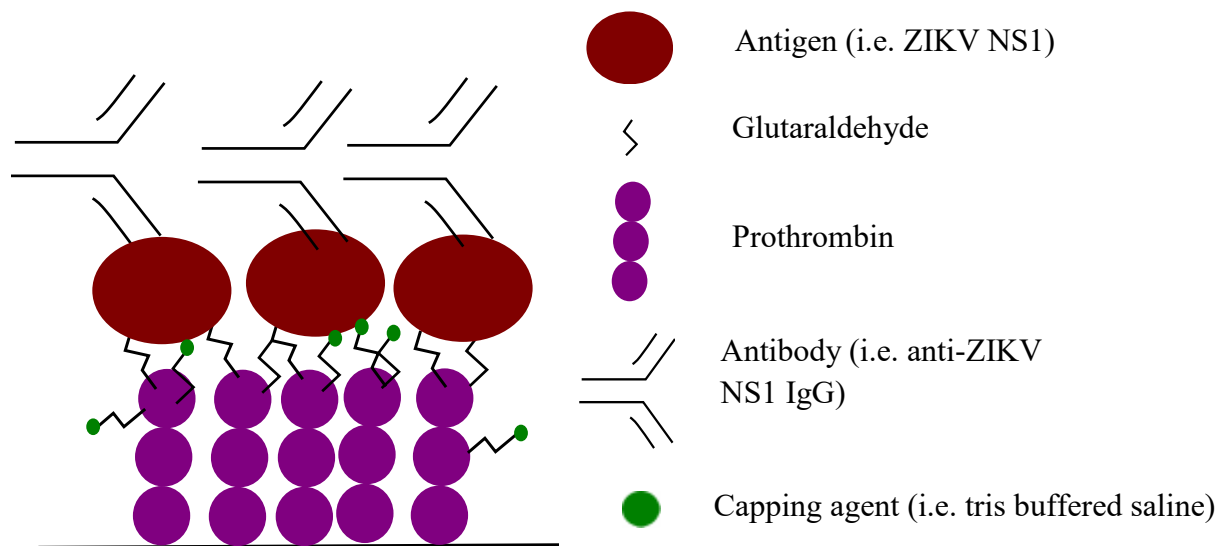


*Figure 6-1. Cartoon depiction of immobilization procedure and the reaction of the antigen with its antibody. Prothrombin is initially immobilized through the GLA domain to the alumina surface. This is then treated with glutaraldehyde, a homo-bifunctional crosslinker, followed by the antigen to attach the antigen to the surface without exposing it to the alumina surface. The surface is then coated in a capping agent, a small molecule that will react with the remaining glutaraldehyde. Finally, the surface is exposed to a solution containing the antibody, which will recognize epitopes on the antigen and bind.*

## Materials and Methods

### *Thin Film Preparation*

All thin film wafers and slides were provided by Prominent Medical Inc. (Edmonton, AB). Unprocessed <100> silicon wafers 100 mm diameter (University Wafers, South Boston, MA) were sputtered with  $226.5 \pm 3.8$  nm of tantalum at the NAIT Nanotechnology Centre for Applied Research, as previously described (Chapter 4.1). Wafers prepared for Part A of this study were sputtered with  $139.8 \pm 6.3$  nm of aluminum as described in Chapter 4.1. Wafers prepared for Part B of this study were sputtered with  $120 \pm 2$  nm of aluminum as described in Chapter 4.2 Study A.

The wafers were then cleaved into slides approximately 2.6cm x 6cm or 1.3cm x 6cm. Each slide was anodized using 0.4M phosphoric acid and 0.1M oxalic acid at  $19 \pm 1^\circ\text{C}$  and 4V until the current decayed to  $<0.02 \text{ mA/cm}^2$ , as described previously in Chapter 4.2. In some cases, the entire wafer was anodized first and then either cleaved into slides afterwards or left intact for further testing.

### *Protein Immobilization*

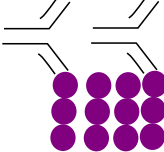
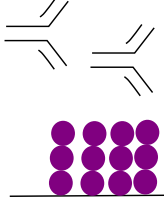
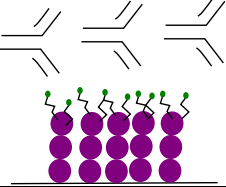
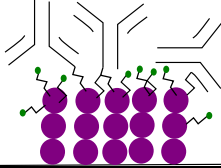
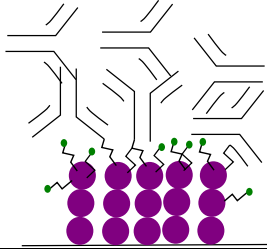
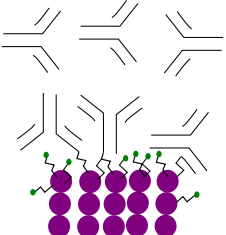
#### Part A – Immunoglobulin G (IgG)

Part A of this study demonstrates the ability to immobilize an immunoglobulin G (IgG) antibody to prothrombin via a glutaraldehyde cross-linker and then visibly detect this immobilized antibody with a polyclonal secondary antibody. Table 6-1 shows the layout of the experiment.

#### Prothrombin Treatment

A Sharpie<sup>®</sup> permanent marker (Sharpie, Oak Brook, IL) was used with a template to draw 8 circles of 1 cm diameter. 20  $\mu\text{L}$  drops of human prothrombin (1 mg/mL, TBS, pH 7.4) (Aniara Diagnostica LLC, West Chester, Ohio) were placed onto each spot using a pipette and left in a Petri dish with wet paper towel underneath at  $20 \pm 2^\circ\text{C}$ . The Petri dish and paper towel provided a humid environment to prevent the protein drying on the surface. After 30 minutes, the prothrombin solution was removed with a pipette and then the slide was rinsed thoroughly with deionized water. The slide was blown dry using a pressurized air can (Electronics Duster Compressed Air, Staples Inc., Framingham, MA) before observing with a polarizing lens at approximately  $75^\circ$  from normal (s-polarized).

Table 6-1. Experimental design for Part A: Immunoglobulin G and the expected result of protein binding on the surface.

Treatment	Cartoon Depiction of Expected Result
Prothrombin (II)	
II + Anti-prothrombin IgG antibody (AII)	
II + Non-specific antibody, mouse anti-influenza B IgG (Nab)	
II + Glutaraldehyde (G) + TBS (Cap) + Antibody, rabbit anti-goat IgG (Ab)	
II + G + Antigen, goat anti-rubella IgG (Ag) + Cap	
II + G + Ag + Cap + Ab	
II + G + Ag + Cap + Nab	

### Initial Controls

Two control spots were placed on a prothrombin coated area: (1) a 20  $\mu\text{L}$  spot of anti-human prothrombin, sheep IgG (200  $\mu\text{g}/\text{mL}$  in PBS, pH 7.3) (Aniara Diagnostica LLC, West Chester, OH) was placed on a prothrombin coated area as a colour reference for an adsorbed antibody layer. After 15 minutes, the spot was removed using a pipette and rinsed with deionized water; (2) in a similar fashion, a 20  $\mu\text{L}$  spot of anti-influenza B, mouse IgG (200  $\mu\text{g}/\text{mL}$  in PBS, pH 7.3) (MyBioSource Inc., San Diego, CA) was placed as a negative control, to test whether non-specific binding would occur between an unrelated antibody and the prothrombin coated surface. After rinsing and drying, the slide was observed with a polarizing lens and colours recorded.

### Antigen Immobilization

The slide was then immersed in a beaker containing 200 mL of 0.5% (v/v) glutaraldehyde (Thermo Fisher Scientific, Waltham, MA) 0.025M phosphate buffer, pH 6.84, for 1 hour while stirring slowly. After removal, the slide was thoroughly rinsed with deionized water and allowed to air dry. The immobilized antigen was a polyclonal goat IgG to the rubella virus. 40  $\mu\text{L}$  of the goat anti-rubella IgG (1 mg/mL, PBS, pH 7.3) (goat polyclonal anti-rubella antibody, EMD Millipore Corp., Temecula, CA) was placed onto three areas with activated prothrombin and left for 1 hour. After removal, these spots were thoroughly rinsed with deionized water and then the slide was immersed into a solution of TBS, pH 7.38, for 1 hour with stirring. The slide was removed and rinsed again with deionized water and allowed to air dry.

### Secondary Antibody

Finally, 20  $\mu\text{L}$  of rabbit polyclonal anti-goat IgG (H&L), HRP conjugated, (200  $\mu\text{g}/\text{mL}$  in PBS, pH 7.3) (Cedarlane Laboratories Corp., Burlington, ON) was placed on two areas, one coated with antigen and one without, and left for one hour. 20  $\mu\text{L}$  of anti-influenza B antibody (200  $\mu\text{g}/\text{mL}$  in

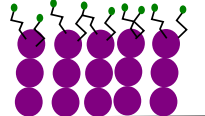
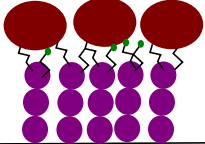
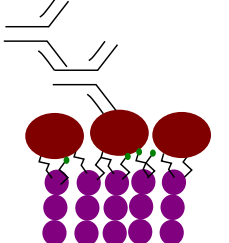
PBS, pH 7.3) was placed on an antigen coated area for 1 hour as a control for non-specific binding. These were removed with a pipette and then rinsed with deionized water and allowed to air dry. Note that before use all antibodies were dialyzed overnight at 4°C in PBS, pH 7.3-7.4, with 8-10 kD MWCO dialysis tubing (Micro Float-A-Lyzer<sup>®</sup>, Spectrum Laboratories Inc., Rancho Dominguez, CA). Slides were observed at 75° from normal using a polarizing lens (s-polarized) and colours recorded.

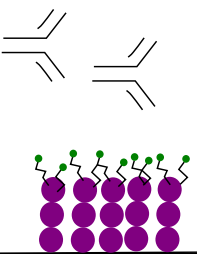
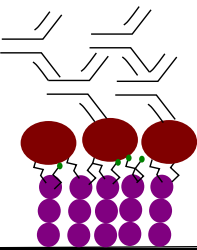
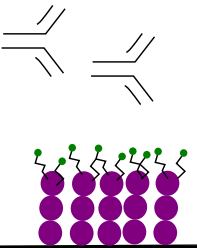
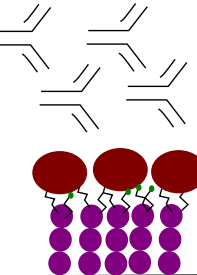
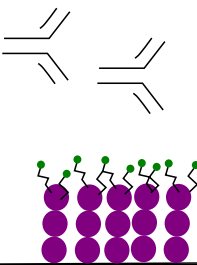
### Part B – Zika NS1 Complex

Part B of this study demonstrates the ability to immobilize a viral antigen to the prothrombin coated surface via glutaraldehyde and then subsequently detect this immobilized antigen with both a polyclonal and monoclonal IgG solution, followed by a secondary antibody to increase the signal.

The experimental design can be found in Table 6-2.

*Table 6-2. Experimental design for Part B: Zika NS1 and the expected result of protein binding on the surface.*

Treatment	Cartoon Depiction of Expected Result
Prothrombin (II) + Glutaraldehyde (G) + TBS (Cap)	
II + G + ZIKV NS1 (Ag) + Cap	
II + G + Ag + Cap + Mouse monoclonal anti-ZIKV NS1 IgG (MAb) + Goat anti-mouse IgG (2° Ab)	

<p>II + G + Cap + MAb + 2°Ab</p>	
<p>II + G + Ag + Cap + Goat polyclonal anti- ZIKV NS1 IgG (PAb) + Rabbit anti- goat IgG (2°Ab)</p>	
<p>II + G + Cap + PAb + 2°Ab</p>	
<p>II + G + Ag + Cap + Non-specific antibody, mouse anti-influenza B IgG (NAb) + Goat anti- mouse IgG (2°Ab)</p>	
<p>II + Cap + NAb + 2°Ab</p>	

### Prothrombin Treatment

Eight, 1 cm diameter circles were drawn on each slide with permanent marker. Prothrombin was placed on spots 1 through 8 (20  $\mu$ L, 0.1 mg/mL,  $20 \pm 2^\circ\text{C}$ , humid environment) for 30 minutes and then removed with a pipette and rinsed with deionized water.

### Glutaraldehyde Treatment

The entire slide was then immersed in a 200mL solution of 0.5% (v/v) glutaraldehyde in 0.025M phosphate buffer, pH 6.8, for two hours with stirring and then rinsed with deionized water. The slide was then immersed in 200mL of PBS, pH 7.4, for a one-hour rinse with stirring to remove any excess glutaraldehyde on the surface.

### ZIKV NS1 Antigen Treatment

After the PBS rinse, the slide was air dried and then 20  $\mu$ L drops of Zika NS1 (0.1 mg/mL, PBS, pH 7.3) (Product code: ZIKVSU-NS1-100, The Native Antigen Company, Oxfordshire, UK) were placed on 4 prothrombin coated spots using a pipette. The drops were left for 15.5 hours at  $4^\circ\text{C}$  in a high relative humidity environment. They were then removed with a pipette and the slide was thoroughly rinsed with deionized water. The slide was then immersed in a 200 mL solution of TBS, pH 7.4, for 1 hour with stirring to cap any unreacted glutaraldehyde, as well as remove excess antigen from the surface.

### Antibody Tests

Finally, antibodies were placed on the surface, 20  $\mu$ L spots at 200  $\mu$ g/mL in PBS, pH 7.3 – 7.4, for 1 hour. A commercial, anti-ZIKV NS1, goat polyclonal IgG (200  $\mu$ g/mL in PBS, pH 7.4) (Catalog No.: MBS5304723, MyBioSource Inc., San Diego, CA) was placed on 2 spots, one previously coated in ZIKV-NS1 and one only coated in prothrombin. A mouse, monoclonal antibody (IgG

10F3) isolated from commercial hybridomas made to ZIKV NS1 Suriname strain was placed on a similar set of spots (courtesy of Dr. Tom Hobman in the Department of Cell Biology at the University of Alberta, hybridomas acquired from ProSci Inc., Poway, CA). A nonspecific antibody, anti-influenza B, mouse IgG (Product code: MBS220959, MyBioSource Inc., San Diego, CA), was placed on two similar spots as a negative control. The antibodies were then removed with a pipette and the spots rinsed with deionized water. The slides air dried and were then observed at approximately 75° with a polarizer (s-polarized). No colour changes could be observed, therefore a secondary antibody was applied to each spot to help increase the signal.

Secondary antibodies were applied as follows: goat anti-mouse IgG (H+L) HRP conjugate (Bio-Rad Laboratories Ltd., Mississauga, ON) was placed on all spots previously coated in mouse IgGs. Rabbit anti-goat IgG (H+L) HRP conjugate (Bio-Rad Laboratories Ltd., Mississauga, ON) was placed on spots previously coated in goat IgGs. The secondary antibodies were left for 1 hour (20 µL, 0.2 mg/mL, PBS pH 7.4, 20 ± 2°C, humid environment) and then rinsed off with deionized water. Photos were taken using a phone camera and a polarizer (s-polarized).

### *Colour Coordinates*

Photos of the interference colours were taken at approximately 75° from normal using a phone camera and a polarizing lens (s-polarized). The slides were placed on a white cardboard sheet and imaged with a matte, white background. The images were then analyzed for RGB coordinates using ImageJ software (Rasband, WS, ImageJ, US National Institutes of Health, Bethesda, MD, <https://imagej.nih.gov/ij/>, 1997-2016). A circular area of each slide was selected in the photo, encompassing between 5,000 and 30,000 pixels. The mean and standard deviation were recorded for the RGB coordinates of each area. Colour difference was calculated using the Euclidean distance between the R, G, and B coordinates as shown in Equation (5.1):

$$\Delta C = \sqrt{(R_s - R_b)^2 + (G_s - G_b)^2 + (B_s - B_b)^2} \quad (5.1)$$

Where  $R$ ,  $G$  and  $B$  are the RGB coordinates measured,  $s$  is the signal or the test spot exposed to both antigen and antibody,  $b$  is the background or the spot only coated in antigen. Note that this method does not consider differences in colour due to human perception and only calculates the differences in the collected data. The colour differences were recorded for each slide and then pooled to get a mean and standard deviation for colour change with each treatment.

### *Statistics*

Numerical results were analyzed using an unpaired T-test. Statistical analysis was conducted with IBM SPSS Statistics for Windows, Version 24.0 (IBM Corp., Released 2016, Armonk, NY).

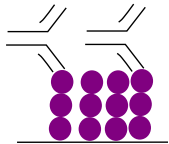
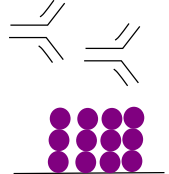
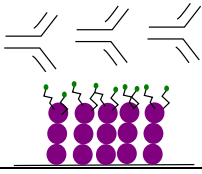
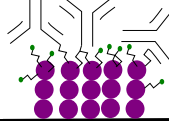
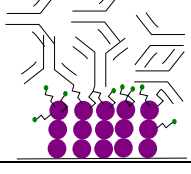
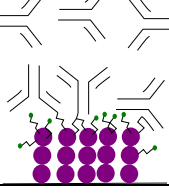
## **Results**

### *Part A – Immunoglobulin G*

The results of Part A are shown in Table 6-3. The base colour of the slide was tan. Prothrombin produced a colour change from tan to purple. Anti-prothrombin antibody produced a change from purple to dark blue. When a non-specific antibody, mouse anti-influenza B antibody, was placed on prothrombin for a similar time, no colour change was observed ( $p < 0.001$ , II+AII vs. II+Nab). Goat antibodies were exposed to prothrombin treated with glutaraldehyde, hereafter known as ‘activated prothrombin’. No colour shift was observed after a 1-hour exposure to the goat antibody solution. After treating the slide with TBS to cap remaining glutaraldehyde, anti-goat antibody was placed on spots with and without previous treatment with goat antibody. Both had colour changes occur and no significant difference was found between the colour differences ( $p = 0.136$ , II+G+Cap+Ab vs. II+G+Ag+Cap+Ab). Therefore, the TBS treatment did not function as a suitable

cap, allowing non-specific binding to occur to the surface and change the colour. An additional spot of activated prothrombin with goat antibody was exposed to a non-specific antibody, mouse anti-influenza B, as a negative control and no observed change in colour was found by eye. However, RGB coordinate analysis found a colour difference for this spot and this again was found to be not significantly different from the test ( $p=0.876$ , II+G+Ag+Cap+Ab vs, II+G+Ag+Cap+Nab).

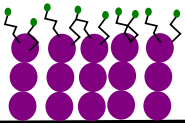
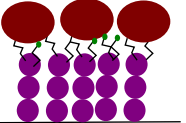
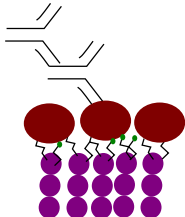
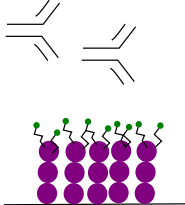
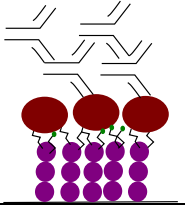
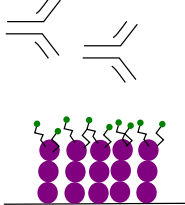
Table 6-3. Results of Part A: Immunoglobulin G immobilization and detection with secondary antibody. Look to Table 6-1 for a detailed understanding of the treatment symbols. Sample size of  $n=3$  for all experiments.

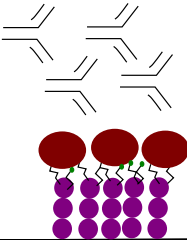
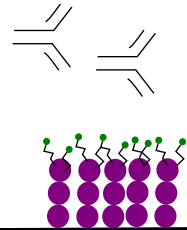
Treatment	Cartoon Depiction of Expected Result	Image with Polarizing Lens (75° from normal, s-polarized light)	Observed Colour and RGB Coordinates	Colour Difference ( $\Delta C$ ) & Observed Difference (Yes/No)
II			Purple R: $55.37 \pm 8.59$ G: $19.51 \pm 2.34$ B: $77.02 \pm 4.37$	N/A
II + AII			Blue R: $34.34 \pm 9.73$ G: $34.75 \pm 6.28$ B: $100.55 \pm 4.71$	Vs. II $34.97 \pm 3.24$ Yes
II + Nab			Purple R: $57.82 \pm 6.85$ G: $19.82 \pm 3.22$ B: $74.00 \pm 4.49$	Vs. II $4.64 \pm 2.27$ No
II + G + Cap + Ab			Purple R: $53.50 \pm 8.12$ G: $21.06 \pm 2.48$ B: $81.51 \pm 4.20$	Vs. II $12.42 \pm 0.23$ No
II + G + Ag + Cap			Purple R: $61.01 \pm 2.79$ G: $20.19 \pm 2.35$ B: $86.85 \pm 2.93$	Vs. II $4.99 \pm 1.77$ No
II + G + Ag + Cap + Ab			Blue R: $45.36 \pm 8.01$ G: $27.49 \pm 4.60$ B: $94.30 \pm 5.18$	Vs. Ag $16.42 \pm 4.18$ Yes
II + G + Ag + Cap + Nab			Dark Purple R: $55.91 \pm 8.39$ G: $23.44 \pm 3.57$ B: $93.67 \pm 4.27$	Vs. Ag $12.79 \pm 2.51$ Yes

### *Part B – Zika NS1 Complex*

The immobilization of Zika virus NS1 protein and detection with both a polyclonal and monoclonal antibody was demonstrated, with results displayed in Table 6-4. The average RGB coordinates for each treatment were converted to Yxy colour coordinates and plotted on a 1931 CIE colour diagram for easy visual comparison of the colours, see Figure 6-3. The initial slide colour was tan. Prothrombin changed the slide to a light purple. After treatment of activated prothrombin with the NS1 protein, the colour changed to purple. The slide was then treated with TBS to cap remaining glutaraldehyde before the antibody solutions were placed on the surface. No colour differences were observed when the primary antibodies were exposed to the surface. Therefore, a secondary antibody was placed on all spots, including the negative control areas. The polyclonal treated area showed the strongest colour change ( $\Delta C = 17.03 \pm 2.12$ ,  $p < 0.001$  vs. non-specific) followed by the monoclonal antibody ( $\Delta C = 11.63 \pm 0.23$ ,  $p < 0.001$  vs. non-specific) and finally the non-specific antibody ( $\Delta C = 3.84 \pm 0.40$ ), which showed no observable colour difference. The negative controls remained visibly purple, however RGB coordinate analysis showed a shift for each negative control relative to the prothrombin treated area, Table 6-4, which again points towards the TBS treatment not functioning as a cap for glutaraldehyde.

Table 6-4. Results of Part B: Zika NS1 immobilization and detection with specific monoclonal and polyclonal antibody solutions followed by secondary antibodies. Look to Table 6-2 for a detailed understanding of the treatment labels. Sample size of n=3 for all experiments.

Treatment	Cartoon Depiction of Expected Result	Image with Polarizing Lens (75° from normal, s-polarized light)	Observed Colour and RGB Coordinates	Colour Difference ( $\Delta C$ ) & Observed Difference (Yes/No)
II + G + Cap			Light Purple R: 96.96 ± 4.11 G: 31.38 ± 5.14 B: 62.66 ± 5.93	N/A
II + G + Ag + Cap			Purple R: 81.61 ± 4.66 G: 24.39 ± 6.09 B: 67.79 ± 5.65	Vs. II 17.65 ± 2.26 Yes
II + G + Ag + Cap + MAb (10F3) + 2°Ab			Dark Purple R: 71.74 ± 4.43 G: 21.90 ± 6.11 B: 73.40 ± 4.87	Vs. Ag 11.63 ± 0.23 Yes
II + G + Cap + MAb (10F3) + 2°Ab			Purple R: 88.02 ± 4.18 G: 25.92 ± 6.14 B: 68.13 ± 5.39	Vs. Ag 7.04 ± 1.94 No
II + G + Ag + Cap + PAb + 2°Ab			Dark Purple R: 67.88 ± 4.58 G: 22.76 ± 6.39 B: 77.18 ± 6.67	Vs. Ag 17.03 ± 2.12 Yes
II + G + Cap + PAb + 2°Ab			Purple R: 87.36 ± 4.23 G: 25.99 ± 6.52 B: 69.65 ± 6.10	Vs. Ag 6.76 ± 3.35 No

<p>II + G + Ag + Cap + Nab + 2°Ab</p>			<p>Purple R: <math>82.74 \pm 4.55</math> G: <math>25.04 \pm 7.08</math> B: <math>68.50 \pm 5.54</math></p>	<p>Vs. Ag <math>3.84 \pm 0.40</math> No</p>
<p>II + Cap + Nab + 2°Ab</p>			<p>Purple R: <math>88.72 \pm 5.50</math> G: <math>26.22 \pm 7.50</math> B: <math>72.16 \pm 6.37</math></p>	<p>Vs. Ag <math>9.66 \pm 3.35</math> No</p>

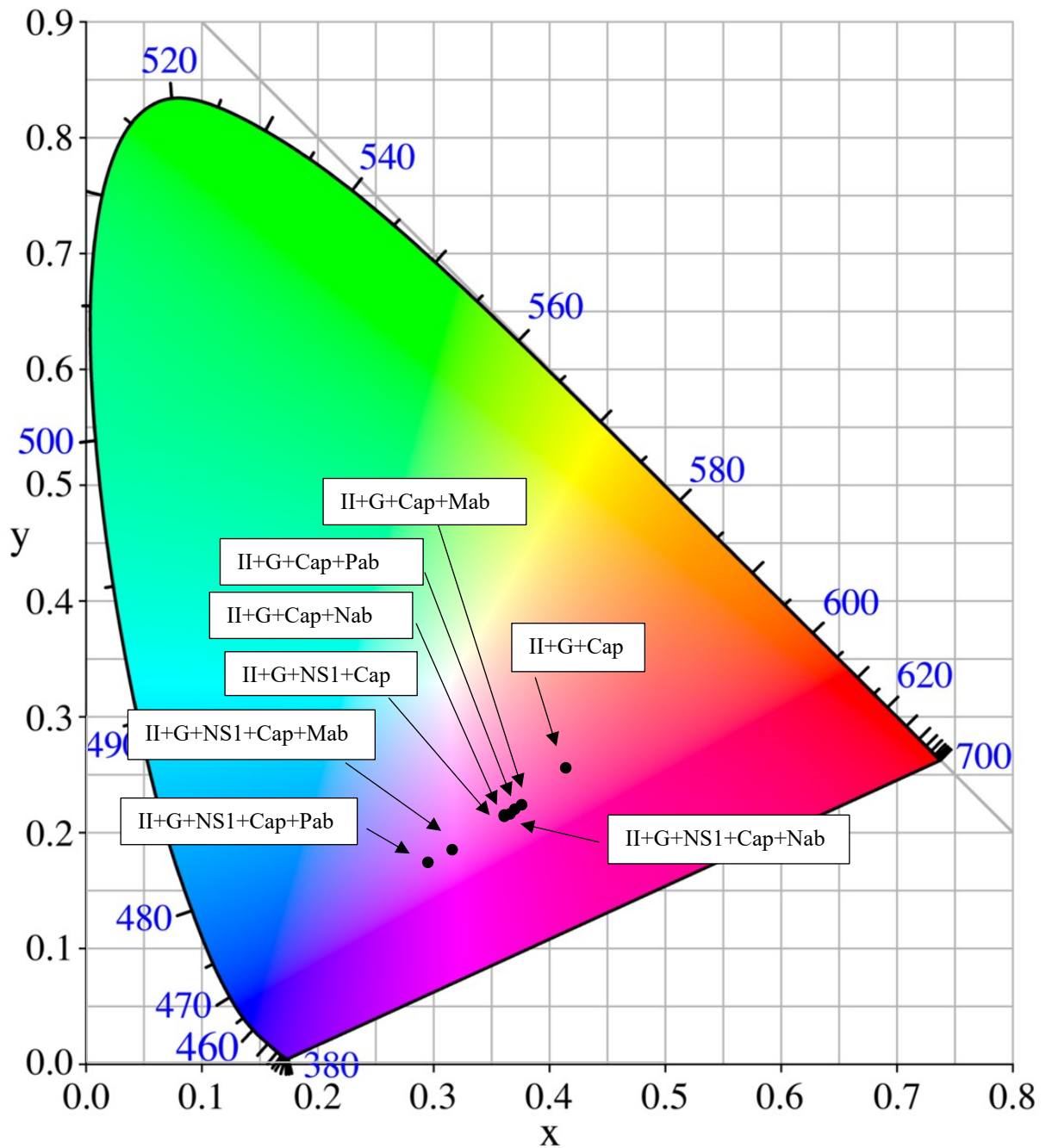


Figure 6-2. Colour coordinate results of Part B, converted to  $Yxy$  coordinates and plotted on a 1931 CIE colour diagram. II: prothrombin, G: glutaraldehyde treatment, Cap: TBS treatment, NS1: Zika non-structural protein 1, Mab: monoclonal anti-NS1 antibody, Pab: polyclonal anti-NS1 antibody, Nab: polyclonal nonspecific antibody.

## Discussion

This work successfully demonstrated the ability to detect an antibody from solution by immobilizing its associated antigen to the thin film surface by using prothrombin as a bridge. Part A demonstrated the ability to bind goat antibodies and detect anti-goat antibodies from a buffered solution. It was found that an antigen may not always show a visible colour shift when bound. The prothrombin showed a shift from tan to purple, corresponding to an 11nm change in thickness (height of prothrombin when GLA domain in contact with the surface [25]). When the antigen was applied there was no visible change in the colour, Table 6-3. It was initially hypothesized that crosslinking rabbit IgG would cause a significant increase in the optical path length and the colour would shift from purple to blue. An IgG has dimensions of 8.5 nm x 4.5 nm x 14.2 nm, with newer models showing that the length is up to 17.1 nm from the apex of one antigen-binding site to the other [31, 32]. A colour shift is strongly visible when anti-prothrombin IgG is complexed with prothrombin on the surface, changing the colour from purple to blue (Table 6-3), with negative controls showing no change. However, no colour shift was observed after crosslinking goat antibody. When the secondary antibody was placed on the antigen coated surface, a change in colour occurred from purple to blue. Therefore, it was concluded that the goat antibody was cross-linked to prothrombin in a configuration that did not significantly increase the optical path length. This could be due to steric effects, i.e. the bound antibody did not increase the thickness of the protein layer, or due to a low surface concentration. Several studies have shown that surface concentration is extremely important in the development of immunoassays based on thin film interference [33, 34, 35]. For example, in Chapter 5.1 of this work, it was found that an antigen could be adsorbed to the surface at such low concentrations (human prothrombin, 20 $\mu$ L spot, 10 $\mu$ g/mL) that no visible colour shift is observed. However, a colour shift was found with the

addition of the antigen's associated antibody. If the reaction of goat antibody with activated prothrombin is of low efficiency, then there may not be enough bound antibody to create a visible colour shift. Glutaraldehyde reacts with proteins through either Schiff base formation or Michael addition depending on the pH conditions, see Figure 6-4 [26, 28]. Both reactions require nucleophilic attack of the aldehyde by the lone pair of the protein amino group, therefore, reaction efficiency is higher with unprotonated amino groups. Since the pKa of  $\epsilon$ -amino groups on lysyl residues is  $> 9.5$ , only a small percentage of unprotonated groups would be present at the pH in these experiments (pH 6.8 for activating prothrombin and pH 7.4 for the goat antibody). Using the Henderson-Hasselbalch equation,  $< 0.8\%$  of lysine groups will be deprotonated (assuming pKa of 9.5 and pH of 7.4). Simply increasing the pH to 8.0, increases the number of deprotonated lysine groups by nearly 4 times to 3%. It is therefore recommended that further testing be carried out with increased pH to improve the efficiency of the glutaraldehyde reaction.

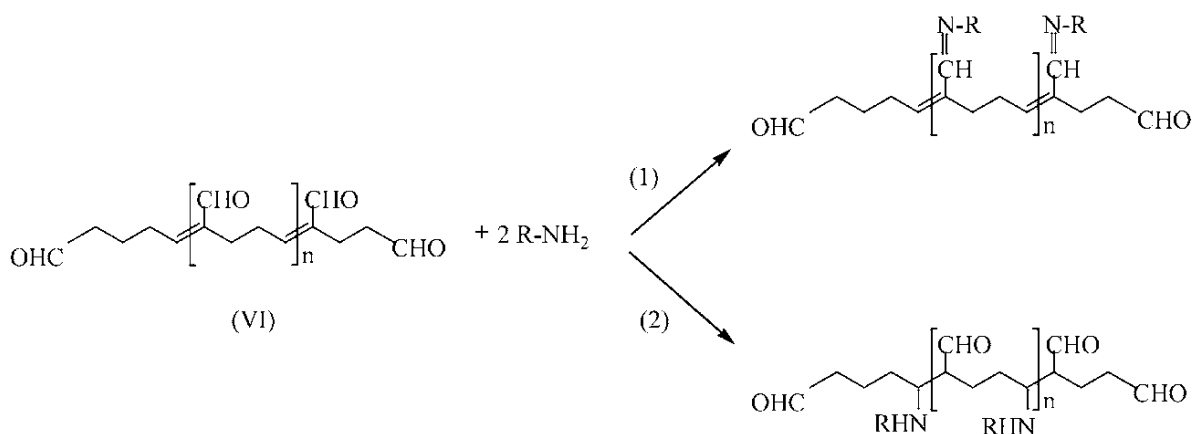


Figure 6-3. Glutaraldehyde reaction with amino groups via (1) Schiff base or (2) Michael-type addition reactions. Figure adapted from [26].

The negative controls, on the other hand, also showed changes in colour after RGB coordinate analysis. As discussed in the introduction, small amine molecules, such as tris(hydroxymethyl)aminomethane as found in TBS buffer, can be used to react with any

remaining glutaraldehyde that has not reacted with the molecule of choice. This helps to prevent non-specific binding from occurring. The shift in colour detected with the negative controls could be due to ineffective capping of all glutaraldehyde. Schiff base reactions are reversible due to acid catalyzed hydrolysis of the double bond [36]. Several studies recommend the reduction of the double bond with sodium borohydride or sodium cyanoborohydride to prevent this [37, 38]. Future work should examine whether reducing agents can be used to prevent false positives.

Part B of this chapter helps develop an understanding of the visual immunoassay as follows: a) demonstrates the ability to test for antibodies associated with Zika virus non-structural protein 1 (NS1), and b) the ability to detect both monoclonal and polyclonal antibodies and differentiate between them based on the intensity of colour shift.

After crosslinking Zika NS1 to prothrombin, the surface changed from light purple to purple. NS1 forms a hexamer composed of three homodimers (MW=270kDa). Xu et al. established the full-length crystal structure for ZIKV NS1 [29]. Brown et al. [39] showed with electron microscopy that the hexamer complex is, roughly, a 10nm diameter cylinder. Depending on the orientation of binding, the thickness change due to a bound IgG can be from 4.5 to 14.2 nm, or an average of 9.4 nm [32] and a change from purple to dark blue for similar surfaces, see Chapter 5.1 Part D - 120nm and 4V slides. Therefore, either the surface density of the ZIKV NS1 is lower than a monolayer, or the refractive index of the film is not matched with the antigen and a mismatch of refractive indices is causing reduced sensitivity in detecting this protein layer. This emphasizes the need for tunability of these films. As was shown in Chapter 5.1, changing the anodization parameters, such as electrolyte and voltage, significantly effects the sensitivity for detecting adsorbed protein layers. Therefore, an experiment could be conducted where ZIKV NS1 is immobilized in a similar fashion as in this study onto films anodized at various voltages. The voltages would change the refractive

index of the alumina film, and the film that best matches the refractive index of the NS1 protein layer would show the strongest of colour shifts.

This study found that the primary antibodies did not produce an observable colour shift, which is why the secondary antibodies were added to increase the signal. The polyclonal antibody coated area showed a stronger shift than the monoclonal, because it is a mixture of antibodies able to recognize various epitopes and would have a higher affinity for a randomly oriented antigen bound to the surface, see Table 6-4. The ability to visibly detect the bound primary antibody could again be improved by varying the refractive index of the aluminum oxide layer.

The negative controls showed weak shifts in colour after application of the secondary antibodies. This weak colour shift is probably occurring due to TBS being an ineffective cap for glutaraldehyde, as discussed earlier. Future work needs to identify the problem and eliminate the non-specific binding by testing other capping agents or employing reducing agents to help stabilize the cross-linked bond.

Some limitations to these experiments are listed: 1) antibodies were exposed to the surface in non-complex solutions containing only buffer. Future tests will need to be done in a complex medium, such as whole blood or serum. 2) Future tests would benefit from the use of radiolabelled antigens and antibodies to affirm whether or not protein surface density, and not the optics of the system, is limiting visible interference colour shifts.

## **Conclusion**

This chapter shows a successful demonstration of visual immuno-assays on anodized aluminum-tantalum thin films. Prothrombin was successfully used as a bridging agent to the surface for both rabbit IgG and ZIKV NS1. The following conclusions were made from these experiments:

- 1) Glutaraldehyde activated prothrombin can be successfully used to bridge rabbit IgG and ZIKV NS1 to the alumina surface. These antigens can then form complexes with their associated antibodies which is observed by a visible colour change of the surface.
- 2) The antigen size, binding time, and antibody type (polyclonal or monoclonal) are all important factors to consider when using these devices as immuno-assays. All these factors will affect the final optical path length change and the ability to observe a colour shift.

## References

- [1] P. Takmakov, I. Vlassioux and S. Smirnov, "Application of anodized aluminum in fluorescence detection of biological species," *Analytical and Bioanalytical Chemistry*, vol. 385, no. 5, pp. 954-958, 2006.
- [2] S. Tanvir, J. Pantigny, P. Boulnois and S. Pulvin, "Covalent immobilization of recombinant human cytochrome CYP2E1 and glucose-6-phosphate dehydrogenase in alumina membrane for drug screening applications," *Journal of Membrane Science*, vol. 329, pp. 85-90, 2009.
- [3] G. Gonzalez, G. Priano, M. Gunther and F. Battaglini, "Mass transport effect of mesoscopic domains in the amperometric response of an electroactive species: Modeling for its applications in biomolecule detection," *Sensors and Actuators B: Chemical*, vol. 144, no. 2, pp. 349-353, 2008.
- [4] P. Milka, I. Krest and M. Keusgen, "Immobilization of alliinase on porous aluminum oxide," *Biotechnology and Bioengineering*, vol. 69, no. 3, pp. 344-348, 2000.
- [5] H. P. Jennissen, "Immobilizing mediator molecules via anchor molecules on metallic implant materials containing oxide layer". USA Patent 6,635,269 B1, 21 Oct 2003.
- [6] D. Hyndman, G. Lever, R. Burrell and T. G. Flynn, "Protein Immobilization to Alumina Supports: I. Characterization of Alumina-Organophosphate Ligand Interactions and Use in the Attachment of Papain," *Biotechnology and Bioengineering*, vol. 40, pp. 1319-1327, 1992.
- [7] D. Hyndman, R. Burrell, G. Lever and T. G. Flynn, "Protein Immobilization to Alumina Supports: II. Papain Immobilization to Alumina via Organophosphate Linkers," *Biotechnology and Bioengineering*, vol. 40, pp. 1328-1336, 1992.

- [8] J. Dai, G. L. Baker and M. L. Bruening, "Use of porous membranes modified with polyelectrolyte multilayers as substrates for protein arrays with low nonspecific adsorption," *Analytical Chemistry*, vol. 78, no. 1, pp. 135-140, 2005.
- [9] G. B. Oliveira, J. L. Filho, M. E. Chaves, W. M. Azevedo and L. B. Carvalho, "Enzyme immobilization on anodic aluminum oxide/polyethyleneimine or polyaniline composites," *Reactive and Functional Polymers*, vol. 68, no. 1, pp. 27-32, 2008.
- [10] R. Zuo, D. Ornek and T. K. Wood, "Aluminum- and mild steel-binding peptides from phage display," *Applied Genetics and Molecular Biotechnology*, vol. 68, pp. 505-509, 2005.
- [11] B. L. Adams, A. S. Finch, M. M. Hurley, D. A. Sarkes and D. N. Stratis-Cullum, "Genetically Engineered Peptides for Inorganics: Study of an Unconstrained Bacterial Display Technology and Bulk Aluminum Alloy," *Materials Views*, vol. 25, pp. 4585-4591, 2013.
- [12] Y. Gwak, J. Park, M. Kim, H. S. Kim, M. J. Kwon, S. J. Oh, Y. Kim and E. Jin, "Creating Anti-icing Surfaces via the Direct Immobilization of Antifreeze Proteins on Aluminum," *Scientific Reports*, vol. 5, no. 12019, pp. 1-9, 2015.
- [13] J. P. Murray and S. J. Laband, "Degradation of Poliovirus by Adsorption on Inorganic Surfaces," *Applied and Environmental Microbiology*, vol. 37, no. 3, pp. 480-486, 1979.
- [14] J. P. Murray, *Physical Chemistry of Virus Adsorption and Degradation on Inorganic Surfaces: Its relation to wastewater treatment*, Cincinnati, OH: United States Environmental Protection Agency, 1980.
- [15] R. B. Thurman and C. P. Gerba, "Characterization of the effect of aluminum metal on poliovirus," *Journal of Industrial Microbiology*, vol. 3, pp. 33-38, 1988.
- [16] W. R. Bowen and Q. Gan, "Properties of Microfiltration Membranes: The Effects of Adsorption and Shear on the Recovery of an Enzyme," *Biotechnology and Bioengineering*, vol. 40, pp. 491-497, 1992.
- [17] A. Wittayanukulluk, D. Jiang, F. E. Regnier and S. L. Hem, "Effect of microenvironment pH of aluminum hydroxide adjuvant on the chemical stability of adsorbed antigen," *Vaccine*, vol. 22, p. 1172, 2004.
- [18] T. Clapp, P. Siebert, D. Chen and L. J. Braun, "Vaccines with Aluminum-Containing Adjuvants: Optimizing Vaccine Efficacy and Thermal Stability," *Journal of Pharmaceutical Science*, vol. 100, no. 2, p. 388, 2011.
- [19] D. C. Kim, A. Jang and D. J. Kang, "Biological functionality of active enzyme structures immobilized on various solid surfaces," *Current Applied Physics*, vol. 9, p. 1454, 2009.

- [20] R. E. Burrell, "Aluminum Oxide Surfaces and Interface Molecules". Provisional Patent. Filed Feb. 20, 2018.
- [21] D. A. Walz, D. Hewett-Emmett and W. H. Seegers, "Amino acid sequence of human prothrombin fragments 1 and 2," *Proceedings of the Natural Academy of Sciences USA*, vol. 74, no. 5, pp. 1969-1972, 1977.
- [22] M. E. Karaman, D. A. Antelmi and R. M. Pashley, "The production of stable hydrophobic surfaces by the adsorption of hydrocarbon and fluorocarbon carboxylic acids onto alumina substrates," *Colloids and Surfaces A: Physicochemical and Engineering Aspects*, vol. 182, no. 1-3, p. 285, 2001.
- [23] D. Muljadi, A. M. Posner and J. P. Quirk, "The Mechanism of Phosphate Adsorption by Kaolinite, Gibbsite, and Pseudoboehmite. Part 2. The Location of the Adsorption Sites," *Journal of Soil Science*, vol. 17, no. 2, pp. 230-237, 1966.
- [24] J. van den Brand, O. Blajiev, P. C. Beentjes, H. Terryn and J. H. de Wit, "Interaction of Anhydride and Carboxylic Acid Compounds with Aluminum Oxide Surfaces Studied Using Infrared Reflection Absorption Spectroscopy," *American Chemical Society*, pp. 6308-6317, 2004.
- [25] T. K. Lim, V. A. Bloomfield and G. L. Nelsestuen, "Structure of the Prothrombin- and Blood Clotting Factor X-Membrane Complexes," *Biochemistry*, vol. 16, no. 19, pp. 4177-4181, 1977.
- [26] I. Migneault, C. Dartiguenave, M. J. Bertrand and K. C. Waldron, "Glutaraldehyde: behavior in aqueous solution, reaction with proteins, and application to enzyme crosslinking," *BioTechniques*, vol. 37, no. 5, p. 790, 2004.
- [27] D. R. Walt and V. I. Agayn, "The chemistry of enzyme and protein immobilization with glutaraldehyde," *Trends in Analytical Chemistry*, vol. 13, no. 10, p. 425, 1994.
- [28] Y. Wine, N. Cohen-Hadar, A. Freeman and F. Frolow, "Elucidation of the Mechanism and End Products of Glutaraldehyde Crosslinking Reaction by X-Ray Structure Analysis," *Biotechnology and Bioengineering*, vol. 98, no. 3, p. 711, 2007.
- [29] X. Xu, H. Song, J. Qi, Y. Liu, H. Wang, C. Su, Y. Shi and G. F. Gao, "Contribution of intertwined loop to membrane association revealed by Zika virus full-length NS1 structure," *The EMBO Journal*, vol. 35, no. 20, p. 2170, 2016.
- [30] Y. Shi and G. F. Gao, "Structural Biology of the Zika Virus," *Trends in Biochemical Sciences*, vol. 1344, p. 1, 2017.

- [31] E. O. Saphire, P. W. Parren, R. Pantophlet, M. B. Zwick, G. M. Morris, P. M. Rudd, R. A. Dwek, R. L. Stanfield, D. R. Burton and I. A. Wilson, "Crystal Structure of a Neutralizing Human IgG Against HIV-1: A Template for Vaccine Design," *Science*, vol. 293, p. 1155, 2001.
- [32] V. R. Sarma, E. W. Silverton, D. R. Davies and W. D. Terry, "The Three-Dimensional Structure at 6 Å Resolution of a Human  $\gamma$ G1 Immunoglobulin Molecule," *The Journal of Biological Chemistry*, vol. 246, no. 11, p. 3753, 1971.
- [33] H. Nygren, T. Sandström and M. Stenberg, "Direct Visual Detection of Protein Antigen: Importance of Surface Concentration," *Journal of Immunological Methods*, vol. 59, pp. 145-149, 1983.
- [34] I. Giaever, "The antigen-antibody reaction: a visual observation," *Journal of Immunology*, vol. 110, pp. 1424-1426, 1973.
- [35] H. Sweet, *Development of a Thin Film Device and Optics System for Protein Detection*, Edmonton, AB: University of Alberta, 2018.
- [36] E. H. Cordes and W. P. Jencks, "On the Mechanism of Schiff Base Formation and Hydrolysis," *Journal of the American Chemical Society*, vol. 84, no. 5, pp. 832-837, 1962.
- [37] K. Matsumoto, O. Hamada, H. Ukeda and Y. Osajima, "Amperometric Flow Injection Determination of Fructose with an Immobilized Fructose 5-Dehydrogenase Reactor," *Analytical Chemistry*, vol. 58, pp. 2732-2734, 1986.
- [38] E. H. Hansen and H. S. Mikkelsen, "Enzyme-Immobilization by the Glutardialdehyde Procedure. An investigation of the effects of reducing the Schiff-bases generated, as based on studying the immobilization of glucose oxidase to silanized controlled pore glass," *Analytical Letters*, vol. 24, no. 8, pp. 1419-1430, 1991.
- [39] W. C. Brown, D. L. Akey, J. R. Konwerski, J. T. Tarrasch, G. Skiniotis, R. J. Kuhn and J. L. Smith, "Extended surface for membrane association in Zika virus NS1 structure," *Nature Structural & Molecular Biology*, vol. 23, no. 9, p. 865, 2016.

## Chapter 7 Conclusion

### Conclusions

This work has increased the understanding of thin film diagnostics based on anodized aluminum-tantalum thin films and has shown the capability to tune the physical and optical properties of these devices to optimize their sensitivity for detection of adsorbed protein layers. The following is a list of key conclusions from this study:

1) Increased working gas pressure during sputtering of tantalum films decreased optical reflectance, even after coating with aluminum and anodizing, by creating a rougher tantalum film surface with voided grain boundaries that scatters light or traps it by internal reflections. The increased gas pressure also caused a phase change from  $\alpha$ -Ta to  $\beta$ -Ta. However, tantalum microstructure was not found to significantly influence the sensitivity of the anodized aluminum-tantalum films to detecting adsorbed protein layers. This likely occurs because of a new mismatch introduced between the effective refractive index of the protein layer and the porous aluminum oxide. At high surface density the refractive index of the adsorbed protein layer is much higher than at lower surface densities. The mismatch of refractive indices introduces a reflection of light at the protein/oxide interface which acts as noise in the system and reduces the interference colour effects.

2) The structure and topography of anodized aluminum is highly dependent on the sputtered microstructure. Sputtering parameters with a lower energy flux lead to voided grain boundaries and defects which increase pore tortuosity, inhomogeneity and pitting of the anodic alumina surface. However, the optical properties of the porous anodic alumina, specifically the refractive index, is robust to changes in the sputtered microstructure when anodizing under the conditions

tested (potentiostatic at 4V in 0.4M phosphoric-0.1M oxalic acid electrolyte). The sensitivity of these films to detecting adsorbed protein layers by a colour shift appears to be minimally improved when films are sputtered to produce dense films with minimal defects. The improved sensitivity is lower than expected likely due to the minimal variation in refractive index found for these films, which was <2% variation regardless of sputtered aluminum microstructure.

3) The anodization electrolyte and voltage strongly influence the optical properties and microstructure of the porous anodic alumina. The addition of oxalic acid has significant effects on the microstructure of films anodized in phosphoric acid leading to reduced surface roughness, increased thickness, smaller pore size, and higher refractive indices due to lower dissolution rates. Norsol Anoad<sup>®</sup> (glycolic acid and glycerol mixture) and citric acid have less of an effect on microstructure and optical properties with phosphoric acid anodization.

Increasing voltage results in an increase of the refractive index of the porous alumina layer in the range of 2 to 8V. The addition of 0.1M oxalic acid to a 0.4M phosphoric acid bath reduces the dissolution of the anodic alumina layer at lower voltages (2V) leading to increased ability to tune the refractive index by pore size. Voltage can also be increased mid-anodization to produce smaller pores at the alumina surface and wider pores below. This results in the ability to tune both the refractive index and the surface pore size of the alumina layer. The engineering of the refractive index and surface pore size was also accomplished through sequential anodization with sulphuric acid followed by the phosphoric-oxalic acid mix. The pores must be small enough to eliminate or reduce the amount of protein adsorption inside the pores, as this will change the refractive index of the alumina layer and reduce sensitivity by a mismatch of refractive indices between the protein and alumina layers.

4) The voltage, electrolyte and sputtered aluminum thickness can all be tailored to optimize the sensitivity of these films to detecting adsorbed protein layers by interference colour shifts. For best sensitivity, the thickness of the sputtered aluminum layer must be controlled to produce films which move through the first order interference colours when protein is adsorbed (approximately,  $0.2 < x < 0.5$  in  $Y_{xy}$  colour coordinate system). This must be combined with matching the refractive index of the alumina layer with the protein layer, preferably through changes in voltage or electrolyte during anodization.

5) Protein size and surface density have significant effects on the colour shifts when adsorbed to anodized aluminum-tantalum thin films. Molecular size can be visibly detected by the colour shift that occurs from the adsorbed protein thickness. Spacing of an antigen, prothrombin, can be achieved by adding a smaller molecule with a similar affinity for the alumina surface (fragment 1).

6) Glutaraldehyde activated prothrombin can be successfully used to bridge rabbit IgG and Zika virus non-structural protein 1 (NS1) to an anodic alumina surface. These antigens remain structurally intact enough for their associated antibodies to bind, create a thickness change, and thereby shift the interference colour of the surface. The antigen size and antibody type (polyclonal or monoclonal) were found to be important factors to consider when using these films as immunoassays.

### Future Direction

The future work can be divided into two main sections, (1) materials and (2) protein testing. On the materials end, it would be highly beneficial to continue the anodization work of this study. Chapter 4.3 introduced the concept of sequential anodization to engineer both the nanostructure

and optical properties of the porous alumina film. It would be helpful to expand the voltage parameters to find the limits of tunability for the refractive index. A thorough study of sensitivity, as that taken in Chapter 5, would also help, as the protein binding characteristics and composition of these films probably differ since they are initially anodized in sulphuric acid. These films likely have a high sulphate content at the surface since it is well known that the electrolyte anion is incorporated into the film [1, 2]. The film composition would also affect shelf-life of the interference colour, as higher phosphate content leads to a better resistance to hydration of the anodic alumina to form boehmite [3]. On the other hand, these films may prove to be more sensitive due to the small pore size preventing protein from adsorbing in the pores and changing the refractive index.

With regards to protein testing, it would be valuable to run the same study in Chapter 5.2 Part C with the use of a radiolabelled antibody. In this section, stronger differences in colour were found for lower antibody concentrations when the antigen spacing was increased on the surface. However, it is unknown whether this improved colour change is a result of the starting colour and where it sits in the first order interference regime, or whether the antigen spacing opened more epitopes for the polyclonal antibody to bind to. A radiolabelled antibody would confirm whether more antibody bound to the surface or not.

It might also help to run a series of tests optimizing the cross-linking procedure with glutaraldehyde. Glutaraldehyde acts through either Schiff base formation or Michael addition, both of which require nucleophilic attack of the aldehyde by the lone pair of electrons on the protein amino group. Increasing pH might improve reaction efficiency by increasing the number of deprotonated amino groups. Increasing glutaraldehyde concentration and reaction time might also improve the efficiency and allow for higher antigen surface density, leading to stronger colour

changes. Schiff base reactions are also susceptible to acid catalyzed hydrolysis of the double bond and therefore some reversibility in the reaction may be occurring. To prevent this a reducing agent can be used to stabilize the double bond to a single bond, where compounds such as sodium borohydride, sodium cyanoborohydride or sodium triacetoxyborohydride can be used.

To further the Zika NS1 antibody detection, the sensitivity could be improved by tuning the refractive index of the alumina layer. As discussed in Chapter 5.1, the voltage of anodization can be used to change the refractive index and the thickness can be adjusted to maintain first order interference colours. For example, increasing voltage leads to higher refractive indices and therefore a higher optical path length. Reducing the thickness of the sputtered aluminum would push the initial colour back into a lower optical path length ( $OPL = \eta d$ , where  $\eta$  is refractive index and  $d$  is physical path length), such that first order colours could be maintained. Films could be anodized at high and low voltages with lower and higher thicknesses, respectively. Then the NS1 protein could be immobilized using glutaraldehyde and the resulting colours measured for improved colour change.

Further testing also needs to be done in various media. Diagnostic tests are not done in pure buffers, but rather in complex solutions such as serum, whole blood, urine and saliva. Sweet [4] showed that serum can have negative effects on immobilized proteins over long periods of time. It needs to be understood what effects other complex media have on the thin film surface and whether there should be time restrictions for tests to reduce non-specific binding or unwanted chemical or enzymatic reactions.

Shelf-life testing would also be beneficial, as it is unknown how long an immobilized protein can remain structurally stable when bridged to an alumina surface via prothrombin. Prothrombin would

help increase the shelf-life by acting as a spacer between the aluminum oxide surface and the protein of interest, thereby preventing the surface from denaturing or catalytically degrading the protein. However, proteins require a hydration shell to maintain their shape and function. Over time the water may be entirely evaporated from the surface, leaving the proteins dry and susceptible to denaturation. In this case, special types of packaging could be used to reduce environmental effects and improve shelf-life.

As discussed previously, there are several benefits to the thin film diagnostic technology over the current standard of antibody-based tests, ELISA. These benefits include, rapidity of testing, reduced sample preparation time, reduced cost, capability of testing at the point-of-care and no need for trained technical staff to carry out the test. However, there are a number of technical challenges that still need to be overcome. Many of these were discussed above, including shelf-life, improved protein binding techniques, and reduced pore size to prevent smaller species that may be found in complex media from binding inside the nanoporous films. One aspect not addressed in this work is the testing of such technology in operational conditions. For example, the method by which a biological solution, i.e. patient blood or urine sample, is exposed to the surface, the mechanical device that holds the films and allows the operator to expose samples to the thin film surface, and the regulation requirements in medical device manufacturing. All these questions need to be addressed before a functional medical device can be commercialized.

## References

- [1] Y. Fukuda and T. Fukushima, "Behavior of Sulfate Ions during Formation of Anodic Oxide Film on Aluminium," *Bulletin of the Chemical Society of Japan*, vol. 53, no. 11, pp. 3125-3130, 1980.
- [2] G. E. Thompson and G. C. Wood, "Porous anodic film formation on aluminium," *Nature*, vol. 290, pp. 230-232, 1981.

[3] G. E. Thompson, R. C. Furneaux and G. C. Wood, "The Morphology of Sealed Anodic Films Formed on Aluminium in Phosphoric Acid," Transactions of the Institute of Metal Finishing, vol. 53, pp. 97-102, 1975.

[4] H. Sweet, Development of a Thin Film Device and Optics System for Protein Detection, Edmonton, AB: University of Alberta, 2018.

## References

### Chapter 1 - Introduction

- [1] C. D. Chin, V. Linder and S. K. Sia, "Commercialization of microfluidic point-of-care diagnostic devices," *Lab Chip*, vol. 12, pp. 2118-2134, 2012.
- [2] C. Dincer, R. Bruch, A. Kling, P. S. Dittrich and G. A. Urban, "Multiplexed Point-of-Care Testing - xPOCT," *Trends in Biotechnology*, pp. 1-15, 2017.
- [3] T. R. Holford, F. Davis and S. P. Higson, "Recent trends in antibody based sensors," *Biosensors and Bioelectronics*, vol. 34, pp. 12-24, 2012.
- [4] R. Burns, "Immunochemical techniques," in *Principles and Techniques of Biochemistry and Molecular Biology*, New York, NY, University Cambridge Press, 2010, pp. 263-299.
- [5] K. M. Koczula and A. Gallotta, "Lateral flow assays," *Essays in Biochemistry*, vol. 60, pp. 111-120, 2016.
- [6] V. Gubala, L. F. Harris, A. J. Ricco, M. X. Tan and D. E. Williams, "Point of Care Diagnostics: Status and Future," *Analytical Chemistry*, vol. 84, pp. 487-515, 2012.
- [7] EMD Millipore Corporation, "Rapid Lateral Flow Test Strips: Considerations for Product Development," EMD Millipore Corporation, Billerica, MA, 2013.
- [8] C. P. Chan, W. C. Mak, K. Y. Cheung, K. K. Sin, C. M. Yu, T. H. Rainer and R. Renneberg, "Evidence-Based Point-of-Care Diagnostics: Current Status and Emerging Technologies," *Annual Reviews of Analytical Chemistry*, vol. 6, pp. 191-211, 2013.
- [9] G. M. Whitesides, S. T. Phillips, A. W. Martinez, M. J. Butte, A. Wong, S. W. Thomas, H. Sindi, S. J. Vella, E. Carrilho, K. A. Mirica and Y. Liu, "Lateral flow and flow-through bioassay devices based on patterned porous media, methods of making same, and methods of using same". USA Patent 8,377,710 B2, 19 February 2013.
- [10] S. A. Dunbar, "Applications of Luminex® xMAP™ technology for rapid, high-throughput multiplexed nucleic acid detection," *Clinica Chimica Acta*, vol. 363, pp. 71-82, 2006.
- [11] C. D. Chin, Y. K. Cheung, T. Laksanasopin, M. M. Modena, S. Y. Chin, A. A. Sridhara, D. Steinmiller, V. Linder, J. Mushingantahe, G. Umviligihozo, E. Karita, L. Mwambarangwe, S. L. Braunstein, J. van de Wijgert, R. Sahabo, J. E. Justman, W. El-Sadr and S. K. Sia, "Mobile Device for Disease Diagnosis and Data Tracking in Resource-Limited Settings," *Clinical Chemistry*, vol. 59, no. 4, pp. 1-12, 2013.
- [12] H. Becker and L. E. Locascia, "Polymer microfluidic devices," *Talanta*, vol. 56, pp. 267-287, 2002.

- [13] J. Hu, X. Cui, Y. Gong, X. Xu, B. Gao, T. Wen, T. Lu and F. Xu, "Portable microfluidic and smartphone-based devices for monitoring of cardiovascular diseases at the point of care," *Biotechnology Advances*, vol. 34, pp. 305-320, 2016.
- [14] C. S. Kosack, A. Page and P. R. Klatser, "A guide to aid the selection of diagnostic tests," *Bullitin of the World Health Organization*, vol. 95, pp. 639-645, 2016.
- [15] A. Charlesby and J. J. Polling, "The Optical Properties of Thin Oxide Films on Tantalum," *Proceedings of the Royal Society of London. Series A, Mathematical and Physical Sciences*, vol. 227, pp. 434-447, 1955.
- [16] E. Hecht, *Optics*, Addison-Wesley Publishing Company, Inc., 1979.
- [17] I. Langmuir and V. J. Schaefer, "Optical measurement of the thickness of a film adsorbed from a solution," *Journal of the American Chemistry Society*, vol. 59, p. 1406, 1937.
- [18] M. F. Shaffer and I. H. Dingle, "A Study of Antigens and Antibodies by the Monolayer Film Technique of Langmuir," *Proceedings of the Society of Experimental Biology & Medicine*, vol. 38, p. 528, 1938.
- [19] E. F. Porter and A. M. Pappenheimer, "Antigen-antibody reactions between layers adsorbed on built up stearate films," *Journal of Experimental Medicine*, vol. 69, pp. 755-765, 1939.
- [20] I. Giaever, "The antigen-antibody reaction: a visual observation," *Journal of Immunology*, vol. 110, pp. 1424-1426, 1973.
- [21] A. L. Adams, M. Kling, G. C. Fischer and L. Vroman, "Three simple ways to detect antibody-antigen complex on flat surfaces," *Journal of Immunological Methods*, vol. 3, pp. 227-232, 1973.
- [22] I. Giaever, "Method and apparatus for immunological detection of biological particles". United States of America Patent 3,853,467, 10 December 1974.
- [23] I. Giaever, "Substrate for immunological tests and method of fabrication thereof". United States of America Patent 3,926,564, 16 December 1975.
- [24] I. Giaever, "Diagnostic device for visually detecting presence of biological particles". United States of America Patent 3,979,184, 7 September 1976.
- [25] I. Giaever and R. J. Laffin, "Visual detection of hepatitis B antigen," *Proceedings of the National Academy of Science USA*, vol. 71, pp. 4533-4535, 1974.
- [26] C. R. Keese and I. Giaever, "Measurement of antigen concentrations with a one-step inhibition assay," *Journal of Immunological Methods*, vol. 43, pp. 313-317, 1981.

- [27] B. H. Nygren, T. Sandstrom, J. E. Stenberg and L. B. Stilbert, "Method and member for detecting and/or measuring the concentration of a chemical substance". United States of America Patent 4,558,012, 10 December 1985.
- [28] H. Nygren, T. Sandström and M. Stenberg, "Direct Visual Detection of Protein Antigen: Importance of Surface Concentration," *Journal of Immunological Methods*, vol. 59, pp. 145-149, 1983.
- [29] T. Sandstrom, M. Stenberg and H. Nygren, "Visual detection of organic monomolecular films by interference colors," *Applied Optics*, vol. 24, no. 4, pp. 472-479, 1985.
- [30] T. Sandstrom, L. Stiblert and D. M. Maul, "Devices and methods for detection of an analyte based upon light interference". USA Patent 5,494,829, 27 February 1996.
- [31] J. M. Smith, M. C. Bauman and P. C. Fuchs, "An Optical Immunoassay for the Direct Detection of Group A Strep Antigen," *Laboratory Medicine*, vol. 26, no. 6, pp. 408-410, 1995.
- [32] T. M. Nguyen, D. W. Gauthier, T. D. Myles, B. S. Nuwayhid, M. A. Viana and P. C. Schreckenberger, "Detection of group B streptococcus: Comparison of an optical immunoassay with direct plating and broth-enhanced cultrue methods," *Journal of Maternal-Fetal Medicine*, vol. 7, pp. 172-176, 1998.
- [33] D. Schultze, Y. Thomas and W. Wunderli, "Evaluation of an Optical Immunoassay for the Rapid Detection of Influenza A and B Viral Antigens," *European Journal of Clinical Microbiology and Infectious Disease*, vol. 20, pp. 280-283, 2001.
- [34] C. I. Banda, E. H. Koumans, M. K. Sawyer, J. Dover, A. O'Connor, J. R. Papp, E. R. Unger, J. Braxton and C. M. Black, "Evaluation of the rapid BioStar optical immunoassay for detection of *Chlamydia trachomatis* in adolescent women," *Journal of Clinical Microbiology*, vol. 47, no. 1, pp. 215-216, 2009.
- [35] R. Ostroff, A. Ettinger, H. La, M. Rihanek, L. Zalman, J. Meador, A. K. Patick, S. Worland and B. Polisky, "Rapid multiserotype detection of human rhinoviruses on optically coated silicon surfaces," *Journal of Clinical Virology*, vol. 21, no. 2, pp. 105-117, 2001.
- [36] L. V. Dong, K. H. Eng, L. K. Quyen and P. Gopalakrishnakone, "Optical immunoassay for snake venom detection," *Biosensors and Bioelectronics*, vol. 19, pp. 1285-1294, 2004.
- [37] I. H. Malitson, "Interspecimen Comparison of the Refractive Index of Fused Silica," *Journal of the Optical Society of America*, vol. 55, no. 10, pp. 1205-1209, 1965.
- [38] T. L. McMeekin, M. L. Groves and N. J. Hipp, "Refractive Indices of Amino Acids, Proteins, and Related Substances," in *Amino Acids and Serum Proteins*, Philadelphia, American Chemical Society, 1964, pp. 54-66.

- [39] J. Vörös, "The Density and Refractive Index of Adsorbing Protein Layers," *Biophysics Journal*, vol. 87, no. 1, pp. 553-561, 2004.
- [40] J. Benesch, A. Askendal and P. Tengvall, "The determination of thickness and surface mass density of mesothick immunoprecipitate layers by null ellipsometry and protein 125iodine labeling," *Journal of Colloid and Interface Science*, vol. 249, no. 1, pp. 84-90, 2002.
- [41] R. G. C. Oudshoorn, R. P. H. Kooyman and J. Greve, "Refractive index and layer thickness of an adsorbing protein as reporters of monolayer formation," *Thin Solid Films*, Vols. 284-285, pp. 836-840, 1996.
- [42] T. Sandstrom, L. Stibler and D. M. Maul, "Method and instrument for detection of change of thickness or refractive index for a thin film substrate". USA Patent 5,613,171, 20 May 1997.
- [43] S. D. Alvarez, C. Li, C. E. Chiang, I. K. Schuller and M. J. Sailor, "A Label-Free Porous Alumina Interferometric Immunosensor," *ACS Nano*, vol. 3, no. 10, pp. 3301-3307, 2009.
- [44] S. Pan and L. J. Rothberg, "Interferometric Sensing of Biomolecular Binding Using Nanoporous Aluminum Oxide Templates," *Nano Letters*, vol. 3, no. 6, pp. 811-814, 2003.
- [45] H. U. Osmanbeyoglu, T. B. Hur and H. K. Kim, "Thin alumina nanoporous membranes for similar size biomolecule separation," *Journal of Membrane Science*, vol. 343, no. 1-2, pp. 1-6, 2009.
- [46] S. Simovic, D. Losic and K. Vasilev, "Controlled drug release from porous materials by plasma polymer deposition," *Chemical Communications*, vol. 46, no. 8, pp. 1317-1319, 2010.
- [47] K. C. Popat, E. E. Swan, V. Mukhatyar, K. Chatvanichkul, G. K. Mor, C. A. Grimes and T. A. Desai, "Influence of nanoporous alumina membranes on long-term osteoblast response," *Biomaterials*, vol. 26, no. 22, pp. 4516-4522, 2005.
- [48] R. E. Burrell, A. G. Naylor and A. M. Rosenfeld. US Patent 5,124,172, 1992.
- [49] S. S. Djokić and R. E. Burrell, "Visual detection of protein adsorption onto electrochemically oxidized aluminum surfaces," *Biosensors & Bioelectronics*, vol. 13, pp. 271-278, 1998.
- [50] D. A. Vermilyea, "The Kinetics of Formation and Structure of Anodic Oxide Films on Tantalum," *Acta Metallurgica*, vol. 1, pp. 283-294, 1953.
- [51] G. Wypych, *Handbook of Fillers 3rd Edition*, ChemTec Publishing, 2010.
- [52] K. Nassau, *The Physics and Chemistry of Color: The Fifteen Causes of Color*, NY: John Wiley & Sons, Inc., 1983.

- [53] "Interference colours," OpenLearn, [Online]. Available: <http://www.open.edu/openlearn/science-maths-technology/science/introduction-minerals-and-rocks-under-the-microscope/content-section-2.2.5>. [Accessed 05 05 2018].
- [54] R. G. Ben, "1931 Colour Space," Wikipedia, [Online]. Available: <https://commons.wikimedia.org/w/index.php?curid=7889658>. [Accessed 18 June 2018].
- [55] L. S. Jung, C. T. Campbell, T. M. Chinowsky, M. N. Mar and S. S. Yee, "Quantitative Interpretation of the Response of Surface Plasmon Resonance Sensors to Adsorbed Films," *Langmuir*, vol. 14, no. 19, pp. 5636-5648, 1998.
- [56] P. G. Sheasby and R. Pinner, *The Surface Treatment and Finishing of Aluminum and its Alloys - 6th Edition*, Finishing Publications Ltd., 2001.
- [57] A. G. Naylor, Interviewee, [Interview]. May 2016.
- [58] J. L. Vossen and W. Kern, *Thin Film Processes*, New York: Academic Press, Inc., 1978.
- [59] R. F. Bunshah, *Handbook of Deposition Technologies for Films and Coatings: Science, Technology and Applications Second Edition*, Park Ridge: Noyes Publications, 1994.
- [60] J. A. Thornton, "The microstructure of sputter-deposited coatings," *Journal of Vacuum Science and Technology*, vol. 4, no. 6, pp. 3059-3065, 1986.
- [61] J. A. Thornton, "Influence of apparatus geometry and deposition conditions on the structure and topography of thick sputtered coatings," *Journal of Vacuum Science & Technology*, vol. 11, pp. 666-670, 1974.
- [62] J. A. Thornton and D. W. Hoffman, "Stress-related Effects in Thin Films," *Thin Solid Films*, vol. 171, pp. 5-31, 1989.
- [63] J. G. Han, "Recent progress in thin film processing by magnetron sputtering with plasma diagnostics," *Journal of Physics D: Applied Physics*, vol. 42, p. 043001, 2009.
- [64] R. Messier, A. P. Giri and R. A. Roy, "Revised structure zone model for thin film physical structure," *Journal of Vacuum Science and Technology A*, vol. 2, pp. 500-503, 1984.
- [65] K. Chan and B. Teo, "Sputtering power and deposition pressure effects on the electrical and structural properties of copper thin films," *Journal of Materials Science*, vol. 40, pp. 5971-5981, 2005.
- [66] D. W. Hoffman and J. A. Thornton, "The compressive stress transition in Al, V, Zr, Nb and W metal films sputtered at low working pressures," *Thin Solid Films*, vol. 45, pp. 387-396, 1977.

- [67] S. Van Gils, T. Dimogerontakis, G. Buytaert, E. Stijns, P. Skeldon, G. E. Thompson and M. R. Alexander, "Optical properties of magnetron-sputtered and rolled aluminum," *Journal of Applied Physics*, vol. 98, 2005.
- [68] W. Lee and S. Park, "Porous Anodic Aluminum Oxide: Anodization and Templated Synthesis of Functional Nanostructures," *Chemical Reviews*, vol. 114, pp. 7487-7556, 2014.
- [69] G. D. Bengough and J. M. Stuart, "Improved process of protecting surfaces of aluminium or aluminium alloys". UK Patent 223,994, 2 August 1923.
- [70] G. D. Sulka, "Highly Ordered Anodic Porous Alumina Formation by Self-Organization Anodizing," in *Nanostructured Materials in Electrochemistry*, Weinheim, Wiley-VCH, 2008, pp. 1-97.
- [71] W. Lee and S. Park, "Porous Anodic Aluminum Oxide: Anodization and Templated Synthesis of Functional Nanostructures," *Chemical Reviews*, vol. 114, pp. 7487-7556, 2014.
- [72] G. E. Thompson, "Porous anodic alumina: fabrication, characterization and applications," *Thin Solid Films*, vol. 297, pp. 192-201, 1997.
- [73] A. Mutalib Md Jani, D. Losic and N. H. Voelcker, "Nanoporous anodic aluminium oxide: Advances in surface engineering and emerging applications," *Progress in Materials Science*, vol. 58, pp. 636-704, 2013.
- [74] R. C. Furneaux, W. R. Rigby and A. P. Davidson, "The formation of controlled-porosity membranes from anodically oxidized aluminum," *Nature*, vol. 337, no. 12, pp. 147-149, 1989.
- [75] G. E. Thompson, "Porous anodic alumina: fabrication, characterization and applications," *Thin Solid Films*, vol. 297, pp. 192-201, 1997.
- [76] G. E. Thompson, R. C. Furneaux, G. C. Wood, J. A. Richardson and J. S. Goode, "Nucleation and growth of porous anodic films on aluminum," *Nature*, vol. 272, pp. 433-435, 1978.
- [77] K. R. Herbert, S. P. Albu, I. Paramasivam and P. Schmuki, "Morphological instability leading to formation of porous anodic oxide films," *Nature Materials*, vol. 11, pp. 162-166, 2012.
- [78] J. Wang, C. Wang, Y. Li and W. Liu, "Optical constants of anodic aluminum oxide films formed in oxalic acid solution," *Thin Solid Films*, vol. 516, pp. 7689-7694, 2008.
- [79] Y. Wang, L. Chen, Z. Wu, S. Xu, H. Cui and W. Xu, "Subtle vertical structures of porous anodic alumina films for use as waveguides," *Nanotechnology*, vol. 28, no. 18, 2017.

- [80] A. Hierro-Rodriguez, P. Rocha-Rodrigues, F. Valdes-Bango, J. M. Alameda, P. A. Jorge, J. L. Santos, J. P. Araujo and J. M. Teixeira, "On the anodic aluminium oxide refractive index of nanoporous templates," *Journal of Physics D: Applied Physics*, vol. 48, no. 45, p. 455105, 2015.
- [81] M. M. Rahman, E. Garcia-Caurel, A. Santos, L. F. Marsal, J. Pallares and J. Ferre-Borrull, "Effect of the anodization voltage on the pore-widening rate of nanoporous anodic alumina," *Nanoscale Research Letters*, vol. 7, no. 474, 2012.
- [82] G. E. Thompson, R. C. Furneaux and G. C. Wood, "The Morphology of Sealed Anodic Films Formed on Aluminium in Phosphoric Acid," *Transactions of the Institute of Metal Finishing*, vol. 53, pp. 97-102, 1975.
- [83] G. D. Davis, T. S. Sun, J. S. Ahearn and J. D. Venables, "Application of surface behaviour diagrams to the study of hydration of phosphoric acid-anodized aluminum," *Journal of Materials Science*, vol. 17, pp. 1807-1818, 1982.
- [84] J. D. Venables, M. E. Tadros and B. M. Ditchek. US Patent 4,308,079, 1981.
- [85] R. L. Parfitt, "Anion Adsorption by Soils and Soil Materials," in *Advances in Agronomy*, Academic Press Inc, 1978, pp. 1-50.
- [86] D. Muljadi, A. M. Posner and J. P. Quirk, "The Mechanism of Phosphate Adsorption by Kaolinite, Gibbsite, and Pseudoboehmite. Part 2. The Location of the Adsorption Sites," *Journal of Soil Science*, vol. 17, no. 2, pp. 230-237, 1966.
- [87] R. D. Ramsier, P. N. Henriksen and A. N. Gent, "Adsorption of Phosphorous Acids on Alumina," *Surface Science*, vol. 203, pp. 72-88, 1988.
- [88] D. Costa, L. Savio and C.-M. Pradier, "Adsorption of Amino Acids and Peptides on Metal and Oxide Surfaces in Water Environment: A Synthetic and Prospective Review," *The Journal of Physical Chemistry B*, vol. 120, pp. 7039-7052, 2016.
- [89] E. Greiner, K. Kumar, M. Sumit, A. Giuffre, W. Zhao, J. Pedersen and N. Sahai, "Adsorption of L-glutamic acid and L-aspartic acid to  $\gamma$ -Al<sub>2</sub>O<sub>3</sub>," *Geochimica et Cosmochimica Acta*, vol. 133, pp. 142-155, 2014.
- [90] M. Trujillo, J. Valencia and J. C. Calvo, "Peptide solubility, structure and charge position effect on adsorption by aluminium hydroxide," *Revista Colombiana de Química*, vol. 35, no. 2, pp. 135-146, 2006.
- [91] R. J. Sepelyak, J. R. Feldkamp, T. E. Moody, J. L. White and S. L. Hem, "Adsorption of Pepsin by Aluminum Hydroxide I: Adsorption Mechanism," *American Pharmaceutical Association*, vol. 73, no. 11, p. 1514, 1984.

- [92] J. P. Murray and S. J. Laband, "Degradation of Poliovirus by Adsorption on Inorganic Surfaces," *Applied and Environmental Microbiology*, vol. 37, no. 3, pp. 480-486, 1979.
- [93] J. P. Murray, *Physical Chemistry of Virus Adsorption and Degradation on Inorganic Surfaces: Its relation to wastewater treatment*, Cincinnati, OH: United States Environmental Protection Agency, 1980.
- [94] R. B. Thurman and C. P. Gerba, "Characterization of the effect of aluminum metal on poliovirus," *Journal of Industrial Microbiology*, vol. 3, pp. 33-38, 1988.
- [95] W. R. Bowen and Q. Gan, "Properties of Microfiltration Membranes: The Effects of Adsorption and Shear on the Recovery of an Enzyme," *Biotechnology and Bioengineering*, vol. 40, pp. 491-497, 1992.
- [96] D. C. Kim, A. Jang and D. J. Kang, "Biological functionality of active enzyme structures immobilized on various solid surfaces," *Current Applied Physics*, vol. 9, p. 1454, 2009.
- [97] A. Wittayanukulluk, D. Jiang, F. E. Regnier and S. L. Hem, "Effect of microenvironment pH of aluminum hydroxide adjuvant on the chemical stability of adsorbed antigen," *Vaccine*, vol. 22, p. 1172, 2004.
- [98] T. Clapp, P. Siebert, D. Chen and L. J. Braun, "Vaccines with Aluminum-Containing Adjuvants: Optimizing Vaccine Efficacy and Thermal Stability," *Journal of Pharmaceutical Science*, vol. 100, no. 2, p. 388, 2011.
- [99] P. Takmakov, I. Vlassioug and S. Smirnov, "Application of anodized aluminum in fluorescence detection of biological species," *Analytical and Bioanalytical Chemistry*, vol. 385, no. 5, pp. 954-958, 2006.
- [100] S. Tanvir, J. Pantigny, P. Boulnois and S. Pulvin, "Covalent immobilization of recombinant human cytochrome CYP2E1 and glucose-6-phosphate dehydrogenase in alumina membrane for drug screening applications," *Journal of Membrane Science*, vol. 329, pp. 85-90, 2009.
- [101] G. Gonzalez, G. Priano, M. Gunther and F. Battaglini, "Mass transport effect of mesoscopic domains in the amperometric response of an electroactive species: Modeling for its applications in biomolecule detection," *Sensors and Actuators B: Chemical*, vol. 144, no. 2, pp. 349-353, 2008.
- [102] P. Milka, I. Krest and M. Keusgen, "Immobilization of alliinase on porous aluminum oxide," *Biotechnology and Bioengineering*, vol. 69, no. 3, pp. 344-348, 2000.
- [103] H. P. Jennissen, "Immobilizing mediator molecules via anchor molecules on metallic implant materials containing oxide layer". USA Patent 6,635,269 B1, 21 Oct 2003.

- [104] P. Rezvanian, M. Arroyo-Hernandez, M. Ramos, R. Daza, M. Elices, G. V. Guinea and J. Pérez-Rigueira, "Development of a versatile procedure for the biofunctionalization of Ti-6Al-4V implants," *Applied Surface Science*, vol. 387, pp. 656-660, 2016.
- [105] D. Hyndman, G. Lever, R. Burrell and T. G. Flynn, "Protein Immobilization to Alumina Supports: I. Characterization of Alumina-Organophosphate Ligand Interactions and Use in the Attachment of Papain," *Biotechnology and Bioengineering*, vol. 40, pp. 1319-1327, 1992.
- [106] D. Hyndman, R. Burrell, G. Lever and T. G. Flynn, "Protein Immobilization to Alumina Supports: II. Papain Immobilization to Alumina via Organophosphate Linkers," *Biotechnology and Bioengineering*, vol. 40, pp. 1328-1336, 1992.
- [107] Y. Lu, D. Zhang, Q. Zhang, Y. Huang, S. Luo, Y. Yao, S. Li and Q. Liu, "Impedance spectroscopy analysis of human odorant binding proteins immobilized on nanopore arrays for biochemical detection," *Biosensors and Bioelectronics*, vol. 79, p. 251, 2016.
- [108] J. Dai, G. L. Baker and M. L. Bruening, "Use of porous membranes modified with polyelectrolyte multilayers as substrates for protein arrays with low nonspecific adsorption," *Analytical Chemistry*, vol. 78, no. 1, pp. 135-140, 2005.
- [109] G. B. Oliveira, J. L. Filho, M. E. Chaves, W. M. Azevedo and L. B. Carvalho, "Enzyme immobilization on anodic aluminum oxide/polyethyleneimine or polyaniline composites," *Reactive and Functional Polymers*, vol. 68, no. 1, pp. 27-32, 2008.
- [110] S. D. Alvarez, C. Li, C. E. Chiang, I. K. Schuller and M. J. Sailor, "A label-free porous alumina interferometric immunosensor," *ACS Nano*, vol. 3, no. 10, pp. 3301-3307, 2009.
- [111] B. L. Adams, A. S. Finch, M. M. Hurley, D. A. Sarkes and D. N. Stratis-Cullum, "Genetically Engineered Peptides for Inorganics: Study of an Unconstrained Bacterial Display Technology and Bulk Aluminum Alloy," *Materials Views*, vol. 25, pp. 4585-4591, 2013.
- [112] R. Zuo, D. Ornek and T. K. Wood, "Aluminum- and mild steel-binding peptides from phage display," *Applied Genetics and Molecular Biotechnology*, vol. 68, pp. 505-509, 2005.
- [113] Y. Gwak, J. Park, M. Kim, H. S. Kim, M. J. Kwon, S. J. Oh, Y. Kim and E. Jin, "Creating Anti-icing Surfaces via the Direct Immobilization of Antifreeze Proteins on Aluminum," *Scientific Reports*, vol. 5, no. 12019, pp. 1-9, 2015.
- [114] R. E. Burrell, "Aluminum Oxide Surfaces and Interface Molecules". Provisional Patent. Filed Feb. 20, 2018.
- [115] M. Huang, A. C. Rigby, X. Morelli, M. A. Grant, G. Huang, B. Furie, B. Seaton and B. C. Furie, "Structural basis of membrane binding by Gla domains of vitamin K-dependent proteins," *Nature Structural Biology*, vol. 10, no. 9, pp. 751-756, 2003.

- [116] T. K. Lim, V. A. Bloomfield and G. L. Nelsestuen, "Structure of the Prothrombin- and Blood Clotting Factor X-Membrane Complexes," *Biochemistry*, vol. 16, no. 19, pp. 4177-4181, 1977.
- [117] K. G. Mann, M. E. Nesheim, W. R. Church, P. Haley and S. Krishnaswamy, "Surface-Dependent Reactions of the Vitamin K-Dependent Enzyme Complexes," *Blood*, vol. 76, no. 1, pp. 1-16, 1990.
- [118] D. A. Walz, D. Hewett-Emmett and W. H. Seegers, "Amino acid sequence of human prothrombin fragments 1 and 2," *Proceedings of the National Academy of Sciences USA*, vol. 74, no. 5, pp. 1969-1972, 1977.
- [119] A. Violante, C. Colombo and A. Buondonno, "Competitive Adsorption of Phosphate and Oxalate by Aluminum Oxides," *Soil Science Society of America Journal*, vol. 55, pp. 65-70, 1991.
- [120] J. van den Brand, O. Blajiev, P. C. Beentjes, H. Terryn and J. H. de Wit, "Interaction of Anhydride and Carboxylic Acid Compounds with Aluminum Oxide Surfaces Studied Using Infrared Reflection Absorption Spectroscopy," *American Chemical Society*, pp. 6308-6317, 2004.
- [121] R. Nave, "Oil Film Interference," *Hyperphysics*, [Online]. Available: <http://hyperphysics.phy-astr.gsu.edu/hbase/phyopt/oilfilm.html>. [Accessed 19 December 2016].
- [122] "Interference by Thin Film," *askIITians.com*, [Online]. Available: <https://www.askiitians.com/iit-jee-wave-optics/interference-by-thin-film/>. [Accessed 05 05 2018].

## **Chapter 2 – Tantalum**

- [1] J. J. Colin, G. Abadias, A. Michel and C. Jaouen, "On the origin of the metastable  $\beta$ -Ta phase stabilization in tantalum sputtered thin films," *Acta Materialia*, vol. 126, p. 481, 2017.
- [2] M. H. Read and C. Altman, "A New Structure in Tantalum Thin Films," *Applied Physics Letters*, vol. 7, p. 51, 1965.
- [3] M. H. Read and D. H. Hensler, "X-ray Analysis of Sputtered Films of Beta-Tantalum and Body-Centered Cubic Tantalum," *Thin Solid Films*, vol. 10, p. 123, 1972.
- [4] D. G. Muth, "Ellipsometer Study of Anodic Oxides Formed on Sputtered Tantalum and Tantalum-Aluminum Alloy Films," *Journal of Vacuum Science and Technology*, vol. 6, p. 749, 1969.
- [5] S. L. Lee, M. Doxbeck, J. Mueller, M. Cipollo and P. Cote, "Texture, structure and phase transformation in sputter beta tantalum coating," *Surface & Coatings Technology*, vol. 177, p. 44, 2004.

- [6] A. A. Navid and A. M. Hodge, "Nanostructured alpha and beta tantalum formation - Relationship between plasma parameters and microstructure," *Materials Science and Engineering A*, vol. 536, p. 49, 2012.
- [7] J. A. Thornton and D. W. Hoffman, "Stress-related Effects in Thin Films," *Thin Solid Films*, vol. 171, pp. 5-31, 1989.
- [8] A. Charlesby and J. J. Polling, "The Optical Properties of Thin Oxide Films on Tantalum," *Proceedings of the Royal Society of London. Series A, Mathematical and Physical Sciences*, vol. 227, pp. 434-447, 1955.
- [9] L. Young, "The determination of the thickness, dielectric constant, and other properties of anodic oxide films on tantalum from the interference colours," *Proceedings of the Royal Society A: Mathematical, Physical, and Engineering Sciences*, vol. 244, p. 41, 1958.
- [10] S. Cui-Cui, C. Yun-Yu, D. En-Mei and L. Chang-Hao, "Tunable structural color of anodic tantalum oxide films," *Chinese Physics B*, vol. 21, p. 088101, 2012.
- [11] D. Y. Smith, "The Optical Properties of Metallic Aluminum," in *Handbook of Optical Constants of Solids*, San Diego, Academic Press Inc., 1985, pp. 369-406.
- [12] J. A. Thornton and D. W. Hoffman, "Internal stresses in titanium, nickel, molybdenum, and tantalum films deposited by cylindrical magnetron sputtering," *Journal of Vacuum Science and Technology*, vol. 14, pp. 164-168, 1977.
- [13] J. A. Thornton, "The microstructure of sputter-deposited coatings," *Journal of Vacuum Science and Technology*, vol. 4, no. 6, pp. 3059-3065, 1986.

### **Chapter 3 – Aluminum**

- [1] C. R. Fuller and P. B. Ghate, "Magnetron-sputtered aluminum films for integrated circuit interconnections," *Thin Solid Films*, vol. 64, pp. 25-37, 1979.
- [2] L. D. Hartsough and P. S. McLeod, "High-rate sputtering of enhanced aluminum mirrors," *Journal of Vacuum Science and Technology*, vol. 14, no. 1, p. 123, 1977.
- [3] I. Hong, C. Chiu, H. Huang and R. Hsieh, "A Study of the Microstructure, Texture and Sputtering Properties of 5N High-purity Aluminum Target," *China Steel Technical Report*, vol. 24, p. 56, 2011.
- [4] L. Piergiovanni and S. Limbo, "Metal Packaging Materials," in *Food Packaging Materials*, NY, Springer, Cham, 2016, pp. 13-21.
- [5] J. A. Thornton, "The microstructure of sputter-deposited coatings," *Journal of Vacuum Science and Technology*, vol. 4, no. 6, pp. 3059-3065, 1986.

- [6] J. A. Thornton, "Influence of apparatus geometry and deposition conditions on the structure and topography of thick sputtered coatings," *Journal of Vacuum Science & Technology*, vol. 11, pp. 666-670, 1974.
- [7] J. A. Thornton and D. W. Hoffman, "Stress-related Effects in Thin Films," *Thin Solid Films*, vol. 171, pp. 5-31, 1989.
- [8] R. K. Waits, "Planar Magnetron Sputtering," in *Thin Film Processes*, New York, Academic Press, Inc., 1978, pp. 131-170.
- [9] R. F. Bunshah, *Handbook of Deposition Technologies for Films and Coatings*, Science, Technology and Applications, Second Edition, New Jersey: Noyes Publications, 1994, pp. 29-.
- [10] J. G. Han, "Recent progress in thin film processing by magnetron sputtering with plasma diagnostics," *Journal of Physics D: Applied Physics*, vol. 42, p. 043001, 2009.
- [11] R. Knepper and R. Messier, "Thin Film Morphology at Low Adatom Mobility," *Proceedings of SPIE*, vol. 4467, p. 87, 2001.
- [12] K. H. Guenther, "Revisiting structure zone models for thin film growth," *SPIE*, vol. 1324, p. 2, 1990.
- [13] I. K. Chin, F. K. Yam, Y. Chai and Z. Hassan, "Comparative study of porous anodic alumina: effects of aluminium deposition methods," *Materials Science and Technology*, vol. 31, no. 6, p. 709, 2015.
- [14] S. Upreti, K. Mukherjee, M. Palit, A. Bag, S. Mallik, S. Chattopadhyay and C. K. Maiti, "Porous Anodic Alumina Template Formation: Deposition Technique Dependence," in *Physics of Semiconductor Devices, Environmental Science and Engineering*, Cham, Springer, 2014, pp. 725-728.
- [15] T. H. Choudhury and S. Raghavan, "Anodization of sputtered metallic films: The microstructural connection," *Scripta Materialia*, vol. 105, pp. 18-21, 2015.
- [16] A. F. Feil, M. V. da Costa, L. Amaral, S. R. Teixeira, P. Migowski, J. Dupont, G. Machado and S. B. Peripolli, "The influence of aluminum grain size on alumina nanoporous structure," *Journal of Applied Physics*, vol. 107, p. 026103, 2010.
- [17] M. W. Liao and C. K. Chung, "Growth of porous anodized alumina on the sputtered aluminum films with 2D-3D morphology for high specific surface area," *Applied Surface Science*, vol. 309, pp. 290-294, 2014.
- [18] C. K. Chung, M. W. Liao, O. K. Khor and H. C. Chang, "Enhancement of pore size distribution in one-step hybrid pulse anodization of aluminum thin films sputtered on Si substrates," *Thin Solid Films*, vol. 544, pp. 374-379, 2013.

- [19] T. Lebyedyeva, S. Kryvyi, P. Lytvyn, M. Skoryk and P. Shpylovyy, "Formation of Nanoporous Anodic Alumina by Anodization of Aluminum Films on Glass Substrates," *Nanoscale Research Letters*, vol. 11, no. 203, 2016.
- [20] W. H. Yu, G. T. Fei, X. M. Chen, F. H. Xue and X. J. Xu, "Influence of defects on the ordering degree of nanopores made from anodic aluminum oxide," *Physics Letters A*, vol. 350, pp. 392-395, 2006.
- [21] J. Goldstein, D. Newbury, D. Joy, C. Lyman, P. Echlin, E. Lifshin, L. Sawyer and J. Michael, *Scanning Electron Microscopy and X-Ray Microanalysis*, 3rd Ed., New York: Springer Science + Business Media LLC, 2003.
- [22] T. Sandström, M. Stenberg and H. Nygren, "Visual detection of organic monomolecular films by interference colors," *Applied Optics*, vol. 24, no. 4, pp. 472-479, 1985.
- [23] R. E. Burrell, A. G. Naylor and A. M. Rosenfeld, "Thin Film Diagnostic". US Patent 5,124,172, 23 June 1992.
- [24] P. Chiggiato, "Vacuum Technology for Ion Sources," in *CAS CERN Accelerator School: Ion Sources*, Senec, Slovakia, CERN, 2013, pp. 463-502.
- [25] S. Van Gils, T. Dimogerontakis, G. Buytaert, E. Stijns, P. Skeldon, G. E. Thompson and M. R. Alexander, "Optical properties of magnetron-sputtered and rolled aluminum," *Journal of Applied Physics*, vol. 98, 2005.
- [26] R. S. Nowicki, "Influence of residual gases on the properties of dc magnetron-sputtered aluminum-silicon," *Journal of Vacuum Science and Technology*, vol. 17, no. 1, p. 384, 1980.
- [27] H. H. Gatzen, V. Saile and J. Leuthold, "Vacuum Technology," in *Micro and Nano Fabrication: Tools and Processes*, Berlin, Springer-Verlag, 2015, pp. 7-63.
- [28] M. F. Ashby, *Materials Selection in Mechanical Design*, Fourth Edition, Burlington, MA: Elsevier Ltd., 2011.
- [29] B. Kim and J. S. Lee, "Formation of Anodic Aluminum Oxide with Branched or Meshed Pores," *Journal of Nanoscience and Nanotechnology*, vol. 16, no. 6, p. 6575, 2016.
- [30] L. Maissel and R. Glang, *Handbook of Thin Film Technology*, NY: McGraw-Hill, 1970.
- [31] H. Sweet, *Development of a Thin Film Device and Optics System for Protein Detection*, Edmonton, AB: University of Alberta, 2018.

## Chapter 4 – Anodization

### Chapter 4.1 – The Effect of Chemical Additives in Phosphoric Acid Anodization of Aluminum-Tantalum Thin Films

- [1] P. G. Sheasby and R. Pinner, *The Surface Treatment and Finishing of Aluminum and its Alloys* - 6th Edition, Finishing Publications Ltd., 2001.
- [2] R. C. Furneaux, W. R. Rigby and A. P. Davidson, "The formation of controlled-porosity membranes from anodically oxidized aluminum," *Nature*, vol. 337, no. 12, pp. 147-149, 1989.
- [3] W. Lee and S. Park, "Porous Anodic Aluminum Oxide: Anodization and Templated Synthesis of Functional Nanostructures," *Chemical Reviews*, vol. 114, pp. 7487-7556, 2014.
- [4] R. E. Burrell, A. G. Naylor and A. M. Rosenfeld. "Thin Film Diagnostic Device. " US Patent 5,124,172, 1992.
- [5] M. A. Jozefowicz and A. M. Rosenfeld, "Optical Interference Structures". US Patent 5,218,472, 8 June 1993.
- [6] A. M. Rosenfeld and P. Smits, "Colour Change Devices Incorporating Thin Anodic Films". US Patent 4,994,314, 19 February 1991.
- [7] P. Smits, A. M. Rosenfeld and H. F. DeFerrari, "Tamper-Evident Structures". US Patent 4,837,061, 6 June 1989.
- [8] P. P. Mardilovich, A. N. Govyadinov, N. I. Mazurenko and R. Paterson, "New and modified anodic alumina membranes Part II. Comparison of solubility of amorphous (normal) and polycrystalline anodic alumina membranes," *Journal of Membrane Science*, vol. 98, pp. 143-155, 1995.
- [9] V. Moutarlier, M. P. Gigandet, J. Pagetti and B. Normand, "Influence of oxalic acid addition to chromic acid on the anodising of Al 2024 alloy," *Surface Coatings and Technology*, vol. 182, pp. 117-123, 2004.
- [10] W. Bensalah, M. Feki, M. Wery and H. F. Ayed, "Chemical dissolution resistance of anodic oxide layers formed on aluminum," *Transactions of Nonferrous Metals Society of China*, vol. 21, pp. 1673-1679, 2011.
- [11] Y. Shang, L. Wang, D. Niu, Z. Liu, Y. Wang and C. Liu, "Effects of Additive for Anodizing Electrolyte on Anodic Film of High Silicon Aluminum Alloy," *International Journal of Electrochemical Science*, vol. 11, pp. 1549-1557, 2016.
- [12] K. Hinrichs and K. Eichhorn, "Ch. 7 Detection of Organic Attachment onto Highly Ordered Three-Dimensional Nanostructured Thin Films by Generalized Ellipsometry and Quartz

Crystal Microbalance with Dissipation Techniques, " in *Ellipsometry of Functional Organic Surfaces and Films*, Heidelberg: Springer, 2014, pp. 142-143.

[13] G. E. Thompson, "Porous anodic alumina: fabrication, characterization and applications," *Thin Solid Films*, vol. 297, pp. 192-201, 1997.

[14] D. A. Skoog, D. M. West and F. J. Holler, "Appendix 4 – Dissociation Constants for Acids, " in *Fundamentals of Analytical Chemistry – 5<sup>th</sup> Edition*, New York, W. B. Saunders Company, 1988, p. 817.

[15] A. Violante, C. Colombo and A. Buondonno, "Competitive Adsorption of Phosphate and Oxalate by Aluminum Oxides," *Soil Science Society of America Journal*, vol. 55, pp. 65-70, 1991.

[16] J. van den Brand, O. Blajiev, P. C. Beentjes, H. Terryn and J. H. de Wit, "Interaction of Anhydride and Carboxylic Acid Compounds with Aluminum Oxide Surfaces Studied Using Infrared Reflection Absorption Spectroscopy," *American Chemical Society*, pp. 6308-6317, 2004.

[17] P. Benoit, J. G. Hering and W. Stumm, "Comparative study of the adsorption of organic ligands on aluminum oxide by titration calorimetry," *Applied Geochemistry*, vol. 8, pp. 127-139, 1993.

[18] "National Center for Biotechnology Information," PubChem Compound Database, [Online]. Available: <https://pubchem.ncbi.nlm.nih.gov/>. [Accessed 13 September 2017].

## Chapter 4.2 - The Effects of Voltage on the Structure and Optical Properties of Anodized Aluminum-Tantalum Thin Films

[1] G. E. Thompson and G. C. Wood, "Porous anodic film formation on aluminium," *Nature*, vol. 290, pp. 230-232, 1981.

[2] P. G. Sheasby and R. Pinner, *The Surface Treatment and Finishing of Aluminum and its Alloys - 6th Edition*, Finishing Publications Ltd., 2001.

[3] J. P. O'Sullivan and G. C. Wood, "The morphology and mechanism of formation of porous anodic films on aluminium," *Proceedings of the Royal Society of London A*, vol. 317, pp. 511-543, 1970.

[4] W. Lee and S. Park, "Porous Anodic Aluminum Oxide: Anodization and Templated Synthesis of Functional Nanostructures," *Chemical Reviews*, vol. 114, pp. 7487-7556, 2014.

[5] G. D. Sulka, "Highly Ordered Anodic Porous Alumina Formation by Self-Organization Anodizing," in *Nanostructured Materials in Electrochemistry*, Weinheim, Wiley-VCH, 2008, pp. 1-97.

- [6] H. U. Osmanbeyoglu, T. B. Hur and H. K. Kim, "Thin alumina nanoporous membranes for similar size biomolecule separation," *Journal of Membrane Science*, vol. 343, no. 1-2, pp. 1-6, 2009.
- [7] R. C. Furneaux, W. R. Rigby and A. P. Davidson, "The formation of controlled-porosity membranes from anodically oxidized aluminum," *Nature*, vol. 337, no. 12, pp. 147-149, 1989.
- [8] Y. Wang, L. Chen, Z. Wu, S. Xu, H. Cui and W. Xu, "Subtle vertical structures of porous anodic alumina films for use as waveguides," *Nanotechnology*, vol. 28, no. 18, 2017.
- [9] J. Wang, C. Wang, Y. Li and W. Liu, "Optical constants of anodic aluminum oxide films formed in oxalic acid solution," *Thin Solid Films*, vol. 516, pp. 7689-7694, 2008.
- [10] T. Shih, P. Wei and Y. Huang, "Optical properties of anodic aluminum oxide films on Al 1050 alloys," *Surface & Coatings Technology*, vol. 202, pp. 3298-3305, 2008.
- [11] A. Hierro-Rodriguez, P. Rocha-Rodrigues, F. Valdes-Bango, J. M. Alameda, P. A. Jorge, J. L. Santos, J. P. Araujo and J. M. Teixeira, "On the anodic aluminium oxide refractive index of nanoporous templates," *Journal of Physics D: Applied Physics*, vol. 48, no. 45, p. 455105, 2015.
- [12] M. M. Rahman, E. Garcia-Caurel, A. Santos, L. F. Marsal, J. Pallares and J. Ferre-Borrull, "Effect of the anodization voltage on the pore-widening rate of nanoporous anodic alumina," *Nanoscale Research Letters*, vol. 7, no. 474, 2012.
- [13] H. Sweet, *Development of a Thin Film Device and Optics System for Protein Detection*, Edmonton, AB: University of Alberta, 2018.
- [14] A. Charlesby and J. J. Polling, "The Optical Properties of Thin Oxide Films on Tantalum," *Proceedings of the Royal Society of London. Series A, Mathematical and Physical Sciences*, vol. 227, pp. 434-447, 1955.
- [15] L. Young, *Anodic Oxide Films*, New York: Academic Press, 1961.
- [16] L. Young, "The determination of the thickness, dielectric constant, and other properties of anodic oxide films on tantalum from the interference colours," *Proceedings of the Royal Society A: Mathematical, Physical, and Engineering Sciences*, vol. 244, p. 41, 1958.
- [17] S. Cui-Cui, C. Yun-Yu, D. En-Mei and L. Chang-Hao, "Tunable structural color of anodic tantalum oxide films," *Chinese Physics B*, vol. 21, p. 088101, 2012.

### Chapter 4.3 - The Effects of Sequential Anodization with Sulphuric Acid and Phosphoric-Oxalic Acid on the Microstructure and Optical Properties of Aluminum-Tantalum Thin Films

- [1] R. E. Burrell, A. G. Naylor and A. M. Rosenfeld, "Thin Film Diagnostic". US Patent 5,124,172, 23 June 1992.
- [2] T. R. Holford, F. Davis and S. P. Higson, "Recent trends in antibody based sensors," *Biosensors and Bioelectronics*, vol. 34, pp. 12-24, 2012.
- [3] R. Burns, "Immunochemical techniques," in *Principles and Techniques of Biochemistry and Molecular Biology*, New York, NY, University Cambridge Press, 2010, pp. 263-299.
- [4] B. Bryne, E. Stack, N. Gilmartin and R. O'Kennedy, "Antibody-Based Sensors: Principles, Problems and Potential for Detection of Pathogens and Associated Toxins," *Sensors*, vol. 9, pp. 4407-4445, 2009.
- [5] D. A. Walz, D. Hewett-Emmett and W. H. Seegers, "Amino acid sequence of human prothrombin fragments 1 and 2," *Proceedings of the Natural Academy of Sciences USA*, vol. 74, no. 5, pp. 1969-1972, 1977.
- [6] M. Huang, A. C. Rigby, X. Morelli, M. A. Grant, G. Huang, B. Furie, B. Seaton and B. C. Furie, "Structural basis of membrane binding by Gla domains of vitamin K-dependent proteins," *Nature Structural Biology*, vol. 10, no. 9, pp. 751-756, 2003.
- [7] R. E. Burrell, "Aluminum Oxide Surfaces and Interface Molecules". Provisional Patent. Filed Feb. 20, 2018.
- [8] H. Sweet, *Development of a Thin Film Device and Optics System for Protein Detection*, Edmonton, AB: University of Alberta, 2018.
- [9] K. Wilson, "Basic Principles," in *Principles and Techniques of Biochemistry and Molecular Biology*, Seventh Edition, New York, NY, Cambridge University Press, 2010, pp. 1-37.
- [10] A. Charlesby and J. J. Polling, "The Optical Properties of Thin Oxide Films on Tantalum," *Proceedings of the Royal Society of London. Series A, Mathematical and Physical Sciences*, vol. 227, pp. 434-447, 1955.
- [11] J. Vörös, "The Density and Refractive Index of Adsorbing Protein Layers," *Biophysical Journal*, vol. 87, pp. 553-561, 2004.
- [12] T. L. McMeekin, M. L. Groves and N. J. Hipp, "Refractive Indices of Amino Acids, Proteins, and Related Substances," in *Amino Acids and Serum Proteins*, Philadelphia, American Chemical Society, 1964, pp. 54-66.

- [13] H. Nagata, A. Yamaguchi and A. Kawai, "Characterization of Thin-Film Interference Effect due to Surface Roughness," *Japan Journal of Applied Physics*, vol. 34, pp. 3754-3758, 1995.
- [14] J. A. Thornton, "Influence of apparatus geometry and deposition conditions on the structure and topography of thick sputtered coatings," *Journal of Vacuum Science & Technology*, vol. 11, pp. 666-670, 1974.
- [15] T. Sandström, M. Stenberg and H. Nygren, "Visual detection of organic monomolecular films by interference colors," *Applied Optics*, vol. 24, no. 4, pp. 472-479, 1985.
- [16] R. G. Ben, "1931 Colour Space," Wikipedia, [Online]. Available: <https://commons.wikimedia.org/w/index.php?curid=7889658>. [Accessed 18 June 2018].
- [17] R. Reverberi and L. Reverberi, "Factors affecting the antigen-antibody reaction," *Blood Transfus*, vol. 5, pp. 227-240, 2007.
- [18] B. Demeule, S. J. Shire and J. Liu, "A therapeutic antibody and its antigen form different complexes in serum than in phosphate-buffered saline: A study by analytical ultracentrifugation," *Analytical Biochemistry*, vol. 388, pp. 279-287, 2009.
- [19] M. Hadzhieva, A. D. Pashov, S. Kaveri, S. Lacroix-Desmazes, H. Mouquet and J. D. Dimitrov, "Impact of Antigen Density on the Binding Mechanism of IgG Antibodies," *Scientific Reports*, vol. 7, p. 3767, 2017.
- [20] H. Nygren, M. Werthen and M. Stenberg, "Kinetics of antibody binding to solid-phase-immobilised antigen," *Journal of Immunological Methods*, vol. 101, pp. 63-71, 1987.

## **Chapter 5 - Optical Sensitivity: Effects of Thin Film Microstructure and Antigen Surface Density on Visual Detection of IgG**

### **Chapter 5.1 – The Effect of Thin Film Microstructure on a Visual Immunoassay for Anti-prothrombin IgG Based on Anodized Aluminum-Tantalum Thin Films**

- [1] R. E. Burrell, A. G. Naylor and A. M. Rosenfeld, "Thin Film Diagnostic". US Patent 5,124,172, 23 June 1992.
- [2] T. R. Holford, F. Davis and S. P. Higson, "Recent trends in antibody based sensors," *Biosensors and Bioelectronics*, vol. 34, pp. 12-24, 2012.
- [3] R. Burns, "Immunochemical techniques," in *Principles and Techniques of Biochemistry and Molecular Biology*, New York, NY, University Cambridge Press, 2010, pp. 263-299.
- [4] B. Bryne, E. Stack, N. Gilmartin and R. O'Kennedy, "Antibody-Based Sensors: Principles, Problems and Potential for Detection of Pathogens and Associated Toxins," *Sensors*, vol. 9, pp. 4407-4445, 2009.

- [5] D. A. Walz, D. Hewett-Emmett and W. H. Seegers, "Amino acid sequence of human prothrombin fragments 1 and 2," *Proceedings of the Natural Academy of Sciences USA*, vol. 74, no. 5, pp. 1969-1972, 1977.
- [6] M. Huang, A. C. Rigby, X. Morelli, M. A. Grant, G. Huang, B. Furie, B. Seaton and B. C. Furie, "Structural basis of membrane binding by Gla domains of vitamin K-dependent proteins," *Nature Structural Biology*, vol. 10, no. 9, pp. 751-756, 2003.
- [7] R. E. Burrell, "Aluminum Oxide Surfaces and Interface Molecules". Provisional Patent. Filed Feb. 20, 2018.
- [8] H. Sweet, *Development of a Thin Film Device and Optics System for Protein Detection*, Edmonton, AB: University of Alberta, 2018.
- [9] K. Wilson, "Basic Principles," in *Principles and Techniques of Biochemistry and Molecular Biology*, Seventh Edition, New York, NY, Cambridge University Press, 2010, pp. 1-37.
- [10] A. Charlesby and J. J. Polling, "The Optical Properties of Thin Oxide Films on Tantalum," *Proceedings of the Royal Society of London. Series A, Mathematical and Physical Sciences*, vol. 227, pp. 434-447, 1955.
- [11] J. Vörös, "The Density and Refractive Index of Adsorbing Protein Layers," *Biophysical Journal*, vol. 87, pp. 553-561, 2004.
- [12] T. L. McMeekin, M. L. Groves and N. J. Hipp, "Refractive Indices of Amino Acids, Proteins, and Related Substances," in *Amino Acids and Serum Proteins*, Philadelphia, American Chemical Society, 1964, pp. 54-66.
- [13] H. Nagata, A. Yamaguchi and A. Kawai, "Characterization of Thin-Film Interference Effect due to Surface Roughness," *Japan Journal of Applied Physics*, vol. 34, pp. 3754-3758, 1995.
- [14] J. A. Thornton, "Influence of apparatus geometry and deposition conditions on the structure and topography of thick sputtered coatings," *Journal of Vacuum Science & Technology*, vol. 11, pp. 666-670, 1974.
- [15] T. Sandström, M. Stenberg and H. Nygren, "Visual detection of organic monomolecular films by interference colors," *Applied Optics*, vol. 24, no. 4, pp. 472-479, 1985.
- [16] R. G. Ben, "1931 Colour Space," Wikipedia, [Online]. Available: <https://commons.wikimedia.org/w/index.php?curid=7889658>. [Accessed 18 June 2018].
- [17] R. Reverberi and L. Reverberi, "Factors affecting the antigen-antibody reaction," *Blood Transfus*, vol. 5, pp. 227-240, 2007.
- [18] B. Demeule, S. J. Shire and J. Liu, "A therapeutic antibody and its antigen form different complexes in serum than in phosphate-buffered saline: A study by analytical ultracentrifugation," *Analytical Biochemistry*, vol. 388, pp. 279-287, 2009.

[19] M. Hadzhieva, A. D. Pashov, S. Kaveri, S. Lacroix-Desmazes, H. Mouquet and J. D. Dimitrov, "Impact of Antigen Density on the Binding Mechanism of IgG Antibodies," *Scientific Reports*, vol. 7, p. 3767, 2017.

[20] H. Nygren, M. Werthen and M. Stenberg, "Kinetics of antibody binding to solid-phase-immobilised antigen," *Journal of Immunological Methods*, vol. 101, pp. 63-71, 1987.

## Chapter 5.2 - The Effect of Antigen Size and Surface Density on a Visual Immunoassay Based on Anodized Aluminum-Tantalum Thin Films

[1] K. D. Elgert, *Immunology: Understanding the Immune System*, Hoboken, NJ: John Wiley & Sons, Inc., 2009.

[2] M. Hadzhieva, A. D. Pashov, S. Kaveri, S. Lacroix-Desmazes, H. Mouquet and J. D. Dimitrov, "Impact of Antigen Density on the Binding Mechanism of IgG Antibodies," *Scientific Reports*, vol. 7, p. 3767, 2017.

[3] H. Nygren, M. Werthen and M. Stenberg, "Kinetics of antibody binding to solid-phase-immobilised antigen," *Journal of Immunological Methods*, vol. 101, pp. 63-71, 1987.

[4] H. Nygren, T. Sandström and M. Stenberg, "Direct Visual Detection of Protein Antigen: Importance of Surface Concentration," *Journal of Immunological Methods*, vol. 59, pp. 145-149, 1983.

[5] H. Sweet, *Development of a Thin Film Device and Optics System for Protein Detection*, Edmonton, AB: University of Alberta, 2018.

[6] T. K. Lim, V. A. Bloomfield and G. L. Nelsestuen, "Structure of the Prothrombin- and Blood Clotting Factor X-Membrane Complexes," *Biochemistry*, vol. 16, no. 19, pp. 4177-4181, 1977.

[7] S. Krishnaswamy, "The Transition of Prothrombin to Thrombin," *Journal of Thrombosis and Haemostasis*, vol. 11, pp. 265-276, 2013.

[8] R. E. Burrell, "Aluminum Oxide Surfaces and Interface Molecules". Provision Patent. Filed Feb. 20, 2018.

[9] M. Huang, A. C. Rigby, X. Morelli, M. A. Grant, G. Huang, B. Furie, B. Seaton and B. C. Furie, "Structural basis of membrane binding by Gla domains of vitamin K-dependent proteins," *Nature Structural Biology*, vol. 10, no. 9, pp. 751-756, 2003.

[10] A. Tulinsky, C. H. Park and T. J. Rydel, "The Structure of Prothrombin Fragment 1 at 3.5 Å Resolution," *The Journal of Biological Chemistry*, vol. 260, no. 19, p. 10771, 1985.

[11] V. R. Sarma, E. W. Silverton, D. R. Davies and W. D. Terry, "The Three-Dimensional Structure at 6 Å Resolution of a Human  $\gamma$ G1 Immunoglobulin Molecule," *The Journal of Biological Chemistry*, vol. 246, no. 11, p. 3753, 1971.

[12] S. D. Alvarez, C. Li, C. E. Chiang, I. K. Schuller and M. J. Sailor, "A label-free porous alumina interferometric immunosensor," *ACS Nano*, vol. 3, no. 10, pp. 3301-3307, 2009.

## **Chapter 6 - Visual Immunoassay for Anti-Zika NS1 IgG and Goat Anti-Rabbit IgG on Anodized Aluminum-Tantalum Thin Films**

[1] P. Takmakov, I. Vlassiouk and S. Smirnov, "Application of anodized aluminum in fluorescence detection of biological species," *Analytical and Bioanalytical Chemistry*, vol. 385, no. 5, pp. 954-958, 2006.

[2] S. Tanvir, J. Pantigny, P. Boulnois and S. Pulvin, "Covalent immobilization of recombinant human cytochrome CYP2E1 and glucose-6-phosphate dehydrogenase in alumina membrane for drug screening applications," *Journal of Membrane Science*, vol. 329, pp. 85-90, 2009.

[3] G. Gonzalez, G. Priano, M. Gunther and F. Battaglini, "Mass transport effect of mesoscopic domains in the amperometric response of an electroactive species: Modeling for its applications in biomolecule detection," *Sensors and Actuators B: Chemical*, vol. 144, no. 2, pp. 349-353, 2008.

[4] P. Milka, I. Krest and M. Keusgen, "Immobilization of alliinase on porous aluminum oxide," *Biotechnology and Bioengineering*, vol. 69, no. 3, pp. 344-348, 2000.

[5] H. P. Jennissen, "Immobilizing mediator molecules via anchor molecules on metallic implant materials containing oxide layer". USA Patent 6,635,269 B1, 21 Oct 2003.

[6] D. Hyndman, G. Lever, R. Burrell and T. G. Flynn, "Protein Immobilization to Alumina Supports: I. Characterization of Alumina-Organophosphate Ligand Interactions and Use in the Attachment of Papain," *Biotechnology and Bioengineering*, vol. 40, pp. 1319-1327, 1992.

[7] D. Hyndman, R. Burrell, G. Lever and T. G. Flynn, "Protein Immobilization to Alumina Supports: II. Papain Immobilization to Alumina via Organophosphate Linkers," *Biotechnology and Bioengineering*, vol. 40, pp. 1328-1336, 1992.

[8] J. Dai, G. L. Baker and M. L. Bruening, "Use of porous membranes modified with polyelectrolyte multilayers as substrates for protein arrays with low nonspecific adsorption," *Analytical Chemistry*, vol. 78, no. 1, pp. 135-140, 2005.

- [9] G. B. Oliveira, J. L. Filho, M. E. Chaves, W. M. Azevedo and L. B. Carvalho, "Enzyme immobilization on anodic aluminum oxide/polyethyleneimine or polyaniline composites," *Reactive and Functional Polymers*, vol. 68, no. 1, pp. 27-32, 2008.
- [10] R. Zuo, D. Ornek and T. K. Wood, "Aluminum- and mild steel-binding peptides from phage display," *Applied Genetics and Molecular Biotechnology*, vol. 68, pp. 505-509, 2005.
- [11] B. L. Adams, A. S. Finch, M. M. Hurley, D. A. Sarkes and D. N. Stratis-Cullum, "Genetically Engineered Peptides for Inorganics: Study of an Unconstrained Bacterial Display Technology and Bulk Aluminum Alloy," *Materials Views*, vol. 25, pp. 4585-4591, 2013.
- [12] Y. Gwak, J. Park, M. Kim, H. S. Kim, M. J. Kwon, S. J. Oh, Y. Kim and E. Jin, "Creating Anti-icing Surfaces via the Direct Immobilization of Antifreeze Proteins on Aluminum," *Scientific Reports*, vol. 5, no. 12019, pp. 1-9, 2015.
- [13] J. P. Murray and S. J. Laband, "Degradation of Poliovirus by Adsorption on Inorganic Surfaces," *Applied and Environmental Microbiology*, vol. 37, no. 3, pp. 480-486, 1979.
- [14] J. P. Murray, *Physical Chemistry of Virus Adsorption and Degradation on Inorganic Surfaces: Its relation to wastewater treatment*, Cincinnati, OH: United States Environmental Protection Agency, 1980.
- [15] R. B. Thurman and C. P. Gerba, "Characterization of the effect of aluminum metal on poliovirus," *Journal of Industrial Microbiology*, vol. 3, pp. 33-38, 1988.
- [16] W. R. Bowen and Q. Gan, "Properties of Microfiltration Membranes: The Effects of Adsorption and Shear on the Recovery of an Enzyme," *Biotechnology and Bioengineering*, vol. 40, pp. 491-497, 1992.
- [17] A. Wittayanukulluk, D. Jiang, F. E. Regnier and S. L. Hem, "Effect of microenvironment pH of aluminum hydroxide adjuvant on the chemical stability of adsorbed antigen," *Vaccine*, vol. 22, p. 1172, 2004.
- [18] T. Clapp, P. Siebert, D. Chen and L. J. Braun, "Vaccines with Aluminum-Containing Adjuvants: Optimizing Vaccine Efficacy and Thermal Stability," *Journal of Pharmaceutical Science*, vol. 100, no. 2, p. 388, 2011.
- [19] D. C. Kim, A. Jang and D. J. Kang, "Biological functionality of active enzyme structures immobilized on various solid surfaces," *Current Applied Physics*, vol. 9, p. 1454, 2009.
- [20] R. E. Burrell, "Aluminum Oxide Surfaces and Interface Molecules". Provisional Patent. Filed Feb. 20, 2018.

- [21] D. A. Walz, D. Hewett-Emmett and W. H. Seegers, "Amino acid sequence of human prothrombin fragments 1 and 2," *Proceedings of the National Academy of Sciences USA*, vol. 74, no. 5, pp. 1969-1972, 1977.
- [22] M. E. Karaman, D. A. Antelmi and R. M. Pashley, "The production of stable hydrophobic surfaces by the adsorption of hydrocarbon and fluorocarbon carboxylic acids onto alumina substrates," *Colloids and Surfaces A: Physicochemical and Engineering Aspects*, vol. 182, no. 1-3, p. 285, 2001.
- [23] D. Muljadi, A. M. Posner and J. P. Quirk, "The Mechanism of Phosphate Adsorption by Kaolinite, Gibbsite, and Pseudoboehmite. Part 2. The Location of the Adsorption Sites," *Journal of Soil Science*, vol. 17, no. 2, pp. 230-237, 1966.
- [24] J. van den Brand, O. Blajiev, P. C. Beentjes, H. Terryn and J. H. de Wit, "Interaction of Anhydride and Carboxylic Acid Compounds with Aluminum Oxide Surfaces Studied Using Infrared Reflection Absorption Spectroscopy," *American Chemical Society*, pp. 6308-6317, 2004.
- [25] T. K. Lim, V. A. Bloomfield and G. L. Nelsestuen, "Structure of the Prothrombin- and Blood Clotting Factor X-Membrane Complexes," *Biochemistry*, vol. 16, no. 19, pp. 4177-4181, 1977.
- [26] I. Migneault, C. Dartiguenave, M. J. Bertrand and K. C. Waldron, "Glutaraldehyde: behavior in aqueous solution, reaction with proteins, and application to enzyme crosslinking," *BioTechniques*, vol. 37, no. 5, p. 790, 2004.
- [27] D. R. Walt and V. I. Agayn, "The chemistry of enzyme and protein immobilization with glutaraldehyde," *Trends in Analytical Chemistry*, vol. 13, no. 10, p. 425, 1994.
- [28] Y. Wine, N. Cohen-Hadar, A. Freeman and F. Frolow, "Elucidation of the Mechanism and End Products of Glutaraldehyde Crosslinking Reaction by X-Ray Structure Analysis," *Biotechnology and Bioengineering*, vol. 98, no. 3, p. 711, 2007.
- [29] X. Xu, H. Song, J. Qi, Y. Liu, H. Wang, C. Su, Y. Shi and G. F. Gao, "Contribution of intertwined loop to membrane association revealed by Zika virus full-length NS1 structure," *The EMBO Journal*, vol. 35, no. 20, p. 2170, 2016.
- [30] Y. Shi and G. F. Gao, "Structural Biology of the Zika Virus," *Trends in Biochemical Sciences*, vol. 1344, p. 1, 2017.
- [31] E. O. Saphire, P. W. Parren, R. Pantophlet, M. B. Zwick, G. M. Morris, P. M. Rudd, R. A. Dwek, R. L. Stanfield, D. R. Burton and I. A. Wilson, "Crystal Structure of a Neutralizing Human IgG Against HIV-1: A Template for Vaccine Design," *Science*, vol. 293, p. 1155, 2001.

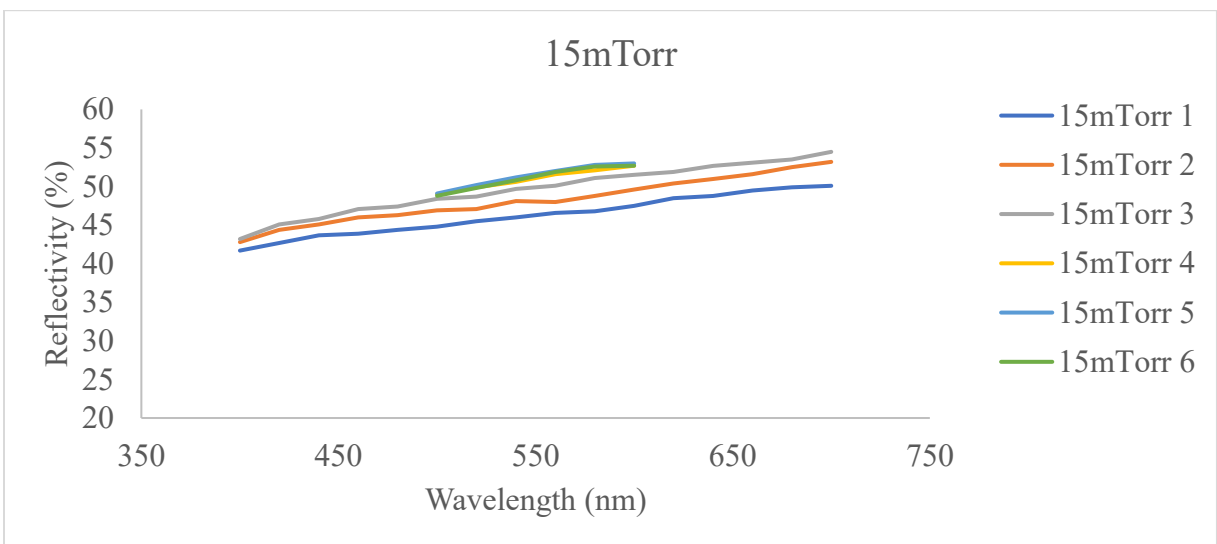
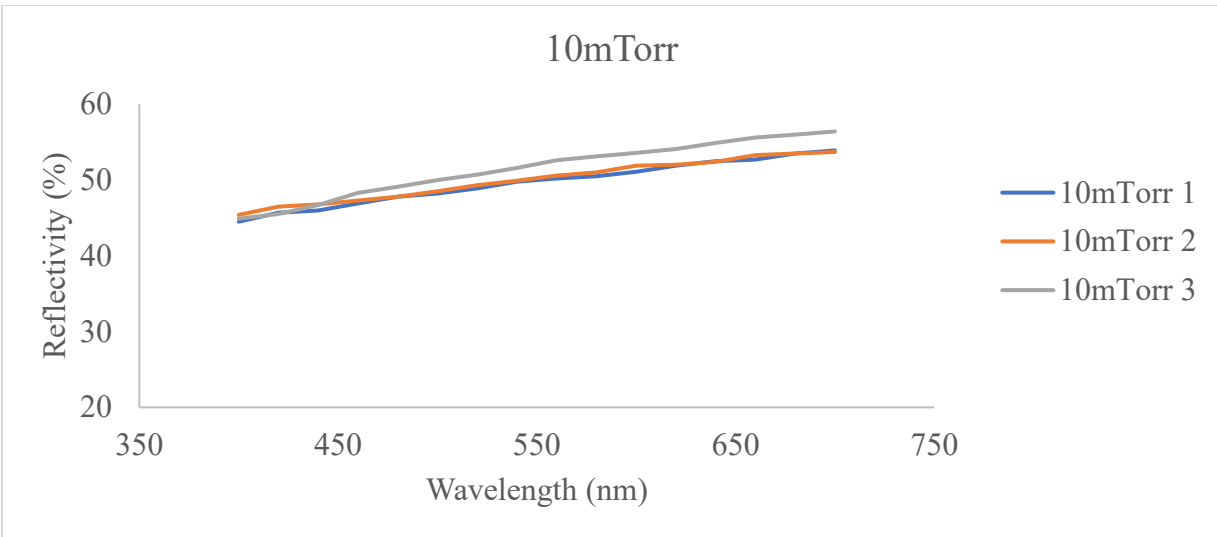
- [32] V. R. Sarma, E. W. Silverton, D. R. Davies and W. D. Terry, "The Three-Dimensional Structure at 6 Å Resolution of a Human  $\gamma$ G1 Immunoglobulin Molecule," *The Journal of Biological Chemistry*, vol. 246, no. 11, p. 3753, 1971.
- [33] H. Nygren, T. Sandström and M. Stenberg, "Direct Visual Detection of Protein Antigen: Importance of Surface Concentration," *Journal of Immunological Methods*, vol. 59, pp. 145-149, 1983.
- [34] I. Giaever, "The antigen-antibody reaction: a visual observation," *Journal of Immunology*, vol. 110, pp. 1424-1426, 1973.
- [35] H. Sweet, *Development of a Thin Film Device and Optics System for Protein Detection*, Edmonton, AB: University of Alberta, 2018.
- [36] E. H. Cordes and W. P. Jencks, "On the Mechanism of Schiff Base Formation and Hydrolysis," *Journal of the American Chemical Society*, vol. 84, no. 5, pp. 832-837, 1962.
- [37] K. Matsumoto, O. Hamada, H. Ukeda and Y. Osajima, "Amperometric Flow Injection Determination of Fructose with an Immobilized Fructose 5-Dehydrogenase Reactor," *Analytical Chemistry*, vol. 58, pp. 2732-2734, 1986.
- [38] E. H. Hansen and H. S. Mikkelsen, "Enzyme-Immobilization by the Glutardialdehyde Procedure. An investigation of the effects of reducing the Schiff-bases generated, as based on studying the immobilization of glucose oxidase to silanized controlled pore glass," *Analytical Letters*, vol. 24, no. 8, pp. 1419-1430, 1991.
- [39] W. C. Brown, D. L. Akey, J. R. Konwerski, J. T. Tarrasch, G. Skiniotis, R. J. Kuhn and J. L. Smith, "Extended surface for membrane association in Zika virus NS1 structure," *Nature Structural & Molecular Biology*, vol. 23, no. 9, p. 865, 2016.

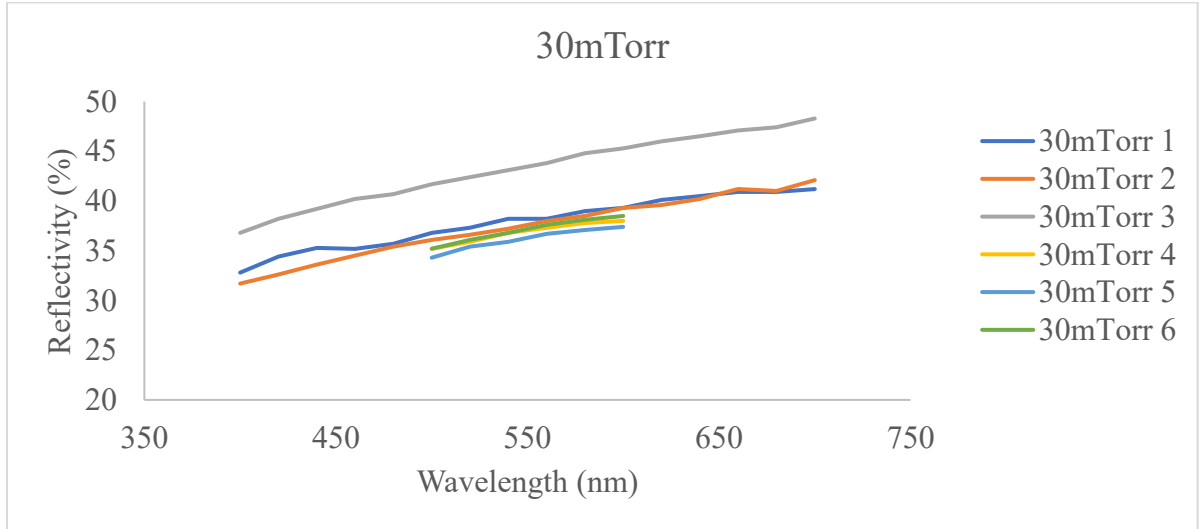
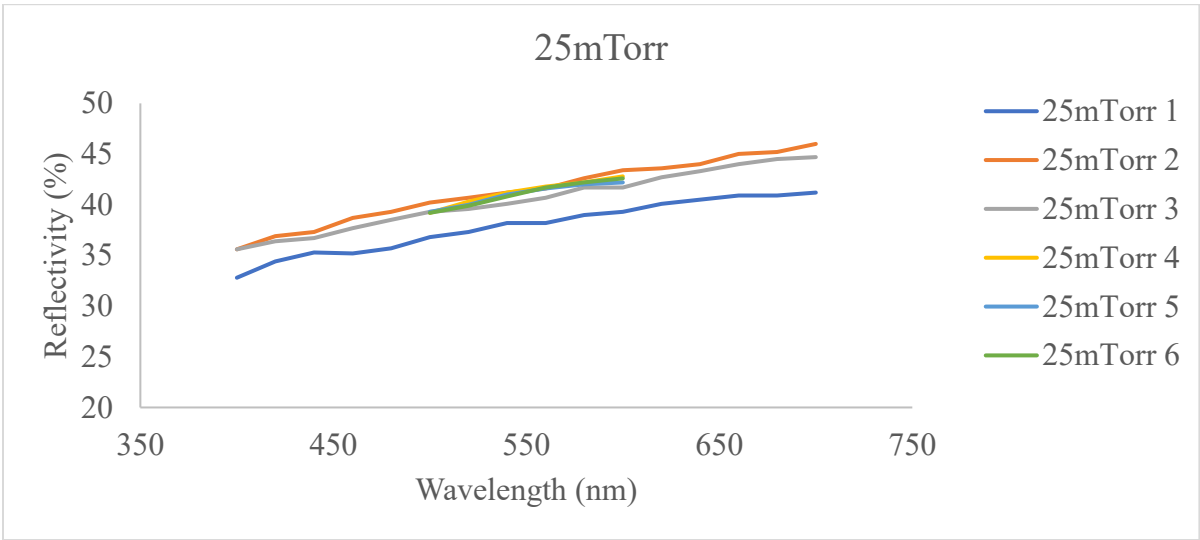
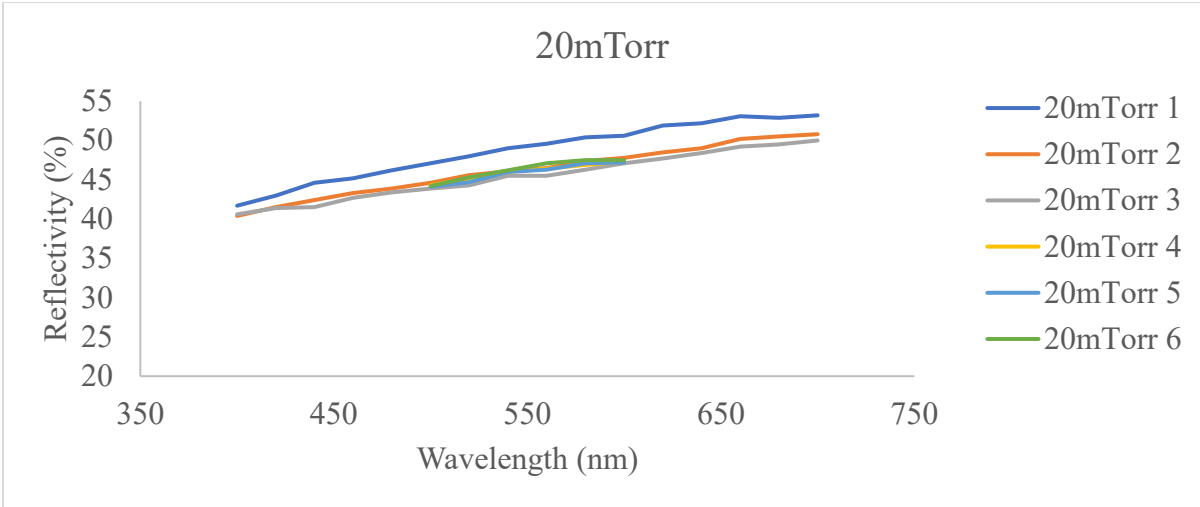
## **Chapter 7 – Conclusion**

- [1] Y. Fukuda and T. Fukushima, "Behavior of Sulfate Ions during Formation of Anodic Oxide Film on Aluminium," *Bulletin of the Chemical Society of Japan*, vol. 53, no. 11, pp. 3125-3130, 1980.
- [2] G. E. Thompson and G. C. Wood, "Porous anodic film formation on aluminium," *Nature*, vol. 290, pp. 230-232, 1981.
- [3] G. E. Thompson, R. C. Furneaux and G. C. Wood, "The Morphology of Sealed Anodic Films Formed on Aluminium in Phosphoric Acid," *Transactions of the Institute of Metal Finishing*, vol. 53, pp. 97-102, 1975.
- [4] H. Sweet, *Development of a Thin Film Device and Optics System for Protein Detection*, Edmonton, AB: University of Alberta, 2018.

## Appendix 1 – Supplementary Data

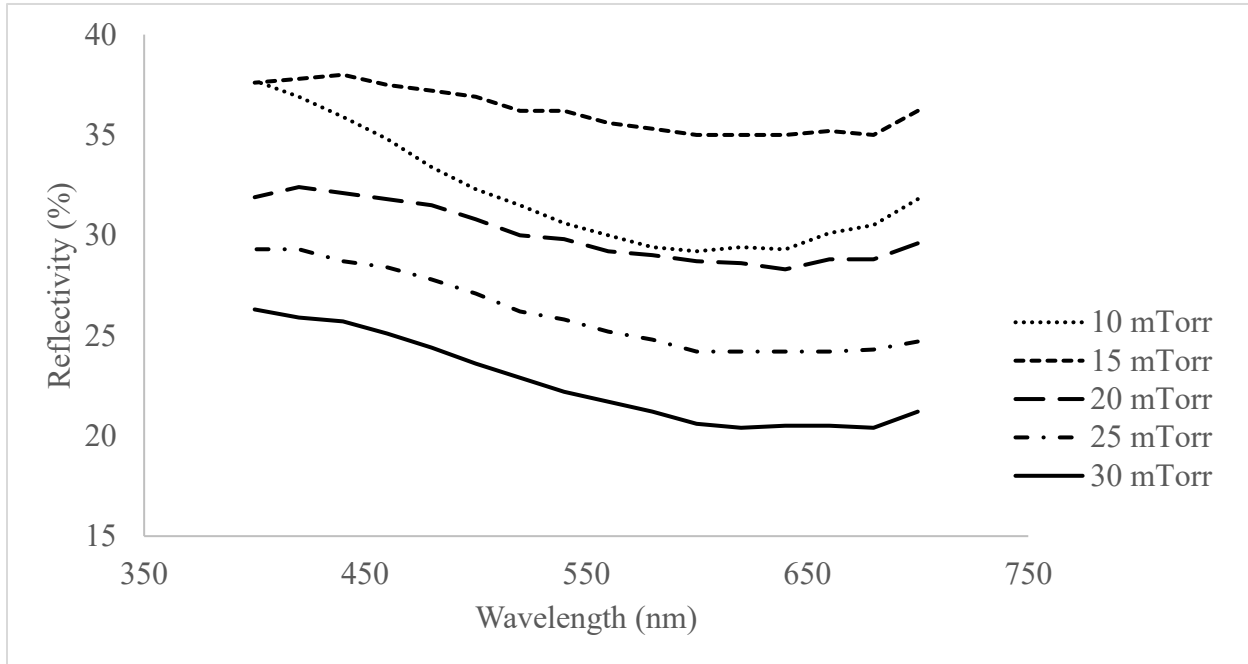
**Spectroscopy Supplementary Data** – Reflectivity vs. wavelength plot for tantalum films sputtered at 10, 15, 20, 25 and 30 mTorr through the visible light spectrum (400nm to 700nm). Samples labelled with numbers 1 through 6; 10mTorr n=3; 15, 20, 25, 30mTorr n=6.





Reflectivity spectrums recorded with spectrophotometer on replicate slides of anodized aluminum-tantalum thin films; 120nm of aluminum deposited on tantalum and anodized in .4M phosphoric – 0.1M oxalic acid at 4V. Tantalum films sputtered under various gas pressures, 10, 15, 20, 25 or 30 mTorr.

### Repeat 2



### Repeat 3

